

**REPORT DOCUMENTATION PAGE**Form Approved  
OMB NO. 0704-0188

Public Reporting burden for this collection of information is estimated to average 1 hour per response, including the time for reviewing instructions, searching existing data sources, gathering and maintaining the data needed, and completing and reviewing the collection of information. Send comment regarding this burden estimate or any other aspect of this collection of information, including suggestions for reducing this burden, to Washington Headquarters Services, Directorate for Information Operations and Reports, 1215 Jefferson Davis Highway, Suite 1204, Arlington, VA 22202-4302, and to the Office of Management and Budget, Paperwork Reduction Project (0704-0188), Washington, DC 20503.

1. AGENCY USE ONLY (Leave Blank)		2. REPORT DATE March 29, 2004	3. REPORT TYPE AND DATES COVERED Final 01/01/01 - 12/31/03 01 July 99 - 30 Jun 03
4. TITLE AND SUBTITLE Hydrologic Modeling of Extreme Floods Using Remote Sensing Observations		5. FUNDING NUMBERS <del>Grant DAAD19-99-1-1063</del> DAAD19-99-1-0163	
6. AUTHOR(S) Professor James A. Smith		8. PERFORMING ORGANIZATION REPORT NUMBER	
7. PERFORMING ORGANIZATION NAME(S) AND ADDRESS(ES) Princeton University Dept. of Civil and Environmental Engineering Princeton, NJ 08544		10. SPONSORING / MONITORING AGENCY REPORT NUMBER <del>33802 GS</del> 39129.7-EV	
9. SPONSORING / MONITORING AGENCY NAME(S) AND ADDRESS(ES) U. S. Army Research Office P.O. Box 12211 Research Triangle Park, NC 27709-2211		11. SUPPLEMENTARY NOTES The views, opinions and/or findings contained in this report are those of the author(s) and should not be construed as an official Department of the Army position, policy or decision, unless so designated by other documentation.	
12 a. DISTRIBUTION / AVAILABILITY STATEMENT Approved for public release; distribution unlimited.		12 b. DISTRIBUTION CODE	
13. ABSTRACT (Maximum 200 words)  The objectives of this research are to develop a comprehensive understanding of extreme floods and to dramatically improve the capability to model these events. Paired diagnostic and modeling studies play a central role in this project. Hydrologic and hydrometeorological studies of extreme floods in the Great Plains, central Appalachians, The Milwaukee metropolitan area, Charlotte, NC metropolitan area and, high-gradient rainforest west of Puerto Rico have been completed. For the large flood events examined in this study, the spatial (1 km) and temporal (15 minutes) resolution of rainfall estimates provided by the WSR-88D was crucial to accurate modeling of extreme flood response. Coupled hydraulic and hydrologic modeling studies using RMA-2V and the Network Model have been carried out to characterize the dependence of flood response on floodwave attenuation and altered runoff processes associated with impervious cover and elaboration of the drainage network.			
14. SUBJECT TERMS Floods, Extreme Rainfall, Hydrologic Models, Remote Sensing		15. NUMBER OF PAGES	
17. SECURITY CLASSIFICATION OR REPORT UNCLASSIFIED		16. PRICE CODE	
18. SECURITY CLASSIFICATION ON THIS PAGE UNCLASSIFIED	19. SECURITY CLASSIFICATION OF ABSTRACT UNCLASSIFIED	20. LIMITATION OF ABSTRACT UL	

**REPORT DOCUMENTATION PAGE (SF298)**  
**(Continuation Sheet)**

**Objectives:**

The objectives of this research are to develop a comprehensive understanding of extreme floods and to dramatically improve the capability to model and forecast these events. We examine the potential improvements in flood characterization and forecasting that can result from use of high-resolution radar rainfall estimates and distributed hydrologic models.

**Approach:**

Hydrologic and hydraulic modeling studies of large floods using WSR-88D (Weather Surveillance Radar – 1988 Doppler) radar rainfall estimates in a range of “flood environments” have formed the core methodology of the project (Morrison and Smith [2001], Giannoni et al. [2003], Zhang et al. [2001 and 2003], and Turner-Gillespie et al. [2003]). Hydrologic modeling studies have utilized a simplified version of CASC2D, denoted the Network Model. The model, which has been coded in JAVA, is designed for fast run times, platform portability, efficient utilization of high-resolution radar rainfall estimates, and the capability for readily examining different representations of the drainage network. Hydrologic modeling studies of large floods have utilized a wide range of land use – land cover (LULC) data sets, derived from both aerial photographs and satellite imagery.

Hydraulic studies of flood wave attenuation have utilized the 2-D open channel flow code RMA-2V. The Network Model and RMA-2V have been coupled to provide a modeling system for examining hydrologic and hydraulic controls of flood response in a 10 km channel reach in an urban stream in Charlotte, North Carolina (Turner-Gillespie et al. [2003]).

High-resolution radar rainfall estimates play a central role in hydrologic modeling studies. Particular attention has been given to estimation of extreme, flood-producing rainfall from weather radar (Smith et al. [2001 and 2002], Krajewski and Smith [2002], Zhang et al. [2001 and 2003], and Uijlenhoet et al. [2003 a and b]).

**Results:**

Hydrologic modeling studies of large floods have been performed for a high-gradient, forested watershed in the Blue Ridge of Virginia (see Giannoni et al. [2003] and Sturdevant-Rees et al. [2001]), urbanizing drainage basins in Charlotte NC (Smith et al. [2002] and Turner-Gillespie et al. [2003]) and Milwaukee WI (Zhang and Smith [2003]), a high-gradient tropical rainforest catchment in Puerto Rico (Smith et al [2004]) and a low-gradient agricultural basin in the Great Plains (Zhang et al. [2001]). The storms responsible for these floods have included tropical storms, mesoscale convective systems (organized systems of thunderstorms) and orographic convective systems (organized systems of thunderstorms in mountainous terrain). Modeling analyses for all storms were based on radar rainfall estimates (at 5-minute time scale and 1 km horizontal resolution) derived from WSR-88D radars from the operational NWS radar network.

Analyses have provided fundamental insights into the hydrology of extreme floods, especially as they relate to the distribution of extreme floods (Morrison and Smith [2001 and 2002], Sturdevant-Rees et al. [2001], Smith et al [2002] and Zhang et al. [2003]).

An important conclusion from our analyses is that radar rainfall estimates for these extreme rainstorms are generally of very high quality and well suited to distributed hydrologic modeling. Furthermore, distributed hydrologic modeling in the CASC2D model environment can capture extreme flood response over a wide range of "flood environments". High-resolution LULC data sets will play an important role in implementation of distributed hydrologic models. Of particular utility are representations of impervious cover in urban and suburban environments.

Hydraulic modeling using RMA-2V has been used to examine flood wave attenuation in urban stream channels (Turner-Gillespie et al. [2002]). In the Charlotte, North Carolina metropolitan region, particular interest focuses on whether flood wave attenuation results from man-made alterations to the channel and floodplain system. For the Charlotte region it has been shown that geologic controls of longitudinal profile and valley bottom width are dominant controls of flood wave attenuation. The relative roles of channel and hillslope processes in determining flood response have been examined by coupling the Network Model with RMA-2V. In this coupled model, high-resolution radar rainfall estimates and the Network Model are used to provide tributary boundary conditions for RMA-2V.

A compendium of the papers published under support by this project has been assembled and included as a contribution to this report.

### **Journal Publications**

Giannoni, F., J. A. Smith, Y. Zhang and G. Roth, 2003, Hydrologic modeling of extreme floods using radar rainfall estimates, *Advances in Water Resources*, 26, 195 - 203.

Krajewski, W. F. and J. A. Smith, 2002, Radar hydrology: rainfall estimation, 2003, *Advances in Water Resources*, 25, 1387 - 1394.

Morrison, J. E. and J. A. Smith, 2001, Scaling properties of flood peak, *Extremes*, 4(1), 5 - 23..

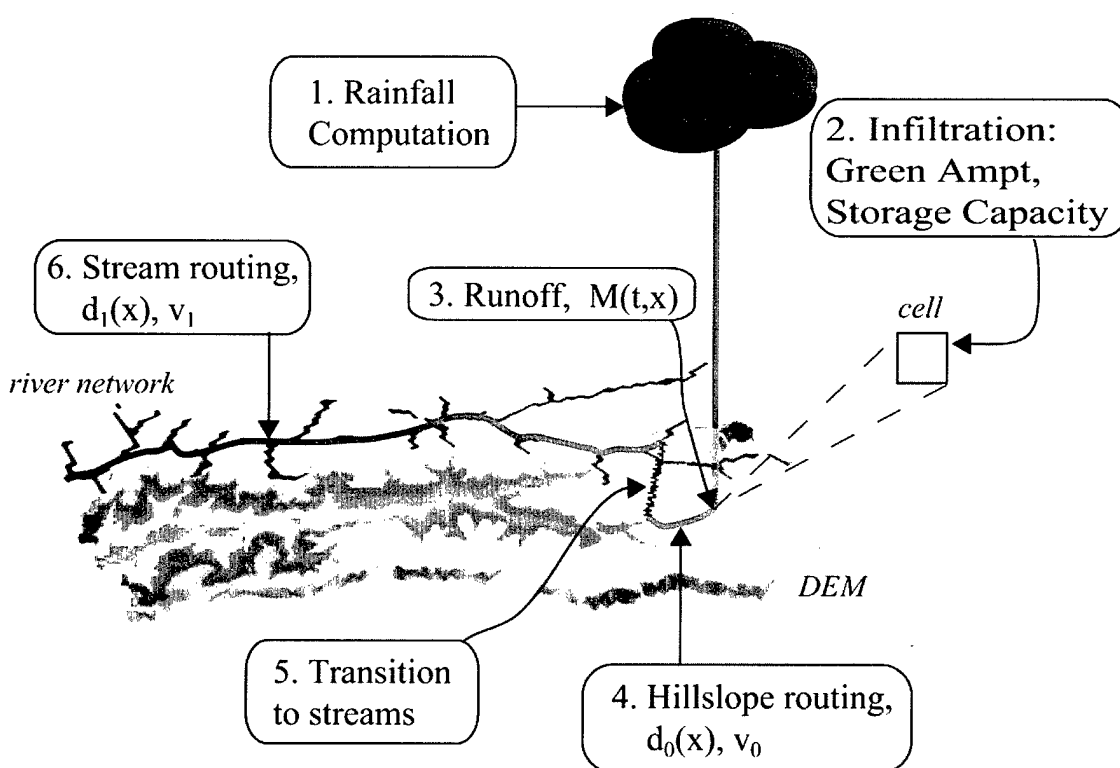
Morrison, J. E. and J. A. Smith, 2002, Stochastic modeling of flood peaks using the generalized extreme value distribution, *Water Resources Research*, 38(12), 3805.

Smith, J. A., M. L. Baeck, J. E. Morrison, P. L. Sturdevant-Rees, D. F. Turner-Gillespie and P. D. Bates, 2002, The regional hydrology of extreme floods in an urbanizing drainage basin, *J. of Hydrometeorology*, 267 - 282.

# ***Hydrologic Modeling of Extreme Floods Using Remote Sensing Observations***

By James A. Smith, Mary Lynn Baeck, Matthias Steiner, Francesca Giannoni,  
Daniel Turner-Gillespie, Julia Morrison, Paula Sturdevant-Rees, Yu Zhang,  
and Remko Uijlenhoet

Princeton University  
Department of Civil and Environmental Engineering



Research funded by  
United States Army Research Office  
DAAD19-99-1063



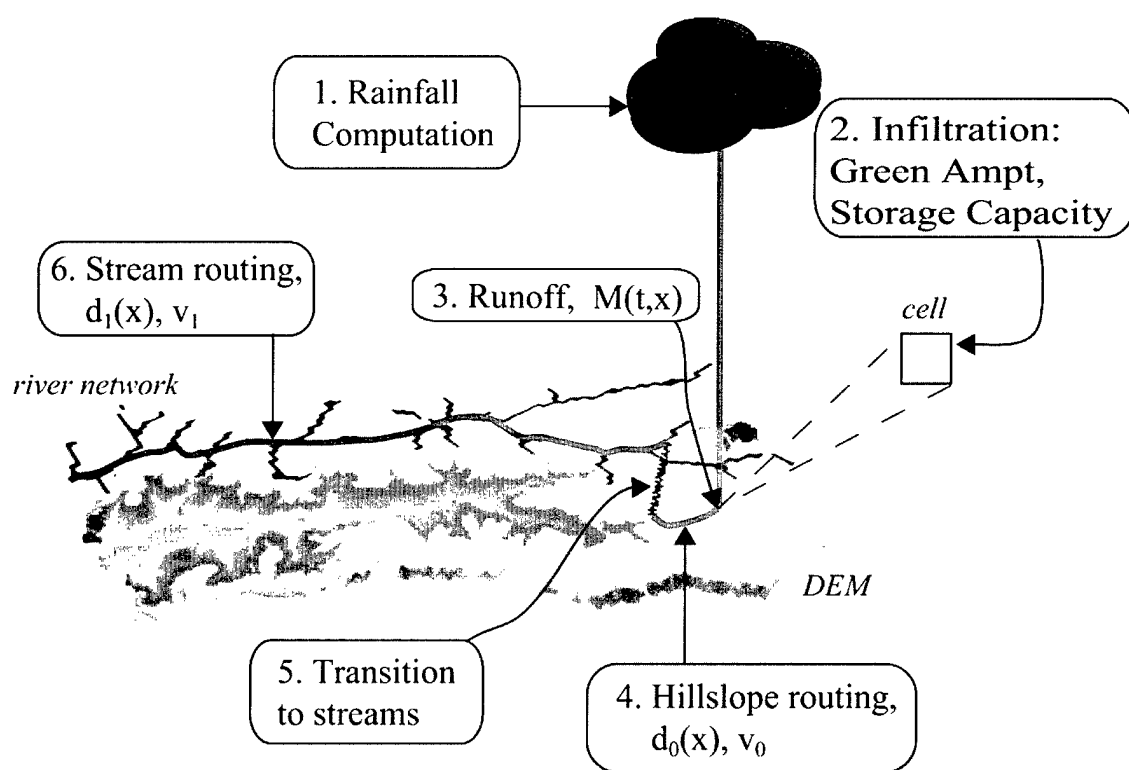
## Table of Contents

1. Hydrologic modeling of extreme floods using radar rainfall estimates, by Francesca Giannoni, James A. Smith, Yu Zhang, and Giorgio Roth. *Advances in Water Resources* 26 (2003) 195-203.
2. Space-Time Variability of Rainfall and Extreme Flood Response in the Menomonee River Basin, Wisconsin, by Yu Zhang and James A. Smith. *Journal of Hydrometeorology*, 4 (2003) 506-517.
3. Attenuating reaches and the regional flood response of an urbanizing drainage basin, by Daniel F. Turner-Gillespie, James A. Smith, and Paul D. Bates. *Advances in Water Resources* 26 (2003) 673-684
4. Variability of Raindrop Size Distribution in a Squall Line and Implications for Radar Rainfall Estimation, by Remko Uijlenhoet, Matthias Steiner, and James A. Smith. *Journal of Hydrometeorology*, (2003) 43-61
5. The Microphysical Structure of Extreme Precipitation as Inferred from Ground-Based Raindrop Spectra, by Remko Uijlenhoet, James A. Smith, and Matthias Steiner. *Journal of Atmospheric Sciences*, 60 (2003) 1220-1238
6. Radar hydrology: rainfall estimation, by W.F. Krajewski and James A. Smith. *Advances in Water Resources* 25 (2002) 1387-1394
7. The Regional Hydrology of Extreme Floods in a Urbanizing Drainage Basin, by James A. Smith and Mary Lynn Baeck. *Journal of Hydrometeorology*, (2002) 267-282
8. Stochastic modeling of flood peaks using the generalized extreme value distribution, by Julia E. Morrison and James A. Smith. *Water Resources Research*, Vol. 38, No. 12, 1305 (2002)
9. Extreme Rainfall and Flooding from Supercell Thunderstorms, by James A. Smith, Mary Lynn Baeck and Yu Zhang. *Journal of Hydrometeorology*, (2001) 469-489
10. Scaling Properties of Flood Peaks, by Julia A. Morrison and James A. Smith. *Kluwer Academic Publishers* (2001) *Extremes* 4:1, 5-22
11. Tropical storms and the flood hydrology of the central Appalachians, by Paula Sturdevant-Rees, James A. Smith, Julia Morrison, and Mary Lynn Baeck. *Water Resources Research*, Vol. 37, No. 8, 2143-2168 (2001)

# ***Hydrologic Modeling of Extreme Floods Using Remote Sensing Observations***

By James A. Smith, Mary Lynn Baeck, Matthias Steiner, Francesca Giannoni,  
Daniel Turner-Gillespie, Julia Morrison, Paula Sturdevant-Rees, Yu Zhang,  
and Remko Uijlenhoet

Princeton University  
Department of Civil and Environmental Engineering



Research funded by  
United States Army Research Office  
DAAD19-99-1063



# Hydrologic modeling of extreme floods using radar rainfall estimates

Francesca Giannoni <sup>a,b</sup>, James A. Smith <sup>a,\*</sup>, Yu Zhang <sup>a</sup>, Giorgio Roth <sup>b</sup>

<sup>a</sup> Department of Civil and Environmental Engineering, Princeton University, Princeton, NJ 08544, USA

<sup>b</sup> Centro di Ricerca Interuniversitario in Monitoraggio Ambientale, Università di Genova, Genova, Italy

## Abstract

High resolution radar rainfall fields and a distributed hydrologic model are combined for analysis and monitoring of extreme floods. Hydrologic modeling is based on a Hortonian infiltration model and a network-based representation of hillslope and channel flow. Model analyses are used to examine the hydrology and hydrometeorology of the 27 June 1995 Rapidan River flood which produced a measured peak discharge of  $3000 \text{ m}^3 \text{ s}^{-1}$  at a drainage area of  $295 \text{ km}^2$ . The unit discharge of  $10.2 \text{ m}^3 \text{ s}^{-1} \text{ km}^{-2}$  is the largest for the US east of the Mississippi River for basins larger than  $100 \text{ km}^2$ . Rainfall estimates at  $1 \text{ km}$  horizontal scale and  $5 \text{ min}$  time scale are used to reconstruct flood response to the Rapidan storm at basin scales ranging from  $1$  to  $295 \text{ km}^2$ . Peak storm total rainfall accumulations for the 27 June 1995 storm exceeded  $600 \text{ mm}$  in a time period of approximately  $6 \text{ h}$ . Scale dependent flood response is related to the structure and motion of the Rapidan storm and the drainage network structure of the Rapidan River basin. The envelope curve of peak discharge for the Rapidan flood at basin scales less than  $295 \text{ km}^2$ , derived from model analyses, is compared with envelope curves, based on extensive indirect discharge measurements, from the 19 July 1942 Smethport, Pennsylvania flood and the 18–19 August 1969 Nelson County, Virginia flood. These three events largely define the envelope curve of flood peaks for the US east of the Mississippi River at basin scales less than  $1000 \text{ km}^2$ . Analyses illustrate how radar rainfall estimates can be combined with conventional stream gaging and indirect discharge measurements to enhance monitoring of extreme floods.

© 2002 Elsevier Science Ltd. All rights reserved.

## 1. Introduction

The Rapidan River flood of 27 June 1995 ([14,17, 20,22,26]; see Fig. 1 for location map) produced the largest unit discharge flood peak at drainage areas greater than  $100 \text{ km}^2$  for the United States east of the Mississippi River ([20]; see also [3,11]). Comparable flood events for drainage areas less than  $1000 \text{ km}^2$  occurred 19 July 1942 near Smethport, Pennsylvania [6] and 19–20 August 1969 in Nelson County Virginia ([2,15,19]. Hydrologic and hydrometeorological analyses of the Smethport and Nelson County flood events have been grounded in “bucket survey” rainfall measurements and extensive indirect discharge measurements (Fig. 2; see [4,7,13] for similar analyses of scale-dependent flood response and a historical perspective on development of procedures for extreme flood analysis).

For the Rapidan River flood, time series of stage at the US Geological Survey (USGS) gaging station at Ruckersville, Virginia and an indirect discharge measurement of the peak are combined to produce a flood hydrograph at  $295 \text{ km}^2$  scale (Fig. 3). Radar rainfall observations [20] provide high temporal ( $5 \text{ min}$ ) and spatial ( $1 \text{ km}^2$ ) representation of rainfall from the Rapidan storm (Figs. 3 and 4). Peak storm total rainfall accumulation exceeded  $600 \text{ mm}$  (Fig. 4) in a time period of approximately  $6 \text{ h}$  and rainfall rates exceeded  $300 \text{ mm h}^{-1}$  [20].

Extensive surveys of flood peaks from indirect discharge measurements were not carried out for the Rapidan flood, so it is difficult to directly characterize the spatial variability of peak flood response in the Rapidan River basin (as in Fig. 2). Numerous questions arise concerning the spatial distribution of flooding in the Rapidan River basin. How large were unit discharge flood peaks in the area of heaviest rainfall (Fig. 4)? How does the envelope curve of flood peaks for the Rapidan flood compare with those of the Smethport and Nelson County floods (Fig. 2)? How did the spatial and temporal distribution of rainfall from the Rapidan storm interact with drainage basin structure to determine

\* Corresponding author. Address: Department of Civil and Environmental Engineering, Princeton University, Princeton, NJ 08544, USA.

E-mail address: [jsmith@princeton.edu](mailto:jsmith@princeton.edu) (J.A. Smith).

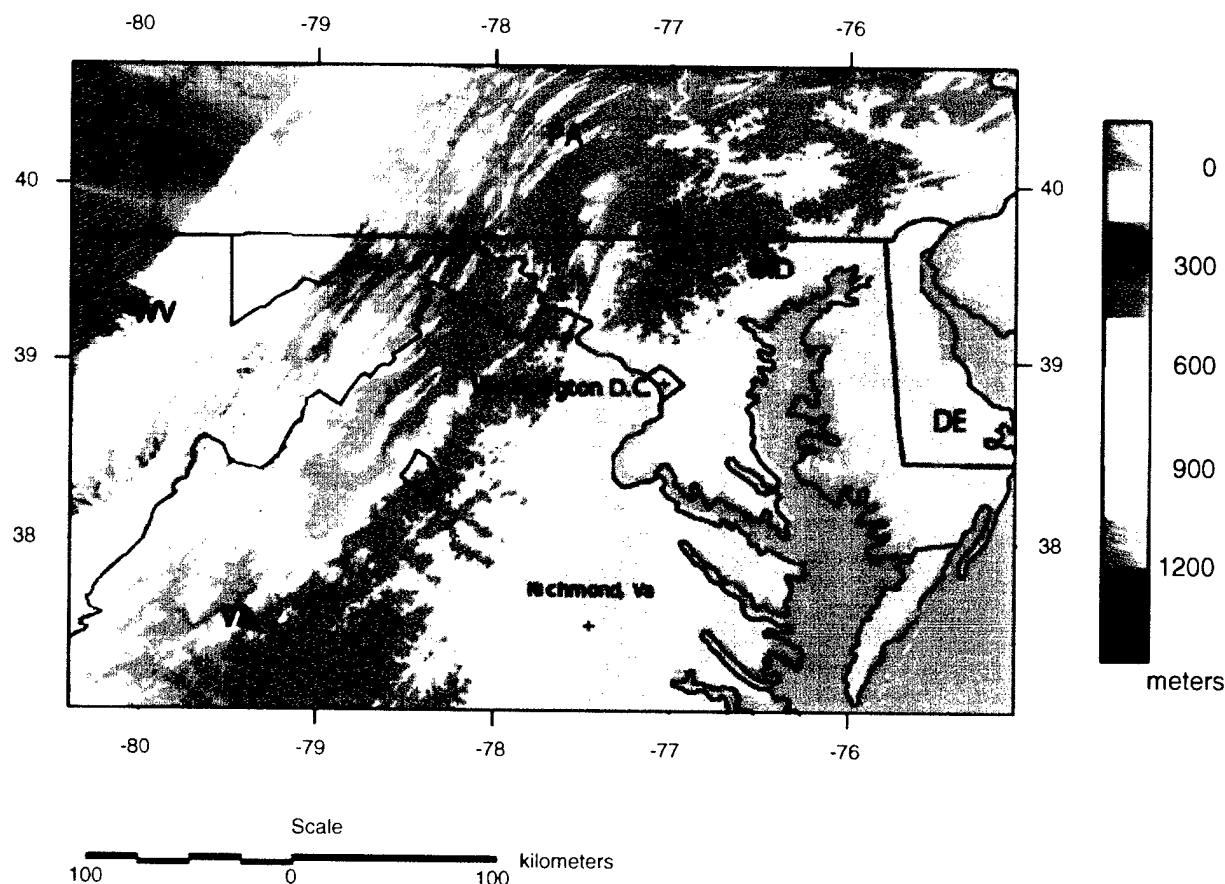


Fig. 1. Location map for the Rapidan River basin. The basin boundary is outlined in black and the stream gaging station is located at 78.3° West and 38.3° North.

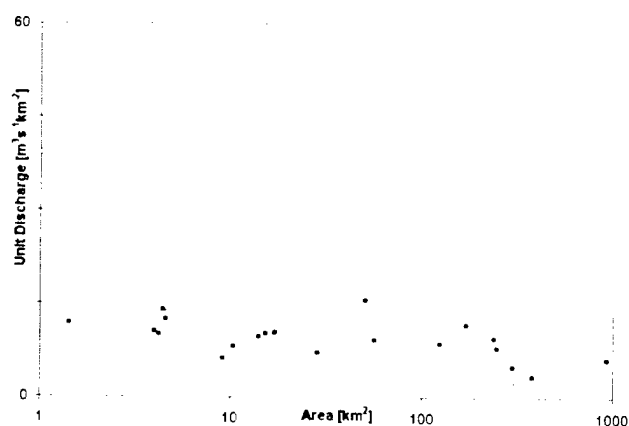


Fig. 2. Observed peak discharge values for the 19 July 1942 Smethport, PA flood (diamonds) and the 18–19 August 1969 Nelson County, Virginia flood (filled circles). Discharge is expressed as a unit discharge ( $\text{m}^3 \text{s}^{-1} \text{km}^{-2}$ ), that is peak discharge divided by drainage area. Data and discussion of the Smethport data are given in [6]; see [2] for Nelson County data and discussion.

scale-dependent response of the Rapidan flood? In this paper, we combine high-resolution rainfall estimates derived from the Sterling, Virginia WSR-88D (Weather

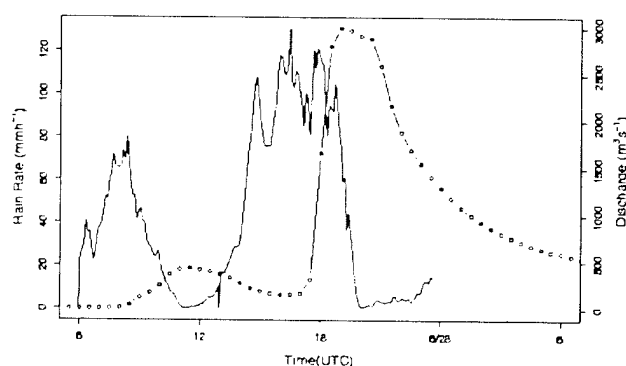


Fig. 3. Time series of basin-averaged rainfall rate ( $\text{mm h}^{-1}$ ; solid line with solid dots) and discharge ( $\text{m}^3 \text{s}^{-1}$ ; solid line with open circles) for the Rapidan River basin from 6 UTC 27 July 1995 to 6 UTC 28 July 1995. Rainfall rate estimates are derived from WSR-88D reflectivity observations and have a time resolution of 5 min.

Surveillance Radar—1988 Doppler) radar with a distributed hydrologic model to examine these questions. Of particular interest is an enhanced understanding of the hydrology of extreme floods and improved assessments of flood hazards and their relation to morphologic properties of drainage basins and land management

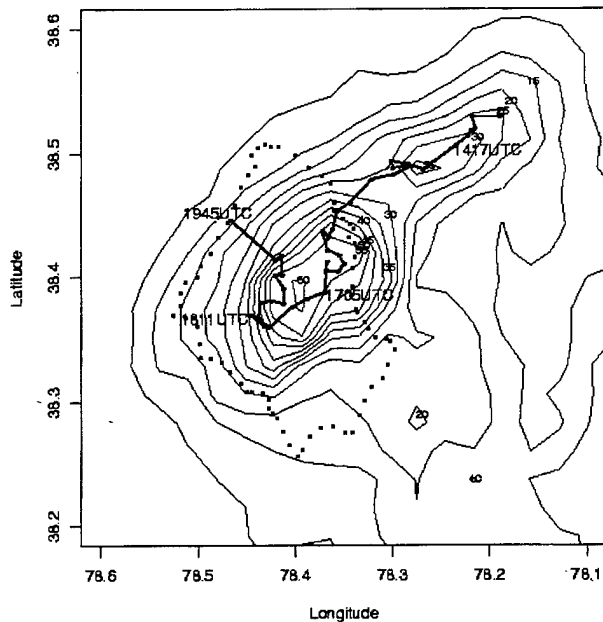


Fig. 4. Storm total rainfall accumulation (cm) for the Rapidan storm. The track of the storm, as represented through the 3-D center of mass projected to the surface, is shown by open circles connected by solid lines (see [20] for additional analyses). Times (UTC) for selected periods are shown. The boundary of the Rapidan basin is outlined by filled circles (see Fig. 1).

practices (see [14] for discussion of hazards issues in the context of the Rapidan storm).

Hydrologic modeling is based on a Hortonian infiltration model (the Green–Ampt model with moisture redistribution; see [16]) and a drainage network based representation of hillslope and channel response [12]. The principal objective of model analyses is to characterize the elements of space–time rainfall distribution and drainage network structure which control extreme flood response. An implicit assumption is that space–time rainfall distribution and drainage network structure provide the most important controls of extreme flood response for events like the Rapidan flood.

In this paper we illustrate new methodologies for monitoring and analysis of extreme floods (see [9] for recent developments). The scientific, engineering and management problems for which these methods can be applied are diverse, as reflected in the range of problems that have been examined surrounding the Rapidan storm and flood [14,17,20,22,26].

## 2. Methodology

The network model [12] is a distributed hydrologic model, which is used in this study to analyze spatially varying flood response in the Rapidan River basin.

Discharge at any location along the drainage network is represented as:

$$Q(t) = \int_A M \left( t - \frac{d_0(x)}{v_0} - \frac{d_1(x)}{v_1}, x \right) dx \quad (1)$$

where  $A$  is the domain of the drainage basin above the specified location,  $x$  is an arbitrary location in  $A$ ,  $M(t, x)$  is the runoff rate ( $\text{mm h}^{-1}$ ) at time  $t$  and location  $x$ ,  $d_0(x)$  denotes the distance from  $x$  to the closest stream channel and  $d_1(x)$  denotes the channel flow distance from  $x$  to the outlet of the basin specified by the region  $A$ . The total flow distance from  $x$  to the basin outlet is  $d_0(x) + d_1(x)$ . The runoff rate  $M(t, x)$  is computed from the rainfall rate  $R(t, x)$  (obtained from Eq. (2) below) using the Green–Ampt infiltration model with moisture redistribution (see [16] for algorithm details). Runoff is assumed to move over hillslopes at a uniform velocity  $v_0$  and through the channel system at velocity  $v_1$  (see [18] for discussion of similar models). In subsequent sections we use (1) to compute discharge at numerous locations upstream of the USGS stream gaging station on the Rapidan River.

Two methods of drainage network extraction are used, the area-threshold method and a slope-area threshold method (see [24] for discussion). In the area-threshold method, stream channels are identified based on exceedance of a specified upstream drainage area threshold,  $|A|$ . In the slope-area method, the smallest channel segments are identified based on the product  $|A|S^k$  exceeding a specified threshold, where  $S$  is the local terrain slope and  $k$  is an extraction parameter. For both methods, we use drainage density as the central parameter for network extraction. An area threshold extraction of the Rapidan drainage network is illustrated in Fig. 5. Drainage density for the network in Fig. 5 is  $0.6 \text{ km km}^{-2}$ .

Radar rainfall estimation is based on a power law  $Z$ – $R$  relationship and raingage-based bias correction (see [1,20]), with the estimation equation formulated as follows:

$$R(t, x) = BaZ(t, x)^b \quad (2)$$

where  $R(t, x)$  is rainfall rate ( $\text{mm h}^{-1}$ ) at time  $t$  and spatial location  $x$ ,  $Z(t, x)$  is the radar reflectivity factor ( $\text{mm}^6 \text{ m}^{-3}$ ) at time  $t$  and location  $x$ ,  $a$  and  $b$  are  $Z$ – $R$  parameters and  $B$  is the multiplicative bias. The default WSR-88D  $Z$ – $R$  relationship [8] is used with  $a = 0.017$  and  $b = 0.71$ . A 55 dBZ cap is applied to reflectivity observations to mitigate the influence of hail contamination. For the Rapidan storm the hail cap did not play a significant role in rainfall analyses. The multiplicative bias  $B$  is estimated as the ratio of total rainfall from rain gage and bucket survey observations to total rainfall from radar bins containing rain gages [20] and takes the value 2.5. Bias correction is a component of operational National Weather Service radar rainfall estimation

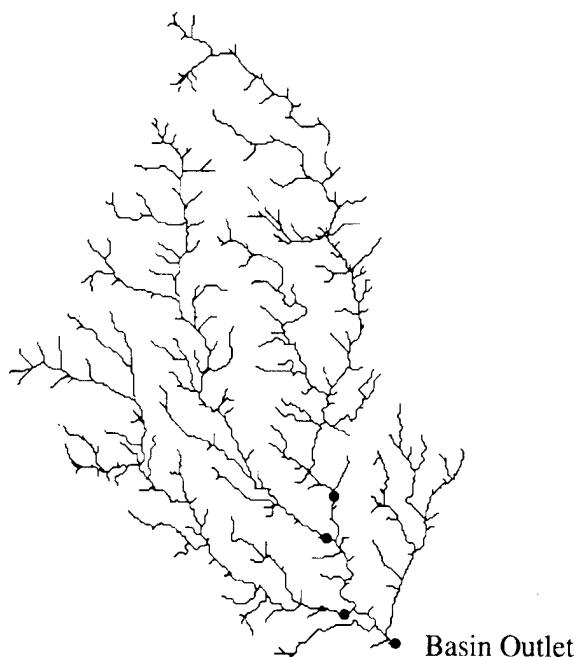


Fig. 5. The extracted drainage network of the Rapidan River basin (see Fig. 1). Solid circles show the locations used for model analyses of flood response (see Figs. 6 and 7). The circles represent the outlets of the three main tributary basins (from top to bottom, the mainstem Rapidan River, the Middle River and the South River). The bottom circle is at the location of the Ruckersville stream gaging station (denoted "basin outlet", which has an upstream area of 295 km<sup>2</sup>).

algorithms ([8]; see [1.8] for discussion of bias estimates for "warm rain" events, like the Rapidan storm).

The storm total rainfall field derived from these observations (Fig. 4) has a maximum rainfall accumulation of 670 mm with areas of 300 mm accumulations covering the central portions of the Rapidan basin. Springer et al. [22] have reported rainfall measurements which exceeded 750 mm and are near the rainfall peak in Fig. 4. The total runoff from the Rapidan storm of 296 mm, computed by integrating the measured discharge over the duration of the event and dividing by drainage area, is approximately the same as the storm total rainfall [20]. The pattern of storm total rainfall distribution corresponds well with the spatial distribution of landslides and debris flows [26]. These and other observations from prior research indicate that the radar rainfall estimates accurately reflect the spatial and temporal distribution of flood-producing rainfall.

The storm total rainfall distribution strongly reflected the size and track of the storm (Fig. 4). During the 4 h period from 14:30 UTC to 18:30 UTC, the storm centroid moved from the east-central boundary of the Rapidan basin to the center of the basin. The storm was multicellular and consisted of 2–3 component cells during much of its life cycle, including the period from 14:30 to 18:30 UTC. Storm motion resulted principally

from feeder cells merging with the parent storm and developing into the dominant cell of the storm (see [20] for additional discussion of terrain controls of storm motion and evolution). The size of storm cells resulted in a characteristic horizontal dimension for the storm of approximately 8 km. As illustrated below, storm motion and structure played an important role in extreme flood response for the event.

### 3. Analyses of the rapidan flood

The network model, which was implemented with a grid resolution of 90 m and drainage density of 1.1 km km<sup>-2</sup>, reproduces peak discharge and the time of peak discharge (Fig. 6) for the Rapidan flood with overland flow velocity  $v_0 = 0.13$  m s<sup>-1</sup> and channel flow velocity  $v_1 = 2.1$  m s<sup>-1</sup> (the saturated hydraulic conductivity for the Green-Ampt model was 5 mm h<sup>-1</sup>). An important feature of the model hydrograph is that it captures the extended period (45–60 min) of near-peak discharge. The model does not capture recession characteristics of the flood or the basin response to the morning storm (Fig. 6; see also Fig. 3). These shortcomings are due to inadequate representation of antecedent soil moisture (for the morning storm), the hydraulics of open channel flow in the transition from overbank to valley bottom full flow and non-Hortonian runoff production mechanisms. The model does, however, provide a good representation of extreme flood response for the 4 h period centered on the peak discharge.

Model analyses indicate that the 45–60 min period of near-peak discharge resulted from differences in the relative timing of contributions from the mainstem Rapidan, Middle River and South River (Fig. 7; see Fig. 5 for locations). The peak discharge of the mainstem Rapidan River of 2000 m<sup>3</sup> s<sup>-1</sup> (Fig. 7) occurred at 18:18 UTC; for the Middle River the peak discharge of

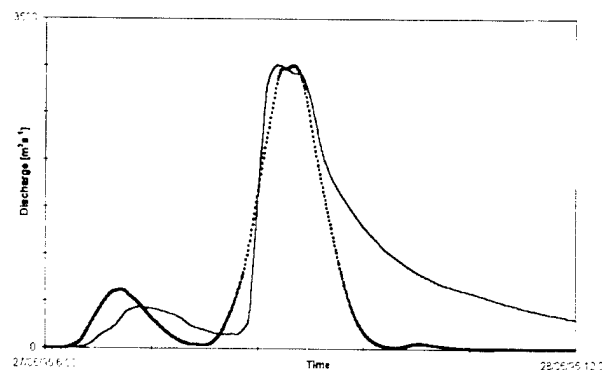


Fig. 6. Observed (solid black line with solid diamonds) and model (solid red line) hydrographs for the Rapidan flood from 27 June 1995 6 UTC–28 June 1995 12 UTC. Tic marks are at 6 h time steps.

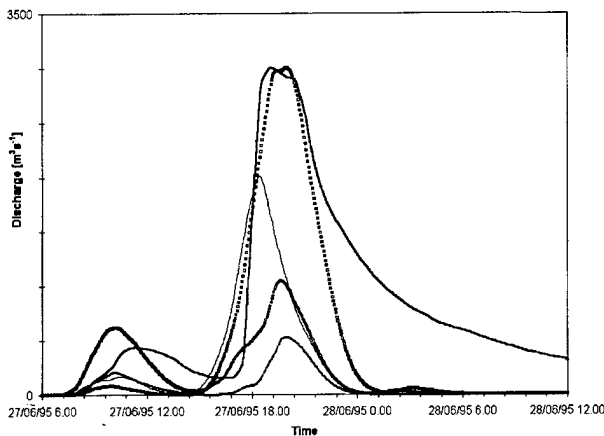


Fig. 7. Observed and model hydrographs for the Rapidan River (as in Fig. 6) with model hydrographs from the three major tributary basins (see Fig. 5 for locations). The solid red line is for the mainstem Rapidan River. The solid, dark blue line represents the Middle River and the solid, purple line is used for the South River.

approximately  $1000 \text{ m}^3 \text{ s}^{-1}$  occurred at 19:48 UTC; for the South River the peak discharge of approximately  $500 \text{ m}^3 \text{ s}^{-1}$  occurred at 20:00 UTC. The initial model peak is principally determined by the mainstem Rapidan with contributions from the Middle River. For the sharp, rising limb of the hydrograph from 14 to 17 UTC, the model discharge at the downstream location is just a lagged version of the discharge from the mainstem Rapidan River (Fig. 7). The second model peak is controlled by the Middle River but includes the receding contributions of the mainstem Rapidan and the rising limb contributions from the South River that result from the late period of rainfall in the lower portion of the South River basin (note the relatively close proximity of the South River to the basin outlet; Fig. 5). These results highlight the importance of storm motion and its control of the timing of rainfall contributions to the watershed (see Fig. 4 and additional discussion below).

The observed peak discharge for the Rapidan River at  $295 \text{ km}^2$ , expressed as a unit discharge, was  $10.2 \text{ m}^3 \text{ s}^{-1} \text{ km}^{-2}$ . The  $2000 \text{ m}^3 \text{ s}^{-1}$  peak discharge of the mainstem Rapidan River from model analyses yields a unit discharge of  $20 \text{ m}^3 \text{ s}^{-1} \text{ km}^{-2}$  at  $100 \text{ km}^2$ . An envelope curve of peak discharge was derived from model analyses (Fig. 8). Unit discharge for the model-derived envelope curve decreases from  $50 \text{ m}^3 \text{ s}^{-1} \text{ km}^{-2}$  at  $1 \text{ km}^2$  to a  $20 \text{ m}^3 \text{ s}^{-1} \text{ km}^{-2}$  plateau for  $10\text{--}100 \text{ km}^2$ . The decrease in unit discharge from  $100$  to  $300 \text{ km}^2$  results from the non-synchronous contributions of the three main tributary basins.

Model analyses suggest that the envelope curve of the Rapidan flood is slightly larger than the Smethport envelope curve (Fig. 2) at small basin scales ( $<10 \text{ km}^2$ ) and slightly larger than the Nelson County envelope curve

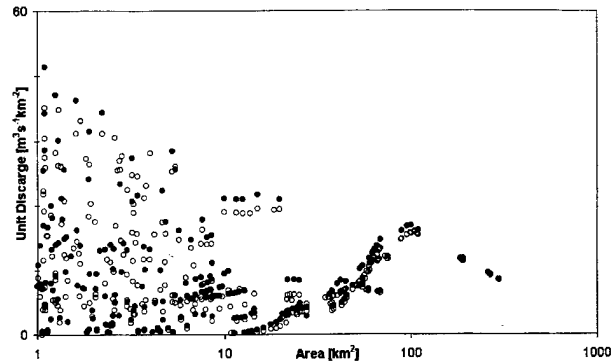


Fig. 8. Peak discharge values throughout the Rapidan basin derived from network model analyses. The open circles represent analyses using drainage network derived using the area-threshold method. The filled circles represent analyses using drainage network derived using the area-slope method (see text for additional details).

(Fig. 2) at large scales ( $100\text{--}300 \text{ km}^2$ ). At small scales the Rapidan envelope curve is much larger than the Nelson County envelope curve and at large scales it is much larger than the Smethport envelope curve.

Peak discharge from small basins is closely linked with peak rainfall rates. Smith et al. [20] concluded from analyses of radar and rain gage observations of the Rapidan storm that peak rainfall rates in both the mainstem Rapidan and Middle River basins exceeded  $300 \text{ mm h}^{-1}$ . The Smethport storm produced the world record rainfall rate of  $185 \text{ mm h}^{-1}$  at  $4.25 \text{ h}$  time scale [6]. Much larger rainfall rates for time intervals less than  $1 \text{ h}$  were reported in [6] and in correspondence surrounding development of the Eisenlohr report. The extreme magnitudes of rainfall rates for the Rapidan storm have played an important role in interpretation of the spatial frequency and intensity of debris flows produced by the Rapidan storm [14,26,22].

The smaller unit discharge flood peaks from the Nelson County flood at small basin scales are possibly due to smaller short-term rainfall rates from the 19–20 August 1969 storm. It is also possible that areas of peak unit discharge were not sampled for the Nelson County flood [15]. The bucket survey observations for the storm [2] provide an ambiguous representation of the  $1\text{--}10 \text{ km}^2$  region with largest storm total rainfall [15] and no information on short-term rainfall rates.

Peak discharge at basin scales between  $100$  and  $300 \text{ km}^2$  for the Rapidan and Nelson County floods reflect a combination of large rainfall rates and extreme rainfall accumulations. For the Rapidan storm, extreme accumulations were linked to terrain controls of storm motion [20]. The Nelson County storm, like the Rapidan storm, occurred on the east slope of the Virginia Blue Ridge in a region of similar terrain to that of the Rapidan River basin. Small net storm motion during the  $6 \text{ h}$  period of peak rainfall played a key role in extreme

rainfall accumulations for the Rapidan Storm. Similar orographic mechanisms are plausible for the Nelson County storm.

During the 4 h period from 14:30 to 18:30 UTC, the Rapidan storm had a net storm motion of approximately 20 km (Fig. 4), which is little more than twice the characteristic horizontal scale of the storm (see below). Storm structure and motion resulted in contrasting temporal patterns of rainfall distribution, which are characterized for the three main tributary basins of the Rapidan River by the mean basin-averaged rainfall and fractional coverage of heavy rainfall (rainfall rates exceeding  $25 \text{ mm h}^{-1}$ ; Fig. 9). The peak basin-averaged rainfall rate of  $90 \text{ mm h}^{-1}$  for the mainstem Rapidan River basin occurred at 16:30 UTC (Fig. 9). The peak for the Middle River basin, also approximately  $90 \text{ mm h}^{-1}$ , occurred 1.5 h later (Fig. 9). Fractional areal coverage of heavy rainfall (Fig. 9) for the mainstem Rapidan ranged from 60% to 80% (approximately 60–80  $\text{km}^2$ ) from 14:30 to 17 UTC. From 17 to 19 UTC, fractional coverage of heavy rainfall in the Middle River basin exceeded 60%.

The spatial scale of heavy rainfall for the Rapidan River basin, as represented by the area of rainfall rates

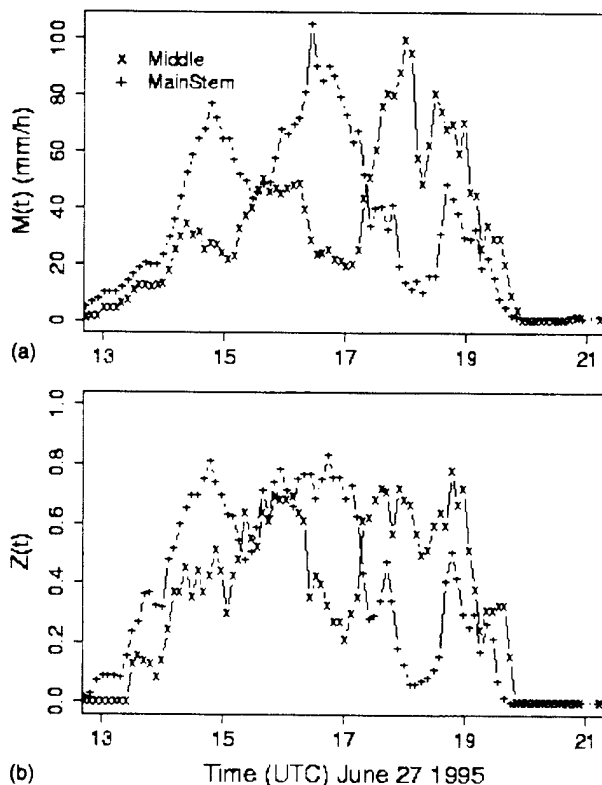


Fig. 9. Time series of mean rainfall ( $\text{mm h}^{-1}$ ) for the mainstem ("+" ) and Middle River ("x") basins (top) and fractional basin coverage by rainfall rates exceeding  $25 \text{ mm h}^{-1}$  (bottom). Drainage network for mainstem Rapidan and Middle River basins are shown in Fig. 5 (see also Fig. 1 for location map).

exceeding  $25 \text{ mm h}^{-1}$  (Fig. 9), ranged from approximately 60–100  $\text{km}^2$ . Model analyses of hydrologic response (Fig. 10a) for the Rapidan storm are most sensitive to spatial averaging of rainfall rates at the 8 km scale, which is approximately the characteristic scale of organization of heavy rainfall. The model peak discharge only decreases to 95% of the observed peak with 4 km averaging of rainfall rates. For rainfall rates averaged over 8 km horizontal scale, the model peak decreases to 87% of the observed peak and the extended period of near-peak response has been lost. With 16 km horizontal averaging of rainfall rate, peak discharge decreases to 67% of the observed peak.

Model results for the Rapidan storm are relatively insensitive to temporal averaging up to 60 min time scale (Fig. 10b). The double peak structure of flood response is retained up to 15 min time averaging. The peak discharge for time averaging of 60 min is quite close to the observed peak, but the double peak structure has been lost. Peak discharge for 3 h averages of rainfall fields is

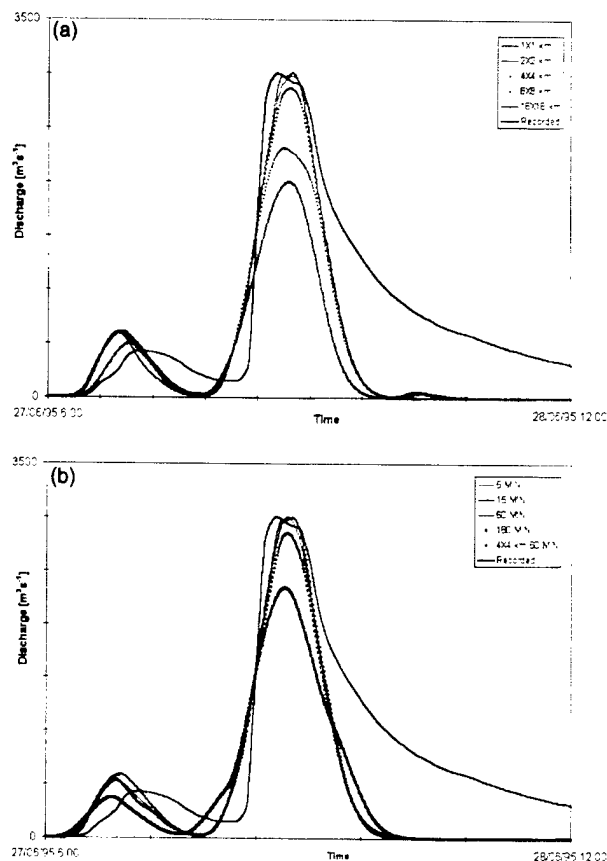


Fig. 10. (a) Model results with spatial averaging of rainfall rate fields at 1, 2, 4, 8 and 16 km ("\*") resolution (see legend for color scheme). The observed discharge is given as solid black line with squares. (b) As in (a), but for time averaging of 5, 15 (note that 5 and 15 min results are indistinguishable), 60, and 180 min (see legend for color scheme). Results for 4 km spatial averaging and hourly time averaging are also shown.



only 75% of the observed peak. Also shown in Fig. 10b are results for 1 h time averaging and 4 km spatial averaging of rainfall rates. The model peak discharge decreases to 95% of the observed peak. These results are of particular importance, because they represent the space and time scales of operational WSR-88D rainfall products [8]. Similar results would not necessarily hold for rapidly propagating convective systems (see [21]).

#### 4. Network structure and extreme flood response

In this section we examine the controls of drainage network structure, and the interaction of drainage network structure and rainfall distribution, on extreme flood response. An important aspect of the drainage network is that it partitions the drainage basin into fast response (channels) and slow response (hillslopes) components. We begin the section with sensitivity analyses of model response to hillslope and channel velocity parameters.

The model hydrograph for the Rapidan flood changes in magnitude and form with changes in the hillslope velocity  $v_0$  (Fig. 11b). Peak discharge increases from 93% of the observed peak to 105% of the observed peak with an increase in  $v_0$  from 0.09 to 0.17  $\text{m s}^{-1}$ . The peak discharge changes from the mainstem Rapidan contribution (first peak) to the Middle River tributary contribution (second peak) as  $v_0$  increases from 0.09 to 0.17  $\text{m s}^{-1}$ .

Dependence of model results on the channel velocity parameter,  $v_1$ , is also characterized by changes in the discharge magnitude and hydrograph form (Fig. 11a). The channel velocity plays a fundamental role in determining the timing of flood response. The time of peak discharge increases from 19:00 to 20:30 UTC as  $v_1$  decreases from 2.5 to 1.7  $\text{m s}^{-1}$ . Decreasing channel velocities also change the form of the hydrograph from one with extended near-peak discharge to a single peak hydrograph.

The network model representation of extreme flood response depends strongly on drainage network properties. Decreasing drainage density from 1.1 to 0.60  $\text{km km}^{-2}$ , but holding  $v_0$  and  $v_1$  constant at 0.13 and 2.1  $\text{m s}^{-1}$  (Fig. 12) results in a 12% decrease in peak discharge, a 30 min delay in the model peak and a change in the form of the hydrograph (the twin-peak structure has been lost).

These results do not imply that the 1.1  $\text{km km}^{-2}$  drainage density provides a more accurate physical representation of the drainage system than the 0.60  $\text{km km}^{-2}$  drainage density. What is clearly implied is that model parameters  $v_0$  and  $v_1$  depend on the model drainage density. With the 0.60  $\text{km km}^{-2}$  network, comparable model results (Fig. 13) to those for the 1.1  $\text{km km}^{-2}$  network are obtained by increasing  $v_0$  to

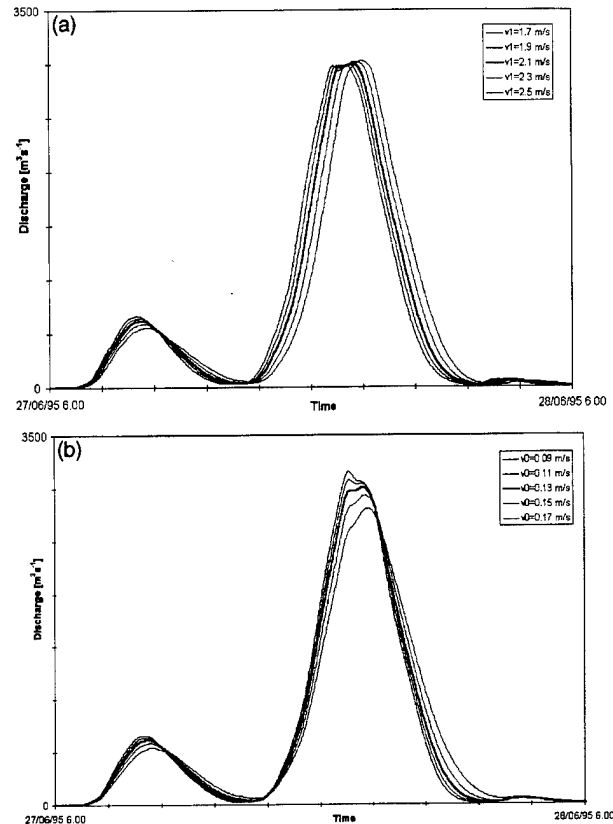


Fig. 11. (a) Model results for changing channel velocity. Time of peak discharge increase with increasing velocity from 1.7 to 2.5  $\text{m s}^{-1}$ . The solid line is for model results in Fig. 6. (b) Model results for changing hillslope velocity. Model peaks decrease with increasing velocity from 0.09 to 0.17  $\text{m s}^{-1}$ . The solid line is for model results in Fig. 6.

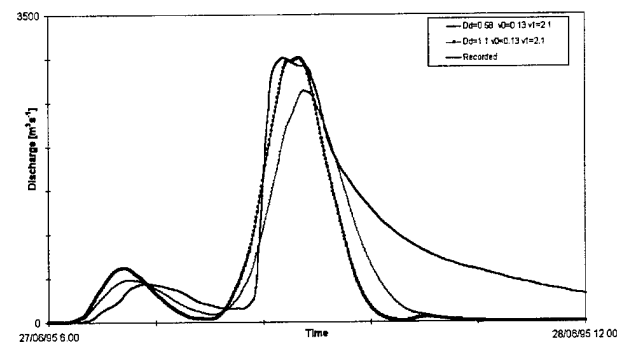


Fig. 12. Model results for changing drainage density (blue line for drainage density of 0.58  $\text{km km}^{-2}$ , dashed purple line for drainage density of 1.1  $\text{km km}^{-2}$ ).

0.2  $\text{m s}^{-1}$  and increasing  $v_1$  to 2.3  $\text{m s}^{-1}$ . Decreasing drainage density leads to longer hillslope flow paths. To maintain the timing of basin response, hillslope and channel velocities must be increased to accommodate the larger mean flow lengths on hillslopes. The results imply that there is a range of drainage densities over

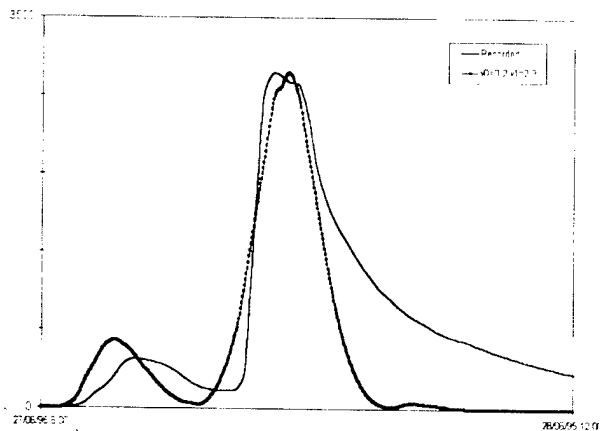


Fig. 13. Model results for drainage density of  $0.6 \text{ km km}^{-2}$ ,  $v_0 = 0.2 \text{ m s}^{-1}$  and  $v_1 = 2.3 \text{ m s}^{-1}$ .

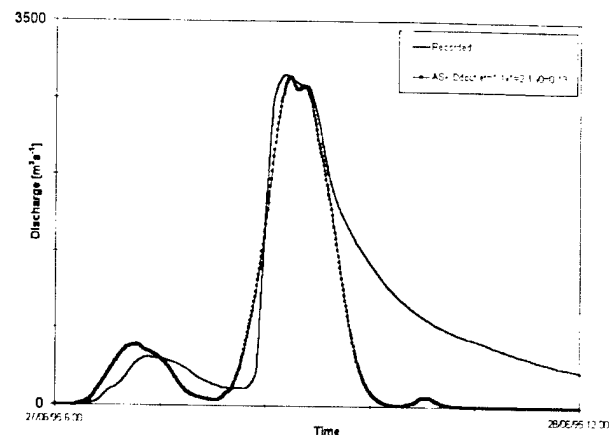


Fig. 14. Model results for drainage network extracted using the area-slope method (density of  $1.1 \text{ km km}^{-2}$ ),  $v_0 = 0.13 \text{ m s}^{-1}$  and  $v_1 = 2.1 \text{ m s}^{-1}$ . Observed discharge is shown in black line with squares.

which the channel and hillslope velocities can be chosen to produce essentially the same Geomorphological Instantaneous Unit Hydrograph (GIUH; see [18]). Physical interpretation of model parameters can be based more readily on derived properties, like the GIUH, than on the parameter values themselves.

The problem of specification of the drainage network is not unique to the model used for the present analyses, but is a fundamental issue for implementation and interpretation of any distributed hydrologic model (see [5,23] for recent physical advances in measuring and interpreting drainage density). For the present analyses model results were not sensitive to drainage density over the range from  $0.6$  to  $1.1 \text{ km km}^{-2}$ , provided that velocity parameters were adjusted to reflect the partitioning of hydrologic response between channel and hillslope response.

From the perspective of flood response, the aggregate drainage density of the basin is only one aspect of the drainage network structure and organization. The distribution of drainage density (see [25]) within the drainage basin can also play an important role in flood response. A drainage network for the Rapidan with  $1.1 \text{ km km}^{-2}$  drainage density was extracted using the area-slope algorithm (see Section 2). The principal difference in the two methods is that the area-slope method places higher drainage density in the high gradient regions of the basin, which typically have longer travel distances to the basin outlet.

Model results for the area-slope network are comparable to those for the area-threshold network. Hillslope and channel velocities increase slightly to accommodate the longer channel flow distances (Fig. 14). There are, however, important differences in model flood response between area-slope and area-threshold networks, but they are not reflected in the flood response at  $295 \text{ km}^2$  scale. The envelope curve of model flood peaks from the area-slope method has larger flood

peaks at small areas than the area-threshold method (Fig. 8).

## 5. Summary and conclusions

There are five principal observations from our work:

1. Extreme flood response to the 27 June 1995 storm in the Rapidan River basin can be reproduced with high resolution radar rainfall estimates from the Sterling, Virginia WSR-88D and a distributed hydrologic model. Storm structure and motion play an important role in determining the timing of rainfall contributions to the Rapidan River basin, which in turn is of primary importance in determining extreme flood response.
2. The envelope curve of the Rapidan flood from model analyses shows a decrease in unit discharge from  $50 \text{ m}^3 \text{ s}^{-1} \text{ km}^{-2}$  at  $1 \text{ km}^2$  to a plateau between 20 and  $30 \text{ m}^3 \text{ s}^{-1} \text{ km}^{-2}$  at basin scales between 10 and  $100 \text{ km}^2$ . Unit discharge decreases to  $10 \text{ m}^3 \text{ s}^{-1} \text{ km}^{-2}$  at  $295 \text{ km}^2$ . This decrease is due to the asynchronous contributions of the three major tributaries to discharge at the basin outlet. The model envelope curve of the Rapidan flood is slightly larger than that for the July 1942 Smethport, Pennsylvania flood at small scales ( $<10 \text{ km}^2$ ) and slightly larger than that for the 18–19 August 1969 Nelson County, Virginia flood at larger scales ( $100\text{--}300 \text{ km}^2$ ).
3. The Rapidan storm was a multicell thunderstorm with a characteristic horizontal scale of approximately  $8\text{--}10 \text{ km}$ . Model results are most sensitive to spatial averaging of rainfall at approximately the  $8 \text{ km}$  scale of organization of heavy rainfall. For the  $1 \text{ h}$ ,  $4 \text{ km}$  scale, which is the space and time scale of

operational WSR-88D radar rainfall products, model results are good.

4. Model results for the Rapidan flood are not sensitive to drainage density, provided that hillslope and channel velocity parameters are adjusted with changing drainage density. The problem of channel/hillslope partitioning is important for all distributed hydrologic models.
5. Model analyses show little difference in extreme flood response between area-threshold and area-slope networks at 295 km<sup>2</sup> scale. There are, however, significant differences in envelope curves at small basin scales. The larger distribution of drainage density in high gradient regions with the area slope method significantly increases the envelope curve for drainage areas <10 km<sup>2</sup>.

The combination of high-resolution radar rainfall estimates and distributed hydrologic models is of great potential utility for flood forecasting. Realizing this potential requires advances in both radar rainfall estimation and hydrologic modeling. Two problems of particular importance for radar rainfall estimation (see also [10]) are: (1) improving rainfall rate estimates for extreme rain rates (roughly speaking, rainfall rates exceeding 50 mm h<sup>-1</sup>) and (2) improving the quantitative characterization of the error structure of radar rainfall estimates (again with special emphasis on extreme rainfall rates). The dominant hydrologic and hydraulic processes associated with extreme floods can differ markedly from those associated with lesser floods. The response to the Rapidan storm during the late morning and afternoon of 27 June 1995, for example, differed significantly from the response to the early morning storm of 27 June 1995. Formulation and verification of hydrologic models used for flood forecasting should be examined from the perspective of extreme floods.

### Acknowledgements

This research was funded in part by the US Army Research Office (Grant No. DAAD19-99-1-0163), NASA (NAG5-7544) and the National Science Foundation (ATM99-06012 and EAR-9706259). This support is gratefully acknowledged.

### References

- [1] Baeck ML, Smith JA. Estimation of heavy rainfall by the WSR-88D. *Weather Forecast* 1988;13:416–36.
- [2] Camp JD, Miller EM. Floods of August 1969 in Virginia. USGS Open File Report, Richmond Virginia: 1970. 120 pp.
- [3] Costa JE. Hydraulics and basin morphometry of the largest flash floods in the conterminous United States. *J Hydrol* 1987;93:313–38.
- [4] Dalrymple T. Major Texas floods of 1935. US Geological Survey Water Supply Paper 796-G, 1937. p. 223–90.
- [5] Dietrich WE, Duhne T. The channel head. In: Beven K, Kirkby MJ, editors. *Channel network hydrology*. Chichester: John Wiley and Son; 1993. p. 175–219.
- [6] Eisenlohr Jr WS. Floods of July 18, 1942 in North-central Pennsylvania. US Geological Survey Water-Supply Paper, 1134-B, 1952. 100 pp.
- [7] Erskine HM. Flood of August 4–5, 1943, in Central West Virginia. US Geological Survey Paper 1134-A, 1951. 47 pp.
- [8] Fulton RA, Breidenbach JP, Seo D-J, Miller DA, O'Bannon T. The WSR-88D rainfall algorithm. *Weather Forecast* 1998;13(2): 377–95.
- [9] Jarrett RD, Tomlinson EM. Regional interdisciplinary paleoflood approach to assess extreme flood potential. *Water Resour Res* 2000;36(10):2957–84.
- [10] Krajewski WF, Smith JA. Radar hydrology: rainfall estimation. *Adv Water Resour* 2002;25(8–12):1387–94.
- [11] Michaud JD, Hirschboeck KK, Winchell M. Regional variations in small-basin floods in the United States. *Water Resour Res* 2001;37(5):1405–16.
- [12] Morrison JE, Smith JA. Scaling properties of flood peaks. *Extremes* 2001;4(1):5–23.
- [13] Morgan AE. Official plan for the protection of the district from flood damage. The Miami Conservancy District, 1916.
- [14] Morgan BA, Wiecek GF, Campbell RH, Gori PL. Debris-flow hazards in areas affected by the June 27, 1995 storm in Madison County, Virginia. US Geological Survey Open File Report 97-438, 1997. 12 pp.
- [15] Morgan BA, Iovine G, Chirico P, Wiecek GF. Inventory of debris flows and floods in the Lovington and Horseshoe Mountain, VA, 7.5' quadrangles from the 19–20 August 1969 storm in Nelson County, Virginia. US Geological Survey Open File Report 99-518, 1999. 9 pp.
- [16] Ogden FL, Saghaian B. Green and Ampt infiltration with redistribution. *J Irrigation Drainage Eng, ASCE* 1997;123(5): 386–93.
- [17] Pontrelli MD, Bryan G, Fritsch JM. The Madison County, Virginia, flash flood of 27 June 1995. *Weather Forecast* 1999; 14(3):384–404.
- [18] Rodriguez-Iturbe I, Rinaldo A. *Fractal river basins*. Cambridge University Press; 1997. pp. 547.
- [19] Schwarz FK. The unprecedented rains associated with the remnants of Hurricane Camille. *Monthly Weather Rev* 1970; 98(11):851–9.
- [20] Smith JA, Baeck ML, Steiner M, Miller AJ. Catastrophic rainfall from an upslope thunderstorm in the Central Appalachians: the Rapidan Storm of June 27, 1995. *Water Resour Res* 1996;32(10):3099–113.
- [21] Smith JA, Baeck ML, Morrison JE, Sturdevant-Rees PL, Bates PD. The regional hydrology of extreme floods in an urbanizing drainage basin. *J Hydrometeorol* 2002;3(3):267–82.
- [22] Springer GS, Dowdy HS, Eaton LS. Sediment budgets for two mountainous basins affected by a catastrophic storm: Blue Ridge Mountains, Virginia. *Geomorphology* 2001;37(1–2):135–48.
- [23] Tarboton DG, Bras RL, Rodriguez-Iturbe I. A physical basis of drainage density. *Geomorphology* 1992;5(1–2):59–76.
- [24] Tarboton DG. A new method for the determination of flow directions and upslope areas in grid digital elevation models. *Water Resour Res* 1997;33(2):309–19.
- [25] Tucker GE, Catani F, Rinaldo A, Bras RL. Statistical analysis of drainage density from digital terrain data. *Geomorphology* 2001;36(3–4):187–202.
- [26] Wiecek GF, n BA, Campbell RH. Debris-flow hazards in the Blue Ridge of Central Virginia. *Environ Eng Geosci* 1999;6(1):3–23.

## Space-Time Variability of Rainfall and Extreme Flood Response in the Menomonee River Basin, Wisconsin

YU ZHANG AND JAMES A. SMITH

*Department of Civil and Environmental Engineering, Princeton University, Princeton, New Jersey*

(Manuscript received 26 December 2001, in final form 5 October 2002)

### ABSTRACT

The hydrometeorological processes that control flash flooding are examined through analyses of space-time rainfall variability and flood response in the Milwaukee metropolitan region. The analyses focus on four flood events in the Menomonee River basin that occurred 21 June 1997, 2 July 1997, 6 August 1998, and 21 July 1999. The June 1997 and August 1998 flood events produced record flood peaks in the Menomonee River and its tributaries. Rainfall analyses, which are based on WSR-88D radar reflectivity observations and rainfall measurements from a dense network of rain gauges maintained by the city of Milwaukee, provide rainfall fields for each event at 1-km spatial resolution and 5-min timescale. The June 1997 and August 1998 storms exhibited striking contrasts in storm structure, evolution, and motion. Analyses of the structure and evolution of these storms are presented in conjunction with scaling analyses of the rainfall fields. The contrasting storm-scale properties of the June 1997 and August 1998 events resulted in sharp contrasts in extreme flood response between the two events. The regional flood response of the Menomonee River basin is examined in terms of space-time rainfall variability and heterogeneous land surface properties. Analyses are based on radar rainfall fields and 15-min discharge observations from stream gauging stations, with drainage area ranging from 47 to 319 km<sup>2</sup> for the four flood events. Extreme flood response is examined in terms of flood peak magnitudes, peak response times, and event water balance. A distributed hydrologic model, which includes a Hortonian infiltration model and a network-based representation of hillslope and channel response, plays a central role in examining the regional flood response.

### 1. Introduction

The Menomonee River, which drains much of the Milwaukee metropolitan region (Fig. 1), experienced record flooding 21 June 1997 and 6 August 1998. Sample flood frequency distributions (Fig. 2) for the Menomonee River at Wauwatosa [319 km<sup>2</sup>; U.S. Geological Survey (USGS) gauge number 04087120] and its tributaries Underwood Creek (47 km<sup>2</sup>; USGS gauge number 04087088) and the Menomonee River at Menomonee Falls (90 km<sup>2</sup>; USGS gauge number 04087030) illustrate the magnitudes of flood peaks for the two events and the contrasting flood response between the urbanized lower basin (Underwood Creek) and the agricultural upper basin (Menomonee River above Menomonee Falls).

The hydrograph of the Menomonee River at Wauwatosa for the 21 June 1997 flood (Fig. 3) exhibited three peaks in response to multiple pulses of heavy rainfall over the basin. The form of flood response in the Menomonee River basin is tied to both storm properties

and land surface properties. In this paper, we examine the hydrometeorological processes that control extreme flood response in the Menomonee River basin. The 21 June 1997 and 6 August 1998 events in the Menomonee River basin provide the principal targets of opportunity for study of space-time variability of rainfall and extreme flood response. Analyses of flood events on 2 July 1997 and 21 July 1999 are used to further examine flood response properties of the Menomonee River basin.

Our approach to extreme flood analysis is by necessity event-based and opportunistic as opposed to driven by observations from carefully designed field campaigns in experimental watersheds. Extreme, flood-producing storms are spatially and temporally rare and are seldom represented in the observations from experimental watersheds. In this study, our experimental base consists of two contrasting storms that produced record floods within the 319 km<sup>2</sup> Menomonee River basin (21 June 1997 and 6 August 1998), a short-duration, extreme rainfall rate storm (2 July 1997) that is used to examine the "unit response" of the Menomonee River basin, and a storm (21 July 1999) consisting of multiple pulses of heavy rainfall, like the 21 June 1997 storm, but with somewhat smaller storm total accumulation than the 21 June 1997 storm.

*Corresponding author address:* Dr. James A. Smith, Dept. of Civil and Environmental Engineering, Princeton University, Princeton, NJ 08544.  
E-mail: jsmith@princeton.edu

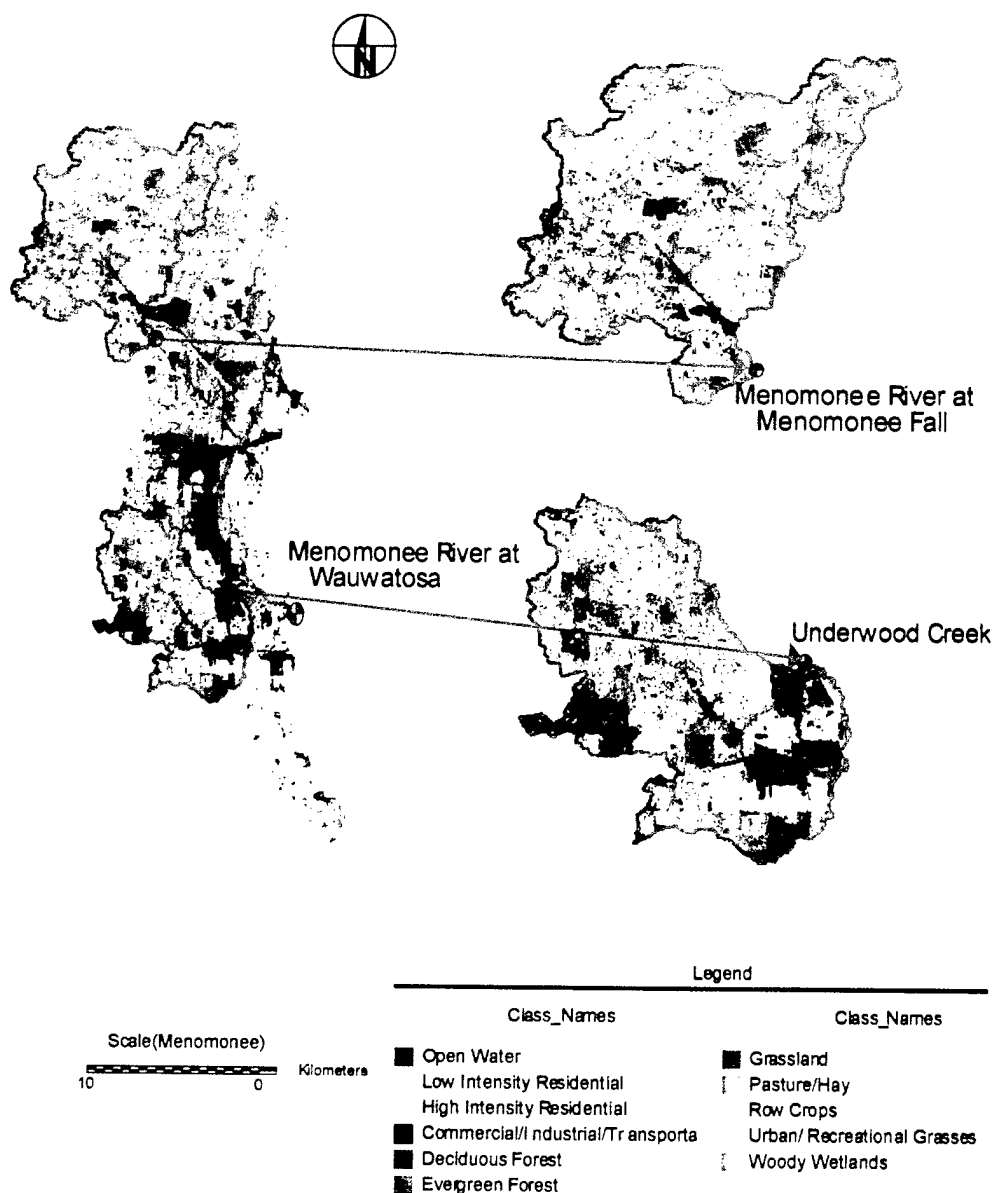


FIG. 1. Land use and land cover (LULC) for the Menomonee River basin. Blowups of the Underwood Creek basin and Menomonee Falls basin are included. Stream gauging stations are denoted by blue-shaded circles.

Extreme flood response in the Menomonee River basin is examined in terms of flood peak magnitudes, peak response times, and event water balance for the four flood events. Discharge observations at 15-min timescale from the three stream gauging stations (see Figs. 1–3) and radar rainfall fields with 1-km horizontal scale and 5-min timescale are used for diagnostic and hydrologic model analyses of peak response and event water balance. The distributed hydrologic model used in this study (see Morrison and Smith 2001; and Giannoni et al. 2003) consists of a Hortonian infiltration model (the Green-Ampt model with moisture redistribution; see Ogden and Saghaian 1997) and a network-based hillslope and channel response model (see also Rodriguez-Iturbe and Rinaldo 1997; Vieux and Bedient 1998).

The Menomonee River basin has a wide range of land use and land cover properties (Fig. 1), resulting in a heterogeneous mix of hydrologic response properties. The basin consists of wetlands, agricultural land, impervious regions distributed throughout the urban portions of the basin, and residential regions, some with and some without detention basins. Storm sewers are found throughout the nonagricultural areas of the basin. Our knowledge of hydrologic response is strongest in homogeneous drainage basins, yet many of the scientific, engineering, and resource management problems concerning flood response are focused on heterogeneous catchments with land surface properties that are changing over time (see, e.g., Potter 1991). Urbanizing regions are especially important in terms of engineering

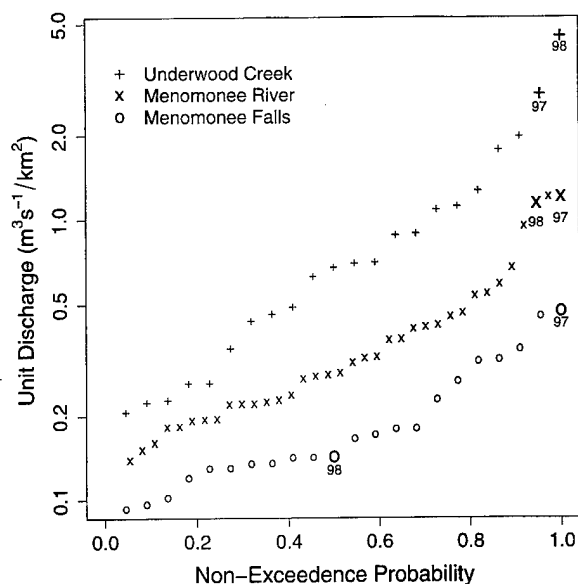


FIG. 2. Quantile plots of annual flood peaks for Menomonee River at Menomonee Falls (USGS ID: 04087030; 25-yr record), Menomonee River at Wauwatosa (USGS ID: 04087120; 39-yr record) and Underwood Creek (USGS ID: 04087088; 22-yr record). Flood peaks on 21 Jun 1997 and 6 Aug 1998 are highlighted 97 and 98, respectively. Peak discharge is represented as a unit discharge ( $\text{m}^3 \text{s}^{-1} \text{km}^{-2}$ ), i.e., discharge divided by drainage area of the basin.

and management problems, but the regional flood response of urbanizing basins is poorly understood (see Leopold 1968; Graf 1977; Smith et al. 2002). In this study, our objective is to examine the regional flood response of the Menomonee River basin and identify land surface and rainfall properties that are dominant controls of extreme flood response.

Space-time variability of rainfall is examined through analyses of rainfall fields derived from Weather Surveillance Radar-1988 Doppler (WSR-88D) volume scan reflectivity observations. Particular attention is given in section 2 to the contrasting structure, motion, and rainfall rates from the 21 June 1997 and 6 August 1998 storms (for related analyses, see Doswell et al. 1996; Smith et al. 1996, 2001, and 2002; Ogden et al. 2000; Sturdevant-Rees et al. 2001; Zhang et al. 2001). In section 3 these contrasting storm elements are revisited in light of extreme flood response.

## 2. Hydrometeorology of the 21 June 1997 and 6 August 1998 storms

In this section, we examine the spatial and temporal variability of rainfall for the 21 June 1997 and 6 August 1998 storms in the Milwaukee metropolitan region. Analyses are based on high-resolution (1-km horizontal scale; 5-min timescale) rainfall estimates derived from volume scan WSR-88D reflectivity observations and rain gauge observations from an urban mesonet main-

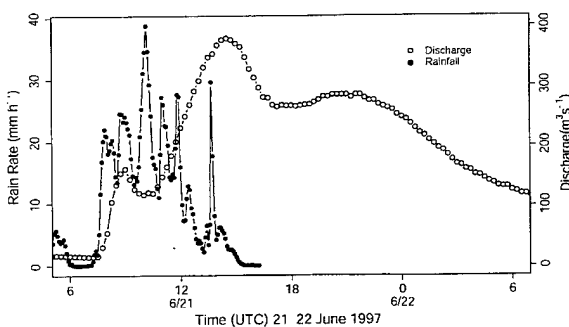


FIG. 3. Basin-averaged rainfall rate and discharge for the Menomonee River at Wauwatosa, 0600 UTC 21 Jun–0600 UTC 22 Jun 1997. Rainfall rate time series are averaged to 15-min time interval.

tained by the city of Milwaukee. Supplemental analyses utilize Geostationary Operational Environmental Satellite (GOES) IR observations and cloud-to-ground (CG) lightning observations from the National Lightning Detection Network (see Orville and Silver 1997). Particular attention is given to contrasts in storm structure, evolution, and motion between the June 1997 and August 1998 storms.

Radar rainfall estimation is based on a power-law  $Z$ - $R$  relationship and bias correction based on rain gauge observations (see Fulton et al. 1998; Baek and Smith 1998), with the estimation equation formulated as follows:

$$R = BaZ^b, \quad (1)$$

where  $R$  is rainfall rate ( $\text{mm h}^{-1}$ ),  $Z$  is the radar reflectivity factor ( $\text{mm}^6 \text{m}^{-3}$ ),  $a$  and  $b$  are  $Z$ - $R$  parameters, and  $B$  is the multiplicative bias. The default WSR-88D  $Z$ - $R$  relationship is used with  $a = 0.017$  and  $b = 0.71$ . A 55-dBZ cap is applied to reflectivity observations to mitigate the influence of hail contamination. For the four events analyzed in this study the hail cap did not play a significant role in the rainfall analyses. The multiplicative bias  $B$  is estimated for each event as the ratio of total rainfall from the rain gauge network and total rainfall from radar bins containing rain gauges. Rainfall estimates are developed at 1-km horizontal resolution and 5-min timescale.

Flooding in the Menomonee River basin on 21 June 1997 resulted from a series of storms that passed over the basin from 0630 until 1330 UTC. At 0700 UTC (Fig. 4a), a small area of convection was developing between a decaying mesoscale convective system (MCS) centered over Michigan and a large MCS over Iowa (see also Roebber and Eise 2001). The MCS developing over Milwaukee intensified and remained nearly stationary until 1100 UTC (Figs. 4b,c). The western MCS passed over the Milwaukee region at 1300 UTC (Fig. 4d) ending the period of heavy rainfall in the Menomonee River basin.

The large-scale evolution of weather systems on 21 June (Fig. 4) was linked with storm-scale evolution over

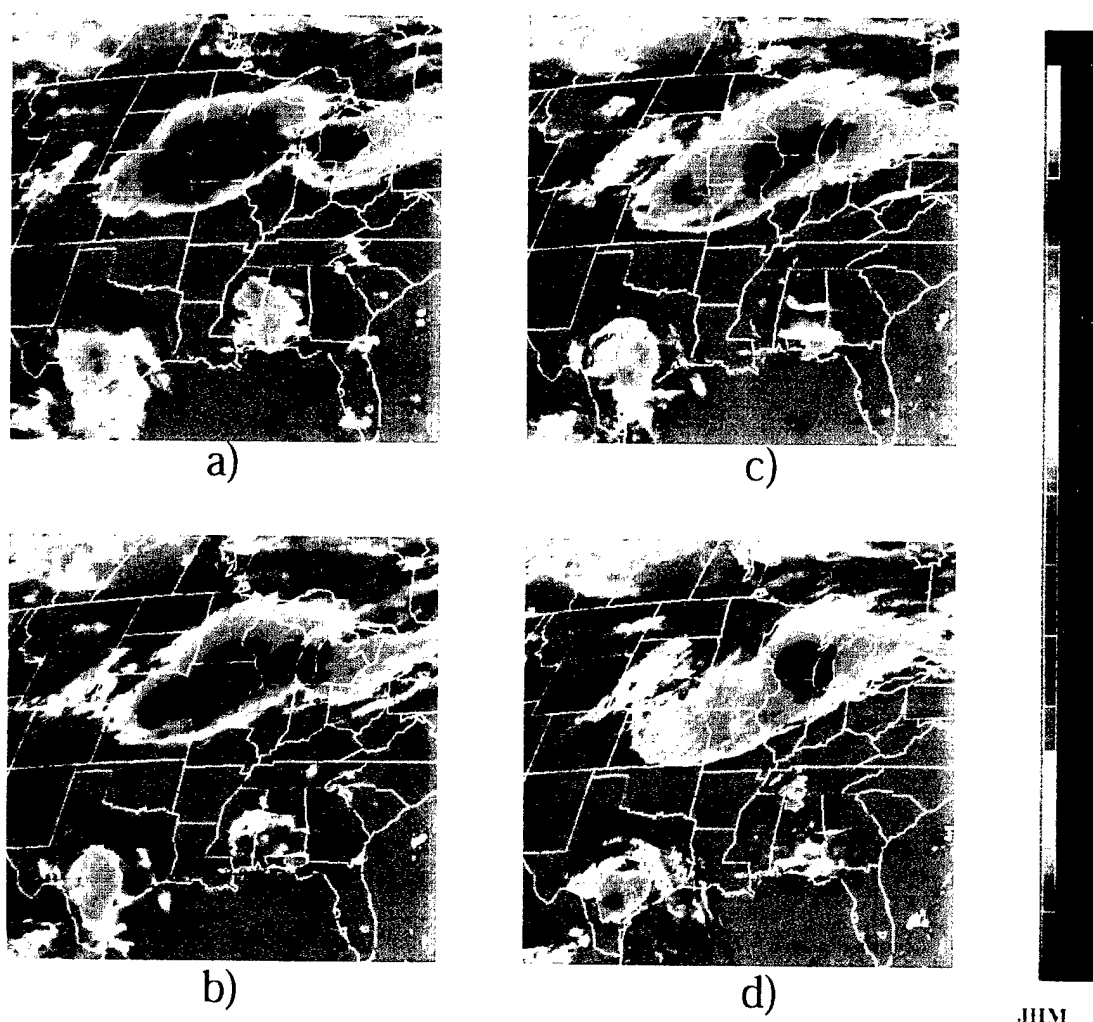


FIG. 4. GOES IR imagery on 21 Jun 1997 at (a) 0700 UTC, (b) 0900 UTC, (c) 1100 UTC, and (d) 1300 UTC.

the Milwaukee region (Fig. 5). At 0717 UTC (Fig. 5a), convective elements were oriented along an east–west boundary. A north–south oriented outflow boundary (apparent in Fig. 5a as a reflectivity *thin line* west of the Menomonee River basin) moving from east to west served as a focusing mechanism for convective development and intensification. Heavy rainfall in the Menomonee River basin was concentrated in the center and lower portion of the basin (Fig. 5a). From this time until the arrival of the western MCS, convective elements tracked repeatedly over the Milwaukee region [see Chappell (1989) for discussion of *quasi-stationary* behavior of storm systems]. Intensification of the Milwaukee MCS (Fig. 5b) resulted in an organized region of convection extending along an east–west axis through the upper half of the Menomonee basin at 0946 UTC. During the decaying phase of the Milwaukee MCS (Fig. 5c; 1126 UTC), a north–south-oriented line of convection covered much of the Menomonee River basin below Menomonee Falls. Passage of the western MCS over the Milwaukee Region (Fig. 4d) was associated with a

rapidly moving arc of convection (Fig. 5d). Time lapse imagery of radar reflectivity fields (not shown) illustrate the rotation of the band of convection about the center of the MCS circulation, which at 1310 UTC was located close to the Milwaukee radar.

Gauge–radar intercomparisons for the 21 June 1997 storm (Figs. 6 and 7a and discussion below; rain gauge locations are shown in Fig. 7a) illustrate the capability of radar rainfall estimates to represent the temporal and spatial variability of extreme storm rainfall. The estimated multiplicative bias,  $B$ , for the event is 1.11, reflecting an 11% underestimation of rainfall with the default  $Z$ – $R$  relationship. The root-mean-square error (rmse) of 15-min rainfall estimates of  $11.5 \text{ mm h}^{-1}$  is 66% of the mean 15-min rainfall rate (for 15-min periods with positive rainfall rates). The rmse of rainfall rate estimates at 60-min timescale,  $5.4 \text{ mm h}^{-1}$ , is 42% of the mean 60-min rainfall rate (for hours with positive rainfall). The storm total RMSE of 14.3 mm is 12% of mean storm total rainfall of 103 mm. A significant contribution to rmse, especially at shorter timescales, arises

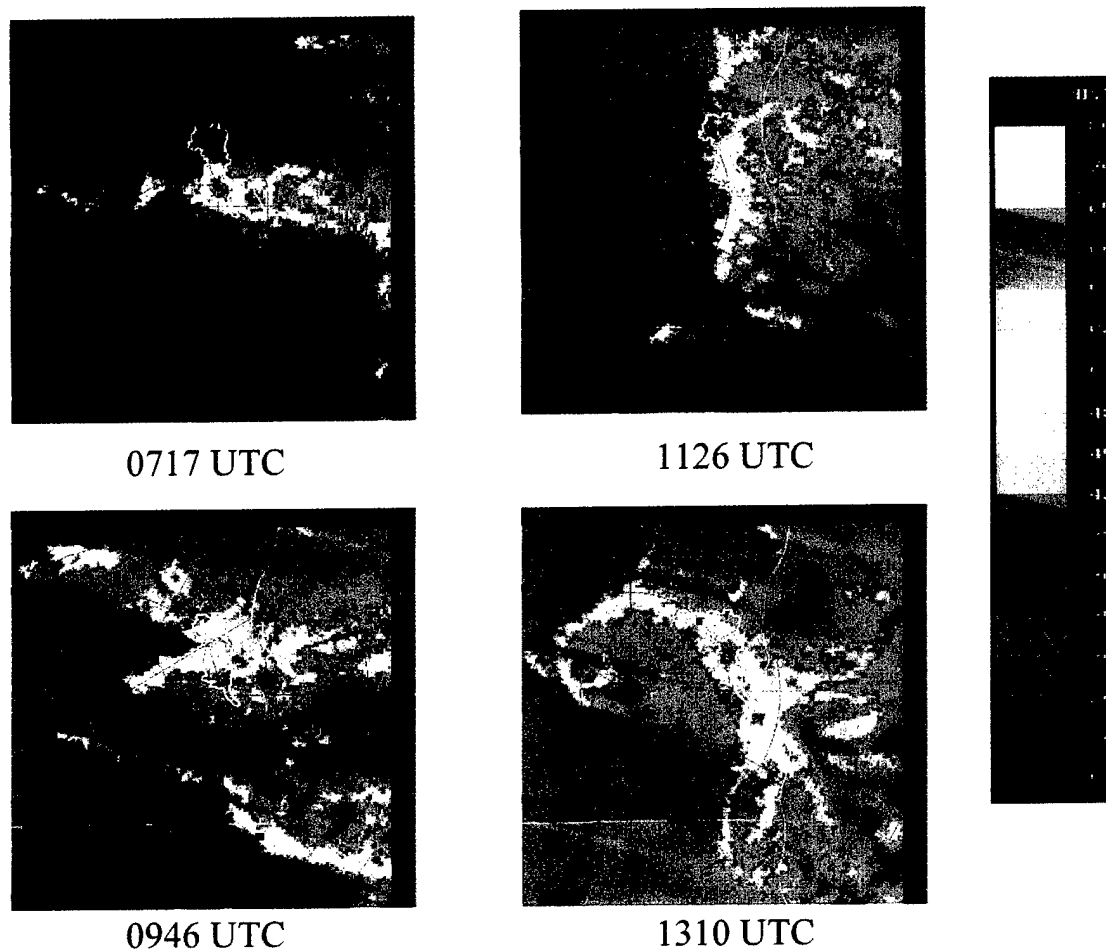


FIG. 5. WSR-88D reflectivity fields on 21 June 1997 at (a) 0717 UTC, (b) 0946 UTC, (c) 1126 UTC, and (d) 1310 UTC.

from the sampling differences between radar and rain gauges (see Ciach and Krajewski 1999; Anagnostou et al. 1999).

The storm total rainfall map (Fig. 7a) for the period 0600–1400 UTC reflects the structure and motion of

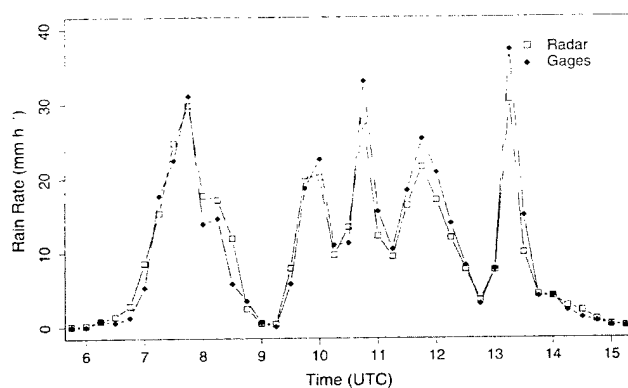


FIG. 6. Time series of radar and rain gauge rainfall estimates at 15-min timescale. Gauge analyses are averaged for 18 rain gauges in Milwaukee urban rain gauge network. Radar analyses are for the 18 1-km bins that contain the rain gauges.

storm elements over the region [see Chappell (1989) for additional discussion], with an elongated rainfall maximum greater than 100 mm extending from 20 km west of the basin to 30 km east of the basin. The 100-mm contour encloses most of the Menomonee River basin.

The synoptic-scale environment of the 6 August 1998 storm included a cold front extending from southwest of the Rio Grande River in Mexico to northern Illinois, and a warm front oriented from southwest to northeast through Milwaukee (National Oceanic and Atmospheric Administration Daily Weather Maps; figures not shown). Widespread convection developed ahead of the cold front and wrapped around the upper-level low. The flood-producing storms over the Milwaukee region tracked along the warm front from 1800 to 2400 UTC on August 6. During this period, storms formed southwest of Underwood Creek along the frontal boundary and were steered over Underwood Creek and the center of the Menomonee River basin (Fig. 8).

The storm total rainfall distribution for the 6 August 1998 storm (Fig. 7b) reflects storm structure and motion, as controlled by the frontal boundary and steering winds aloft. Of particular importance for flooding in Under-



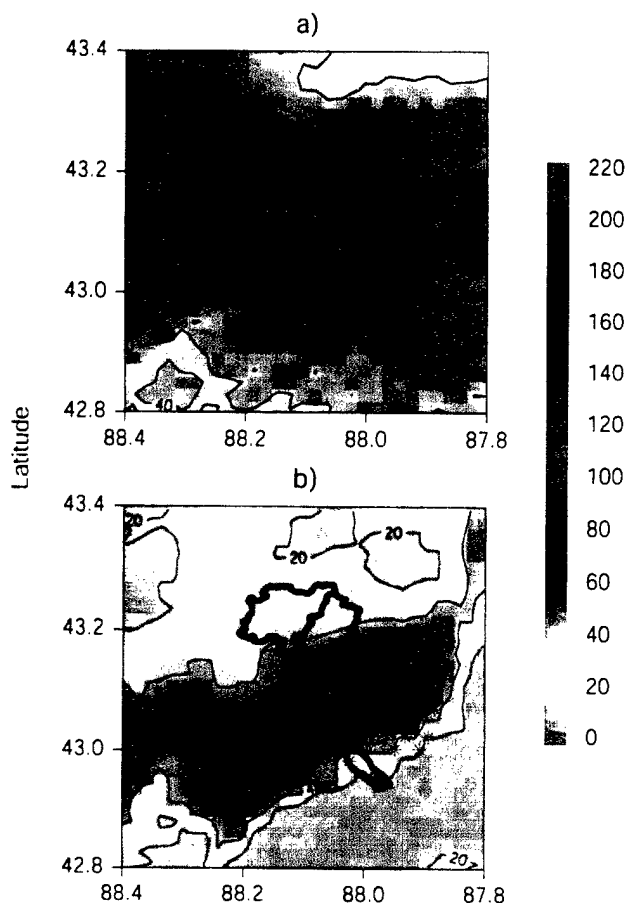


FIG. 7. Storm total rainfall (mm) for (a) 21 Jun 1997 and (b) 6 Aug 1998 storms. Rain gauges are shown as red asterisks.

wood Creek was the 2.5-h period beginning of 2030 UTC (Fig. 8) during which persistent high rainfall rates occurred over Underwood Creek. As with the 21 June 1997 storm, there was good agreement (not shown) between radar rainfall estimates and rain gauge observations. Four rain gauges were located within the 140-mm storm total contour (Fig. 7b). Storm total accumulations for these gauges ranged from 160 to 200 mm.

Scaling analyses of rainfall fields (Figs. 9 and 10) illustrate contrasting temporal evolution and spatial structure of the 21 June 1997 and 6 August 1998 storms [see Perica and Foufoula-Georgiou (1996) and references therein for related analyses]. Analyses were carried out for rainfall fields averaged over length scales of 1, 4, and 16 km. The domain used for scaling analyses is a 128 km by 128 km region centered on the Menomonee River basin. A rainfall threshold of  $1 \text{ mm h}^{-1}$  was used to distinguish rain–no rain areas at 1-km resolution (results are similar in form over a range of rain-rate thresholds,  $0.25\text{--}2.5 \text{ mm h}^{-1}$ , commonly used for rain–no rain analyses; see Baek and Smith 1995). Analyses of fractional coverage, mean rainfall (for positive bins), and coefficient of variation (mean divided by standard deviation) of rainfall rate (for positive bins) were per-

formed for rainfall rate fields averaged over the 1-, 4-, and 16-km grids.

Scaling analyses highlight the contrasting temporal evolution of two storms that exhibit “quasistationary” (Chappel 1989) behavior. For the June 1997 storm there was a sharp increase in fractional rain area with evolution of the Milwaukee MCS and arrival of the western MCS (Fig. 9). At 0700 UTC, fractional coverage of rainfall was 25% at 1-km resolution, 40% at 4-km resolution, and 70% at 16-km resolution. Fractional coverage increased sharply at 0900 UTC with explosive growth of the Milwaukee MCS (Figs. 4 and 5). By 1300 UTC, fractional coverage was 95% at 16-km resolution, 90% at 4-km resolution, and 70% at 1-km resolution. The 6 August 1998 storm, by contrast, exhibited relatively minor changes in storm properties with time (Fig. 10). Fractional coverage of rainfall for the 6 August 1998 storm increased gradually during the period of peak rainfall. From 1930 to 2300 UTC fractional coverage increased from 10% to 20% at 1-km resolution. The uniform temporal features (and spatial structures; see Fig. 8) of the 6 August 1998 storm are likely due to the role of the frontal boundary in organizing the evolution of convection during the 4-h period of peak rainfall.

There were also contrasts in variability of rainfall rate between the June 1997 and August 1998 storms. For the June 1997 storm, the coefficient of variation of rainfall rate fluctuated around 1.3 for 1- and 4-km analyses and 1.0 for 16-km analyses. For the August 1998 storm, the coefficient of variation fluctuated between 1.5 and 2.0 at all scales from 2000 to 2300 UTC. The August 1998 storm was composed of small cores with high rainfall rates grading to low rainfall rates over short distances. Rainfall rate observations from the Milwaukee rain gauge network at 5-min timescale exceeded  $140 \text{ mm h}^{-1}$  during the August 1998 storm. Peak rainfall rates from the 21 June 1997 storm were  $100 \text{ mm h}^{-1}$ .

The storm microphysical and dynamical processes that control the spatial and temporal distribution of extreme rainfall rates are poorly understood, especially at space–time scales relevant to flood production in urban basins, like Underwood Creek. During the period of peak rainfall intensity over Underwood Creek, the August 1998 storm is discernible in GOES IR imagery (figure not shown) only as a small cloud streak with relatively warm cloud-top temperatures ( $-50^{\circ}\text{C}$ , as compared with  $-80^{\circ}\text{C}$  for the 21 June 1997 storms; see Fig. 4). In this respect, the August 1998 storm is similar to storms like the 28 July 1997 Fort Collins, Colorado, storm in which extreme rainfall rates were linked to efficient warm rain precipitation processes (Petersen et al. 1999; see also Maddox et al. 1978; Smith et al. 1996). Unlike the Fort Collins storm, the August 1998 Milwaukee storm produced large storm total cloud-to-ground lightning flash densities (as did the June 1997 storm; see Fig. 11). For the August 1998 storm, peak flash densities were on the northeast (“downstream”)

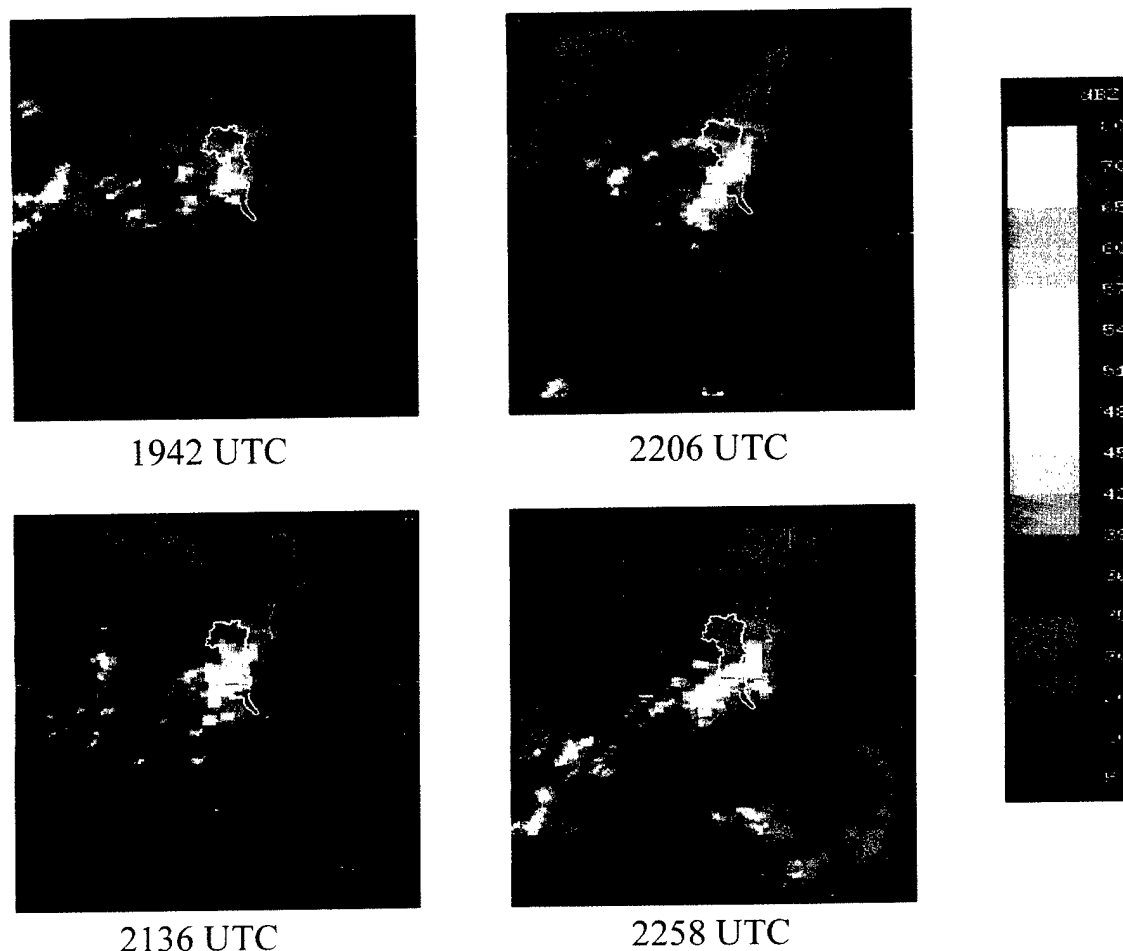


FIG. 8. WSR-88D reflectivity field on 6 Aug 1997 at (a) 1942 UTC, (b) 2136 UTC, (c) 2206 UTC, and (d) 2258 UTC.

end of the region of peak rainfall and followed the period of extreme rainfall production. For the June 1997 storm, peak flash densities were concentrated to the west ("upstream") of the largest rainfall accumulations (Fig. 11) and preceded production of peak rainfall rates. Advances in understanding microphysical and dynamical processes controlling extreme rainfall rates are needed both for characterizing space-time structure of flood-producing rainfall and for improving remote sensing procedures used for estimating rainfall rate.

### 3. Flood response of the Menomonee River basin

In this section we examine flood response of the Menomonee River basin with particular emphasis on contrasting response of the lower basin and the upper basin (Fig. 1). Analyses focus on Underwood Creek (in the lower basin) and the Menomonee River above Menomonee Falls (in the upper basin; see Figs. 1 and 2). Land use in the upper basin is dominated by a mix of agricultural and residential regions, with a core of urban development in the lower portion of the basin (Fig. 1). Residential and urban land use categories dominate the Underwood Creek basin. Differences in flood response

are examined in terms of the spatial and temporal variability of rainfall forcing. In addition to the 21 June 1997 and 6 August 1998 events, we examine flood response to smaller events on 2 July 1997 and 21–22 July 1999.

The 2 July 1997 storm produced rainfall accumulations ranging from 15 to 40 mm over the Menomonee River basin during the 45-min period beginning 0800 UTC. The storm was a rapidly moving, long-lived thunderstorm system, which produced large hail, damaging winds, and lightning, in addition to extreme rainfall rates over the Milwaukee region. The storm entered the western edge of the Milwaukee WSR-88D area of coverage at 0424 UTC and reached the western margin of the Menomonee River basin at 0754 UTC for an average speed of  $71 \text{ km h}^{-1}$ . The storm exhibited the hook echo signature of a supercell thunderstorm at the western margin of the radar area of coverage and produced peak reflectivity values between 65 and 70 dBZ [compare with the storms described in Smith et al. (2001)]. Reports of damaging winds, large hail, and lightning were concentrated in the area west of the Menomonee River basin. Peak rainfall rates from the Milwaukee rain gauge network exceeded  $150 \text{ mm h}^{-1}$  at 5-min timescale. At

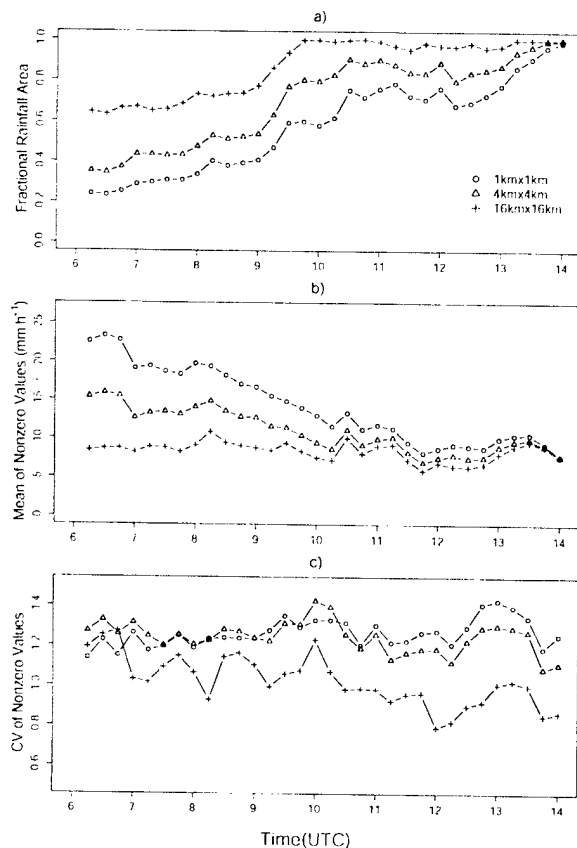


FIG. 9. Time series of (a) fractional coverage ( $\text{km}^2 \text{km}^{-2}$ ) of positive rain rates, (b) mean rain rate of nonzero bins, and (c) coefficient of variation of nonzero rain rates on 21 Jun 1997.

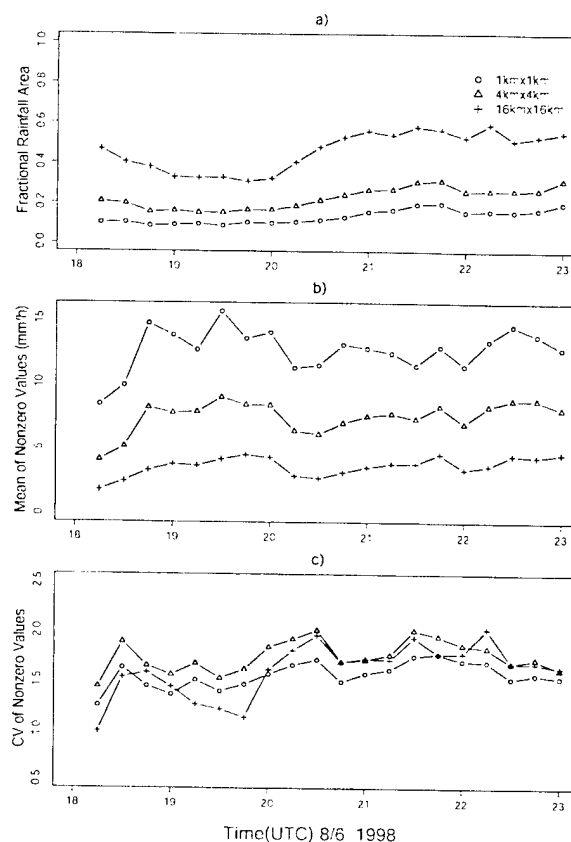


FIG. 10. Time series of (a) fractional coverage ( $\text{km}^2 \text{km}^{-2}$ ) of positive rain rates, (b) mean rain rate of nonzero bins, and (c) coefficient of variation of nonzero rain rates on 6 Aug 1998.

any location within the Menomonee River basin, virtually all of the storm total rainfall was delivered during a time period of less than 20 min. Rainfall accumulations in the Menomonee Falls basin ranged from less than 5 mm in the upper basin to 30 mm near the basin outlet. Rainfall accumulations in Underwood Creek ranged from 20 to 40 mm.

The 21 July 1999 storm was a multicellular thunderstorm that produced rainfall accumulations in the Menomonee River basin ranging from 60 to 110 mm during a 4-h period beginning 0400 UTC. Although the storm produced lightning and there were reports of damaging winds, the most significant impacts of the storm centered on flash flooding throughout southern Wisconsin. Like the 21 June 1997 storm, large rainfall accumulations resulted from multiple storm elements tracking over the region from west to east. Peak rainfall rates from the Milwaukee rain gauge network exceeded  $100 \text{ mm h}^{-1}$  at 5-min timescale. Rainfall accumulations above Menomonee Falls ranged from 80 to 110 mm. For Underwood Creek, rainfall accumulations ranged from 50 to 80 mm.

Unit Values discharge observations at 15-min time

interval from the USGS gauging stations at Menomonee Falls and Underwood Creek were used in conjunction with radar rainfall fields to construct water budgets for the 21 June 1997, 2 July 1997, 6 August 1998, and 21 July 1999 flood events (Tables 1 and 2). Storm total runoff (in mm) was computed by integrating discharge over the duration of the flood and scaling by the basin area.

There are large contrasts in runoff volumes and flood peak magnitudes between Underwood Creek and the Menomonee River above Menomonee Falls (Tables 1 and 2). Runoff ratios for Menomonee Falls range from less than 10% to a maximum of 24%, with little correspondence to rainfall totals. For Underwood Creek, runoff ratio ranged from 30% for low rainfall totals to 70% for the largest rain event. Unit discharge flood peaks ranged from  $0.13 \text{ m}^3 \text{ s}^{-1} \text{ km}^{-2}$  to  $0.47 \text{ m}^3 \text{ s}^{-1} \text{ km}^{-2}$  for Menomonee Falls. For Underwood Creek unit discharge peaks ranged from  $1.02 \text{ m}^3 \text{ s}^{-1} \text{ km}^{-2}$  to  $4.20 \text{ m}^3 \text{ s}^{-1} \text{ km}^{-2}$ . The differences in peak unit discharge between Underwood Creek and Menomonee Falls for the four flood events reflect the long-term flood frequency contrasts between the two basins (Fig. 2).

The June 1997 and August 1998 floods in Underwood

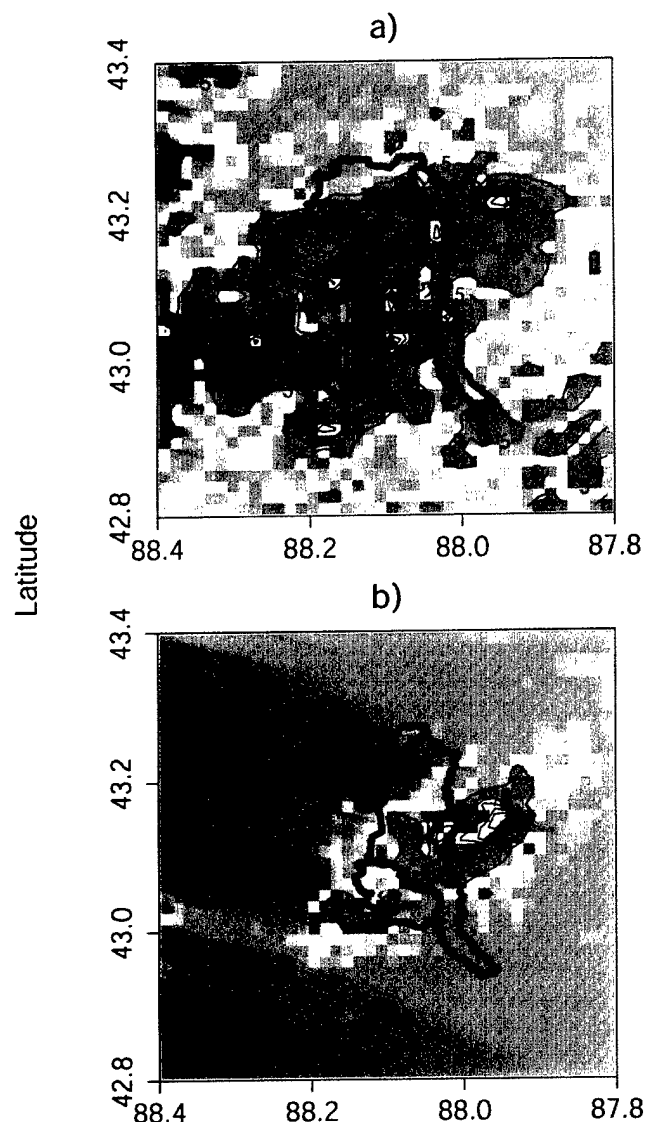


FIG. 11. Storm total cloud-to-ground (CG) lightning strikes (CG strikes  $\text{km}^{-2}$ ) for (a) the 21 Jun 1997 and (b) the 6 Aug 1998 storms. Contours are 5 CG strikes  $\text{km}^{-2}$  interval. Color scale ranges from less than 1 CG strikes  $\text{km}^{-2}$  (orange), 5–10 CG strikes  $\text{km}^{-2}$  (green to blue), 10–15 CG strikes  $\text{km}^{-2}$  (dark blue to purple) and greater than 15 CG strikes  $\text{km}^{-2}$  (white).

Creek resulted from comparable storm total rainfall accumulations, 131 mm for the June 1997 event and 113 mm for the August 1998 event. The flood peak magnitudes and runoff volumes (Table 2) for the two events, however, were quite different, 62 mm of runoff (runoff ratio of 56%) for the June 1997 event versus 93 mm of runoff (runoff ratio of 70%) for the August 1998 event, and peak discharge values of  $130 \text{ m}^3 \text{ s}^{-1}$  for the June 1997 event versus  $212 \text{ m}^3 \text{ s}^{-1}$  for the August 1998 event. The August 1998 storm produced higher basin-averaged rainfall rates and a continuous 3-h period (2030–2330 UTC) of heavy rainfall over much of the basin. The June 1997 storm was characterized by multiple pulses of heavy rainfall separated by periods of low rainfall

TABLE 1. Summary of flood events in the Menomonee River basin above Menomonee Falls.

Event	Total rainfall (mm)	Total runoff (mm)	Runoff ratio	Peak discharge ( $\text{m}^3 \text{ s}^{-1}$ )	Peak unit discharge ( $\text{m}^3 \text{ s}^{-1} \text{ km}^{-2}$ )
21–22 Jun 1997	103	NA	NA	42	0.47
2–3 Jul 1997	18	4.5	0.24	11	0.13
6–7 Aug 1998	28	2.6	0.09	12	0.14
21–22 Jul 1999	96	7.5	0.08	25	0.28

rate (Figs. 5 and 6). The August 1998 storm exhibited larger gradients in storm total rainfall distribution, from 80 mm at the northwest border of the basin to 210 mm in the central core to 80 mm at the southeastern boundary.

A distributed hydrologic model is used to further examine contrasting hydrologic response associated with space–time rainfall variability and heterogeneous land surface properties. The Network Model (Morrison and Smith 2001; Giannoni et al. 2003) combines a grid-based Hortonian infiltration model and network-based hillslope and channel response model. Discharge in the Network Model can be represented as follows:

$$Q(t) = |A|^{-1} \int_A M \left[ t - \frac{d_o(x)}{v_o} - \frac{d_i(x)}{v_i}, x \right] dx, \quad (2)$$

where  $A$  is the domain of the drainage basin above the specified location,  $M(t, x)$  is the runoff rate ( $\text{mm h}^{-1}$ ) at time  $t$  and location  $x$  ( $\in A$ ),  $d_o(x)$  denotes the distance from  $x$  to the closest stream channel, and  $d_i(x)$  denotes the channel distance from  $x$  to the outlet of the basin specified by the region  $A$ . The total flow distance from  $x$  to the basin outlet is  $d_o(x) + d_i(x)$ . The drainage network for the Menomonee River basin was extracted from a 30-m Digital Elevation Models data using an area threshold criterion; the aggregate drainage density of the extracted drainage network is  $1.7 \text{ km km}^{-2}$ . The runoff rate  $M(t, x)$  is computed from the rainfall rate  $R(t, x)$  ( $\text{mm h}^{-1}$ ) using the Green-Ampt infiltration model with moisture redistribution [see Ogden and Saghaian (1997) for algorithm details]. Runoff is assumed to move over hillslopes at a uniform velocity  $v_o$  and through the channel system at velocity  $v_i$  [see Rodriguez-Iturbe and Rinaldo (1997) for discussion of similar models]. Giannoni et al. (2003) present sensitivity anal-

TABLE 2. Summary of flood events in Underwood Creek.

Event	Total rainfall (mm)	Total runoff (mm)	Runoff ratio	Peak discharge ( $\text{m}^3 \text{ s}^{-1}$ )	Peak unit discharge ( $\text{m}^3 \text{ s}^{-1} \text{ km}^{-2}$ )
21–22 Jun 1997	111	62	0.56	130	2.56
2–3 Jul 1997	33	10	0.30	56	1.10
6–7 Aug 1998	131	93	0.70	212	4.16
21–22 Jul 1999	60	24	0.40	92	1.82

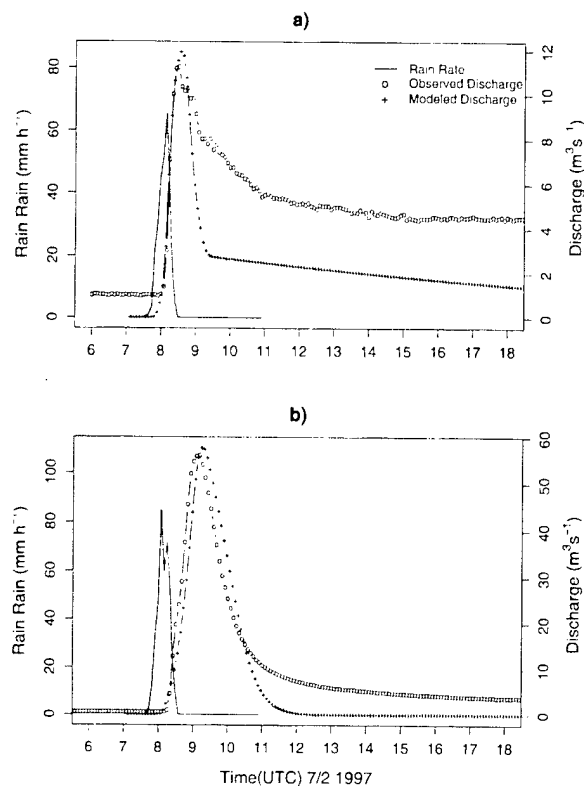


FIG. 12. Modeled and observed hydrographs for (a) Menomonee Falls and (b) Underwood Creek 2 Jul 1997. Solid line represents basin-averaged rain rate.

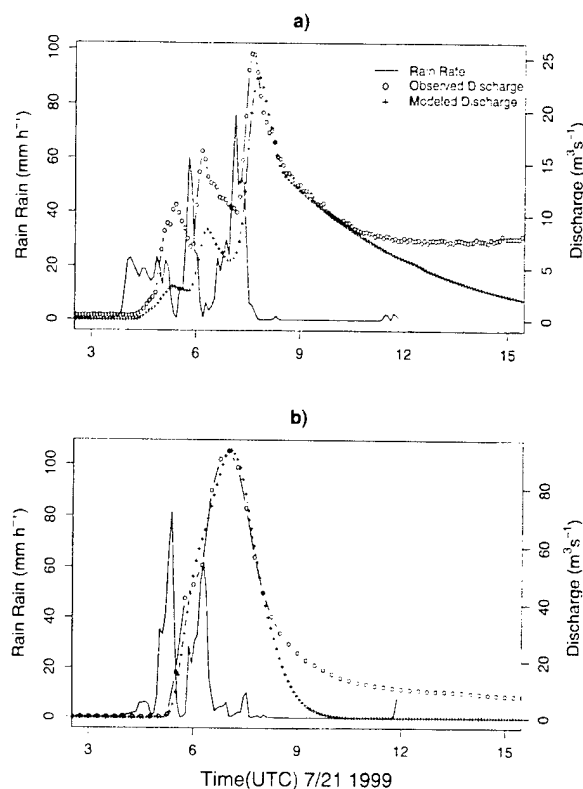


FIG. 13. Modeled and observed hydrographs for (a) Menomonee Falls and (b) Underwood Creek 21–22 Jul 1999. Solid line represents basin-averaged rain rate.

yses of model results to spatial and temporal averaging of rainfall fields.

The 2 July 1997 flood reflects basin response to a unit pulse of rainfall. Model results for Underwood Creek reproduced the flood peak magnitude and timing, as well as the structure of the rising and falling limbs of the hydrograph (Fig. 12b). For Menomonee Falls, it is possible to reproduce the peak magnitude and time to peak, but not the receding portion of the hydrograph (Fig. 12a). The results for Menomonee Falls are consistent with a rapid, Hortonian response in the small, urbanized portion of the basin near the basin outlet (note also water balance analyses in Tables 1 and 2 and discussion below). The slow, attenuated response at Menomonee Falls is due to a combination of non-Hortonian runoff production mechanisms from agricultural and residential portions of the basin and the response of detention basins in the residential areas of the basin.

The July 1999 storm provides a more complex response to several pulses of rainfall in both basins. The Underwood Creek hydrograph can be accurately reproduced but the Menomonee Falls hydrograph cannot (Fig. 13). The model response for Menomonee Falls reproduces the peak discharge and time to peak, but severely underestimates preceding peaks and is unable to capture the falling limb of the hydrograph. The ob-

served hydrograph shows a sharp peak associated with each of the pulses of rainfall. The inability of the model to capture all of the hydrograph peaks is likely due to an inadequate representation of the area producing the peak response.

A notable feature of the Menomonee Falls response is that the lag-to-peak (time difference between peak discharge and time centroid of rainfall) is shorter than for Underwood Creek (recall that the drainage area for Menomonee Falls is 90 km<sup>2</sup>; for Underwood Creek the drainage area is 47 km<sup>2</sup>). These results support the conclusion presented above that peak response at Menomonee Falls is determined by urbanized portions of the lower watershed (Fig. 1). Runoff production for the remainder of the basin is dominated by non-Hortonian mechanisms and is characterized by a highly attenuated response, relative to the impervious portion of the basin. As noted above, detention basins in areas of residential land use also play a significant role in the attenuated response of the basin. Sensitivity to temporal and spatial variability of rainfall is highest in the small, impervious portion of the Menomonee Falls basin. In regions dominated by non-Hortonian runoff production mechanisms, sensitivity of flood response to spatial and temporal variability is greatly reduced. Storm total rainfall plays a

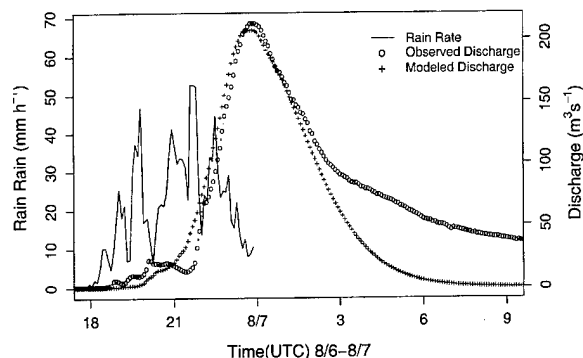


FIG. 14. Modeled and observed hydrographs for Underwood Creek 6-7 Aug 1998. Solid line represents basin-averaged rain rate.

far greater role in determining flood response in these portions of the basin.

For Underwood Creek, the contrasts in flood response between the June 1997 and August 1998 storms are tied to spatial and temporal variability of rainfall rate over the basin, and not basin-averaged storm total rainfall. Structure and motion of the August 1998 storms resulted in a single peak hydrograph (Fig. 14), in which the principal storm elements contributed to peak response [see Smith et al. (2000, 2001, and 2002) and Sturdevant-Rees et al. (2001) for additional discussion of the role of storm structure and motion for extreme flood response].

Flood response in the Menomonee River basin to the 21 June 1997 storm (see Fig. 3) represents a complex interplay of space-time rainfall variability and heterogeneous land surface response. The multippeak structure of the flood hydrograph reflects the quasistationary organization of storm elements and contrasts in runoff production mechanisms over the basin. The peak discharge is primarily associated with Hortonian runoff production in the lower, urbanized portion of the watershed. The final peak, which is characteristic in timing and structure of flood response for other events, results from non-Hortonian mechanisms in the upper basin. Heterogeneous land surface response accentuates the role of space-time variability of rainfall for extreme flood response.

#### 4. Summary and observations

The 21 June 1997 and 6 August 1998 storms were organized systems of thunderstorms that produced record flooding in the Menomonee River basin and its tributaries. The storms exhibited contrasts in structure, motion, and magnitudes of rainfall rates. Scaling analyses based on 1 km, 5-min radar rainfall fields illustrate the contrasting structure and evolution of rainfall for the two events.

Contrasting storm properties between the June 1997 and August 1998 storms resulted in differences in extreme flood response, especially in the most urbanized

area of the Menomonee River basin. Although storm total rainfall in Underwood Creek ranged only from 111 to 131 mm for the events, timing and magnitude of flood peaks differed markedly for the events. The mode of convective organization plays an important role in flood response, especially for small urban watersheds. Microphysical controls of extreme rainfall rates from convective systems also play an important role in extreme flood response of small urban watersheds.

There are large contrasts in flood response in the Menomonee River basin between regions of contrasting land use and cover. Unit discharge flood peaks in Underwood Creek are 5-10 times larger than those in the upper basin. Flood response for the upper basin is characterized by a fast-responding peak, which is generated from a small impervious region close to the basin outlet. For the Menomonee River above Menomonee Falls runoff processes controlling flood peaks are largely decoupled from processes controlling flood volume. Regional flood response of the Menomonee River basin to extreme rainfall is strongly dependent on both space-time variability of rainfall rate and heterogeneities of runoff production.

**Acknowledgments.** This research was funded in part by the U.S. Army Research Office (Grant No. DAAD19-99-1-0163), NASA (NAG5-7544), the National Science Foundation (EAR99-09696 and EAR-0208269), and the National Weather Service. This support is gratefully acknowledged.

#### REFERENCES

- Anagnostou, E. N., W. F. Krajewski, and J. A. Smith, 1999: Uncertainty quantification of mean-areal radar-rainfall estimates. *J. Atmos. Oceanic Technol.*, **16**, 206-215.
- Baeck, M. L., and J. A. Smith, 1995: Climatological analysis of manually digitized radar data for the United States east of the Rocky Mountains. *Water Resour. Res.*, **31**, 3033-3049.
- , and —, 1998: Estimation of heavy rainfall by the WSR-88D. *Wea. Forecasting*, **13**, 416-436.
- Chappell, C., 1989: Quasistationary convective events. *Mesoscale Meteorology and Forecasting*, P. Ray, Ed., Amer. Meteor. Soc., 289-310.
- Ciach, J. G., and W. F. Krajewski, 1999: On the estimation of radar rainfall error variance. *Adv. Water Resour.*, **22**, 585-595.
- Doswell, C. A., III, H. E. Brooks, and R. A. Maddox, 1996: Flash flood forecasting: An ingredients-based methodology. *Wea. Forecasting*, **11**, 560-581.
- Fulton, R. A., J. P. Breidenbach, D.-J. Seo, D. A. Miller, and T. O'Bannon, 1998: The WSR-88D rainfall algorithm. *Wea. Forecasting*, **13**, 377-395.
- Giannoni, F., J. A. Smith, Z. Zhang, and G. Roth, 2003: Hydrologic modeling of extreme floods using radar rainfall observations. *Adv. Water Resour.*, **26**, 195-203.
- Graf, W. L., 1977: Network characteristics in suburbanizing streams. *Water Resour. Res.*, **13**, 459-463.
- Leopold, L. B., 1968: Hydrology for urban land planning—A guidebook on the hydrologic effects of urban land use. U.S. Geological Survey Circular 554, 18 pp.
- Maddox, R. A., L. R. Hoxit, C. F. Chappell, and F. Caracena, 1978: Comparison of meteorological aspects of the Big Thompson and Rapid City flash floods. *Mon. Wea. Rev.*, **106**, 375-389.

- Morrison, J. E., and J. A. Smith, 2001: Scaling properties of flood peaks. *Extremes*, **4**, 5–22.
- Ogden, F. L., and B. Sagharian, 1997: Green and Ampt infiltration with redistribution. *J. Irrig. Drain. Eng.*, **123**, 386–393.
- , H. O. Sharif, S. U. S. Senarath, J. A. Smith, M. L. Baeck, and J. R. Richardson, 2000: Hydrologic analysis of the Fort Collins, Colorado, flash flood of 1997. *J. Hydrol.*, **228**, 82–100.
- Orville, R. E., and A. C. Silver, 1997: Lightning ground flash density in the contiguous United States, 1992–1995. *Mon. Wea. Rev.*, **125**, 631–638.
- Perica, S., and E. Foufoula-Georgiou, 1996: Linking of scaling and thermodynamic parameters of rainfall. *J. Geophys. Res.*, **101** (D3), 7431–7448.
- Petersen, W. A., and Coauthors, 1999: Mesoscale and radar observations of the Fort Collins flash flood of 28 July 1997. *Bull. Amer. Meteor. Soc.*, **80**, 191–216.
- Potter, K. W., 1991: Hydrological impacts of changing land management practice in a moderate-sized agricultural catchment. *Water Resour. Res.*, **27**, 845–855.
- Rodriguez-Iturbe, I., and A. Rinaldo, 1997: *Fractal River Basins*. Cambridge University Press, 547 pp.
- Roebber, P. J., and J. Eise, 2001: The 21 June 1997 flood: Storm-scale simulations and implications for operational forecasting. *Wea. Forecasting*, **16**, 197–218.
- Smith, J. A., M. L. Baeck, M. Steiner, and A. J. Miller, 1996: Catastrophic rainfall from an upslope thunderstorm in the Central Appalachians: The Rapidan Storm of June 27, 1995. *Water Resour. Res.*, **32**, 3099–3113.
- , J. E. Morrison, and P. Sturdevant-Rees, 2000: Catastrophic rainfall and flooding in Texas. *J. Hydrometeorol.*, **1**, 5–25.
- , Y. Zhang, and C. A. Doswell III, 2001: Extreme rainfall and flooding from supercell thunderstorms. *J. Hydrometeorol.*, **2**, 469–489.
- , P. Sturdevant-Rees, J. E. Morrison, D. Turner-Gillespie, and P. Bates, 2002: The regional hydrology of extreme floods in an urbanizing drainage basin. *J. Hydrometeorol.*, **3**, 267–282.
- Sturdevant-Rees, P. L., J. A. Smith, J. Morrison, and M. L. Baeck, 2001: Tropical storms and the flood hydrology of the Central Appalachians. *Water Resour. Res.*, **37**, 2143–2168.
- Vieux, B. E., and P. B. Bedient, 1998: Estimation of rainfall for flood prediction from WSR-88D reflectivity: A case study, 17–18 October 1994. *Wea. Forecasting*, **13**, 407–415.
- Zhang, Y., J. A. Smith, and M. L. Baeck, 2001: The hydrology and hydrometeorology of extreme floods in the Great Plains of eastern Nebraska. *Adv. Water Resour.*, **24**, 1037–1050.



## Attenuating reaches and the regional flood response of an urbanizing drainage basin

Daniel F. Turner-Gillespie<sup>a</sup>, James A. Smith<sup>a,\*</sup>, Paul D. Bates<sup>b</sup>

<sup>a</sup> Department of Civil and Environmental Engineering, Princeton University, Princeton, NJ 08544, USA

<sup>b</sup> School of Geographical Sciences, University of Bristol, Bristol, UK

Received 9 January 2002; received in revised form 20 January 2003; accepted 22 January 2003

### Abstract

The Charlotte, North Carolina metropolitan area has experienced extensive urban and suburban growth and sharply increasing trends in the magnitude and frequency of flooding. The hydraulics and hydrology of flood response in the region are examined through a combination of numerical modeling studies and diagnostic analyses of paired discharge observations from upstream–downstream gaging stations. The regional flood response is shown to strongly reflect urbanization effects, which increase flood peaks and decrease response times, and geologically controlled attenuating reaches, which decrease flood peaks and increase lag times. Attenuating reaches are characterized by systematic changes in valley bottom geometry and longitudinal profile. The morphology of the fluvial system is controlled by the bedrock geology, with pronounced changes occurring at or near contacts between intrusive igneous and metamorphic rocks. Analyses of wave celerity and flood peak attenuation over a range of discharge values for an 8.3 km valley bottom section of Little Sugar Creek are consistent with Knight and Shiono's characterization of the variation of flood wave velocity from in-channel conditions to valley bottom full conditions. The cumulative effect of variation in longitudinal profile, expansions and contractions of the valley bottom, floodplain roughness and sub-basin flood response is investigated using a two-dimensional, depth-averaged, finite element hydrodynamic model coupled with a distributed hydrologic model. For a 10.1 km stream reach of Briar Creek, with drainage area ranging from 13 km<sup>2</sup> at the upstream end of the reach to 49 km<sup>2</sup> at the downstream end, it is shown that flood response reflects a complex interplay of hydrologic and hydraulic processes on hillslopes and valley bottoms.

© 2003 Published by Elsevier Science Ltd.

### 1. Introduction

Urbanization has altered the timing and magnitude of flood peaks in the Charlotte, North Carolina metropolitan region ([10,24,26]; see Fig. 1 for location map). Hydrologic analyses for the most intensely urbanized portion of the region (Little Sugar Creek above gaging station 1; see Figs. 1 and 2) suggest more than a doubling of flood peak magnitudes due to urbanization effects for a short duration (2–4 h) moderate intensity (50 mm h<sup>-1</sup> peak 5-min rain rates; 50 mm storm total accumulation) storm on 9 April 1998 [24,26]. For the same event, flood peak magnitudes in the lower portion of Little Sugar Creek (between gages 4 and 5 in Fig. 2) decreased by approximately a factor of two (Fig. 3). In this paper we examine the regional flood response of

Little Sugar Creek and surrounding basins in terms of changing hydrologic response associated with urbanization and geologic controls of flood wave attenuation.

The importance of flood wave attenuation has been recognized for many years. Following the Ohio River flood of March 1913, Arthur Morgan observed that “the Miami River, like many other streams, is proportioned not for carrying excessive flood water. . . In case of even moderate floods, that occur every 1 or 2 years, lowlands lying along the river are overflowed” [19]. The flood control plan developed by Morgan for the Miami River basin reflected, and built upon, an intuitive understanding of the role of floodplains. Floodplain storage, variations in channel and floodplain roughness, and channel and valley bottom morphology all contributed to the comprehensive flood control plan for the Miami River. Morgan's intuitive understanding of flood wave propagation through a valley bottom reach has been supplemented by more rigorous scientific advances (see, for example, [1,3,13,18]). Flood wave attenuation has

\* Corresponding author.

E-mail address: [jsmith@princeton.edu](mailto:jsmith@princeton.edu) (J.A. Smith).



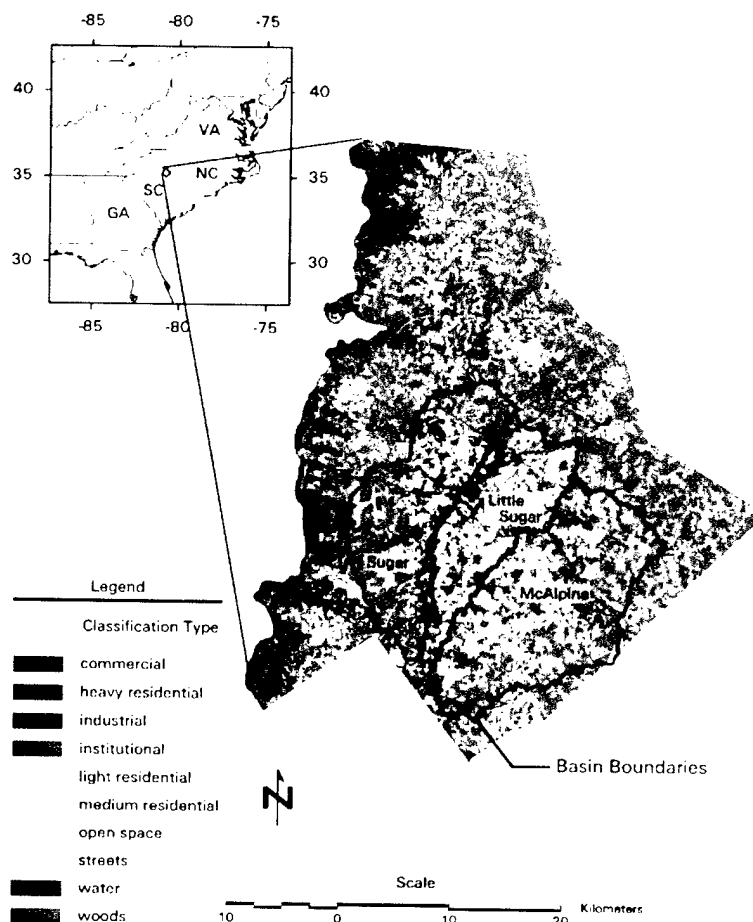


Fig. 1. Study area location and land use/land cover map showing the basin boundaries of Little Sugar Creek, Sugar Creek and McAlpine Creek. Drainage area is 128 km<sup>2</sup> for the Little Sugar Creek basin, 169 km<sup>2</sup> for the Sugar Creek basin and 239 km<sup>2</sup> for the McAlpine Creek basin.

been extensively examined in terms of energy losses resulting from boundary friction, secondary flow, turbulence and constriction-expansion of the flow field (see [25]; for a review). Despite these advances, it remains a difficult problem to characterize attenuating valley bottom reaches [27,28], especially for settings like the Little Sugar Creek basin in which the regional flood response reflects a complex interplay of valley bottom attenuation effects and heterogeneous hydrologic response due to urbanization.

The Little Sugar Creek basin (Figs. 1 and 2) is located within the Piedmont physiographic province. It is bounded on the west by Sugar Creek and on the east by McAlpine Creek (Figs. 1 and 2). The river downstream of the confluence of these three tributaries is named Sugar Creek and we use "Sugar Creek" both for the western tributary basin and the larger basin comprising Little Sugar, McAlpine and Sugar Creek. The region has low relief consisting of rounded ridges and valleys underlain by intrusive igneous rock with zones of metamorphic rock [8]. Regional studies in the North Carolina Piedmont and Blue Ridge provinces have

demonstrated profound bedrock controls of stream longitudinal profiles [9] and depth of soil weathering [5].

Analyses focus on two stream reaches within the Little Sugar Creek basin. The "Archdale–Pineville" reach comprises an 8.3 km section between the Archdale (USGS ID 02146507) and Pineville (USGS ID 02146530) stream gaging stations (gages 4 and 5, respectively, in Fig. 2). The drainage area is 111 km<sup>2</sup> above the Archdale gage and 128 km<sup>2</sup> above the Pineville gage. The intervening drainage area between the two gaging stations is relatively small, implying that channel–floodplain processes will typically play a dominant role in determining differences in flood response properties between the Archdale and Pineville gaging stations. Analyses of 15-min discharge data from both stations for 96 flood events are used to characterize flood wave attenuation in the Archdale–Pineville reach.

The Briar Creek reach is 10.1 km in length and bounded at the upper end by the Shamrock gaging station (USGS ID 0214642825; gage 6 in Fig. 2) and on the lower end by the Colony Road gaging station (USGS ID 0214645022; gage 2 in Figs. 2 and 3).

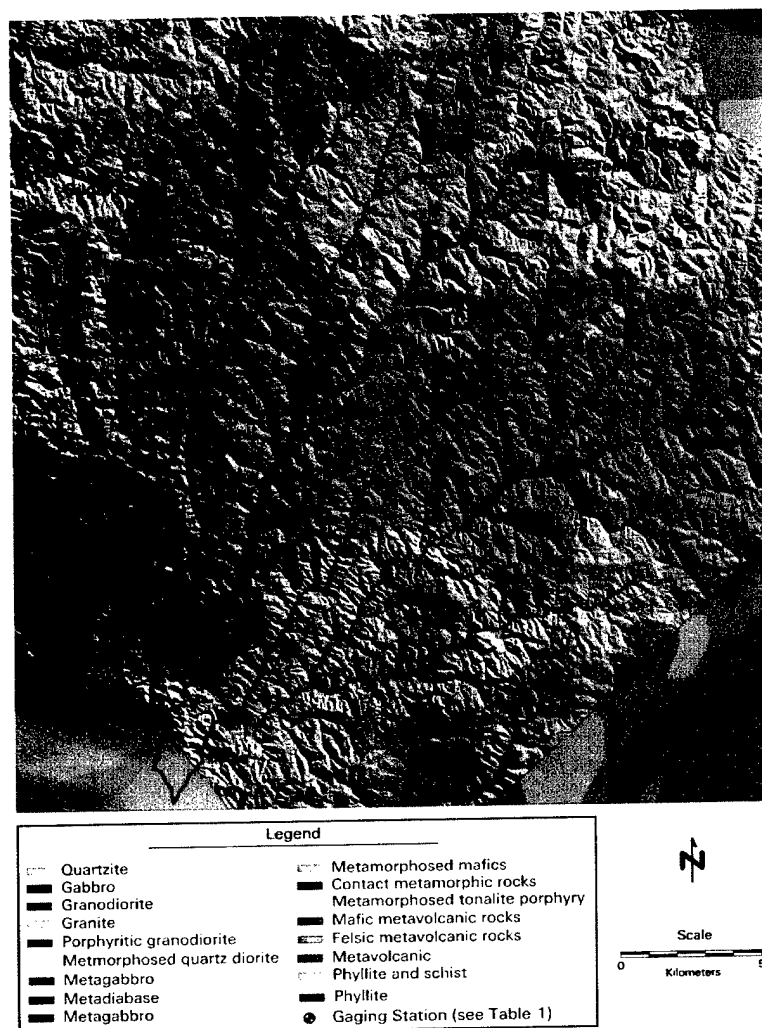


Fig. 2. Bedrock geology of the Charlotte metropolitan area (see [8]). Stream gage locations used in the paper are identified by numbers (see text for additional details).

Drainage area ranges from 13 km<sup>2</sup> above the Shamrock gage to 49 km<sup>2</sup> for the basin above Colony Road. The discharge at Colony Road for the 9 April 1998 flood (Fig. 3) peaked several hours after the downstream Archdale gaging station suggesting that attenuation may play an important role in flood response for Briar Creek.

To analyze flood response in the Briar Creek reach, a two-dimensional depth-averaged hydrodynamic model of the channel–floodplain system (RMA-2; see [3,7,18]) has been coupled with a distributed hydrologic model for tributary inflow [21,26]. The coupled modeling system provides a useful tool for analyses of the integrated effects of hydrologic and hydraulic processes on flood-wave attenuation. Coupled models of this type are of potential utility for regional design of urban flood control systems and for short-term (0–12 h) forecasting of flood inundation (see, for example, developments in [14,15,17]).

## 2. Analyses of flood wave attenuation

Flood events on lower Little Sugar Creek between the Archdale and Pineville gages (gages 4 and 5, respectively, in Figs. 2 and 3) were analyzed for the period June 1997 until June 2000 using 15-min discharge data from the two gaging stations. During this period 96 flood events had peak discharge values greater than 14 m<sup>3</sup> s<sup>-1</sup> at the upstream gage. For each event, the peak discharge at both stations and the time between peak discharge at the two stations, or lag time, were computed. For multiple peak events, where the hydrographs were not separable, only the largest peak was considered. Runoff volumes for the two basins were computed for each event and used as a quality control check on the discharge measurements.

There is a reversal in the lag time–discharge relationship in the lower Little Sugar Creek which occurs at approximately the bankfull discharge of 80 m<sup>3</sup> s<sup>-1</sup>

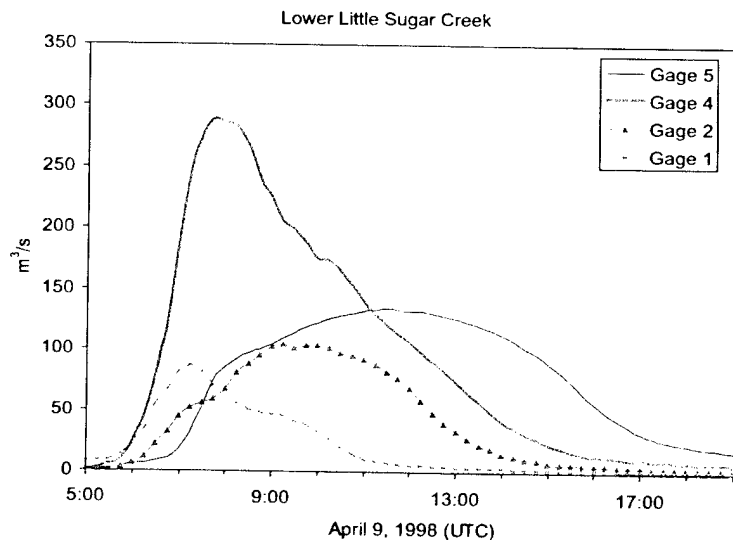


Fig. 3. Observed hydrographs from the 9 April 1998 flood event (see Fig. 2 for gage locations) for stations in the Little Sugar Creek basin. Discharge is given in  $\text{m}^3 \text{s}^{-1}$  and time is in universal time coordinated (UTC).

(Fig. 4a). Determination of bankfull discharge was based on analyses of width, depth and velocity observations from direct discharge measurements at the Archdale gaging station and field surveys. The  $80 \text{ m}^3 \text{s}^{-1}$  value for bankfull discharge corresponds to a slope break in the width discharge relationship. When discharge is less than bankfull, the lag time generally decreases with increasing discharge. Lag time increases with discharge for values greater than bankfull conditions up to the maximum discharge in the data set. These results are consistent with theoretical analyses of Knight and Shiono [16], in which it is concluded that wave speed peaks between  $2/3$  bankfull depth and the bankfull depth. Wave speed is at a minimum at some shallow overbank depth where momentum exchange between main channel and floodplain is at a maximum and acts as an energy loss mechanism to slow the flow.

Knight and Shiono [16] also show that at very large stage the channel and floodplain begin to act as a single unit, dominated by floodplain flow, and the wave speed again begins to increase. This feature was not observed for the lag time analyses, which include events with return intervals less than 25 years.

Lag time analyses can be converted to analyses of wave celerity by dividing the measured flow distance by the lag time. Wave celerity for the largest event on the lower Little Sugar Creek was approximately  $0.6 \text{ m s}^{-1}$ . Flood wave celerity at bankfull stage is approximately  $1.3 \text{ m s}^{-1}$ .

The ratio between the upstream and downstream discharge generally increases for events that exceed bankfull discharge (Fig. 4b). The peak discharge ratios between the downstream and upstream gages for the three largest events with discharge hydrographs at both

stations are 0.58 (23 January 1999), 0.65 (27 July 1998), and 0.54 (9 April 1998). The 27 July 1998 flood, which had a peak discharge of  $250 \text{ m}^3 \text{s}^{-1}$  (Fig. 4), had somewhat less peak attenuation and shorter lag time than the other two events. The relatively large downstream discharge (and short lag time; Fig. 4a) for the July 1998 flood resulted from anomalous storm motion that concentrated heavy rainfall in the lower basin between the two stream gaging stations [24].

The record flood in the Little Sugar Creek basin occurred 23 July 1997 and had a measured peak discharge at Pineville ( $317 \text{ m}^3 \text{s}^{-1}$ ) that was 82% of the measured peak discharge at Archdale ( $385 \text{ m}^3 \text{s}^{-1}$ ; return interval for the Archdale peak discharge exceeded 100 years; see [23,24]). The Pineville peak discharge estimate was derived from an indirect discharge measurement, which was based on surveyed high-water marks and hydraulic computations using Manning's equation [23]. The relatively large Pineville Archdale peak discharge ratio suggests that flood wave attenuation is markedly diminished as Archdale discharge increases from 300 to  $400 \text{ m}^3 \text{s}^{-1}$ . This conclusion is consistent with Knight and Shiono's [16] analysis and places the transition zone between maximum energy loss (due to momentum exchange between channel and floodplain) and increasing wave speed at stages corresponding to discharges between 300 and  $400 \text{ m}^3 \text{s}^{-1}$  at Archdale. These peak discharges have return intervals between 10 and 100 years.

Flood wave attenuation is a prominent feature of flood response throughout the Charlotte metropolitan region. Stream gaging stations in Sugar Creek to the west of Little Sugar Creek (Figs. 1 and 2) are not as ideally positioned as the Archdale-Pineville pair for characterizing attenuation, but the importance of

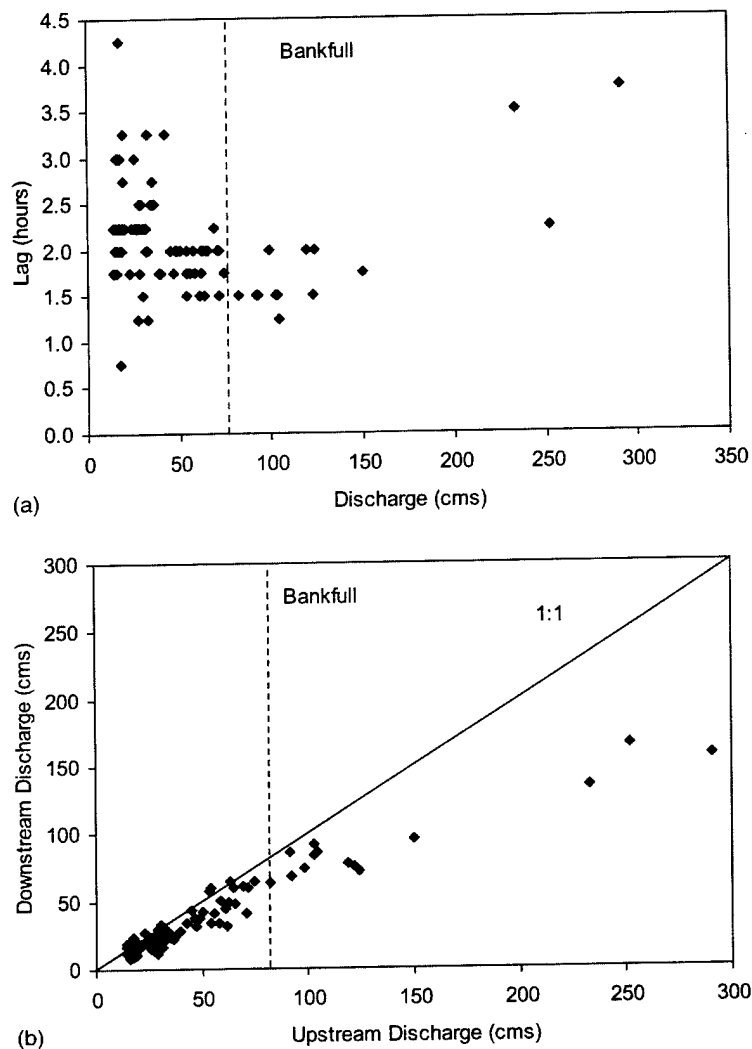


Fig. 4. Comparison of flood response along lower Little Sugar Creek between gage 4 (upstream) and gage 5 (downstream): (a) shows the lag time (h) between the gages in relation to discharge at the upstream gage and (b) shows the discharge at the upstream gage versus discharge at the downstream gage. The discharge corresponding to bankfull stage (approximately  $80 \text{ m}^3 \text{ s}^{-1}$ ) is identified by vertical dashed lines.

attenuation can be readily identified for discharge observations (Fig. 5). For the 23 July 1997 flood, the peak discharge of  $330 \text{ m}^3 \text{ s}^{-1}$  in the Sugar Creek basin at  $80 \text{ km}^2$  (Irwin Creek [gage 9]; Fig. 2) was 20% larger than the peak discharge at  $170 \text{ km}^2$  (Sugar Creek at Pineville [gage 10]; Fig. 2). This corresponds to a decrease in unit discharge from  $4.1 \text{ m}^3 \text{ s}^{-1} \text{ km}^{-2}$  at the upstream station to  $1.6 \text{ m}^3 \text{ s}^{-1} \text{ km}^{-2}$  at the downstream station. In Turner-Gillespie [26], the spatial patterns of attenuating stream reaches are examined in terms of geologic controls of valley bottom form and morphology. We examine these issues below for Little Sugar Creek and Briar Creek.

Hack [9] used observations from the Piedmont and Blue Ridge physiographic provinces, including the Charlotte metropolitan region, to demonstrate the controls of bedrock geology and differential uplift on longitudinal profiles of rivers. At the smaller scale of the

Sugar Creek basin, bedrock geology exerts strong controls on both longitudinal profile and valley bottom morphology of streams (Figs. 1 and 2). Furthermore, these features are linked with observed patterns of floodwave attenuation.

The elevation profile of the channel and the width of the valley bottom were calculated along streams in the Sugar Creek basin and related to bedrock geology. A 10-m resolution digital elevation model (DEM) was created via linear rubber-sheeting from elevation data provided by Mecklenburg County, North Carolina. The valley bottom width is based on the Federal Emergency Management Agency's (FEMA) 100-year floodplain. The drainage network was derived from the Mecklenburg County DEM using an area-threshold algorithm.

In general, the reaches through metagabbro and metavolcanic rocks have a higher valley bottom width

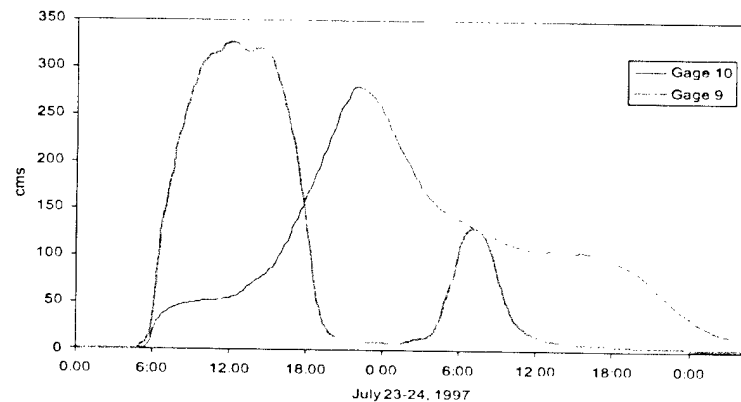


Fig. 5. Flood hydrographs for upstream and downstream gaging stations in Sugar Creek. The discharge hydrographs are given for Irwin Creek (gage 9 in Fig. 2) and Sugar Creek (gage 10 in Fig. 2) on 23–24 July 1997.

than adjacent reaches (Table 1 and Fig. 6a–d). Reaches through granodiorite have areas of high slope resulting in a “stair-step” profile and are typically narrower than adjacent reaches. Reaches with pronounced attenuation, including lower Little Sugar Creek, lower Sugar Creek, McAlpine Creek, and Briar Creek (see Section 3), have geologically controlled areas of wide valley bottom and low stream slope (Figs. 2 and 6).

For the lower Little Sugar Creek reach between Archdale and Pineville (gages 4 and 5, respectively, in Figs. 3 and 6a), the valley bottom widens from 80 to 430 m as the stream crosses a contact between granodiorite and metagabbro. The slope of the reach between the Medical Center (1) and the Archdale (4) gages is 0.0023. The slope between the Archdale and Pineville (5) gages is 0.0010. Two hundred meters below the Archdale gage there is a sharp 2 m drop in the channel profile. Field reconnaissance indicates that the channel is bedrock-controlled at this location with extensive outcrops in the channel and floodplain.

Bedrock geology also exerts strong control on the valley bottom morphology of Briar Creek (Fig. 6b). As the stream flows from metavolcanic rocks into grandio-

rite, the valley bottom width decreases from 350 to 50 m over 3 km. The slope of the channel upstream of the granodiorite–metavolcanic contact is 0.0011 while downstream it is 0.0025. Much of Briar Creek between the Colony and Shamrock gages (gages 2 and 6, respectively, Figs. 2 and 6b) flows along the contact of metavolcanic rocks and granodiorite (in the lower portion) and metamorphosed quartz diorite (in the upper portion; see Fig. 2). As the river crosses the region between these two zones there is a 3.2 m drop in elevation of the channel (labeled “\*” in Fig. 6b).

### 3. Modeling studies of flood response

In this section, we examine the effects of channel and valley bottom morphology and sub-basin hydrologic response on flood peak attenuation using a two-dimensional hydraulic model of the channel and floodplain and a distributed hydrologic model. The study reach is the 10.1 km section of Briar Creek between the stream gage at Shamrock Road (gage 6 in Fig. 2) and the gage at Colony Road (gage 2 in Fig. 2). Hydraulic and hydrologic modeling are carried out for the 23 September 2000 flood event. The peak discharge at the Shamrock gage was  $88 \text{ m}^3 \text{ s}^{-1}$  ( $5.7 \text{ m}^3 \text{ s}^{-1} \text{ km}^{-2}$  unit discharge). At the downstream gage the peak discharge was  $63 \text{ m}^3 \text{ s}^{-1}$  ( $1.3 \text{ m}^3 \text{ s}^{-1} \text{ km}^{-2}$  unit discharge). The peak discharge at the downstream gage was the fourth largest in a 6-year record. At the upstream gage, the peak discharge was the largest in a 3-year record. Unlike the lower reach of Little Sugar Creek (see Section 2), timing and magnitude of tributary contributions play a major role in determining the flood response of the 10.1 km channel reach.

The Briar Creek floodplain reflects a diverse land use and cover with approximately 48% forest, 30% residential, 9% high-intensity development, 12% grassland, and 1% ponds. Development of the floodplain is associated with reduction in the hydraulic roughness. Width

Table 1  
Valley bottom (100-year floodplain) width and slope for Briar Creek, McAlpine Creek and Little Sugar Creek (see Fig. 2 for geologic divisions)

Creek name with rock type	Average slope (m/m)	Average width (m)
<i>Briar Creek</i>		
Metavolcanic	0.0014	265
Granodiorite	0.0026	127
<i>McAlpine Creek</i>		
Metavolcanic	0.0008	325
Granite	0.0011	195
<i>Little Sugar Creek</i>		
Metamorphosed quartz diorite	0.0029	164
Granodiorite	0.0023	122

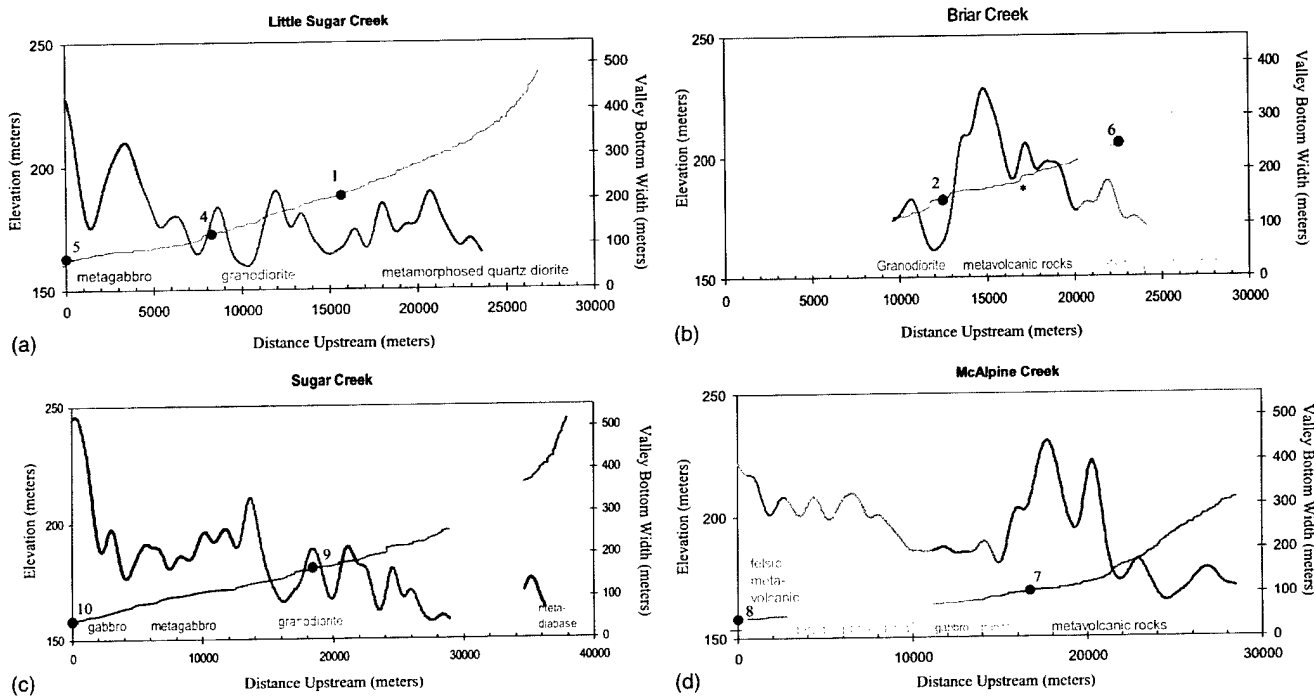


Fig. 6. Channel elevation profile (thin line) and valley bottom width (thick line) in relation to bedrock geology (summarized along horizontal axis; see also Fig. 2) for: (a) Little Sugar Creek, (b) Briar Creek, (c) Sugar Creek and (d) McAlpine Creek. Black dots and reference numbers correspond to gage locations shown in Fig. 2. The \* in (b) marks the location on Briar Creek where upstream the channel flows along the boundary of metavolcanic rock and metamorphosed quartz diorite while downstream of this point along metavolcanic rock and granodiorite (see Fig. 2).

of the floodplain between Shamrock and Colony Road varies from a maximum of 350 m to a minimum of 50 m in constricted reaches. As discussed in the previous section, the channel slope and valley bottom width are closely related to the bedrock geology.

The flood response of Briar Creek was investigated using RMA-2, a two-dimensional, depth-averaged, finite element hydrodynamic model (see [3,7,29] for similar applications of RMA-2). The governing equations are

$$h \frac{\partial u}{\partial t} + hu \frac{\partial u}{\partial x} + hv \frac{\partial u}{\partial y} - \frac{h}{\rho} \left( E_{xx} \frac{\partial^2 u}{\partial x^2} + E_{xy} \frac{\partial^2 u}{\partial y^2} \right) + gh \left( \frac{\partial a}{\partial x} + \frac{\partial h}{\partial x} \right) + \frac{g u n^2 (u^2 + v^2)^{1/2}}{h^{1/3}} = 0 \quad (1)$$

$$h \frac{\partial v}{\partial t} + hu \frac{\partial v}{\partial x} + hv \frac{\partial v}{\partial y} - \frac{h}{\rho} \left( E_{yx} \frac{\partial^2 v}{\partial x^2} + E_{yy} \frac{\partial^2 v}{\partial y^2} \right) + gh \left( \frac{\partial a}{\partial y} + \frac{\partial h}{\partial y} \right) + \frac{g v n^2 (u^2 + v^2)^{1/2}}{h^{1/3}} = 0 \quad (2)$$

$$\frac{\partial h}{\partial t} + u \frac{\partial h}{\partial x} + v \frac{\partial h}{\partial y} = -h \left( \frac{\partial u}{\partial x} + \frac{\partial v}{\partial y} \right) \quad (3)$$

where

$t$  time (s)  
 $x, y$  horizontal coordinates (m)

$u, v$  depth-averaged velocity in  $x$ - and  $y$ -directions, respectively ( $\text{m s}^{-1}$ )  
 $h$  flow depth (m)  
 $\rho$  density of fluid ( $\text{kg m}^{-3}$ )  
 $E$  eddy viscosity coefficient  
for  $xx$  = normal direction on  $x$ -axis surface  
for  $yy$  = normal direction on  $y$ -axis surface  
for  $xy$  and  $yx$  = shear direction on each surface  
 $g$  gravitational acceleration ( $9.8 \text{ m s}^{-2}$ )  
 $a$  elevation of bottom (m)  
 $n$  Manning's roughness coefficient

Elevation data from Mecklenburg County, the FEMA 100-year floodplain map, and digital orthophoto quads were used as guides in mesh generation. The mesh (Fig. 7) consists of 5880 nodes and 1845 elements. The channel is represented as a trapezoid with a flat bottom and sloping sides. The longitudinal lines of the elements tended to be parallel to the channel, so that floodwater advances and retreats smoothly. The RMA-2 marsh porosity option was utilized to cope with wetting and drying of elements (see [4,6] for discussion). A spatially constant eddy viscosity value of  $1440 \text{ N s m}^{-2}$  was used. Roughness coefficients were initially set at 0.030 for the channel and 0.055 for the floodplain (based on [2]).

A transient upstream boundary condition, using observed discharge data, was implemented. The downstream boundary was located 600 m downstream of the

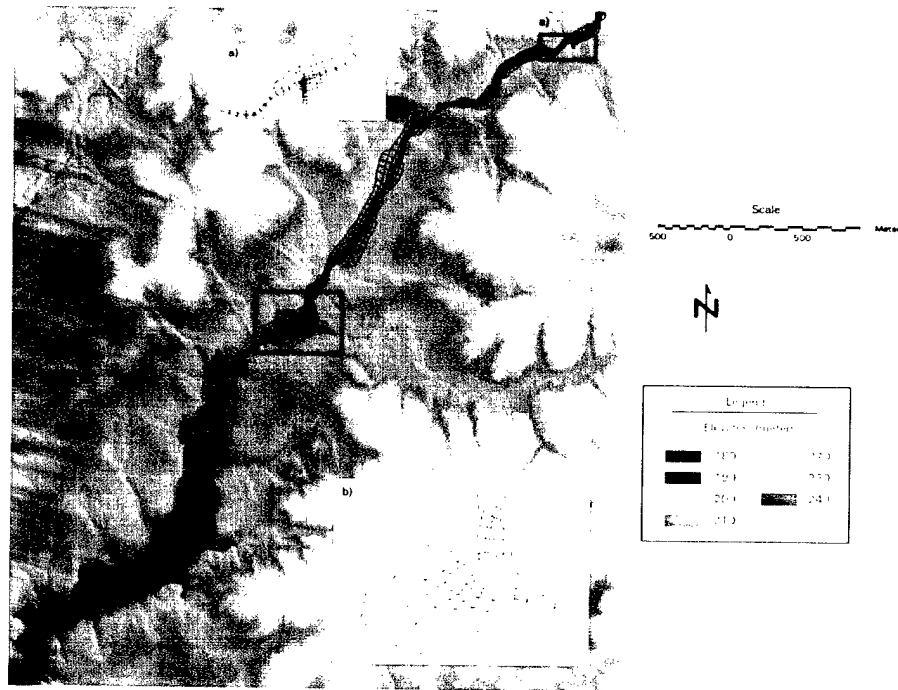


Fig. 7. Finite element mesh used for RMA-2 analyses. The background map illustrates topography of the domain. Insets show two of four tributaries modeled along the reach.

Colony stream gaging station. The mesh below the Colony gaging station was extended smoothly to the downstream boundary. A fixed head condition was implemented at the downstream boundary and had no significant impact on the model results at the Colony gaging station 600 m upstream. Discharge boundary conditions were implemented at major tributaries within the reach (Fig. 7) using model-derived hydrographs (as discussed below).

Tributaries located between the Shamrock and Colony gaging stations contributed 35% of the total runoff at the downstream gage (from 70% of the basin). The hydrographs of the intervening tributaries were generated using a distributed hydrologic model, the Network Model [20,21]. Discharge at the outlet of a drainage basin is represented as:

$$Q(t) = \int_A M \left( t - \frac{d_0(x)}{v_0} - \frac{d_1(x)}{v_1}, x \right) dx \quad (4)$$

where  $Q(t)$  denotes discharge ( $\text{m}^3 \text{s}^{-1}$ ) at time  $t(s)$ ,  $A$  is the domain of the drainage basin,  $x$  is a point within  $A$ ,  $d_0(x)$  is the distance (m) from  $x$  to the closest stream channel,  $v_0$  is the overland flow velocity ( $\text{m s}^{-1}$ ),  $d_1(x)$  is the distance (m) along the channel from  $x$  to the basin outlet,  $v_1$  is the channel flow velocity and  $M(t, x)$  is the runoff rate ( $\text{m s}^{-1}$ ) at time  $t$  and location  $x$ . The total flow distance from  $x$  to the basin outlet is  $d_0(x) + d_1(x)$ , the sum of the overland flow distance and the channel flow distance.

The Network Model partitions the drainage basin into hillslope and channel components. The drainage network for Briar Creek represented both natural and constructed elements of the drainage system (digital representations of the stormwater drainage system were obtained from the City of Charlotte).

The runoff rate  $M(t, x)$  ( $\text{mm h}^{-1}$ ) at time  $t$  and location  $x$  was computed from the rainfall rate  $R(t, x)$  and a Hortonian infiltration model (the Green–Ampt model with moisture redistribution [22]). The rainfall forcing  $R(t, x)$  for the 23 September 2000 events was represented as a spatially uniform, temporally varying field. The rainfall time series was computed as the average of two rain gages in the intervening drainage between the upstream and downstream stream gaging stations. The temporal resolution of rainfall observations is 5 min.

Soil properties were considered homogeneous except for the distinction between pervious and impervious regions. Saturated hydraulic conductivity values for the impervious region, which was computed from planimetric data provided by Mecklenburg County, were taken to be 0. The saturated hydraulic conductivity for the pervious portion of the basin was estimated to maintain the water balance of the reach. The hillslope and channel velocity parameters were taken to be 0.07 and  $5.0 \text{ m s}^{-1}$ , based on detailed analyses of hydrologic response in the upper portion of Little Sugar Creek [26]. The large channel velocity parameter is an artifact of representations of channel flow distances (channel

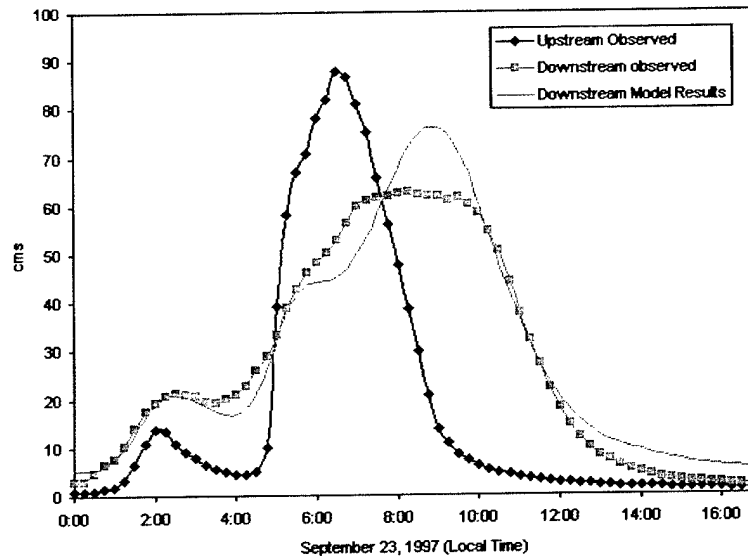


Fig. 8. Observed and model hydrographs for the Briar Creek reach are shown for the 23 September 2000 flood event. The observed upstream (denoted 6 in Fig. 2) hydrograph is denoted by filled diamonds and the observed downstream (denoted 2 in Fig. 2) hydrograph by filled squares.

velocities in the model are computed as flow distances along the channel network in a unit time; see [26]).

The coupled hydrologic and hydraulic model is able to reproduce many of the observed features of the hydrograph at the downstream gage (Fig. 8), including rise, recession and peak properties of the first peak and rise and recession properties of the main peak. The model does not reflect the extended period (more than 2 h) of constant discharge around the peak discharge from the stream gaging record. The differences in model peak response and observed peak response may be due to one or more of the following: (1) errors in representing the valley bottom topography, especially in the margins of the floodplain (see, for example, [17]) (2) roughness el-

ements associated with structures and vegetation (see, for example, [12]) and (3) errors in discharge measurement (see, for example, Potter and Walker [30]).

The coupled model is sensitive to changes in the velocity parameters of the hydrologic model (Fig. 9). Decreasing channel velocity from  $5 \text{ m s}^{-1}$  (Parameter Set 1 in Fig. 9) to  $2 \text{ m s}^{-1}$  (Parameter Set 2) and  $0.7 \text{ m s}^{-1}$  (Parameter Set 3) leads to large changes in the structure of model response for the first peak. A somewhat surprising result is that parameter sets representing less urbanized conditions result in higher peak discharges at the downstream location. Peak discharge increases by more than 10% ( $8.9 \text{ m}^3 \text{ s}^{-1}$ ) as channel velocity decreases from

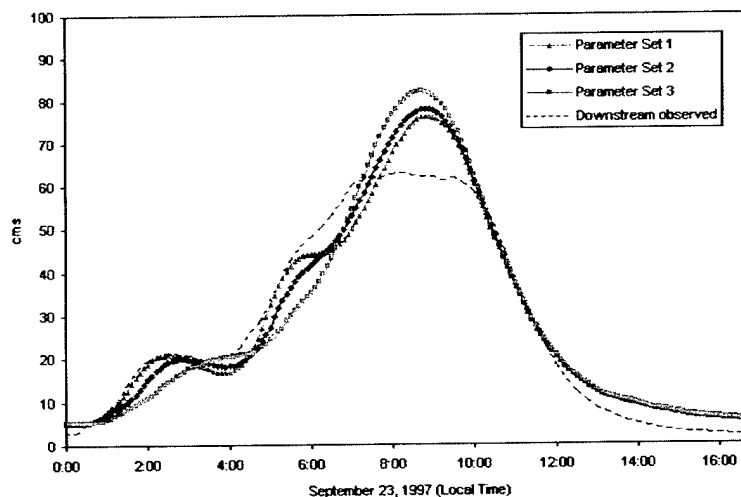


Fig. 9. Comparison of model results and observed discharge for different parameterizations of the hydrologic model. See text for details on the three parameter sets.



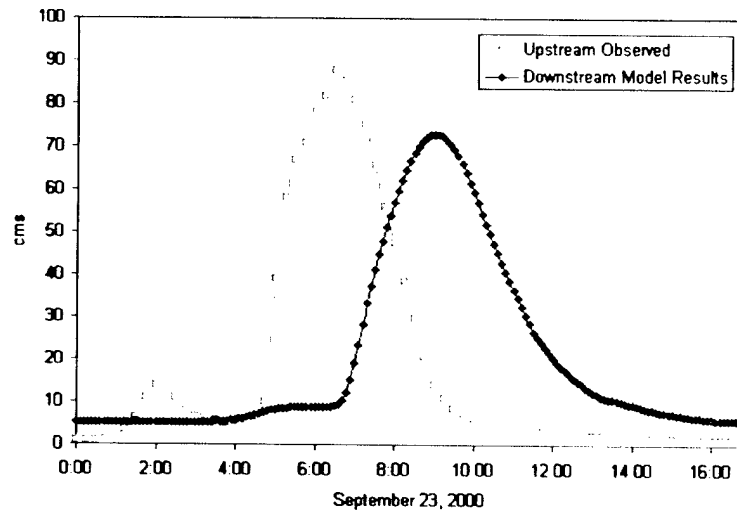


Fig. 10. Upstream observed hydrograph and downstream model hydrograph under the assumption of no input from intervening tributaries.

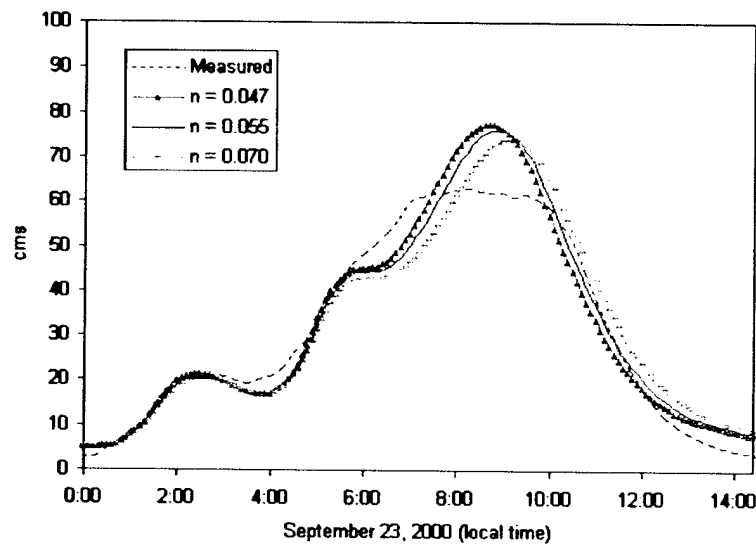


Fig. 11. Comparison of model discharge and observed discharge for varying values of the uniform floodplain roughness ( $n = 0.047$ ,  $0.055$  and  $0.070$ ).

$5.0$  to  $0.7 \text{ m s}^{-1}$ . Parameter set 3 was derived to reproduce peak discharge at the upstream (Shamrock) gaging station and reflects the least urbanized basin conditions. Parameter set 2 represents intermediate conditions. The general conclusion of these analyses is that fast response times in the reach between Shamrock and Colony Road result in the upper Briar Creek basin (above Shamrock) and the lower basin (between Shamrock and Colony Road) contributing “out-of-phase.”

Model analyses indicate that without tributary input, the flood wave from the upstream gage would be conveyed through the reach with a 17% decrease ( $16 \text{ m}^3 \text{ s}^{-1}$ ) in the peak magnitude (Fig. 10). A decrease in the floodplain roughness from  $0.055$  to  $0.047$  resulted in a  $1.4 \text{ m}^3 \text{ s}^{-1}$  increase in peak discharge and a decrease in lag time of 12 min (Fig. 11). Conversely, with a higher

value of floodplain roughness,  $0.070$ , the peak discharge decreased by  $2.3 \text{ m}^3 \text{ s}^{-1}$  and the lag time increased by 12 min. Changing from a constant floodplain roughness of  $0.055$  to variable roughness dependent on land cover ( $0.065$  for forest and  $0.045$  for residential urban and grassland) resulted in a slight decrease in the peak discharge (Fig. 12). In this case, the average roughness over the floodplain is  $0.055$ , the constant floodplain roughness of the base analyses. The spatially variable roughness results in a slightly lower peak discharge.

Flood response in the 10.2 km reach of Briar Creek reflects the complex interplay of hydrologic and hydraulic processes on hillslopes and valley bottoms. In the lower portion of Little Sugar Creek, valley bottom hydraulic processes dominate flood response. For stream reaches like Briar Creek, the relative timing of

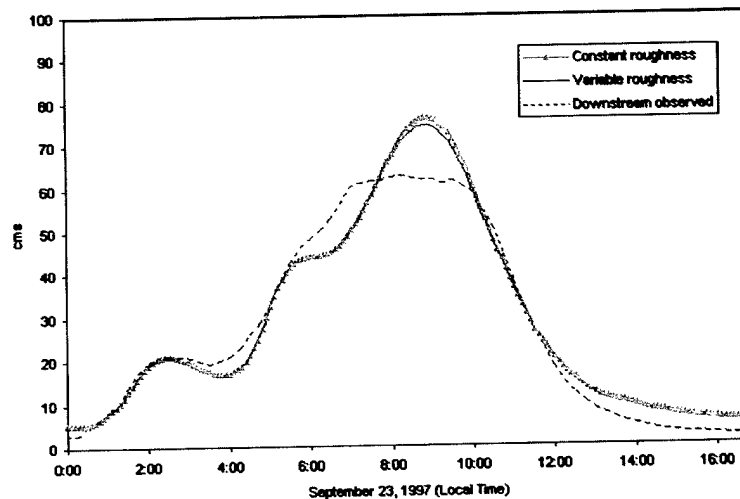


Fig. 12. Comparison of model results for spatially uniform roughness versus variable floodplain roughness values. Uniform roughness is 0.055. For the variable roughness case, forested regions have a roughness of 0.065 and all other land cover (principally residential and grassland) has a roughness of 0.045. The mean roughness over the Briar Creek floodplain for the variable roughness case is 0.055.

local and upstream contributions to flood response play a critical role in determining the cumulative flood response of the reach.

#### 4. Conclusions

The principal observations of this work are the following.

- Paired discharge analyses for an 8.3 km stream reach in Little Sugar Creek demonstrate pronounced flood-wave attenuation. The magnitude of attenuation is dependent on the peak discharge. For in-channel events, the magnitude of flood peak attenuation generally decreases with discharge up to the bankfull discharge. For overbank floods, the magnitude of peak attenuation increases with discharge up to the maximum discharge for which upstream–downstream hydrographs are available. For flood events approaching valley bottom full conditions, there is evidence that the magnitude of peak attenuation decreases. The observed dependence of floodwave attenuation (and floodwave celerity) on flow depth, relative to bankfull depth, is consistent with theoretical analyses of Knight and Shiono [16].
- Attenuating reaches are characterized by geologically controlled regions of wide valley bottoms and low stream slope. Pronounced changes in morphology of the fluvial system occur at or near boundaries between intrusive igneous and metamorphic rocks.
- A distributed hydrologic model and 2-D depth-averaged hydrodynamic model of the channel floodplain system are coupled to analyze flood response for a 10.1 km reach of Briar Creek. The coupled modeling system reproduces flood response for a major

flood event on 23 September 2000. The magnitude of flood peak attenuation, independent of tributary contributions, was approximately 17%.

- Peak flood response for the Briar Creek stream reach is quite sensitive to changing tributary response times associated with urbanization. A surprising aspect of model analyses is that increasing response times in tributary basins between the upstream and downstream gaging stations would result in larger flood peaks at the downstream gaging station.
- The model peak discharge increased by little more than 1% with a decrease in floodplain roughness from 0.055 to 0.047. The decrease in peak discharge was approximately 3% for an increase in floodplain roughness from 0.055 to 0.070. Representation of the spatial variation in roughness with land cover resulted in little change in flood response properties over the reach.

#### Acknowledgements

This research was funded in part by the US Army Research Office (Grant No. DAAD19-99-1-1063), NASA (Grant No. NAG5-7544) and the National Science Foundation (Grant No. EAR-9909696 and EAR-0208269). The authors would like to thank Bill Hazell of the US Geological Survey for providing discharge data and helpful discussions.

#### References

- [1] Babaeyan-Koopaei K, Ervine DA, Carling PA, Cao Z. Velocity and turbulence measurements for two overbank flow events in the River Severn. *J Hydraul Eng ASCE* 2002;128(10):891–900.

- [2] Barnes HH. Roughness characteristics of natural channels. US Geological Survey Water-supply Paper 1849, Washington, DC; 1967. 213 p.
- [3] Bates PD, Anderson MG, Baird L, Walling DE, Simm D. Modelling floodplain flows using a two-dimensional finite element model. *Earth Surface Process Landforms* 1992;17:575–88.
- [4] Bates PD. Development and testing of a subgrid-scale model for moving boundary hydrodynamic problems in shallow water. *Hydrol Process* 2000;14(11–12):2073–88.
- [5] Cady JG. Rock weathering and soil formation in the North Carolina Piedmont Region. In: *Proceedings of Soil Science Society*; 1950. p. 337–42.
- [6] Defina A. Two-dimensional shallow flow equations for partially dry areas. *Water Resour Res* 2000;13(11):3251–64.
- [7] Gee DM, Anderson MG, Baird L. Large-scale floodplain modeling. *Earth Surface Process Landforms* 1990;15:513–23.
- [8] Goldsmith R, Milton DJ, Horton Jr JW. Geologic map of the Charlotte 1° × 2° Quadrangle, North Carolina and South Carolina. Department of the Interior, US Geological Survey; 1988.
- [9] Hack JT. Physiographic divisions and differential uplift in the Piedmont and Blue Ridge, US Geological Survey Professional Paper 1265; 1982.
- [10] Hazell WF, Bales JD. Real-time rainfall measurements in the City of Charlotte and Mecklenburg County, North Carolina. US Geological Survey Fact Sheet Fs-052-97; 1997.
- [12] Hervouet J-M, van Haren L. Recent advances in numerical methods for fluid flows. In: Anderson M, Walling G, Bates P, editors. *Floodplain processes*. New York: Wiley and Sons; 1996.
- [13] Hervouet J-M, Pettijean A. Malpasset dam-break revisited with two-dimensional computations. *J Hydraul Res* 1999;37(6):777–88.
- [14] Horritt MS. Calibration of a two-dimensional finite element flood flow model using satellite radar imagery. *Water Resour Res* 2000;36(11):3279–91.
- [15] Horritt MS, Bates PD. Predicting floodplain inundation: raster-based modeling versus the finite-element approach. *Hydrol Process* 2001;15(5):825–42.
- [16] Knight DW, Shiono K. Channel floodplain interactions. In: Anderson MG, Walling DE, Bates PD, editors. *Floodplain processes*. New York: John Wiley and Sons; 1996.
- [17] Marks K, Bates PD. Integration of high-resolution topographic data with floodplain flow models. *Hydrol Process* 2000;14(11–12):2109–22.
- [18] Miller AJ, Cluer BL. Modeling considerations for simulation of flow in Bedrock Channels, in *Rivers Over Rock: fluvial processes Bedrock Channels*. *Geophys Monogr* 1998;107:61–104.
- [19] Morgan AE. Official plan for the protection of the district from flood damage. The Miami Conservancy District, State of Ohio; 1916.
- [20] Morrison JE. Extreme value statistics with applications in hydrology and financial engineering. PhD thesis, Princeton University; 2001.
- [21] Morrison JE, Smith JA. Scaling properties of flood peaks. *Extremes* 2001;4(1):5–23.
- [22] Ogden FL, Saghaian B. Green and Ampt infiltration with redistribution. *Journal of Irrigation and Drainage Engineering*, ACSE 1997;123(5):386–93.
- [23] Robinson JB, Hazell WF, Young WS. Effects of August 1995 and July 1997 storms in the City of Charlotte and Mecklenburg County, North Carolina. US Geological Survey Fact Sheet FS-036-98; 1998.
- [24] Smith JA, Baeck ML, Morrison JE, Sturdevant-Rees P, Turner-Gillespie DF, Bates PD. The regional hydrology of extreme floods in an urbanizing drainage basin. *J Hydrometeorol* 2002;3(3):267–82.
- [25] Shiono K, Muto Y, Knight DW, Hyde AFL. Energy losses due to secondary flow and turbulence in meandering channels with overbank flows. *J Hydraul Res* 2000;37(5):641–64.
- [26] Turner-Gillespie DF. The urban drainage network and extreme flood response. MS thesis, Department of Civil and Environmental Engineering, Princeton University, Princeton, NJ; June 2001.
- [27] Wolff GC, Burges SJ. An analysis of the influence of river channel properties on flood frequency. *J Hydrol* 2000;153:317–37.
- [28] Woltemade CJ, Potter KW. A watershed modeling analysis of fluvial geomorphologic influences on flood peak attenuation. *Water Resour Res* 1994;30(6):1933–42.
- [29] Miller AJ. Debris from constrictions and flood hydraulics in river canyons—some implications from 2-dimensional flow modeling. *Earth Surface Process Landforms* 1994;19(8):681–97.
- [30] Potter KW, Walker JF. An empirical study of flood measurement error. *Water Resour Res* 1985;21(3):403–6.

## Variability of Raindrop Size Distributions in a Squall Line and Implications for Radar Rainfall Estimation

REMKO UIJLENHOET, MATTHIAS STEINER, AND JAMES A. SMITH

*Environmental Engineering and Water Resources Program, Department of Civil and Environmental Engineering, Princeton University, Princeton, New Jersey*

(Manuscript received 14 November 2001, in final form 26 July 2002)

### ABSTRACT

The intrastorm variability of raindrop size distributions as a source of uncertainty in single-parameter and dual-parameter radar rainfall estimates is studied using time series analyses of disdrometer observations. Two rain-rate ( $R$ ) estimators are considered: the traditional single-parameter estimator using only the radar reflectivity factor ( $Z$ ) and a dual-polarization estimator using a combination of radar reflectivity at horizontal polarization ( $Z_H$ ) and differential reflectivity ( $Z_{DR}$ ). A case study for a squall-line system passing over the Goodwin Creek experimental watershed in northern Mississippi is presented. Microphysically, the leading convective line is characterized by large raindrop concentrations ( $>500$  drops per cubic meter), large mean raindrop sizes ( $>1$  mm), and wide raindrop size distributions (standard deviations  $>0.5$  mm), as compared to the transition region and the trailing stratiform rain. The transition and stratiform phases have similar raindrop concentrations and mean raindrop sizes. Their main difference is that the distributions are wider in the latter. A scaling-law analysis reveals that the shapes of the scaled spectra are bent downward for small raindrop sizes in the leading convective line, slightly bent upward in the transition zone, and strongly bent upward in the trailing stratiform rain. The exponents of the resulting  $Z$ - $R$  relationships are roughly the same for the leading convective line and the trailing stratiform rain ( $\approx 1.4$ ) and slightly larger for the transition region ( $\approx 1.5$ ), with prefactors increasing in this order: transition ( $\approx 200$ ), convective ( $\approx 300$ ), stratiform ( $\approx 450$ ). In terms of rainfall estimation bias, the best-fit mean  $R(Z_H, Z_{DR})$  relationship outperforms the best-fit mean  $R(Z)$  relationship, both for each storm phase separately and for the event as a whole.

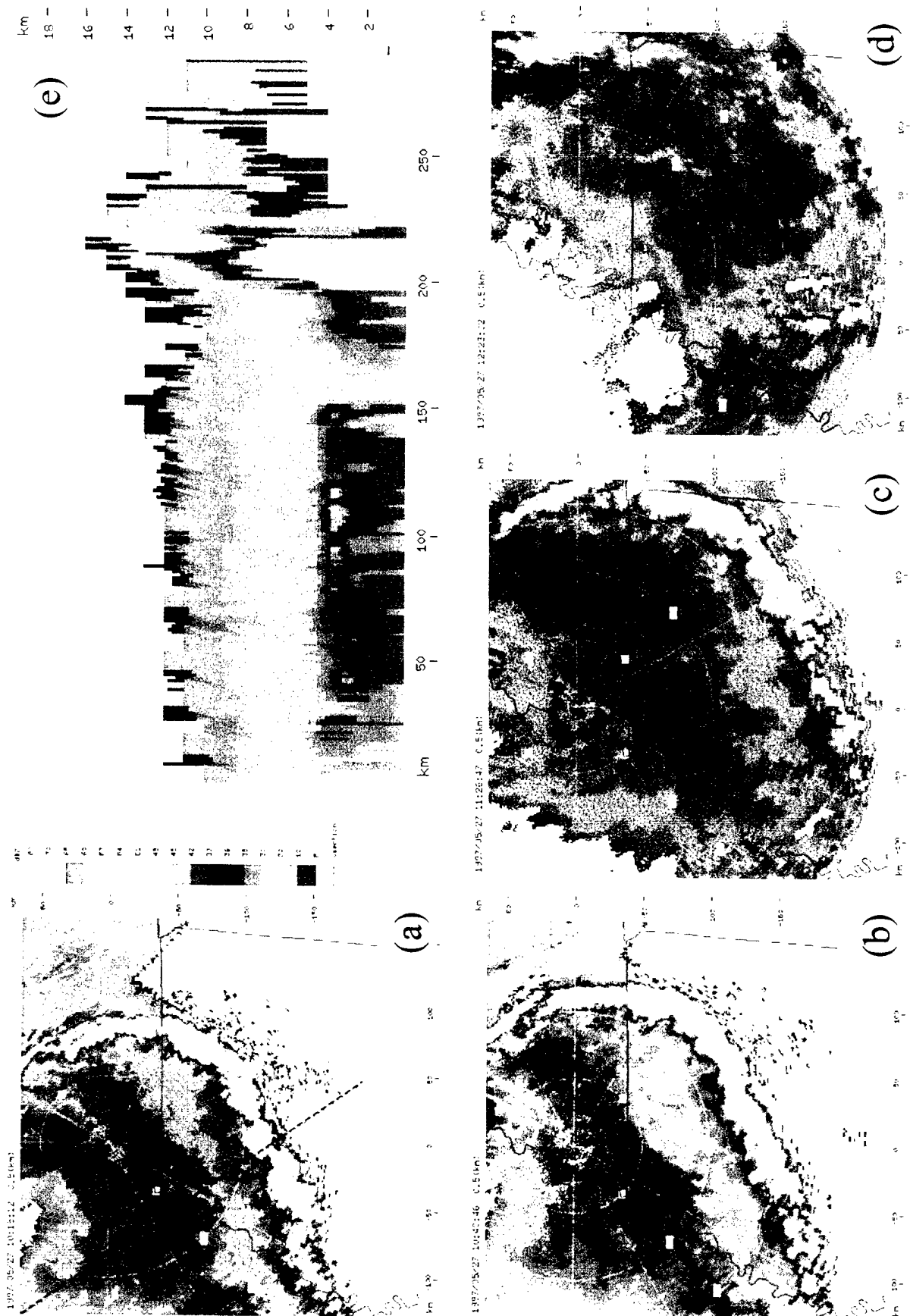
### 1. Introduction

A fundamental step in the hydrometeorological application of single-parameter weather radar is the conversion of radar-measured reflectivities aloft to estimates of the spatial and temporal distribution of rainfall at the ground. Although many different sources of error and uncertainty affect this conversion (e.g., Wilson and Brandes 1979; Zawadzki 1984; Joss and Waldvogel 1990; Steiner et al. 1999; Sánchez-Diezma et al. 2001), a key issue is the limited spatial and temporal representativeness of radar reflectivity-rain rate ( $Z$ - $R$ ) relationships. Fixed  $Z$ - $R$  relationships will inevitably lead to errors in radar rainfall estimates, because raindrop size distributions exhibit an appreciable amount of spatial and temporal variability (e.g., Dingle and Hardy 1962; Waldvogel 1974; Carbone and Nelson 1978; Smith 1993; Smith and De Veaux 1994). Although the storm-to-storm (i.e., *interstorm*) variability of  $Z$ - $R$  relationships is relatively well established (e.g., Fujiwara

1965; Battan 1973; Smith and Krajewski 1993; Steiner and Smith 2000), the variability within storms (i.e., *intra*-storm variability) has received less attention until recently (e.g., Waldvogel 1974; Carbone and Nelson 1978). Yet, there exist appreciable spatial variations in microphysical environments within a storm at any given time and corresponding temporal variations through the course of a storm at any given place within that storm (e.g., Steiner et al. 1995; Houze 1997; Petersen et al. 1999). Since the coefficients of  $Z$ - $R$  relationships are closely related to the microphysical structure of rainfall (e.g., Marshall and Palmer 1948; Battan 1973; Waldvogel 1974; Jameson and Kostinski 2001a), the intrastorm variability of  $Z$ - $R$  relationships is inevitably a source of uncertainty in radar rainfall estimates.

We present a case study of the variability of raindrop size distributions for a squall line passing over a small watershed in northern Mississippi. Because of its particular mesoscale structure, consisting of three different regions with distinctly different microphysical regimes, namely *initial convection*, *transition*, and *trailing stratiform* precipitation (Houze 1977, 1993; Leary and Houze 1979; Smull and Houze 1987; Biggerstaff and Houze 1991, 1993; Brown and Houze 1994; Maki et al. 2001; Bringi et al. 2002), the squall line represents an

*Corresponding author address:* Dr. Remko Uijlenhoet, Hydrology and Quantitative Water Management Group, Department of Environmental Sciences, Wageningen University, Nieuwe Kanaal 11, 6709 PA Wageningen, Netherlands.  
E-mail: remko.uijlenhoet@wur.nl



ideal model for analyzing the variability of raindrop size distributions and associated uncertainties in radar rainfall estimates. In particular, the fact that the squall line combines stratiform and convective rainfall in one single (mesoscale) event will allow a comparison of the results of our analyses with the many approaches toward distinguishing stratiform from convective rainfall that have recently appeared in the literature (e.g., Steiner et al. 1995; Tokay and Short 1996; Houze 1997; Steiner and Smith, 1998; Tokay et al. 1999; Atlas and Ulbrich 2000; Atlas et al. 2000; Sempere Torres et al. 2000; Rao et al. 2001). Such a distinction is important from a radar hydrometeorological perspective (e.g., Smith et al. 1996, 2000, 2001), because different types of rainfall are associated with different  $Z$ - $R$  relationships.

The raindrop size distributions, collected with a Joss-Waldvogel disdrometer (Joss and Waldvogel 1967), are analyzed using both established moment methods for the study of the variability of raindrop size distributions (e.g., Waldvogel 1974; Tokay and Short 1996) and a method describing the raindrop size distribution as a scaling law (Sempere Torres et al. 1994, 1998; Uijlenhoet 1999). The results of these analyses provide us with explanations for the intrastorm variations of the coefficients of  $Z$ - $R$  relationships and the associated uncertainties in reflectivity-based rainfall estimates. In addition, we provide an evaluation of the potential of polarimetric weather radar for rainfall estimation in which we limit ourselves to a measurable that is highly relevant from an operational perspective, namely differential reflectivity. The extra measurable provided by such radar systems in principle allows the estimation of an additional parameter of the raindrop size distribution [see Bringi et al. (2002) for a recent application of polarimetric radar for the estimation of gamma drop size distribution parameters]. This should lead to improved rain-rate estimates as compared to single-parameter weather radar, especially in highly variable environments. This is particularly relevant since the U.S. National Weather Service is considering upgrading the radars in the Next Generation Weather Radar (NEXRAD) network to polarimetric systems (Zrnich and Ryzhkov 1999).

## 2. Methodology

### a. Data

The data selected for our analysis consist of a 2.5-h time series of 1-min raindrop size distributions collected with a Joss-Waldvogel disdrometer (Joss and Waldvogel

1967) during a squall line that passed over the Goodwin Creek experimental watershed in northern Mississippi on 27 May 1997. The disdrometer is located at the climate station in the center of the 21.4-km<sup>2</sup> watershed. Alonso and Bingner (2000) provide further details about the catchment. The total rainfall accumulation for the event exceeds 35 mm, and the peak rain rate associated with the leading convective line as derived from the disdrometer observations approaches 140 mm h<sup>-1</sup> (Steiner et al. 1999).

The Joss-Waldvogel disdrometer is a momentum transducer, receiving raindrops on a 50-cm<sup>2</sup> styrofoam cone, determining their size and classifying them into 20 diameter intervals ranging from 0.3 to 5.5 mm (Joss and Waldvogel 1967). The 1-min histograms of drop counts obtained in this manner represent samples of raindrop size distributions. The limited representativeness of such samples has been discussed by Joss and Waldvogel (1969), Gertzman and Atlas (1977), Smith et al. (1993), Porrà et al. (1998), and Jameson and Kostinski (2001b). It should be noted that the so-called deadtime correction (e.g., Sauvageot and Lacaux 1995) was not applied in obtaining the results reported in this paper, in accordance with Tokay and Short (1996) and J. Joss (2000, personal communication). Calculations (not reproduced here) demonstrate that, although there is definitely an effect, application of this correction does not qualitatively alter the conclusions of this paper. Additional details concerning the measurement process and the associated data analysis are provided by Steiner and Smith (2000). The data for the 27 May 1997 squall line are part of a larger dataset of 30 events that has been studied to assess the effects of radar bias adjustment and rain gauge data quality control on radar rainfall estimation (Steiner et al. 1999).

Steiner et al. (1999) show that the 27 May 1997 squall line was associated with the development of a mesoscale convective complex (MCC) the previous night over eastern Oklahoma. Initially, a series of intense storms started to move rapidly in an easterly direction. Within 6 h, these scattered storms had evolved into a well-organized squall line. Figure 1 shows radar imagery [based on level 2 reflectivity data of the Memphis Weather Surveillance Radar-1988 Doppler (WSR-88D)] of the movement of the squall line as it passes over northern Mississippi and the bordering regions of Arkansas and Tennessee. Figure 1a shows a horizontal cross section [constant altitude plan position indicator (CAPPI)] image of the storm at 500 m above the ground. The image corresponds to a time around 1015 UTC, just

FIG. 1. Horizontal cross section (CAPPI) at 0.5 km of the 27 May 1997 squall line at (a) 1015 UTC, based on level 2 reflectivity data from the Memphis WSR-88D, when leading convective line passes over the Goodwin Creek watershed (delineated in black); (b) 1040 UTC, when transition region reaches the Goodwin Creek watershed; (c) 1126 UTC, when trailing stratiform rain reaches the Goodwin Creek watershed; and (d) 1223 UTC, which marks end of trailing stratiform rain passing over the Goodwin Creek watershed. (e) Vertical cross section (RHI), corresponding to dashed line in (a), showing typical squall-line structure (Houze 1977, 1993).

after the squall line has reached the Goodwin Creek watershed (which is delineated in black). Figure 1e shows a vertical cross section [range height indicator (RHI)] image along the dashed line in Fig. 1a, cutting through the squall line and over the Goodwin Creek watershed. These images show a typical squall-line structure with a leading convective line, an intermediate or transition region, and a trailing region with stratiform rain (e.g., Houze 1977, 1993). Note the high reflectivities (>50 dBZ) in the leading convective line, the low reflectivities (<30 dBZ) in the transition region, and the intermediate reflectivities ( $\approx 35$  dBZ) in the trailing stratiform region (Fig. 1a). Also note the distinct differences in vertical structure among the three regions, with high reflectivities towering up to 16 km in the leading convective line (180–220 km, Fig. 1e), the virtual absence of vertical structure in the transition region (150–180 km), and the radar bright band at 3–4 km in the stratiform region (40–150 km). These distinctly different vertical reflectivity profiles are indicators of strongly contrasting microphysical environments and associated differences in the mechanisms of precipitation production (e.g., Houze 1977, 1993). In section 3 we will investigate the “footprints” of these different production mechanisms as we analyze the time series of raindrop size spectra collected in the Goodwin Creek watershed during the overpass of the squall line. Figures 1a–d mark the beginning and end of each of these regions as they pass over the watershed. The actual event lasted longer, but the additional rainfall after 1230 UTC will not be considered here. After this moment, the event lost the distinct brightband structure that characterized the previous stratiform period (Fig. 1e). In addition, rainfall rates dropped dramatically after 1230 UTC (Fig. 2a).

## b. Definitions

### 1) RAINDROP SIZE DISTRIBUTION AND CHARACTERISTIC DIAMETERS

If  $N_v(D)$  ( $\text{mm}^{-1} \text{m}^{-3}$ ), the subscript  $V$  standing for “volume,” represents the raindrop size distribution, then  $N_v(D)dD$  ( $\text{m}^{-3}$ ) is the mean number of raindrops with (equivalent spherical) diameters between  $D$  and  $D + dD$  (mm) present per unit volume of air. A widely used parameterization for the raindrop size distribution is the gamma form (e.g., Ulbrich 1983; Tokay and Short 1996; Ulbrich and Atlas 1998)

$$N_v(D) = N_0 D^\mu \exp(-\Lambda D), \quad (1)$$

which reduces to the exponential form (e.g., Marshall and Palmer 1948; Waldvogel 1974; Carbone and Nelson 1978; Joss and Gori 1978) for  $\mu = 0$ .

Under certain conditions, the raindrop size distribution can be interpreted probabilistically as the product of the expected (mean) raindrop concentration  $N_T$  ( $\text{m}^{-3}$ ) and the probability density function  $f_D(D)$  ( $\text{mm}^{-1}$ ) of

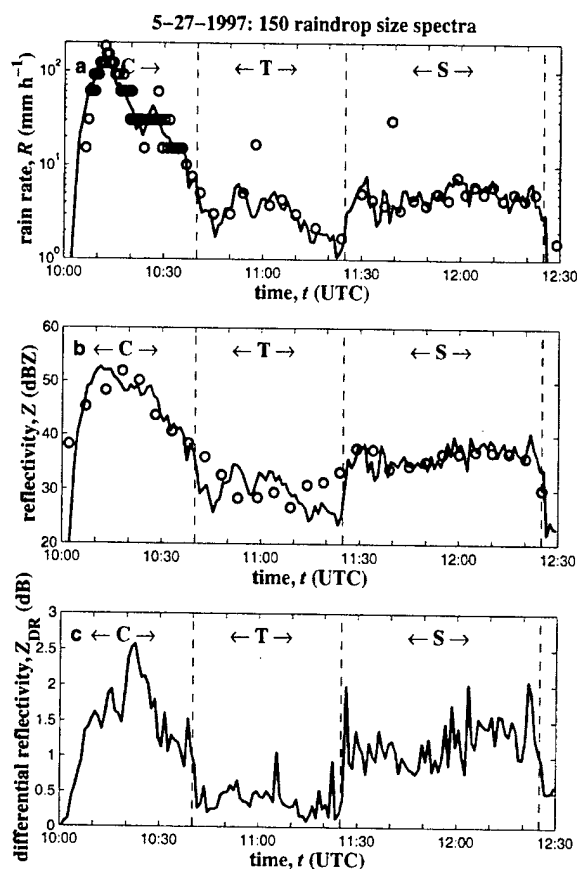


FIG. 2. Temporal evolution of (a) rain rate, (b) radar reflectivity factor, and (c) differential reflectivity during the three phases of the 27 May 1997 squall line, derived from 1-min Joss–Waldvogel disdrometer observations at the Goodwin Creek climate station (Fig. 3), where C, T, and S indicate convective, transition, and stratiform phases, respectively, and dashed vertical lines show their boundaries (1040, 1125, and 1225 UTC). Circles in (a) indicate measurements from nearby tipping-bucket rain gauge. Circles in (b) indicate base scan reflectivity measurements from the Memphis WSR-88D (closest radial pixel to disdrometer).

the stochastic diameter of raindrops present in a volume of air; that is,

$$N_v(D) = N_T f_D(D) \quad (2)$$

(Uijlenhoet and Stricker 1999). Such a product representation of the raindrop size distribution was first explicitly considered by Chandrasekar and Bringi (1987), for the special case of gamma raindrop size distributions. For the general case of any parametric form for the raindrop size distribution, it was discussed by Semper Torres et al. (1998, appendix). Jameson and Kostinski (2001a) stress the importance of Eq. (2) for the physical interpretation of empirical  $Z$ – $R$  relationships in radar meteorology. Porra et al. (1998) and Uijlenhoet (1999) discuss in detail the implicit hypotheses on which this product representation is based. The most important of these is the assumption that it is not necessary to

know exactly the multivariate statistical properties (e.g., size, speed, and position) of the entire raindrop population in the sample volume (including the interdrop dependencies), but sufficient to have a measure for the average raindrop size properties in the air, as defined by the univariate probability density function of raindrop sizes  $f_D(D)$ .

The raindrop concentration  $N_T$  ( $\text{m}^{-3}$ ) is the moment of order zero of the raindrop size distribution, that is, the total integral over the raindrop size distribution,

$$N_T = \int_0^\infty N_V(D) dD. \quad (3)$$

The effects of truncation of the raindrop size distribution (Ulbrich 1985) have been disregarded. Truncation at the large-diameter end of the spectrum mainly affects high-order moments. Even then, mainly the prefactors of power-law relationships between rainfall integral variables will be affected, and the exponents much less.

The first two moments of the probability density function  $f_D(D)$  are the mean raindrop diameter in a volume of air  $\mu_D$  (mm),

$$\mu_D = \int_0^\infty D f_D(D) dD = N_T^{-1} \int_0^\infty D N_V(D) dD, \quad (4)$$

and the variance of the corresponding raindrop diameters  $\sigma_D^2$  ( $\text{mm}^2$ ),

$$\begin{aligned} \sigma_D^2 &= \int_0^\infty D^2 f_D(D) dD - \mu_D^2 \\ &= N_T^{-1} \int_0^\infty D^2 N_V(D) dD - \mu_D^2, \end{aligned} \quad (5)$$

where  $\sigma_D$  (mm) is the standard deviation. Note that  $\mu_D^2 + \sigma_D^2$ , that is, the integral in Eq. (5), is proportional to the mean raindrop surface area. A widely used characteristic raindrop diameter is the median-volume diameter  $D_0$  (mm), which in combination with  $\mu_D$  and  $\sigma_D$  provides information about the skewness (i.e., asymmetry) of  $N_V(D)$ , and is defined as the 50th percentile of the normalized distribution of liquid rain water content [Eq. (7)] over all drop diameters,

$$\begin{aligned} \int_0^{D_0} D^3 N_V(D) dD &= \int_{D_0}^\infty D^3 N_V(D) dD \\ &= 0.5 \int_0^\infty D^3 N_V(D) dD \end{aligned} \quad (6)$$

(Atlas 1953). In an entirely analogous manner, other percentiles can be defined.

## 2) RAINFALL INTEGRAL VARIABLES

The liquid rain water content  $W$  ( $\text{mg m}^{-3}$ ) is related to the raindrop size distribution according to

$$W = 10^{-3} \frac{\pi \rho_w}{6} \int_0^\infty D^3 N_V(D) dD, \quad (7)$$

where  $\rho_w$  ( $\text{kg m}^{-3}$ ) is the density of water, which for all practical purposes can be taken as  $1000 \text{ kg m}^{-3}$ . If the effects of wind (notably updrafts and downdrafts), turbulence, and raindrop interaction are neglected, the (stationary) rain rate  $R$  ( $\text{mm h}^{-1}$ ) is related to the raindrop size distribution  $N_V(D)$  according to

$$R = 6\pi \times 10^{-4} \int_0^\infty D^3 v(D) N_V(D) dD, \quad (8)$$

where  $v(D)$  represents the functional relationship between the raindrop terminal fall speed in still air  $v$  ( $\text{m s}^{-1}$ ) and the equivalent spherical raindrop diameter  $D$  (mm). The simplest and most widely used form of the  $v(D)$  relationship is the power law

$$v(D) = cD^\gamma. \quad (9)$$

Atlas and Ulbrich (1977) demonstrate that Eq. (9), with  $c = 3.778$  (if  $v$  is expressed in meters per second and  $D$  in millimeters) and  $\gamma = 0.67$ , provides a close fit to the data of Gunn and Kinzer (1949) in the range  $0.5 \leq D \leq 5.0$  mm (the diameter interval contributing most to rain rate). Although more sophisticated relationships have been proposed in the literature (e.g., Best 1950; Atlas et al. 1973; Beard 1976), the power-law form for the  $v(D)$  relationship is the only functional form that is consistent with power-law relationships between rainfall-related variables, notably between  $Z$  and  $R$  (Sempere Torres et al. 1994; Uijlenhoet 1999, 2001).

The central variable of most operational rainfall retrieval algorithms is the radar reflectivity factor  $Z$  ( $\text{mm}^6 \text{ m}^{-3}$ ), defined as (e.g., Battan 1973)

$$Z = \int_0^\infty D^6 N_V(D) dD, \quad (10)$$

which is sometimes expressed in dBZ using the transformation  $10 \log Z$ . This definition of the radar reflectivity factor implicitly assumes Rayleigh scattering and spherical particles (Battan 1973). In case of nonspherical particles, polarization effects need to be taken into account. The copolar linear reflectivity factors at horizontal and vertical polarization  $Z_{H,V}$  ( $\text{mm}^6 \text{ m}^{-3}$ ) are defined as (e.g., Seliga and Bringi 1976; Balakrishnan et al. 1989; Doviak and Zrnica 1993)

$$Z_{H,V} = \frac{\lambda^4}{\pi^3 |K|^2} \int_0^\infty \sigma_{H,V}(D) N_V(D) dD, \quad (11)$$

where  $Z_{H,V}$  is a short notation for " $Z_H$  or  $Z_V$ ,"  $\lambda$  (mm) is the wavelength of the transmitted signal,  $|K|^2$  (—) is a coefficient related to the dielectric constant of water ( $\approx 0.93$ ), and  $\sigma_{H,V}(D)$  ( $\text{mm}^2$ ) are the copolar linear backscattering cross sections at horizontal and vertical polarization, respectively. In our calculations, we use the backscattering cross sections provided by Goddard and



Cherry (1984). The differential reflectivity  $Z_{DR}$  is defined as (e.g., Seliga and Bringi 1976; Balakrishnan et al. 1989; Doviak and Zrnic 1993)

$$Z_{DR} = Z_H/Z_V, \quad (12)$$

which is generally expressed in dB using the transformation  $10 \log Z_{DR}$ .

### c. Scaling-law formalism

Sempere Torres et al. (1994, 1998) have demonstrated that many previously proposed parameterizations for the raindrop size distribution are special cases of a general formulation, which takes the form of a scaling law. In this formulation, the raindrop size distribution depends both on the raindrop diameter ( $D$ ) and on the value of a so-called reference variable, commonly taken to be the rain rate ( $R$ ). The generality of this formulation stems from the fact that it is no longer necessary to impose an a priori functional form for the raindrop size distribution, as opposed to the normalization approaches recently proposed by Testud et al. (2001) and Illingworth and Blackman (2002), which are both based on the gamma parameterization. Moreover, it naturally leads to the ubiquitous power-law relationships between rainfall integral parameters, notably that between the radar reflectivity factor ( $Z$ ) and  $R$ . A major advantage over previous scaling approaches (e.g., Sekhon and Srivastava 1971; Willis 1984; Willis and Tattelman 1989) is that this approach explicitly considers the issue of the *internal consistency* of parameterizations for the raindrop size distribution (e.g., Bennett et al. 1984; Delrieu et al. 1991; Uijlenhoet 1999, 2001; Uijlenhoet and Stricker 1999).

According to the scaling-law formalism, raindrop size distributions can be parameterized as (Sempere Torres et al. 1994, 1998)

$$N_v(D, R) = R^\alpha g(R^{-\beta} D), \quad (13)$$

where  $N_v(D, R)$  ( $\text{mm}^{-1} \text{m}^{-3}$ ) is the raindrop size distribution as a function of rain rate  $R$  ( $\text{mm h}^{-1}$ ),  $\alpha$  and  $\beta$  are (dimensionless) *scaling exponents*, and  $g(x)$  is the *general raindrop size distribution* as a function of scaled raindrop diameter  $x = R^{-\beta} D$ . Substitution of  $R = 1 \text{ mm h}^{-1}$  in Eq. (13) shows that  $N_v(D, 1) = g(D)$ , in other words that  $g(x)$  represents the *equivalent* (i.e., scaled) raindrop size distribution at a rain rate of  $1 \text{ mm h}^{-1}$  (Uijlenhoet 1999). In agreement with common practice,  $R$  is used as the reference variable in Eq. (13), although any other rainfall integral variable could serve as such (notably  $Z$ ). According to this formulation, the values of  $\alpha$  and  $\beta$  and the form and dimensions of  $g(x)$  depend on the *choice* of the reference variable but do not bear any functional dependence on its *value*. The values of the scaling exponents indicate whether it is the variability of the raindrop sizes or the variability of the raindrop concentration (or some combination thereof) that controls the variability of the raindrop size dis-

tribution. In general, the closer  $\beta$  is to zero, the more pronounced is the relative contribution of number-controlled variability (Uijlenhoet 1999; Uijlenhoet et al. 2003, hereafter USS).

The importance of the scaling-law formalism for radar hydrometeorology stems from the fact that it allows an interpretation of the coefficients of  $Z$ - $R$  relationships in terms of the values of the scaling exponents and the shape of the general raindrop size distribution. Substituting the scaling law for the raindrop size distribution [Eq. (13)] into the definition of  $Z$  [Eq. (10)] leads to the power law

$$Z = aR^b, \quad (14)$$

with

$$a = \int_0^\infty x^6 g(x) dx, \quad \text{and} \quad (15)$$

$$b = \alpha + 7\beta \quad (16)$$

(Uijlenhoet 1999, 2001). Hence, the *prefactor* of a power-law  $Z$ - $R$  relationship is entirely determined by the shape of the general raindrop size distribution (its sixth moment), whereas a linear combination of the values of the scaling exponents completely determines the *exponent* of such a power-law  $Z$ - $R$  relationship. This approach for determining power-law relationships complements the traditional regression-based methods (e.g., Steiner and Smith 2000). It has the advantage that it guarantees consistency between the coefficients of power-law relationships and the parameters of the corresponding parameterization for the raindrop size distribution.

Substituting Eqs. (13) and (9) into the definition of  $R$  in terms of the raindrop size distribution [Eq. (8)] leads to the *self-consistency constraints*

$$6\pi \times 10^{-4} c \int_0^\infty x^{3+\gamma} g(x) dx = 1 \quad \text{and} \quad (17)$$

$$\alpha + (4 + \gamma)\beta = 1 \quad (18)$$

(Sempere Torres et al. 1994). Hence,  $g(x)$  must satisfy an integral equation (which reduces its degrees of freedom by one), and there is only *one* free scaling exponent. These self-consistency constraints guarantee that substitution of the parameterization for the raindrop size distribution [Eq. (13)] into the defining expression for  $R$  [Eq. (8)], leads to  $R = R$ .

For the purpose of this paper, consider a gamma parameterization for the general raindrop size distribution,

$$g(x) = \kappa x^\mu \exp(-\lambda x), \quad (19)$$

which for  $\mu = 0$  reduces to an exponential parameterization. In this general form,  $g(x)$  is not an admissible description of the general raindrop size distribution, because it does not satisfy the self-consistency constraint on  $g(x)$  [Eq. (17)]. Substitution of Eq. (19) into (17)

yields, for a given value of the parameter  $\mu$ , a power-law relationship of  $\kappa$  in terms of  $\lambda$ ,

$$\kappa = [6\pi \times 10^{-4} c \Gamma(4 + \gamma + \mu)]^{-1} \lambda^{4+\gamma+\mu}. \quad (20)$$

This is an explicit form of the self-consistency constraint on  $g(x)$  for the case of a gamma parameterization. For the applied units, with  $c = 3.778$  and  $\gamma = 0.67$  (Atlas and Ulbrich 1977), Eq. (20) reduces to  $\kappa = 9.50\lambda^{4.67}$  for the special case of an exponential parameterization for  $g(x)$  ( $\mu = 0$ ).

It is of considerable interest to establish a link between the scaling-law formalism and the traditional analytical parameterizations for the raindrop size distribution. For the case of the gamma raindrop size distribution, this can be achieved through substituting Eq. (19) into (13). This yields

$$N_v(D, R) = \kappa R^{\alpha-\mu\beta} D^\mu \exp(-\lambda R^{-\beta} D). \quad (21)$$

Equation (21) reduces to the classical gamma parameterization for the raindrop size distribution [Eq. (1)] if  $N_0$  and  $\Lambda$  depend on  $R$  according to the power laws

$$N_0 = \kappa R^{\alpha-\mu\beta} \quad \text{and} \quad (22)$$

$$\Lambda = \lambda R^{-\beta}. \quad (23)$$

For the special case of an exponential parameterization for the raindrop size distribution of the form initially proposed by Marshall and Palmer (1948), that is, Eq. (1) with  $\mu = 0$ , Eq. (22) reduces to  $N_0 = \kappa R^\alpha$ . Recall that the self-consistency of Eq. (21) requires that  $\alpha$  and  $\beta$  be related to each other via Eq. (18), and  $\kappa$  and  $\lambda$  via Eq. (20).

Sempere Torres et al. (1994) have demonstrated that the scaling exponents  $\alpha$  and  $\beta$  may be estimated as the intercept and slope of a plot of the exponents  $\gamma_m$  (of power laws between the moments of order  $m$  and  $R$ ) versus the order of the moment  $m + 1$ . In general, the lower-order moments, which mainly depend on the counts in the smallest raindrop bins, are very sensitive to instrumental limitations (Uijlenhoet 1999). The higher-order moments, on the other hand, depending strongly on the counts in the larger raindrop bins, are more sensitive to sampling fluctuations (e.g., Smith et al. 1993). Therefore, as a general rule, we only estimate the values of the scaling exponents on the basis of moments of orders between two and six ( $2 \leq m \leq 6$ ). In fact, to guarantee self-consistency, we only estimate  $\beta$  in this manner and subsequently invoke the constraint on the scaling exponents [Eq. (18)] to estimate  $\alpha$ . Finally, we employ a moment method developed by Uijlenhoet (1999) to estimate self-consistent values of the parameters of the scaled raindrop size distribution  $g(x)$ . Effectively, this method uses the moments of orders  $4 + \gamma$  and  $5 + \gamma$  (with  $\gamma = 0.67$ ) of  $g(x)$  to estimate  $\lambda$  and  $\mu$ . This corresponds closely to the moment orders (i.e., central in the range 0–6) that are commonly used to estimate the parameters of the gamma raindrop size distribution (e.g., Tokay and Short 1996; Ulbrich and

Atlas 1998). The corresponding self-consistent value of  $\kappa$  is subsequently estimated using Eq. (20). USS provide a more detailed discussion of this scaling analysis (which is applied to our disdrometer data in section 3b).

### 3. Results and discussion

#### a. Time series analyses

##### 1) RAINFALL INTEGRAL VARIABLES

Figure 2 shows the time traces of rain rate  $R$  [Eq. (8)], radar reflectivity factor  $Z$  [Eq. (10)], and differential reflectivity  $Z_{DR}$  [Eq. (12)] during the three phases of the 27 May 1997 squall line, as derived from the 1-min Joss–Waldvogel disdrometer observations at the climate station in the Goodwin Creek watershed. The dashed vertical lines separate the three phases of the squall line: convective (C), transition (T), and stratiform (S). These times closely correspond to the times associated with Figs. 1b–d. The classification into C, T, and S is a subjective one, based on raindrop size distributions and radar imagery. A comparison with data from a nearby tipping bucket rain gauge (Fig. 2a) shows that, although the overall correspondence between both rain-rate traces is acceptable, the peak rain rates from the tipping bucket gauge (circles) are significantly larger than those derived from the spectra (bold line). Note that the volume of the employed bucket corresponds to a rainfall depth of 0.01 in. (0.254 mm) and that the gauge data were available as numbers of tips per 30 s. The resulting quantization effect is clearly visible in Fig. 2a, particularly for high rain rates (i.e., from 1000 to 1030 UTC). There are two readings from the tipping bucket gauge (one shortly before 1100 UTC, the other around 1140 UTC), however, that seem to be in error by almost an order of magnitude [see Steiner et al. (1999) for a discussion of rain gauge data quality control].

A comparison between the reflectivity trace derived from the spectra (Fig. 2b, bold line) and base scan reflectivity data from the Memphis WSR-88D (circles) shows a good correspondence. The deviations during the convective and transition phases are likely due to differences in sampling characteristics between both devices. The correspondence during the stratiform phase is striking. This comparison demonstrates that a 50-cm<sup>2</sup> disdrometer collecting 1-min rainfall samples at the ground can be quite representative for a weather radar with a sample volume aloft of the order of cubic kilometers.

Concentrating on the values derived from the spectra (bold lines), all three rainfall integral variables in Fig. 2 show a similar behavior, namely high values during the leading convective line, low values in the transition region, and intermediate values in the trailing stratiform rain (similar to the reflectivity values in Fig. 1). The noisy appearance of the differential reflectivity trace, particularly during the stratiform phase of the squall-

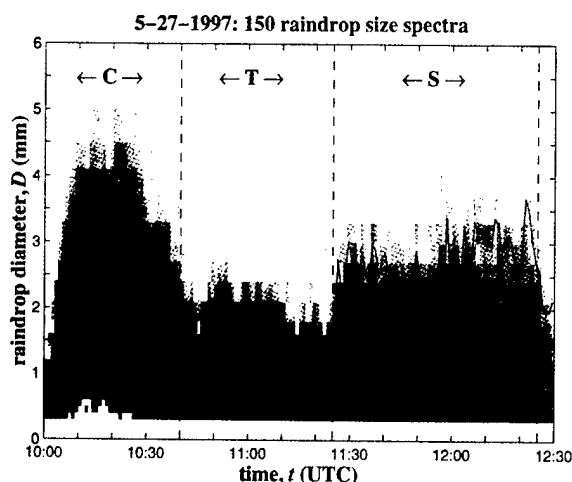


FIG. 3. Temporal evolution of 1-min raindrop size distributions measured with Joss–Waldvogel disdrometer at the climate station in the Goodwin Creek watershed during three phases of the 27 May 1997 squall line. Grayscale indicates number of raindrops in size interval (arbitrary units). Bold solid line indicates median-volume diameter  $D_0$  (mm), thin solid lines indicate 10th and 90th percentiles of distribution of normalized liquid rain water content over raindrop diameters (by definition,  $D_0$  is 50th percentile).

line system, is attributed to sampling fluctuations. Figure 2c shows that at the transition–stratiform boundary  $Z_{DR}$  increases from values close to zero, indicating spherical (i.e., small) drops, to values in excess of 1 dB, indicating quite oblate (i.e., large) drops. The value of  $Z_{DR}$  effectively serves as a characteristic raindrop size for the tail of the raindrop size distribution. It would be interesting to verify whether polarimetric radars are able to capture the convective–transition and transition–stratiform boundaries in squall lines as well as the remarkable data in Fig. 2c suggest.

Figure 3 shows the time evolution of the raindrop size distributions themselves. This figure demonstrates that the convective phase produces wide spectra (large drops), the transition phase narrow spectra (small drops), and the stratiform phase intermediate spectra (average-sized drops). This is consistent with the microphysical processes that take place in a squall-line system (Houze 1977, 1993): growth associated with convection tends to produce a wide array of raindrop sizes; the transition phase is characterized by a fallout of smaller particles (as the larger ones have already disappeared); and the stratiform phase is associated with new growth as a result of diffusion and aggregation in weak mesoscale updrafts, hence larger particles and a wider distribution. However, this analysis does not prove that the raindrop size distributions are fundamentally different in the three regions considered, because a significant part of the variations observed in Fig. 3 will be due to variations in the rain rate (Fig. 2a). The scaling analysis in section 3b filters the effects

of rain-rate variations and therefore leads to more conclusive results.

To indicate which parts of the raindrop size distributions most significantly contribute to the liquid rain water content, a quantity of core hydrometeorological interest, we have included in Fig. 3 time traces of the 10th, 50th (i.e.,  $D_0$ ), and 90th percentiles (all in mm) of the normalized distribution of the liquid water content  $W$  over raindrop size  $D$  [see Eqs. (6) and (7)]. The difference between the 90th and the 10th percentiles is the range of raindrop diameters that corresponds to the central 80% of the liquid water content (excluding the 10% of  $W$  caused by the smallest drops and the 10% of  $W$  caused by the largest drops). As such, this difference is also a measure of the width of raindrop size distributions, an alternative to  $\sigma_D$  perhaps better suited to skewed distributions. Clearly, the main contribution to the liquid water content comes from significantly larger drops than does the main contribution to the number concentration. The behavior of  $D_0$  in the convective phase also indicates that there seem to exist different regimes within the convection. A similar observation, although less pronounced, can be made for the differential reflectivity (Fig. 2c). The 90th percentile (Fig. 3) is seen to be strongly prone to sampling fluctuations, particularly during the stratiform phase. Nevertheless, there exist significant differences between the percentile values in each of the three regions considered.

Figure 4 shows the time evolution of the raindrop concentration  $N_T$  [Eq. (3)], the mean raindrop diameter  $\mu_D$  [Eq. (4)], and the standard deviation of the raindrop diameters  $\sigma_D$  [Eq. (5)] during the event. There is a clear contrast between the first two of those and the corresponding time series for  $R$ ,  $Z$ , and  $Z_{DR}$  (Fig. 2). First of all, there is hardly any difference between the raindrop concentration in the transition region and that in the stratiform region. In contrast to the abrupt increase in  $R$ ,  $Z$ , and  $Z_{DR}$  at the transition–stratiform boundary (Fig. 2), the mean raindrop concentration even decreases slightly. This reduction could have been caused by aggregation, which reduces the number of particles. On the other hand, the change is very gradual and the difference may not be significant given the relatively large statistical fluctuations. The only feature of the raindrop concentration time series that is present in Fig. 2 as well is the increase during the leading convective line. However, this increase is less pronounced for  $N_T$  (by roughly a factor of 2) than it is for  $R$ ,  $Z$ , and  $Z_{DR}$ . Moreover, the reduction of  $N_T$  shortly after 1020 UTC is much more pronounced than that of  $R$  and, particularly, that of  $Z$ .

The increases in  $R$ ,  $Z$ , and  $Z_{DR}$  during the leading convective line (Fig. 2) have been caused by combined increases in the raindrop concentration (Fig. 4a), the mean raindrop diameter (Fig. 4b), and the standard deviation (Fig. 4c). What remains to be solved is the problem of explaining the sudden increases in  $R$ ,  $Z$ , and  $Z_{DR}$  at the transition–stratiform boundary (Fig. 2, 1125 UTC). Neither the raindrop concentration nor the mean

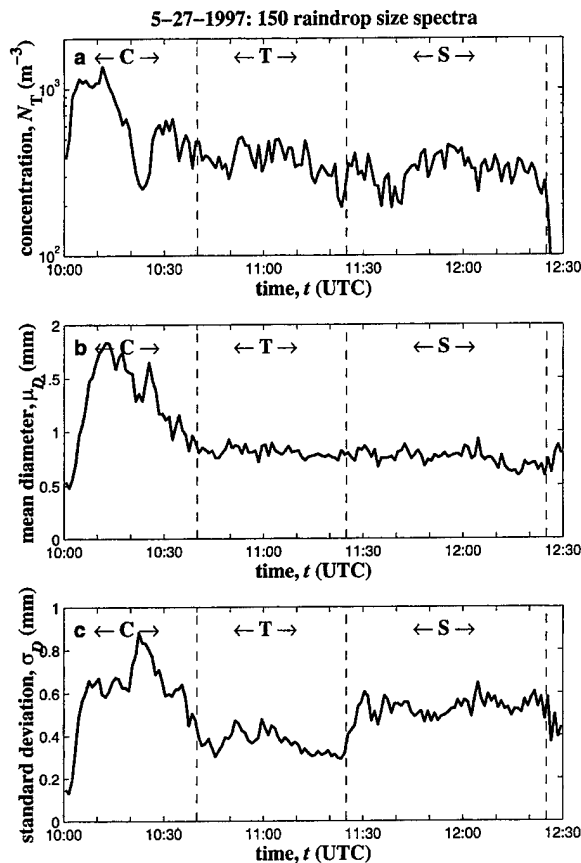


FIG. 4. Temporal evolution of (a) raindrop concentration, (b) mean raindrop diameter, and (c) standard deviation of raindrop diameters during the three phases of the 27 May 1997 squall line, derived from 1-min Joss–Waldvogel disdrometer observations (Fig. 3).

raindrop diameter (Figs. 4a,b) changes enough during this phase to explain the observed increases in  $R$ ,  $Z$ , and  $Z_{DR}$ . The answer is provided by the temporal structure of the standard deviation of the raindrop diameters (Fig. 4c). Where the raindrop concentration and the mean raindrop diameter remain unaffected at the transition–stratiform boundary, the standard deviation shows a sudden increase. In general, if the standard deviation of a distribution, which is a measure for its spread, changes while its mean stays the same, the relative proportions of small and large drops must have changed. Figure 3 shows how this happened in this case. Comparing the transition and stratiform regions, we observe 1) an increase in the number of small raindrops ( $D < 0.5$  mm), 2) a decrease in the number of intermediate drops ( $0.5 < D < 1.0$  mm), and 3) an increase in the number of large drops ( $D > 1.0$  mm). In this particular case, where the total raindrop concentration approximately remains the same as well, the absolute number of small and large drops together must have increased by roughly the same amount as the decrease in the number of intermediate drops. The behavior at the large-drop end of the spec-

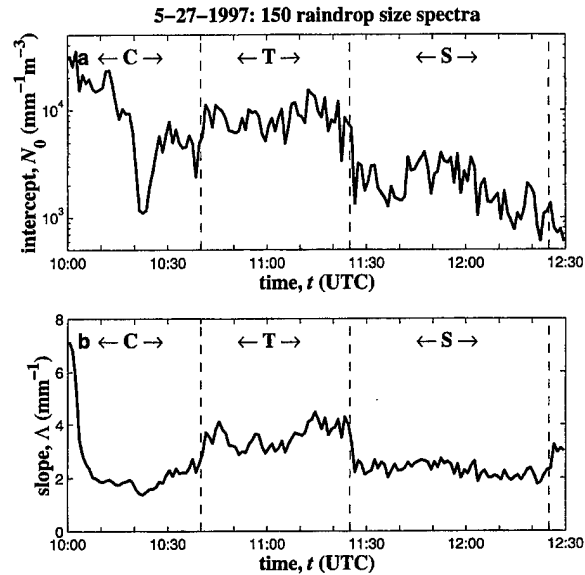


FIG. 5. Temporal evolution of (a) intercept and (b) slope parameters of exponential fit to raindrop size distributions according to Waldvogel's (1974) method during the three phases of the 27 May 1997 squall line.

trum can be explained microphysically by the aggregation of ice particles above the melting layer, which upon melting produces larger raindrops at the expense of intermediate ones.

## 2) EQUIVALENT EXPONENTIAL AND GAMMA DISTRIBUTIONS

In his study of the temporal variability of raindrop size distributions and the associated  $Z$ – $R$  relationships, Waldvogel (1974) proposes to adjust to each empirical raindrop size distribution an “equivalent” exponential distribution of the form  $N_0 \exp(-\Lambda D)$ , that is, Eq. (1) with  $\mu = 0$ , with the same liquid rain water content and radar reflectivity as the empirical distribution. We have applied Waldvogel's procedure to the values of  $W$  [Eq. (7)] and  $Z$  [Eq. (10)] derived from the spectra. Figure 5 shows the resulting time series of the intercept parameter  $N_0$  ( $mm^{-1} m^{-3}$ ) and the slope parameter  $\Lambda$  ( $mm^{-1}$ ) of the equivalent exponential raindrop size distributions. Waldvogel reports “ $N_0$  jumps,” that is, sudden increases of  $N_0$  while the rain rate remained approximately constant, which he related to the disappearance of the radar bright band and the associated presence of convective activity (showers or thunderstorms). According to Waldvogel, large values of  $N_0$  are associated with “small-drop spectra” (at a given rain rate) and small  $Z$ – $R$  prefactors, whereas small values of  $N_0$  are associated with “large-drop spectra” (at the same rain rate) and large  $Z$ – $R$  prefactors. This interpretation is consistent with the results of our previous analysis of the variability of rainfall integral variables during the

passage of the squall line. Note, however, that during the event analyzed here the rain rate was not constant (Fig. 2a).

Moving "against nature" from right to left in Fig. 5a, that is, from stratiform via transition to convective, the occurrence of an  $N_0$  jump is evident at the stratiform–transition boundary (1125 UTC), corresponding to the disappearance of the radar bright band (Fig. 1e). During the transition phase  $N_0$  is seen to remain relatively constant, whereas during the convective phase there is a sudden drop and a new jump, after which  $N_0$  reaches an even larger value than during the transition phase. A similar drop during convection is present in  $R$  (Fig. 2a), whereas  $Z$  remains fairly constant during this period (Fig. 2b). On the other hand, the " $N_0$  drop" corresponds to peaks in both  $Z_{DR}$  (Fig. 2c) and  $D_0$  (Fig. 3). In Fig. 4, we see that this drop is related to a sudden decrease of the raindrop concentration (Fig. 4a), a slight decrease of the mean raindrop diameter (Fig. 4b), and a peak in the standard deviation of the raindrop diameters (Fig. 4c). This points again toward a sequence of contrasting regimes within the convective phase of the squall-line system.

In accordance with Waldvogel's (1974) results, the temporal structure of  $\Lambda$  (Fig. 5b) follows that of  $N_0$  to a large extent, including what may be called " $\Lambda$  jumps," which indicates that  $N_0$  and  $\Lambda$  are not independent variables. In fact, although the  $\Lambda$  jumps (Fig. 5b) may be less dramatic in magnitude than those in  $N_0$  (Fig. 5a), the values of  $\Lambda$  within each of the three considered phases of the squall line seem to be much more stable. For instance, the  $N_0$  drop between 1020 and 1025 UTC is completely absent in the temporal structure of  $\Lambda$ , resulting in a remarkably constant slope parameter during the convective phase. The increased numbers of small and intermediate size raindrops and the disappearance of the large drops during the transition phase (Fig. 3) produce, besides decreasing values of the integral variables (Fig. 2), a higher intercept (Fig. 5a) and a steeper slope (Fig. 5b) of the fitted exponential drop size distribution. When large drops reappear during the stratiform phase, the intercept decreases again and the slope becomes less steep (with corresponding increases in the integral variables).

Although for exponential raindrop size distributions of the form  $N_0 \exp(-\Lambda D)$  the inverse of  $\Lambda$  should theoretically equal the mean raindrop diameter, that is,  $\mu_D = \Lambda^{-1}$  (Uijlenhoet and Stricker 1999), such an interpretation is not warranted here. According to Waldvogel's procedure,  $\Lambda$  is calculated from the values of  $W$  and  $Z$  for each spectrum, not from a direct exponential adjustment. As a result,  $\Lambda$  loses its physical meaning as the inverse mean raindrop diameter. On the other hand,  $\mu_D$  is affected by instrumental limitations at the small-drop end of the spectrum (as is evident in Fig. 3 around 1015 UTC). It is therefore not surprising that  $\mu_D$  (Fig. 4b) and  $\Lambda$  (Fig. 5b) are not, as theory predicts, the inverse of each other. In fact, the inverse relationship

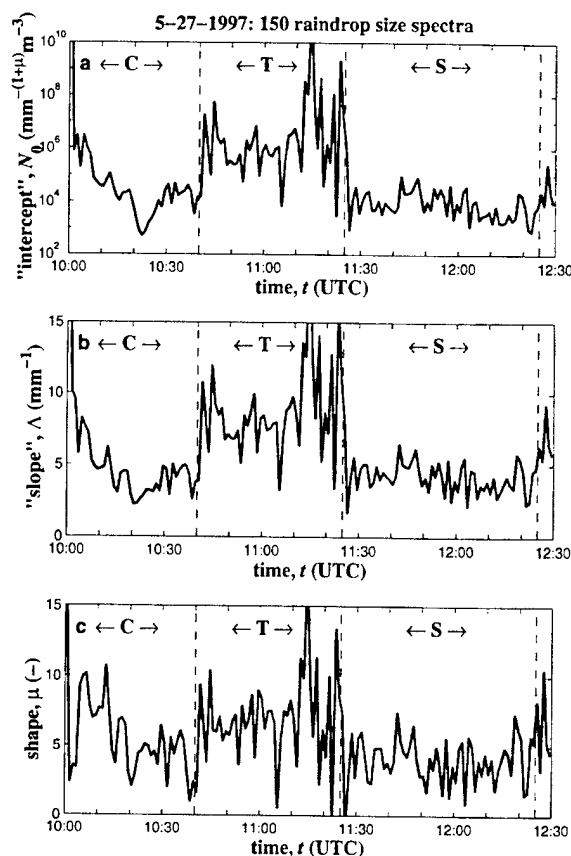


FIG. 6. Temporal evolution of (a) "intercept," (b) "slope," and (c) shape parameters of gamma fit to raindrop size distributions according to Tokay and Short's (1996) method during the three phases of the 27 May 1997 squall line (note: "intercept" and "slope" are used because gamma distribution does not really have intercept or slope, as opposed to exponential distribution; see Fig. 5).

between  $D_0$  (Fig. 3) and  $\Lambda$ , also predicted by theory (e.g., Uijlenhoet and Stricker 1999), is a lot tighter (except between 1020 and 1025 UTC). This is because  $D_0$  does not depend as strongly on small raindrops as does  $\mu_D$ .

Tokay and Short (1996) employ the method of moments (using moments of orders 3, 4, and 6) to fit a gamma parameterization of the form of Eq. (1) to their empirical raindrop size distributions. Figure 6 provides the time series of the parameters  $N_0$ ,  $\Lambda$ , and  $\mu$ , adjusted using Tokay and Short's procedure for the 27 May 1997 squall line. The general behavior of the three time series is rather similar, with minimum values occurring in the convective and stratiform regions, and maxima in the transition region. In case of  $\mu$ , it is not clear if these differences are significant, given the large statistical fluctuations. In addition, the physical interpretation of the parameter  $N_0$  is hampered by the fact that its units depend on the value of the parameter  $\mu$ . This may introduce spurious correlations between  $N_0$  and  $\mu$  (e.g., Chandrasekar and Bringi 1987; Uijlenhoet 1999). The

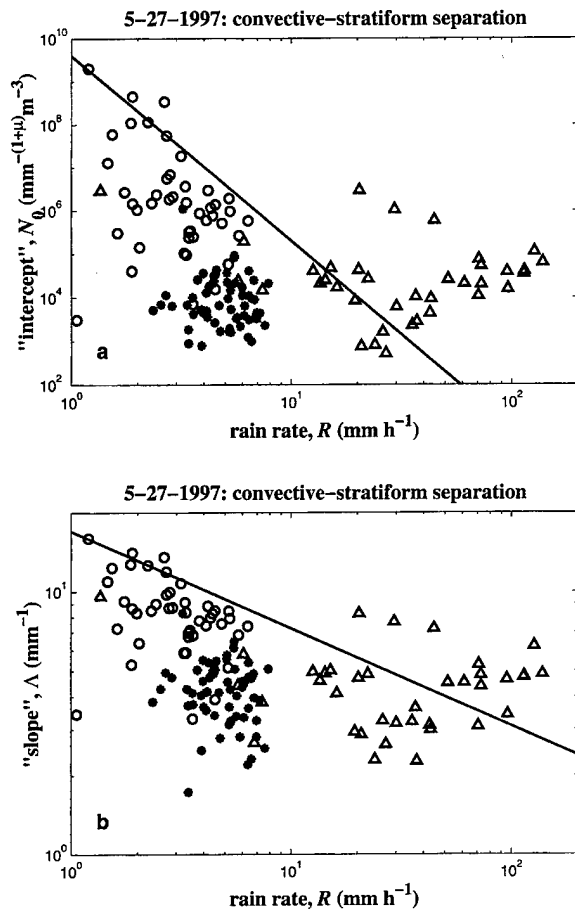


FIG. 7. Empirical relationship between the "intercept" parameter of gamma fit (Fig. 6a) and rain rate (Fig. 2a) for the 27 May 1997 squall line. Triangles indicate raindrop size distributions collected during the leading convective phase, circles show distributions collected during the transition phase, and asterisks indicate distributions collected during the trailing stratiform phase. The solid line indicates the separator between tropical convective (above) and tropical stratiform (below) rain proposed by Tokay and Short (1996). (b) Same as (a) but for the "slope" parameter of gamma fit (Fig. 6b).

temporal evolution of the parameter  $\Lambda$  (Fig. 6b) is reasonably close to that of the  $\Lambda$  parameter estimated using Waldvogel's (1974) procedure (Fig. 5b). The mean value of  $\mu$  during the 27 May 1997 storm is about 5. This closely corresponds to the mode of the empirical  $\mu$  distribution reported by Tokay and Short (1996) for tropical rainfall and to  $\mu = 6$  found by Steiner (1991) for rainfall in Switzerland.

Tokay and Short (1996) propose a stratiform-convective classification based on the adjusted parameter values. Figure 7 provides scatterplots of  $N_0$  versus  $R$  (Fig. 7a) and  $\Lambda$  versus  $R$  (Fig. 7b) for the three rainfall types considered. Also included are curves (straight lines in log-log space) proposed by Tokay and Short (1996) to discriminate between convective (above) and stratiform precipitation (below),  $N_0 = 4 \times 10^9 R^{-4.3}$  and

$\Lambda = 17R^{-0.37}$ , respectively. Evidently, this algorithm is not successful in correctly classifying the convective and the stratiform distributions. This may be due to the fact that Tokay and Short derived their results for "tropical oceanic" rainfall, whereas the 27 May 1997 squall line could be classified as "midlatitude continental."

Motivated by a lack of detailed microphysical and dynamic information in space and time, precipitation type classification schemes generally rely upon integral parameters such as radar reflectivity or rain rate (e.g., Steiner et al. 1995). Figures 7 and 11a (section 3c) show that a simple approach such as thresholding the rain rate (e.g., Ciach et al. 1997) or radar reflectivity will be reasonably successful in separating convective ( $\geq 10 \text{ mm h}^{-1}$  or  $\geq 40 \text{ dBZ}$ ) from stratiform ( $< 10 \text{ mm h}^{-1}$  or  $< 40 \text{ dBZ}$ ) rainfall, except for the onset of convection. This approach will work reasonably well for organized storm systems but not necessarily otherwise. Tokay and Short's (1996) method of classifying precipitation types on the basis of fitted raindrop size distribution parameters does not appear to be very robust (Fig. 7). Based on the analyses presented above, the mean raindrop diameter and the width of the raindrop size distribution (i.e., the standard deviation of the drop diameters), if available, seem to be more suitable parameters to assist in the classification. Figure 4 shows that the leading convective line exhibits mean drop diameters  $\mu_D \geq 1 \text{ mm}$  and standard deviations  $\sigma_D \geq 0.5 \text{ mm}$ . The transition phase has very narrow raindrop spectra with  $\mu_D < 1 \text{ mm}$  and  $\sigma_D < 0.5 \text{ mm}$ . For the trailing stratiform region,  $\mu_D < 1 \text{ mm}$  and  $\sigma_D \geq 0.5 \text{ mm}$ . Thus, the mean drop diameter separates the convective phase from the rest of the storm system, while the width of the raindrop size distribution assists in the more subtle distinction between transition and stratiform rainfall.

#### b. Scaling analysis

To reveal the typical shapes of the raindrop size distributions during the passage of the squall-line system, we have applied the scaling-law analysis outlined in section 2c to the spectra from each of the three storm phases. We have only considered spectra associated with rain rates exceeding  $1 \text{ mm h}^{-1}$ .

In Fig. 8a the exponents  $\gamma_m$  of power-law relationships between the  $m$ th order moment of the raindrop size distribution (for  $0 \leq m \leq 6$ ) and the reference variable  $R$  are plotted against the corresponding moment orders  $m + 1$  for the 38 convective spectra considered. The power-law relationships have been adjusted using linear regression on the logarithmic values, using  $\log R$  as the independent variable. The error bars indicate 68% confidence limits, estimated from 1000 bootstrap samples (Efron and Tibshirani 1993). According to the scaling-law theory (Sempere Torres et al. 1994), a plot like Fig. 8a should yield a straight line with intercept  $\alpha$  and slope  $\beta$ . The dashed line indicates a linear regression between  $\gamma_m$  and  $m + 1$  for  $2 \leq m \leq 6$ . The straight-

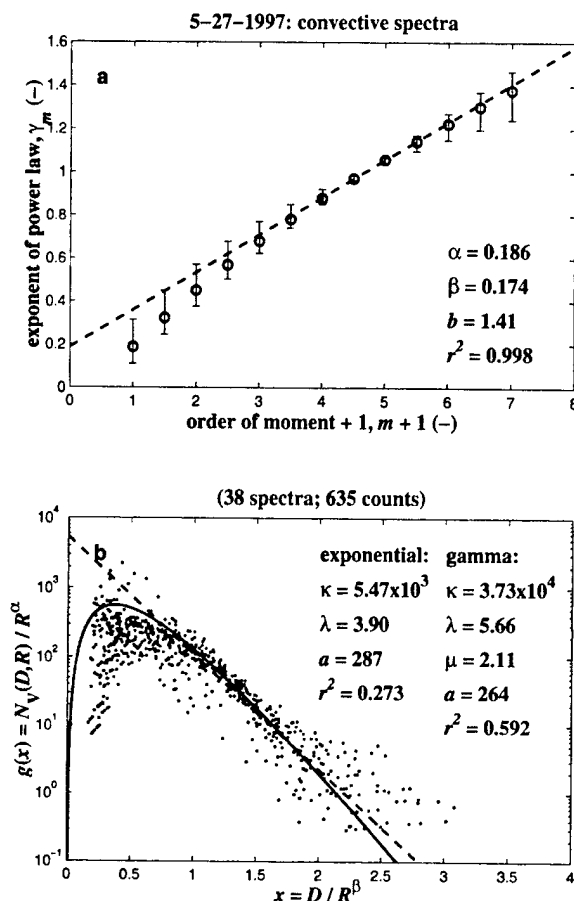


FIG. 8. Scaling analysis of raindrop size distributions collected during the convective phase of the 27 May 1997 squall line. (a) Estimation of scaling exponents ( $\alpha$ ,  $\beta$ ) as intercept and slope of the plot of exponents  $\gamma_m$  (of power laws with  $R$ ) vs order of moment  $m + 1$  for  $2 \leq m \leq 6$  (error bars indicate 68% confidence limits obtained using 1000 bootstrap samples). Corresponding values of exponent  $b$  (—) of the  $Z$ - $R$  relationship and of coefficient of determination  $r^2$  (—) of the regression line are indicated as well. (b) Application of exponents to scale spectra and infer general raindrop size distribution (dots) and adjustment of theoretical parameterizations for  $g(x)$ , with corresponding parameter values, prefactors  $a$  (—) of  $Z$ - $R$  relationships, and coefficients of determination  $r^2$  (—): exponential parameterization (dashed line) and gamma parameterization (solid line).

line behavior predicted by the scaling-law formalism holds reasonably well over a large part of the range of moment orders from 0 to 6. This is confirmed by the high value of the coefficient of determination  $r^2$  (computed as the square of the correlation coefficient between  $\gamma_m$  and  $m + 1$  for  $2 \leq m \leq 6$ ).

As explained in section 2c, in order to guarantee self-consistency, the value of  $\beta$  has been determined as the slope of the dashed line in Fig. 8a, and the value of  $\alpha$  from the self-consistency constraint on the scaling exponents [Eq. (18)], although the difference with the intercept of the dashed line is small. The indicated value of  $b$  is the exponent of the corresponding  $Z$ - $R$  relationship implied by the scaling-law formalism [Eq. (16)].

Note that this value is very close to the exponent of the standard NEXRAD  $Z$ - $R$  relationship  $Z = 300R^{1.4}$  (Fulton et al. 1998). As we have shown in section 2c, the estimated value of  $b$  is independent of any assumption regarding the shape of the (scaled) raindrop size distribution.

In Fig. 8b the inferred values for the scaling exponents are used to identify the shape of the corresponding general raindrop size distribution  $g(x)$ . The scaling analysis is successful in the sense that it eliminates a large part of the rain-rate-induced variability, as predicted by the scaling-law formalism. The fact that not all dots fall perfectly on one single curve indicates that one reference variable (in this case the rain rate  $R$ ) is apparently not able to explain *all* observed variability (which is a lot during the convective phase; see Fig. 3). Two different analytical parameterizations have been fitted to the empirical general raindrop size distribution indicated by the dots: an exponential parameterization (bold dashed line) and a gamma parameterization (bold solid line). Equations (19) and (20) explain the meaning of the parameter values indicated in Fig. 8b (recall that  $\mu = 0$  for the exponential parameterization). The indicated values of  $a$  are the values for the prefactors of the corresponding  $Z$ - $R$  relationships implied by the scaling-law formalism [Eq. (15)] for the two parameterizations. These values are just a little bit less than that of the standard NEXRAD  $Z$ - $R$  relationship.

Also shown are the corresponding values of the coefficient of determination (or model efficiency)  $r^2$  (—). This goodness-of-fit statistic indicates the fraction of the observed variance explained by the model:  $r^2 = 1$  indicates a perfect agreement between model and observations,  $r^2 = 0$  indicates that the model does not perform better than the mean of the observations, and  $r^2 < 0$  indicates a serious lack of agreement (e.g., Mood et al. 1974). In terms of the computed value of  $r^2$ , the gamma parameterization provides a better fit to the data than does the exponential parameterization. This is mainly due to a closer agreement for values of the scaled raindrop diameter  $x$  smaller than 0.5.

Similar scaling analyses have been carried out for the transition (Fig. 9) and the stratiform (Fig. 10) phases of the squall-line system. These analyses reveal that the shapes of the scaled spectra are wide and bent downward for small raindrop sizes in the leading convective line, narrow and slightly bent upward in the transition zone, and wide and strongly bent upward in the trailing stratiform rain. Although the fits are reasonable (see  $r^2$  values in Figs. 9 and 10), the scaled distributions during the transition and stratiform phases display shapes that the gamma parameterization for the raindrop size distribution is not able to accommodate very well. With regard to the shapes during the different phases, our results differ somewhat from those obtained by Sempere Torres et al. (2000), which may be due to the fact that they employed an optical spectroprecipitometer instead of a Joss-Waldvogel disdrometer (with the associated

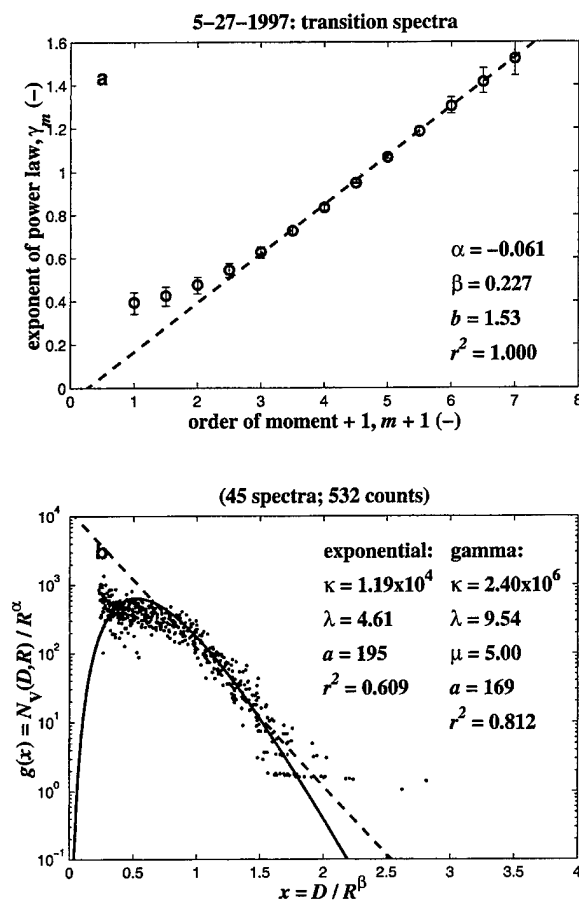


FIG. 9. Same as Fig. 8 but for raindrop size distributions collected during the transition phase of the 27 May 1997 squall line.

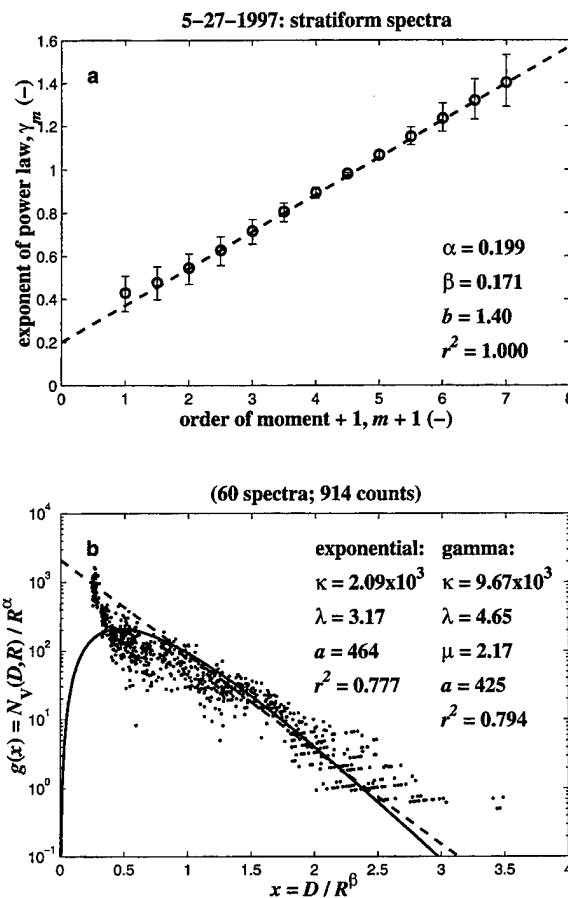


FIG. 10. Same as Fig. 8 but for raindrop size distributions collected during the stratiform phase of the 27 May 1997 squall line.

deadtime problem affecting the small-drop end of the scaled spectra). Nevertheless, in terms of the width of the distributions, this is consistent with the results from the time series analyses presented in section 3a. The dispersion among the scaled spectra (i.e., the scatter of the data points about the fitted curve) during the transition and stratiform phases is significantly smaller than during the convective phase. The exponents of the resulting  $Z$ - $R$  relationships are roughly the same for the leading convective line and the trailing stratiform rain ( $\approx 1.4$ ) and slightly larger for the transition region ( $\approx 1.5$ ), with prefactors increasing in this order: transition ( $\approx 200$ ), convective ( $\approx 300$ ), stratiform ( $\approx 450$ ). Table 1 summarizes the inferred parameter values and their associated uncertainties. Note the difference between the  $\mu$  values in Table 1 and those in Fig. 6c.

### c. Implications for rainfall estimation

In this section we investigate the implications of the variability of the raindrop size distributions reported in sections 3a and 3b for single-parameter and dual-parameter radar rainfall estimates. Figure 11a is a scat-

terplot of the values of the radar reflectivity factor  $Z$  and the rain rate  $R$  shown before in Figs. 2a,b. The three phases of the squall line occupy distinct regions in the  $Z$ - $R$  phase space. There is hardly any overlap (Steiner et al. 1999). To show the time dependence of the  $Z$ - $R$  relation during the convective phase of the storm, the data points have been connected. The separate regimes within the convective phase that were discussed previously are clearly distinguishable in Fig. 11a.

We have derived power-law  $Z$ - $R$  relationships based on linear regression of  $\log Z$  on  $\log R$  for each of the three storm phases separately and for three combinations (Table 2). The motivation for studying these combinations is the observation that classification schemes proposed in the literature (e.g., Steiner et al. 1995; Tokay and Short 1996; Ciach et al. 1997) only distinguish between convective and stratiform precipitation. It is therefore important to assess the effect of classification of a transition phase (as a separate category, or incorporated either in the convective or stratiform category) on the radar rainfall estimates. The coefficients obtained via regression are close to the ones obtained in section 3b using the scaling-law formalism, notwithstanding



TABLE 1. Means and 68% confidence limits (obtained using 1000 bootstrap samples) of the following parameters for the convective, transition, and stratiform phases of the 27 May 1997 squall line: scaling exponents ( $\alpha$ ,  $\beta$ ) and corresponding exponent  $b$  of the  $Z$ - $R$  relationship; intercept  $\kappa$ , (semilogarithmic) slope  $\lambda$  of exponential fit to general raindrop size distribution  $g(x)$ , and corresponding prefactor  $a$  of the  $Z$ - $R$  relationship; parameters  $\kappa$ ,  $\lambda$ , and  $\mu$  of gamma parameterization for general raindrop size distribution  $g(x)$ , and corresponding prefactor  $a$  of the  $Z$ - $R$  relationship.

Parameter		16%	Mean	85%
Convective phase (38 spectra; 27.75 mm)				
General	$\alpha$	0.014	0.186	0.436
	$\beta$	0.121	0.174	0.211
	$b$	1.28	1.41	1.49
Exponential	$\kappa$	$2.17 \times 10^3$	$5.47 \times 10^3$	$1.03 \times 10^4$
	$\lambda$	3.20	3.90	4.47
	$a$	209	287	455
Gamma	$\kappa$	$1.19 \times 10^4$	$3.73 \times 10^4$	$1.06 \times 10^5$
	$\lambda$	4.82	5.66	6.60
	$\mu$	1.73	2.11	2.73
	$a$	192	264	413
Transition phase (45 spectra; 2.35 mm)				
General	$\alpha$	-0.197	-0.061	0.048
	$\beta$	0.204	0.227	0.256
	$b$	1.47	1.53	1.60
Exponential	$\kappa$	$1.05 \times 10^4$	$1.19 \times 10^4$	$1.40 \times 10^4$
	$\lambda$	4.49	4.61	4.77
	$a$	180	195	207
Gamma	$\kappa$	$1.32 \times 10^6$	$2.40 \times 10^6$	$5.54 \times 10^6$
	$\lambda$	8.97	9.54	10.3
	$\mu$	4.57	5.00	5.54
	$a$	155	169	180
Stratiform phase (60 spectra; 5.00 mm)				
General	$\alpha$	-0.015	0.199	0.395
	$\beta$	0.130	0.171	0.217
	$b$	1.30	1.40	1.51
Exponential	$\kappa$	$1.51 \times 10^3$	$2.09 \times 10^3$	$2.98 \times 10^3$
	$\lambda$	2.96	3.17	3.42
	$a$	389	464	545
Gamma	$\kappa$	$6.18 \times 10^3$	$9.67 \times 10^3$	$1.66 \times 10^4$
	$\lambda$	4.35	4.65	5.05
	$\mu$	2.00	2.17	2.39
	$a$	356	425	498

their radically different methods of derivation. In this section we employ the regression-based coefficients rather than the scaling-based ones to allow a direct comparison with polarimetric rainfall estimators, which are also derived using regression (Table 3). The  $Z$ - $R$  relationships for the three phases separately and the mean relationship for the entire event are shown in Fig. 11a. The convective relationship and the mean event relationship differ only a little. Also indicated in Table 2 are the 68% confidence limits associated with the estimated coefficients obtained using 1000 bootstrap samples (Efron and Tibshirani 1993) and the associated coefficients of determination in logarithmic space (i.e., squares of the correlation coefficients between  $\log Z$  and  $\log R$ ). High values of  $r^2$ , indicating that the data points closely follow a power-law relationship, correspond to narrow confidence limits. It should be noted that the

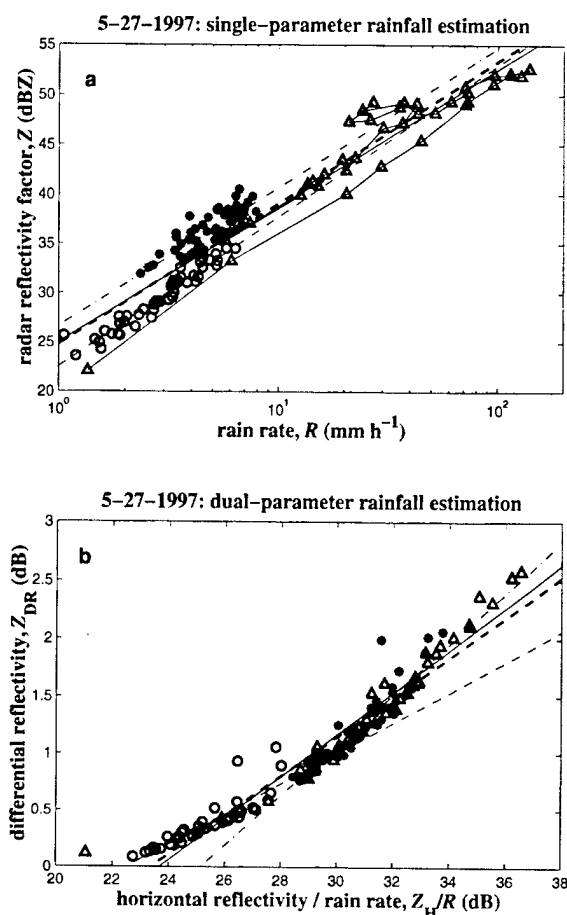


FIG. 11. (a) Empirical radar reflectivity-rain rate relationship for the 27 May 1997 squall line. Triangles indicate raindrop size distributions collected during the leading convective phase (connected with thin solid lines to show time dependence), circles indicate distributions collected during the transition phase, and asterisks indicate distributions collected during the trailing stratiform phase. The bold dashed line indicates the best-fit  $Z$ - $R$  relationship for the entire event, the thin solid line shows the best-fit relationship for the convective phase, the thin dashed line is the best-fit relationship for the transition phase, and the thin dash-dotted line indicates the best-fit relationship for the stratiform phase (see Table 2 for corresponding values of prefactors, exponents, and coefficients of determination). (b) Same as (a) but for the empirical relationship between differential reflectivity and the (horizontal) reflectivity-rain rate ratio (see Table 3 for corresponding values of prefactors, exponents, and coefficients of determination).

confidence limits for the prefactors and those for the exponents are not independent of each other.

Figure 11b shows the corresponding empirical relationships between  $Z_{DR}$  and  $Z_H/R$  (i.e., the ratio of  $Z_H$  to  $R$ ) for the three storm phases. Note the significantly reduced scatter as compared to the empirical  $Z$ - $R$  relationships in Fig. 11a. Except for a few outliers, all data points roughly follow a single curve. Interestingly, this curve seems to consist of two more or less straight lines, one with a gentle slope (corresponding to the transition phase) and one with a steep slope (corresponding

TABLE 2. Means and 68% confidence limits (obtained using 1000 bootstrap samples) of prefactors  $a$  and exponents  $b$  of the  $Z$ - $R$  relationship (obtained using linear regression of  $\log Z$  on  $\log R$ ) for the convective (C), transition (T), and stratiform (S) phases (and combinations thereof) of the 27 May 1997 squall line, and corresponding coefficients of determination ( $-$ ).

Phase	$a$ in $Z = aR^b$			$b$ in $Z = aR^b$			$r^2$
	16%	Mean	85%	16%	Mean	85%	
C	232	315	529	1.24	1.38	1.46	0.897
T	158	178	198	1.44	1.52	1.62	0.932
S	381	463	565	1.28	1.40	1.52	0.667
C + T	177	189	200	1.48	1.51	1.55	0.972
T + S	126	144	163	1.93	2.00	2.10	0.829
C + T + S	273	299	323	1.40	1.43	1.47	0.917

to both the convective and the stratiform phases). Recall that transition represents a decay phase, whereas the convective and stratiform phases include growth. Table 3 provides the corresponding estimated coefficients of the  $R(Z_H, Z_{DR})$  relationships, the associated 68% confidence limits obtained using 1000 bootstrap samples, and the corresponding coefficients of determination. The latter pertain to the linear regression of  $Z_{DR}$  on  $Z_H/R$  in logarithmic space, employed to infer the reported coefficients. As would be expected based on the data (Fig. 11b), the  $R(Z_H, Z_{DR})$  relationships for the entire event and for the convective and stratiform phases are quite similar. They are also reasonably close to a relationship reported by Doviak and Zrnic (1993). Only the relationship for the transition phase deviates significantly. However, rain rates during that phase are very low anyway (Fig. 2a), so this does not seem to be a major obstacle for the successful application of a mean  $R(Z_H, Z_{DR})$  relationship.

Tables 4 and 5 provide the biases in the simulated radar rainfall estimates obtained using the derived single-parameter  $Z$ - $R$  algorithms (Table 2) and dual-parameter polarimetric algorithms (Table 3) for each of the storm phases and combinations thereof. The rows in Tables 4 and 5 correspond to the mean relationships presented in Tables 2 and 3, respectively. The columns in Tables 4 and 5 correspond to the phases of the squall line to which these relationships are applied. Thus, the entries on the diagonals of Tables 4 and 5 are the biases associated with the regressions presented in Tables 2 and 3. Although these biases are small, they are generally not zero, demonstrating the fact that (unconstrained) linear regression on logarithmic values leads to biased estimators (e.g., Steiner and Smith 2000).

The best  $Z$ - $R$  algorithm in terms of overall bias is actually the best-fit relationship for the convective phase of the squall line. It outperforms both the best-fit relationship for the entire event and the "optimal" combination of three dedicated relationships for each of the three storm phases. It is not surprising that the "convective"  $Z$ - $R$  algorithm performs as well as it does, because almost 80% of the total rainfall (27.75 out of 35.10 mm) is produced during the convective phase of

TABLE 3. Means and 68% confidence limits (obtained using 1000 bootstrap samples) of prefactors  $c$  and exponents  $d$  of the  $R(Z_H, Z_{DR})$  relationships [obtained using linear regression of  $\log Z_{DR}$  on  $\log(Z_H/R)$ ] for the convective (C), transition (T), and stratiform (S) phases (and combinations thereof) of the 27 May 1997 squall line, and corresponding coefficients of determination ( $-$ ).

Phase	$c$ in $R = c \times 10^{-3} Z_H Z_{DR}^{-d}$			$d$ in $R = c \times 10^{-3} Z_H Z_{DR}^{-d}$			$r^2$
	16%	Mean	85%	16%	Mean	85%	
C	3.06	4.29	5.25	4.53	5.44	6.01	0.919
T	5.36	5.62	5.97	6.81	7.49	8.40	0.769
S	2.84	3.06	3.28	4.25	4.54	4.81	0.884
C + T	4.64	4.81	5.01	5.61	5.77	5.96	0.960
T + S	4.67	4.83	4.99	5.94	6.12	6.31	0.930
C + T + S	4.42	4.60	4.79	5.62	5.79	5.95	0.940

the squall-line system. The fact that it even performs better than a combination of three separate relationships for each of the storm phases is a result of underestimations during the convective and transition phases that are compensated by an overestimation during the stratiform phase.

With regard to the polarimetric algorithms, the attention should be focused entirely on the best-fit relationship for the entire event because of its potential operational applicability. Its bias is negligible, both for each of the storm phases separately and for the event as a whole. This is also evident from the comparison with the best-fit  $Z$ - $R$  relationship for the entire event in Figs. 12a,b. Note the close correspondence between the rainfall accumulations derived from the best-fit  $R(Z_H, Z_{DR})$  relationship for the entire event (circles) and those derived directly from the raindrop size spectra (bold solid line), as compared to those derived from the best-fit  $R(Z)$  relationship (thin solid line). Although this is a promising result, it should be realized that 1) simulating radar rainfall estimates from disdrometer measurements "does not consider radar errors and the needed dwell times to make the measurements" (Doviak and Zrnic 1993), and 2) the result obtained here needs to be repeatable in order to have operational significance (a remark that applies in fact not only to the polarimetric algorithm but to all analyses presented in this paper). With regard to the latter, we are currently investigating the potential of polarimetric algorithms on several dozen other severe storms. We are particularly interested in the interevent variability of the coefficients of the polarimetric estimator. If we want this to be a robust estimator, the variability of its coefficients should be small.

The major advantage of a polarimetric algorithm over the traditional single-parameter  $Z$ - $R$  algorithm in situations of appreciable intrastorm variability of raindrop size distributions (such as during the 27 May 1997 squall line) is that it accounts for most variability using one single mean relationship. In case of a single-parameter algorithm, one would have to resort to using different  $Z$ - $R$  relationships for different microphysical conditions, such as, in the case of a squall line, different

TABLE 4. Biases (mm) associated with single-parameter rain-rate estimates, obtained from reflectivities alone using best-fit  $R(Z)$  relationships (Table 2) for the convective (C), transition (T), and stratiform (S) phases (and combinations thereof) of the 27 May 1997 squall line. For comparison, rainfall accumulations obtained from raindrop size distributions are 27.75 mm (C), 2.35 mm (T), and 5.00 mm (S)

$R(Z)$	Bias (mm)					
	C	T	S	C + T	T + S	C + T + S
C	-0.94	-0.56	1.93	-1.51	1.37	0.42
T	-0.94	0.02	3.36	-0.92	3.38	2.44
S	-8.68	-1.02	0.10	-9.70	-0.92	-9.60
C + T	-1.36	-0.05	3.15	-1.42	3.10	1.73
T + S	-16.11	-0.39	0.53	-16.50	0.15	-15.97
C + T + S	-3.69	-0.56	1.69	-4.25	1.13	-2.56

relationships for each of the three storm phases. The latter, however, would be difficult to implement in an operational setting because it would require a classification of precipitation types. A single polarimetric rainfall estimation algorithm, independent of precipitation type, would alleviate this problem.

#### 4. Summary and conclusions

The intrastorm variability of raindrop size distributions as a source of uncertainty in single-parameter and dual-parameter radar rainfall estimates has been studied using time series analyses of disdrometer observations. Two rain-rate ( $R$ ) estimators have been considered: the traditional single-parameter estimator using only the radar reflectivity factor ( $Z$ ) and a dual-polarization estimator using a combination of radar reflectivity at horizontal polarization ( $Z_H$ ) and differential reflectivity ( $Z_{DR}$ ). A case study for a squall-line system passing over the Goodwin Creek experimental watershed in northern Mississippi has been presented. The main conclusions of this work can be summarized as follows.

- 1) The mesoscale features of the 27 May 1997 squall line, as observed using the Memphis WSR-88D, and its microphysical characteristics, as observed using a Joss-Waldvogel disdrometer, correspond closely.
- 2) Microphysically, the leading convective line is characterized by large raindrop concentrations ( $>500$  drops per cubic meter), large mean raindrop sizes ( $>1$  mm), and wide raindrop size distributions (stan-

dard deviations  $>0.5$  mm), as compared to the transition region and the trailing stratiform rain.

- 3) The transition and stratiform phases have similar raindrop concentrations (200–500 drops per cubic meter) and mean raindrop sizes (0.6–0.9 mm). Their main difference is that the distributions are wider in the latter (standard deviations  $>0.5$  mm).
- 4) Fits of equivalent exponential and gamma raindrop size distributions according to Waldvogel's (1974) and Tokay and Short's (1996) methods support the idea of narrow (small size) spectra in the transition region, wider (intermediate size) spectra in the trailing stratiform rain, and even wider (large size) spectra in the leading convective line.
- 5) Tokay and Short's (1996) scheme to distinguish between tropical oceanic convective and stratiform rainfall does not to apply to the midlatitude continental squall line studied here.
- 6) A scaling-law analysis (Sempere Torres et al. 1994, 1998; Uijlenhoet 1999) reveals that the shapes of the scaled spectra are bent downward for small raindrop sizes in the leading convective line, slightly bent upward in the transition zone, and strongly bent upward in the trailing stratiform rain. However, these results should be interpreted with care, given the (yet unknown) sensitivity of this type of analysis to sampling fluctuations.
- 7) The exponents of the resulting  $Z$ - $R$  relationships are roughly the same for the leading convective line and the trailing stratiform rain ( $\approx 1.4$ ) and slightly larger

TABLE 5. Biases (mm) associated with dual-parameter rain-rate estimates, obtained from combination of (horizontal) reflectivities and differential reflectivities using best-fit  $R(Z_H, Z_{DR})$  relationships (Table 3) for the convective (C), transition (T), and stratiform (S) phases (and combinations thereof) of the 27 May 1997 squall line. For comparison, rainfall accumulations obtained from raindrop size distributions are 27.75 mm (C), 2.35 mm (T), and 5.00 mm (S).

$R(Z_H, Z_{DR})$	Bias (mm)					
	C	T	S	C + T	T + S	C + T + S
C	1.60	-0.06	0.53	1.54	0.47	2.08
T	-9.12	0.10	-0.82	-9.02	-0.71	-9.84
S	1.24	-0.56	0.05	0.67	-0.51	0.72
C + T	1.46	0.14	0.67	1.60	0.80	2.27
T + S	-1.91	0.06	0.17	-1.85	0.22	-1.69
C + T + S	0.03	0.02	0.39	0.05	0.42	0.44

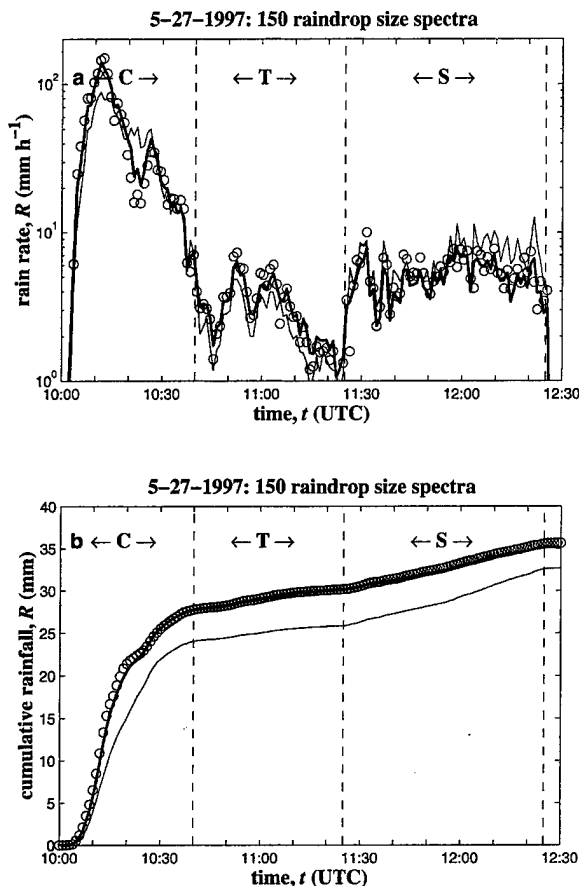


FIG. 12. (a) Comparison of single-parameter rain-rate estimates, obtained from reflectivities alone using the best-fit  $R(Z)$  relationship for the entire event (thin solid line), and dual-parameter rain-rate estimates, obtained from combination of (horizontal) reflectivities and differential reflectivities using the best-fit  $R(Z_H, Z_{DR})$  relationship for the entire event (circles), with those computed directly from raindrop size distributions for the 27 May 1997 squall line (bold solid line). (b) Same as (a) but for rainfall accumulations.

for the transition region ( $\approx 1.5$ ), with prefactors increasing in this order: transition ( $\approx 200$ ), convective ( $\approx 300$ ), stratiform ( $\approx 450$ ).

- 8) In terms of rainfall estimation bias, the best-fit mean  $R(Z_H, Z_{DR})$  relationship outperforms the best-fit mean  $R(Z)$  relationship, both for each storm phase separately and for the event as a whole. Further investigations are necessary to test the performance of these algorithms on independent data.
- 9) Ignoring transition rain as a category will not significantly affect rainfall estimates because rain rates and associated accumulations in that category are typically small. However, for the purpose of fitting  $Z$ - $R$  relations, one should make sure that transition rain does not "contaminate" the convective and stratiform rain categories to avoid significantly biased  $Z$ - $R$  coefficients.

**Acknowledgments.** The extraordinary assistance of the staff of the USDA/ARS National Sedimentation Laboratory in Oxford, Mississippi, in maintaining and operating the disdrometer is greatly appreciated. We would like to thank Paul Smith and two other reviewers (anonymous) for their detailed and helpful comments. This work was supported by National Science Foundation Grants EAR-9909696 and ATM-9906012, the National Weather Service and the NEXRAD Operations Support Facility under Cooperative Agreement NA87WH0518, National Aeronautics and Space Administration Grant NAG5-7744, and United States Army Research Office Grant DAAD19-99-1-0163. The lead author is currently supported by the Netherlands Organization for Scientific Research (NWO), through Grant 016.021.003 in the framework of the Innovational Research Incentives Scheme (Vernieuwingsimpuls).

#### REFERENCES

- Alonso, C. V., and R. L. Bingner, 2000: Goodwin Creek Experimental Watershed: A unique field laboratory. *ASCE J. Hydraul. Eng.*, **126**, 174–177.
- Atlas, D., 1953: Optical extinction by rainfall. *J. Meteor.*, **10**, 486–488.
- , and C. W. Ulbrich, 1977: Path- and area-integrated rainfall measurement by microwave attenuation in the 1–3 cm band. *J. Appl. Meteor.*, **16**, 1322–1331.
- , and —, 2000: An observationally based conceptual model of warm oceanic convective rain in the Tropics. *J. Appl. Meteor.*, **39**, 2165–2181.
- , R. C. Srivastava, and R. S. Sekhon, 1973: Doppler radar characteristics of precipitation at vertical incidence. *Rev. Geophys. Space Phys.*, **11**, 1–35.
- , C. W. Ulbrich, F. D. Marks, R. A. Black, E. Amitai, P. T. Willis, and C. E. Samsury, 2000: Partitioning tropical oceanic convective and stratiform rains by draft strength. *J. Geophys. Res.*, **105**, 2259–2267.
- Balakrishnan, N., D. S. Zrnic, J. Goldhirsh, and J. Rowland, 1989: Comparison of simulated rain rates from disdrometer data employing polarimetric radar algorithms. *J. Atmos. Oceanic Technol.*, **6**, 476–486.
- Battani, L. J., 1973: *Radar Observation of the Atmosphere*. The University of Chicago Press, 324 pp.
- Beard, K. V., 1976: Terminal velocity and shape of cloud and precipitation drops aloft. *J. Atmos. Sci.*, **33**, 851–864.
- Bennett, J. A., D. J. Fang, and R. C. Boston, 1984: The relationship between  $N_0$  and  $\lambda$  for Marshall–Palmer type raindrop-size distributions. *J. Climate Appl. Meteor.*, **23**, 768–771.
- Best, A. C., 1950: Empirical formulae for the terminal velocity of water drops falling through the atmosphere. *Quart. J. Roy. Meteor. Soc.*, **76**, 302–311.
- Biggerstaff, M. I., and R. A. Houze Jr., 1991: Kinematic and precipitation structure of the 10–11 June 1985 squall line. *Mon. Wea. Rev.*, **119**, 3034–3065.
- , and —, 1993: Kinematics and microphysics of the transition zone of the 10–11 June 1985 squall line. *J. Atmos. Sci.*, **50**, 3091–3110.
- Bringi, V. N., G.-J. Huang, V. Chandrasekar, and E. Gorgucci, 2002: A methodology for estimating the parameters of a gamma raindrop size distribution model from polarimetric radar data: Application to a squall-line event from the TRMM/Brazil campaign. *J. Atmos. Oceanic Technol.*, **19**, 633–645.
- Brown, S. A., and R. A. Houze Jr., 1994: The transition zone and secondary maximum of radar reflectivity behind a midlatitude

- squall line: Results retrieved from Doppler radar data. *J. Atmos. Sci.*, **51**, 2733–2755.
- Carbone, R. E., and L. D. Nelson, 1978: The evolution of raindrop spectra in warm-based convective storms as observed and numerically modeled. *J. Atmos. Sci.*, **35**, 2302–2314.
- Chandrasekar, V., and V. N. Bringi, 1987: Simulation of radar reflectivity and surface measurements of rainfall. *J. Atmos. Oceanic Technol.*, **4**, 464–478.
- Ciach, G. J., W. F. Krajewski, E. N. Anagnostou, M. L. Baeck, J. A. Smith, J. R. McCollum, and A. Kruger, 1997: Radar rainfall estimation for ground validation studies of the Tropical Rainfall Measuring Mission. *J. Appl. Meteor.*, **36**, 735–747.
- Delrieu, G., J.-D. Creutin, and I. Saint André, 1991: Mean  $K$ - $R$  relationships: Practical results for typical weather radar wavelengths. *J. Atmos. Oceanic Technol.*, **8**, 467–476.
- Dingle, A. N., and K. R. Hardy, 1962: The description of rain by means of sequential raindrop-size distributions. *Quart. J. Roy. Meteor. Soc.*, **88**, 301–314.
- Doviak, R. J., and D. S. Zrnic, 1993: *Doppler Radar and Weather Observations*. Academic Press, 562 pp.
- Efron, B., and R. Tibshirani, 1993: *An Introduction to the Bootstrap*. Chapman and Hall, 436 pp.
- Fujiwara, M., 1965: Raindrop-size distribution from individual storms. *J. Atmos. Sci.*, **22**, 585–591.
- Fulton, R. A., J. P. Breidenbach, D.-J. Seo, D. A. Miller, and T. O'Bannon, 1998: The WSR-88D rainfall algorithm. *Wea. Forecasting*, **13**, 377–395.
- Gertzman, H. R., and D. Atlas, 1977: Sampling errors in the measurement of rain and hail parameters. *J. Geophys. Res.*, **82**, 4955–4966.
- Goddard, J. W. F., and S. M. Cherry, 1984: The ability of dual-polarization radar (copolar linear) to predict rainfall rate and microwave attenuation. *Radio Sci.*, **19**, 201–208.
- Gunn, R., and G. D. Kinzer, 1949: The terminal velocity of fall for water droplets in stagnant air. *J. Meteor.*, **6**, 243–248.
- Houze, R. A., Jr., 1977: Structure and dynamics of tropical squall-line system. *Mon. Wea. Rev.*, **105**, 1540–1567.
- , 1993: *Cloud Dynamics*. Academic Press, 573 pp.
- , 1997: Stratiform precipitation in regions of convection: A meteorological paradox? *Bull. Amer. Meteor. Soc.*, **78**, 2179–2196.
- Illingworth, A. J., and T. M. Blackman, 2002: The need to represent raindrop size spectra as normalized gamma distributions for the interpretation of polarization radar observations. *J. Appl. Meteor.*, **41**, 286–297.
- Jameson, A. R., and A. B. Kostinski, 2001a: Reconsideration of the physical and empirical origins of  $Z$ - $R$  relations in radar meteorology. *Quart. J. Roy. Meteor. Soc.*, **127**, 517–538.
- , and —, 2001b: What is a raindrop size distribution? *Bull. Amer. Meteor. Soc.*, **82**, 1169–1177.
- Joss, J., and A. Waldvogel, 1967: Ein Spektrograph für Niederschlags-tropfen mit automatischer Auswertung. *Pure Appl. Geophys.*, **68**, 240–246.
- , and —, 1969: Raindrop size distribution and sampling size errors. *J. Atmos. Sci.*, **26**, 566–569.
- , and E. G. Gori, 1978: Shapes of raindrop size distributions. *J. Appl. Meteor.*, **17**, 1054–1061.
- , and A. Waldvogel, 1990: Precipitation measurements and hydrology. *Radar in Meteorology*, D. Atlas, Ed., Amer. Meteor. Soc., 577–606.
- Leary, C. A., and R. A. Houze Jr., 1979: Melting and evaporation of hydrometeors in precipitation from the anvil clouds of deep tropical convection. *J. Atmos. Sci.*, **36**, 669–679.
- Maki, M., T. D. Keenan, Y. Sasaki, and K. Nakamura, 2001: Characteristics of the raindrop size distribution in tropical continental squall lines observed in Darwin, Australia. *J. Appl. Meteor.*, **40**, 1393–1412.
- Marshall, J. S., and W. M. Palmer, 1948: The distribution of raindrops with size. *J. Meteor.*, **5**, 165–166.
- Mood, A. M., F. A. Graybill, and D. C. Boes, 1974: *Introduction to the Theory of Statistics*. McGraw-Hill, 564 pp.
- Petersen, W. A., and Coauthors, 1999: Mesoscale and radar observations of the Fort Collins flash flood of 28 July 1997. *Bull. Amer. Meteor. Soc.*, **80**, 191–216.
- Porrà, J. M., D. Sempere Torres, and J.-D. Creutin, 1998: Modeling of drop size distribution and its applications to rainfall measurements from radar. *Stochastic Methods in Hydrology: Rain, Landforms, and Floods*, V. K. Gupta et al., Eds., World Scientific, 73–84.
- Rao, T. N., D. N. Rao, K. Mohan, and S. Raghavan, 2001: Classification of tropical precipitating systems and associated  $Z$ - $R$  relationships. *J. Geophys. Res.*, **106D**, 17 699–17 711.
- Sánchez-Diezma, R., D. Sempere Torres, J.-D. Creutin, I. Zawadzki, and G. Delrieu, 2001: Factors affecting the precision of radar measurement of rain. An assessment from a hydrological perspective. Preprints, *30th Conf. on Radar Meteorology*, Munich, Germany, Amer. Meteor. Soc., 573–575.
- Sauvageot, H., and J.-P. Lacaux, 1995: The shape of averaged raindrop size distributions. *J. Atmos. Sci.*, **52**, 1070–1083.
- Sekhon, R. S., and R. C. Srivastava, 1971: Doppler radar observations of drop-size distributions in a thunderstorm. *J. Atmos. Sci.*, **28**, 983–994.
- Seliga, T. A., and V. N. Bringi, 1976: Potential use of radar differential reflectivity measurements at orthogonal polarizations for measuring precipitation. *J. Appl. Meteor.*, **15**, 69–76.
- Sempere Torres, D., J. M. Porrà, and J.-D. Creutin, 1994: A general formulation for raindrop size distribution. *J. Appl. Meteor.*, **33**, 1494–1502.
- , —, and —, 1998: Experimental evidence of a general description of raindrop size distribution properties. *J. Geophys. Res.*, **103D**, 1785–1797.
- , R. Sánchez-Diezma, I. Zawadzki, and J.-D. Creutin, 2000: Identification of stratiform and convective areas using radar data with application to the improvement of DSD analysis and  $Z$ - $R$  relations. *Phys. Chem. Earth*, **25**, 985–990.
- Smith, J. A., 1993: Marked point process models of raindrop-size distributions. *J. Appl. Meteor.*, **32**, 284–296.
- , and W. F. Krajewski, 1993: A modeling study of rainfall rate-reflectivity relationships. *Water Resour. Res.*, **29**, 2505–2514.
- , and R. D. De Veaux, 1994: A stochastic model relating rainfall intensity to raindrop processes. *Water Resour. Res.*, **30**, 651–664.
- , M. L. Baeck, M. Steiner, and A. J. Miller, 1996: Catastrophic rainfall from an upslope thunderstorm in the central Appalachians: The Rapidan storm of June 27, 1995. *Water Resour. Res.*, **32**, 3099–3113.
- , —, J. E. Morrison, and P. Sturdevant-Rees, 2000: Catastrophic rainfall and flooding in Texas. *J. Hydrometeorol.*, **1**, 5–25.
- , —, Y. Zhang, and C. A. Doswell III, 2001: Extreme rainfall and flooding from supercell thunderstorms. *J. Hydrometeorol.*, **2**, 469–489.
- Smith, P. L., Z. Liu, and J. Joss, 1993: A study of sampling-variability effects in raindrop size observations. *J. Appl. Meteor.*, **32**, 1259–1269.
- Smull, B. F., and R. A. Houze Jr., 1987: Dual-Doppler analysis of a midlatitude squall line with a trailing region of stratiform rain. *J. Atmos. Sci.*, **44**, 2128–2148.
- Steiner, M., 1991: A new relationship between mean Doppler velocity and differential reflectivity. *J. Atmos. Oceanic Technol.*, **8**, 430–443.
- , and J. A. Smith, 1998: Convective versus stratiform rainfall: An ice-microphysical and kinematic conceptual model. *Atmos. Res.*, **48**, 317–326.
- , and —, 2000: Reflectivity, rain rate, and kinetic energy flux relationships based on raindrop spectra. *J. Appl. Meteor.*, **39**, 1923–1940.
- , R. A. Houze Jr., and S. E. Yuter, 1995: Climatological characterization of three-dimensional storm structure from operational radar and rain gauge data. *J. Appl. Meteor.*, **34**, 1978–2007.

- , J. A. Smith, S. J. Burgess, C. V. Alonso, and R. W. Darden, 1999: Effect of bias adjustment and rain gauge data quality control on radar rainfall estimation. *Water Resour. Res.*, **35**, 2487–2503.
- Testud, J., S. Oury, R. A. Black, P. Amayenc, and X. Dou, 2001: The concept of “normalized” distribution to describe raindrop spectra: A tool for cloud physics and cloud remote sensing. *J. Appl. Meteor.*, **40**, 1118–1140.
- Tokay, A., and D. A. Short, 1996: Evidence from tropical raindrop spectra of the origin of rain from stratiform versus convective clouds. *J. Appl. Meteor.*, **35**, 355–371.
- , —, C. R. Williams, W. L. Ecklund, and K. S. Gage, 1999: Tropical rainfall associated with convective and stratiform clouds: Intercomparison of disdrometer and profiler measurements. *J. Appl. Meteor.*, **38**, 302–320.
- Uijlenhoet, R., 1999: Parameterization of rainfall microstructure for radar meteorology and hydrology. Ph.D. dissertation, Wageningen University, Wageningen, Netherlands, 279 pp. [Available from R. Uijlenhoet, Hydrology and Quantitative Water Management Group, Dept. of Environmental Sciences, Wageningen University, Nieuwe Kanaal 11, 6709 PA Wageningen, Netherlands.]
- , 2001: Raindrop size distributions and radar reflectivity–rain rate relationships for radar hydrology. *Hydrol. Earth Syst. Sci.*, **5**, 615–627.
- , and J. N. M. Stricker, 1999: A consistent rainfall parameterization based on the exponential raindrop size distribution. *J. Hydrol.*, **218**, 101–127.
- , J. A. Smith, and M. Steiner, 2003: The microphysical structure of extreme precipitation as inferred from ground-based raindrop spectra. *J. Atmos. Sci.*, in press.
- Ulbrich, C. W., 1983: Natural variations in the analytical form of the raindrop size distribution. *J. Climate Appl. Meteor.*, **22**, 1764–1775.
- , 1985: The effects of drop size distribution truncation on rainfall integral parameters and empirical relations. *J. Climate Appl. Meteor.*, **24**, 580–590.
- , and D. Atlas, 1998: Rainfall microphysics and radar properties: Analysis methods for drop size spectra. *J. Appl. Meteor.*, **37**, 912–923.
- Waldvogel, A., 1974: The  $N_0$  jump of raindrop spectra. *J. Atmos. Sci.*, **31**, 1067–1078.
- Willis, P. T., 1984: Functional fits to some observed drop size distributions and parameterization of rain. *J. Atmos. Sci.*, **41**, 1648–1661.
- , and P. Tattelman, 1989: Drop-size distributions associated with intense rainfall. *J. Appl. Meteor.*, **28**, 3–15.
- Wilson, J. W., and E. A. Brandes, 1979: Radar measurement of rainfall—A summary. *Bull. Amer. Meteor. Soc.*, **60**, 1048–1058.
- Zawadzki, I., 1984: Factors affecting the precision of radar measurements of rain. Preprints, *22d Conf. on Radar Meteorology*, Zurich, Switzerland, Amer. Meteor. Soc., 251–256.
- Zrnica, D. S., and A. V. Ryzhkov, 1999: Polarimetry for weather surveillance radar. *Bull. Amer. Meteor. Soc.*, **80**, 389–406.

## The Microphysical Structure of Extreme Precipitation as Inferred from Ground-Based Raindrop Spectra

REMKO UIJLENHOET, JAMES A. SMITH, AND MATTHIAS STEINER

*Department of Civil and Environmental Engineering, Environmental Engineering and Water Resources Program, Princeton University, Princeton, New Jersey*

(Manuscript received 14 November 2001, in final form 14 November 2002)

### ABSTRACT

The controls on the variability of raindrop size distributions in extreme rainfall and the associated radar reflectivity–rain rate relationships are studied using a scaling-law formalism for the description of raindrop size distributions and their properties. This scaling-law formalism enables a separation of the effects of changes in the scale of the raindrop size distribution from those in its shape. Parameters controlling the scale and shape of the scaled raindrop size distribution may be related to the microphysical processes generating extreme rainfall. A global scaling analysis of raindrop size distributions corresponding to rain rates exceeding  $100 \text{ mm h}^{-1}$ , collected during the 1950s with the Illinois State Water Survey raindrop camera in Miami, Florida, reveals that extreme rain rates tend to be associated with conditions in which the variability of the raindrop size distribution is strongly number controlled (i.e., characteristic drop sizes are roughly constant). This means that changes in properties of raindrop size distributions in extreme rainfall are largely produced by varying raindrop concentrations. As a result, rainfall integral variables (such as radar reflectivity and rain rate) are roughly proportional to each other, which is consistent with the concept of the so-called equilibrium raindrop size distribution and has profound implications for radar measurement of extreme rainfall. A time series analysis for two contrasting extreme rainfall events supports the hypothesis that the variability of raindrop size distributions for extreme rain rates is strongly number controlled. However, this analysis also reveals that the actual shapes of the (measured and scaled) spectra may differ significantly from storm to storm. This implies that the exponents of power-law radar reflectivity–rain rate relationships may be similar, and close to unity, for different extreme rainfall events, but their prefactors may differ substantially. Consequently, there is no unique radar reflectivity–rain rate relationship for extreme rain rates, but the variability is essentially reduced to one free parameter (i.e., the prefactor). It is suggested that this free parameter may be estimated on the basis of differential reflectivity measurements in extreme rainfall.

### 1. Introduction

Appreciable effort has been devoted to modeling and observing the storm-scale structure of extreme precipitation phenomena; however, their microphysical structure has received relatively little attention (e.g., Hudson 1963; Blanchard and Spencer 1970; Shiotsuki 1976; Willis and Tattelman 1989). The spatiotemporal variability of its hydrometeor size spectra can provide us with more information about the physical processes causing extreme precipitation. As an example, consider the world record 1-min rainfall rate of  $1872 \text{ mm h}^{-1}$  (i.e.,  $>30 \text{ mm}$  in 1 min), measured with a rain gauge in Unionville, Maryland, on 4 July 1956 (Willis and Tattelman 1989). What are the factors controlling the shapes of raindrop size distributions corresponding to

such extraordinary fluxes of water, and what are the microphysical environments that are able to produce them? In this paper, we provide a framework for analyzing raindrop size distributions in extreme rainfall that allows us to make a first step toward tackling these issues. In addition, we present the results of detailed case studies where we apply this framework.

An improved understanding of the microphysical structure of extreme precipitation is not only interesting in its own right. It is crucial in developing improved techniques for the remote measurement of extreme precipitation as well (e.g., Baeck and Smith 1998; Tokay et al. 1999; Atlas et al. 2000). Since accurate measurement is the basis for any reliable prediction, this is a particularly relevant issue in hydrometeorological applications (see Steiner et al. 1999; Smith et al. 1996, 2000, 2001 for antecedents of the present study). Two major problems when using single-parameter radar in combination with a standard (fixed) relationship between radar reflectivity ( $Z$ ) and rain rate ( $R$ ) for rainfall estimation are the overestimation of extreme “cold pro-

*Corresponding author address:* Dr. Remko Uijlenhoet, Hydrology and Quantitative Water Management Group, Department of Environmental Sciences, Wageningen University, Nieuwe Kanaal 11, Wageningen 6709 PA, Netherlands.  
E-mail: remko.uijlenhoet@wur.nl

cess" rain (associated with hail contamination; e.g., Smith et al. 2001) and the underestimation of extreme "warm process" rain (associated with equilibrium raindrop size distributions and the associated linearity of the  $Z$ - $R$  relationship; e.g., Smith et al. 1996; Petersen et al. 1999; American Meteorological Society 2000; Atlas and Ulbrich 2000).

The purpose of this paper is to learn more about the microphysical structure of extreme precipitation through an analysis of measured raindrop size distributions at the ground in extreme rainfall using an extension of a recently developed technique for the analysis of raindrop size spectra and their properties. Section 2 presents a review of previous work concerning raindrop size distributions associated with extreme rainfall conditions. In section 3, a formulation for the raindrop size distribution in terms of a scaling law (Sempere Torres et al. 1994, 1998; Uijlenhoet 1999) will be extended to provide a general framework that allows an evaluation of 1) hypotheses regarding the shapes and variability of raindrop size distributions in extreme rainfall and 2) implications for the radar remote measurement of extreme rainfall. This framework will be applied in section 4 to analyze ground-based raindrop size distributions for which the maximum rain rate approaches 500 mm  $\text{h}^{-1}$ , collected during the 1950s with the Illinois State Water Survey raindrop camera in Miami, Florida (Mueller 1962; Fujiwara 1965; Stout and Mueller 1968; Smith and de Veaux 1994). Particular attention will be paid to the hypothesis that the underestimation of extreme warm-process rain may be associated with raindrop spectra evolving to (multimodal) equilibrium distributions and the resulting proportionality between  $Z$  and  $R$  (e.g., List 1988; Zawadzki and de Agostinho Antonio 1988; Uijlenhoet 1999; Atlas and Ulbrich 2000; Jameson and Kostinski 2001a,b). Finally, section 5 presents the conclusions of this work.

## 2. Raindrop size distributions in extreme rainfall

Hudson (1963) presents one of the first experiments designed to measure and parameterize raindrop size distributions in high intensity storms. One of the aims of Hudson's study was to extend the previously reported analyses of Laws and Parsons (1943), already covering rain rates up to 150 mm  $\text{h}^{-1}$ , to even higher rain rates (up to 225 mm  $\text{h}^{-1}$ ). The main conclusion of his analyses is that up to rain rates of about 100 mm  $\text{h}^{-1}$  both the modal and the median raindrop size increased with increasing rain rates, whereas at higher rain rates "the results show a previously unreported phenomenon with both modal and median drop sizes decreasing [with increasing rain rates]." A closer inspection of Hudson's data, however, reveals that in the rain-rate range between 50 and 150 mm  $\text{h}^{-1}$ , these characteristic raindrop sizes remain approximately constant.

Blanchard and Spencer (1970), hypothesizing about the microphysical processes that generate raindrop size

distributions, argue that because in "light rains" (which they define as events with rain rates less than 25 mm  $\text{h}^{-1}$ ) drops are relatively sparse and most of them are small, both spontaneous and collisional breakup are probably of little importance in shaping raindrop size distributions. The microphysical processes that initiate rainfall must then be the main factor controlling the shape of raindrop size distributions. In heavy rain (with rain rates exceeding 100 mm  $\text{h}^{-1}$ ), on the other hand, where the spatial distribution of drops is relatively dense and there are larger drops, "there is a possibility that the drop size distribution here is determined mainly by raindrop breakup and very little by the microphysical processes that initiate the rainfall." Blanchard and Spencer provide empirical evidence for this hypothesis, both from their own artificial rain column experiments and from previously published experimental data (among others, those of Hudson). They find that, in the range of rain rates between roughly 100 and 700 mm  $\text{h}^{-1}$ , the median volume diameter remains relatively constant. They argue that "for a given intensity in heavy rain, we might find a steady state drop size distribution, where drop growth is balanced by drop breakup, that is the same whether it originates from marine shower clouds or continental thunderstorms." Mueller (1966), Srivastava (1971), Pasqualucci (1982), and Hodson (1986) provide additional evidence for (approximately) constant characteristic raindrop sizes during episodes of high rain rates.

Blanchard and Spencer's hypothesis is supported by List's (1988) finding that, as a result of the compensating effects in the competing microphysical processes shaping raindrop size distributions, "any raindrop size distribution will develop with time into an equilibrium distribution regardless of the initial spectrum." On the basis of the stationary form of the stochastic collection equation, List et al. (1987) show analytically that equilibrium raindrop size distributions are by definition the product of the rain rate  $R$  (or any other rainfall integral variable, such as  $Z$ ) and a generic shape function, implying that during equilibrium conditions 1) all moments of the raindrop size distribution must be proportional to each other and 2) all characteristic raindrop sizes must be constant. List (1988), Zawadzki and de Agostinho Antonio (1988), and Atlas and Ulbrich (2000) provide experimental evidence for such a proportionality in persistent tropical rain. Jameson and Kostinski (2001a,b) interpret this linearity as evidence for what they call "statistically homogeneous rain."

With regard to the shape of equilibrium distributions, computer simulations of the temporal evolution of raindrop size distributions in both zero-dimensional (box) and one-dimensional (shaft) models have demonstrated that raindrop size distributions evolve with time to multimodal equilibrium distributions (e.g., List et al. 1987; Hu and Srivastava 1995). The higher the rain rate, the faster equilibrium is reached (Srivastava 1971; List et al. 1987; McFarquhar and List 1991). Empirical evi-



dence for multiple peaks in raindrop size distributions associated with extreme rain rates has been provided by Shiotsuki (1976), Zawadzki and de Agostinho Antonio (1988), and Willis and Tattelman (1989). Recently, Sauvageot and Koffi (2000) have provided new (statistical) evidence for the occurrence of persistent multimodal raindrop size distributions and a conceptual model to explain their ("synthetic") shapes as resulting from overlapping rain shafts. Sheppard (1990) argues that some of the reported empirical evidence for multimodal raindrop size distributions may be due to instrumental artifacts associated with the Joss–Waldvogel disdrometer (see also Steiner and Waldvogel 1987; McFarquhar and List 1993).

In summary, there is both theoretical and empirical support for the hypothesis that in extreme rainfall, raindrop size distributions evolve toward an equilibrium-like state in which 1) the characteristic raindrop sizes (such as the median volume diameter  $D_0$ ) are constants, independent of  $R$  (although, as we will see later, they may still exhibit storm-to-storm variability, resulting in prefactors of power-law relationships that may vary between storms); 2) the moments of the raindrop size distribution (such as  $Z$  and  $R$ ) are proportional to each other (implying that the exponents of power-law relationships between such moments are unity); and 3) the shapes of the distributions may display a tendency toward multimodality (although the support for this last aspect is less convincing than that for the other two). If we want to test this hypothesis and assess its practical implications using empirical raindrop size distributions at the ground, we need a methodology to extract meaningful information about the intrinsic shape of raindrop size distributions and their variability from the empirical data without imposing an a priori functional form, as has been the common approach since Marshall and Palmer's (1948) work [see e.g., Martinez and Gori (1999) for a recent example of this approach]. The next section will present such a methodology.

### 3. Scaling-law framework for analyzing raindrop size distributions

#### a. Scaling-law formalism

Sempere Torres et al. (1994, 1998) have demonstrated that many previously proposed parameterizations for the raindrop size distribution are special cases of a general formulation, which takes the form of a scaling law. In this formulation, the raindrop size distribution depends both on the raindrop diameter ( $D$ ) and on the value of a so-called reference variable, commonly taken to be the rain rate ( $R$ ). The generality of this formulation stems from the fact that it is no longer necessary to impose an a priori functional form for the raindrop size distribution. Moreover, it naturally leads to the ubiquitous power-law relationships between rainfall integral parameters, notably that between the radar reflectivity

factor ( $Z$ ) and  $R$ . A major advantage over previous scaling approaches (e.g., Sekhon and Srivastava 1971; Willis 1984; Willis and Tattelman 1989) is that this approach explicitly considers the issue of the *internal consistency* of parameterizations for the raindrop size distribution (e.g., Bennett et al. 1984; Delrieu et al. 1991; Uijlenhoet 1999, 2001; Uijlenhoet and Stricker 1999).

According to the scaling-law formalism, raindrop size distributions can be parameterized as (Sempere Torres et al. 1994, 1998; Porrà et al. 1998)

$$N_v(D, R) = R^\alpha g(R^{-\beta}D), \quad (1)$$

where  $N_v(D, R)dD$  (per cubic meter), the subscript  $V$  standing for volume, represents the mean number of raindrops with (equivalent spherical) diameters between  $D$  and  $D + dD$  (in millimeters) present per unit volume of air as a function of the rain rate  $R$  (in millimeters per hour),  $\alpha$  and  $\beta$  are (dimensionless) *scaling exponents*, and  $g(x)$  is a *scaled raindrop size distribution* as a function of the scaled raindrop diameter  $x = R^{-\beta}D$ . Note that  $g(x)$  has been referred to as the "general raindrop size distribution" in earlier studies dealing with the scaling-law formalism (Sempere Torres et al. 1994, 1998; Porrà et al. 1998; Uijlenhoet 1999, 2001; Uijlenhoet et al. 2003). According to this formulation, the values of  $\alpha$  and  $\beta$  and the form and dimensions of  $g(x)$  depend on the *choice* of the reference variable, but do not bear any functional dependence on its *value*. Substitution of  $R = 1 \text{ mm h}^{-1}$  in Eq. (1) shows that  $N_v(D, 1) = g(D)$ , in other words that  $g(x)$  represents the *equivalent* (i.e., scaled) raindrop size distribution at a rain rate of  $1 \text{ mm h}^{-1}$  (Uijlenhoet 1999). Note that  $g(x)$  is *not* a probability density function [which will be derived later, see Eq. (20)]. In agreement with common practice,  $R$  is used as the reference variable in Eq. (1), although any other rainfall integral variable could serve as such (notably  $Z$ ). The main difference between Eq. (1) and the normalization approaches recently proposed by Testud et al. (2001) and Illingworth and Blackman (2002), is that the latter use *two* reference variables instead of only *one*.

The importance of the scaling-law formalism for radar meteorology stems from the fact that it allows an interpretation of the coefficients of power-law  $Z$ – $R$  relationships in terms of the values of the scaling exponents and the shape of the scaled raindrop size distribution. By definition,  $Z$  is related to the size distribution of the raindrops in the radar sample volume according to

$$Z = \int_0^\infty D^6 N_v(D, R) dD \quad (2)$$

(e.g., Battan 1973). Substituting the scaling law for the raindrop size distribution [Eq. (1)] into Eq. (2) leads to the power law

$$Z = aR^b, \text{ with} \quad (3)$$

$$a = \int_0^\infty x^6 g(x) dx, \text{ and} \quad (4)$$

$$b = \alpha + 7\beta \quad (5)$$

(Uijlenhoet 1999, 2001). Hence, the *prefactor* of a power-law  $Z$ - $R$  relationship is entirely determined by the shape of the scaled raindrop size distribution (its sixth moment), whereas a linear combination of the values of the scaling exponents completely determines the *exponent* of such a power-law  $Z$ - $R$  relationship. Any physical interpretation of the scaling exponents and of the scaled raindrop size distribution will therefore directly lead to a physical interpretation of the coefficients of power-law  $Z$ - $R$  relationships.

In a similar manner, the scaling-law formalism leads to power-law relationships between any other pair of rainfall integral variables. In particular, the rain rate  $R$  (in millimeters per hour) is defined in terms of the raindrop size distribution  $N_v(D, R)$  according to

$$R = 6\pi \times 10^{-4} \int_0^\infty D^3 v(D) N_v(D, R) dD, \quad (6)$$

where  $v(D)$  represents the functional relationship between the raindrop terminal fall speed in still air  $v$  (in meters per second) and the equivalent spherical raindrop diameter  $D$  (in millimeters). The simplest and most widely used form of the  $v(D)$  relationship is the power law

$$v(D) = cD^\gamma. \quad (7)$$

Atlas and Ulbrich (1977) demonstrate that Eq. (7) with  $c = 3.778$  and  $\gamma = 0.67$  (if  $v$  is expressed in meters per second and  $D$  in millimeters) provides a close fit to the data of Gunn and Kinzer (1949) in the range  $0.5 \leq D \leq 5.0$  mm (the diameter interval contributing most to rain rate). Although more sophisticated relationships have been proposed in the literature (e.g., Best 1950; Atlas et al. 1973; Beard 1976), the power-law form for the  $v(D)$  relationship is the only functional form that is consistent with power-law relationships between rainfall-related variables, notably between  $Z$  and  $R$  (Sempere Torres et al. 1994; Uijlenhoet 1999, 2001).

Substituting Eqs. (1) and (7) into the definition of  $R$  in terms of the raindrop size distribution [Eq. (6)] leads to the *self-consistency constraints*

$$6\pi \times 10^{-4} c \int_0^\infty x^{3+\gamma} g(x) dx = 1 \quad \text{and} \quad (8)$$

$$\alpha + (4 + \gamma)\beta = 1 \quad (9)$$

(Sempere Torres et al. 1994). Hence,  $g(x)$  must satisfy an integral equation (which reduces its degrees of freedom by one) and there is only *one* free scaling exponent. These self-consistency constraints guarantee that substitution of the parameterization for the raindrop size

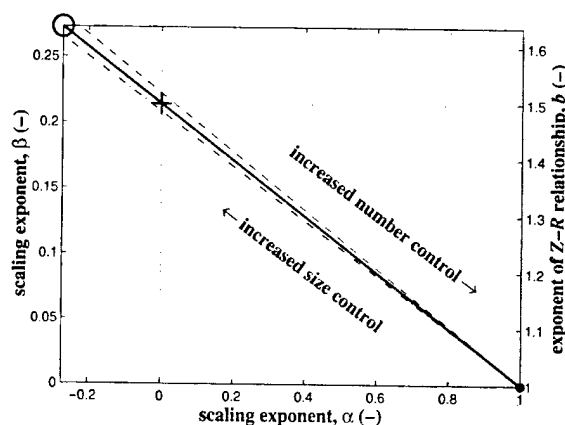


FIG. 1. Theoretical self-consistency relationship between scaling exponents  $\alpha$  (—) and  $\beta$  (—),  $\beta = (1 - \alpha)/(4 + \gamma)$ , and corresponding values of exponent  $b$  (—) of  $Z$ - $R$  relationship, for three different values of exponent  $\gamma$  (—) of power-law relationship between raindrop terminal fall speed and equivalent spherical raindrop diameter (bold solid line:  $\gamma = 0.67$ ; thin dashed line:  $\gamma = 0.5$ ; thin dash-dotted line:  $\gamma = 0.8$ ). The circle at the point with coordinates  $(\alpha, \beta) = (-0.273, 0.273)$  corresponds to raindrop size-controlled rainfall; the plus at the point with coordinates  $(\alpha, \beta) = (0, 0.214)$  and associated thin dotted lines corresponds to Marshall and Palmer's (1948) exponential raindrop size distribution; the dot at the point with coordinates  $(\alpha, \beta) = (1, 0)$  corresponds to equilibrium rainfall (i.e., raindrop concentration controlled) conditions (adapted from Uijlenhoet 1999).

distribution [Eq. (1)] into the defining expression for  $R$  [Eq. (6)] leads to  $R = R$ . Figure 1 provides a graphical representation of the self-consistency constraint on the scaling exponents [Eq. (9)] for different values of  $\gamma$  (Spilhaus 1948; Sekhon and Srivastava 1971; Atlas and Ulbrich 1977). Apparently, the sensitivity to different forms of the power-law  $v(D)$  relationship is not dramatic.

Substitution of the self-consistency constraint on the scaling exponents [Eq. (9)] for  $\gamma = 0.67$  (Atlas and Ulbrich 1977) into the definition of  $b$  in terms of those scaling exponents [Eq. (5)] yields  $b = 1.50 - 0.50\alpha$ , or equivalently  $b = 1 + 2.33\beta$  (Uijlenhoet 2001). Hence, the exponents of power-law  $Z$ - $R$  relationships can be expressed explicitly in terms of both scaling exponents [which are related to each other via the self-consistency constraint Eq. (9)], *independent* of any assumption regarding the shape of the scaled raindrop size distribution (see the right y axis in Fig. 1).

#### b. Gamma scaled raindrop size distribution

For the purpose of this paper, consider a gamma parameterization for the scaled raindrop size distribution:

$$g(x) = \kappa x^\mu \exp(-\lambda x), \quad (10)$$

which, for  $\mu = 0$ , reduces to an exponential parameterization. In this general form,  $g(x)$  is not an admissible description of the scaled raindrop size distribution, because it does not necessarily satisfy the self-consistency

constraint on  $g(x)$  [Eq. (8)]. Substitution of Eq. (10) into (8) yields, for a given value of the parameter  $\mu$ , a power-law relationship of  $\kappa$  in terms of  $\lambda$ :

$$\kappa = [6\pi \times 10^{-4} c \Gamma(4 + \gamma + \mu)]^{-1} \lambda^{4+\gamma+\mu}. \quad (11)$$

This is an explicit form of the self-consistency constraint on  $g(x)$  for the case of a gamma parameterization. For the applied units, with  $c = 3.778$  and  $\gamma = 0.67$  (Atlas and Ulbrich 1977), Eq. (11) reduces to  $\kappa = 9.50\lambda^{4.67}$  for the special case of an exponential parameterization for  $g(x)$  ( $\mu = 0$ ) (Uijlenhoet 2001).

A self-consistent expression for the prefactor of a power-law  $Z$ - $R$  relationship for the case of a gamma parameterization for  $g(x)$  can now be obtained by substituting Eqs. (10) and (11) into (4). For the applied units, with  $c = 3.778$  and  $\gamma = 0.67$  (Atlas and Ulbrich 1977), this yields  $a = 2.10 \times 10^4 \kappa^{-0.50}$  or, equivalently,  $a = 6.84 \times 10^3 \lambda^{-2.33}$  for the special case of an exponential parameterization for  $g(x)$  ( $\mu = 0$ ) (Uijlenhoet 2001). The scaling-law approach for determining power-law relationships complements the traditional regression-based methods (e.g., Steiner and Smith 2000). It has the advantage that it guarantees consistency between the coefficients of power-law relationships and the parameters of the corresponding parameterization for the raindrop size distribution.

It is of considerable interest to establish a link between the scaling-law formalism and the traditional analytical parameterizations for the raindrop size distribution. For the case of the gamma raindrop size distribution, this can be achieved through substituting Eq. (10) into (1). This yields

$$N_v(D, R) = \kappa R^{\alpha-\mu\beta} D^\mu \exp(-\lambda R^{-\beta} D). \quad (12)$$

Equation (12) reduces to the classical gamma parameterization for the raindrop size distribution:

$$N_v(D) = N_0 D^\mu \exp(-\Lambda D) \quad (13)$$

(Ulbrich 1983; Chandrasekar and Bringi 1987; Tokay and Short 1996; Ulbrich and Atlas 1998), if  $N_0$  and  $\Lambda$  depend on  $R$  according to the power laws

$$N_0 = \kappa R^{\alpha-\mu\beta} \quad \text{and} \quad (14)$$

$$\Lambda = \lambda R^{-\beta}. \quad (15)$$

Recall that the self-consistency of Eq. (12) requires that  $\alpha$  and  $\beta$  be related to each other via Eq. (9), and  $\kappa$  and  $\lambda$  via Eq. (11). For the special case of an exponential parameterization for the raindrop size distribution—that is, Eq. (13) with  $\mu = 0$ —Eq. (14) reduces to  $N_0 = \kappa R^\alpha$ . In Marshall and Palmer's (1948) parameterization,  $N_0 = 8.00 \times 10^3 \text{ mm}^{-1} \text{ m}^{-3}$ , independent of  $R$ . This implies  $\kappa = N_0 = 8.00 \times 10^3$ ,  $\alpha = 0$ ,  $\lambda = 4.23$  [Eq. (11)], and  $\beta = 0.214$  [Eq. (9)]. The corresponding self-consistent values of  $a$  and  $b$  are 237 [Eq. (4)] and 1.50 [Eq. (5)], respectively (see the bold plus and the dotted lines in Fig. 1).

### c. Controls on the variability of raindrop size distributions

What can be said about the shape of  $g(x)$  and the values of the scaling exponents (and hence the coefficients of  $Z$ - $R$  relationships) under equilibrium conditions? It has already been mentioned in section 2 that, on the basis of the stationary form of the stochastic collection equation, List et al. (1987) have shown analytically that equilibrium raindrop size distributions are the product of the rain rate  $R$  (or any other rainfall integral variable, e.g.,  $Z$ ) and a generic shape function. This implies that equilibrium raindrop size distributions are a family of curves defined by

$$N_v(D, R) = R g(D). \quad (16)$$

Comparison with Eq. (1) shows immediately that Eq. (16) is in fact a limiting case of the scaling law, obtained for  $\alpha = 1$  and  $\beta = 0$ . Equivalently, it may be stated that the scaling law is a generalization of Eq. (16) for nonequilibrium conditions. Because these values of  $\alpha$  and  $\beta$  satisfy the constraint imposed by Eq. (9), they form a self-consistent pair (indicated by the bold dot in Fig. 1). As such, Eq. (16) is an admitted form of the scaling law. Because in equilibrium  $\alpha = 1$  and  $\beta = 0$  independent of  $\gamma$ , the three theoretical self-consistency relationships presented in Fig. 1 meet in the equilibrium point. Substituting  $\alpha = 1$  and  $\beta = 0$  into Eq. (5) yields  $b = 1$  (Fig. 1, right  $y$  axis), implying that, under equilibrium conditions,  $Z$  and  $R$  are proportional to each other; that is,  $Z$ - $R$  relationships become linear. This has been noted earlier by Hodson (1986) and has been discussed in a more formal way by List (1988). The analysis presented here shows that this linearity is also consistent with the scaling-law formalism.

At this point, it is useful to express the raindrop size distribution  $N_v(D, R)$  (in  $\text{mm}^{-1} \text{ m}^{-3}$ ) as the product of the mean (expected) raindrop concentration  $N_T$  (per cubic meter) and the probability density function  $f_D(D, R)$  (per millimeter) of the (stochastic) diameters of raindrops present in a volume of air; that is,

$$N_v(D, R) = N_T f_D(D, R). \quad (17)$$

Such a probabilistic interpretation of the raindrop size distribution has been considered previously by Chandrasekar and Bringi (1987), Porrà et al. (1998), Sempere Torres et al. (1998, their appendix), Kostinski and Jameson (1999), and Uijlenhoet (1999). Jameson and Kostinski (2001a) stress its importance for the physical interpretation of empirical  $Z$ - $R$  relationships in radar meteorology. Note that, in accordance with the definition of the scaling law [Eq. (1)], we have retained the explicit dependence on the reference variable  $R$  in Eq. (17).

The raindrop concentration  $N_T$  (per cubic meter) is by definition equal to the total integral over the raindrop size distribution:

$$N_T = \int_0^\infty N_v(D, R) dD. \quad (18)$$

TABLE 1. Three special cases of controls on variability of raindrop size distributions, with associated values of scaling exponents  $\alpha$  (–) and  $\beta$  (–), and exponents of power-law relationships between raindrop concentration  $N_r$  and rain rate  $R$  ( $\alpha + \beta$ ), and between  $m$ th order moment of raindrop size distribution  $\Omega_m$  and rain rate  $R$  [ $\gamma_m$ , not to be confused with  $\gamma$ , exponent of power-law relationship between raindrop terminal fall speed and diameter; Eq. (7)]: 1) raindrop size-controlled rainfall; 2) intermediate case with equal proportions of size-controlled and number-controlled rainfall (Marshall–Palmer rainfall); 3) raindrop concentration-controlled— that is, number-controlled—rainfall (equilibrium rainfall). Note that radar reflectivity factor  $Z$  is a special case of  $\Omega_m$  for  $m = 6$  (adapted from Uijlenhoet 1999).

Case	$\alpha$ (–)	$\beta$ (–)	$\alpha + \beta$ (–)	$\gamma_m$ (–)
Size-controlled rainfall	$-(3 + \gamma)^{-1}$	$(3 + \gamma)^{-1}$	0	$m(3 + \gamma)^{-1}$
Intermediate	0	$(4 + \gamma)^{-1}$	$(4 + \gamma)^{-1}$	$(m + 1)(4 + \gamma)^{-1}$
Number-controlled rainfall	1	0	1	1

Substituting the scaling law for the raindrop size distribution [Eq. (1)] into Eq. (18) leads to the power law

$$N_r = \left[ \int_0^\infty g(x) dx \right] R^{\alpha+\beta}. \quad (19)$$

Substituting Eqs. (1) and (19) into (17), and rearranging leads to

$$f_D(D, R) = R^{-\beta} g'(R^{-\beta} D), \quad (20)$$

where  $g'(x)$  is the normalized (density) form of  $g(x)$ , that is,

$$g'(x) = \left[ \int_0^\infty g(x) dx \right]^{-1} g(x). \quad (21)$$

Equation (20) represents a scaling law for the probability density function of the diameters of raindrops present in a volume of air. These equations will allow us to investigate different types of control on the variability of raindrop size distributions.

We have seen that under equilibrium conditions  $\alpha = 1$  and  $\beta = 0$  (the bold dot in Fig. 1), as noted before by Sempere Torres et al. (1994). Substituting these values into Eqs. (19) and (20) shows that this corresponds to a situation where the raindrop concentration  $N_r$  is proportional to  $R$  and where the probability density function of the raindrop diameters in a volume of air satisfies  $f_D(D, R) = g'(D)$ , independent of  $R$ . The latter implies that under equilibrium conditions all characteristic raindrop sizes must be constants, independent of  $Z$  or  $R$  or any other moment of the raindrop size distribution. If characteristic raindrop sizes are constants, then any change in  $Z$  or  $R$  during equilibrium must be caused by changes in the raindrop concentration. This is also evident from the functional form of Eq. (16), which shows that raindrop size distributions for different rain rates are multiples of each other in equilibrium. Equilibrium conditions represent a limiting case, where all variability of the shape of the raindrop size distribution is controlled by variations in the raindrop concentration, that is, where the variability is *number controlled*. As we have seen in section 2, this constancy of characteristic raindrop sizes is a property of raindrop size distributions that has been observed by many previous authors during extreme rainfall conditions. As

such, these observations suggest that extreme rain rates often correspond to equilibrium-like conditions.

It follows from Eq. (19) that the other limiting case, that is, where all variability is controlled by variations in the characteristic raindrop sizes, that is, where the variability is *size controlled*, occurs if  $\alpha + \beta = 0$ . In this situation, the raindrop concentration  $N_r$  (per cubic meter) is a constant independent of  $R$  [Eq. (19)]. The corresponding values of the scaling exponents are  $\alpha = -\beta = -0.273$  [Eq. (9)] and that of the  $Z$ – $R$  exponent is 1.63 (Fig. 1, bold circle). For intermediate values of  $\beta$ , we have a combination of number and size control, as in Marshall and Palmer's (1948) exponential parameterization for the raindrop size distribution, for which  $\alpha = 0$  as we have seen before (the bold plus and the dotted lines in Fig. 1). Table 1 summarizes the three special cases we have identified.

#### d. Estimation of scaling exponents and scaled raindrop size distribution parameters

The scaling exponents  $\alpha$  and  $\beta$  can be estimated from empirical raindrop size distributions using regression-based power-law relationships between moments of different orders and the reference variable  $R$ . The moment of order  $m$  is defined as

$$\Omega_m = \int_0^\infty D^m N_r(D, R) dD. \quad (22)$$

Note that the raindrop concentration  $N_r$  [Eq. (19)] and the radar reflectivity  $Z$  [Eq. (2)] are special cases of  $\Omega_m$  for  $m = 0$  and  $m = 6$ , respectively. Similarly, the rain rate  $R$  [Eq. (6)] is proportional to  $\Omega_m$  for  $m = 3 + \gamma$ , if we assume a power-law  $v(D)$  relationship [Eq. (7)]. Substituting the scaling law for the raindrop size distribution [Eq. (1)] into Eq. (22) leads to the power law

$$\Omega_m = \left[ \int_0^\infty x^m g(x) dx \right] R^{\alpha+(m+1)\beta} \quad (23)$$

(Sempere Torres et al. 1994). Hence, the scaling exponents  $\alpha$  and  $\beta$  may be estimated as the intercept and slope of a plot of the exponent  $\gamma_m = \alpha + (m + 1)\beta$  of this power law versus the order of the moment  $m + 1$  for different values of  $m$  (Sempere Torres et al. 1994).

In general, the lower-order moments, which mainly depend on the counts in the first few raindrop size bins (associated with the smallest drops), are very sensitive to instrumental limitations (Uijlenhoet 1999). The higher-order moments, on the other hand, depending strongly on the counts in the larger raindrop bins, are more sensitive to sampling fluctuations (e.g., Smith et al. 1993; Uijlenhoet et al. 2002, manuscript submitted to *J. Atmos. Sci.*). Therefore, as a general rule, we only estimate the values of the scaling exponents on the basis of moments of orders between two and six ( $2 \leq m \leq 6$ ). In fact, to guarantee self-consistency, we only estimate  $\beta$  in this manner and subsequently invoke the constraint on the scaling exponents [Eq. (9)] to estimate  $\alpha$ .

We employ a moment method developed by Uijlenhoet (1999) to estimate self-consistent values of the parameters of the scaled raindrop size distribution  $g(x)$ . Effectively, this method uses the moments of orders  $4 + \gamma$  and  $5 + \gamma$  (with  $\gamma = 0.67$ ) of  $g(x)$  to estimate  $\lambda$  and  $\mu$ . This corresponds closely to the moment orders (i.e., central in the range 0–6) that are commonly used to estimate the parameters of the gamma raindrop size distribution (e.g., Tokay and Short 1996; Ulbrich and Atlas 1998). The corresponding self-consistent value of  $\kappa$  is subsequently estimated using Eq. (11).

In summary, the scaling-law formalism allows a separation of the effects of the variability of rainfall integral variables from changes in the form of an intrinsic raindrop size distribution. In other words, it separates the effects of changes in the *scale* of the raindrop size distribution from those in its *shape*. The parameters controlling the scale and the shape of the scaled raindrop size distribution are directly related to the microphysical processes producing extreme precipitation. All effects of the variability of rainfall integral variables are entirely contained in the values of the scaling exponents. The values of these exponents determine whether it is the variability of the raindrop sizes or the variability of the raindrop concentration (or some combination thereof), which controls the variability of the raindrop size distribution. In general, the closer  $\beta$  is to zero (i.e., the closer  $b$  is to one), the more pronounced is the relative contribution of number-controlled variability (Fig. 1). In other words, the values of  $\beta$  and  $b$  are measures of how far the raindrop size distributions under consideration are away from equilibrium (Uijlenhoet 1999). The remaining challenge is now to try to relate the values of the scaling exponents and those of the parameters of the scaled raindrop size distribution to the (micro) physical processes shaping raindrop spectra during conditions of extreme rainfall. Although tackling this ambitious issue is beyond the scope of this paper, a first step toward understanding the variability of ground-based raindrop size distributions in extreme rainfall will be taken in the case studies presented in the next section.

#### 4. Scaling analysis of Miami ISWS raindrop camera data

In this section, scaling analyses of raindrop size distributions corresponding to maximum rain rates reaching almost  $500 \text{ mm h}^{-1}$  are presented. The data have been collected in Miami, Florida, from 20 August 1957 through 14 August 1958, using the Illinois State Water Survey (ISWS) raindrop camera. This instrument provides 1-min information about the numbers of drops in 75 diameter intervals of 0.1-mm width, from 0.5 to 7.9 mm, in an approximately  $1\text{-m}^3$  sample volume [see Jones (1992) for a more detailed description of the workings of the raindrop camera]. Note that wind sorting may be a source of error for the ISWS raindrop camera, with the effect of reducing the number of drops being sampled (Rinehart 1983). The Miami dataset comprises a total of 2506 1-min spectra (Mueller 1962; 1966), that is, almost 42 h of rainfall. Previous analyses involving this dataset include the ones presented by Fujiwara (1965), Stout and Mueller (1968), and Smith (1993).

##### a. Global analysis

Figures 2–5 present the results of a global analysis of the data, that is, a climatological analysis of the dataset as a whole, without regard to its internal temporal structure. To investigate the possible emergence of equilibrium-like conditions as rain rates increase toward extreme values, the rain-rate dependence of the scaling exponents and the parameters of the scaled raindrop size distribution has been determined. Concretely, the scaling methodology presented in section 3 has been applied to those spectra in the Miami ISWS raindrop camera dataset for which rain rates exceed given thresholds of 1, 10, and  $100 \text{ mm h}^{-1}$  (Figs. 2, 3, and 4, respectively).

##### 1) GENERAL OBSERVATIONS

In Figs. 2a, 3a, and 4a the exponents  $\gamma_m$  of power-law relationships between the  $m$ th order moment of the raindrop size distribution (for  $0 \leq m \leq 6$ , in steps of 0.5) and the reference variable  $R$  are plotted against  $m + 1$  for the three rain-rate thresholds considered. The power-law relationships have been adjusted using linear regression on the logarithmic values, using  $\log R$  as the independent variable. The error bars indicate 68% confidence limits associated with the inferred values of  $\gamma_m$ , estimated from 100 bootstrap samples (Efron and Tibshirani 1993). If the sampling distributions of  $\gamma_m$  would be normal (Gaussian), then the 68% confidence limits would correspond to an interval from minus to plus one standard deviation about the mean. The sampling uncertainties associated with Figs. 2a and 3a are negligible compared to those associated with Fig. 4a. This is because the number of data points involved in estimating the power-law exponents in Fig. 4a is significantly less than those in Figs. 2a and 3a (139 versus 2341 and 1131, respectively).

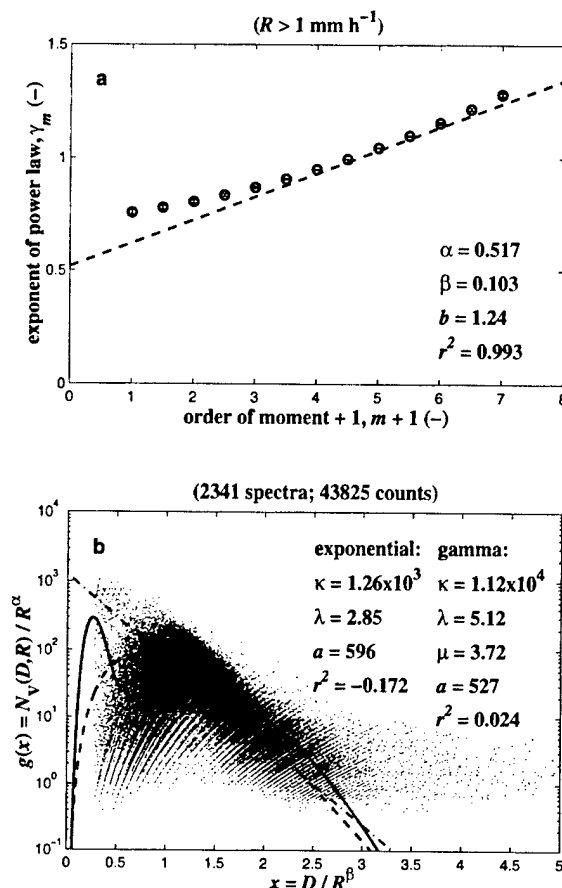


FIG. 2. Global scaling analysis for Miami ISWS raindrop camera data for rain-rate threshold of  $1 \text{ mm h}^{-1}$ . (a) Estimation of scaling exponents ( $\alpha$ ,  $\beta$ ) as intercept and slope of plot of exponents  $\gamma_m$  (of power laws with  $R$ ) vs order of moment  $m + 1$  for  $2 \leq m \leq 6$  (error bars indicate 68% confidence limits obtained using bootstrap method). Corresponding values of exponent  $b$  (—) of Z-R relationship and of coefficient of determination  $r^2$  (—) of regression line are indicated as well. (b) Application of exponents to scale spectra and to infer scaled raindrop size distribution (dots) and adjustment of theoretical parameterizations for  $g(x)$ , with corresponding parameter values, pre-factors  $a$  (—) of Z-R relationships, and coefficients of determination  $r^2$  (—): exponential parameterization (dash-dotted line) and gamma parameterization (dashed line). For comparison, List's (1988) parameterization for three-peak equilibrium distribution (solid line) is shown as well.

According to the scaling-law theory (Sempere Torres et al. 1994), plots like Figs. 2a, 3a, and 4a should yield straight lines with intercepts  $\alpha$  and slopes  $\beta$  [Eq. (23)]. The dashed lines indicate linear regressions between  $\gamma_m$  and  $m + 1$  for  $2 \leq m \leq 6$ . As explained in section 3d, in order to guarantee self-consistency, the values of  $\beta$  have been estimated as the slopes of these regression lines and the values of  $\alpha$  from the self-consistency constraint on the scaling exponents [Eq. (9)]. The indicated values of  $b$  are the exponents of the corresponding Z-R relationships implied by the scaling-law formalism [Eq. (5)]. The straight-line behavior predicted by the

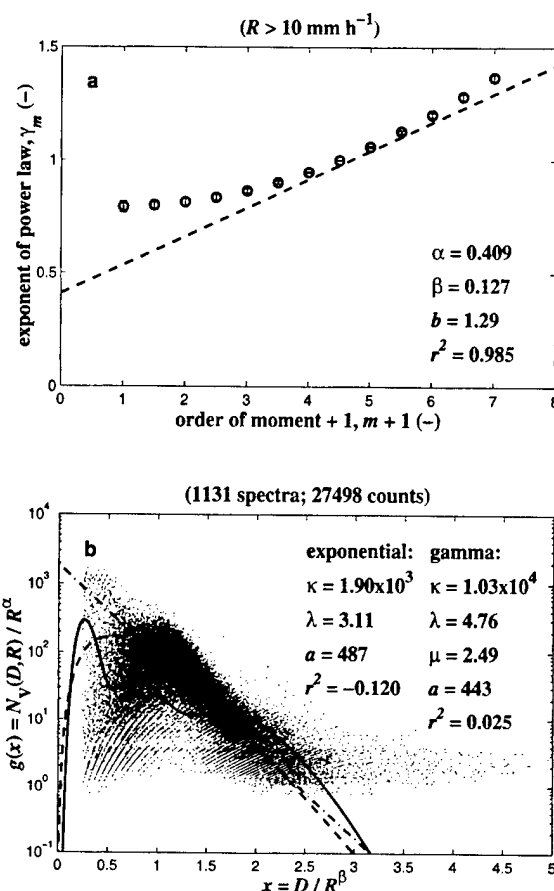


FIG. 3. Same as Fig. 2, but for rain-rate threshold of  $10 \text{ mm h}^{-1}$ .

scaling-law formalism holds reasonably well, in particular for  $m + 1 \geq 3$ . This is confirmed by the high values of the coefficient of determination  $r^2$  (computed as the square of the correlation coefficient between  $\gamma_m$  and  $m + 1$  for  $2 \leq m \leq 6$ ). The curvature of the plots in Figs. 2a–4a may be indicating that one single-scaling exponent does not suffice to explain all variability of the moments of the Miami raindrop size distributions. In addition, there may be an instrumental effect at the small-diameter end of the spectra associated with the manual analysis of the drop camera data and wind effects on the samples collected.

In Figs. 2b, 3b, and 4b the inferred values for the scaling exponents are used to identify the shapes of the corresponding scaled raindrop size distributions  $g(x)$ . The fact that not all data points fall perfectly on one single curve indicates that one reference variable (in this case the rain rate  $R$ ) is not able to explain all observed variability. However, the appreciable amount of scatter present in Fig. 2b, for instance, should not be regarded as surprising, because what we try to do here is explain all variability present in over 2000 individual raindrop size spectra using only one single explanatory variable ( $R$ ).

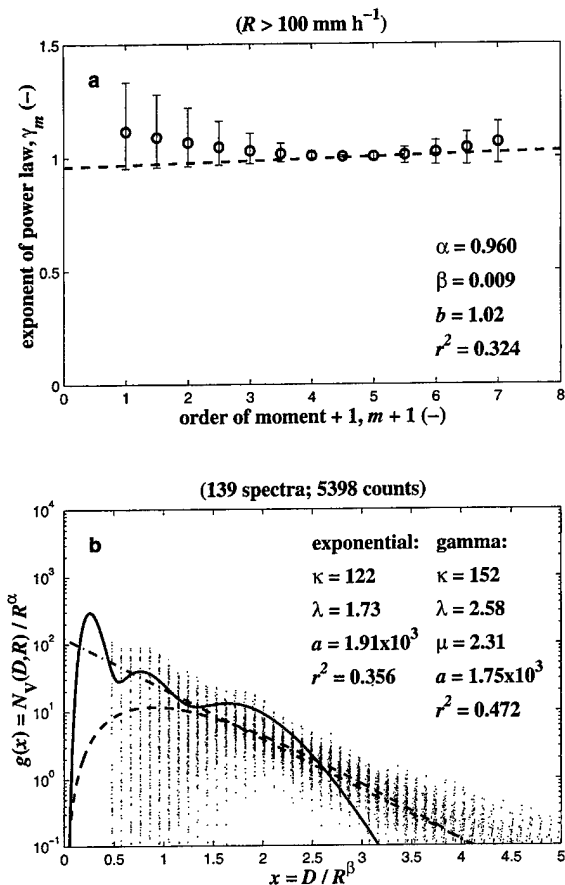


FIG. 4. Same as Figs. 2 and 3, but for rain-rate threshold of 100 mm h<sup>-1</sup>.

The "streaky" nature of the empirical scaled raindrop size distributions is an artifact of the data analysis. The streaks correspond to single count raindrop size bins that reappear for spectra with widely varying rain rates. The amount of curvature of the streaks is related to the combined scaling of the  $x$  axis and the  $y$  axis and is therefore determined by the values of the scaling exponents. Compare for instance the direction of the streaks in Figs. 2b and 3b with those in Fig. 4b, for which the scaling of the  $x$  axis is almost absent because  $\beta \approx 0$  (Fig. 4a). The scattered, streaky appearance of these figures is entirely consistent with previously published results of scaling analyses (e.g., Sempere Torres et al. 1994, 1998).

Two different analytical parameterizations have been fitted to the empirical scaled raindrop size distributions indicated by the data points in Figs. 2b–4b (following the procedure outlined in section 3d): an exponential parameterization (bold dash-dotted line) and a gamma parameterization (bold dashed line). Equations (10) and (12) explain the meaning of the indicated parameter values (recall that  $\mu = 0$  for the exponential parameterization). The indicated values of  $a$  are the prefactors

of the corresponding  $Z$ – $R$  relationships implied by the scaling-law formalism [Eq. (4)] for the two parameterizations. Note that these differ by more than 10% depending on whether one assumes an exponential or a gamma functional form for  $g(x)$ . For comparison, List's (1988) approximation to the three-peak equilibrium distribution as the sum of three gamma distributions is included in Figs. 2b–4b as well. Also shown are the corresponding values of the coefficient of determination (or model efficiency)  $r^2$  (–). This goodness-of-fit statistic indicates the fraction of the observed variance explained by the model:  $r^2 = 1$  indicates a perfect agreement between model and observations,  $r^2 = 0$  indicates that the model does not perform better than the mean of the observations, and  $r^2 < 0$  indicates a serious lack of agreement (e.g., Mood et al. 1974).

## 2) SCALING EXPONENTS AND SCALED RAINDROP SIZE DISTRIBUTIONS

The difference between employing a threshold of 1 mm h<sup>-1</sup> or one of 10 mm h<sup>-1</sup> in the scaling analysis is not very pronounced, either in terms of the inferred scaling exponents (Figs. 2a and 3a), or in terms of the identified scaled raindrop size distributions (Figs. 2b and 3b). However, as the rain-rate threshold increases from 10 to 100 mm h<sup>-1</sup>, the value of the scaling exponent  $\beta$  decreases roughly from 0.1 to 0 (Fig. 4a). This indicates a change from a combination of size- and number-controlled variability to a situation where the rainfall variability is almost purely number controlled, consistent with equilibrium conditions (Fig. 1). Figure 4a shows that in this situation all moments of the raindrop size distribution are approximately proportional to each other. Hence, their relationships are linear, consistent with the equilibrium hypothesis (section 3c).

The shape of the scaled raindrop size distribution reflects a similar behavior (Figs. 2b–4b). It also changes relatively little when the rain-rate threshold is increased from 1 to 10 mm h<sup>-1</sup>, while it changes much more markedly when the threshold is increased from 10 to 100 mm h<sup>-1</sup>. Table 2 summarizes the identified scaling exponents and parameters of exponential and gamma fits to the empirical scaled raindrop size distributions and their associated uncertainties for the three rain-rate thresholds. Note how the uncertainties increase as the rain-rate threshold increases and the number of spectra in the sample decreases. Of the different parameters listed in Table 2, the "normalization" parameter  $\kappa$  seems to be the most sensitive to sampling errors.

Figure 5 provides a direct graphical representation of the effect of increasing the rain-rate threshold on the values of the scaling exponents (top left-hand side) and the parameters of exponential (top right-hand side) and gamma (bottom four panels) fits to the empirical scaled raindrop size distributions. The rain-rate threshold is increased in 5 mm h<sup>-1</sup> steps from 0 to 100 mm h<sup>-1</sup>. The error bars again indicate 68% confidence limits

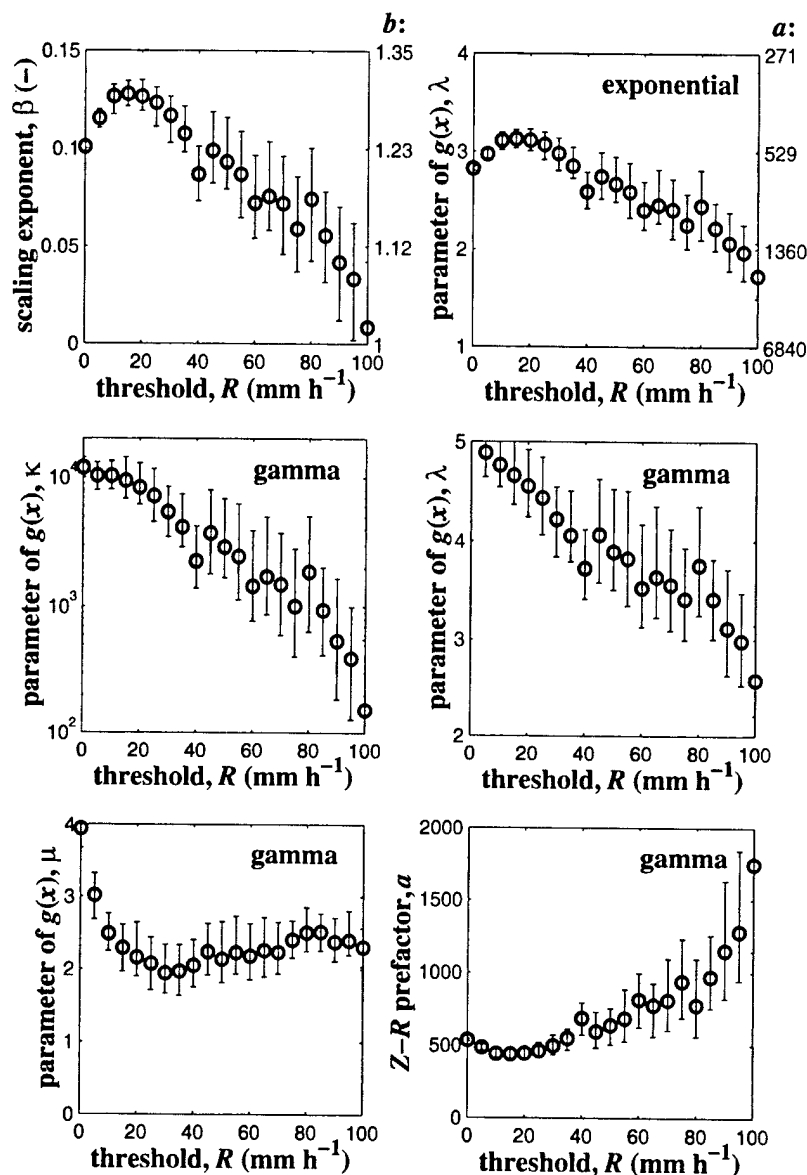


FIG. 5. Dependence of values of scaling exponent  $\beta$  (—), parameters of exponential (top right) and gamma parameterizations (bottom four panels) for scaled raindrop size distribution  $g(x)$ , and corresponding coefficients of Z-R relationships on value of rain-rate threshold for Miami ISWS raindrop camera data (error bars indicate 68% confidence limits obtained using bootstrap method). In the top panels  $b$  is the Z-R exponent and  $a$  is the Z-R prefactor.

based on 100 bootstrap samples, increasing gradually for all parameters as the rain-rate threshold increases and the sample size decreases. The “curves” in Fig. 5 should not be interpreted as functional relationships. They demonstrate the change in estimated parameter values as the rain-rate threshold increases, that is, if the analysis is limited to those raindrop size spectra that correspond to rain rates exceeding a given threshold.

The scaling exponent  $\beta$  is seen to increase as the rain-rate threshold increases from 0 to 10  $\text{mm h}^{-1}$ , and sub-

sequently decreases steadily to almost its equilibrium value of zero (actually 0.009, see Fig. 4a) for a rain-rate threshold of 100  $\text{mm h}^{-1}$  (Fig. 5, top left-hand side). Because Eq. (15) with  $\beta \approx 0$  implies  $\Lambda \approx \lambda$ , the semi-logarithmic slope of an exponential fit to the Miami data [i.e.,  $\Lambda$  in Eq. (13), with  $\mu = 0$ ] nearly becomes a constant, independent of rain rate, for rain rates exceeding 100  $\text{mm h}^{-1}$  (actually  $\Lambda \approx \lambda = 1.73 \text{ mm}^{-1}$ ; see Fig. 4b). This is consistent with Mueller’s (1966) finding, for the same dataset, that “at Miami the slope



TABLE 2. Means and 68% confidence limits (obtained using bootstrap method) of the following parameters for rain-rate thresholds of 1, 10, and 100 mm h<sup>-1</sup> applied to Miami ISWS raindrop camera data: scaling exponents ( $\alpha$ ,  $\beta$ ) and corresponding exponents  $b$  of  $Z$ - $R$  relationship; intercept  $\kappa$  and (semilogarithmic) slope  $\lambda$  of exponential fit to scaled raindrop size distribution  $g(x)$ ; corresponding prefactor  $a$  of  $Z$ - $R$  relationship (with  $\mu = 0$ ); parameters  $\kappa$ ,  $\lambda$ , and  $\mu$  of gamma parameterization for scaled raindrop size distribution  $g(x)$ ; corresponding prefactor  $a$  of  $Z$ - $R$  relationship.

Parameter	16%	Mean	85%
$R > 1 \text{ mm h}^{-1}$ (2341 spectra)			
General	$\alpha$	0.504	0.517
	$\beta$	0.100	0.103
	$b$	1.23	1.24
Exponential	$\kappa$	$1.22 \times 10^3$	$1.26 \times 10^3$
	$\lambda$	2.83	2.85
	$a$	582	596
Gamma	$\kappa$	$9.33 \times 10^3$	$1.12 \times 10^4$
	$\lambda$	4.93	5.12
	$\mu$	3.46	3.72
	$a$	514	527
$R > 10 \text{ mm h}^{-1}$ (1131 spectra)			
General	$\alpha$	0.385	0.409
	$\beta$	0.119	0.127
	$b$	1.28	1.29
Exponential	$\kappa$	$1.68 \times 10^3$	$1.90 \times 10^3$
	$\lambda$	3.03	3.11
	$a$	467	487
Gamma	$\kappa$	$7.25 \times 10^3$	$1.03 \times 10^4$
	$\lambda$	4.45	4.76
	$\mu$	2.16	2.49
	$a$	422	443
$R > 100 \text{ mm h}^{-1}$ (139 spectra)			
General	$\alpha$	0.817	0.960
	$\beta$	-0.028	0.009
	$b$	0.94	1.02
Exponential	$\kappa$	50	122
	$\lambda$	1.43	1.73
	$a$	$1.31 \times 10^3$	$1.91 \times 10^3$
Gamma	$\kappa$	39	152
	$\lambda$	2.11	2.58
	$\mu$	2.04	2.31
	$a$	$1.20 \times 10^3$	$1.75 \times 10^3$

remains constant or even increases slightly with large values of  $R$ . Note that the Marshall-Palmer value for  $\beta$  is 0.214 (section 3b, Fig. 1). Recall that  $\beta$  determines  $\alpha$  via the self-consistency constraint on the scaling exponents [Eq. (9), Fig. 1]. All values in Fig. 5 correspond to the strongly number-controlled convective regime (Sempere Torres et al. 1998).

The parameter  $\lambda$  of the exponential parameterization for  $g(x)$  follows a similar behavior as  $\beta$  (Fig. 5, top right-hand side), with increasing values for rain-rate thresholds between 0 and 10 mm h<sup>-1</sup> and decreasing values for thresholds between 10 and 100 mm h<sup>-1</sup>. Recall that  $\lambda$  determines  $\kappa$  via the self-consistency constraint Eq. (11), with  $\mu = 0$ . One should be careful when trying to find a physical interpretation for the correspondence between  $\beta$  and  $\lambda$ . Their relationship is strongly influenced by the fact that the units of  $\lambda$  depend

on the value of  $\beta$  [Eq. (15)], causing spurious correlations (Mood et al. 1974). Note that, for the units employed here, the Marshall-Palmer value for  $\lambda$  is 4.23 (section 3b). The values in Fig. 5 are all significantly smaller, indicating wider raindrop size distributions and larger mean raindrop diameters at a given rain rate than what would result from the Marshall-Palmer parameterization, which is generally considered typical for stratiform conditions. This is consistent with the previous "convective" interpretation of  $\beta$ .

Specifically, for a rain-rate threshold of 100 mm h<sup>-1</sup> (when  $\beta \approx 0$ ),  $\Lambda \approx \lambda = 1.73 \text{ mm}^{-1}$  (independent of rain rate), as we have seen before (Fig. 4b). For exponential raindrop size distributions all characteristic raindrop sizes are inversely proportional to  $\Lambda$ , notably the mean raindrop diameter  $\mu_D = \Lambda^{-1}$  and the median-volume diameter  $D_0 = 3.67\Lambda^{-1}$  (e.g., Uijlenhoet and Stricker 1999). This implies that if the exponential distribution is assumed a reasonable description of the data,  $\mu_D \approx 0.56 \text{ mm}$  and  $D_0 \approx 2.12 \text{ mm}$  for rain rates exceeding 100 mm h<sup>-1</sup> (both characteristic sizes are approximately constants, in agreement with the equilibrium hypothesis).

The parameters  $\kappa$  and  $\lambda$  of gamma fits to the empirical scaled raindrop size distributions decrease nearly monotonically as the rain-rate threshold increases from 0 to 100 mm h<sup>-1</sup> (Fig. 5, middle two panels). The parameter  $\mu$  (bottom left-hand side), on the other hand, decreases rapidly from roughly 4 to 2 as the rain-rate threshold increases from 0 to 30 mm h<sup>-1</sup>, then increases slowly to a value smaller than 2.5 as the rain-rate threshold increases further towards 100 mm h<sup>-1</sup>. Between the thresholds of 10 and 100 mm h<sup>-1</sup>, the value of  $\mu$  always stays between 2 and 2.5. Some care should be exercised here however, as instrumental effects such as undercounting of small drops can cause  $\mu$  to be always biased positive (Ulbrich and Atlas 1998). Since the parameter  $\mu$  is inversely related to the relative width of the raindrop size distribution, the spread of the raindrop sizes relative to the mean drop size is roughly constant for rain rates exceeding 10 mm h<sup>-1</sup>.

### 3) RADAR REFLECTIVITY-RAIN RATE RELATIONSHIPS

Figures 2-5 also provide insight into the implications of these analyses for the corresponding (climatological)  $Z$ - $R$  relationships. Figures 2a-4a and the top left-hand side of Fig. 5 (right y axis) show that the exponents  $b$  of power-law  $Z$ - $R$  relationships for the Miami data roughly decrease from 1.3 to 1 as the rain-rate threshold increases from 0 to 100 mm h<sup>-1</sup>, independent of the choice of parameterization for  $g(x)$ . Figures 2b-4b and the top right-hand side of Fig. 5 (right y axis) show that in case of an exponential form for  $g(x)$ , the corresponding prefactors  $a$  roughly increase from 500 to 2000. In case of a gamma form for  $g(x)$ , the general tendency is the same, although the values of  $a$  are consistently of

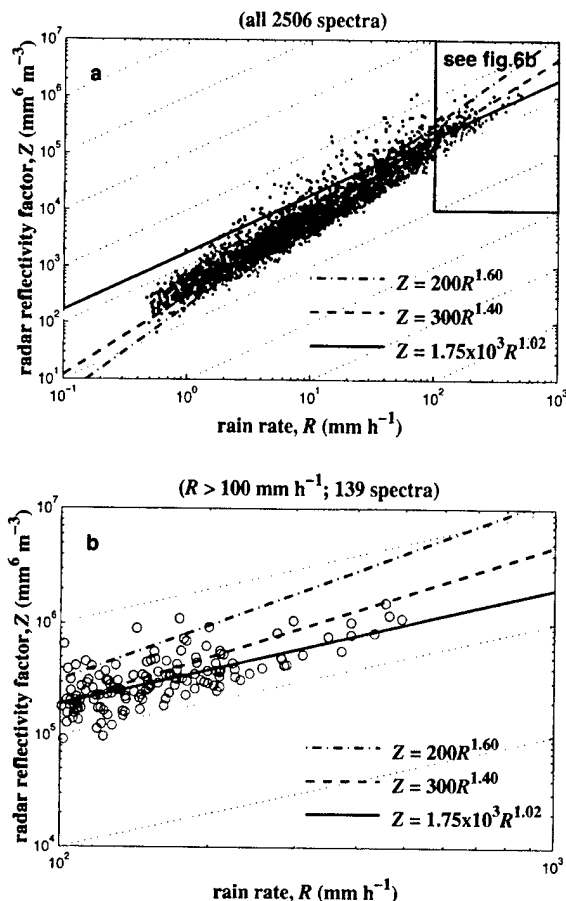


FIG. 6. Empirical  $Z$ - $R$  relationships for Miami, FL (dots, circles), as compared to Marshall-Palmer  $Z$ - $R$  relationship ( $Z = 200R^{1.6}$ , dash-dotted lines), standard NEXRAD  $Z$ - $R$  relationship ( $Z = 300R^{1.4}$ , dashed lines), and nearly linear  $Z$ - $R$  relationship ( $Z = 1.75 \times 10^3 R^{1.02}$ , solid lines) resulting from scaling analysis using rain-rate threshold of  $100 \text{ mm h}^{-1}$  and gamma parameterization for  $g(x)$  (parallel dotted lines indicate direction of linear  $Z$ - $R$  relationships). (a) All 2506 raindrop size distributions regardless of rain rate. (b) Magnification of 139 raindrop size distributions with rain rates exceeding  $100 \text{ mm h}^{-1}$ .

the order of 10% smaller, as is evident from Figs. 2b-4b and Fig. 5 (bottom right-hand side).

The scaling exponents and scaled raindrop size distribution parameters inferred from a global scaling analysis using a rain rate threshold of  $100 \text{ mm h}^{-1}$  and a gamma parameterization for  $g(x)$  lead to the nearly linear  $Z$ - $R$  relationship  $Z = 1.75 \times 10^3 R^{1.02}$  (Figs. 4a,b). Although the linearity of this relationship is consistent with the equilibrium hypothesis, its prefactor differs significantly from the 742 speculated by List (1988) to be "a universal constant for steady tropical rain." This suggests that, whereas the  $Z$ - $R$  exponent  $b$  seems to have a fixed value of one, the  $Z$ - $R$  prefactor  $a$  under equilibrium conditions may not be considered constant. Since  $a$  is equivalent to the sixth moment of  $g(x)$  [Eq. (4)], this suggests that  $g(x)$  cannot be considered a fixed

TABLE 3. Goodness-of-fit statistics corresponding to different subsamples of Miami ISWS raindrop camera data (Fig. 6) for Marshall-Palmer  $Z$ - $R$  relationship ( $Z = 200R^{1.6}$ ), standard NEXRAD  $Z$ - $R$  relationship ( $Z = 300R^{1.4}$ ), and nearly linear  $Z$ - $R$  relationship ( $Z = 1.75 \times 10^3 R^{1.02}$ ) resulting from scaling analysis using rain-rate threshold of  $100 \text{ mm h}^{-1}$  and gamma parameterization for  $g(x)$ : mean bias error (mbe), rmse, and coefficient of determination ( $r^2$ ).

Relationship	Mbe ( $\text{mm h}^{-1}$ )	Rmse ( $\text{mm h}^{-1}$ )	$r^2$ (-)
All 2506 spectra			
$Z = 200R^{1.6}$	-5.62	23.2	0.733
$Z = 300R^{1.4}$	-0.265	19.6	0.809
$Z = 1.75 \times 10^3 R^{1.02}$	-2.97	28.5	0.597
$R > 100 \text{ mm h}^{-1}$ (139 spectra)			
$Z = 200R^{1.6}$	-66.4	86.1	-0.234
$Z = 300R^{1.4}$	-16.0	54.9	0.498
$Z = 1.75 \times 10^3 R^{1.02}$	18.6	82.7	-0.139
$R > 200 \text{ mm h}^{-1}$ (32 spectra)			
$Z = 200R^{1.6}$	-141	151	-2.04
$Z = 300R^{1.4}$	-64.9	79.6	0.151
$Z = 1.75 \times 10^3 R^{1.02}$	14.7	93.1	-0.162

function for equilibrium conditions either. The larger prefactor we find, as compared to List (1988), is indicative of larger raindrop diameters at the same rain rate (Steiner and Smith 1998).

Figure 6 and Table 3 compare the performance of the nearly linear  $Z$ - $R$  relationship  $Z = 1.75 \times 10^3 R^{1.02}$  (solid line) with two standard  $Z$ - $R$  relationships: the Next Generation Weather Radar (NEXRAD)  $Z$ - $R$  relationship (Fulton et al. 1998)  $Z = 300R^{1.4}$  (dashed line) and the Marshall-Palmer  $Z$ - $R$  relationship (Marshall et al. 1955)  $Z = 200R^{1.6}$  (dash-dotted line). In addition to the coefficient of determination  $r^2$  (-), Table 3 also provides values of the mean bias error (mbe;  $\text{mm h}^{-1}$ ) and of the root-mean-square error (rmse;  $\text{mm h}^{-1}$ ). Figure 6a qualitatively shows that the overall fit of the standard NEXRAD  $Z$ - $R$  relationship (dashed line) to all 2506 raindrop size distributions regardless of rain-rate is much better than that of the nearly linear relationship (solid line) and also slightly better than the Marshall-Palmer relationship (dash-dotted line). However, if the analysis is restricted to the 139 raindrop size distributions with rain-rates exceeding  $100 \text{ mm h}^{-1}$  (Fig. 6b), then the nearly linear  $Z$ - $R$  relationship does a very good job as compared to the two standard relationships, in particular at the extreme rain-rate end. Interestingly, both in terms of the fraction of explained variance ( $r^2$ ) and in terms of the rmse, the standard NEXRAD  $Z$ - $R$  relationship outperforms the other two on all occasions, even if we limit the analysis to the 32 raindrop size distributions with rain rates exceeding  $200 \text{ mm h}^{-1}$  (Table 3). For these extreme rain rates, however, the nearly linear  $Z$ - $R$  relationship derived on the basis of the scaling-law formalism yields by far the smallest bias. As we will see later (Fig. 12), the requirement of a small bias error is of fundamental importance when estimating rainfall volumes over entire events.

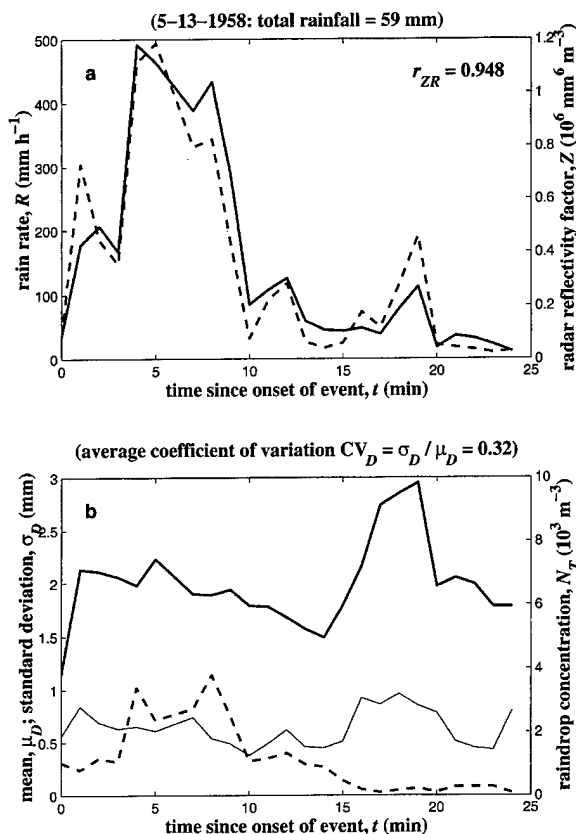


FIG. 7. Time series analysis for 13 May 1958 event of Miami ISWS raindrop camera data. (a) Temporal evolution of rain rate  $R$  (solid line) and radar reflectivity factor  $Z$  (dashed line), with corresponding linear correlation coefficient  $r_{ZR}$  (—). (b) Temporal evolution of mean  $\mu_D$  (bold solid line) and standard deviation  $\sigma_D$  (thin solid line) of [with corresponding average coefficient of variation  $CV_D$  (—)] and of raindrop concentration (bold dashed line).

#### b. Analysis of two contrasting extreme rainfall events

The contrasting behavior of two individual extreme rainfall events is exemplified in Figs. 7–12. The 13 May 1958 event (Figs. 7 and 8) exhibits a maximum 1-min rain rate of  $492 \text{ mm h}^{-1}$  and a maximum 1-min liquid water content of  $18.95 \text{ g m}^{-3}$  (as derived from the spectra), both absolute maxima for the entire ISWS raindrop camera dataset (which includes, apart from Miami, a dozen other locations around the world). The synoptic weather type for this event is characterized by Mueller (1962) as “trough aloft.” The 21 June 1958 event (Figs. 9 and 10), on the other hand, contains the largest 1-min raindrop concentration (9091 drops per cubic meter) of the entire dataset. Its maximum 1-min rain rate is  $284 \text{ mm h}^{-1}$ . Mueller (1962) characterizes this event as “air mass.”

##### 1) 13 MAY 1958 EVENT

Figure 7a provides the time series of the rain rate  $R$  (solid line) and the radar reflectivity  $Z$  (dashed line) as

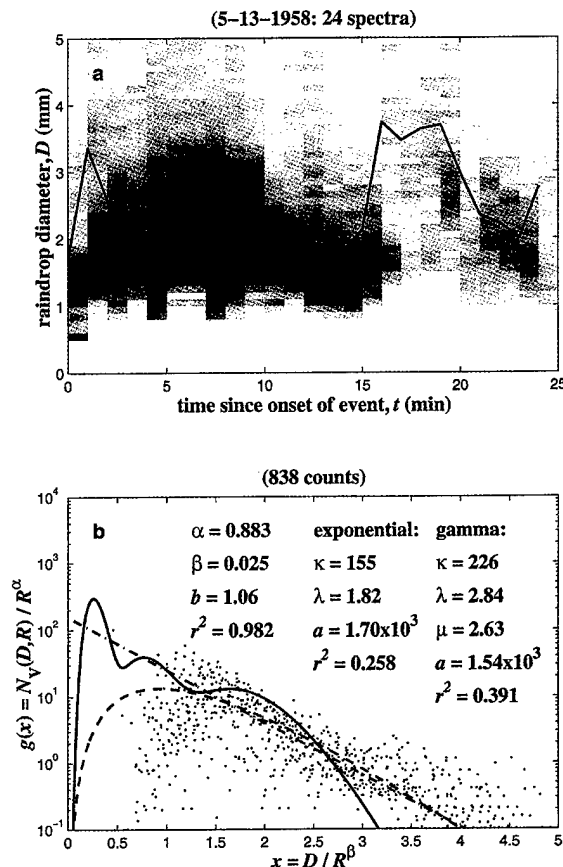


FIG. 8. Time series and scaling analyses for 13 May 1958 event of Miami ISWS raindrop camera data. (a) Temporal evolution of entire spectra [grayscale indicates number of raindrops in size interval, with darker shades showing greater density (arbitrary units); solid line is the median volume diameter  $D_0$  (mm)]. (b) Scaled raindrop size distributions  $g(x) = N_V(D,R)/R^\alpha$  versus  $x = D/R^\beta$  [corresponding values of exponent  $b$  (—) of  $Z$ - $R$  relationship and of coefficient of determination  $r^2$  (—) of regression line are indicated as well] and adjusted parameter values, prefactors  $a$  (—) of  $Z$ - $R$  relationships, and coefficients of determination  $r^2$  (—): exponential parameterization (dash-dotted line) and gamma parameterization (dashed line). For comparison, List's (1988) parameterization for three-peak equilibrium distribution (solid line) is shown as well.

derived from the raindrop spectra. To demonstrate the striking proportionality between  $Z$  and  $R$  for this event, linear axes are used for both variables. The fact that  $Z$  and  $R$  are almost perfectly linearly related throughout the event (the linear correlation coefficient  $r$  between  $Z$  and  $R$  equals 0.948) provides evidence for equilibrium-like conditions during this event. This means that the rainfall variability must be strongly, if not entirely, number-biased (section 3c, Fig. 1).

Figure 7b shows the time evolution of the mean raindrop diameter  $\mu_D$  (bold solid line), the standard deviation of the raindrop diameters  $\sigma_D$  (thin solid line), and the raindrop concentration  $N_T$  (bold dashed line) during the event. The standard deviation closely follows the

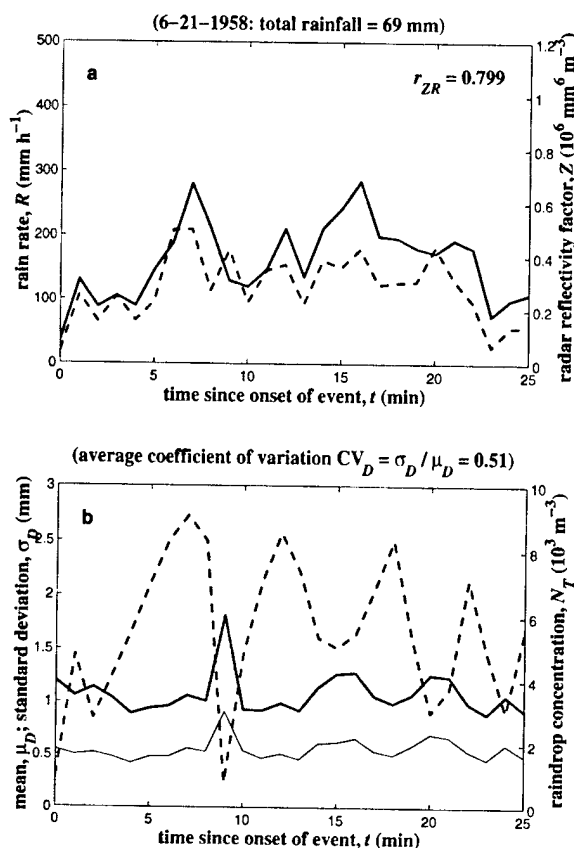


FIG. 9. Same as Fig. 7, but for 21 Jun 1958 event.

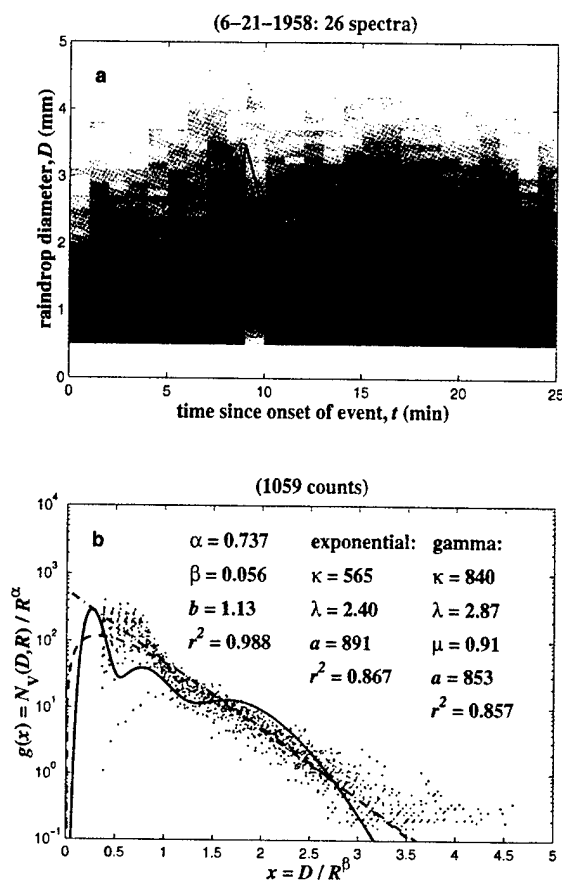


FIG. 10. Same as Fig. 8, but for 21 Jun 1958 event.

mean, indicating a roughly constant coefficient of variation (average  $CV_D \approx 0.32$ ). The mean diameter does not change dramatically during the period of maximum rain rate, between 3 and 10 min after the onset of the event, neither does the median volume diameter  $D_0$  (Fig. 8a, bold line). This indicates that the peak rain rate, which is approximately 3–5 times as large as the rain rates directly before and after the peaks (Fig. 7a), must have been caused mainly by a significant increase in the raindrop concentration, pointing toward a situation of number-controlled variability.

This is essentially confirmed by Fig. 7b, showing a 1-min increase of the raindrop concentration from about 1000 drops per cubic meter to between 3000 and 4000 drops per cubic meter. The rain rate  $R$  is proportional to the raindrop concentration  $N_T$  and, assuming  $\gamma = 0.67$ , to the 3.67th power of any characteristic raindrop size [see Eqs. (6) and (7)], such as the mean diameter  $\mu_D$  or the median volume diameter  $D_0$ . Hence, for comparison, to achieve a comparable tripling of the rain rates without increasing the raindrop concentrations would have required an approximately 35% increase in  $\mu_D$  or  $D_0$  (or any other characteristic raindrop size).

Interestingly, the second (smaller) rainfall peak of just over  $100 \text{ mm h}^{-1}$ , which occurs between 17 and 20 min

after the onset of the event, has been caused mainly by increases of the characteristic raindrop sizes  $\mu_D$  and  $D_0$  (Figs. 7b and 8a), with the raindrop concentration remaining more or less constant (Fig. 7b). This points towards a relatively rare situation of size-controlled variability. Figure 8a, which gives the temporal evolution of the raindrop size spectra during the event, shows that the mentioned increases of the characteristic raindrop sizes (and the relatively small raindrop concentrations during this time period, see Fig. 7b), are apparently caused by a depletion of small raindrops (possibly associated with size sorting due to wind effects).

Figure 8b provides the results of the scaling analysis applied to the raindrop size distributions of Fig. 8a. The value of  $\beta$  ( $\approx 0$ ) and  $b$  ( $\approx 1$ ) provide further evidence for the overwhelming influence of number-controlled rainfall variability during this event. The values of the parameters of the exponential and gamma parameterizations fitted to the empirical  $g(x)$  resemble those of the global scaling analysis for a rain-rate threshold of  $100 \text{ mm h}^{-1}$  (Fig. 4b).

## 2) 21 JUNE 1958 EVENT

Figures 9 and 10 repeat the same analysis, but now for the 21 June 1958 event. The fundamental difference

between both events, besides the differences in the maximum rain rates, is that for the 13 May 1958 event the mean raindrop diameter is about 2 mm, whereas for the 21 June 1958 event it is of the order of 1 mm (Figs. 7b and 9b). These smaller mean diameters are compensated to a certain extent by tremendous bursts of the raindrop concentration, occasionally approaching 10 000 drops per cubic meter (Fig. 9b). A similar contrast exists between the modal raindrop diameters for both events, that is, the diameters for which the peaks of the raindrop size distributions occur (see the dark shaded areas in Figs. 8a and 10a). The median volume diameters show a less pronounced difference (Figs. 8a and 10a), although  $D_0$  remains surprisingly constant during the 21 June 1958 event (except for one minute, possibly due to a sampling effect or a problem associated with the manual analysis of the drop camera data). In summary, the 13 May 1958 event is characterized by broad gamma spectra (Fig. 8b), the 21 June 1958 event by narrow exponential spectra (Fig. 10b).

Figure 9a shows again a strong linear relationship between  $Z$  and  $R$ , although not as strong as for the 13 May 1958 event. The linear correlation coefficient between  $Z$  and  $R$  is 0.799 in this case. Figure 9b shows a largely constant mean raindrop diameter and standard deviation, except for one interval. The average coefficient of variation is slightly larger than for the previous event (average  $CV_D \approx 0.51$ ). What is striking about Fig. 9b is the seemingly negative correlation between the raindrop concentration and the mean raindrop diameter (and its standard deviation). This indicates that the bursts of raindrop concentration in Fig. 9b are not as evenly distributed over all raindrop sizes as true equilibrium conditions would demand, but must be concentrated on the small-diameter end of the spectra. Figure 10a seems to confirm this hypothesis (see the dark shaded areas corresponding to the  $N_T$  bursts in Fig. 9b). Hence, although the rainfall variability during this event is strongly number controlled, it is not entirely number controlled. This also explains the smaller linear correlation coefficient in Fig. 9a and the larger values of  $\beta$  and  $b$  in Fig. 10b, as compared to the previous event. The three-peak equilibrium distribution of List (1988) fits the data shown in Fig. 10b relatively well (much better than for the 13 May 1958 event; see Fig. 8b) and also the prefactors of the  $Z$ - $R$  relationships are closer to List's "universal constant" ( $a = 742$ ).

### 3) RADAR REFLECTIVITY-RAIN RATE RELATIONSHIPS

The  $Z$ - $R$  relationships derived on the basis of the scaling-law formalism for both events, obtained using a gamma fit to the scaled raindrop size distribution, are  $Z = 1.54 \times 10^3 R^{1.06}$  (13 May 1958) and  $Z = 853 R^{1.13}$  (21 June 1958). Although there is empirical evidence that the rainfall variability during both events is strongly number controlled (although stronger during the first

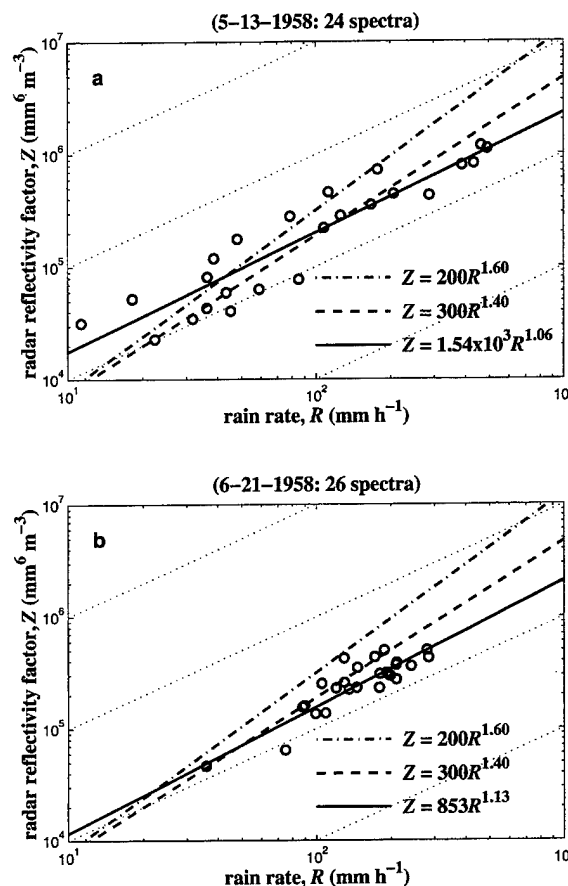


FIG. 11. Empirical  $Z$ - $R$  relationships for Miami, FL, for two contrasting extreme rainfall events (circles), as compared to Marshall-Palmer  $Z$ - $R$  relationship ( $Z = 200R^{1.6}$ , dash-dotted lines), standard NEXRAD  $Z$ - $R$  relationship ( $Z = 300R^{1.4}$ , dashed lines), and nearly linear  $Z$ - $R$  relationships resulting from scaling analyses (see Figs. 8b and 10b) and gamma parameterizations for  $g(x)$  (solid lines). Parallel dotted lines indicate direction of linear  $Z$ - $R$  relationships: (a) 13 May 1958 event; (b) 21 Jun 1958 event.

event), the shapes of the corresponding (scaled) distributions differ substantially. The net result of this is that both  $Z$ - $R$  relationships have exponents that are relatively close to unity, but strongly different prefactors. This indicates that there exists no single linear  $Z$ - $R$  relationship for "warm process" extreme rainfall, as List (1988) suggests.

Figure 11 and Table 4 compare the performance of the nearly linear  $Z$ - $R$  relationships derived for the two rainfall events discussed above,  $Z = 1.54 \times 10^3 R^{1.06}$  (Fig. 11a, solid line) and  $Z = 853 R^{1.13}$  (Fig. 11b, solid line), with the two standard  $Z$ - $R$  relationships presented earlier (Fig. 6): the NEXRAD  $Z$ - $R$  relationship (Fulton et al. 1998)  $Z = 300R^{1.4}$  (dashed line) and the Marshall-Palmer  $Z$ - $R$  relationship (Marshall et al. 1955)  $Z = 200R^{1.6}$  (dash-dotted line). In this case, the  $Z$ - $R$  relationships derived on the basis of the scaling-law for-

TABLE 4. Goodness-of-fit statistics corresponding to two contrasting extreme rainfall events in Miami, FL (Fig. 11), for Marshall–Palmer  $Z$ – $R$  relationship ( $Z = 200R^{1.6}$ ), standard NEXRAD  $Z$ – $R$  relationship ( $Z = 300R^{1.4}$ ), and nearly linear  $Z$ – $R$  relationships ( $Z = 1.54 \times 10^3 R^{1.06}$ ,  $Z = 853R^{1.13}$ ) resulting from scaling analysis using gamma parameterization for  $g(x)$ : mbe, rmse, and  $r^2$ .

Relationship	Mbe (mm h <sup>-1</sup> )	Rmse (mm h <sup>-1</sup> )	$r^2$ (–)
13 May 1958 (24 spectra)			
$Z = 200R^{1.6}$	–56.7	108	0.473
$Z = 300R^{1.4}$	–13.6	62.9	0.823
$Z = 1.54 \times 10^3 R^{1.06}$	8.84	50.6	0.885
21 Jun 1958 (26 spectra)			
$Z = 200R^{1.6}$	–68.9	80.9	–0.766
$Z = 300R^{1.4}$	–29.3	46.8	0.410
$Z = 853R^{1.13}$	8.01	40.4	0.560

malism outperform the standard relationships both in terms of the mean bias error, the root-mean-square error, and the coefficient of determination (Table 4). Their fits to the data also seem better from a qualitative perspective (Figs. 11a,b).

Although the assessment of the quality of instantaneous radar rainfall estimates (such as in Figs. 6 and 11) is of intrinsic interest, for practical hydrometeorological applications it is much more important to assess their quality over entire rainfall events. Figure 12 provides a comparison of cumulative rainfall distributions estimated using the  $Z$ – $R$  relationships presented in Fig. 11 with the measured cumulative rainfall distributions for the two contrasting rainfall events discussed above. In both cases the  $Z$ – $R$  relationships derived on the basis of the scaling-law formalism slightly overestimate the measured accumulations. This can be attributed to the small positive bias errors associated with these  $Z$ – $R$  relationships (Table 4). Nevertheless, in an absolute sense they outperform both standard  $Z$ – $R$  relationships, which significantly underestimate cumulative rainfall. Moreover, a slight overestimate of rainfall accumulation is more acceptable than an underestimate because of the systematic error in the measurements caused by wind sorting (Rinehart 1983).

## 5. Summary and conclusions

A scaling-law formalism for the description of raindrop size distributions and their properties (Sempere Torres et al. 1994, 1998) has been extended to provide a framework that allows an investigation of the controls on the variability of raindrop size distributions and the associated radar reflectivity–rain rate relationships in extreme rainfall. This scaling methodology has been applied to ground-based raindrop size distributions collected with the ISWS raindrop camera, corresponding to rain rates reaching almost 500 mm h<sup>-1</sup>.

The main conclusions of this work can be summarized as follows.

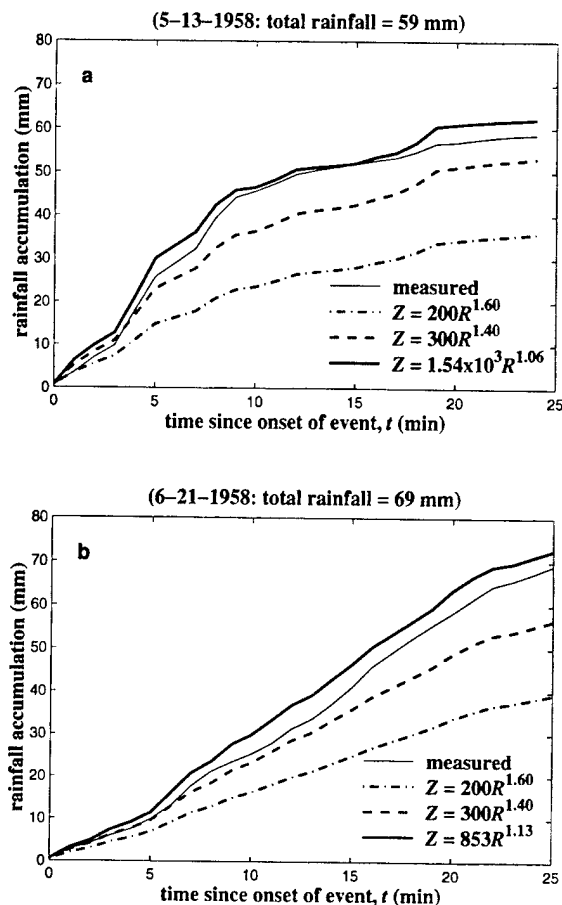


FIG. 12. Measured rainfall accumulations (derived from empirical raindrop size spectra) for Miami, FL, for two contrasting extreme rainfall events (thin solid lines), as compared to rainfall accumulations obtained from empirical radar reflectivity factors  $Z$  and different  $Z$ – $R$  relationships: Marshall–Palmer  $Z$ – $R$  relationship ( $Z = 200R^{1.6}$ , bold dash-dotted lines), standard NEXRAD  $Z$ – $R$  relationship ( $Z = 300R^{1.4}$ , bold dashed lines), and nearly linear  $Z$ – $R$  relationships resulting from scaling analyses (see Figs. 8, 10, and 11) and gamma parameterizations for  $g(x)$  (bold solid lines): (a) 13 May 1958 event; (b) 21 Jun 1958 event.

- 1) A global analysis of the data (employing increasing rain rate thresholds) and a time series analysis for two contrasting extreme rainfall events show that extreme rain rates (exceeding 100 mm h<sup>-1</sup>) tend to be produced in environments where the variability of raindrop size distributions is strongly number controlled. This implies that changes in raindrop size distribution properties in extreme rainfall are mainly caused by varying raindrop concentrations. Apparently, the competing microphysical processes shaping raindrop size distributions in extreme rainfall (coalescence on the one hand, and spontaneous and collisional breakup on the other hand) compensate each other in such a manner that an equilibrium state is reached, in which the probability density function

of the raindrop sizes (hence all characteristic diameters) remains largely constant.

- 2) The result is that rainfall integral variables (such as radar reflectivity and rain rate) are roughly proportional to each other (e.g., List 1988), which is consistent with the concept of equilibrium raindrop size distributions. Because default  $Z$ - $R$  relationships are always of a power-law form with exponents significantly larger than one (typically around 1.5), this proportionality has important implications for radar remote sensing of extreme rainfall. It may provide an explanation for the underestimation reported in extreme warm-process rain (e.g., American Meteorological Society 2000).
- 3) Although equilibrium raindrop size distributions produced by numerical models exhibit multiple peaks (List et al. 1987; Hu and Srivastava 1995), the scaled raindrop size distributions fitted to the raindrop camera data display little or no tendency toward multimodality [as opposed to the experimental findings of Zawadzki and de Agostinho Antonio (1988) on the basis of Joss-Waldvogel disdrometer data].
- 4) In contrast to prior speculation (List 1988), the shapes of the (measured and scaled) raindrop size spectra may differ significantly from event to event. This implies that, although the exponents of power-law  $Z$ - $R$  relationships may be similar for different extreme rainfall events (i.e., close to unity), their prefactors may differ substantially. As a result, there is no "universal" linear radar reflectivity-rain rate relationship for extreme rain rates, but the variability is essentially reduced to one free parameter (i.e., the prefactor).
- 5) This free parameter may be estimated on the basis of differential reflectivity ( $Z_{DR}$ ) measurements in extreme rainfall (e.g., Zrnica and Ryzhkov 1999). Specific differential phase ( $K_{DP}$ ) may also prove to be a promising weather radar measurable for this purpose (e.g., Bringi et al. 2002). It is highly relevant in this respect to extend the simple (i.e., single) scaling-law formalism proposed by Sempere Torres et al. (1994, 1998) to a more general *multiscaling* approach that would be able to employ (two or more) Doppler polarimetric radar measurables to infer (normalized) raindrop size distributions (Uijlenhoet 1999; Zawadzki 2002, personal communication).
- 6) Further research is needed to establish closer connections between the identified shapes of the scaled raindrop spectra (and consequently the prefactors of power-law  $Z$ - $R$  relationships) and the microphysics of the "warm rain" process.

**Acknowledgments.** We thank Dr. Ken Beard (University of Illinois/ISWS) for making his version of the raindrop camera data available to us. We are indebted to both him and Dr. Gene Mueller (who was instrumental in collecting the original data) for discussions

concerning issues of data quality control. The comments of two reviewers (anonymous) are greatly appreciated. This work was supported by National Aeronautics and Space Administration Grant NAG5-7744, National Science Foundation Grants ATM-9906012 and EAR-9909696, the National Weather Service and the NEXRAD Operations Support Facility under Cooperative Agreement NA87WH0518, and United States Army Research Office Grant DAAD19-99-1-0163. The lead author is currently supported by the Netherlands Organization for Scientific Research (NWO), through Grant 016.021.003 in the framework of the Innovative Research Incentives Scheme (*Vernieuwingsimpuls*).

#### REFERENCES

- American Meteorological Society, 2000: Policy statement: Prediction and mitigation of flash floods. *Bull. Amer. Meteor. Soc.*, **81**, 1338-1340.
- Atlas, D., and C. W. Ulbrich, 1977: Path- and area-integrated rainfall measurement by microwave attenuation in the 1-3 cm band. *J. Appl. Meteor.*, **16**, 1322-1331.
- , and —, 2000: An observationally based conceptual model of warm oceanic convective rain in the Tropics. *J. Appl. Meteor.*, **39**, 2165-2181.
- , R. C. Srivastava, and R. S. Sekhon, 1973: Doppler radar characteristics of precipitation at vertical incidence. *Rev. Geophys. Space Phys.*, **11**, 1-35.
- , C. W. Ulbrich, F. D. Marks, R. A. Black, E. Amitai, P. T. Willis, and C. E. Samsury, 2000: Partitioning tropical oceanic convective and stratiform rains by draft strength. *J. Geophys. Res.*, **105D**, 2259-2267.
- Baeck, M. L., and J. A. Smith, 1998: Rainfall estimation by the WSR-88D for heavy rainfall events. *Wea. Forecasting*, **13**, 416-436.
- Battani, L. J., 1973: *Radar Observation of the Atmosphere*. The University of Chicago Press, 324 pp.
- Beard, K. V., 1976: Terminal velocity and shape of cloud and precipitation drops aloft. *J. Atmos. Sci.*, **33**, 851-864.
- Bennett, J. A., D. J. Fang, and R. C. Boston, 1984: The relationship between  $N_0$  and  $\lambda$  for Marshall-Palmer type raindrop-size distributions. *J. Climate Appl. Meteor.*, **23**, 768-771.
- Best, A. C., 1950: Empirical formulae for the terminal velocity of water drops falling through the atmosphere. *Quart. J. Roy. Meteor. Soc.*, **76**, 302-311.
- Blanchard, D. C., and A. T. Spencer, 1970: Experiments on the generation of raindrop-size distributions by drop breakup. *J. Atmos. Sci.*, **27**, 101-108.
- Bringi, V. N., G.-J. Huang, V. Chandrasekar, and E. Gorgucci, 2002: A methodology for estimating the parameters of a gamma raindrop size distribution model from polarimetric radar data: Application to a squall-line event from the TRMM/Brazil campaign. *J. Atmos. Oceanic Technol.*, **19**, 633-645.
- Chandrasekar, V., and V. N. Bringi, 1987: Simulation of radar reflectivity and surface measurements of rainfall. *J. Atmos. Oceanic Technol.*, **4**, 464-478.
- Delrieu, G., J.-D. Creutin, and I. Saint André, 1991: Mean  $K$ - $R$  relationships: Practical results for typical weather radar wavelengths. *J. Atmos. Oceanic Technol.*, **8**, 467-476.
- Efron, B., and R. Tibshirani, 1993: *An Introduction to the Bootstrap*. Chapman and Hall, 436 pp.
- Fujiwara, M., 1965: Raindrop-size distribution from individual storms. *J. Atmos. Sci.*, **22**, 585-591.
- Fulton, R. A., J. P. Breidenbach, D.-J. Seo, D. A. Miller, and T. O'Bannon, 1998: The WSR-88D rainfall algorithm. *Wea. Forecasting*, **13**, 377-395.
- Gunn, R., and G. D. Kinzer, 1949: The terminal velocity of fall for water droplets in stagnant air. *J. Meteor.*, **6**, 243-248.

- Hodson, M. C., 1986: Raindrop size distribution. *J. Climate Appl. Meteor.*, **25**, 1070–1074.
- Hu, Z., and R. C. Srivastava, 1995: Evolution of raindrop size distribution by coalescence, breakup, and evaporation: Theory and observations. *J. Atmos. Sci.*, **52**, 1761–1783.
- Hudson, N. W., 1963: Raindrop size distribution in high intensity storms. *Rhod. J. Agric. Res.*, **1**, 6–11.
- Illingworth, A. J., and T. M. Blackman, 2002: The need to represent raindrop size spectra as normalized gamma distributions for the interpretation of polarization radar observations. *J. Appl. Meteor.*, **41**, 286–297.
- Jameson, A. R., and A. B. Kostinski, 2001a: Reconsideration of the physical and empirical origins of Z–R relations in radar meteorology. *Quart. J. Roy. Meteor. Soc.*, **127**, 517–538.
- , and —, 2001b: What is a raindrop size distribution? *Bull. Amer. Meteor. Soc.*, **82**, 1169–1177.
- Jones, D. M. A., 1992: Raindrop spectra at the ground. *J. Appl. Meteor.*, **31**, 1219–1225.
- Kostinski, A. B., and A. R. Jameson, 1999: Fluctuation properties of precipitation. Part III: On the ubiquity and emergence of the exponential drop size spectra. *J. Atmos. Sci.*, **56**, 111–121.
- Laws, J. O., and D. A. Parsons, 1943: The relation of raindrop-size to intensity. *Trans. Amer. Geophys. Union*, **22**, 709–721.
- List, R., 1988: A linear radar reflectivity–rainrate relationship for steady tropical rain. *J. Atmos. Sci.*, **45**, 3564–3572.
- , N. R. Donaldson, and R. E. Stewart, 1987: Temporal evolution of drop spectra to collisional equilibrium in steady and pulsating rain. *J. Atmos. Sci.*, **44**, 362–372.
- Marshall, J. S., and W. M. Palmer, 1948: The distribution of raindrops with size. *J. Meteor.*, **5**, 165–166.
- , W. Hirschfeld, and K. L. S. Gunn, 1955: Advances in radar weather. *Advances in Geophysics*, Vol. 2, Pergamon, 1–56.
- Martinez, D., and E. G. Gori, 1999: Raindrop size distributions in convective clouds over Cuba. *Atmos. Res.*, **52**, 221–239.
- McFarquhar, G. M., and R. List, 1991: The raindrop mean free path and collision rate dependence on rainrate for three-peak equilibrium and Marshall–Palmer distributions. *J. Atmos. Sci.*, **48**, 1999–2003.
- , and —, 1993: The effect of curve fits for the disdrometer calibration on raindrop spectra, rainfall rate, and radar reflectivity. *J. Appl. Meteor.*, **32**, 774–782.
- Mood, A. M., F. A. Graybill, and D. C. Boes, 1974: *Introduction to the Theory of Statistics*. McGraw-Hill, 564 pp.
- Mueller, E. A., 1962: Raindrop size distributions at Miami, Florida. Research Rep. 9B, Illinois State Water Survey Meteorological Laboratory at the University of Illinois, 281 pp.
- , 1966: Radar cross sections from drop size spectra. Ph.D. dissertation, University of Illinois, 89 pp. [Available from the author.]
- Pasqualucci, F., 1982: The variation of drop-size distribution in convective storms: A comparison between theory and radar measurements. *Geophys. Res. Lett.*, **9**, 839–841.
- Petersen, W. A., and Coauthors, 1999: Mesoscale and radar observations of the Fort Collins flash flood of 28 July 1997. *Bull. Amer. Meteor. Soc.*, **80**, 191–216.
- Porrà, J. M., D. Sempere Torres, and J.-D. Creutin, 1998: Modeling of drop size distribution and its applications to rainfall measurements from radar. *Stochastic Methods in Hydrology: Rain, Landforms, and Floods*, V. K. Gupta et al., Eds., World Scientific, 73–84.
- Rinehart, R. E., 1983: Out-of-level instruments: Errors in hydro-meteor spectra and precipitation measurements. *J. Climate Appl. Meteor.*, **22**, 1404–1410.
- Sauvageot, H., and M. Koffi, 2000: Multimodal raindrop size distributions. *J. Atmos. Sci.*, **57**, 2480–2492.
- Sekhon, R. S., and R. C. Srivastava, 1971: Doppler radar observations of drop-size distributions in a thunderstorm. *J. Atmos. Sci.*, **28**, 983–994.
- Sempere Torres, D., J. M. Porrà, and J.-D. Creutin, 1994: A general formulation for raindrop size distribution. *J. Appl. Meteor.*, **33**, 1494–1502.
- , —, and —, 1998: Experimental evidence of a general description of raindrop size distribution properties. *J. Geophys. Res.*, **103D**, 1785–1797.
- Sheppard, B. E., 1990: Effect of irregularities in the diameter classification of raindrops by the Joss–Waldvogel disdrometer. *J. Atmos. Oceanic Technol.*, **7**, 180–183.
- Shiotsuki, Y., 1976: An estimation of drop-size distribution in the severe rainfall. *J. Meteor. Soc. Japan*, **54**, 259–263.
- Smith, J. A., 1993: Marked point process models of raindrop-size distributions. *J. Appl. Meteor.*, **32**, 284–296.
- , and R. D. de Veaux, 1994: A stochastic model relating rainfall intensity to raindrop processes. *Water Resour. Res.*, **30**, 651–664.
- , M. L. Baeck, M. Steiner, and A. J. Miller, 1996: Catastrophic rainfall from an upslope thunderstorm in the central Appalachians: The Rapidan storm of June 27, 1995. *Water Resour. Res.*, **32**, 3099–3113.
- , —, J. E. Morrison, and P. Sturdevant-Rees, 2000: Catastrophic rainfall and flooding in Texas. *J. Hydrometeor.*, **1**, 5–25.
- , —, Y. Zhang, and C. A. Doswell III, 2001: Extreme rainfall and flooding from supercell thunderstorms. *J. Hydrometeor.*, **2**, 469–489.
- Smith, P. L., Z. Liu, and J. Joss, 1993: A study of sampling-variability effects in raindrop size observations. *J. Appl. Meteor.*, **32**, 1259–1269.
- Spilhaus, A. F., 1948: Drop size, intensity, and radar echo of rain. *J. Meteor.*, **5**, 161–164.
- Srivastava, R. C., 1971: Size distribution of raindrops generated by their breakup and coalescence. *J. Atmos. Sci.*, **28**, 410–415.
- Steiner, M., and A. Waldvogel, 1987: Peaks in raindrop size distributions. *J. Atmos. Sci.*, **44**, 3127–3133.
- , and J. A. Smith, 1998: Convective versus stratiform rainfall: An ice-microphysical and kinematic conceptual model. *Atmos. Res.*, **48**, 317–326.
- , and —, 2000: Reflectivity, rain rate, and kinetic energy flux relationships based on raindrop spectra. *J. Appl. Meteor.*, **39**, 1923–1940.
- , —, S. J. Burgess, C. V. Alonso, and R. W. Darden, 1999: Effect of bias adjustment and rain gauge data quality control on radar rainfall estimation. *Water Resour. Res.*, **35**, 2487–2503.
- Stout, G. E., and E. A. Mueller, 1968: Survey of relationships between rainfall rate and radar reflectivity in the measurement of precipitation. *J. Appl. Meteor.*, **7**, 465–474.
- Testud, J., S. Oury, R. A. Black, P. Amayenc, and X. Dou, 2001: The concept of “normalized” distribution to describe raindrop spectra: A tool for cloud physics and cloud remote sensing. *J. Appl. Meteor.*, **40**, 1118–1140.
- Tokay, A., and D. A. Short, 1996: Evidence from tropical raindrop spectra of the origin of rain from stratiform versus convective clouds. *J. Appl. Meteor.*, **35**, 355–371.
- , —, C. R. Williams, W. L. Ecklund, and K. S. Gage, 1999: Tropical rainfall associated with convective and stratiform clouds: Intercomparison of disdrometer and profiler measurements. *J. Appl. Meteor.*, **38**, 302–320.
- Uijlenhoet, R., 1999: Parameterization of rainfall microstructure for radar meteorology and hydrology. Ph.D. dissertation, Wageningen University, Netherlands, 279 pp. [Available from the author.]
- , 2001: Raindrop size distributions and radar reflectivity–rain rate relationships for radar hydrology. *Hydrol. Earth Syst. Sci.*, **5**, 615–627.
- , and J. N. M. Stricker, 1999: A consistent rainfall parameterization based on the exponential raindrop size distribution. *J. Hydrol.*, **218**, 101–127.
- , M. Steiner, and J. A. Smith, 2003: Variability of raindrop size



- distributions in a squall line and implications for radar rainfall estimation. *J. Hydrometeor.* **4**, 43–61.
- Ulbrich, C. W., 1983: Natural variations in the analytical form of the raindrop size distribution. *J. Climate Appl. Meteor.*, **22**, 1764–1775.
- , and D. Atlas, 1998: Rainfall microphysics and radar properties: Analysis methods for drop size spectra. *J. Appl. Meteor.*, **37**, 912–923.
- Willis, P. T., 1984: Functional fits to some observed drop size distributions and parameterization of rain. *J. Atmos. Sci.*, **41**, 1648–1661.
- , and P. Tattelman, 1989: Drop-size distributions associated with intense rainfall. *J. Appl. Meteor.*, **28**, 3–15.
- Zawadzki, I., and M. de Agostinho Antonio, 1988: Equilibrium raindrop size distributions in tropical rain. *J. Atmos. Sci.*, **45**, 3452–3459.
- Zrnic, D. S., and A. V. Ryzhkov, 1999: Polarimetry for weather surveillance radar. *Bull. Amer. Meteor. Soc.*, **80**, 389–406.

## Radar hydrology: rainfall estimation

W.F. Krajewski<sup>a,\*</sup>, J.A. Smith<sup>b</sup>

<sup>a</sup> IIHR—Hydrosience & Engineering, The University of Iowa, Iowa City, IA 52242, USA

<sup>b</sup> Department of Civil & Environmental Engineering, Princeton University, Princeton, NJ 08544, USA

Received 12 October 2001; received in revised form 11 May 2002; accepted 12 May 2002

### Abstract

Radar observations of rainfall and their use in hydrologic research provide the focus for the paper. Radar-rainfall products are crucial for input to runoff and flood prediction models, validation of satellite remote sensing algorithms, and for statistical characterization of extreme rainfall frequency. In this context we discuss the issues of radar-rainfall product development, and the theoretical and practical requirements of validating radar-rainfall maps and new radar technologies. We discuss a framework for reflectivity based rainfall estimation, including estimation of uncertainty of radar-rainfall estimates. Validation of radar-rainfall products is a major challenge for broad utilization of these products in hydrologic applications. In the discussion of radar-rainfall prediction we focus on orographically induced extreme rainfall and flooding, discuss the issues of detection, statistical sample size, and scale effects. We conclude the paper with a set of recommendations for research priorities and experimental requirements to address them.  
© 2002 Elsevier Science Ltd. All rights reserved.

### 1. Introduction

Radar has assisted weather predictions for over forty years but its operational use in hydrologic applications spans only a decade or so. We approached writing this paper on radar hydrology for the 25th Anniversary Special Issue of *Advances in Water Resources* as an opportunity to discuss the research needs in the field. Our approach is not a comprehensive one, we focus on selected issues of radar data use in hydrology drawing on examples mainly from the NEXRAD system in the United States [23,27,29]. We limit our considerations to the use of weather radar for quantitative estimation of rainfall. We do not consider the quantitative precipitation forecasting problem as a recent issue of *Journal of Hydrology* [69] was devoted to it. Our objectives are to discuss those aspects of radar-rainfall estimation for use in hydrology that we consider general yet critically important for the future. The paper contributes to the discussion solicited by [21] on emerging issues in hydrologic research.

Quantitative estimation of rainfall from radar observations is a complex process. It involves issues of

engineering design of a complicated and sophisticated hardware with both electronic and mechanical subsystems, signal processing, propagation and interaction of electromagnetic waves through the atmosphere and with the ground, image analysis and quality control, physics of precipitation processes, optimal estimation and uncertainty analysis, database organization and data visualization, and hydrologic applications. The scope of our paper is limited to the estimation and uncertainty quantification issues. Rather than focusing on a particular algorithm or method, we discuss the generic issue of developing radar-rainfall products and their validation. We discuss the questions of estimating the bias and evaluating the random errors of the rainfall products. We also discuss observations of extreme rainfall. Weather radar offers an unprecedented opportunity to improve our ability of observing extreme storms and quantifying their associated precipitation. These events trigger floods and flash-floods, debris flow, and landslides. As they often occur in complex terrain their detection is associated with additional difficulties and their treatment warrants a separate section in our paper.

We close the paper with a set of recommendations for future research. These involve not only theoretical and modeling studies but also the observational and experimental infrastructure necessary to answer many questions we pose herein.

\* Corresponding author. Tel.: +1-319-335-5231; fax: +1-319-335-5238.

E-mail addresses: witold-krajewski@uiowa.edu, wkrajew@engineering.uiowa.edu (W.F. Krajewski).

## 2. Radar-rainfall estimation

The basics of radar-based observations of rainfall are discussed by many authors including popular textbooks by Battan [8], Doviak and Zrinc [20], Sauvageot [47], and Reinhart [45] (see also [5,31]). Here we only briefly repeat selected definitions for the sake of consistence of our use of these terms in the subsequent discussion. Radar measurements of power of electromagnetic waves backscattered by raindrops are directly related to a physical quantity called *reflectivity*,  $Z$ , with units of  $\text{mm}^6/\text{m}^3$ . Estimation of rainfall amounts (rain intensity,  $R$  in  $\text{mm}/\text{h}$ , or rainfall accumulation,  $R_A$  in  $\text{mm}$ ) involves using reflectivity via a  $Z$ – $R$  relationship. This relationship could be given in terms of a power law of the type  $Z = aR^b$  as discussed in [8], a look-up table [46], or, perhaps, a neural network. We will come back to this issue shortly.

Radar reflectivity data are typically obtained in the form of a volume scan, i.e. a sequence of sweeps for increasing antenna elevation angles. A volume scan is available every 5–15 min and consists of data given in polar coordinates. The volume scan reflectivity data, collected on a polar grid with a resolution of about  $1^\circ$  by 1 km, are converted to radar-rainfall maps (here we call them *products*), i.e. regular grids with a typical resolution of 2 km by 2 km, or 4 km by 4 km. The conversion includes applying a  $Z$ – $R$  relationship, usually in polar coordinates, averaging the polar grid to a rectangular grid, and selecting or averaging the information on the vertical extent of the storm.

How is the  $Z$ – $R$  relationship selected in the above procedure? We distinguish two general approaches. In the first approach, which we will term the drop size distribution (DSD) approach,  $Z$ – $R$  relations are derived from raindrop size distribution observations, typically made at the surface and representing a sample volume of the order  $1 \text{ m}^3$ . Because rainfall rate and radar reflectivity factor can both be derived from observed raindrop size distributions,  $Z$ – $R$  relations can be computed directly by statistical methods (for example, regression of natural logarithms of reflectivity versus natural logarithms of rainfall rate in the case of power law  $Z$ – $R$  relationships). In this approach, a  $Z$ – $R$  relationship is selected based on analysis of raindrop size distribution data for a given dominant rainfall regime.

The second approach is similar in relying on statistical estimation procedures to relate measured values of radar reflectivity to rainfall rate. The fundamental difference is that in the second approach, which we will term the optimization approach, radar reflectivity measured in the atmosphere by a radar is related to surface observations of rainfall rate (typically from rain gauge networks). In this case, radar reflectivity observations with a characteristic scale of approximately  $1 \text{ km}^3$  are related to surface rainfall rate observations. This approach is motivated

by the observation [5] that the largest sources of error in radar-rainfall estimates are not driven by DSD control of  $Z$ – $R$  relations, but by sampling properties that relate radar reflectivity factor at the surface to radar reflectivity aloft (incomplete beam filling, bright band, evaporation below cloud base, updraft/downdrafts, hail contamination aloft, etc.). In the optimization-based approach, some measure of “closeness” of the radar-rainfall products and the surface rainfall reference data obtained by rain gauges is minimized.

The DSD approach avoids the scale compatibility problem of comparing radar measured reflectivity at  $1 \text{ km}^3$  scale to rainfall rate at  $1 \text{ m}^3$  scale, but introduces other problems. There is little evidence that point approximation of  $Z$ – $R$  relationship is adequate in view of the existing evidence of spatial and temporal variability of rainfall rate. Another problem with the DSD approach, as demonstrated by numerous authors [15,49,55], the parameters of these point relationships are highly sensitive to (1) statistical approach used in their estimation; (2) sample size of the data used; and (3) instrument type used to collect the data [12]. It should also be noted that instrumental errors both in the disdrometer used to collect the DSD data and the radar used to perform rainfall estimation are ignored in this approach. This potentially leads to difficulty identifying effects such as bias [59] and non-linear transformation of radar-reflectivity measurements [15].

The optimization approach (e.g. [1,17]) treats the  $Z$ – $R$  relationship as an empirical formula, in which the key step in algorithm implementation is estimation of the unknown  $Z$ – $R$  parameters. The radar-rainfall products are optimized in a well-defined sense, according to a criterion deemed appropriate by the user for a particular application. The approach acknowledges explicitly that products optimal according to one criterion are not necessarily optimal according to another. For example, Ciach et al. [16] show, that root mean square criterion is in conflict with, what they term, “total conditional bias criterion”.

The main reason for this is the non-linear character of  $Z$ – $R$  combined with the existence of random errors for both the radar-reflectivity measurements as well as the rain gauge data that suffer from significant uncertainty in representing the scale of the rainfall product [25,33,66]. Another manifestation of the optimization-based approach is scale dependency. As specific radar-rainfall products correspond to well-defined space and time scales, different solutions are obtained at different scales. In other words, optimizing products at a certain scale results in better estimates than simply averaging them from a lower scale [41].

### 2.1. Bias

Identifying and quantifying bias is perhaps the most important step in characterizing the error structure of

radar-rainfall estimates. By “bias” we mean the systematic departure from the true, and unknown, rainfall. There are numerous causes of radar-rainfall bias, including miscalibrated radar, overshooting the cloud systems, improper  $Z-R$  relationship, and subcloud evaporation of raindrops. All will cause systematic departure of estimated rainfall from the true rainfall. In the following discussion we approach the problem of bias identification from the real-time estimation point of view. This is because in the off-line mode, with the availability of sufficiently large sample the problem of bias adjustment is much simpler.

We also recognize that identification of the bias due to any or all of the above causes is difficult due to the existence of significant spatial and temporal variability of rainfall and the sampling area mismatch of radar and rain gauge sensors. To eliminate the effects of random factors—which include in addition to the rainfall variability, the reflectivity and rain gauge measurement errors—on bias identification, radar-rainfall and rain gauge rainfall accumulation should be integrated over a certain time scale prior to a meaningful comparison. What is that scale? There is no simple answer to this question. If the scale is too short, for example 15 min, clearly significant spatial variability of rainfall will mask the effect of the bias. From one period to the next, from one gauge to the next, we could have large positive and negative differences between the radar and rain gauge estimates of rainfall. As we allow time integration of the data, the random effects average out, and the bias, if present, becomes more obvious. On the other hand, if we wait too long, we may be mixing seasonal effects. The bias in the cold season is likely to be different from that of the warm season as the typical vertical extent of the cloud system and the DSDs are quite different [2,50].

In the past, the problem of bias estimation and correction in real-time has been approached in the mean-field sense, i.e. trying to ensure that the entire rainfall field in view of a radar does not deviate from that represented by rain gauges. Several authors conducted studies of statistical techniques for this approach, including [2,48,53]. Recently, we note a tendency documented in the literature towards eliminating some of the range dependent biases based on their physical causes [53]. In particular, Vignal et al. [60–62] demonstrated good performance of a vertical profile of reflectivity correction that mitigates the effect of bright band, among other effects. As these effects operate on a short time scale, their effects should be corrected also on such a scale. Vignal and Krajewski [62] also report decrease of random effects in the VPR-corrected radar-rainfall estimates. This is understandable since some of the effects work in the opposite directions, as we discussed above, and thus, when taken together, they “look” random.

Anagnostou et al. [2], McCollum et al. [37] and Seo and Breidenbach [54], attempted to investigate the effect of different time scales on the effectiveness of the bias removal. Still, due to the lack of long-term high-quality radar and rain gauge data sets the question remains largely unanswered. A Monte Carlo simulation study would be an alternative to provide some guidance but its realism is likely to be compromised by the fact that we know little about the statistical characterization of the errors of radar-rainfall.

Our discussion above has implications for the design of operational rain gauge networks. Qualitatively, the rain gauges should be placed in such a way to capture the range effects in all the directions that characterize the rainfall regimes present under a given radar umbrella. It is preferred to place them along the same radar ray as this would eliminate the potential for the near-radar effects due to ground clutter that may affect different azimuths in a different way. Directions where additional effects are expected, such as orographic or synoptic, should be covered by separate gauge sets. The number of gauges per direction does not need to be high as the systematic effects change gradually (but not necessarily monotonically, see [50,62]) with range. We estimate that 4–6 gauges would do the job.

## 2.2. Polarimetric methods

Research conducted over the past 20 years indicates that radar-rainfall estimation may be improved with additional radar measurements. Research radar systems simultaneously measure reflectivity and phase at horizontal (H) and vertical (V) polarization [11,32,68]. The physical concept behind polarization diversity measurements exploits the fact, that under aerodynamical stress, falling raindrops take oblate shapes, and as a result impact differently the propagation and backscattering of an incoming H and V electromagnetic radar wave. The most common polarimetric radar measurements are (1) the reflectivity factors at H and V polarization ( $Z_H$ ,  $Z_V$ ); (2) the differential reflectivity factor ( $Z_{DR}$ ); and (3) the propagation differential phase ( $\Phi_{DP}$ ). These measurements provide information that can be related to DSD characteristics, and in turn provide improved rainfall estimate.

Additionally, the polarimetric measurements provide new means for classifying precipitating particles (rain, hail, graupel and snow) and for distinguishing the ground echo due to local clutter and anomalous propagation conditions from precipitation. The two most beneficial aspects of polarimetric measurements may be the elimination of hail contamination effects in heavy rainfall and improved detection of ground returns.

Use of polarimetric measurements in an operational setting presents a host of new challenges. It is not our goal to discuss them herein as others have already done

this effectively (e.g. [26,32,68]). Some of the challenges deal primarily with radar system design. Other issues concern the fundamental physics of propagation and interaction of radar waves with precipitating medium.

Our goal is to bring attention to the issue of estimation. The polarimetric measurements are not a panacea to many of radar-rainfall uncertainty sources (with the possible exception of hail contamination). Within-beam variability, subcloud evaporation, cloud overshooting, etc., cannot be solved with the polarimetric measurements. Also, the measurements of some of the polarimetric variables are associated with significant uncertainties. For example, estimation of specific differential phase shift ( $K_{DP}$ ) is subject to random phase errors of the  $\Phi_{DP}$  measurements and the backscattering phase shift ( $\delta$ ), which cannot be readily separated from  $\Phi_{DP}$ . The  $\delta$  value, which increases with an increase in raindrop size, can be significant at high rainfall intensities and high radar frequencies. This non-Rayleigh effect can introduce serious complications in the evaluation of  $K_{DP}$  at the X-band and moderate to high rainfall intensities, and requires careful investigation [36].

Studies on radar polarimetry have concentrated mainly on the S-band frequency and shown that  $K_{DP}$  based radar estimators are not affected by radar calibration errors and partial beam occlusion (e.g. [65,67,68]). However, at S-band, these estimators are characterized by relatively low sensitivity to rainfall rate and this, consequently, has negative impact on the product resolution. Since  $\Phi_{DP}$  sensitivity to the raindrop size is proportional to the radar wavelength, one would expect that at X-band, these limiting values could be lowered by a factor of three. Consequently, the use of X-band wavelength should allow more accurate estimation of light to moderate rainfall rates at higher spatial resolutions. These improvements are primarily important for the accurate prediction of floods in small to medium size watersheds with rapid response to precipitation and for real-time urban water management. Furthermore, partial signal attenuation, which is significant at X-band, is not an important issue for the  $K_{DP}$  estimator unless there is complete attenuation. The main complications in  $K_{DP}$  rainfall estimation at X-band that need to be investigated are (1) the presence of significant  $\delta$  in cases of high rainfall intensities, and (2) the effect of DSD variability and oblateness shape model selection on the estimator parameters. To date, research on the use of polarimetric radar measurements at X-band has been limited to a few theoretical [13,30] and experimental studies [36,57] but the proposed estimators lack adequate quantitative validation and error analysis.

Thus, if we realize that rainfall estimates based on polarimetric data are uncertain, the task remains to quantify these uncertainties. From this point of view the requirements for validation of radar-rainfall are the same as for single-parameter radar.

### 2.3. Validation

The central question for hydrologic application of radar-rainfall products is "How good are these estimates?" In our view this is a question of validation. According to Webster's Ninth New Collegiate Dictionary, *valid* means "being at once relevant and meaningful," and *validation* is the "process of determination of the degree of validity of a measuring device". In this paper, we define validation consistently with the common definition quoted above. Validation is determination of the space-time statistical structure of errors of the radar-rainfall products, i.e. "the degree of validity".

Clearly, identifying and estimating the full structure of the error distribution is a challenging task. It may be prudent to simplify it to begin with and focus on the first two moments of the error distribution. In the section above we discussed the issue of bias, here we will focus on the error variance. Ciach and Krajewski [14] proposed a general framework for the error variance estimation. They proposed to separate the radar/rain gauge difference variance into two components: one due to the natural variability of rainfall in space over scales smaller than that of the radar-rainfall products, and the second one being the radar-rainfall error variance. The subgrid variability, if substantial, implies lack of good representativeness of the grid scale rainfall by the rain gauges that measure the process at a point [33,66]. The use of this approach, coined error variance separation (EVS) method, requires two important components. First, it requires making an assumption about lack of correlation between the errors of the radar-rainfall and the rain gauge approximation of the grid scale rainfall. Second, it requires knowledge of rainfall variability, at least in terms of its spatial correlation function, at scales below that of the grid dimensions.

The EVS approach was explored by Anagnostou et al. [3] who lacked information on the correlation structure of rainfall, and by Habib and Krajewski [25], who used experimentally derived information on the correlation structure of rainfall fields. Nevertheless, the problem of error covariance remains unresolved. To resolve this problem requires a special experimental setup in which rainfall can be accurately estimated by independent means. With the current technologies this implies a dense rain gauge network, so dense that spatial sampling error could be considered negligible and radar-rainfall products could be directly compared to the cluster-based estimate [39]. High-density cluster data would permit developing and testing framework for estimation of error probability distribution, thus extending the scope of the EVS approach.

In closing of this section, let us also mention another fundamental issue of operational and experimental rainfall measurement and estimation. There is a growing recognition that the historical rain gauge data are of

very poor quality. This concerns most of the 15-min, hourly, and daily rainfall data. Following the earlier suggestion by Ciach and Krajewski [14], supported by evidence discussed by Steiner et al. [56], we strongly recommend deployment of dual rain gauge platforms. In view of very high variability of rainfall only gauges sited side by side can provide independent information needed for fault detection and data record collection. Rain gauge data are vital in our quest for improved understanding of radar-based rainfall estimation technologies.

### 3. Radar estimation of extreme rainfall

Radar estimation of extreme rainfall rates plays an important role in a range of applications dealing with the hydrology and hydraulics of flooding. The extreme rainfall rate setting also raises special challenges for development of radar-rainfall estimation algorithms, validation of rainfall algorithms and design of radar-rainfall estimation experiments. Because of the hydrologic importance of extreme rainfall, we examine these challenges in detail below.

Hudson [28] presented one of the first experiments designed to measure and parameterize raindrop size distributions in extreme rainfall rate storms (see also [9,63]). Blanchard and Spencer [9] concluded that breakup of raindrops controls the raindrop size distribution for extreme rainfall rates and they observed that for rainfall rates in the range between 100 and 700 mm/h, the median diameter remains relatively constant. These features of drops size distributions are used to infer that for a given rainfall rate in intense rainfall, a steady-state drops size distribution develops in which drop growth is balanced by drop breakup. List [35] presents theoretical arguments supporting an “equilibrium” drops size distribution in heavy rain and shows that in this case  $Z$  and  $R$  will be linearly related, that is, the exponent  $b$  in the  $Z$ – $R$  relation for extreme rainfall rates will be 1.

Uijlenhoet et al. [58] show that the linear  $Z$ – $R$  relationship holds for extreme rainfall rate drop spectra from Florida (rainfall rates exceeding 100 mm/h). It is also shown in [58] that the prefactor of the  $Z$ – $R$  relation varies over a large range. It follows that, even under equilibrium conditions for extreme rainfall rates, bias estimation will play an important role in reflectivity-based estimation of extreme rainfall rates. This point is further illustrated in analyses of radar-rainfall estimates from “warm rain process” storms, which produce extreme rainfall rates [44,50,51]. Development of  $Z$ – $R$  estimation procedures, as discussed above, will be sensitive to the weighting of observations from the extreme tail of the rainfall rate distribution. For applications in which extreme rainfall rates are of special interest, val-

idation procedures should explicitly characterize the error of rainfall rate estimates as a function of rainfall rate.

The extreme rainfall estimation problem provides one setting in which ideas from the DSD approach and the optimization approach can be usefully combined to enhance radar-rainfall estimation algorithms. The extreme rainfall setting is one in which previous studies provide a strong basis for presuming that variations in DSDs play a significant role in the accuracy of radar-rainfall estimates. Information on key aspects of the variability in DSD properties can be obtained from polarimetric measurements, like differential reflectivity and differential phase shift. Including these additional radar observations should lead to significant improvements in estimation of extreme rainfall rates. The framework for including polarimetric measurements, however, should be the optimization approach, in which radar observations aloft are compared with surface measurements of rainfall rate.

The climatology of rainfall rates exceeding 100 mm/h is heavily influenced by warm season systems of thunderstorms. The climatology of radar reflectivity observations for these storms, in turn, is strongly influenced by hail contamination [6,7]. The presence of hail in a radar sample volume can severely distort radar-rainfall estimates, due the sixth power dependence of  $Z$  on drop diameter. An extreme example of the hail contamination problem is provided by supercell thunderstorms, which are often prolific hail producers and the agents of extreme rainfall rates. The Dallas Hailstorm of 5 May 1995 [52] was a supercell thunderstorm, which produced hailstones (more than 2 cm in diameter) in close proximity to regions experiencing 15-min rainfall rates exceeding 200 mm/h. More than 15 fatalities resulted from flash floods produced the Dallas Hailstorm. Smith et al. [52] argue that supercell thunderstorms play an important role in determining the frequency of extreme rainfall rates in much of the US east of the Rocky Mountains. Hail contamination precludes the development of useful climatologies of extreme rainfall from single parameter radar-rainfall estimates. As discussed in Section 2.2, polarimetric measurements could significantly reduce errors in rainfall rates due to hail contamination.

Warm season thunderstorms in urban environments present an important challenge to radar-rainfall estimation procedures. Flood response of small drainage basins in urban environments is particularly sensitive to “fine-scale” temporal and spatial variability of rainfall. The precise scale boundaries will depend on details of the drainage basin (see [52], for example), but in many settings the relevant scales of variability are comparable or smaller than the minimum observation scales of operational weather radar systems like the WSR-88D (6 min, 1 km). Experimental programs for radar estimation

at rainfall at fine space and time scales will play an important role in advances in urban flood hydrology.

The utility of radar-rainfall estimates for extreme flood analysis can be viewed in terms of enhanced capabilities for modeling flood response of a drainage basin. The potential benefits of high-resolution rainfall estimates have motivated advances in hydrologic modeling [10,18,34,38,40,42,43,64]. Advances in operational forecasting and hydrologic design have progressed more slowly although there are exceptions (e.g. see [22]). Radar-rainfall estimates hold particular promise for enhanced flash flood forecasting procedures and for engineering design and management applications in small basins. For these problems, hydrologic processes forced by rainfall rate play a comparable or even more important role than hydraulic processes associated with flood wave propagation. The central difficulty here is often the non-linear response of drainage basins to rainfall rate.

These observations have important implications for development of radar-rainfall estimation procedures. One of the major obstacles to increased utilization of radar-rainfall estimates for hydrologic modeling has been the absence of quantitative assessments of the accuracy of radar-rainfall estimates. As discussed in previous sections, development of formalized procedures for estimating the error structure of radar-rainfall fields and for validating radar-rainfall estimates is of central importance to radar hydrology. In some settings, the hydrologic application may impose useful constraints on the error assessment problem. In particular, assessment of error structure of radar-rainfall estimates that are used for hydrologic modeling should consider the propagation of errors through hydrologic models. The non-linear response of drainage basins to rainfall forcing implies that errors in extreme rainfall rates will play an important role in hydrologic modeling. Quantification and validation of radar-rainfall estimates for extreme rain conditions are also an important challenge for radar hydrology.

The challenges of extreme rainfall estimation are particularly acute in mountainous terrain. Some of the largest measured rainfall accumulations in the United States and the world [19] have occurred in complex terrain. Landslides and debris flows are added to flooding as major hazards associated with extreme rainfall in mountainous terrain. Radar-rainfall estimation in complex terrain is complicated by ground returns and signal loss associated with beam blockage [31] (see also Andrieu et al. [4] for novel approaches dealing with radar sampling problems in complex terrain). An additional problem is that orographic storms may differ from storms forming away from terrain in terms of microphysical and dynamical properties [44,50]. Despite these difficulties, radar-rainfall estimates hold great

promise in improving hazards assessment capabilities in mountainous terrain.

#### 4. Conclusions and recommendations

From the discussion on radar-rainfall estimation we conclude that there is much that we do not understand about the instrument that has been in use for over 40 years. We cannot answer numerous basic questions about radar-rainfall estimation error structure. What is the probability distribution of the errors? Are they dependent in space and time from pixel to pixel and from scan to scan? How do they depend on the rainfall regime? To what extent are they caused by the radar hardware characteristics and to what extent can rainfall estimation algorithms mitigate the error sources? We also know little about the rainfall processes at scales that affect radar-rainfall estimates. What is the spatial correlation structure of rainfall at scales below 2 km? What is the spatial correlation structure of reflectivity and other moments of DSD?

We could ask many similar questions regarding our knowledge of rainfall scaling. Does rainfall rate scale according to a certain way at scales below that of the typical radar-rainfall products? To what extent radar-rainfall error structure affects our understanding of rainfall scaling at higher spatial scales? How does rainfall integration in time affect its scaling properties?

It is clear that the above questions—if we as community consider them important—form a research agenda for the upcoming years. Here we propose several recommendations for the community to consider.

1. Long term monitoring and validation sites, providing detailed information on precipitation, should be developed. The sites should have an areal extent on the order of 100 km<sup>2</sup> and include a mix of radar, surface (rain gauge, disdrometer, and conventional meteorological) and upper air observations. Experimental design should be structured in a way to provide both information of the spatial dependence of rainfall as well as good estimates of areal rainfall for direct comparisons with radar-based estimates.
2. New technologies for in situ measurement of precipitation are needed. If we could build reliable and inexpensive disdrometers to replace rain gauges this would address many needs of remote sensing of precipitation. Instruments with sampling volume just one or two orders of magnitude greater than the current instruments would go a long way towards closing the scale gap in our abilities to observe precipitation. Optical technologies seem to be particularly attractive here.

3. Methodological advances are needed in several areas of radar-rainfall estimation. Of particular importance are advances in rainfall estimation using radar polarimetric observations, estimation of the error structure of rainfall rate estimates, and validation of radar-rainfall algorithms.
4. Most important for radar hydrology is the diffusion of radar-rainfall products into a diverse array of hydrologic applications. The potential of radar-rainfall products for operational flood forecasting is going to be realized in application. There is still tremendous potential for advances in flash flood forecasting. Numerous other applications provide important areas of exploration in radar hydrology. These include engineering design of flood control structures, precipitation frequency analysis, operation and control of urban storm and waste water treatment systems, water supply forecasting, groundwater recharge assessments and non-point source pollution assessments.

#### Acknowledgements

Many of the problems we discussed were inspired by our research in support of the NASA's Tropical Rainfall Measuring Mission Ground Validation Program and the NWS Office's of Hydrology efforts to improve NEXRAD rainfall estimation. We would like to also acknowledge receiving support from NOAA GCIP grants NA96GP0416 and NA96GP0417, NSF grant EAR00-01249 and their role in organizing many ideas forwarded herein. We acknowledge many stimulating discussions with Drs. Mary Lynn Baeck, Grzegorz J. Ciach, Emad Habib, Anton Kruger, Brian Nelson, Matthias Steiner and Remko Uijlenhoet.

#### References

- [1] Anagnostou EN, Krajewski WF. Calibration of the NEXRAD precipitation processing subsystem. *Weather Forecast* 1998; 13:396–406.
- [2] Anagnostou EN, Krajewski WF, Seo D-J, Johnson ER. Mean-field radar rainfall bias studies for WSR-88D. *ASCE J Eng Hydrol* 1998;3:149–59.
- [3] Anagnostou EN, Krajewski WF, Smith JA. Uncertainty quantification of mean-areal radar rainfall estimates. *J Atmos Oceanic Technol* 1999;16:206–15.
- [4] Andrieu H, Creutin JD, Delrieu G, Faure D. Use of a weather radar for the hydrology of a mountainous area. 1. Radar measurement interpretation. *J Hydrol* 1997;193:1–25.
- [5] Austin PM. Relation between measured radar reflectivity and surface rainfall. *Mon Weather Rev* 1987;115:1053–69.
- [6] Baeck ML, Smith JA. Climatological analysis of Manually Digitized Radar data for the United States. *Water Resour Res* 1995;31:3033–49.
- [7] Baeck ML, Smith JA. Estimation of heavy rainfall by the WSR-88D. *Weather Forecast* 1998;13:416–36.
- [8] Battan LJ. Radar observation of the atmosphere. The University of Chicago Press; 1973.
- [9] Blanchard DC, Spencer AT. Experiments of the generation of raindrop size distributions by drop breakup. *J Atmos Sci* 1970;27:101–8.
- [10] Borga M, Anagnostou ET, Frank E. On the use of real-time radar rainfall estimates for flood prediction in mountainous basins. *J Geophys Res Atmos* 2000;105:2269–80.
- [11] Bringi VN, Goddard JWF, Cherry SM. Comparison of dual polarization radar measurements of rain with ground based disdrometer measurements. *J Appl Meteor* 1982;21:252–64.
- [12] Campos E, Zawadzki I. Instrument uncertainties in Z–R relations. *J Appl Meteor* 2000;39:1088–102.
- [13] Chandrasekar V, Bringi VN, Balakrishnan VN, Zrnic DS. Error structure of multiparameter radar and surface measurements of rainfall. Part III: Specific differential phase. *J Atmos Oceanic Technol* 1990;7:621–9.
- [14] Ciach GJ, Krajewski WF. On the estimation of radar rainfall error variance. *Adv Water Resour* 1999;22:585–95.
- [15] Ciach GJ, Krajewski WF. Radar-rain gauge comparisons under observational uncertainties. *J Appl Meteor* 1999;38:1519–25.
- [16] Ciach GJ, Morrissey ML, Krajewski WF. Conditional bias in radar rainfall estimation. *J Appl Meteor* 2000;39:1941–6.
- [17] Ciach GJ, Krajewski WF, Anagnostou EN, Baeck ML, Smith JA, McCollum JR, et al. Radar rainfall estimation for ground validation studies of the tropical Rainfall Measuring Mission. *J Appl Meteor* 1997;36:735–47.
- [18] Corral C, Sempere-Torres D, Revilla M, Berenguer M. A semi-distributed hydrological model using rainfall estimates by radar. Application to Mediterranean basins. *Phys Chem Earth Part B: Hydrol Oceans Atmos* 2000;25:1133–6.
- [19] Costa JE. Hydraulics and basin morphometry of the largest flash floods in the conterminous United States. *J Hydrol* 1987;93:313–38.
- [20] Doviak RJ, Zrnic DS. Doppler Radar and Weather Observations. San Diego, CA: Academic Press Inc; 1993.
- [21] Entekhabi D, Asrar GR, Betts AK, Beven KJ, Bras RL, Duffy CJ, et al. An agenda for land surface hydrology research and a call for the second international hydrological decade. *Bull Am Meteorol Soc* 1999;80:2043–58.
- [22] Finnerty BD, Smith MB, Seo D-J, Koren V, Moglen GE. Space-time scale sensitivity of the Sacramento model to radar-gauge precipitation inputs. *J Hydrol* 1997;203:21–38.
- [23] Fulton RA, Breidenbach JP, Seo D-J, Miller DA, O'Bannon T. The WSR-88D rainfall algorithm. *Weather Forecast* 1998;13:377–95.
- [24] Habib E, Krajewski WF. Uncertainty analysis of the TRMM ground validation radar-rainfall products application to the TEFLUN-B field campaign. *J Appl Meteor* 2002;41:558–72.
- [25] Hubbert JV, Bringi VN. An iterative filtering technique for the analysis of coplanar differential phase and dual-frequency radar measurements. *J Atmos Oceanic Technol* 1995;12:643–8.
- [26] Hudlow MD. Technological developments in real-time operational hydrologic forecasting in the United States. *J Hydrol* 1988;102:69–92.
- [27] Hudson NW. Raindrop size distribution in high intensity rain. *Rhod J Agric Res* 1963;1:6–11.
- [28] Hunter S. WSR-88D Radar rainfall estimation: capabilities, limitations and potential improvements. *NWA Digest* 1996; 20:26–36.
- [29] Jameson AR. An alternative approach to estimating rainfall rate by radar using propagation differential phase shift. *J Atmos Oceanic Technol* 1994;11:122–31.
- [30] Joss J, Waldvogel A. Precipitation measurement and hydrology. In: Atlas D, editor. *Radar in Meteorology*. Boston: AMS; 1990. p. 577–606 (Chapter 29A).



- [32] Keenan TD et al. The BMRC/NCAR C-Band polarimetric (C-POL) radar system. *J Atmos Oceanic Technol* 1998;15:871–86.
- [33] Kitchen M, Blackall RM. Representativeness errors in comparisons between radar and gauge measurements of rainfall. *J Hydrol* 1992;134:13–33.
- [34] Krajewski WF, Lakshmi V, Georgakakos KP, Jain SC. A Monte-Carlo study of rainfall sampling effect on a distributed catchment model. *Water Resour Res* 1991;27:119–28.
- [35] List R. A linear radar reflectivity rain rate relationship for steady tropical rain. *J Atmos Sci* 1991;45:3564–72.
- [36] Matrosov SY, Kropfli RA, Reinking RF, Martner BE. Prospects for measuring rainfall using propagation differential phase in X- and Ka-radar bands. *J Appl Meteor* 1999;38:766–76.
- [37] McCollum JR, Krajewski WF, Ferraro RR, Ba MB. Evaluation of biases of satellite rainfall estimation algorithms over the continental United States. *J Appl Meteor*, in press.
- [38] Michaud JD, Sorooshian S. Effect of rainfall-sampling errors on simulations of desert flash floods. *Water Resour Res* 1994;30:2765–75.
- [39] Moore RJ, Jones DA, Cox DR, Isham VS. Design of the HYREX raingauge network. *Hydrol Earth Syst Sci* 2000;4:523–30.
- [40] Morin E, Enzel Y, Shamir U, Garti R. The characteristic time scale for basin hydrological response using radar data. *J Hydrol* 2001;252:85–99.
- [41] Morin E., Krajewski WF, Goodrich DC, Gao X, Sorooshian S. Estimating rainfall intensities from meteorological radar data: The scale dependency problem. *J Hydrometeorol*, submitted for publication.
- [42] Ogden FL, Julien PY. Runoff model sensitivity to radar rainfall resolution. *J Hydrol* 1994;158:1–18.
- [43] Pessoa ML, Bras RL, Williams ER. Use of weather radar for flood forecasting in the Sieve-River basin—a sensitivity analysis. *J Appl Meteor* 1993;32:462–75.
- [44] Petersen WA, Carey LD, Rutledge SA, Knievel JC, Doesken NJ, Johnson RH, et al. Mesoscale and radar observations of the Fort Collins flash flood of 28 July 1997. *Bull Am Meteorol Soc* 1999;80:191–216.
- [45] Reinhardt R. Radar for meteorologists. Reinhardt Publications; 1997.
- [46] Rosenfeld D, Wolff DB, Amitai E. The window probability matching method for rainfall measurement with radar. *J Appl Meteor* 1994;33:682–93.
- [47] Sauvageot H. Radar Meteorology. Artech House, Inc; 1991. p. 315.
- [48] Smith JA, Krajewski WF. Estimation of the mean field bias of radar rainfall estimates. *J Appl Meteor* 1991;30:397–412.
- [49] Smith JA, Krajewski WF. A modeling study of rainfall rate–reflectivity relationships. *Water Resour Res* 1993;29:2505–14.
- [50] Smith JA, Seo DJ, Baeck ML, Hudlow MD. An intercomparison study of NEXRAD precipitation estimates. *Water Resour Res* 1996;32:2035–45.
- [51] Smith JA, Baeck ML, Steiner M, Miller AJ. Catastrophic rainfall from an upslope thunderstorm in the Central Appalachians: the Rapidan Storm of June 27, 1995. *Water Resour Res* 1996;32:3099–113.
- [52] Smith JA, Baeck ML, Zhang Y, Doswell Jr CA. Extreme rainfall and flooding from supercell thunderstorms. *J Hydrometeorol* 2001;2:469–89.
- [53] Seo D-J, Breidenbach JP, Fulton R, Miller D, O'Banion T. Real time adjustment of range dependent biases in WSR-88D rainfall estimates due to nonuniform vertical profile of reflectivity. *J Hydrometeorol* 2000;1:222–40.
- [54] Seo D-J, Breidenbach JP. Real-time correction of spatially nonuniform bias in radar rainfall data using rain gauge measurements. *J Hydrometeorol* 2002;3:93–111.
- [55] Steiner M, Smith JA. Reflectivity rain rate and kinetic energy flux relationships based on raindrop spectra. *J Appl Meteor* 2000;39:1923–40.
- [56] Steiner M, Smith JA, Burges SJ, Alonso CV, Darden RW. Effect of bias adjustment and rain gauge data quality control on radar rainfall estimation. *Water Resour Res* 1999;35:2487–503.
- [57] Tan J, Holt AR, Hendry A, Bebbington DHO. Extracting rainfall rates from X-band CDR radar data by using differential propagation phase shift. *J Atmos Oceanic Technol* 1991;8:790–801.
- [58] Uijlenhoet R, Smith JA, Steiner M. The microphysical structure of extreme precipitation. *J Atmos Sci*, in press.
- [59] Ulbrich CW, Miller NE. Experimental test of the effects of Z–R law variations on comparison of WSR-88D rainfall amounts with surface rain gauge and disdrometer data. *Weather Forecast* 2001;16:369–74.
- [60] Vignal B, Andrieu H, Creutin JD. Identification of vertical profiles of reflectivity from volumetric radar data. *J Appl Meteor* 1999;38:1214–28.
- [61] Vignal B, Galli G, Joss J, Germann U. Three methods to determine profiles of reflectivity from volumetric radar data to correct precipitation estimates. *J Appl Meteor* 2000;39:1715–26.
- [62] Vignal B, Krajewski WF. Large sample evaluation of two methods to correct range-dependent error for WSR-88D rainfall estimates. *J Hydrometeorol* 2001;2(5):490–504.
- [63] Willis PT, Tattleman P. Drop-size distributions associated with extreme rainfall. *J Appl Meteor* 1989;28:3–15.
- [64] Winchell M, Gupta HV, Sorooshian S. On the simulation of infiltration- and saturation-excess runoff using radar-based rainfall estimates: effects of algorithm uncertainty and pixel aggregation. *Water Resour Res* 1998;34:2655–70.
- [65] Vivekanandan J, Yates DN, Brandes EA. The influence of terrain on rainfall estimates from radar reflectivity and specific propagation phase observations. *J Atmos Oceanic Technol* 1999;16:837–45.
- [66] Zawadzki I. On radar–raingauge comparison. *J Appl Meteor* 1975;14:1430–6.
- [67] Zrnic DS, Ryzhkov AV. Advantages of rain measurements using specific differential phase. *J Atmos Oceanic Technol* 1996;13:454–64.
- [68] Zrnic DS, Ryzhkov AV. Polarimetry for weather surveillance radars. *Bull Am Meteorol Soc* 1999;80:389–406.
- [69] *J Hydrol* 2000;239(1–4).

## The Regional Hydrology of Extreme Floods in an Urbanizing Drainage Basin

JAMES A. SMITH AND MARY LYNN BAECK

*Department of Civil and Environmental Engineering, Princeton University, Princeton, New Jersey*

JULIA E. MORRISON

*Department of Operations Research, Princeton University, Princeton, New Jersey*

PAULA STURDEVANT-REES

*Department of Civil and Environmental Engineering, University of Massachusetts—Amherst, Amherst, Massachusetts*

DANIEL F. TURNER-GILLESPIE

*Department of Civil and Environmental Engineering, Princeton University, Princeton, New Jersey*

PAUL D. BATES

*School of Geographical Sciences, University of Bristol, Bristol, United Kingdom*

(Manuscript received 16 January 2001, in final form 14 November 2001)

### ABSTRACT

The Charlotte, North Carolina, metropolitan area has experienced extensive urban and suburban growth since 1960. Five of the largest flood peaks in the 74-yr discharge record of Little Sugar Creek, which drains the central urban corridor of Charlotte, have occurred since August of 1995. A central objective of this study is to explain how these two observations are linked. To achieve this goal, a series of hypotheses of broad importance to the hydrology and hydrometeorology behavior of extreme floods will be examined. These hypotheses concern the roles of 1) space–time variability of rainfall, 2) antecedent soil moisture, 3) expansion of impervious area, and 4) alterations of the drainage network for extreme floods in urbanizing drainage basins. The methodology used to examine these hypotheses centers on diagnostic studies of flood response for the five major flood events that have occurred since August of 1995. Diagnostic studies exploit the diverse range of extreme precipitation forcing for the five events and heterogeneity of land surface properties for catchments with stream gauging records. The observational resources for studying flood response in the Charlotte metropolitan region are exceptional. They include two National Weather Service WSR-88D radars that were deployed in 1995, a dense network of rain gauges and stream gauges installed by the U.S. Geological Survey in 1995, and extensive land surface datasets developed by Mecklenburg County. This study focuses on the *regional* hydrology of extreme flood response, as opposed to the specific effects of individual elements of the constructed environment. Of particular interest are the hydrologic, hydraulic, and hydrometeorological controls of extreme flood response at basin scales ranging from 1 to 500 km<sup>2</sup>.

### 1. Introduction

The Charlotte, North Carolina, metropolitan area (Fig. 1) has experienced rapid growth since the early 1960s (Martens 1968). A striking feature of the flood record for the region is the series of extreme floods during the 1990s. The four largest flood peaks, and five of the largest seven flood peaks, in the 74-yr discharge record of Little Sugar Creek, which drains the central

urban corridor of Charlotte at a drainage area of 110 km<sup>2</sup>, have occurred since August of 1995 (Fig. 2).

The five flood events in Little Sugar Creek since 1995 were produced by a diverse collection of storms: 1) Tropical Storm Jerry (27 August 1995), 2) an organized system of thunderstorms that repeatedly tracked over the Charlotte region (23 July 1997), 3) Hurricane Danny (24 July 1997), 4) a fast-moving, prefrontal squall line (9 April 1998), and 5) a small, relatively short-lived thunderstorm system (27 July 1998). Storm total, basin-averaged rainfall in Little Sugar Creek ranged from 50 mm for the 24 July 1997 storm to more than 180 mm for the 23 July 1997 storm. Peak rainfall accumulations

---

Corresponding author address: James A. Smith, Dept. of Civil and Environmental Engineering, Princeton University, Princeton, NJ 08544.  
E-mail: jsmith@princeton.edu

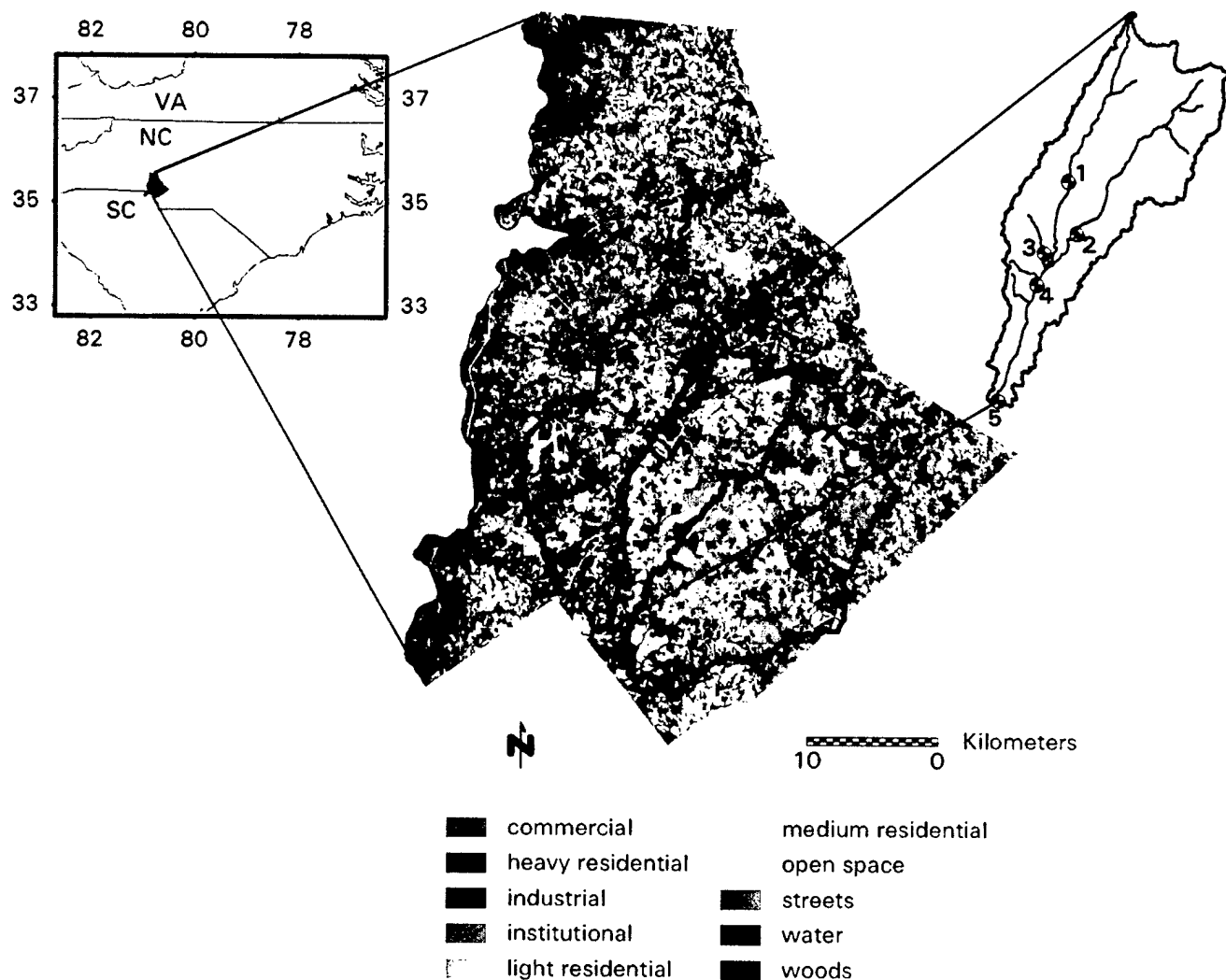


FIG. 1. Location map for Mecklenburg County, North Carolina, with LULC and drainage basin boundaries for Little Sugar Creek (middle), McAlpine Creek (eastern catchment), and Irwin-Sugar Creek (western catchment). The upper right-hand inset provides an expanded view of Little Sugar Creek with the drainage network and location of stream gauges used for analyses of 1995–98 floods. The numbers beside gauging-station locations correspond to the numbers in Table 2.

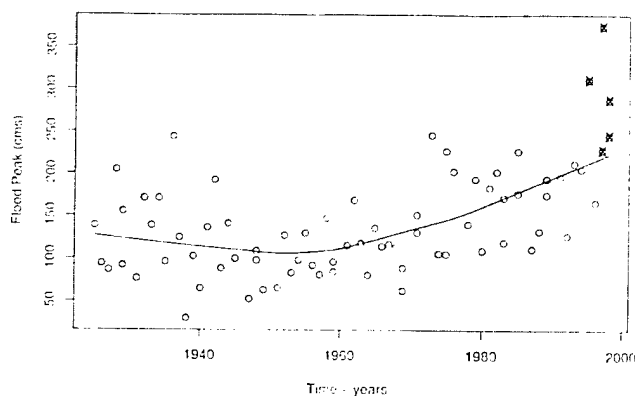


FIG. 2. Annual flood peaks ( $\text{m}^3 \text{s}^{-1}$ ) for Little Sugar Creek at Archdale (station 4 in Fig. 1 and Table 2). A lowess smoothing of the data is shown by the solid line. The five flood events analyzed in sections 3 and 4 are marked by an "X". The 24 Jul 1997 and 27 Jul 1998 peaks are not annual peaks but are included for comparison purposes.

from the 23 July 1997 storm reached 280 mm during a 12-h period, nearly doubling the daily rainfall record of 150 mm for Charlotte, which has a gauging record of more than 100 yr. In addition to the contrasts in storm total rainfall, there were also significant differences in the spatial and temporal distribution of rainfall over the Little Sugar Creek basin, as described in section 3.

A central objective of this study is to provide an explanation for the series of extreme floods in Little Sugar Creek during the late 1990s. To achieve this objective, the following hypotheses, which are of general interest to flood hydrology, will be examined:

- Increasing flood peak magnitudes in the Charlotte metropolitan region are due to increased drainage density associated with elaboration of the drainage network through streets, culverts, and other elements of the constructed environment (Graf 1977). An alternative hypothesis is that increasing flood magnitudes

TABLE 1. Summary of flood response and trends in flood response based on stream-gauging observations for annual flood peaks from 1962 to 1995 for five catchments in the Charlotte metropolitan area. USGS identification codes for the gauging stations are given in the first column. McMullen Creek is located on the western boundary of the McAlpine Creek basin (Fig. 1). Irwin Creek drains the northeastern portion of the Irwin-Sugar Creek basin. Long Creek is northwest of Little Sugar Creek. The median annual flood peak is expressed as a unit discharge, i.e., discharge divided by drainage area. The fifth column provides the linear trend in annual flood peaks, expressed as a percentage of the median flood peak from the fourth column. The V/P ratio (h) is the median value for the station, computed using procedures described in the text.

Basin	Drainage area (km <sup>2</sup> )	V/P ratio (h)	Median flood (m <sup>3</sup> s <sup>-1</sup> km <sup>-2</sup> )	Trend (% yr <sup>-1</sup> )
Little Sugar (02146507)	110	8.4	1.39	1.8
McAlpine (02146600)	103	13.6	0.86	2.3
McMullen (02146700)	18	5.7	1.97	3.4
Irwin-Sugar (02146300)	79	9.1	1.22	1.6
Long Creek (02142900)	43	14.1	0.89	0.4

result primarily from increasing runoff volumes associated with increases in impervious area (Leopold 1968).

- The importance of antecedent soil moisture for flood response decreases with urbanization because of the effects of increased impervious area. The importance of antecedent soil moisture diminishes with the return interval of the event (Wood et al. 1990). For very large flood events in urban areas, the role of antecedent soil moisture can be neglected in assessing flood response.
- The series of anomalously large flood peaks since 1995 resulted principally from anomalously large rainfall.

A paired objective of this study is to characterize the hydrologic, hydraulic, and hydrometeorological controls of extreme flood response and to determine their dependence on basin scale. For Little Sugar Creek and surrounding catchments, analyses span basin scales ranging from 1 to 500 km<sup>2</sup>. This range of basin scales encompasses the region of anomalous scaling behavior of annual flood peaks for the central Appalachian region of Maryland and Virginia (Smith 1992). Scaling behavior of central Appalachian flood peaks can be characterized by a maximum scale of variability [as represented by the coefficient of variation (CV) of annual flood peaks] at approximately 100 km<sup>2</sup>. This feature is inconsistent with simple scaling theories, which are equivalent to the index flood assumption (Smith 1992) and multiscaling theories of regional flood frequency. Explanations for this scaling property of flood response have centered on 1) space-time organization of rainfall, 2) drainage network structure, and 3) channel/floodplain processes (Smith 1992; Gupta et al. 1994; Woods and Sivapalan 1999; Morrison and Smith 2001). Analyses of scale-dependent flood response for Little Sugar Creek exploit the diverse range of extreme precipitation forcing for the five flood events since 1995 and heterogeneity of land surface properties, both natural and anthropogenic.

The observational resources for studying flood response in the Charlotte metropolitan region are excep-

tional. The region is covered by two National Weather Service WSR-88D (Weather Surveillance Radar-1988 Doppler) radars, both of which were deployed in 1995. A dense network of rain gauges and stream gauges was installed by the U.S. Geological Survey (USGS) in 1995 (Hazell and Bales 1997; Robinson et al. 1998). Mecklenburg County has developed extensive land surface datasets. For this study, these datasets have been adapted to provide high-resolution (5–30 m) gridded datasets of terrain elevation, impervious cover, soil texture classification, and land use-land cover (LULC).

## 2. Long-term trends in hydrologic response

The focus of this study is the Little Sugar Creek basin (Fig. 1), for which five USGS stream-gauging stations (see inset of Fig. 1) provide discharge observations for the five flood events during the period of 1995–98. Little Sugar Creek is one of the three main tributaries to Sugar Creek. It is bounded on the west by Irwin-Sugar Creek and on the east by McAlpine Creek (Fig. 1). The Sugar Creek catchment, downstream of the confluence of Little Sugar Creek, McAlpine Creek, and Irwin-Sugar Creek, has a drainage area of 550 km<sup>2</sup>.

The LULC map for Mecklenburg County (Fig. 1) was developed from imagery taken during the mid-1990s. The Sugar Creek region is characterized by an inner core of urban and dense residential land use and an outer region of lower density residential land use and forest cover (Fig. 1). The downtown core of Charlotte is located principally in the Little Sugar Creek basin, and the most intense urbanization has occurred in the northwestern portion of the basin.

Table 1 provides a summary of flood response properties and temporal trends in flood response for five drainage basins in the Charlotte metropolitan area with long stream gauging records (1962–95). Each of the five basins has a drainage area of less than 111 km<sup>2</sup>. Two of the basins (Little Sugar Creek and Irwin Creek) have experienced significant urbanization. Four of the basins (Little Sugar Creek, Irwin Creek, McMullen Creek, and McAlpine Creek) experienced suburbanization during the period of 1962–96. Long Creek has experienced only

minor suburban development and serves as a control catchment.

Leopold (1968) notes that hydrologic response to urbanization is typically characterized by increasing flood peak magnitudes, decreasing lag time, and increasing runoff volumes. These elements of hydrologic response are interpreted as a direct consequence of decreasing saturated conductivity and overland flow roughness. Graf (1977) shows that timing and magnitude of flood peaks in a suburbanizing region can be very sensitive to elaboration of the drainage network, which increases the drainage density of the basin and the hydraulic efficiency of the drainage system (see also Anderson 1970; Hollis 1988).

Marked increases in flood peak magnitudes have occurred for all areas experiencing urbanization and suburbanization (Table 1). Flood magnitude is represented in Table 1 by the median annual flood peak, expressed as a unit discharge (i.e., discharge divided by drainage area). The time trend in flood peaks, which was computed by linear regression of annual flood peak magnitude versus record year, is expressed as a percent of the median annual flood peak. The largest percent increase in flood peaks is for McMullen Creek. The 3.4% increase per year in flood peaks for McMullen Creek translates to a doubling of the median annual flood in approximately 30 years. Changes in flood peak magnitudes for Long Creek, the control catchment, are small relative to those for the other four catchments.

Basin response times are strongly tied to LULC properties (Table 1). Response time is represented by the median volume-to-peak (V/P) ratio, which is the ratio of the runoff volume associated with the annual flood peak ( $m^3$ ; computed from the USGS mean daily discharge observations 1 day prior to the day of the peak discharge to 2 days after the peak discharge) to the annual flood peak ( $m^3 s^{-1}$ ). Bradley and Potter (1992) discuss V/P ratios as a measure of basin response time. The median response time in Little Sugar Creek at 110- $km^2$  scale of 8.4 h is more than 5 h faster than the response time of Long Creek at 42.5  $km^2$ . The median response time of the suburbanizing McAlpine Creek at 102.5  $km^2$  is 0.5 h faster than that of Long Creek. Median flood peak magnitudes also strongly reflect LULC properties. The median (unit discharge) flood peak in McMullen Creek is 2 times the median (unit discharge) flood peak in Long Creek at drainage areas of 18.2 and 42.5  $km^2$ , respectively. The median unit discharge flood peaks of Irwin Creek and Little Sugar Creek at 70–110- $km^2$  scale are approximately 50% larger than that of McAlpine Creek.

Large increases in annual runoff volume have occurred in the Little Sugar Creek basin since the early 1960s (Fig. 3; runoff is expressed as a depth by dividing annual runoff volume by drainage area). The trend line [computed using the "lowess" locally weighted polynomial regression and scatterplot smoothing algorithm; see Venables and Ripley (1997)] for annual runoff vol-

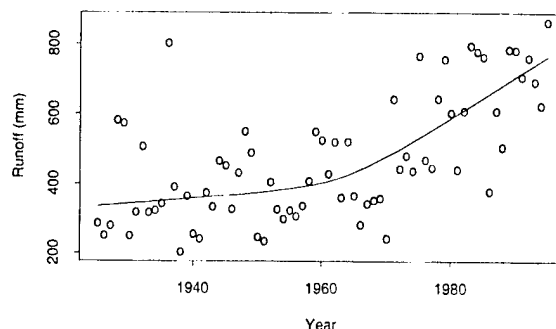


FIG. 3. Time series of annual runoff (mm) for Little Sugar Creek at Archdale (station 4 in Fig. 1) during the period of 1927–96. A lowess smoothing of the time series is provided.

ume increases from approximately 400 mm in 1962 to 800 mm in 1995, representing a doubling of the annual runoff during a 33-yr period. The annual runoff ratio (that is, the ratio of annual runoff to annual rainfall) increased from 0.35 to 0.70 during this period. The largest increases in runoff volume have occurred during the autumn season (September, October, November) with roughly a tripling of runoff volume (figure not shown).

It is generally difficult to relate time trends in hydrologic response to time trends in LULC (Potter 1991). For the Charlotte region, we can assess temporal changes in LULC for certain time periods. USGS 7.5-min (1:24 000) topographic maps provide insight to changing land cover in the region. The Charlotte East quadrangle was published in 1967 based on aerial photographs from 1965 and was photo-revised in 1984 based on imagery from 1984. Extensive revisions to the topographic map reflect residential development within the McMullen Creek basin to the point that we can conclude that McMullen Creek was near full development conditions by 1984. During the period of 1964–84, the McMullen Creek basin was transformed from mixed woodland/residential to dense residential. From 1984 to the present, changes in land cover within McMullen Creek have been small in comparison with the preceding 15-yr period. Changes in flood response of McMullen Creek (Table 1) are presumed to be closely linked to changes in land surface properties from 1964 to 1984. As Wolman (1967) notes, some of the changes to the fluvial system that accompany intense suburban development are episodic and have relatively rapid recovery times (1–10 yr). Other changes to the land surface, especially those that augment the drainage network, are permanent changes (Graf 1977). Persistence of elevated flood peaks into the late 1990s suggests that permanent, engineered changes to the drainage and channel system dominate McMullen Creek time trends.

The Derita quadrangle (north of Charlotte East), which was published in 1971 and was revised based on 1993 photogrammetry, provides information on time trends in Little Sugar Creek land use. Martens (1968) notes that in 1962 the most extensive impervious area

TABLE 2. Summary of basin characteristics for catchments of five stream-gauging stations in Little Sugar Creek (Fig. 1), where  $K_{sat}$  denotes the mean saturated hydraulic conductivity over the basin. The effective impervious cover for current conditions is the sum of the percent impervious and percent urban soils values (see text).

Basin	Drainage area (km <sup>2</sup> )	Percent impervious 1962	Percent impervious 1995	Percent urban soils	$K_{sat}$ (mm h <sup>-1</sup> )
Little Sugar at Medical Center (station 1, 02146409)	32	22	32	20	3.8
Brian Creek (station 2, 021465022)	49	9	25	5	5.0
Little Hope Creek (station 3, 02146470)	6.7	—	30	8	3.6
Little Sugar at Archdale (station 4, 02146507)	110	15	27	10	4.9
Little Sugar at NC 51 (station 5, 02146530)	128	—	26	9	5.5

within the Charlotte region was located in the central portion of the Little Sugar Creek basin in the downtown area. The most extensive changes to the Derita quadrangle reflect the extension of urban development into the uppermost portions of the Little Sugar Creek basin. Little Sugar Creek was gauged from 1962 to 1970 just downstream of the downtown region (at 39.9 km<sup>2</sup>), and annual peaks were reported in Martens (1968) and subsequent data reports. Annual flood peaks ranged from 1.03 to 2.34 m<sup>3</sup> s<sup>-1</sup> km<sup>-2</sup>, with a median value of 2.03 m<sup>3</sup> s<sup>-1</sup> km<sup>-2</sup>. The stream-gauging station for Little Sugar Creek at Medical Center (31.6 km<sup>2</sup>; Fig. 1) was installed in 1995. The annual peaks of 2.76 (April 1998), 3.21 (August 1995), and 4.76 m<sup>3</sup> s<sup>-1</sup> km<sup>-2</sup> (July 1997) all exceeded the maximum flood peak of 2.34 m<sup>3</sup> s<sup>-1</sup> km<sup>-2</sup> during the 1960s. These observations suggest significant changes in flood response from 1970 to the present within the most intensively urbanized catchment as of 1962 (Martens 1968).

Quantitative assessment of change in impervious cover for the Little Sugar Creek basin (Table 2) was based on planimetric data developed by Mecklenburg County from 1962 (reported in Martens 1968) and 1995. The algorithms used for computing the 1995 impervious area are designed to mimic those used by Martens (1968) for the 1962 analysis in which impervious area was computed manually from hard-copy planimetric maps. Impervious area is defined as any area covered by buildings, roads, and parking lots (paved areas other than roads). Impervious cover for Little Sugar Creek above Archdale increased from 15% in the early 1960s to 27% in the mid-1990s. Impervious cover for the Briar Creek catchment increased by almost a factor of 3, from 9% to 25%. Little Sugar Creek, above Medical Center, retained the highest impervious cover at 32%, but its increase was smaller than in other portions of the basin. The current impervious cover for Little Hope Creek, at 30%, is only 2% smaller than that for Little Sugar Creek above Medical Center. Contrasts in hydrologic response of these two basins play an important role in the flood response analyses of section 4.

The pattern of impervious cover (Fig. 4), in particular

the contrasts between residential and urban areas, can play a role in hydrologic response. Connectivity of impervious area with the drainage system is an important element of the pattern of impervious cover. A house surrounded by vegetated lawn may have a combined impervious cover of 30%, but the contribution of this impervious cover to downstream hydrologic response will depend on connectivity with stream channels, sewers, or streets. Although the impervious fraction of suburban watersheds has approached that of urban watersheds in Mecklenburg County, significant contrasts in annual water balance remain between urban and suburban watersheds. The mean annual runoff in Little Sugar Creek at Archdale (Fig. 3) during the period of 1995–98 was more than 20% larger than those in the suburbanizing watersheds of Irwin Creek and McAlpine Creek. The mean unit discharge of Little Sugar Creek at Medical Center during the period of 1995–98 of  $1.73 \times 10^{-2}$  m<sup>3</sup> s<sup>-1</sup> km<sup>-2</sup> was 21% larger than the  $1.44 \times 10^{-2}$  m<sup>3</sup> s<sup>-1</sup> km<sup>-2</sup> value for Little Hope Creek (compare with water balance analyses of large floods in section 4).

Soil hydraulic information for Little Sugar Creek (Table 2), based on U.S. Department of Agriculture soil surveys, augments the regional picture of impervious cover and associated infiltration potential. The “urban soils” classification (Table 2) includes compacted soils that behave hydraulically as impervious in short-duration heavy rain. The effective impervious cover of a catchment is the fraction of impervious cover shown in the fourth column of Table 2 plus the fraction of urban soils (fifth column). The area above the Medical Center gauging station has the largest effective impervious cover of 52%. For Little Hope Creek, the effective impervious fraction is 38%.

Saturated hydraulic conductivity was estimated from soil texture classification using the Rawls and Brakensiek relationships (Rawls et al. 1993) along with masks for the zero conductivity regions that are either impervious or urban soils. Mean saturated hydraulic conductivity for Archdale is 4.9 mm h<sup>-1</sup>. The mean (areally averaged) saturated hydraulic conductivity for

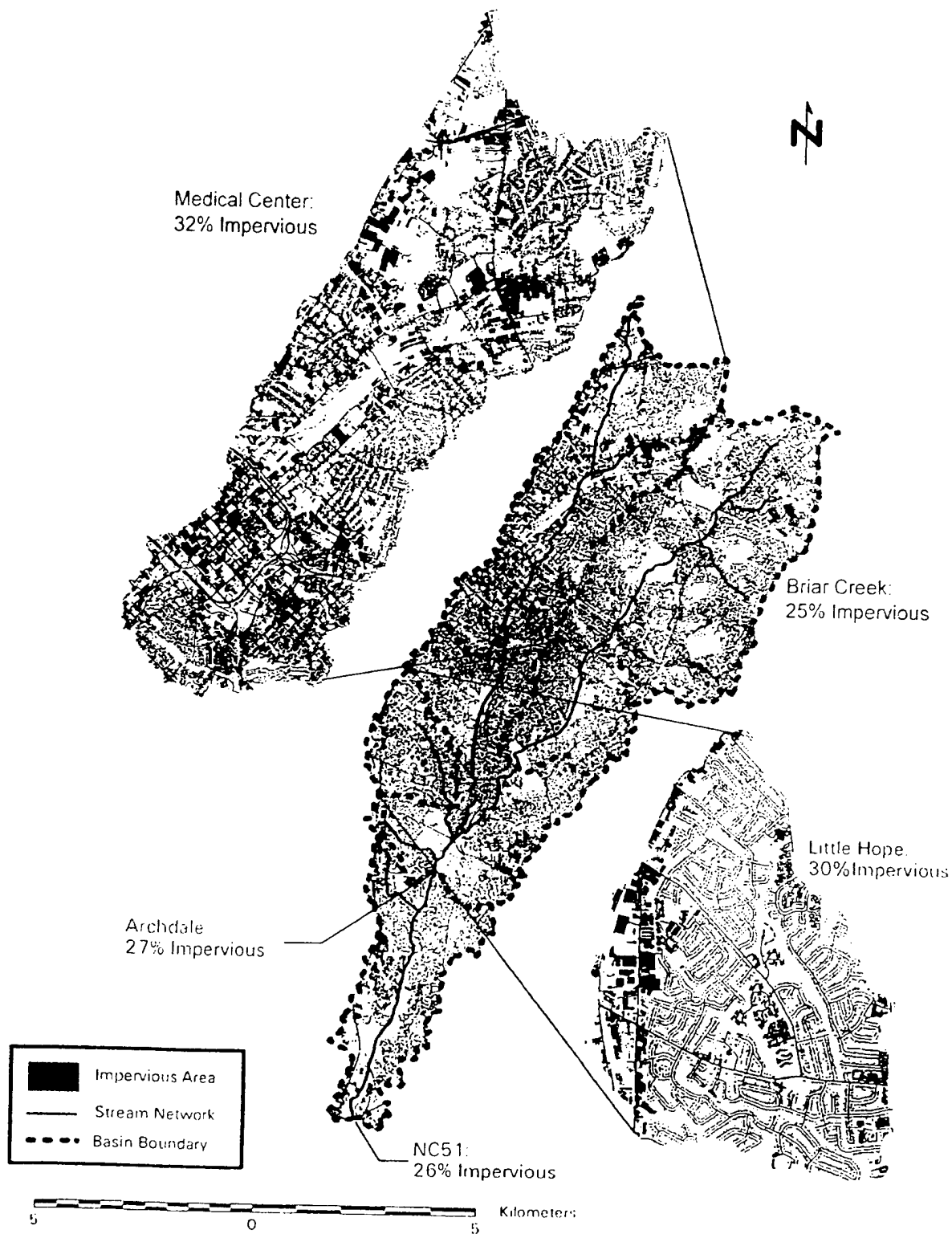


FIG. 4. Impervious area field for Little Sugar Creek with basin boundaries corresponding to the areas upstream of the five stream-gauging stations shown in Fig. 1. In the upper left-hand corner a blowup of Little Sugar Creek at Medical Center (station 1 in Fig. 1) is presented. A blowup of Little Hope Creek (station 3 in Fig. 1) is given in the lower right-hand corner. Black areas represent impervious cover; white areas represent regions with vegetation or soil cover.

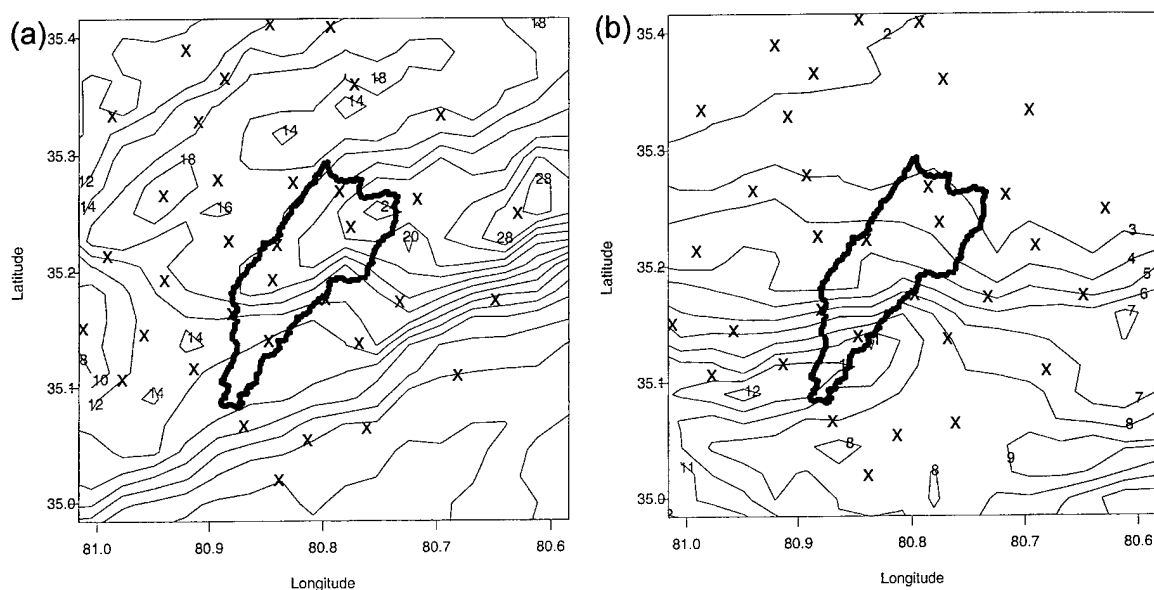


FIG. 5. Storm total rainfall fields (cm) for (a) the 23 Jul 1997 and (b) 27 Jul 1998 storms. Rain gauge locations are denoted by "X". The basin boundary of Little Sugar Creek is shown as a solid black line (see Fig. 1).

the basin above Medical Center at  $3.8 \text{ mm h}^{-1}$  is slightly larger than that of Little Hope at  $3.6 \text{ mm h}^{-1}$ . The mean saturated hydraulic conductivity for the 48% of the Medical Center area that is not effectively impervious is approximately  $8 \text{ mm h}^{-1}$ . These values will be compared in the following sections with the magnitudes of rainfall rates from the five 1995–98 storms.

### 3. Hydrometeorology of the five storms

The five flood events in Little Sugar Creek were produced by a diverse collection of storms. In this section we briefly describe each storm and present analyses of the spatial and temporal distribution of rainfall for each event. These analyses are linked in section 4 to flood response properties of Little Sugar Creek.

Tropical Storm Jerry produced record flooding over a broad area of the southeastern United States during 26–28 August 1995. Rainfall accumulations during a 12-h period on 27 August 1995 exceeded 200 mm in the Little Sugar Creek basin, with heaviest rainfall concentrated during two intense rain periods separated by 8 h. On 23 July 1997, heavy rainfall developed along an east–west-oriented frontal boundary, producing record rainfall in Charlotte, as storms repeatedly tracked over the region during a 12-h period [see Chappell (1988) and Doswell et al. (1996) for discussion of quasi-stationary convective systems and flash flooding]. Less than 24 h after the heavy rainfall on 23 July 1997 produced record flooding in Charlotte, Hurricane Danny grazed the region. Charlotte was spared even more catastrophic flooding because the heaviest rainfall from Danny passed to the south and east. The 9 April 1998 squall line passed through South Carolina and southern

North Carolina, producing a 2-h period of heavy rainfall in Charlotte. The 27 July 1998 storm was a convective system with low echo centroid structure in radar reflectivity observations and shallow, warm cloud tops in satellite infrared observations. These storms are small but can produce extreme rainfall rates (Maddox et al. 1978; Smith et al. 1996; Peterson et al. 1999) over periods of several hours.

Rainfall analyses for the five storms are based on both rain gauge and WSR-88D reflectivity observations, with the exception of the August 1995 event for which WSR-88D volume scan reflectivity observations are not available. The USGS rain gauge network in Mecklenburg County (Hazell and Bales 1997; and Robinson et al. 1998) consists of 46 tipping-bucket rain gauges, 9 of which are in or adjacent to the Little Sugar Creek basin. Radar rainfall estimates were computed using methods described in Baeck and Smith (1998). Key elements of the procedure are rainfall rate–reflectivity ( $Z$ – $R$ ) conversion using the standard WSR-88D  $Z$ – $R$  relationship ( $Z = 300R^{1.4}$ ; with a 55-dBZ threshold on reflectivity observations) and a multiplicative bias correction using rain gauge storm totals from all of the rain gauges in the USGS network (and radar-based storm totals for the 1-km bins containing rain gauges). Radar-based rainfall estimates captured variability of rainfall at sufficiently fine timescales (5–15 min) and space scales (1 km; Fig. 5) to analyze response times and event water balance for gauged subbasins of Little Sugar Creek (Fig. 1).

Rainfall summaries for the five flood events (Tables 3 and 4 and Figs. 5a,b) present a contrasting picture of the series of extreme flood events during the late 1990s. The rain gauge analyses in Tables 3 and 4 are based on



TABLE 3. Rainfall summaries based on rain gauges in the Little Sugar Creek basin for five flood events. The maxima of the second to fifth columns are taken over the nine rain gauges covering the basin.

Event	Storm total max (mm)	Max 5 min (mm h <sup>-1</sup> )	Max 15 min (mm h <sup>-1</sup> )	Max 60 min (mm h <sup>-1</sup> )
Aug 1995	218	122	101	70
23 Jul 1997	230	161	144	78
24 Jul 1997	64	70	50	22
Apr 1998	64	76	50	35
Jul 1998	102	80	64	51

observations from the nine rain gauges in or adjacent to the Little Sugar Creek basin (no corrections were made for potential undercatch by the tipping-bucket rain gauges). The first two flood events, 27 August 1995 and 23 July 1997, were the product of excessive rainfall. In contrast, the 1998 flood events and flooding from Hurricane Danny (24 July 1997) were the product of modest rainfall accumulations, by historical standards, in Charlotte.

The 27 August 1995 and 23 July 1997 storms produced peak rain gauge accumulations in the Little Sugar Creek basin that exceeded 200 mm in 12 h. Peak rain gauge accumulations were 100 mm or less for the other three events. Basin-averaged rainfall for the 27 August 1995 and 23 July 1997 storms were 169 and 181 mm; basin-averaged rainfall for the other three events ranged from 50 to 60 mm (Table 4). The peak rainfall accumulation for the 23 July 1997 event of 280 mm, which was located approximately 10 km northeast of the Little Sugar Creek basin (Fig. 5a), nearly doubled the previous maximum daily rainfall accumulation from the Charlotte rain gauge. The median value of maximum annual daily rainfall from the Charlotte rain gauge during the 100-yr period from 1895 to 1994 is 65 mm.

The 27 August 1995 and 23 July 1997 storms produced markedly higher rainfall rates than did the other three events. Peak rainfall rates at a 5-min timescale were greater than 120 mm h<sup>-1</sup> for both events. The 161 mm h<sup>-1</sup> 5-min peak rainfall rate for the 23 July 1997 storm is 64% of the 100-yr, 5-min rainfall rate for Charlotte (Frederick et al. 1977) and is 111% of the 2-yr, 5-min rainfall rate. The 78 mm h<sup>-1</sup> 60-min peak rainfall rate is 86% of the 100-yr, 60-min rainfall rate for Charlotte and is 181% of the 2-yr, 60-min rainfall rate (Frederick et al. 1977). For the 27 August 1995, 23 July 1997, and 27 July 1998 storms, more than 50% of storm total rainfall was delivered at 5-min rainfall rates exceeding 25 mm h<sup>-1</sup> and more than 25% of storm total rainfall was delivered at rainfall rates exceeding 50 mm h<sup>-1</sup>. For the 23 July 1997 storm, 78 mm of rainfall were delivered at rainfall rates exceeding 50 mm h<sup>-1</sup> and 20 mm of rainfall were delivered at rainfall rates exceeding 100 mm h<sup>-1</sup> (Table 4).

To characterize the temporal variability of rainfall over the Little Sugar Creek drainage basin, we utilize 5-min, 1-km radar rainfall fields to compute the follow-

TABLE 4. Basin-averaged rainfall and fraction of storm total rainfall at rainfall rates exceeding 5, 25, 50, and 100 mm h<sup>-1</sup>, based on rain gauge observations (as in Table 3).

Event	Total (mm)	% > 5 (mm h <sup>-1</sup> )	% > 25 (mm h <sup>-1</sup> )	% > 50 (mm h <sup>-1</sup> )	% > 100 (mm h <sup>-1</sup> )
Aug 1995	169	92	54	28	5
23 Jul 1997	181	97	73	43	11
24 Jul 1997	50	79	15	6	0
Apr 1998	57	94	38	5	0
Jul 1998	59	96	60	25	0

ing quantities: 1) the mean rainfall rate over the catchment at time  $t$  during the storm,  $M(t)$ ; 2) the fractional coverage of the basin by rainfall rates exceeding 25 mm h<sup>-1</sup> at  $t$ ,  $Z(t)$ ; and 3) the normalized distance of rainfall from the basin outlet at  $t$ ,  $D(t)$ . The mean rainfall rate and fractional coverage time series provide basic information on rainfall mass balance and distribution of rainfall rates over the catchment. They do not provide information on the spatial distribution of rainfall relative to the basin network structure, however. The drainage network, as represented by the distance function  $d(x)$ , provides a natural metric for analyzing the spatial distribution of rainfall. The value of  $d(x)$  for each point  $x$  within the drainage basin is computed as the sum of the overland flow distance from  $x$  to the nearest channel and the distance along the channel to the basin outlet [using the algorithms of Tarboton (1997); see additional discussion in section 4].

The normalized distance time series  $D(t)$  is a function of the rainfall field  $R(t, x)$  and the distance function  $d(x)$ . It is defined as the ratio of the rainfall-weighted centroid distance to the basin outlet  $D_1(t)$  and the maximum distance from the basin outlet  $d_{\max}$ . The distance time series  $D_1(t)$  can be represented as

$$D_1(t) = |A|^{-1} \int_A w(t, y) d(y) dy, \quad (1)$$

where  $A$  is the spatial domain of the drainage basin and the weight function  $w(t, y)$  is given by

$$w(t, y) = \frac{R(t, y)}{|A|^{-1} \int_A R(t, u) du}. \quad (2)$$

The random variable  $D_1(t)$  takes values from 0 to the maximum distance from the basin outlet  $d_{\max}$ . Values of  $D(t)$  range from 0 to 1, with values close to 0 indicating that rainfall is distributed near the basin outlet; values of  $D(t)$  close to 1 reflect a rainfall distribution concentrated at the far periphery of the drainage basin. If rainfall is uniformly distributed over the catchment, then the weights do not vary spatially, and we obtain the mean distance

$$d_{\text{mean}} = |A|^{-1} \int_A d(y) dy. \quad (3)$$

For the Little Sugar Creek basin, spatially uniform rainfall produces a value of  $D(t)$  equal to 0.62.

The 23 July 1997 storm included two main pulses of heavy rainfall (Fig. 6a), at 0500–0900 and 1200–1400 UTC. The first period was characterized by a series of small storm elements passing over the basin, resulting in large temporal and spatial variability of rainfall. The second period was characterized by growth of the rain area within the Little Sugar Creek catchment. At 1320 UTC, the basin rain area exceeding 25 mm  $\text{h}^{-1}$  (Fig. 6a) reached its maximum value of 80% of the total basin area. During both periods, the rainfall distribution, as represented by the normalized distance  $D(t)$ , moved from the lower to the upper basin during a 2-h time period (0430–0630 and 1200–1400 UTC). This pattern and timescale of motion was important for flood response in Little Sugar Creek (as discussed further in section 4).

The temporal structure of rainfall distribution in Little Sugar Creek for the 9 April 1998 event (Fig. 6b) reflects the squall line organization of the storm (Houze 1993). The storm moved rapidly through the region and was large in linear extent relative to the dimensions of the drainage basin. The sharp spike in fractional coverage of heavy rainfall  $Z(t)$  reflects passage of the main line of convection. Throughout the rainfall period, the storm exhibited relatively uniform spatial rainfall distribution throughout the basin [i.e.,  $D(t)$  is close to the spatially uniform value of 0.62 for Little Sugar Creek].

The spatial distribution of storm total rainfall for the 27 July 1998 event (Fig. 5b) was characterized by very large accumulations in the lower basin (120 mm) and relatively small accumulations in the upper basin (40 mm). During the 2-h period of the storm, this rainfall distribution resulted from an initial period of rainfall concentrated in the lower basin and a later period of expanding rain area, with large contributions in the upper portions of the basin. At 1220 UTC, the rain area exceeding 25 mm  $\text{h}^{-1}$  had grown to cover 80% of the basin, and the rainfall distribution was nearly uniform over the basin [i.e.,  $D(t)$  is close to 0.62].

The time series  $M(t)$ ,  $Z(t)$ , and  $D(t)$  for the 23 July 1997 storm (figures not shown) were computed for the Little Sugar Creek basin above Medical Center (31.2  $\text{km}^2$ ) and for the Sugar Creek basin (550  $\text{km}^2$ ). The principal differences in rainfall distribution with changing basin scale are tied to fractional coverage of rainfall. In decreasing the basin size from 110 to 31  $\text{km}^2$ , we reach a scale at which flood response is dominated by periods in which the entire basin receives heavy rainfall. In converse, the increase of basin size from 110 to 550  $\text{km}^2$  reflects the transition from a scale at which peak periods of the storm produce fractional coverage values of heavy rainfall close to 100% to a scale at which no more than 50% of the basin receives heavy rainfall. These results have particular relevance to analyses of scaling behavior of annual flood peaks (Smith 1992; Gupta et al. 1994; Robinson and Sivapalan 1997; Woods

and Sivapalan 1999). In Smith (1992), it is proposed that the 100- $\text{km}^2$  scale at which the peak in CV of annual flood peaks occurs for the central Appalachian region is linked to spatial organization of flood-producing rainfall. For the series of heavy rainfall events in Charlotte, the aspect of spatial organization of rainfall that varies most strikingly around a scale of 100  $\text{km}^2$  is fractional coverage of heavy rainfall.

#### 4. Hydrologic response for extreme floods

Hydrologic response for extreme floods in Charlotte is examined in this section through analyses of the five flood events described in previous sections. Particular attention is given to analyses for the Little Sugar Creek basin at Medical Center, which reflects the most intense urban development within the catchment (Figs. 1, 4), and the Little Hope Creek basin, which is suburban and is dominated by residential development (Figs. 1, 4).

Hydrograph plots (Fig. 7) for the five flood events in the Little Sugar Creek basin illustrate systematic spatial heterogeneities in flood response, independent of the details of the rainfall distribution. Of most importance, flood peaks for Little Sugar Creek at Archdale (station 4 in Fig. 1) are largely determined by contributions from the urbanized western portion of the drainage basin (as represented by station 1 in Fig. 1, Little Sugar Creek above Medical Center, and the region immediately downstream). Briar Creek (station 2 in Fig. 1) peaks well after the downstream gauge at Archdale and contributes mainly to the recession at Archdale (see especially Figs. 7a,c,e). Flood peaks decrease (Figs. 7c,d) from Archdale at 110  $\text{km}^2$  to the most downstream gauge at North Carolina Route 51 (NC 51; 128  $\text{km}^2$ ).

Flood summaries for Little Hope Creek (Table 5) and Little Sugar Creek at Medical Center (Table 6) were carried out for seven flood periods: the two peaks from 27 August 1995 (as illustrated in Fig. 8), the two peaks from 23 July 1997 (as illustrated in Fig. 9), and the 24 July 1997, 9 April 1998, and 27 July 1998 events. For each period, the water balance is summarized by basin-averaged rainfall (mm) and runoff (mm). Flood magnitude is represented by the peak discharge, expressed as a unit discharge ( $\text{m}^3 \text{s}^{-1} \text{km}^{-2}$ ). Flood response time is represented by the lag-to-peak value, which was computed as the time difference between the peak discharge and the time centroid of basin-averaged rainfall. As detailed below, these analyses suggest that expansion of the drainage network, and the associated enhancement of hydraulic efficiency of the drainage system, is the dominant control of increasing flood peaks in Little Sugar Creek.

There are large differences in the timing of flood response between urban and suburban catchments. The median lag time of 1.0 h for Little Sugar Creek at Medical Center at 31.6  $\text{km}^2$  is smaller than the 1.1 h for Little Hope Creek at 6.7  $\text{km}^2$ . Lag time was computed for a subset of flood events in Little Sugar Creek at

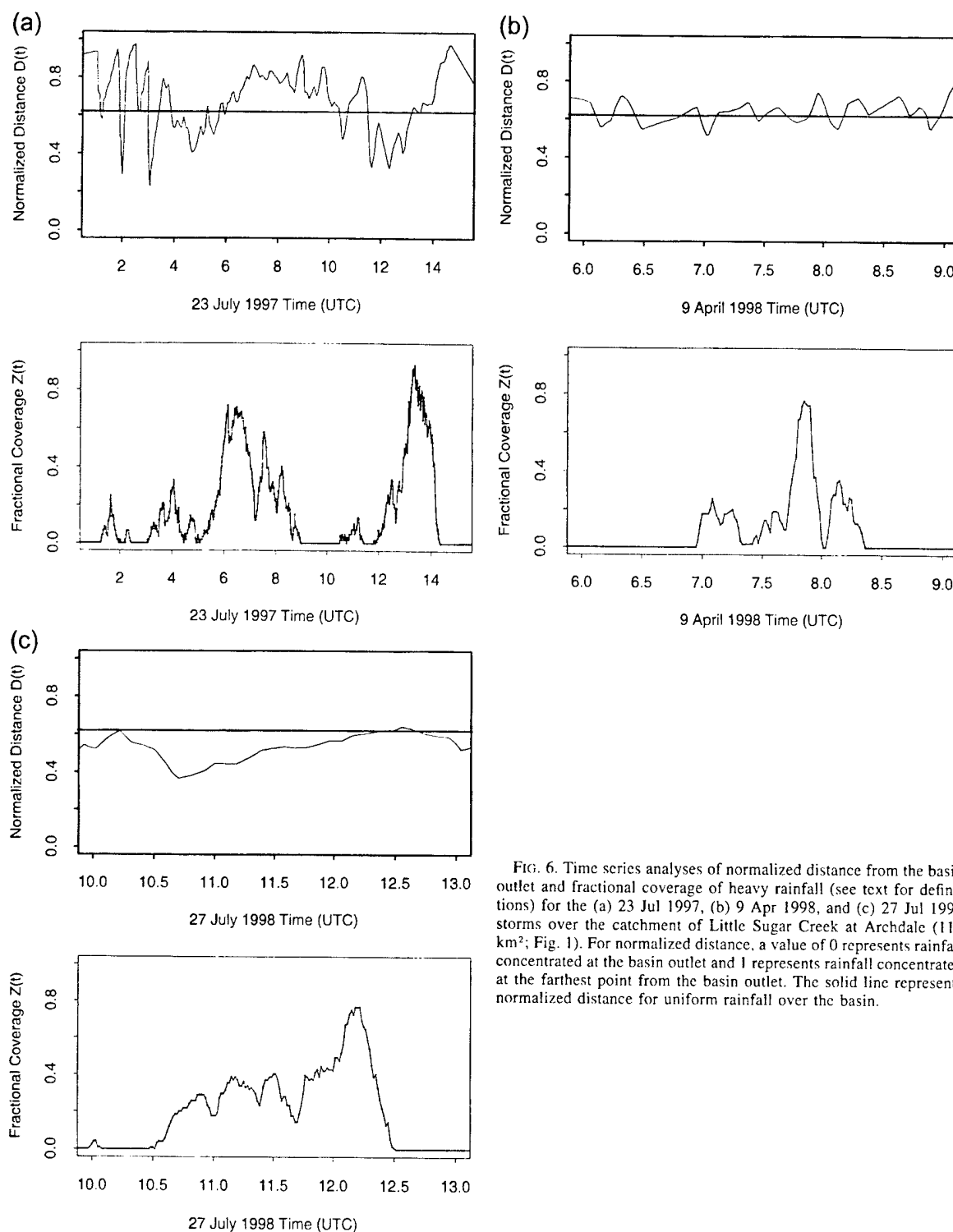


FIG. 6. Time series analyses of normalized distance from the basin outlet and fractional coverage of heavy rainfall (see text for definitions) for the (a) 23 Jul 1997, (b) 9 Apr 1998, and (c) 27 Jul 1998 storms over the catchment of Little Sugar Creek at Archdale (110 km<sup>2</sup>; Fig. 1). For normalized distance, a value of 0 represents rainfall concentrated at the basin outlet and 1 represents rainfall concentrated at the farthest point from the basin outlet. The solid line represents normalized distance for uniform rainfall over the basin.

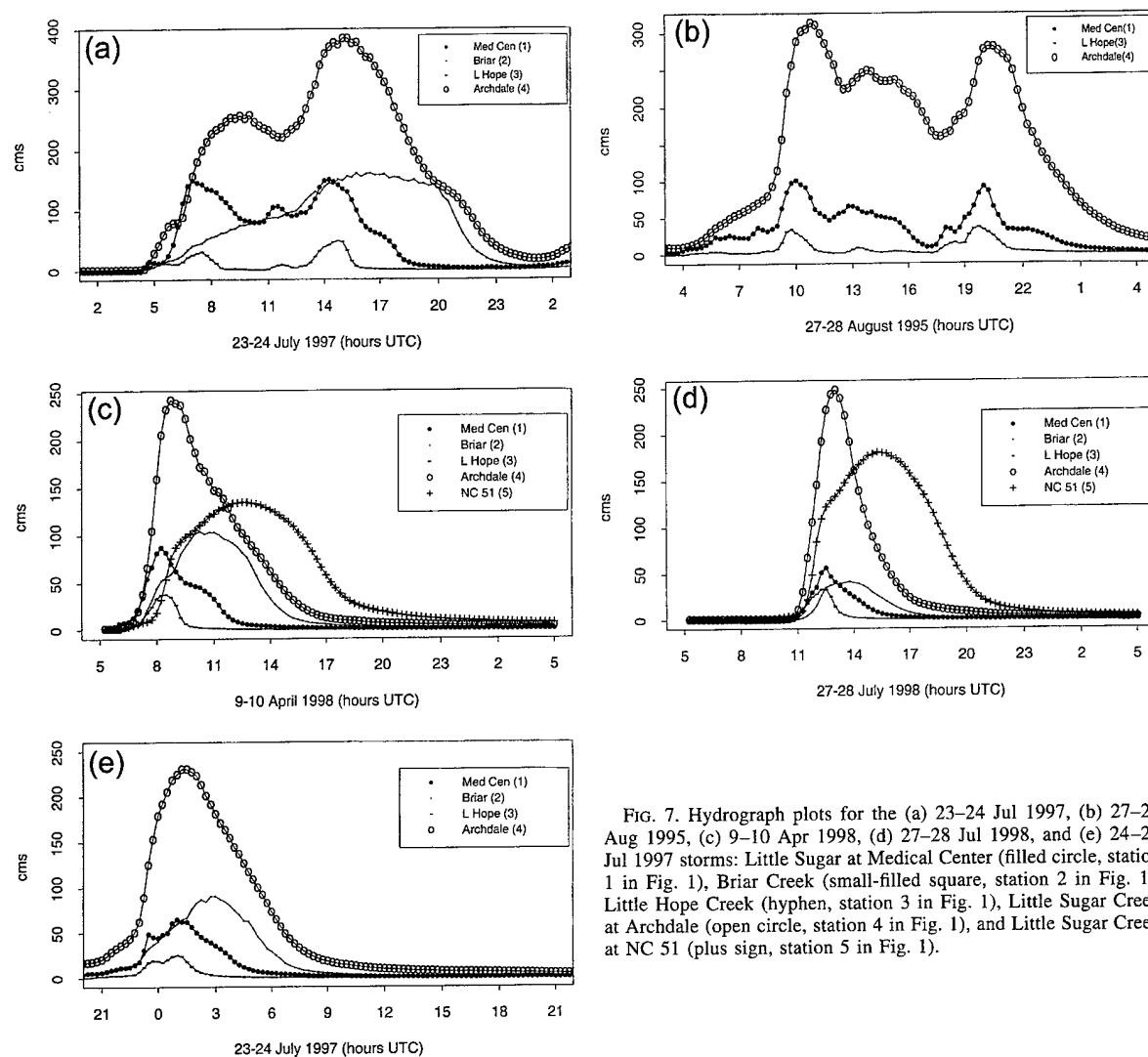


FIG. 7. Hydrograph plots for the (a) 23–24 Jul 1997, (b) 27–28 Aug 1995, (c) 9–10 Apr 1998, (d) 27–28 Jul 1998, and (e) 24–25 Jul 1997 storms: Little Sugar at Medical Center (filled circle, station 1 in Fig. 1), Briar Creek (small-filled square, station 2 in Fig. 1), Little Hope Creek (hyphen, station 3 in Fig. 1), Little Sugar Creek at Archdale (open circle, station 4 in Fig. 1), and Little Sugar Creek at NC 51 (plus sign, station 5 in Fig. 1).

TABLE 5. Flood summaries for Little Sugar Creek at Medical Center for the five storms (note that the 23 Jul 1997 and 27 Aug 1995 events are each broken into two periods; see Figs. 9 and 10). “Runoff ratio” is the ratio of runoff (“runoff” column) to storm total rainfall (“rain” column). “Lag time,” or lag-to-peak time, is the difference between the time of peak discharge and the time centroid of basin-averaged rainfall.

Little Sugar at Medical Center (event)	Rain (mm)	Runoff (mm)	Runoff ratio	Peak ( $\text{m}^3 \text{s}^{-1} \text{km}^{-2}$ )	Lag time (h)
27 Aug 1995 (1)	120	66	0.55	3.2	1.0
27 Aug 1995 (2)	50	36	0.72	2.9	1.7
23 Jul 1997 (1)	134	86	0.64	4.8	2.2
23 Jul 1997 (2)	60	60	1.00	4.8	0.9
24 Jul 1997	41	33	0.81	2.0	1.2
9 Apr 1998	58	33	0.58	2.8	0.8
27 Jul 1998	39	16	0.40	1.8	0.7

Archdale, McAlpine Creek at Sardis, McMullen Creek, Irwin Creek, and Long Creek (compare with results in Table 1), yielding values of 2.8, 6.2, 2.0, 3.1, and 6.8 h, respectively.

Additional support for the conclusion that expansion

TABLE 6. Flood summaries for Little Hope Creek for the seven storm periods (as described in Table 5).

Little Hope Creek (event)	Rain (mm)	Runoff (mm)	Runoff ratio	Peak ( $\text{m}^3 \text{s}^{-1} \text{km}^{-2}$ )	Lag time (h)
27 Aug 1995 (1)	100	45	0.45	5.0	1.1
27 Aug 1995 (2)	60	45	0.75	5.4	1.4
23 Jul 1997 (1)	97	35	0.36	4.6	3.3
23 Jul 1997 (2)	70	55	0.80	7.2	1.1
24 Jul 1997	55	39	0.70	3.7	1.2
9 Apr 1998	61	41	0.68	5.7	0.9
27 Jul 1998	55	30	0.56	4.9	1.0

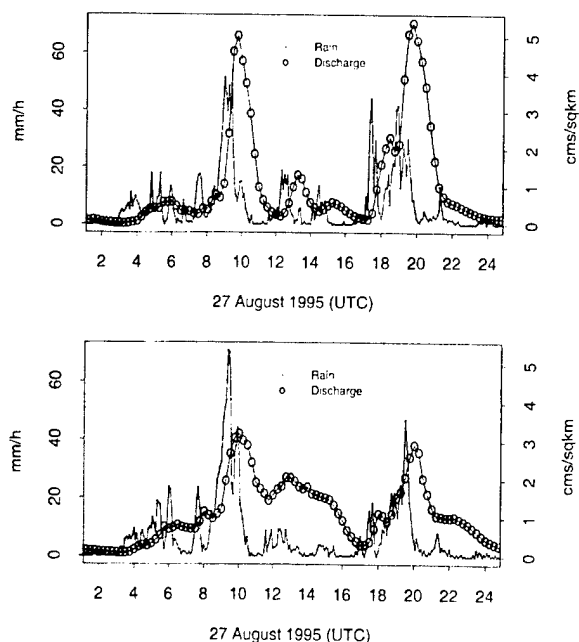


FIG. 8. Time series of basin-averaged rainfall and discharge in (top) Little Hope Creek and (bottom) Little Sugar Creek at Medical Center for the 27 Aug 1995 event.

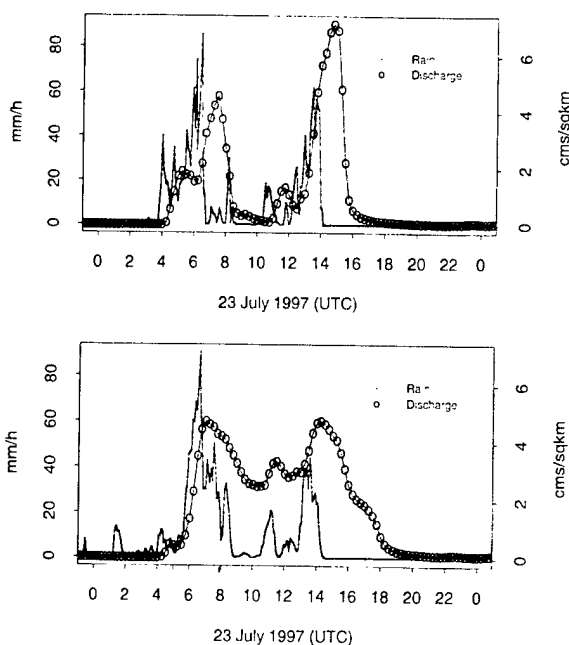


FIG. 9. Time series of basin-averaged rainfall and discharge in (top) Little Hope Creek and (bottom) Little Sugar Creek at Medical Center for the 23 Jul 1997 event.

of the drainage network (and the resulting decrease in response time) is a dominant control of increasing flood magnitudes in Little Sugar Creek is provided by two representations of the drainage network (Fig. 10). One representation (right-hand side) is derived from a high-resolution (10 m) DEM using an area-threshold algorithm. The second representation (left-hand side) includes the sewer network in addition to the natural drainage network. The cumulative drainage density for both networks is comparable (the contribution of the natural drainage network is smaller for the second representation). The role of drainage network structure (Fig. 10) for hydrologic response can be summarized through the width function (Fig. 11), that is, the number of channel links at a specified distance from the basin outlet (Rodríguez-Iturbe and Rinaldo 1997). The width function is proportional to the geomorphological instantaneous unit hydrograph (GIUH) of the basin [see Rodríguez-Iturbe and Rinaldo (1997) for assumptions linking the width function and GIUH]. The effect of urban development in Little Sugar Creek has been principally to amplify the width function in the lower section of the basin (Fig. 11). A direct consequence has been a decrease in the response time and an increase in flood magnitudes for the Little Sugar Creek basin at Medical Center and downstream.

There is little difference in the water balance of flood events between the Little Hope Creek basin and the Little Sugar basin above Medical Center. For Little Sugar Creek at Medical Center, the cumulative runoff ratio for the seven events is 0.66 (502 mm rainfall to 330

mm runoff). For Little Hope Creek the runoff ratio is 0.59 (496 mm rainfall to 291 mm of runoff) for the seven events. The difference in runoff ratio is due to the first pulse of rainfall from the largest event, the 23 July 1997 flood (Fig. 8). The 134 mm of rain in Little Sugar Creek above Medical Center for the first pulse of the 23 July 1997 storm resulted in 86 mm of runoff; in Little Hope Creek 35 mm of runoff resulted from 97 mm of rainfall. If the 23 July 1997 event is removed from the computation, the runoff ratio is 0.61 for Little Hope and 0.60 for Little Sugar Creek at Medical Center. As noted in section 2, cumulative runoff during 1995–99 was 20% larger in the Little Sugar Creek basin above Medical Center than in the Little Hope Creek basin.

The water balance results are consistent with the soil hydraulic properties (Table 2) and rainfall rate analyses (Table 3) presented in sections 2 and 3. The differences in extreme flood response between an impervious region and a pervious region with saturated hydraulic conductivity values of less than  $10 \text{ mm h}^{-1}$  (Table 2) are small for rain rates experienced during the series of extreme storms in Charlotte (Table 3). Extreme flood response in Little Sugar Creek, for both impervious and pervious regions, is dominated by infiltration excess mechanisms. Runoff ratios close to 1, especially for periods during which large portions of the basin are receiving heavy rainfall (see analyses in Fig. 6), are at odds with previous analyses of the maximum extent of saturated portions of a drainage basin (Dunne 1978). The decreasing runoff ratios between the second and third 23–24 July 1997 events are consistent with rainfall rate-controlled infil-

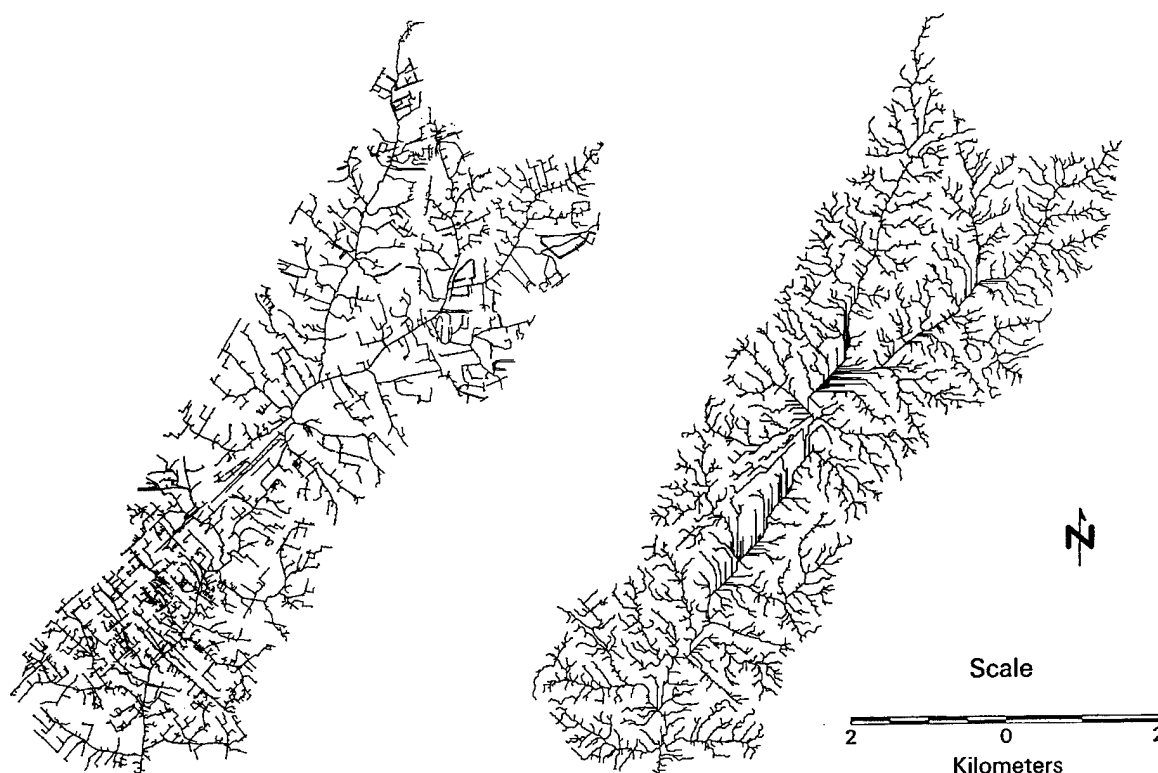
## Little Sugar Creek above Medical Center

### Stormwater Drainage System

from City of Charlotte, Storm Water Services

### Equivalent Natural Network

derived from constant area threshold with similar drainage density



Drainage Densities = 0.010 m<sup>-1</sup>

FIG. 10. The drainage network of Little Sugar Creek above Medical Center (left) including the sewer system and (right) derived from a 10-m DEM (with the same drainage density as on the left).

tration excess runoff production but are at odds with expanding saturated area control of runoff.

Antecedent soil moisture plays an important role in the flood response of Little Sugar Creek, even for extreme events in the most urbanized portion of the watershed, as illustrated by flood response for the three storm periods from 0400 UTC 23 July until 1200 UTC 24 July 1997. For Little Hope Creek, the runoff ratio increased from 36% (97 mm rain to 35 mm runoff) for the first event to 80% for the second event (70 mm rainfall to 55 mm runoff) and back to 70% for the third event (55 mm rainfall to 39 mm runoff). For Little Sugar Creek at Medical Center, the runoff ratio increased from 64% (134 mm of rainfall to 86 mm of runoff) for the first event to 100% for the second event (60 mm of rainfall and runoff) and back to 81% for the third event (41 mm of rainfall and 33 mm of runoff). For the two August 1995 rain periods, the runoff ratios increased

from 55% and 45% for Little Sugar Creek at Medical Center and Little Hope Creek, respectively, during the first event to 72% and 75% for the second rain period. For Little Sugar Creek at Medical Center, 40 mm of rainfall produces 33 mm of runoff for the 24 July 1997 event (immediately following 160 mm of rainfall on 23 July) but only 16 mm of runoff for the July 1998 event.

Antecedent discharge (minimum discharge preceding flood rise), which was computed for the 27 August 1995, 23 July 1997, 9 April 1998, and 27 July 1998 events, provides a useful surrogate for antecedent soil moisture. For Little Sugar Creek at Medical Center, antecedent discharge ranged from  $3.0 \times 10^{-5} \text{ m}^3 \text{ s}^{-1} \text{ km}^{-2}$  for the 23 July 1997 event to  $6.8 \times 10^{-5} \text{ m}^3 \text{ s}^{-1} \text{ km}^{-2}$  for the April 1998 event. For Little Hope Creek, it ranged from  $1.4 \times 10^{-5} \text{ m}^3 \text{ s}^{-1} \text{ km}^{-2}$  for the 23 July 1997 event to  $5.6 \times 10^{-5} \text{ m}^3 \text{ s}^{-1} \text{ km}^{-2}$  for the April 1998 event. The consequences of high antecedent soil moisture preceded-

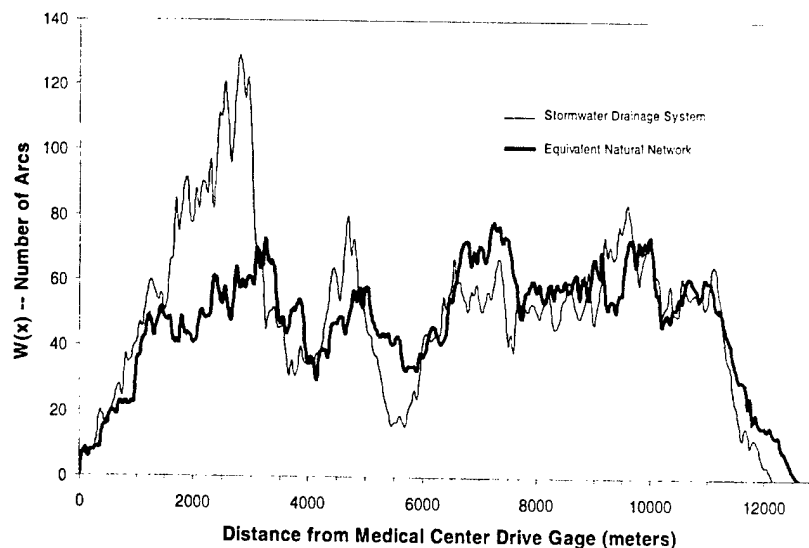


FIG. 11. The width function of the Little Sugar Creek drainage network (above Medical Center), derived from the complete stormwater drainage system (thin line; see Fig. 10) and the equivalent natural drainage network (thick line; see Fig. 10).

ing the 23 July 1997 event likely would have included catastrophic flooding in the major urban corridor of Charlotte. Runoff ratios close to 1 for the 0500–0800 UTC rainfall maximum in the upper portion of Little Sugar Creek would have produced an 0700 UTC flood peak at Medical Center of far greater magnitude than that shown in Fig. 9.

Flood response to the July 1998 and April 1998 storms (Fig. 7), combined with analyses of temporal variability of rainfall (Fig. 6), provides additional insight into the role of space-time rainfall distribution for the flood hydrology of Little Sugar Creek. The April and July 1998 floods had comparable peak discharges at Archdale (Fig. 7). The July 1998 flood was notable for its large peak discharge, relative to the storm total rainfall and runoff, especially in comparison with the April 1998 event. The volume-to-peak ratio at the Archdale gauge for the July 1998 event was 3.2 h; for the April 1998 event it was 5.0 h (c.f. the results in Table 1). The April 1998 event exhibited relatively uniform

rainfall distribution (Fig. 6b). For the 27 July 1998 event, heavy rainfall was initially concentrated in the lower portion of the basin, with a trend toward more uniform distribution at the peak intensity of the storm (Fig. 6c). Storm total rainfall over the Little Sugar Creek basin for the 27 July 1998 storm (Fig. 5b) ranged from 25 mm in the upper boundary of the basin to 120 mm at the lower boundary. Runoff ratio ranged from 20%–40% in the upper basin to 60%–80% in the lower basin (Table 7). The residual term in Table 7 includes water that infiltrates into the soil column, interception storage on vegetation, and retention storage on the land surface.

If hillslope and channel velocities were uniform over the basin, storm movement down the basin would result in maximum flood peaks at the basin outlet for a given storm total accumulation over the basin [see Ogden et al. (1995) and Smith et al. (2000) for detailed analyses]. For the Little Sugar Creek basin, however, the highest velocities are concentrated in the central and upper areas of the basin. The response time of the upper urbanized basin (at 30-km<sup>2</sup> scale) is approximately 1.5 h. Storm motion over a 2-h period from the lower basin to the upper basin, as occurred with the 27 July 1998 storm, would result in the upper basin contributing synchronously with the lower basin to the hydrograph at Archdale. The rainfall maximum in the lower basin (Fig. 5b) for the 27 July 1998 storm was the principal control of peak discharge for the event. As a consequence of storm motion and evolution, peak discharge at Archdale was augmented by rapidly responding portions of the middle and upper basin. Similar aspects of storm motion and evolution play an important role in flood response for the 23 July 1997 storm (see Fig. 6a and discussion in section 3).

TABLE 7. Basin-averaged rainfall, runoff, runoff ratio, and rainfall minus runoff for the five basins of Table 1 (and Fig. 1) during the 27 Jul 1998 storm. The final row is for the intervening area between the NC 51 gauge (station 5) and the Archdale gauge (station 4). Infiltration accounts for much of the difference between storm total rainfall and runoff ("Residual").

Station	Rain (mm)	Runoff (mm)	Ratio	Residual (mm)
1	39.2	15.7	0.40	23.5
2	44.7	12.0	0.27	32.7
3	54.4	30.2	0.56	24.2
4	49.8	26.2	0.44	23.6
5	58.9	34.5	0.59	24.4
5 – 4	117.7	88.1	0.75	29.6

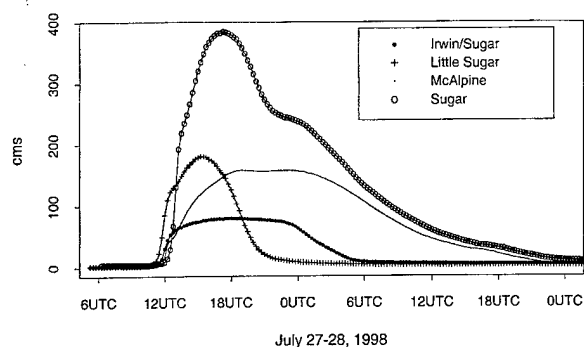


FIG. 12. Hydrographs for Irwin-Sugar Creek (169 km<sup>2</sup>), Little Sugar Creek (128 km<sup>2</sup>), McAlpine Creek (240 km<sup>2</sup>), and Sugar Creek (550 km<sup>2</sup>) during the 27 Jul 1998 flood event.

Flood-wave attenuation in the reach between Archdale and NC 51 (stations 4 and 5 in Fig. 1) is of comparable importance to urbanization effects in determining flood response properties at NC 51 [see Woltemade and Potter (1994) and Wolff and Burges (2000) for related analyses]. The July 1998 and April 1998 flood events provide clear illustration of the magnitude of attenuation in the reach between Archdale and NC 51 (Fig. 7). Flood-wave attenuation in this reach is associated with a geologically controlled drop in the longitudinal profile (Turner-Gillespie 2001) of the channel and expansion of the valley bottom. Flood-wave attenuation is also an important element of the delayed contribution of Briar Creek to Little Sugar Creek at Archdale (Fig. 7), noted at the beginning of this section (see Turner-Gillespie 2001). Geologically controlled variation in longitudinal profile and valley bottom width also play an important role in flood-wave attenuation in Briar Creek.

The regional flood response of Sugar Creek reflects the major changes in response times associated with urbanization and suburbanization (Fig. 7; Tables 5, 6), the influence of attenuating reaches (Fig. 7), and the scale-dependent space-time structure of rainfall forcing (Figs. 5, 6). Figure 12 shows time series for Sugar Creek (550 km<sup>2</sup>) and the contributions from Irwin-Sugar Creek (169 km<sup>2</sup>), Little Sugar Creek (128 km<sup>2</sup>), and McAlpine Creek (240 km<sup>2</sup>) for the July 1998 flood. Timing of the peak response at Sugar Creek reflects the rapid contributions from the urbanized portion of the basin. Attenuating reaches serve to mix the effects of upstream heterogeneities of flood response, resulting in a rapid decline in the influence of urbanization on flood response with increasing drainage area. Of fundamental importance for the flood response illustrated in Fig. 12, as with other extreme floods, is the spatial and temporal pattern of heavy rainfall (Figs. 5, 6).

## 5. Summary and conclusions

The seven principal observations from our work are the following.

- 1) There are large differences in the timing and magnitude of flood response among catchments of different land use and cover in the Charlotte metropolitan region. Differences in land use and cover do not, however, result in large differences in the water balance of flood response for the five extreme flood events. Expansion of the drainage network (Graf 1977) and the associated increase in hydraulic efficiency play a central role in controlling the increasing trend in flood magnitudes.
- 2) Increases in runoff associated with impervious area are important for the overall water balance of the watershed but are of secondary importance for extreme flood response in the Little Sugar Creek basin. Extreme flood response, both for pervious and impervious regions, is dominated by infiltration excess runoff mechanisms in which the magnitude of rainfall rate is much larger than saturated hydraulic conductivity values.
- 3) Antecedent soil moisture plays an important role in the flood response of Little Sugar Creek for extreme floods even in the most intensely urbanized portion of the basin. The most striking example is the 23 July 1997 flood peak, which resulted from rainfall accumulations that were approximately 2 times the previous daily record from the 100-yr Charlotte rain gauge record and which produced the largest flood peak in the 74-yr gauging record of Little Sugar Creek. It seems likely that the dry antecedent conditions preceding the 23 July 1997 event prevented catastrophic flooding in the major urban corridor of Charlotte.
- 4) Fractional basin coverage of heavy rainfall is a key element of scale-dependent flood response in the Sugar Creek basin. For small basins such as Little Sugar Creek at Medical Center (31.2 km<sup>2</sup>), flooding results from storms with fractional coverage of heavy rainfall approaching 100% of the basin for the characteristic response times of the basin (0–2 h). For large basins, such as Sugar Creek (550 km<sup>2</sup>), fractional coverage of the basin by heavy rainfall is small, and the heavy rainfall periods are short in comparison with basin response times (24–48 h). The drainage area of Little Sugar Creek at Archdale (110 km<sup>2</sup>) falls in the transition range between these two extremes. It also falls near the scale of maximum variability of central Appalachian flood peaks (Smith 1992). These results suggest that fractional coverage of heavy rainfall should be examined more closely as an explanation for anomalous scaling behavior of flood peaks.
- 5) Storm structure and motion play an important role in the event-to-event variability in flood response. For the 23 July 1997 and 27 July 1998 events, storm motion from the lower basin to the upper basin on a timescale of approximately 2 h served to amplify peak discharge at Archdale, relative to other modes of storm motion. The link between storm structure,



motion, and peak discharge is strongly dependent on the spatially varying response times described in observation 1 of this section.

- 6) Attenuating reaches play a major role in the regional flood hydrologic behavior of Sugar Creek. Attenuation results primarily from geologically controlled variations in longitudinal profile and valley bottom width (hydraulic modeling studies are being carried out to examine this issue in more detail). Flood-wave attenuation serves to diminish the effects of urbanization on downstream flood response.
- 7) The regional flood response of Sugar Creek reflects the major changes in response times associated with urbanization and suburbanization (observation 1), the scale-dependent space-time structure of rainfall forcing (observation 4), and the influence of attenuating reaches (observation 6).

**Acknowledgments.** This research was funded in part by the U.S. Army Research Office (Grant DAAD19-99-1-1063), NASA (Grant NAG5-7544), and the National Science Foundation (Grants EAR-9706259 and EAR99-09696). This support is gratefully acknowledged. Special thanks are given to William Hazell (USGS) for providing stream gauge and rain gauge data from the USGS network in Mecklenburg County and for helpful discussions. Justin Niedzialek undergraduate class of 1999, Princeton University, assisted with GIS analyses and provided useful discussions.

#### REFERENCES

- Anderson, D. G., 1970: Effects of urban development on floods in northern Virginia. U.S. Geological Survey Water Supply Paper 2001-C, 22 pp.
- Baeck, M. L., and J. A. Smith, 1998: Estimation of heavy rainfall by the WSR-88D. *Wea. Forecasting*, **13**, 416–436.
- Bradley, A. A., and K. W. Potter, 1992: Flood frequency analysis of simulated flows. *Water Resour. Res.*, **28**, 2375–2385.
- Chappell, C., 1988: Quasi-stationary convective events. *Mesoscale Meteorology and Forecasting*, P. S. Ray, Ed., Amer. Meteor. Soc., 289–310.
- Doswell, C. A., III, H. E. Brooks, and R. A. Maddox, 1996: Flash flood forecasting: An ingredients-based methodology. *Wea. Forecasting*, **11**, 560–581.
- Dunne, T., 1978: Experimental studies of hillslope flow processes. *Hillslope Hydrology*, R. Chorley and M. Kirkby, Eds., Academic Press, 227–293.
- Frederick, R. H., V. A. Myers, and E. P. Auciello, 1977: Five- to 60-minute precipitation frequency for the eastern and central United States. NOAA Tech. Memo. NWS Hydro-35, 35 pp.
- Graf, W. L., 1977: Network characteristics in suburbanizing streams. *Water Resour. Res.*, **13**, 459–463.
- Gupta, V. K., O. Mesa, and D. R. Dawdy, 1994: Multiscaling theory of flood peaks: Regional quantile analysis. *Water Resour. Res.*, **30**, 3405–3421.
- Hazell, W. F., and J. D. Bales, 1997: Real-time rainfall measurements in the city of Charlotte and Mecklenburg County, North Carolina. U.S. Geological Survey Fact Sheet FS-052-97, 4 pp.
- Hollis, G. E., 1988: Rain, roads, roofs and runoff: Hydrology in cities. *Geography*, **73**, 9–18.
- Houze, R. A., 1993: *Cloud Dynamics*. Academic Press, 570 pp.
- Leopold, L. B., 1968: Hydrology for urban land planning—A guidebook on the hydrologic effects of urban land use. U.S. Geological Survey Circular 554, 18 pp.
- Maddox, R. A., L. R. Hoxit, C. F. Chappell, and F. Caracena, 1978: Comparison of meteorological aspects of the Big Thompson and Rapid City flash floods. *Mon. Wea. Rev.*, **106**, 375–389.
- Martens, L. A., 1968: Flood inundation and effects of urbanization in metropolitan Charlotte North Carolina. U.S. Geological Survey Water Supply Paper 1591-C, 60 pp.
- Morrison, J. E., and J. A. Smith, 2001: Scaling properties of flood peaks. *Extremes*, **4** (1), 5–23.
- Ogden, F. L., J. R. Richardson, and P. Y. Julien, 1995: Similarity in catchment response, 2. Moving rainstorms. *Water Resour. Res.*, **31**, 1543–1547.
- Peterson, W. A., and Coauthors, 1999: Mesoscale and radar observations of the Fort Collins flash flood of 28 July 1997. *Bull. Amer. Meteor. Soc.*, **80**, 191–216.
- Potter, K. W., 1991: Hydrological impacts of changing land management practices in a moderate-sized agricultural catchment. *Water Resour. Res.*, **27**, 845–855.
- Rawls, W. J., L. R. Ahuja, D. L. Brakensiek, and A. Shirmohammadi, 1993: Infiltration and soil water movement. *Handbook of Hydrology*, D. R. Maidment, Ed., McGraw-Hill, 5.1–5.51.
- Robinson, J. B., W. F. Hazell, and W. S. Young, 1998: Effects of August 1995 and July 1997 storms in the city of Charlotte and Mecklenburg County, North Carolina. U.S. Geological Survey Fact Sheet FS-036-98, 6 pp.
- Robinson, J. S., and M. Sivapalan, 1997: An investigation into the physical causes of scaling and heterogeneity of regional flood frequency. *Water Resour. Res.*, **33**, 1045–1059.
- Rodriguez-Iturbe, I., and A. Rinaldo, 1997: *Fractal River Basins*. Cambridge University Press, 547 pp.
- Smith, J. A., 1992: Representation of basin scale in flood peak distributions. *Water Resour. Res.*, **28**, 2993–2999.
- , M. L. Baeck, M. Steiner, and A. J. Miller, 1996: Catastrophic rainfall from an upslope thunderstorm in the central Appalachians: The Rapidan storm of June 27, 1995. *Water Resour. Res.*, **32**, 3099–3113.
- , —, J. L. Morrison, and P. Sturdevant-Rees, 2000: Catastrophic rainfall and flooding in Texas. *J. Hydrometeorol.*, **1**, 5–25.
- Tarboton, D. G., 1997: A new method for the determination of flow directions and upslope areas in grid digital elevation models. *Water Resour. Res.*, **33**, 309–319.
- Turner-Gillespie, D., 2001: The urban drainage system and extreme flood response. M.S. thesis, Dept. of Civil and Environmental Engineering, Princeton University, 69 pp.
- Venables, W. N., and B. D. Ripley, 1997: *Modern Applied Statistics with S-Plus*. Springer-Verlag, 548 pp.
- Wolff, G. C., and S. J. Burges, 2000: An analysis of the influence of river channel properties on flood frequency. *J. Hydrol.*, **153**, 317–337.
- Wolman, M. G., 1967: A cycle of sedimentation and erosion in urban river channels. *Geograf. Ann.*, **49A**, 385–395.
- Woltemade, C. J., and K. W. Potter, 1994: A watershed modeling analysis of fluvial geomorphic influences on flood peak attenuation. *Water Resour. Res.*, **30**, 1933–1942.
- Wood, E. F., M. Sivapalan, and K. Beven, 1990: Similarity and scale in catchment storm response. *Rev. Geophys.*, **28**, 1–18.
- Woods, R., and M. Sivapalan, 1999: A synthesis of space-time variability in storm response: Rainfall, runoff generation and routing. *Water Resour. Res.*, **35**, 2469–2485.

## Stochastic modeling of flood peaks using the generalized extreme value distribution

Julia E. Morrison

Department of Operations Research and Financial Engineering, Princeton University, Princeton, New Jersey, USA

James A. Smith

Department of Civil and Environmental Engineering, Princeton University, Princeton, New Jersey, USA

Received 9 March 2001; revised 22 April 2002; accepted 22 April 2002; published 19 December 2002.

[1] The generalized extreme value (GEV) distribution is a standard tool for modeling flood peaks, both in annual maximum series (AMS) and in partial duration series (PDS). In this paper, combined maximum likelihood estimation (MLE) and L moment (LMOM) procedures are developed for estimating location, shape, and scale parameters of the GEV distribution. Particular attention is given to estimation of the shape parameter, which determines the “thickness” of the upper tail of the flood frequency distribution. Mixed MLE–LMOM methods avoid problems with both MLE (estimator variance) and LMOM (estimator bias) estimators of the shape parameter. The mixed MLE–LMOM procedure is extended to use the two largest flood peaks in a year. This extension is developed in a PDS framework. Estimation procedures are applied to flood peak observations from 104 central Appalachian basins. The estimated values of the shape parameter for the central Appalachian basins are more negative than has been considered physically reasonable, independent of the estimation procedure that is used. Twenty-eight percent of mixed method estimators of the shape parameter have values less than  $-0.5$ , implying that the moments of order 2 and above are infinite. The estimated shape parameters for the central Appalachian basins do not depend on basin morphological parameters (such as drainage area) or land cover properties (such as percent urban, forest, or agricultural land use). Estimated values of the location and scale parameters for the central Appalachian watersheds correspond well with GEV-based simple scaling theory. Estimated values of the shape parameter for central Appalachian watersheds are shown to differ markedly from those of southern Appalachian watersheds and the difference is shown to be linked to contrasting properties of extreme floods. To conclude the paper, analyses of mixture distribution models are presented to address the question of whether flood peaks really have extreme “heavy tail” behavior or whether the GEV distribution is not the appropriate model for flood peaks. **INDEX TERMS:** 1821 Hydrology: Floods; 1869 Hydrology: Stochastic processes; **KEYWORDS:** Floods, extreme value theory

**Citation:** Morrison, J. E., and J. A. Smith, Stochastic modeling of flood peaks using the generalized extreme value distribution, *Water Resour. Res.*, 38(12), 1305, doi:10.1029/2001WR000502, 2002.

### 1. Introduction

[2] The development of stochastic methods for the characterization of flood peaks in drainage basins has both motivated and benefited from the treatment of classical problems in extreme value statistics. The generalized extreme value (GEV) distribution has been widely used for modeling the distribution of flood peaks in at-site and regional settings [Hosking *et al.*, 1985a; Smith, 1987; Stedinger and Lu, 1995; Rosbjerg and Madsen, 1995; Hosking and Wallis, 1996]. In addition to flood modeling, the GEV distribution is commonly used to model many other natural extreme events [Smith, 1986; Bauer, 1996; Kuchenhoff and Themerus, 1996; Bruun and Tawn, 1998;

Parret, 1998]. “Extreme events” are often defined to be the maximum value of a quantity over a given period of time, such as the maximum annual discharge in a river. Extreme value theory, in particular the extremal types theorem [Leadbetter *et al.*, 1983], suggests that the distribution of these maxima should be close to one of the extreme value types. The GEV distribution, introduced by Jenkinson [1955], is a three-parameter distribution that combines all three extreme value types into a single form (see section 2).

[3] Parameter estimation procedures for the three-parameter GEV distribution have been extensively studied (see the work of Martins and Stedinger [2000] for a literature review). The most commonly used methods are the maximum likelihood estimation (MLE) [Prescott and Walden, 1980], the method of L moments (LMOM) [Hosking, 1990], and the method of moments (MOM). It has been noted that estimates of the shape parameter  $k$  of the GEV distribution

for flood peak data are usually negative [Smith, 1987; Madsen et al., 1997; Martins and Stedinger, 2000], implying heavy tails in the distribution. It has been shown that MLE parameter estimators have a very large variance for negative values of  $k$ , and result in large errors in quantile estimation. Although both LMOM and MOM estimators tend to produce biased estimates, they are still considered preferable to MLE because of smaller variances in their quantile estimates [Hosking et al., 1985b; Madsen et al., 1997]. MLE-based methods, however, can easily incorporate additional information, such as censored data [Prescott and Walden, 1983] or a known prior distribution for  $k$  [Martins and Stedinger, 2000, 2001].

[4] In this paper (section 3), we show how MLE and LMOM methods can be combined to produce improved GEV parameter estimators based on annual maximum series (AMS) of flood peaks. The resulting "mixed" method estimators of the shape parameter of the GEV distribution have reduced variance compared to the MLE estimator and reduced bias compared to the LMOM estimator. The root mean square errors (RMSE) of mixed method estimators of the GEV location, scale, and shape parameters are superior to those of LMOM estimators for flood-size samples. The RMSE of LMOM estimators of extreme flood quantiles (100 and 1000 year flood magnitude analyses are presented) are slightly smaller than those for mixed method estimators. The contrasting properties of quantile and parameter estimators are examined and provide interesting insights to both LMOM and mixed method estimators.

[5] Partial duration series (PDS) [Shane and Lynn, 1964; Todorovich and Zelenhasic, 1970] models assume that the arrival times of peaks above a specified threshold form a Poisson process in time, and that the distribution of the peak magnitudes has a particular form. The attraction of these procedures is that additional information can be used, relative to AMS-based techniques. There are, for example, many flood records in which the second largest flood peak during a year is larger than the majority of other flood peaks. The generalized Pareto (GP) distribution is a common choice for the peak magnitude distribution both because it corresponds to a limiting distribution for excesses over a threshold as that threshold is increased [Leadbetter et al., 1983], and the resulting distribution of annual flood peaks is GEV [Smith, 1984; Madsen and Rosbjerg, 1997]. Madsen et al. [1997] showed that errors in parameter estimation under the GP/PDS approach under certain conditions are smaller than those of the GEV/AMS approach.

[6] In section 4 we introduce a MLE method that uses the values of the two largest observations for a given year (MLE2) and extend the method to a mixed method estimator. The MLE2 method is developed in the GP/PDS framework and tested via Monte Carlo simulations. Analyses illustrate the flexibility of the mixed method framework and the potential for improving parameter and quantile estimators through incorporation of flood observations from PDS records.

[7] The GEV distribution has played an important role in regional flood frequency analyses [Hosking et al., 1985a; Lettenmaier et al., 1987; Chowdhury et al., 1991; Stedinger and Lu, 1995; Hosking and Wallis, 1996]. A commonly used foundation for regional flood frequency analyses is the simple scaling theory, which assumes that appropriately

scaled annual flood peaks have the same distribution in a hydrologically homogeneous geographical region. In the GEV approach, this means that the shape parameter  $k$  of the GEV distribution and the ratio of scale and location parameters are constant for all basins in the region.

[8] In the work of Smith [1992], a sample of 104 basin from the central Appalachian region was studied, and the hypothesis that simple scaling theory holds for this sample was rejected. In section 6 we further investigate the applicability of the index-flood theory to the central Appalachian region. In particular, we estimate the parameters of the GEV distribution for the same sample of basins used by Smith [1992] and Hosking and Wallis [1996] and study the dependence of parameter estimates on morphological and land cover characteristics of the basins.

## 2. MLE and LMOM Methods

[9] The GEV distribution combines into a single form all three Extreme Value (EV) distributions: Gumbel (EVI,  $k = 0$ ), Frechet (EVII,  $k < 0$ ), and Weibull (EVIII,  $k > 0$ ). The GEV distribution has the following cumulative distribution function:

$$G(x) = \begin{cases} \exp \left\{ - \left( 1 - \frac{k(x-b)}{a} \right)^{1/k} \right\} & k \neq 0, \\ \exp \left\{ - \left( e^{-\frac{(x-b)}{a}} \right) \right\} & k = 0. \end{cases} \quad (1)$$

It has three parameters: scale  $a > 0$ , location  $b$ , and shape  $k$ . Here,  $-\infty < x \leq b + a/k$  for  $k > 0$ ,  $-\infty < x < \infty$  for  $k = 0$ , and  $b + a/k \leq x < \infty$  for  $k < 0$ . To simplify our notation, we will write  $\theta$  for the vector  $(b, a, k)^T$ , and to refer to this distribution form with a particular set of parameters, we will write  $G_\theta(x)$ . The corresponding probability density function will be denoted as  $g_\theta(x)$ . In this paper, we will focus on parameter estimation procedures for negative values of the shape parameter  $k$ . Because the GEV distribution does not have a third moment when  $k < -1/3$ , MOM estimators will not be considered here.

[10] The log likelihood function of a random sample  $\{x_1, x_2, \dots, x_n\}$  from the GEV distribution is:

$$\log L(\theta|x) = \dots n \log a - \sum_{i=1}^n \left\{ 1 - \frac{k(x_i - b)}{a} \right\}^{1/k} + \left( \frac{1}{k} - 1 \right) \sum_{i=1}^n \log \left\{ 1 - \frac{k(x_i - b)}{a} \right\} \quad (2)$$

and the corresponding MLE estimator  $\hat{\theta} = (\hat{b}, \hat{a}, \hat{k})^T$  is the point at which  $\log L(\theta|x)$  attains its maximum. It can also be expressed as the solution to the following optimization problem:

$$\begin{aligned} &\text{maximize} && \log L(\theta|x) \\ &\text{subject to} && k(x_i - b) \leq a \quad i = 1, \dots, n \\ &&& a > 0 \end{aligned} \quad (3)$$

The constraints in the problem correspond to the condition that the probability density function of the GEV distribution must be positive at  $\{x_1, x_2, \dots, x_n\}$ .

[11] Traditionally, the problem (3) is solved by setting the partial derivatives of the log likelihood function (2) to zero

and then using Newton–Raphson iterations to solve for the parameters [Prescott and Walden, 1980; Hosking, 1985; MacLeod, 1989]. These methods have only local convergence and experience difficulty when the objective function is nonconvex. In this study, the method of steepest descent was used without second-order information about the objective function. It was found that convergence problems associated with nonconvexity of the objective function could be largely avoided in this manner. Although these methods require a larger number of function evaluations, the overall increase in computational time was nonetheless insignificant for the cases we tested.

[12] The LMOM estimator  $\hat{k}$  for the shape parameter is the solution of the following equation:

$$\frac{1 - 3^{-\hat{k}}}{1 - 2^{-\hat{k}}} = \frac{\hat{\tau}_3 + 3}{2}, \quad (4)$$

The corresponding LMOM estimators for  $a$  and  $b$  are:

$$\hat{a} = \frac{\hat{\lambda}_2 \hat{k}}{(1 - 2^{-\hat{k}}) \Gamma(1 + \hat{k})}, \quad (5)$$

$$\hat{b} = \hat{\lambda}_1 - \frac{\hat{a}}{\hat{k}} [1 - \Gamma(1 + \hat{k})], \quad (6)$$

where  $\hat{\lambda}_1$ ,  $\hat{\lambda}_2$ , and  $\hat{\tau}_3 = \hat{\lambda}_3 / \hat{\lambda}_2$  are the estimators of the first two LMOMs and the L skewness obtained from the sample [Hosking, 1990]. Equation (4) is usually solved using Newton's method or by an approximate solution [see Hosking et al., 1985b].

[13] The bias of LMOM estimates of  $k$  increases with decreasing  $k$ , and is larger than 0.07 when  $k = -0.4$ . The MLE method produces almost unbiased estimates of  $k$ , but the variance of these estimates is large in comparison with those of LMOM. In addition, MLE frequently produces absurd estimates of  $k$  ( $< -1$ ), which lead to very large errors in the quantile estimates [Martins and Stedinger, 2000]. In the next section, we present a combination of LMOM and MLE methods and show that it provides improved estimates of the shape parameter  $k$ .

[14] The quantile function of the GEV distribution is given by:

$$Q(p) = \begin{cases} b + \frac{a}{k} (1 - (-\log p)^k) & k \neq 0, \\ b - a \log(-\log p) & k = 0. \end{cases} \quad (7)$$

For a given value of  $p$ , quantile estimates are obtained by substituting estimated values of the parameters to the formula above. Of particular interest are large quantile values, for example, the 100 year return interval flood magnitude  $Q(0.99)$ . In subsequent sections, we examine properties of quantile estimators  $\hat{Q}(p)$ , in addition to properties of parameter estimators  $\hat{k}$ ,  $\hat{a}$ , and  $\hat{b}$ .

### 3. Mixed LMOMs: MLE Methods

[15] One of the ways to improve MLE estimates of  $k$  is to impose additional constraints on the optimization problem in (3). We would like these constraints to be based on our

sample rather than on additional assumptions about the process that we have observed. One such constraint could be posed by LMOMs, for example, we can require the first LMOM of the estimated GEV distribution to be the same as determined from the sample. The addition of this constraint to the MLE problem (3) produces the first Mixed (MIX1) method.

[16] In the MIX1 method, we maximize the log likelihood function  $L(\theta|x)$ , as a function of  $a$  and  $k$  after substituting  $b$  from the LMOM equation (6). The MIX1 estimator  $\hat{\theta}$  of the parameters of the GEV distribution, then, is the solution to the following optimization problem:

$$\begin{aligned} &\text{maximize} && \log L(\theta|x) \\ &\text{subject to} && b = \hat{\lambda}_1 - \frac{a}{k} [1 - \Gamma(1 + k)] \\ & && k(x_i - b) \leq a \quad i = 1, \dots, n \\ & && a > 0 \end{aligned} \quad (8)$$

[17] In the second mixed method (MIX2), we maximize the likelihood function  $L(\theta|x)$  as a function of  $k$  after taking both  $b$  and  $a$  from the LMOM (equation (5) and (6)). The optimization problem for this method is

$$\begin{aligned} &\text{maximize} && \log L(\theta|x) \\ &\text{subject to} && b = \hat{\lambda}_1 - \frac{a}{k} [1 - \Gamma(1 + k)] \\ & && a = \frac{\hat{\lambda}_2 k}{(1 - 2^{-k}) \Gamma(1 + k)}, \\ & && k(x_i - b) \leq a \quad i = 1, \dots, n \end{aligned} \quad (9)$$

[18] We can also consider the method MIX2 to be an LMOM method where, instead of using (4) to obtain estimates of  $k$ , we maximize the likelihood function to obtain  $k$ . In this case, we avoid using the estimator for  $\tau_3$ , which has a large bias if the true value of  $k$  is less than  $-0.2$  and the sample size is small (less than 50).

[19] Both MIXed methods are based on the solution of a nonlinear optimization problem with nonlinear constraints involving 1 or 2 variables. Modern optimization solvers can solve similar problems with hundreds of variables in a matter of seconds, so, from the computational point of view, these problems are very tractable. In our implementation of the MIXed methods, we used the steepest descent method [Bazaraa et al., 1993] for solving these problems. The initial point was taken to be the LMOM estimate, and if it was infeasible (relative to the constraint in (9)), the value of  $k$  was adjusted to allow it to be feasible. At each iteration, the bounds on the step size were set such that the current solution remained feasible at all times. Although we coded the methods ourselves, standard optimization solvers (such as LOQO [Vanderbei, 1999] or MINOS [Mutagh and Saunders, 1998]) can be readily used.

[20] In order to evaluate the performance of the MIXed methods, we conducted a series of simulation experiments. We simulated random samples of different sizes  $n$  from the GEV distribution corresponding to different values of  $k$  in the range  $-0.5$  to  $0.0$ . For each sample, we estimated the parameters of the GEV distribution using MLE, LMOM, MIX1, and MIX2 methods. We are most interested in the estimates of the shape parameter, but we also present the

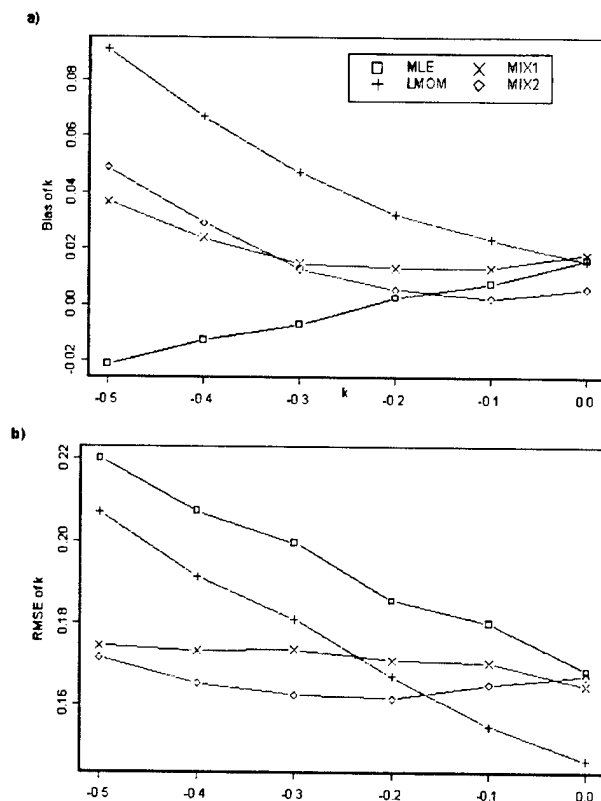


**Figure 1.** Bias (a) and RMSE (b) of the estimator  $\hat{k}$  for a sample size  $n = 30$  and four different estimation methods: MLE, LMOM, MIX1, and MIX2.

results for estimators of location, scale, and flood quantiles. Each simulation experiment was performed 10,000 times.

[21] The bias and RMSE (defined as  $(E[(\hat{k} - k)^2])^{1/2}$ ) were computed for MLE, LMOM, MIX1, and MIX2 estimators of  $k$  for sample size  $n = 30$  (Figure 1). For  $k < -0.1$ , the MIX1 and MIX2 estimators have smaller biases

than the LMOM methods and smaller variances than MLE, resulting in smaller RMSE in the estimation of  $k$  compared to LMOM and MLE. Neither MIXed method produced absurd estimates for  $k$ . The differences in performance decrease with increasing sample size (Table 1). An attractive feature of the MIX1 method is that the RMSE of the estimator  $\hat{k}$  is insensitive to the value of  $k$ . This is a very desirable property for the estimator if we would like to examine the dependence of  $k$  on drainage basin and climatological properties. In section 5, we examine the regional distribution of estimators of  $k$  for central Appalachian drainage basins and examine the dependence of estimators of  $k$  on basin properties, such as basin area, land use and land cover (LULC), and drainage density.

[22] The RMSE of LMOM, MLE, MIX1, and MIX2 estimators of the quantile function  $Q(p)$  ( $(E[(\hat{Q}(p) - Q(p))^2])^{1/2}$ ) were computed for  $p = 0.99$  (100 year flood) and  $p = 0.999$  (1000 year flood) for different values of  $n$  (Table 2). The ratio  $RMSE_Q - MIX1 / RMSE_Q - LMOM$  takes values between 0.98 and 1.02, implying that, in terms of quantiles, the two methods perform almost equally well. This result seems somewhat unusual in comparison to the estimation results in parameter space, where similar ratios range from 0.84, when  $k = -0.5$  to 0.97 when  $k = -0.1$ .

[23] The differences between performance of MIXed method and LMOM estimators in parameter and quantile spaces lead to a more detailed analysis of the distribution of the quantile estimators. A surprising conclusion was that the bias of the LMOM estimator of  $k$  plays an important role in producing good LMOM quantile estimators. We demonstrate this feature with an example using  $n = 30$  and parameter values of the GEV distribution of  $b = 0$ ,  $a = 1$ , and  $k = -0.3$ . The covariance matrix of MIX2 estimators (Table 3, based on 10,000 simulation runs) is smaller than that for LMOM estimators for each element. Only the bias of  $\hat{a}$  is larger for MIX2 than for LMOM.

[24] Under the assumption that the estimators have a joint Gaussian distribution, we can compute the moments of  $\hat{Q}(99)$  by numerically integrating expression (7) with the appropriate pdf of the estimators. If we neglect the bias of

**Table 1.** RMSE of Parameter Estimates for MLE, LMOM, MIX1, and MIX2 Methods for Selected Sample Sizes and Negative Values of  $k$

$n$	$k$	$\hat{a}$ RMSE				$\hat{b}$ RMSE				$\hat{k}$ RMSE			
		MLE	LMOM	MIX1	MIX2	MLE	LMOM	MIX1	MIX2	MLE	LMOM	MIX1	MIX2
30	-0.5	0.21	0.26	0.21	0.21	0.22	0.23	0.22	0.22	0.22	0.21	0.18	0.17
30	-0.4	0.19	0.23	0.20	0.19	0.22	0.22	0.22	0.21	0.21	0.19	0.17	0.17
30	-0.3	0.18	0.21	0.19	0.19	0.22	0.22	0.22	0.22	0.20	0.18	0.17	0.16
30	-0.2	0.17	0.19	0.18	0.17	0.21	0.21	0.21	0.21	0.19	0.17	0.17	0.16
30	-0.1	0.17	0.17	0.17	0.17	0.21	0.21	0.22	0.21	0.18	0.16	0.17	0.17
30	0	0.16	0.16	0.16	0.17	0.21	0.21	0.22	0.21	0.17	0.15	0.17	0.17
50	-0.5	0.16	0.2	0.17	0.16	0.16	0.17	0.17	0.17	0.16	0.17	0.14	0.14
50	-0.4	0.15	0.18	0.15	0.15	0.17	0.17	0.17	0.17	0.15	0.16	0.13	0.13
50	-0.3	0.14	0.16	0.14	0.14	0.17	0.17	0.17	0.16	0.14	0.14	0.13	0.12
50	-0.2	0.13	0.14	0.13	0.13	0.16	0.16	0.17	0.16	0.13	0.13	0.12	0.12
50	-0.1	0.13	0.13	0.13	0.13	0.17	0.16	0.17	0.16	0.13	0.12	0.13	0.12
50	0	0.12	0.12	0.12	0.12	0.16	0.16	0.16	0.16	0.12	0.11	0.12	0.12
100	-0.5	0.11	0.14	0.12	0.11	0.12	0.12	0.12	0.12	0.10	0.13	0.10	0.10
100	-0.4	0.10	0.13	0.11	0.10	0.12	0.12	0.12	0.12	0.10	0.12	0.09	0.10
100	-0.3	0.10	0.11	0.10	0.10	0.12	0.12	0.12	0.11	0.09	0.10	0.09	0.09
100	-0.2	0.091	0.10	0.09	0.09	0.11	0.12	0.12	0.11	0.09	0.09	0.08	0.08
100	-0.1	0.09	0.10	0.09	0.09	0.12	0.12	0.12	0.11	0.08	0.08	0.08	0.08
100	0	0.08	0.08	0.08	0.08	0.11	0.11	0.11	0.11	0.08	0.07	0.08	0.08

**Table 2.** RMSE of Quantile Estimates for MLE, LMOM, MIX1, and MIX2 Methods for Selected Sample Sizes and Values of  $k$ 

$n$	$k$	$\hat{Q}(0.99)RMSE/Q(0.99)$				$\hat{Q}(0.999)RMSE/Q(0.999)$			
		MLE	LMOM	MIX1	MIX2	MLE	LMOM	MIX1	MIX2
30	-0.5	1.53	0.56	0.58	0.56	9.12	1.10	1.19	1.14
30	-0.4	1.03	0.53	0.552	0.54	3.63	1.12	1.16	1.14
30	-0.3	0.96	0.50	0.51	0.50	5.44	1.08	1.09	1.07
30	-0.2	0.63	0.44	0.45	0.44	2.04	0.90	0.91	0.88
30	-0.1	0.53	0.37	0.40	0.39	1.70	0.67	0.77	0.73
30	0	0.37	0.30	0.33	0.33	0.77	0.52	0.61	0.60
50	-0.5	0.74	0.48	0.54	0.50	1.87	0.97	1.14	1.01
50	-0.4	0.62	0.45	0.46	0.46	1.86	0.96	0.95	0.96
50	-0.3	0.48	0.39	0.39	0.39	1.05	0.79	0.73	0.74
50	-0.2	0.39	0.34	0.34	0.34	0.77	0.65	0.62	0.62
50	-0.1	0.32	0.29	0.30	0.29	0.62	0.50	0.53	0.51
50	0	0.26	0.24	0.25	0.25	0.44	0.38	0.41	0.41
100	-0.5	0.40	0.37	0.37	0.37	0.79	0.72	0.71	0.72
100	-0.4	0.35	0.34	0.33	0.34	0.66	0.68	0.60	0.64
100	-0.3	0.3	0.29	0.28	0.28	0.54	0.56	0.49	0.51
100	-0.2	0.25	0.24	0.24	0.23	0.44	0.42	0.40	0.39
100	-0.1	0.20	0.19	0.20	0.19	0.33	0.32	0.32	0.31
100	0	0.17	0.16	0.17	0.17	0.26	0.25	0.26	0.26

the estimators and assume that they are centered at  $(0, 1, -0.3)^T$ , we will find that the MIX2 method performs better (Table 3, center). Note that the bias of the quantile estimator that we obtain under this assumption is large, nearly 12%. Taking into account the biases of the parameter estimators in the computation, we obtain better results for quantile estimators: biases and variances of the quantile estimators are decreased and the  $RMSE_Q$  obtained from LMOM is slightly smaller than that from MIX2. This agrees with the estimated  $RMSE_Q$  obtained from the simulation experiments, where equation (7) is calculated for every simulation experiment and appropriate statistics are computed (Table 3, bottom).

[25] The difference between theoretically computed and simulated variances and RMSEs can be attributed to non-Gaussian properties of one or more estimators. Further

analyses suggested that  $RMSE_Q$  is most sensitive to  $E[\hat{k}]$ . This is not surprising, because  $k$  contributes to (7) exponentially and  $RMSE_Q$  decreases with increasing  $E[\hat{k}]$ , provided that the covariance between  $\hat{k}$  and  $\hat{a}$  is positive (see Table 3). This result agrees well with results of *Lu and Stedinger* [1992], who show that, for certain pairs of  $k$  and  $n$ , smaller  $RMSE_Q$  can be achieved by setting  $\hat{k} = 0$ . In addition, it is clear that decreasing covariance between  $\hat{k}$  and  $\hat{a}$  will result in better estimators of the quantiles. Although accurate estimation of the shape parameter  $k$  is important for proper characterization of the tail of the flood peak distribution, slight overestimation of  $k$  for the LMOM procedure results in smaller values of  $RMSE_Q$ . Improvement of the parameter estimators, therefore, does not necessarily mean improvement of the quantile estimators.

[26] We also compared the performance of the four methods for positive values of  $k$ . We found that the MIX2 methods and MLE performed roughly the same, and LMOM performed slightly better than the other methods.

[27] It is important to note here that, if we have prior knowledge of the underlying physical process, we can add associated constraints to the MLE optimization problem accordingly, and there is a good chance that the estimates of the model parameters will be improved. One example of such prior knowledge is including an estimate of the lower bound of the peak magnitude in the GEV distribution ( $b + a/k$ ). Indeed, absurd estimates of  $k$  usually occur in situations where the smallest value in the sample is very close to the estimated lower bound. If, in addition to our sample  $\{x_1, x_2, \dots, x_n\}$ , we know that a value  $x_0 < \min\{x_1, \dots, x_n\}$  is a possible flood value, then we must have  $b + a/k < x_0$ . Adding this lower bound condition to the MLE problem (3) will reduce the chance of obtaining absurd estimates, if not eliminate it completely (see the work of *Stedinger and Cohn* [1986] for additional development of this idea). *Martins and Stedinger* [2000] discuss a sample of size 15, generated from the GEV distribution with parameters  $a = 1$ ,  $b = 0$ , and  $k = -0.2$  for which the MLE estimate of  $k$  is less than  $-2.4$ . This resulted in an estimate of the 0.999 quantile on the

**Table 3.** Comparison of Performance of LMOM and MIX2 Methods in Parameter and Quantile Spaces (See Text for More Details)<sup>a</sup>

	LMOM	MIX2
Expected values of the estimators, $[(\hat{b}, \hat{a}, \hat{k})^T]$	$\begin{pmatrix} 1.002 \\ 0.0142 \\ -0.2529 \end{pmatrix}$	$\begin{pmatrix} 0.9538 \\ -0.0010 \\ -0.2871 \end{pmatrix}$
Covariance matrix of the estimators, $B$	$\frac{1}{100} \begin{pmatrix} 4.7896 & 2.9063 & 1.2575 \\ 2.9063 & 4.2565 & 1.0176 \\ 1.2575 & 1.0176 & 3.0540 \end{pmatrix}$	$\frac{1}{100} \begin{pmatrix} 4.6026 & 2.4660 & 1.0321 \\ 2.4660 & 3.2099 & 0.5423 \\ 1.0321 & 0.5423 & 2.6157 \end{pmatrix}$
det $B$	$3.2212 \times 10^5$	$2.0724 \times 10^5$
Theoretically computed values for $Q(0.99)$ , assuming unbiased parameter estimators		
Expected value	11.1817	11.0946
Variance	36.2456	31.9329
RMSE	6.1519	5.7723
Theoretically computed values for $Q(0.99)$ , accounting for biased parameter estimators		
Expected value	9.7986	10.1838
Variance	26.3093	26.7793
RMSE	5.1305	5.1817
Simulation results		
Expected value	9.7756	10.1427
Variance	24.4626	24.6872
RMSE	4.9475	4.9733

<sup>a</sup> The true values of the parameters are  $(0, 1, -0.3)^T$  and the true value for  $Q(0.99)$  is 9.9169.

order of  $6 \times 10^6$ , while the value of the real quantile was only 14.9. The true distribution has a lower bound of  $-5$ , while the lowest value in the sample was  $-0.39$ . Suppose that we had the additional information that the value  $x_0 = -1$  is feasible, i.e., there is a strictly positive probability of obtaining  $-1$  from the underlying process. If we add this information into the problem (3), our estimate of  $k$  will be  $-0.74$ , resulting in an estimate of the 0.999 quantile of 208. Although the error of this estimate is still quite large, it is almost 30,000 times smaller than without the condition. Simulation experiments show that adding this condition reduces the overall error in quantile estimates by a factor of 8 in comparison with the standard MLE method. In applications involving natural events (floods, winds, etc.), it is possible that some useful additional information of this kind is available. For instance, the data might say that there was no flood peak above a certain threshold during a certain year, but the value of the maximum flood peak for that year was not recorded. While it is very hard to incorporate such information into the LMOM method, it is very easy to insert it into MLE. We will discuss this approach further in later sections.

[28] To summarize this section, we conclude that for the negative values of  $k$ : (1) MIXed methods produce better estimates of the parameters of the GEV distribution than MLE and LMOM; (2) Quantile estimates produced by MIXed methods have RMSE close to that of LMOM; (3) Difference between relative performances of the MIXed and LMOM methods in the quantile and parameter spaces can be explained by the correlation between parameter estimates, nonlinear quantile function, and the favorable bias of the LMOM estimates; and (4) MIXed methods preserve the attractive large sample properties of MLE estimators (see the work of Morrison [2001] for derivation of large sample properties of MIXed method estimators; it is shown that estimators are strongly consistent, under certain regularity conditions, and have a limiting multivariate Gaussian distribution).

#### 4. Extension to PDS Methods

[29] PDS models of flood peaks (sometimes referred to as the peaks-over-threshold approach) [Shane and Lynn, 1964; Todorovich and Zelenhasic, 1970] assume that the arrival times of peaks greater than a specified threshold form a Poisson process in time, and that the distribution of peak magnitudes has a particular form. If we assume that the distribution is a GP distribution (as in the works of Davison and Smith [1990] and Madsen and Rosbjerg [1997]), the annual flood peaks derived from this model have a GEV distribution (with an atom at zero) [see Smith, 1984; Hosking and Wallis, 1987].

[30] Assume that flood peaks above the threshold  $\delta$  arrive according to a (stationary) Poisson process with rate  $\lambda$ , and that the peaks' magnitudes  $V_1, V_2, \dots$  are i.i.d. random variables independent of the arrival process, each having a GP distribution with location parameter  $\delta$ , scale parameter  $\alpha$ , and shape parameter  $\kappa$ . The cumulative distribution function of  $V_j$  is then

$$F(x) = \begin{cases} 1 - (1 - \kappa \frac{x-\delta}{\alpha})^{1/\kappa} & \kappa \neq 0, \\ 1 - \exp\{-\frac{x-\delta}{\alpha}\} & \kappa = 0. \end{cases} \quad (10)$$

[31] To simplify our notation, we will write  $\eta$  to represent the vector  $(\alpha, \delta, \kappa)^T$ , and to refer to the distribution function with this particular set of parameters  $\eta$ , we will write  $F_\eta(x)$ . The corresponding probability density function will be denoted as  $f_\eta(x)$ . Under our assumptions, the distribution of annual flood peaks (for values greater than  $\delta$ ) is the same as the GEV distribution with parameters

$$\begin{aligned} k &= \kappa, \\ a &= \alpha \lambda^{-\kappa}, \\ b &= \delta + \frac{\alpha}{\kappa} (1 - \lambda^{-\kappa}). \end{aligned} \quad (11)$$

After estimating the parameters for GP/PDS model, then, we can subsequently deduce the appropriate parameters for the GEV model. Madsen and Rosbjerg [1997] showed that the PDS approach can improve MLE and LMOM estimates if both the arrival rate of flood peaks above threshold is greater than 2 peaks per year and  $\kappa < 0$ .

[32] We developed a MLE method based on the magnitudes of the two largest floods each year (MLE2). Methods based on more than one peak per year, have been studied before in the application to sea level heights [Smith, 1986; Dupuis, 1997].

[33] Suppose that the flood peaks for a basin follow the GP/PDS process described above. Let  $X$  and  $Y$  be random variables representing the annual maximum flood peak and the second largest flood peak for a given year, respectively.

[34] Under the GP/PDS model, we can write the probability distribution for  $X$ :

$$\mathbb{P}\{X \leq x\} = \begin{cases} e^{-\lambda(1-F_\eta(x))} & \text{for } x \geq \delta, \\ e^{-\lambda} & \text{for } x < \delta \end{cases} \quad (12)$$

The joint distribution for two largest peaks during a given year is then:

$$\mathbb{P}\{X \leq x, Y \leq y\} = \begin{cases} e^{-\lambda(1-F_\eta(y))} (1 + \lambda F_\eta(x) - \lambda F_\eta(y)) & \text{for } \delta < y < x, \\ e^{-\lambda} (1 + \lambda F_\eta(x)) & \text{for } 0 \leq y < \delta < x, \\ e^{-\lambda} & \text{for } 0 \leq y < x < \delta, \\ 0 & \text{otherwise} \end{cases} \quad (13)$$

[35] Under the GEV/AMS approach, we approximate the expression in (12) by  $G_\theta(x)$  with the parameters  $\theta$  related to those of GP/PDS  $\eta$  through relationships (11). That means that (13) will be approximated by:

$$\mathbb{P}\{X \leq x, Y \leq y\} = G_\theta(y) [1 + \log G_\theta(x) - \log G_\theta(y)] \quad \text{for } \delta < y < x \quad (14)$$

and the joint probability density function for  $X$  and  $Y$  is then just  $g_\theta(y)g_\theta(x)/G_\theta(x)$  for  $\delta < y < x$ . Using this argument, we can construct a likelihood function of the observations of the two largest peaks per year. Also note that

$$\mathbb{P}\{X < \delta\} = G_\theta(\delta) = e^{-\lambda}. \quad (15)$$

[36] Consider a basin with  $m$  years of PDS record with threshold  $\delta$ . Among these  $m$  years of PDS record, there are  $m_0$  with no peaks above  $\delta$ ,  $m_1$  years with only one peak above  $\delta$  (let  $z_1, z_2, \dots, z_{m_1}$  denote the magnitudes of these peaks), and  $m_2$  years with 2 or more peaks (the largest peaks per year will be denoted by  $x_1, x_2, \dots, x_{m_2}$ , and the second largest by  $y_1, y_2, \dots, y_{m_2}$ ). The log likelihood function of these observations is, then:

$$\begin{aligned} \log \Lambda(\theta|z, x, y) = & -m_0 \lambda + m_1 (\log(\lambda) - \lambda) \\ & + m_2 \log(1 - e^{-\lambda} - \lambda e^{-\lambda}) + \sum_{i=1}^{m_1} \log(f_{\eta}(z_i)) \\ & + \sum_{j=1}^{m_2} [\log(g_{\theta}(y_j) + \log(g_{\theta}(x_j)) - \log(G_{\theta}(x_j))], \end{aligned} \quad (16)$$

where the parameters  $\theta$ ,  $\eta$ , and  $\lambda$  are connected through the relationships in (11). Here, the first three terms on the right hand side correspond to the probability of having 0, 1, or "2 or more" peaks in a given year, respectively. The term on the second line is the log likelihood of obtaining the particular values  $z_1, z_2, \dots, z_{m_1}$  of the single flood peaks over threshold that occurred during the  $m_1$  years, and the term on the last line corresponds to the log likelihood of obtaining the particular pairs of two largest peaks for the  $m_2$  years that we observed two or more peaks. Substituting into (16) the derivative of (10) for  $f_{\eta}$ , and  $G_{\theta}$  and  $g_{\theta}$  from (1), and using the relationships (11) we obtain the following expression for the likelihood function of the two maxima:

$$\begin{aligned} \log \Lambda(\theta|z, x, y) = & -m_0 e^{h(\delta)} + m_1 (h(\delta) - e^{h(\delta)}) \\ & + m_2 \log(1 - \exp(-e^{h(\delta)})(1 + e^{h(\delta)})) \\ & - (m_1 + 2m_2) \log a + (1 - k) \sum_{i=1}^{m_1} h(z_i) \\ & + (1 - k) \sum_{j=1}^{m_2} [h(y_j) + h(x_j)] - \sum_{j=1}^{m_2} e^{h(y_j)}, \\ \text{where } h(x) = & \frac{1}{k} \log \left( 1 - \frac{k(x - b)}{a} \right). \end{aligned} \quad (17)$$

The time required to evaluate this expression computationally is not much more than the time necessary to evaluate the standard likelihood function for the MLE method.

[37] The maximum likelihood estimator based on the two largest maxima per year (MLE2) is the (local) maximum of the likelihood function in (17). This can be equivalently written as the solution to the following optimization problem:

$$\begin{aligned} \text{minimize } & -\log \Lambda(\theta|z, x, y) \\ \text{subject to } & k(z_i - b) \leq a \quad i = 1, \dots, m_1 \\ & k(x_j - b) \leq a \\ & k(y_j - b) \leq a, \quad j = 1, \dots, m_2 \\ & k(\delta - b) \leq a, \\ & a > 0 \end{aligned} \quad (18)$$

The first three conditions correspond to the restriction that the measured peak magnitudes must be feasible values for the varying GP distribution. The last condition is the restriction that the scale parameter is positive. The second to

last constraint ("the  $\delta$  constraint") is the condition that the threshold level itself must be a feasible value for the GEV distribution. This constraint is necessary because it ensures that the likelihood function can be evaluated. When  $k > 0$ , since all  $z_i$ ,  $x_j$ , and  $y_j$  are greater than  $\delta$ , the  $\delta$  constraint never becomes binding on the problem (the upper bound of the GEV distribution is obviously greater than  $\delta$ ); when  $k = 0$  the  $\delta$  constraint becomes  $a \geq 0$ , which is less restrictive than the last constraint. For  $k < 0$ , the  $\delta$  constraint has an effect, as it requires that the lower bound for annual flood peaks be less than  $\delta$ . This corresponds to the positive probability of having no peaks above the threshold during a given year.

[38] As with the regular MLE method, we investigated different possible constraints that we can add to the problem (18) in order to improve the estimates of the quantiles. The equivalent of the MIX1 method in this case involves adding the following constraint to the problem (18):

$$b = \frac{\hat{\lambda}_1}{1 - e^{-h_0(\delta)}} - \frac{a}{k} (1 + \Gamma(1 + k)), \quad (19)$$

where  $\hat{\lambda}_1$  is the mean value (estimate of the first LMOM) of all annual maxima above the threshold  $\delta$ , that is,  $\hat{\lambda}_1 = \frac{1}{m_1 + m_2} \left[ \sum_{i=1}^{m_1} z_i + \sum_{j=1}^{m_2} x_j \right]$ . This condition helps to eliminate all absurd estimates of  $k$ , and improves the estimation. We will refer to this method as MLE2-MIX1.

[39] The procedure that we used for Monte Carlo simulations in order to test our methods is the same as described by Madsen *et al.* [1997]. It is designed so that we can compare the performance of the AMS methods to that of PDS-based methods. It exploits the fact that in GP/PDS peaks above higher threshold levels from the same process also have GP distribution with the same value of  $k$ . Specifically, if peaks over the threshold level  $\delta_0$  arrive according to a Poisson process with rate  $\lambda_0$ , and the peaks' magnitudes are i.i.d., independent of the Poisson process, and have a GP distribution with parameters  $\eta_0 = (\alpha_0, \delta_0, \kappa)$ , then peaks above the higher threshold  $\delta_1$  for  $\lambda_1 < \lambda_0$

$$\delta_1 = \begin{cases} \delta_0 + \frac{\alpha_0}{\kappa} \left[ 1 - \left( \frac{\lambda_1}{\lambda_0} \right)^{\kappa} \right] & \kappa \neq 0, \\ \delta_0 + \alpha_0 \log \left( \frac{\lambda_0}{\lambda_1} \right) & \kappa = 0. \end{cases} \quad (20)$$

arrive according to a Poisson process with rate  $\lambda_1$ , are i.i.d., and have a GP distribution with scale parameter  $\alpha_1 = \alpha_0 + \kappa(\delta_1 - \delta_0)$ , location parameter  $\delta_1$ , and the same value of shape parameter  $\kappa$  [see Madsen *et al.*, 1997].

[40] The simulation procedure can be described as follows:

1. Pick parameters to simulate data from the GP/PDS model: Choose a large arrival rate  $\lambda_0$ , so that the probability of obtaining zero peaks during any given year is very small. Choose a threshold level  $\delta_0$ , scale parameter  $\alpha_0$ , and the number of years in the record  $m$ . Also, choose the value of the shape parameter  $\kappa$  and the arrival rate  $\lambda_1$  for which we would like to test the procedure. Compute  $\delta_1$  from (20) and  $\alpha_1 = \alpha_0 + \kappa(\delta_1 - \delta_0)$ .

2. Generate arrival times from the Poisson process with rate  $\lambda_0$ , and generate a flood peak magnitude from the GP distribution with parameters  $\delta_0$ ,  $\alpha_0$ , and  $\kappa$  for each arrival time.



3. Extract the PDS sample corresponding to all peaks higher than  $\delta_1$  and their arrival times: compute the number of years with no peaks,  $m_0$ , the number of years with 1 peak,  $m_1$ , and the number of years with more than one peak,  $m_2 = m - m_0 - m_1$ . For years with only one peak, record the magnitude of the peak  $z_i$ ,  $i = 1, \dots, m_1$ , and for years with two or more peaks record the magnitudes of the largest and second largest peaks,  $x_j$  and  $y_j$ ,  $j = 1, \dots, m_2$ .

4. Solve the optimization problem (18) and record the MLE2 estimates.

5. Extract the AMS sample from the original process by recording the largest peak for each year.

6. Use LMOM and MIX1 method to estimate the parameters of the GEV distribution based on the AMS sample.

[41] Monte Carlo simulations were performed according to the procedure above for records 20–100 years long, values of  $\lambda_1$  from 2 to 7, shape parameter  $k$  between  $-0.5$  and  $0.0$ . Results (Figure 2) show that incorporating information about second maxima leads to a decrease in the estimation error of the shape parameter for all sample sizes. The results obtained for all other sets of the model parameters were similar to this one (Table 4). This was especially significant for very negative values of  $k$ . Although the MLE2 method sometimes produces absurd results, it does so less frequently than MLE, in part due to the “ $\delta$  condition” in problem (18) (see the example above). The MLE2–MIX1 method did not produce any absurd estimates of  $k$ , and its estimates of  $k$  have the smallest RMSE. In terms

**Table 4.** RMSE of the Estimates of  $k$  LMOM, MLE2, and MLE2–MIX1 Methods for Selected Sample Sizes and Negative Values of  $k$

$n$	$k$	$\hat{k}$ RMSE		
		LMOM	MLE2	MLE2–MIX1
35	−0.5	0.19	0.14	0.13
35	−0.4	0.17	0.14	0.12
35	−0.3	0.17	0.13	0.12
35	−0.2	0.15	0.12	0.11
35	−0.1	0.14	0.11	0.11
35	0	0.14	0.11	0.11
50	−0.5	0.18	0.12	0.12
50	−0.4	0.15	0.11	0.10
50	−0.3	0.15	0.11	0.10
50	−0.2	0.13	0.10	0.10
50	−0.1	0.11	0.09	0.09
50	0	0.11	0.09	0.09
100	−0.5	0.13	0.08	0.08
100	−0.4	0.12	0.08	0.08
100	−0.3	0.11	0.07	0.07
100	−0.2	0.09	0.07	0.07
100	−0.1	0.08	0.07	0.07
100	0	0.08	0.06	0.06

of quantiles, though incorporating second maximum decreased the RMSE in the quantiles by a factor of 8 in comparison with the standard MLE method, the LMOM/AMS and MIX1/AMS methods still produce better quantile estimates than MLE2, primarily due to the absurd estimates of  $k$ . MLE2–MIX1 has the smallest RMSE<sub>Q</sub> (see Table 5) for  $k \leq -0.2$ .

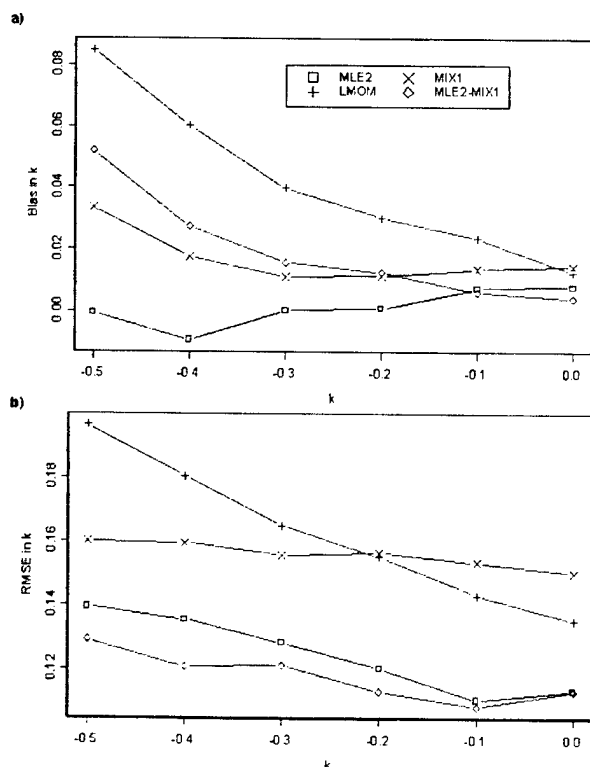


**Figure 2.** Bias (a) and RMSE (b) of the estimator  $\hat{k}$  for a sample size  $n = 30$  and four different estimation methods: MLE2, LMOM, MIX1, and MLE2–MIX1.

## 5. Analysis of Flood Peak Data From the Central Appalachian Region

[42] GEV parameter estimation procedures were applied to flood peak observations from a sample of 104 USGS stream gauging stations in the central Appalachian region (see the works of Smith [1992] and Hosking and Wallis [1996] for previous analyses of this data set). These basins have at least 30 years of data and are not regulated by dams [see Smith, 1992]. The questions that we would like to address in our analysis are (1) How variable are at-site estimates of the shape parameter  $k$  within the region; (2) How can this variability be explained; and (3) How do the estimates of the three GEV parameters depend on morphological and land cover properties of the drainage basins? To address the third question, basin morphological and land cover information was computed for each of the basins from digital elevation data (DEM) and LULC data (based on Landsat Thematic Mapper images from 1990 to 1992). From these data sets we computed drainage area, measures of basin slope and shape (including basin relief, relief ratio and elongation ratio) [Rodriguez-Iturbe and Rinaldo, 1997], and percent cover for various LULC categories (including urban, forest and agricultural classifications) for each of the 104 basins.

[43] Based on analyses of previous sections and for ease of comparison with prior studies, the MLE2–MIX1 method and LMOM method were used to estimate the parameters of the GEV distribution for each of the basins. The range of LMOM estimates of  $k$  for the central Appalachian basins was between  $-0.74$  and  $0.02$ , with a median value of  $-0.37$ . For the MLE2–MIX1 method, estimates of  $k$  ranged from  $-0.82$

**Table 5.** RMSE of Quantile Estimates for LMOM, MLE2, and MLE2-MIX1 Methods for Selected Sample Sizes and Values of  $k$ 

$n$	$k$	$\hat{Q}(0.99)$ RMSE/ $Q(0.99)$			$\hat{Q}(0.999)$ RMSE/ $Q(0.999)$		
		LMOM	MLE2	MLE2-MIX1	LMOM	MLE2	MLE2-MIX1
35	-0.5	0.48	0.66	0.50x2	1.02	1.67	1.02
35	-0.4	0.42	0.55	0.41	0.88	1.23	0.80
35	-0.3	0.42	0.45	0.40	1.01	1.03	0.83
35	-0.2	0.30	0.33	0.30	0.64	0.66	0.55
35	-0.1	0.25	0.24	0.24	0.54	0.46	0.45
50	-0.5	0.46	0.54	0.47	0.96	1.16	0.92
50	-0.4	0.38	0.41	0.37	0.81	0.81	0.72
50	-0.3	0.36	0.34	0.33	0.81	0.68	0.64
50	-0.2	0.26	0.26	0.25	0.56	0.50	0.47
50	-0.1	0.20	0.19	0.19	0.40	0.32	0.33
100	-0.5	0.36	0.33	0.38	0.80	0.61	0.74
100	-0.4	0.321	0.27	0.31	0.72	0.49	0.60
100	-0.3	0.26	0.22	0.23	0.60	0.39	0.43
100	-0.2	0.19	0.17	0.17	0.37	0.30	0.30
100	-0.1	0.15	0.14	0.15	0.27	0.25	0.25

to 0.01 with a median value of  $-0.40$ . As given by *Hosking and Wallis* [1996] the same sample of basins is divided into 5 groups, and the regional estimates of  $k$  for each group were determined. The values of these estimates ranged from  $-0.45$  to  $-0.24$ , which agrees with our distribution of at-site estimates. These values are more negative than what has conventionally been considered physically reasonable [*Martins and Stedinger*, 2000]. When  $k$  is less than  $-1/3$ , the flood peak distribution has an infinite third moment and when  $k$  is less than  $-1/2$ , the distribution has infinite variance. Very negative values of  $k$  suggest that the distribution of flood peaks has very heavy tails.

[44] Figure 3 shows the values of at-site estimates of  $k$  obtained using the LMOM and MLE2-MIX1 methods plotted against the corresponding empirical quantiles of the standard Gaussian distribution. The lines on the plot correspond to a Gaussian approximation of the distribution of the respective estimators of  $k$  for the two methods, if the true value of  $k$  is  $-0.42$  and the period of record is 46 (the average number of years of record available for our sample). From this plot, we conclude that the distribution of the estimates of  $k$  for our sample is approximately Gaussian, and the variability of the estimates can be explained by the variability of the estimators used.

[45] The estimates of the shape parameter  $k$  for the central Appalachian basins do not exhibit systematic dependence on basin morphometric properties or land cover properties. The relationship between estimates of  $k$  and basin area (Figure 4) is representative of those for other basin descriptors. Regression analysis between the estimates of  $k$  and the basin drainage area produced an  $R^2$  value of 0.007.  $R^2$  values for regression analyses of estimates of  $k$  versus basin morphological and land cover variables were less than 0.06 for all variables.

[46] According to simple scaling theory, values of the scaling parameter  $a$  and the location parameter  $b$  should exhibit a log-log relationship with drainage area  $A$ . For the central Appalachian basins, this property generally holds (Figures 5a and 5b). A significant contribution to the variability in this scaling relationship for estimates of the GEV location and scale parameters is related to land cover properties. It was found that basins with a higher percentage

of urbanized land have higher values of the scaling parameter  $a$  and  $b$  (Figures 5a and 5b). These basins respond as though they have larger effective areas [see *Leopold*, 1968; *Smith et al.*, 2002]. Notably, the urbanization effects on GEV parameter estimates are quite important for location and scale, but not for the shape parameter  $k$  (see the work of *Iacobellis and Fiorentino* [2000] for additional discussion).

[47] GEV flood estimation analyses were also carried out for a sample of 34 drainage basins from the southern Appalachians yielding estimates of  $k$  ranging from  $-0.53$  to  $0.24$  with a median value of  $-0.11$ . Selection of the 34 basins (all of which are in North Carolina) was based on identical constraints to those used for the 104 central Appalachian basins. A systematic difference in flood peak distributions between the two regions is that the southern

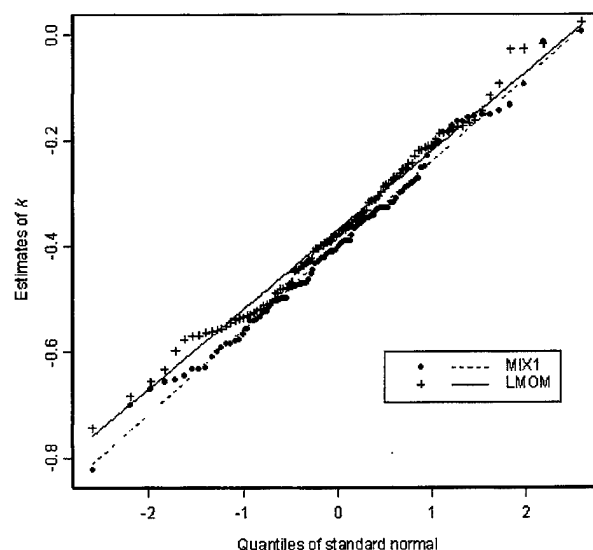


**Figure 3.** A normal QQ plot of at-site estimates of  $k$  for the central Appalachians basins. The lines on the plot correspond to a Gaussian approximation of the distribution of the LMOM and MIX1 estimator of  $k$ .

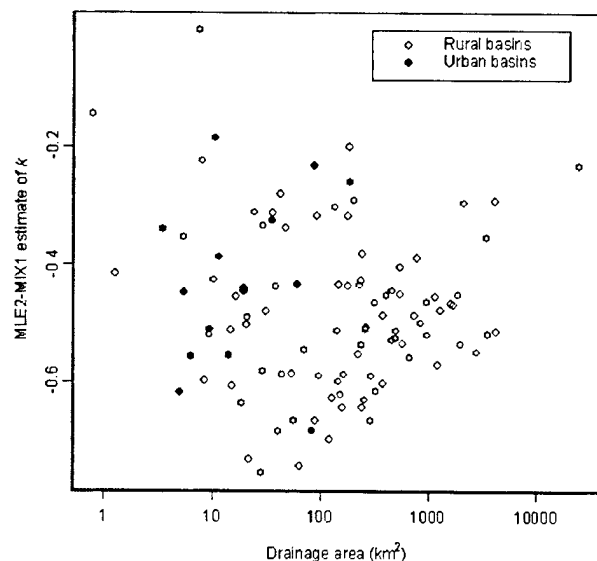


**Figure 4.** Dependence of MLE2-MIX1 estimate of  $k$  on basin's drainage area.

Appalachian basins exhibit markedly lower variability, as represented by the coefficient of variation of annual flood peaks, than central Appalachian basins. This contrast in flood peak distributions is reflected in contrasting magnitudes of extreme flood peaks, as illustrated in Figure 6 by envelope curves of flood peaks for the two samples. The "extreme" estimates of the shape parameter  $k$  for the central Appalachian region are linked to the hydrology and hydrometeorology of extreme floods in the region. The central Appalachian region has experienced some of the largest unit discharge flood peaks in the United States east of the Rocky Mountains [Smith *et al.*, 1996; Eisenlohr, 1952; Hack and Goodlett, 1960]. The Three Floods paradigm of Miller

[1990] interprets the flood hydrology of the central Appalachian region in terms of the contributions of (1) organized systems of thunderstorms, (2) tropical storms, and (3) extratropical cyclones. The relative importance of these three flood-producing storm systems is scale dependent, with thunderstorm systems of most importance at the smallest basin scales (less than  $100 \text{ km}^2$ ) and extratropical cyclones of greatest importance at the largest basin scales (greater than  $10,000 \text{ km}^2$ ).

[48] A key question is whether extreme estimates of the GEV tail parameter  $k$  necessarily mean that flood peak distributions indeed have heavy tails or whether alternative stochastic models can explain the estimated values of  $k$ . One possible scenario for negative estimates of  $k$  from thin-tailed flood distributions is based on the GEV distribution not being the correct distribution for annual flood peaks. If, for example, we estimate the three parameters of the GEV distribution from samples of size  $n = 50$  from the exponential distribution, then the estimated values of  $k$  will be centered at  $-0.38$  for MIX1 estimators and at  $-0.2$  for the LMOM estimators. The exponential distribution is from the Gumbel domain of attraction ( $k = 0$ ), so it does not have thick tails. The exponential distribution, however, can be shown to be a poor choice for modeling flood peak distributions. Are there good alternative models for annual flood peak distributions with thin tails, but large negative estimates of  $k$ ?

[49] The heuristic explanation for the contrasts in flood distributions between the central and southern Appalachians given above, rests on the influence of particular types of flood events. This notion points to a class of alternative models that involve a mixture of different distributions. Let  $V_1$  and  $V_2$  be independent random variables having distributions from the same family, with  $E[V_2] > E[V_1]$ . Again, let  $X$  be a random variable representing an annual flood, and suppose that  $X = V_1$  with probability  $p$  and  $X = V_2$  with probability  $(1 - p)$ .  $V_1$  and  $V_2$  can be thought of as flood

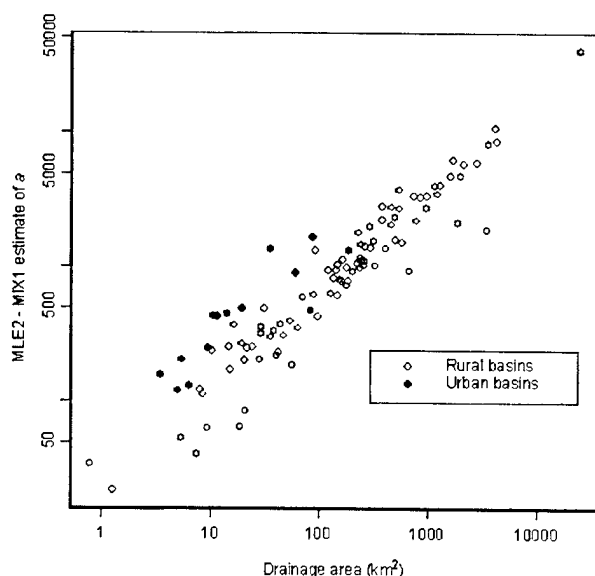


**Figure 5.** (a) Dependence of MLE2-MIX1 estimate of  $a$  on basin's drainage area. Solid circles denote urban basins and empty circles denote rural basins. (b) Dependence of MLE2-MIX1 estimate of  $b$  on basin's drainage area. Solid circles denote urban basins and empty circles denote rural basins.

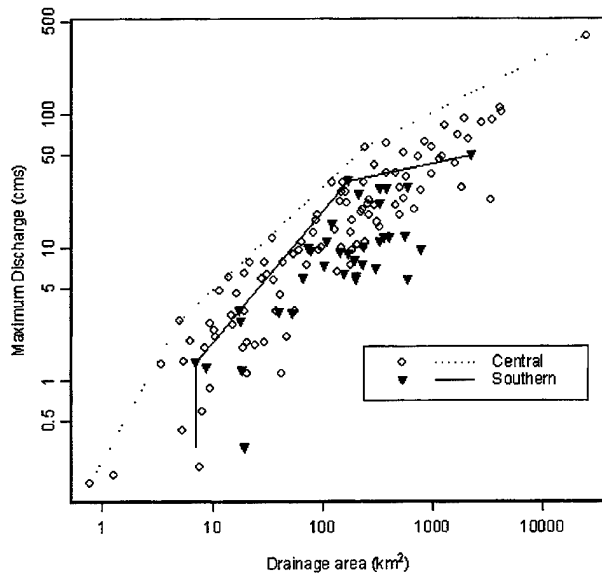


**Figure 6.** Envelope curves of flood peaks for central and southern Appalachians region.

peaks occurring from different classes of storms. For example,  $V_1$  might represent flood peaks produced by tropical storms [Sturdevant-Rees *et al.*, 2001] and  $V_2$  might then represent flood peaks due to summer thunderstorms [Smith *et al.*, 1996]. If  $V_1$  and  $V_2$  have a GEV distribution with  $k=0$ , i.e., both flood populations have a Gumbel distribution, is it possible to obtain estimates of  $k$  centered at  $-0.4$  for flood-length samples? The answer is yes for the following formulation: (1)  $V_1 \sim \text{GEV}$  with  $k_1=0$ ,  $a_1=1$ ,  $b_1=0$ , (2)  $V_2 \sim \text{GEV}$  with  $k_2=0$ ,  $a_2=3.3$ ,  $b_2=6.6$ , and (3)  $p=0.83$ .

[50] If one estimates parameters of the GEV distribution from samples of size 50 from the Gumbel mixture model above using the GEV LMOM estimators, the estimator of the shape parameter  $k$  is distributed about  $-0.4$  (Figure 7). For samples of size 50 from a GEV distribution with parameters  $a=1.4$ ,  $b=0.2$ , and  $k=-0.42$  (a "best fit" GEV parameter set for the Gumbel mixture model) the LMOM estimator of  $k$  is centered about  $-0.4$ . The GEV distribution with  $a=1.4$ ,  $b=0.2$ , and  $k=-0.42$  is close to the Gumbel mixture distribution for the 10 year event, taking a value of 5.3 for the GEV distribution and 5.6 for the Gumbel mixture. The distributions are quite different in the upper tails with a 0.99 quantile of 18.7 for the GEV distribution versus 8.2 for the Gumbel mixture model and a 0.999 quantile of 52.2 for the GEV and 10.6 for the Gumbel mixture. The preceding analyses demonstrate that if we estimate parameters of the GEV distribution from a flood sample whose true distribution is a Gumbel mixture, we can overestimate the upper tail thickness. Furthermore, the differences in assessment of upper tail thickness can have a marked impact on estimates of extreme flood quantiles.

## 6. Conclusions

[51] New *Mixed Method* parameter estimators for the GEV distribution are introduced based on a combination of the MLE and LMOM methods. These procedures can be viewed as LMOM-constrained MLE methods. The new

estimation procedures were motivated by problems in estimating the GEV shape parameter using MLE and LMOM procedures. The performance of GEV parameter and quantile estimators is studied via simulation. MIX1 and MIX2 estimators do not produce absurd estimates of  $k$  (unlike MLE estimators), and the RMSE of these estimators are smaller than that of LMOM and MLE for  $k < -0.1$ . The Mixed Method estimators are based on the MLE principle and are readily extended to incorporate additional information. These estimators also possess the attractive large sample properties of MLE estimators.

[52] Despite the fact that *Mixed Method* estimators provide better estimators of the GEV location, shape, and scale parameters (for negative values of  $k$ ), the resulting *Mixed Method* quantile estimators are not superior to LMOM quantile estimators. Analyses of the distribution of the quantile estimators demonstrate that bias of the LMOM estimator of the GEV shape parameter is an important element of the performance of LMOM quantile estimators.

[53] The Mixed Method estimators are extended to use the largest two flood peaks in a year. This extension is developed in a PDS framework. Performance of the MLE2 and MLE2-MIX1 estimators are also studied via simulation. It is shown that for negative  $k$ , incorporation of the additional information on flood peaks from the PDS record into *Mixed Method* estimators can result in quantile estimators with smaller values of RMSE than for LMOM quantile estimators.

[54] The GEV estimation techniques were applied to flood samples from 104 basins in the central Appalachians. Estimates of the GEV shape parameter, which are centered at  $-0.4$ , are more negative than what has conventionally been considered physically reasonable. Comparison of estimators of the shape parameter with basin descriptors uncovered no significant dependences. The dependence of estimated location and scale parameters on drainage area was consistent with simple scaling theory. It was also concluded that basins with a higher percentage of urban area have larger values of the scale and location parameters.

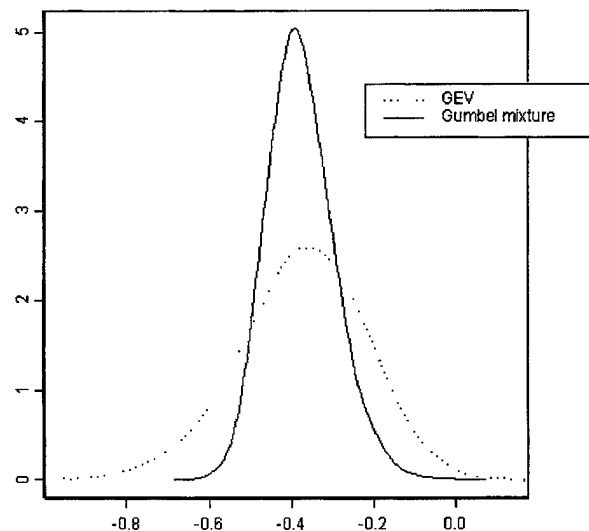


**Figure 7.** Distribution of the estimates of  $k$  for GEV distribution and the Gumbel mixture model (with parameters described in text) with sample size  $n=50$ .

The estimates of  $k$  for central Appalachian watersheds are shown to differ from those of southern Appalachian watersheds and the difference is linked to contrasting properties of extreme floods. Gumbel mixture distribution models were examined to determine whether the negative values of  $k$  might be explained by a stochastic model with tails thinner than those implied by the GEV distribution.

[55] The methods described in this paper were implemented by the authors in the EVANESCE ("Extreme Value Analysis Employing Statistical Copula Estimation") package for S-Plus [Venables and Ripley, 1997]. The package is available from the authors free of charge.

[56] **Acknowledgments.** This research was funded in part by the U.S. Army Research Office (grant DAAD19-99-1-1063), NASA (grant NAG5-7544), and National Science Foundation (grant EAR-9706259). This support is gratefully acknowledged. The authors are thankful to Jery Stedinger for his valuable comments and suggestions.

## References

- Bauer, E., Characteristic frequency distributions of remotely sensed in situ and modelled wind speeds, *Int. J. Climatol.*, 16(10), 1087–1102, 1996.
- Bazaraa, M. S., et al., (Eds.), *Nonlinear Programming: Theory and Algorithms*, John Wiley, New York, 1993.
- Brunn, J. T., and J. A. Tawn, Comparison of approaches for estimating the probability of coastal flooding, *J. R. Stat. Soc., Ser. C Appl. Stat.*, 47, 405–423, 1998.
- Chowdhury, J. U., J. R. Stedinger, and L.-H. Lu, Goodness-of-fit tests for regional generalized extreme value flood distributions, *Water Resour. Res.*, 27(7), 1765–1776, 1991.
- Davison, A. C., and R. L. Smith, Models for exceedances over high thresholds, *J. R. Stat. Soc., Ser. B Stat. Methodol.*, 52(3), 393–442, 1990.
- Dupuis, D. J., Extreme Value Theory based on the  $r$  largest annual events: A robust approach, *J. Hydrol.*, 200, 295–306, 1997.
- Eisenlohr, W. S., Floods of July 12, 1942 in north-central Pennsylvania, *U.S. Geol. Surv. Water Supply Pap.*, 1134-B, 1–155, 1952.
- Hack, J. T., and J. C. Goodlett, Geomorphology and forest ecology of a mountain region in the central Appalachians, *U.S. Geol. Surv. Prof. Pap.*, 347, 1–66, 1960.
- Hosking, J. R. M., Algorithm AS 215: Maximum-likelihood estimation of the parameters of the Generalized Extreme Value distribution, *Appl. Stat.*, 34, 3001–3010, 1985.
- Hosking, J. R. M., L-moments: Analysis and estimation of distributions using linear combinations of order statistics, *J. R. Stat. Soc., Ser. B Stat. Methodol.*, 52(1), 105–124, 1990.
- Hosking, J. R. M., and J. R. Wallis, Parameter and quantile estimation for the generalized Pareto distribution, *Technometrics*, 29(3), 339–349, 1987.
- Hosking, J. R. M., and J. R. Wallis, Regional frequency analysis of floods in central Appalachia, *Res. Rep. RC20349*, IBM Res., Yorktown Heights, N. Y., 1996.
- Hosking, J. R. M., J. R. Wallis, and E. F. Wood, An appraisal of the regional flood frequency procedure in the UK Flood Studies Report, *Hydrol. Sci. J.*, 30(1), 85–109, 1985a.
- Hosking, J. R. M., J. R. Wallis, and E. F. Wood, Estimation of the generalized extreme value distribution by the Method of Probability-Weighted Moments, *Technometrics*, 27(3), 251–261, 1985b.
- Iacobellis, V., and M. Fiorentino, Derived distribution of floods based on the concept of partial area coverage with a climatic appeal, *Water Resour. Res.*, 36(2), 469–482, 2000.
- Jenkinson, A. F., The frequency distribution of the maximum (or minimum) of meteorological elements, *Q. J. R. Meteorol. Soc.*, 81, 158, 1955.
- Kuchenhoff, H., and M. Thamerus, Extreme value analysis of Munich air pollution data, *Environ. Ecol. Stat.*, 3(2), 127–141, 1996.
- Leadbetter, M. R., G. Lindren, and H. Rootzén, *Extremes and Related Properties of Random Sequences and Processes*, Springer-Verlag, New York, 1983.
- Leopold, L. B., Hydrology of urban land planning: A guidebook on the hydrologic effects of urban land use, *U.S. Geol. Surv. Circ.*, 554, 1–3, 1968.
- Lettenmaier, D. P., J. R. Wallis, and E. F. Wood, Effect of regional heterogeneity on flood frequency estimation, *Water Resour. Res.*, 23(2), 313–323, 1987.
- Lu, L.-H., and J. R. Stedinger, Variance of two- and three-GEV/PWM quantile estimators: Formulae, confidence intervals, and a comparison, *J. Hydrol.*, 138, 247–267, 1992.
- MacLeod, A. J., R76-A a remark on algorithm AS 215: Maximum-likelihood estimation of the parameters of the GEV distribution, *Appl. Stat.*, 38, 198–199, 1989.
- Madsen, H., and D. Rosbjerg, The partial duration series method in regional index-flood modeling, *Water Resour. Res.*, 33(4), 737–746, 1997.
- Madsen, H., P. F. Rasmussen, and D. Rosbjerg, Comparison of annual maximum series and partial duration series methods for modeling extreme hydrologic events, 1, At-site modeling, *Water Resour. Res.*, 33(4), 746–757, 1997.
- Martins, E. S., and J. R. Stedinger, Generalized maximum-likelihood generalized extreme-value quantile estimators for hydrologic data, *Water Resour. Res.*, 36(3), 737–744, 2000.
- Martins, E. S., and J. R. Stedinger, Generalized maximum likelihood Pareto–Poisson flood risk analysis for partial duration series, *Water Resour. Res.*, 37(10), 2559–2567, 2001.
- Miller, A. J., Flood hydrology and geomorphic effectiveness in the central Appalachians, *Earth Surf. Processes*, 15(1), 119–134, 1990.
- Morrison, J. E., Extreme value statistics with applications in hydrology and financial engineering, Ph.D. dissertation, Princeton Univ., Princeton, NJ, 2001.
- Murtagh, B. A., and M. A. Saunders, MINOS 5.5 user's guide, *Rep. SOL 83-20R*, Dept. of Operations Res., Stanford Univ., Stanford, Calif., 1998.
- Parrett, C., Regionalization of precipitation characteristics in Montana using L-moments, *Gen. Design Roadside Safety Features*, 1647, 43–52, 1998.
- Prescott, P., and A. T. Walden, Maximum likelihood estimation of the parameters of the generalized extreme-value distribution, *Biometrika*, 67(3), 723–724, 1980.
- Prescott, P., and A. T. Walden, Maximum likelihood estimation of the parameters of the three-parameter generalized extreme-value distribution from censored samples, *J. Stat. Comput. Simul.*, 16, 241–250, 1983.
- Rodriguez-Iturbe, I., and A. Rinaldo, *Fractal River Basins*, Cambridge Univ. Press, New York, 1997.
- Rosbjerg, D., and H. Madsen, Uncertainty measures of regional flood frequency estimators, *J. Hydrol.*, 167, 209–224, 1995.
- Shane, R. M., and W. R. Lynn, Mathematical model for flood risk evaluation, *J. Hydrol. Div. Am. Soc. Civ. Eng.*, 90(HY6), 1–20, 1964.
- Smith, R. L., Threshold methods in statistics, in *Statistical Extremes and Applications*, NATO ASI Ser., vol. 131, edited by J. Tiago de Oliveira, pp. 621–638, D. Reidel, Norwell, Mass., 1984.
- Smith, R. L., Extreme Value Theory based on the  $r$  largest annual events, *J. Hydrol.*, 86, 27–43, 1986.
- Smith, J. A., Estimating the upper tail of flood frequency distributions, *Water Resour. Res.*, 23(8), 1657–1666, 1987.
- Smith, J. A., Representation of basin scale in flood peak distributions, *Water Resour. Res.*, 28(11), 2993–2999, 1992.
- Smith, J. A., M. L. Baack, M. Steiner, and A. Miller, Catastrophic rainfall from an upslope thunderstorm in the central Appalachians: The Rapidan storm of June 27, 1995, *Water Resour. Res.*, 32(10), 3099–3113, 1996.
- Smith, J. A., M. L. Baack, J. E. Morrison, P. Sturdevant-Rees, D. Turner-Gillespie, and P. Bates, The regional hydrology of extreme floods in an urbanizing drainage basin, *J. Hydrometeorol.*, 3(3), 267–282, 2002.
- Stedinger, J. R., and T. Cohn, Flood frequency analysis with historical and paleoflood information, *Water Resour. Res.*, 22(5), 785–793, 1986.
- Stedinger, J. R., and L.-H. Lu, Appraisal of regional and index flood quantile estimators, *Stoch. Hydrol. Hydraul.*, 9(1), 49–75, 1995.
- Sturdevant-Rees, P., J. A. Smith, M. L. Baack, and J. E. Morrison, Tropical storms and the flood hydrology of the central Appalachians, *Water Resour. Res.*, 37(8), 2143–2168, 2001.
- Todorovich, P., and E. Zelenhasic, A stochastic model for flood peaks, *Water Resour. Res.*, 6(6), 1641–1648, 1970.
- Vanderbei, R. J., LOQO user's manual: Version 3.10, *Optim. Methods Softw.*, 11(2), 485–514, 1999.
- Venables, W. N., and B. D. Ripley, *Modern Applied Statistics with S-Plus*, Springer-Verlag, New York, 1997.
- J. E. Morrison, Department of Operations Research and Financial Engineering, Princeton University, Princeton, NJ 08544, USA.
- J. A. Smith, Department of Civil and Environmental Engineering, Princeton University, Princeton, NJ 08544, USA.

## Extreme Rainfall and Flooding from Supercell Thunderstorms

JAMES A. SMITH, MARY LYNN BAECK, AND YU ZHANG

*Department of Civil and Environmental Engineering, Princeton University, Princeton, New Jersey*

CHARLES A. DOSWELL III

*National Severe Storms Laboratory, Norman, Oklahoma*

(Manuscript received 13 September 2000, in final form 25 May 2001)

### ABSTRACT

Supercell thunderstorms, the storm systems responsible for most tornadoes, have often been dismissed as flood hazards. The role of supercell thunderstorms as flood agents is examined through analyses of storm systems that occurred in Texas (5–6 May 1995), Florida (26 March 1992), Nebraska (20–21 June 1996), and Pennsylvania (18–19 July 1996). Particular attention is given to the “Dallas Supercell,” which resulted in 16 deaths from flash flooding and more than \$1 billion in property damage during the evening of 5 May 1995. Rainfall analyses using Weather Surveillance Radar-1988 Doppler (WSR-88D) reflectivity observations and special mesonet rain gauge observations from Dallas, Texas, show that catastrophic flash flooding resulted from exceptional rainfall rates at 5–60-min timescales. The spatial structure of extreme rainfall was linked to supercell structure and motion. The “Orlando Supercell” produced extreme rainfall rates (greater than  $300 \text{ mm h}^{-1}$ ) at 1–5-min timescales over a dense rain gauge network. The Nebraska and Pennsylvania storm systems produced record flooding over larger spatial scales than the Texas and Florida storms, by virtue of organization and motion of multiple storms over the same region. For both the Nebraska and Pennsylvania storms, extreme rainfall and tornadoes occurred in tandem. Severe rainfall measurement problems arise for supercell thunderstorms, both from conventional gauge networks and weather radar. It is hypothesized that supercell storms play a significant role in the “climatology” of extreme rainfall rates (100-yr return interval and greater) at short time intervals (1–60 min) in much of the central and eastern United States.

### 1. Introduction

During the past 20 years there have been major advances in understanding the dynamics of supercell thunderstorms and their role in tornadogenesis (see Doswell and Burgess 1993). Supercell storms have often been dismissed as heavy rainfall producers based on arguments revolving around low precipitation efficiency and rapid storm motion. Cotton and Anthes 1989, for example, note that “storms producing the largest hailstones occur in strongly sheared environments; thus, in general, we should not expect that the storm systems producing the largest hailstones are also heavy rain-producing storms.” Doswell et al. 1996 provide a different perspective, noting that “the combination of intense updrafts and substantial low-level moisture suggests some potential for heavy rainfall rates” (see also Moller et al. 1990, 1994; Doswell 1998).

The 559-mm rainfall accumulation during 2.75 h in D’Hannis, Texas, on 31 May 1935 is a world record

for the 2–3-h time period (WMO 1986). The *Hondo Anvil Herald* of 7 June 1935 noted that “a cyclone and severe electrical storm accompanied the rain” (see Dalrymple et al. 1937; “cyclone” is used colloquially to mean tornado), suggesting that a supercell thunderstorm contributed to this record. This observation is intriguing but raises more questions than it answers. How much rainfall was contributed in this case by supercell thunderstorms? Was there one storm or multiple storms? Were the storms moving rapidly or was anomalous storm motion a key ingredient of the rainfall record?

During the evening of 5 May 1995, a supercell thunderstorm (Fig. 1) passed over the Dallas–Fort Worth metropolitan area, producing softball-sized hail in Fort Worth and flash floods that resulted in 16 fatalities in Dallas. Total damages from flooding and hail made the “Dallas Supercell” the first \$1 billion thunderstorm in U.S. history (NOAA 1995). Unlike the 31 May 1935 storm, there were exceptional observations of the Dallas Supercell from the Dallas–Fort Worth Weather Surveillance Radar-1988 Doppler (WSR-88D) and a dense network of rain gauges in the Dallas metropolitan area.

In this paper, it is demonstrated that supercell thun-

*Corresponding author address:* James A. Smith, Environmental Engineering and Water Resources, Dept. of Civil and Environmental Engineering, Princeton University, Princeton, NJ 08544.  
E-mail: jsmith@princeton.edu



FIG. 1. Reflectivity image (0.5-km elevation) from the Dallas WSR-88D at 2312 UTC 5 May 1995 showing the Dallas Supercell approximately 30 km west of radar. Range rings are 20 km. Trailing squall line is approximately 50 km west of the Dallas Supercell. The bottom image depicts a vertical cross section along the dotted red line shown in the top image.

derstorms can indeed represent a major flood hazard by using analyses of the Dallas Supercell and three other storm systems that produced extreme rainfall and flooding in Florida (26 March 1992), Nebraska (21 June

1996), and Pennsylvania (18–19 July 1996). Locations and timing of the events are representative of the seasonal and geographic occurrence of supercell storms (as illustrated in the following sections). Detailed analyses

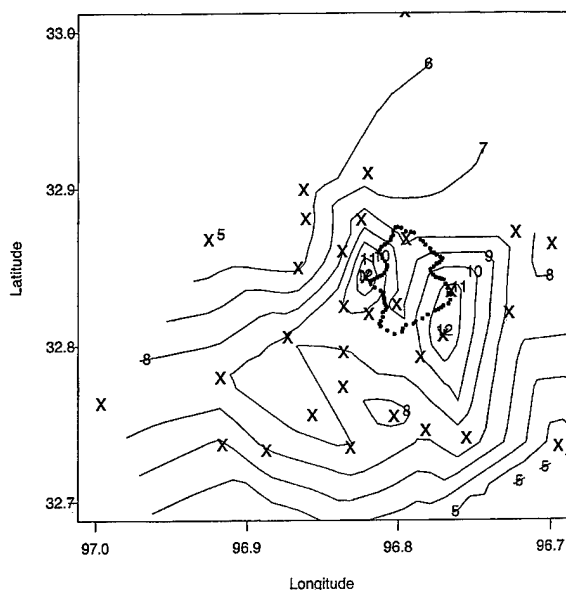


FIG. 2. Storm total rainfall distribution for 5–6 May 1995 over the Dallas metropolitan region, based on rain gauge observations from the Dallas mesonet (locations denoted by "x"). The boundary of Turtle Creek is outlined by dots. Contours represent storm total precipitation isohyets (cm).

of the Dallas Supercell are carried out, using the dense rain gauge observations along with WSR-88D radar observations to characterize spatial and temporal variability of supercell rainfall. The Orlando, Florida, storm provides a second opportunity to examine supercell rainfall over a dense rain gauge network. The Nebraska and Pennsylvania storm systems resulted in flooding at larger spatial scales than those of the Dallas Supercell and "Orlando Supercell," owing to multiple storms tracking over the same area for an extended period of time. For both the Nebraska and Pennsylvania storms, extreme rainfall and tornadoes occurred in tandem over the flood area.

The objectives of this study are

- 1) to identify the aspects of supercell structure, motion, and evolution that control the spatial and temporal distribution of extreme rainfall and flooding;
- 2) to characterize the magnitude of rainfall rates and their relation to supercell structure and motion;
- 3) to provide a depiction of the "climatology" of extreme rainfall from supercell thunderstorms; and
- 4) to illustrate the rainfall measurement problem for supercell thunderstorms.

The focus of this paper is on the spatial and temporal structure of extreme rainfall from supercell thunderstorms. A particular motivation for this study is the desire to understand the scale-dependent hydrologic response of drainage basins for extreme flood events at basin scales ranging from 1 to 1000 km<sup>2</sup> (see Smith 1992; Gupta et al. 1994; Woods and Sivapalan 1999;

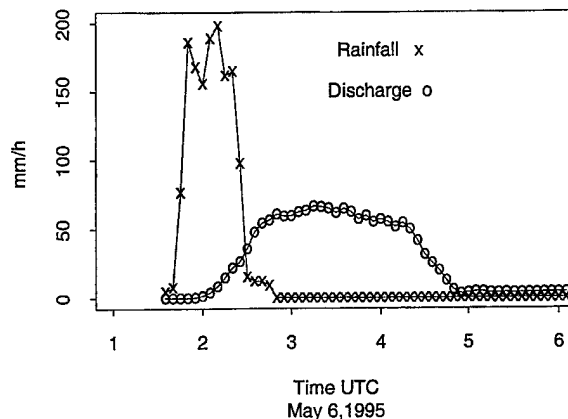


FIG. 3. Time series of basin-averaged rainfall (mm h<sup>-1</sup>; derived from rain gauge observations) and discharge (mm h<sup>-1</sup>) for Turtle Creek (see Fig. 2 for basin boundary). Discharge is expressed as a unit discharge by dividing discharge (m<sup>3</sup> s<sup>-1</sup>) by drainage area (km<sup>2</sup>) and converting to millimeters per hour.

Smith et al. 2000). This study is further motivated by applications in engineering design that require detailed understanding of the geographic distribution of flood hazards associated with extreme rainfall. As noted in NRC (1994), there are particular difficulties in characterizing the spatial occurrence of extreme rainfall for short durations and small areas. This paper does not attempt to identify the physical mechanisms distinguishing supercell storms that produce extreme rainfall from those that do not (see, e.g., Moller et al. 1994). We do, however, attempt to identify physical mechanisms that control rainfall distribution at timescales and space scales relevant to flood production.

## 2. Dallas Supercell: 5–6 May 1995

The Dallas Supercell is illustrated in Fig. 1 through observations from the Dallas–Fort Worth WSR-88D. The supercell and squall line were moving eastward with speeds of approximately 40 and 60 km h<sup>-1</sup>, respectively. Maximum reflectivity values in the supercell were 77 dBZ at the time of the volume scan shown in Fig. 1, and reflectivity values greater than 60 dBZ extended above 10 km. Reports of grapefruit-sized hail were received by the National Weather Service (NWS) at this time. The squall line overtook the supercell thunderstorm at approximately 0130 UTC along the western boundary of Dallas. Catastrophic rainfall during the 45-min period ending at 0215 UTC resulted in the 16 flash-flood deaths in Dallas. The synoptic-scale environment of the Dallas Supercell is summarized and discussed in the National Disaster Survey Report for the event (NOAA 1995).

The storm total rainfall distribution for the Dallas region (Fig. 2), as determined from the Dallas metropolitan rain gauge network, exhibited large spatial variability. Catastrophic rainfall and flooding were con-



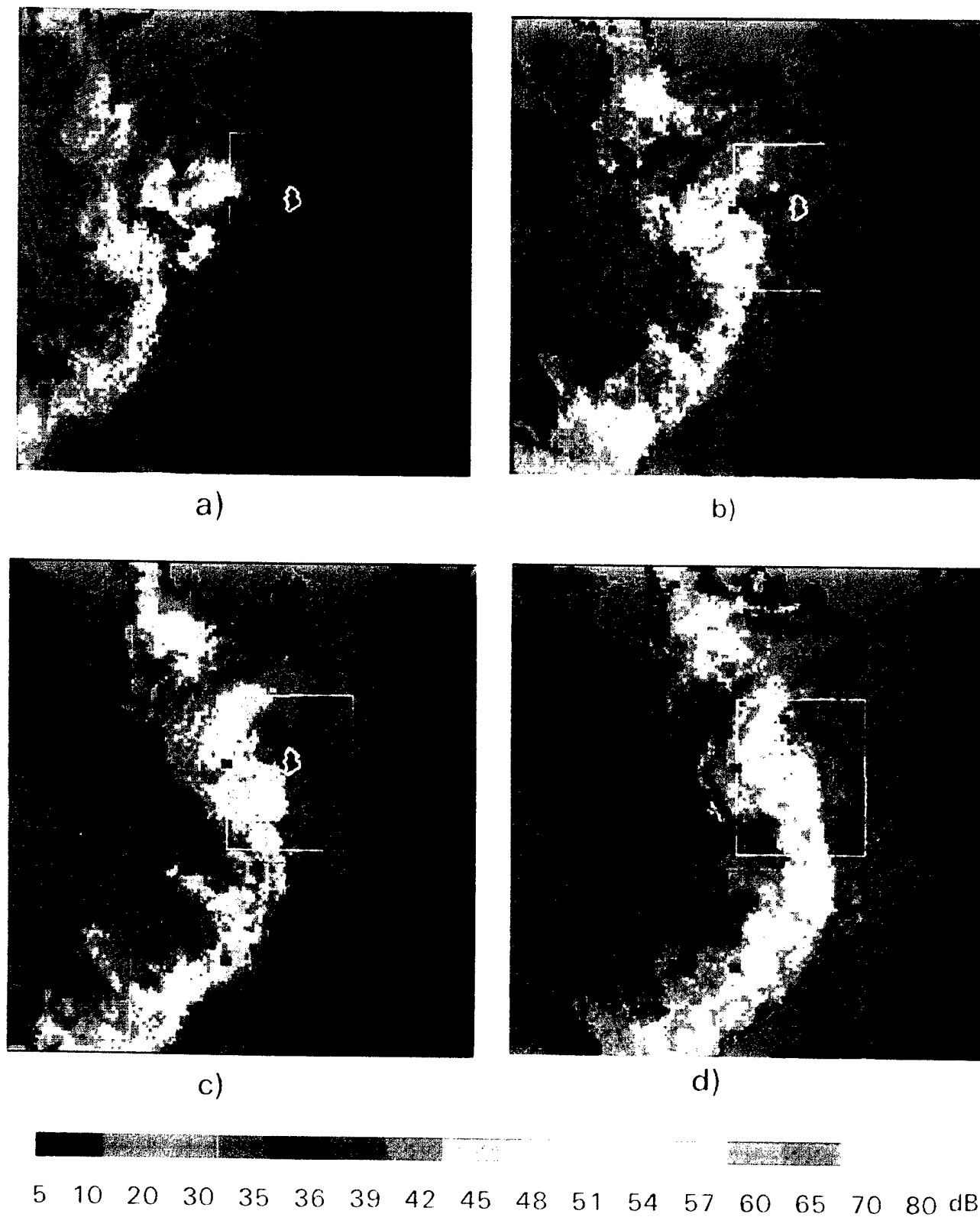


FIG. 4. Low-level (0.5 km) reflectivity images of Dallas Supercell and squall line at (a) 0057, (b) 0120, (c) 0132, (d) 0144, (e) 0201, and (f) 0219 UTC 6 May 1995. The white box corresponds to the region shown in Fig. 2. The basin boundary of Turtle Creek is outlined in white within the box.

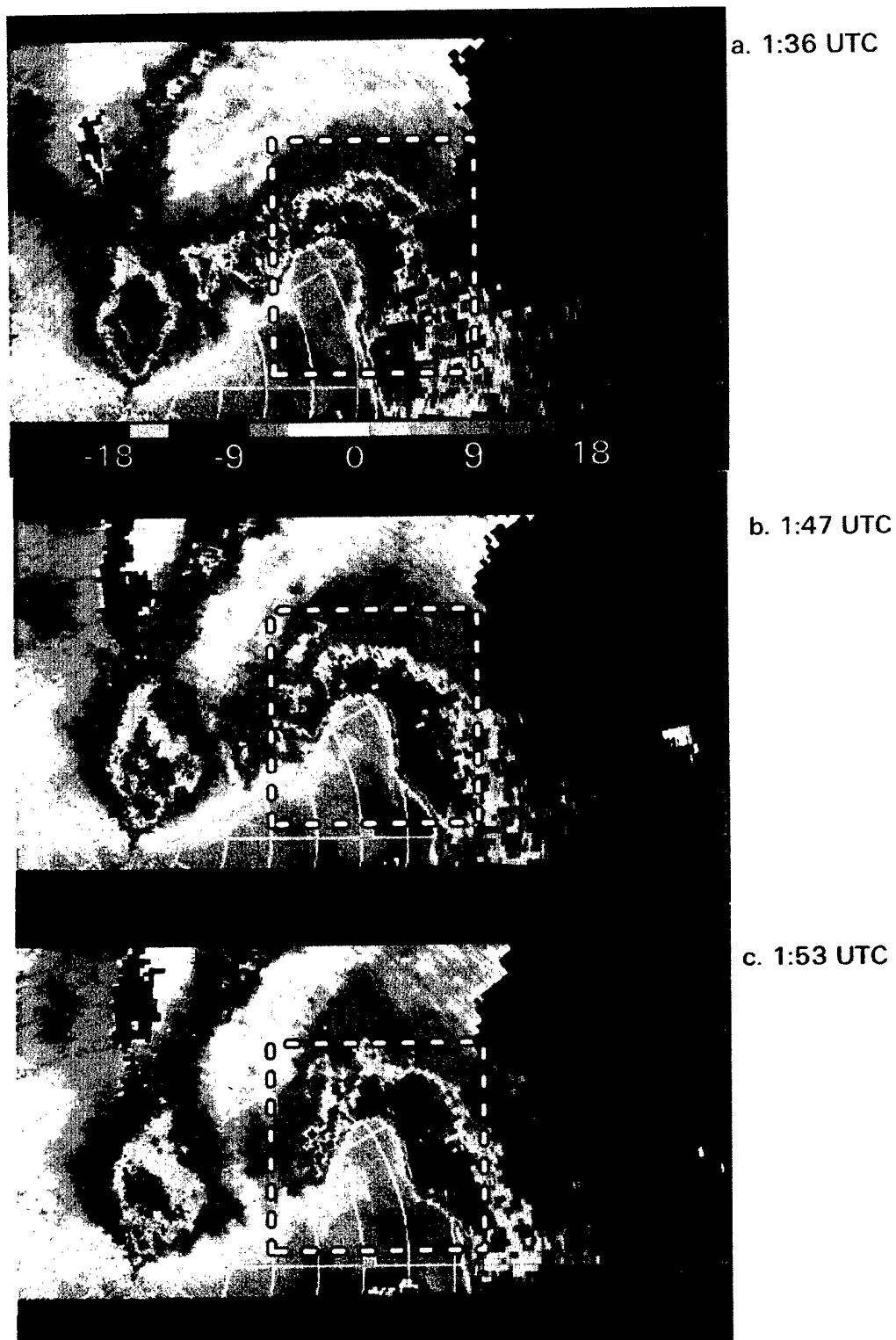


FIG. 5. Doppler velocity images from the  $0.5^\circ$  elevation angle at (a) 0136, (b) 0147, and (c) 0153 UTC. The white box corresponds to the region shown in Fig. 2 and the boxed region in Fig. 4.

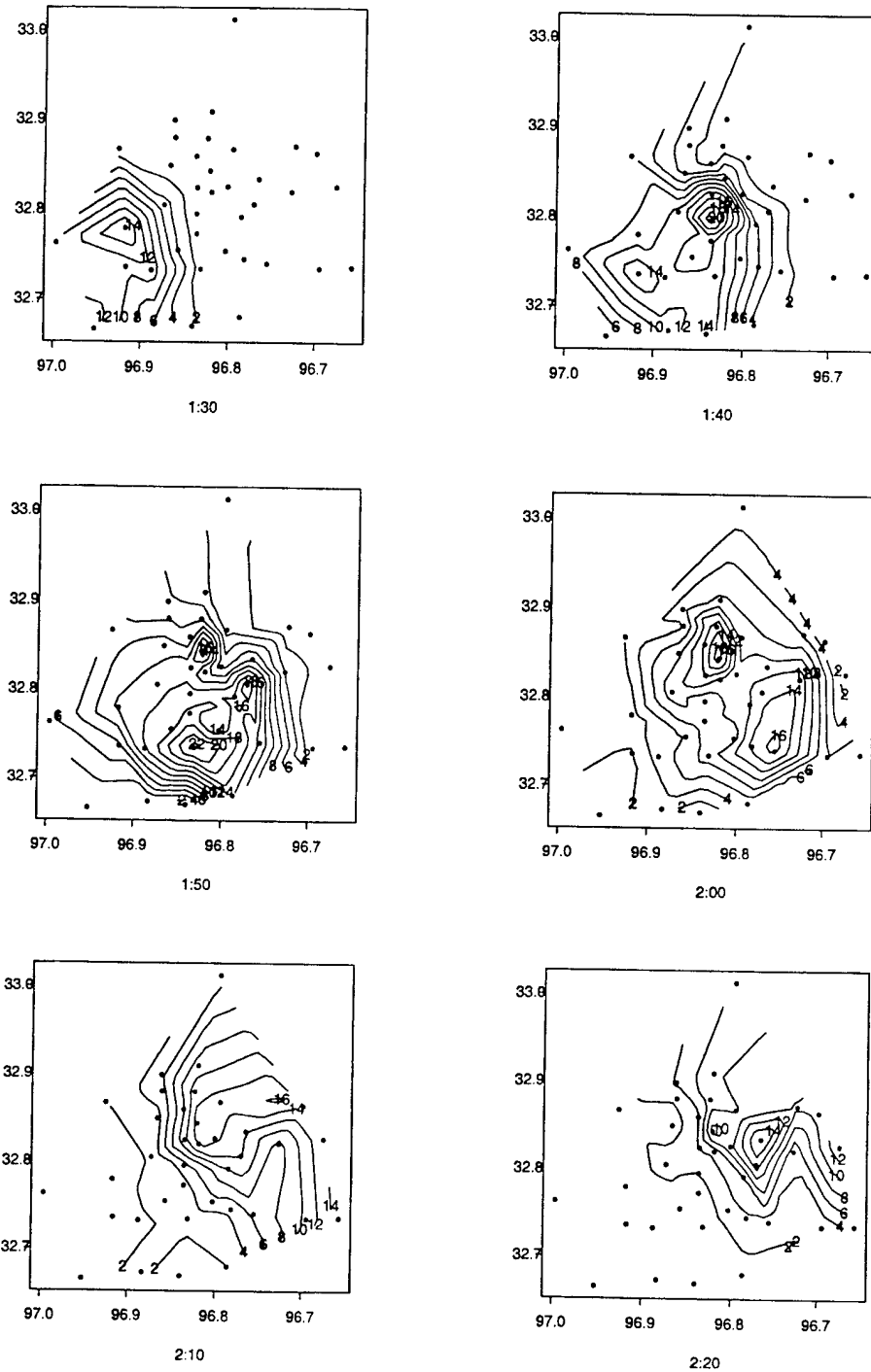


FIG. 6. Rainfall-rate ( $\text{cm h}^{-1}$ ) contour maps for the Dallas metropolitan area during the period of 0125–0220 UTC 6 May (corresponding to the area in Fig. 2). Each contour map is derived from 5-min rainfall-rate observations at gauges (denoted by dots). The time period shown below each map is the ending time of the 5-min period for the rainfall field.

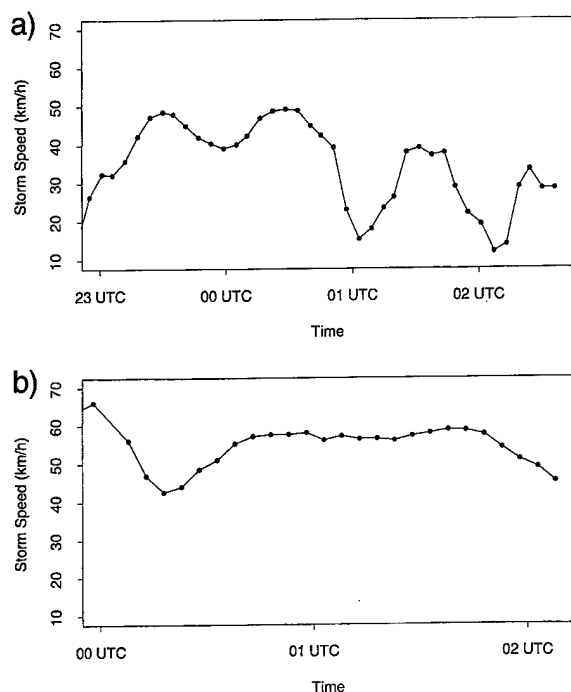


FIG. 7. Storm speed ( $\text{km h}^{-1}$ ) for (a) the Dallas Supercell from 2300 UTC 5 May to 0230 UTC 6 May 1995 and (b) the Orlando Supercell from 0000 to 0200 UTC 26 Mar 1992.

centrated in a small area of central Dallas, with two maxima of 120 mm on the western boundary and south-eastern boundary of Turtle Creek. Spatial gradients of 50 mm over a distance of approximately 4 km separated the area of heaviest rainfall from the large swath of 50–70-mm storm total accumulations. The local maxima exceeding 120 mm on the western and southeastern boundary of Turtle Creek were associated with different structural elements of the Dallas Supercell, as detailed below.

Stream-gauging observations in Turtle Creek provided a 5-min record of water surface elevation. A discharge hydrograph (Fig. 3) was constructed from the stage observations using stage–discharge relations developed from observations reported in Band et al. (1982). The peak discharge at 20- $\text{km}^2$  drainage area was  $400 \text{ m}^3 \text{ s}^{-1}$ , resulting in a unit discharge, that is, discharge divided by drainage area, of  $20 \text{ m}^3 \text{ s}^{-1} \text{ km}^{-2}$ . The peak unit discharge can also be expressed as a runoff rate of  $60 \text{ mm h}^{-1}$ , which provides useful comparison with basin-averaged rainfall-rate time series (Fig. 3). The lag time (i.e., the time difference between time centroid of rainfall and peak discharge) for Turtle Creek at 20- $\text{km}^2$  scale was approximately 1.2 h. The lag time provides a useful timescale for analysis of space–time variability of rainfall over the catchment. For the 20- $\text{km}^2$  drainage basin of Turtle Creek, rainfall separated by more than 1.2 h will not contribute synchronously to the peak at the basin outlet. The lag time

for a drainage basin can be viewed as an upper bound on the timescales of rainfall distribution that are relevant to flood magnitudes at the basin outlet.

Volume-scan reflectivity and Doppler velocity fields (Figs. 4 and 5) for the period of 0130–0215 UTC illustrate storm-scale evolution during the period of heavy rainfall in Dallas. The links between storm structure and evolution and rainfall distribution can be inferred from 5-min rainfall fields derived from the Dallas mesonet rain gauge observations (Fig. 6). Combining the information from these analyses leads to the following conclusions.

- 1) Between 0130 and 0140 UTC, the key elements of storm structure (Figs. 5 and 4c) included an inflow notch, with inbound Doppler velocities greater than  $25 \text{ m s}^{-1}$  at the  $0.5^\circ$  elevation angle, a “precipitation cascade” centered at the apex of the inflow region and which drapes around the inflow region; a rear-flank downdraft (RFD) region, most clearly seen as the near-circular region of outbound Doppler velocities adjacent to the inflow notch and squall line; and the squall line, with a line of reflectivity values greater than 60 dBZ. The precipitation cascade is linked with the forward-flank downdraft of the supercell [see Lemon and Doswell (1979) and Weisman and Klemp (1986) for classical models of supercell thunderstorms]. At 0132 UTC (Fig. 4c) there is a region of lower reflectivity values at the southwestern boundary of Turtle Creek separating peak reflectivities in the precipitation cascade from those in the RFD.
- 2) Rainfall analyses for the 5-min period ending at 0150 UTC (Fig. 6) show a region of extreme rainfall rates to the rear of the RFD. A small region of increased rainfall rates is located to the northwest and is centered at approximately  $32.85^\circ\text{N}$ ,  $96.82^\circ\text{W}$ . The largest 5-min rainfall rates for the event occurred in the RFD region along a 10-km southwest-to-northeast-oriented swath. Low-level inflow to the storm peaked between 0136 and 0147 UTC (Fig. 5 and additional images that are not shown).
- 3) At 0200 UTC, similar rainfall structure prevailed, with two key additional observations. The RFD region has moved, whereas the region of increased precipitation to the north has not (Figs. 4–6). Extreme rainfall rates for the northern region have expanded along the western margin of the Turtle Creek catchment.
- 4) From 0145 to 0220 UTC, the RFD moved at a speed of  $30 \text{ km h}^{-1}$ , the squall line (tracking the leading edge of the 0-Doppler velocity boundary) moved at  $60 \text{ km h}^{-1}$ , and the precipitation cascade remained virtually stationary. Motion of these three storm elements was closely related to the space–time distribution of flood-producing rainfall.

The composite motion of the supercell was computed from storm-tracking analyses of WSR-88D reflectivity

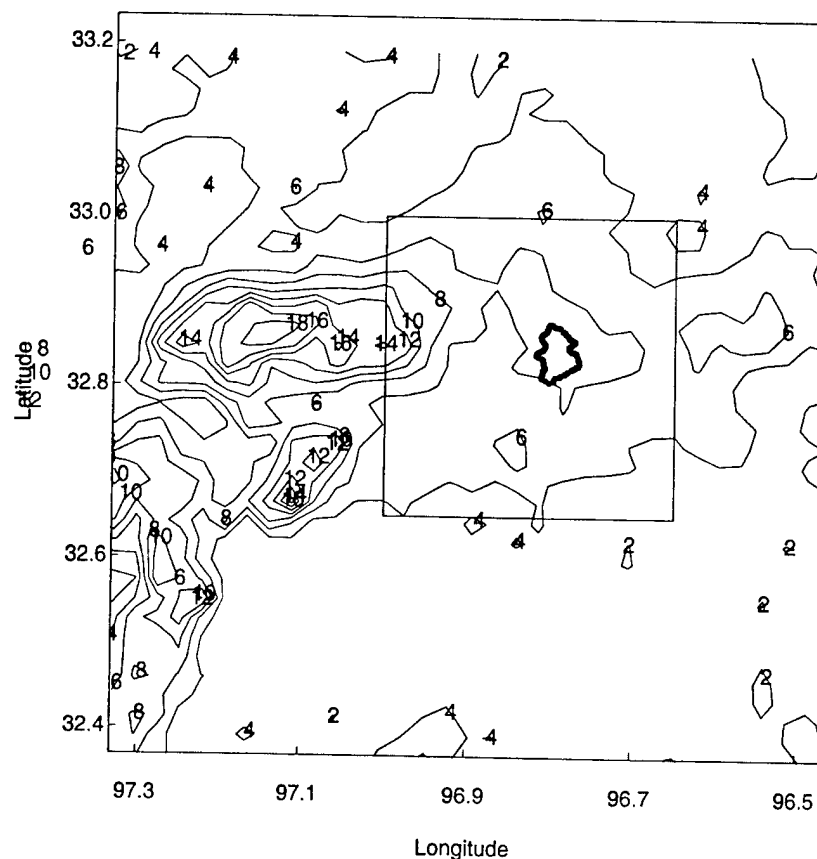


FIG. 8. Storm total rainfall (cm) field (2000 UTC 5 May–0400 UTC 6 May 1995) derived from volume-scan WSR-88D reflectivity observations using the WSR-88D  $Z$ - $R$  relationship ( $Z = 300R^{1.4}$ ) and a 55-dBZ reflectivity threshold. The box corresponds to the region illustrated in Fig. 2, and the basin boundary of Turtle Creek is outlined as in Fig. 2.

observations. The motion vector is obtained from storm locations computed for each volume scan. Storm locations are the surface projection of the 3D center of mass of the storm (Dixon and Wiener 1993). The most important element of the analysis is that from 0130 to 0215 storm speed of the supercell decreased from 35 to less than  $15 \text{ km h}^{-1}$  (Fig. 7a). As noted above, storm speed from 0130 to 0215 UTC included differential rates of motion from the precipitation cascade and rear-flank downdraft. The net effect of storm speed was to increase rainfall accumulations dramatically at a 5–30-min time-scale.

The largest rainfall rates at 5-, 15-, and 60-min time intervals from the Dallas rain gauge network were, respectively, 231, 210, and  $115 \text{ mm h}^{-1}$  (no corrections have been made for systematic underestimation of rainfall rates, which for tipping bucket gauges can be significant at high rainfall rates; see Groisman and Legates 1994). The peak rainfall rates at 5-, 15-, and 60-min time intervals are respectively 87%, 110%, and 115% of the 100-yr rainfall rates for Dallas at these time intervals (265, 191, and  $100 \text{ mm h}^{-1}$ ; see Frederick et al. 1977). The peak 60-min rainfall effectively provides the

storm total rainfall for the event. Rainfall rates from the Dallas Supercell were most extreme at the 15–60-min time period, which is close to the lag time of the  $20\text{-km}^2$  Turtle Creek watershed. To place the rainfall magnitudes in a broader context, record rainfall observations for the conterminous United States range from 1860  $\text{mm h}^{-1}$  at 1 min (Unionville, MD; 4 July 1956), to 437  $\text{mm h}^{-1}$  at 42 min (Holt, MO; 22 June 1947) and 203  $\text{mm h}^{-1}$  at 2.75 h (D'Hanniss, TX; 31 May 1935).

Extreme rainfall rates can be obtained through various combinations of (a) large values of storm inflow velocity, humidity, and inflow area; (b) small values of surface rain area; (c) large rates of decrease in cloud water storage; and (d) small losses of water from the storm via evaporation. Surface observations on 5 May (not shown) show that wind speed increased steadily from 4 to  $12 \text{ m s}^{-1}$  during the 4-h period preceding storm arrival and that specific humidity increased from  $8 \text{ g kg}^{-1}$  at 1200 UTC to  $16 \text{ g kg}^{-1}$  immediately prior to storm arrival. Doppler velocity observations at 0136 UTC (Fig. 5) show a 10-km-wide region in the inflow notch of the storm with Doppler velocities that average  $20 \text{ m s}^{-1}$  (inflow is oriented in close to a radial direction

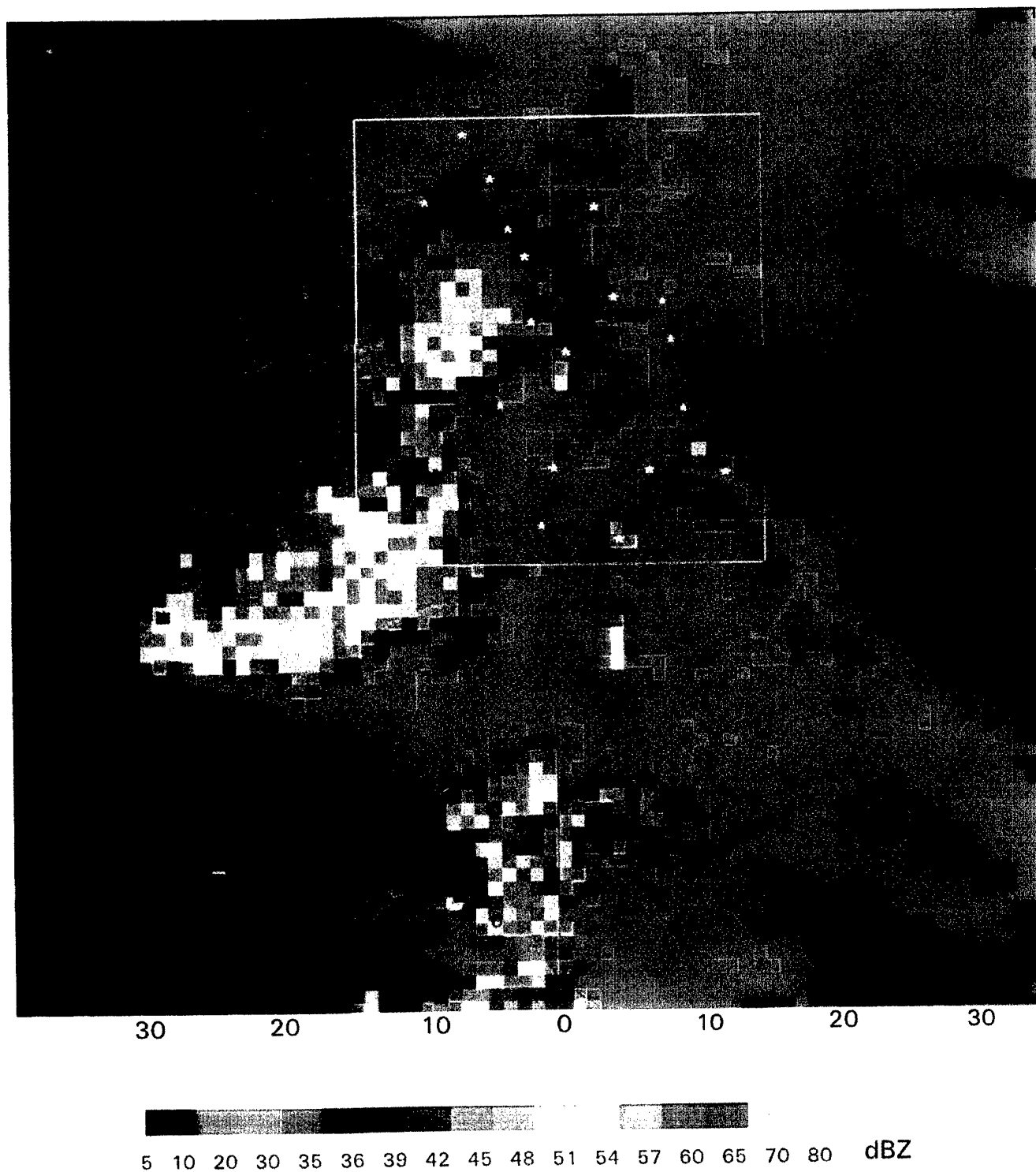


FIG. 9. Reflectivity image (0.5-km elevation) from the Melbourne, FL, WSR-88D at 0143 UTC 26 Mar 1992 illustrating the Orlando Supercell. Range rings are 10 km. The boxed region contains the KSC rain gauge network (Fig. 10), and dots indicate locations of rain gauges.

from the radar). If we take inflow width to be 10 km, inflow depth to be 2 km, inflow velocity to be 20 m  $s^{-1}$ , and specific humidity to be 12 g  $kg^{-1}$ , a cloud water balance would produce a rainfall rate of 104 mm  $h^{-1}$

over 100 km<sup>2</sup>, assuming an efficiency of 50% and no net change in cloud water storage. A doubling of the rainfall rate can be achieved by doubling the product of area, width, and inflow velocity or by decreasing the

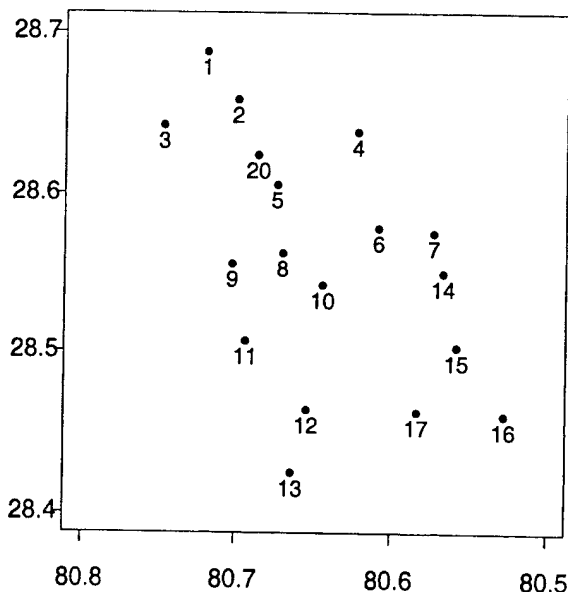


FIG. 10. Locations of rain gauges from the KSC network. Boxed region is the same as that shown in Fig. 9. Gauge numbers are used in time series plots of Fig. 12.

area over which rainfall is distributed from 100 to 50 km<sup>2</sup>. Precipitation efficiency clearly reflects only one aspect of the water budget representation of surface rainfall rates. Relatively low values of precipitation efficiency can be balanced by large values of moisture inflow (Doswell et al. 1996).

Interaction of the supercell with the overtaking squall line appears to have played an important role in the space-time rainfall distribution. Extreme rainfall rates in Dallas were associated with a *dissipating* supercell. Maximum reflectivity values decreased from 77 dBZ at 2300 UTC to 61 dBZ at 0200 UTC. Echo-centroid elevation decreased from 5.8 km above ground level at 2300 UTC to 3 km at 0200 UTC. The decreasing centroid elevation suggests that storage change may have played a role in the water budget of extreme rainfall rates for the Dallas Supercell.

As illustrated in Figs. 4 and 6, the spatial distribution of rainfall rate within the rain area plays an important role in determining maximum point rainfall rates. During the 5-min period of peak rainfall rates ending at 0150 UTC (Fig. 6), rainfall rates that exceeded 50 mm h<sup>-1</sup> covered a region of 427 km<sup>2</sup>. The mean rainfall rate over this region was 113 mm h<sup>-1</sup>. The subareas with rainfall rate that exceeded 100, 150, and 200 mm h<sup>-1</sup> were, respectively, 242, 89, and 7 km<sup>2</sup>.

One of the major obstacles to a better understanding of the role of supercell storms as flood hazards is the difficulty of measuring rainfall for these storms. Neither conventional weather radar observations nor observations from operational rain gauge networks provide a reliable observational basis for analyzing supercell rain-

fall. Analysis based on the standard WSR-88D Next-generation Weather Radar  $Z-R$  relationship ( $Z = 300R^{1.4}$ , where  $Z$  is radar reflectivity and  $R$  is rainfall rate), with a 55-dBZ reflectivity cap and Dallas WSR-88D reflectivity observations shows peak storm total rainfall over Fort Worth instead of Dallas [Fig. 8; see Baek and Smith (1998) for algorithm details and discussion of difficulties in measuring extreme rainfall rates from radar reflectivity observations]. The analysis captures the west-to-east movement of the supercell but does not capture the peak rainfall in Dallas. Reflectivity-based methods for estimating rainfall from radar will often be compromised by hail contamination. The problem with hail contamination can be seen by observing that a 10-mm hydrometeor in a 1-m<sup>3</sup> sample volume has the same reflectivity, 10<sup>6</sup> mm<sup>6</sup> m<sup>-3</sup> (or 60 dBZ), as 10<sup>6</sup> hydrometeors of 1-mm diameter in the same volume. The presence of hail in a radar sample volume can seriously degrade the capability of resolving extreme rainfall rates by radar. Use of the 55-dBZ cap presumes that the sample volume contains a mixture of hail and heavy rainfall. Radar polarimetric measurements (see Zrnić and Ryzhkov 1999) provide significant potential for eliminating hail-contamination problems in estimating rainfall from weather radar.

Operational rain gauge networks are also unable to capture the rainfall distribution from supercell thunderstorms. Rain gauge spacing from conventional networks is inadequate to resolve spatial patterns of rainfall associated with storm structure (as illustrated in Figs. 4–6). Rain gauges from the operational network in the Dallas metropolitan area sampled the periphery of the storm and consequently did not capture the maximum rainfall over Dallas.

### 3. Orlando Supercell: 26 March 1992

The Orlando Supercell of 26 March 1992 (Fig. 9) passed over Orlando, Florida, producing severe hail damage, and then passed over the Kennedy Space Center (KSC) mesonet (Fig. 10). For the 26 March 1992 storm, 18 of 20 rain gauges were operational and provided rainfall-rate observations at 1-min time interval. The largest 1-min rainfall rate measured at the KSC mesonet during the period of 1988–93 of 330 mm h<sup>-1</sup> occurred when the Orlando Supercell passed over the network. In this section, structure, motion, and rainfall of the Orlando Supercell are compared with those of the Dallas Supercell.

There were a series of large hail reports associated with the Orlando Supercell from 0000 to 0100 UTC 26 March 1992. The largest report was for a 3-in.-diameter hailstone at approximately 0045 UTC. Maximum reflectivity values for the storm decreased from 76 dBZ shortly before 0000 UTC to 60 dBZ at 0200 UTC. By 0132 UTC (Fig. 11), the RFD region of the supercell had begun to surge ahead of the storm center, beginning the transition from supercell to bow echo (Moller et al.

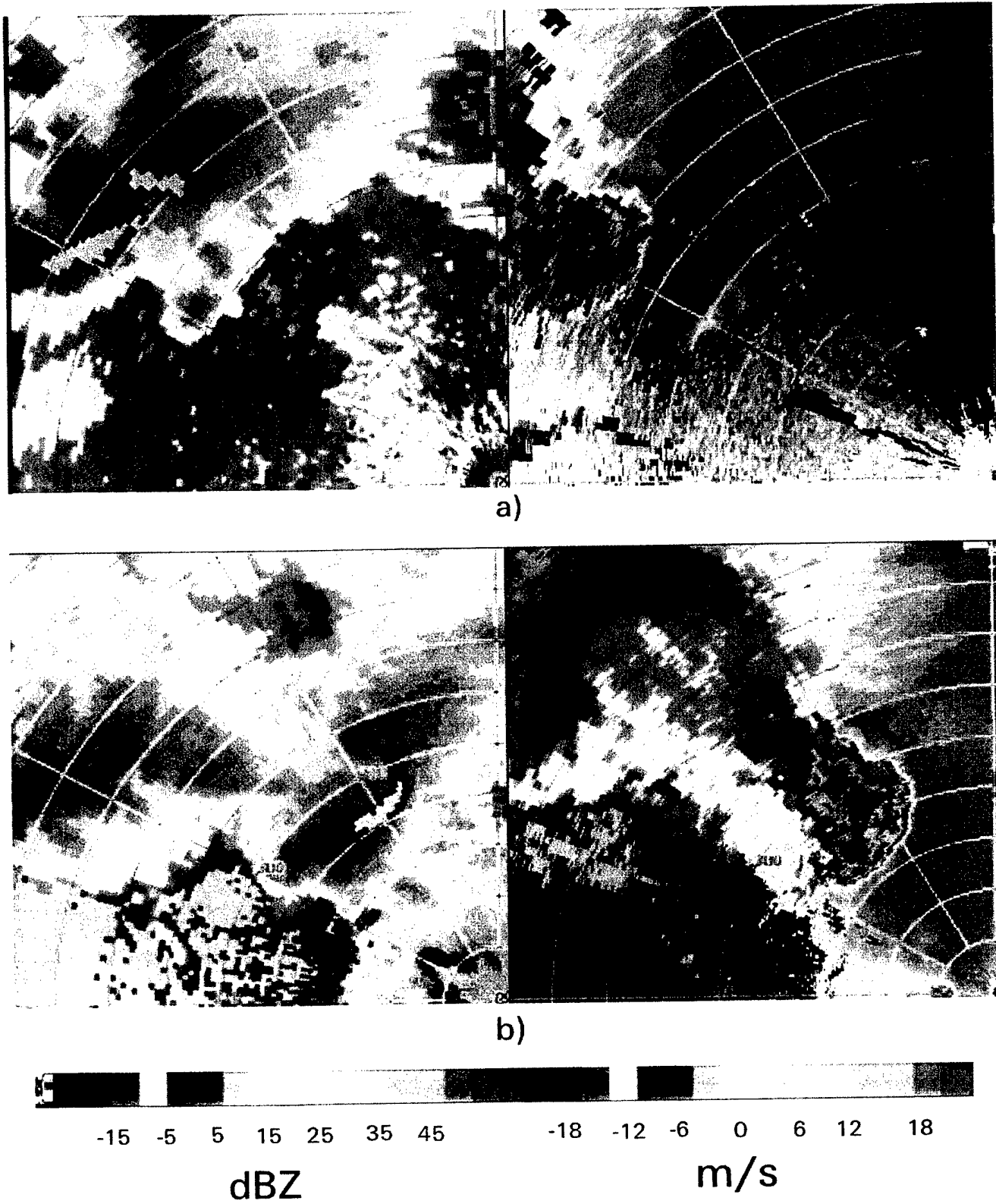


FIG. 11. Reflectivity and Doppler velocity observations from the Melbourne WSR-88D at (a) 0041 UTC 26 Mar and (b) 0132 UTC 26 Mar 1992.



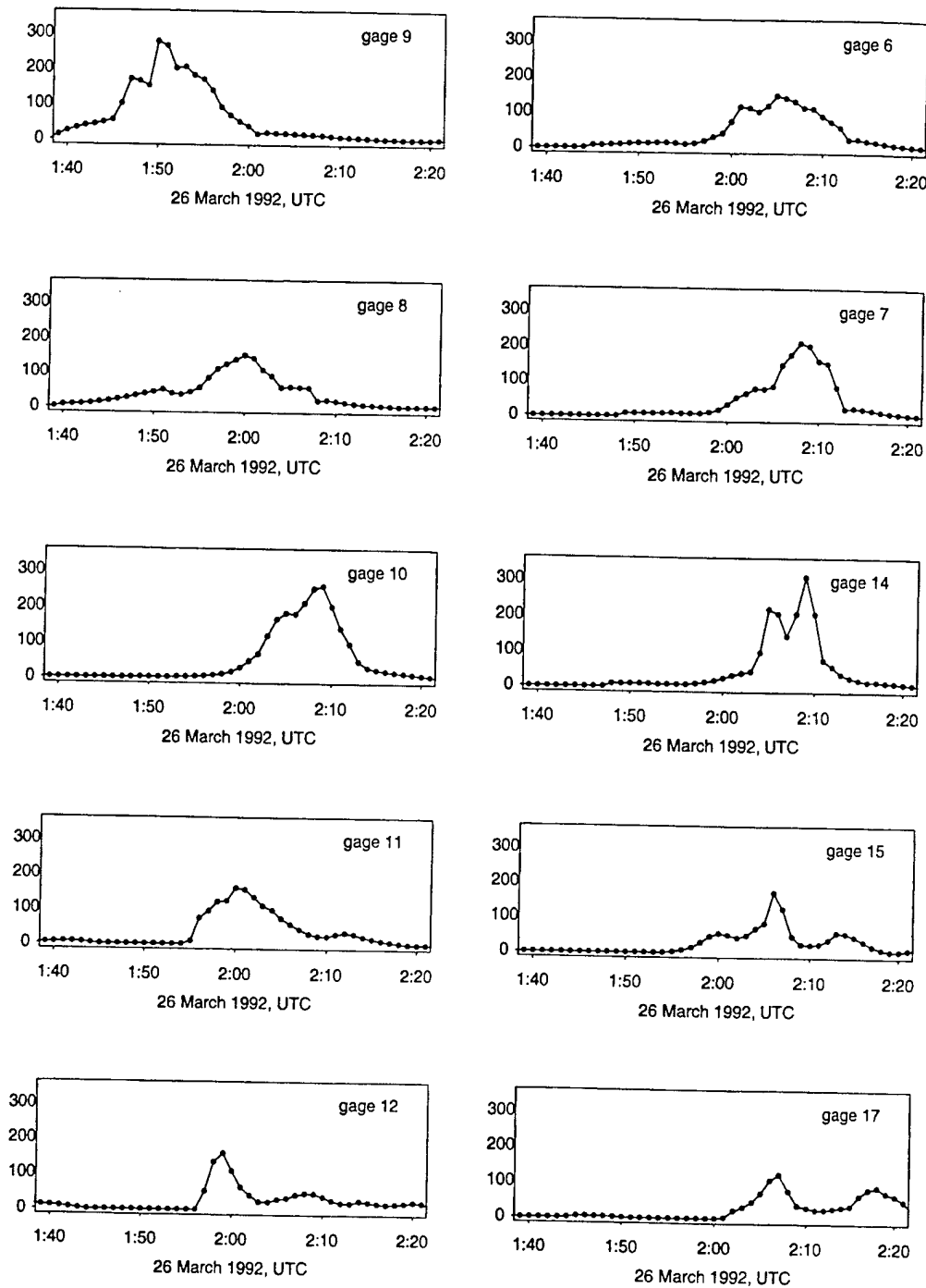


FIG. 12. Time series of 1-min rainfall rate ( $\text{mm h}^{-1}$ ) for 10 rain gauges from the KSC network. Gauge numbers given in the upper-right-hand corner of each time series plot correspond to the identification numbers in Fig. 10.

1994; Przyblinski 1995). Storm structure of the Orlando Supercell at 0145 UTC (Fig. 9), immediately preceding the time when extreme rainfall was observed at the KSC mesonet, included a precipitation cascade and an RFD region. The KSC mesonet sampled rainfall from the

precipitation cascade with only the southernmost gauges sampling rainfall from the expanding RFD region.

Rain gauge observations from the KSC network (Fig. 12) illustrate the role of storm motion for space-time rainfall variability. A major control of space-time rain-

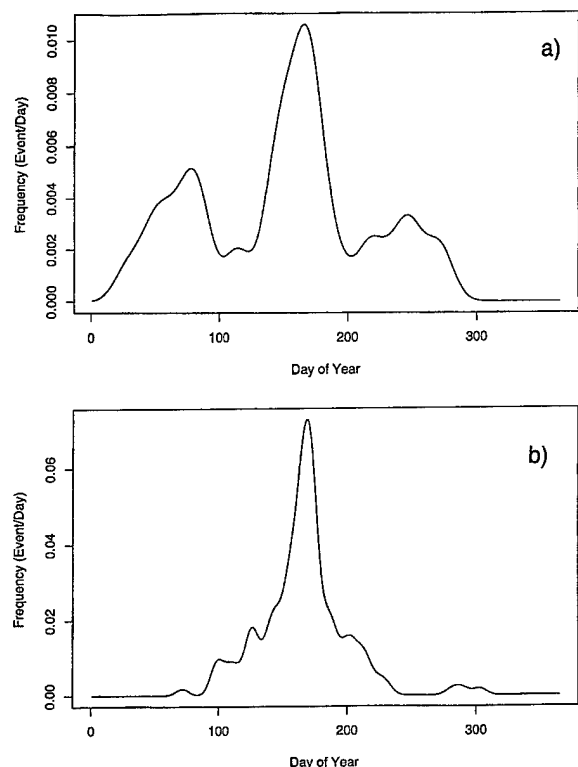


FIG. 13. (a) Seasonal frequency (events per day) of flood peaks in Maple Creek. (b) Seasonal frequency (events per day) of tornadoes for counties drained by Maple Creek.

fall variability is the west-to-east motion of the precipitation-cascade region through the center of the KSC network. The west-to-east progression of the heavy-rain region from 0150 to 0210 is clearly seen in the time series of rainfall progressing from gauge 9 to gauge 8 to gauge 10 (Fig. 12). Interpretation of space-time rainfall variability as resulting from a steady-state storm of fixed size moving at uniform speed is, however, not consistent with analyses in Fig. 12. Most notable, from 0205 until 0215 the eastern gauges 7 and 14 peak synchronously with the central gauge 10 at rain rates larger than  $200 \text{ mm h}^{-1}$ . Superimposed on variability associated with mean storm motion is large temporal variability associated with storm evolution and spatial variability associated with storm microstructure.

Rainfall rates for the Orlando Supercell were most exceptional at the shortest timescales (1–5 min). Peak rainfall rates ranged from  $330 \text{ mm h}^{-1}$  at 1 min to  $222 \text{ mm h}^{-1}$  at 5 min,  $136 \text{ mm h}^{-1}$  at 15 min and  $37 \text{ mm h}^{-1}$  at 60 min. The maximum rainfall rate at 5-min time interval ( $222 \text{ mm h}^{-1}$ ) was 85% of the 100-yr, 5-min rainfall rate for the region (Frederick et al. 1977; precipitation frequency estimates are not provided at timescales of less than 5 min). At 15-min timescales, the maximum rainfall rate ( $136 \text{ mm h}^{-1}$ ) was 70% of the 100-yr rainfall rate for the east coast of Florida. The

maximum hourly rainfall rate was not exceptional for Florida.

Storm speed for the Orlando Supercell is contrasted in Fig. 7b with that of the Dallas Supercell (Fig. 7a). Storm speed remained nearly constant at approximately  $55 \text{ km h}^{-1}$ , unlike the Dallas Supercell, for which storm speed slowed dramatically following merger with the trailing squall line. Because of steady, rapid storm motion, extreme rainfall rates over the KSC rain gauge network were limited to very short time intervals (1–5 min) and storm total accumulations were modest (less than 50 mm).

#### 4. Nebraska: 20–21 June 1996

A series of tornadic supercell thunderstorms tracked through eastern Nebraska on 20–21 June 1996, producing record flooding at a number of U.S. Geological Survey (USGS) stream-gauging stations. In this and the following section, attention shifts from storm systems that produce extreme floods at small basin scales ( $<20 \text{ km}^2$ ) to those that produce extreme floods at larger spatial scale ( $>100 \text{ km}^2$ ). Analyses presented in this section are based largely on WSR-88D observations and stream-gauging observations. The focus of these analyses is the Pebble Creek watershed, for which virtually all rainfall was associated with supercell thunderstorms. Pebble Creek, located in eastern Nebraska, has a drainage area of  $528 \text{ km}^2$ . It is bounded on the west by Maple Creek, a  $1165\text{-km}^2$  catchment with a stream-gauging record of more than 40 yr.

The long-term observed frequency of flooding in eastern Nebraska is characterized by a sharp peak in seasonal flood frequency (Fig. 13a, based on Maple Creek annual flood peak observations) during late June. June storms in eastern Nebraska are prominently represented in the occurrence of catastrophic rainfall in small areas of the United States. Three of 25 storms with measured rainfall exceeding 50% of probable maximum precipitation for the United States east of the Rocky Mountains (6-h duration,  $10\text{-mi}^2$  area) occurred in and near Maple and Pebble Creeks (Riedel and Schreiner 1980; Foufoula-Georgiou and Wilson 1990).

The seasonal occurrence of tornadoes (Fig. 13b) for the counties in and adjacent to Maple and Pebble Creeks exhibits a sharp late-June peak, corresponding in time with the peak in flood occurrence. The joint occurrence of flood events in Maple Creek (based on the partial-duration flood record series) and tornadic thunderstorms was examined by determining the flood events in Maple Creek for which a tornado report occurred the previous day (based on tornado reports for counties which Maple Creek drains). During the 1990s, there were seven flood events that could be linked in this manner to tornadoes. The count drops to three in the 1980s, one during the 1970s, four during the 1960s, and none in the 1950s. The increase in incidence of floods that are linked to tornadoes over time is probably related to increased de-

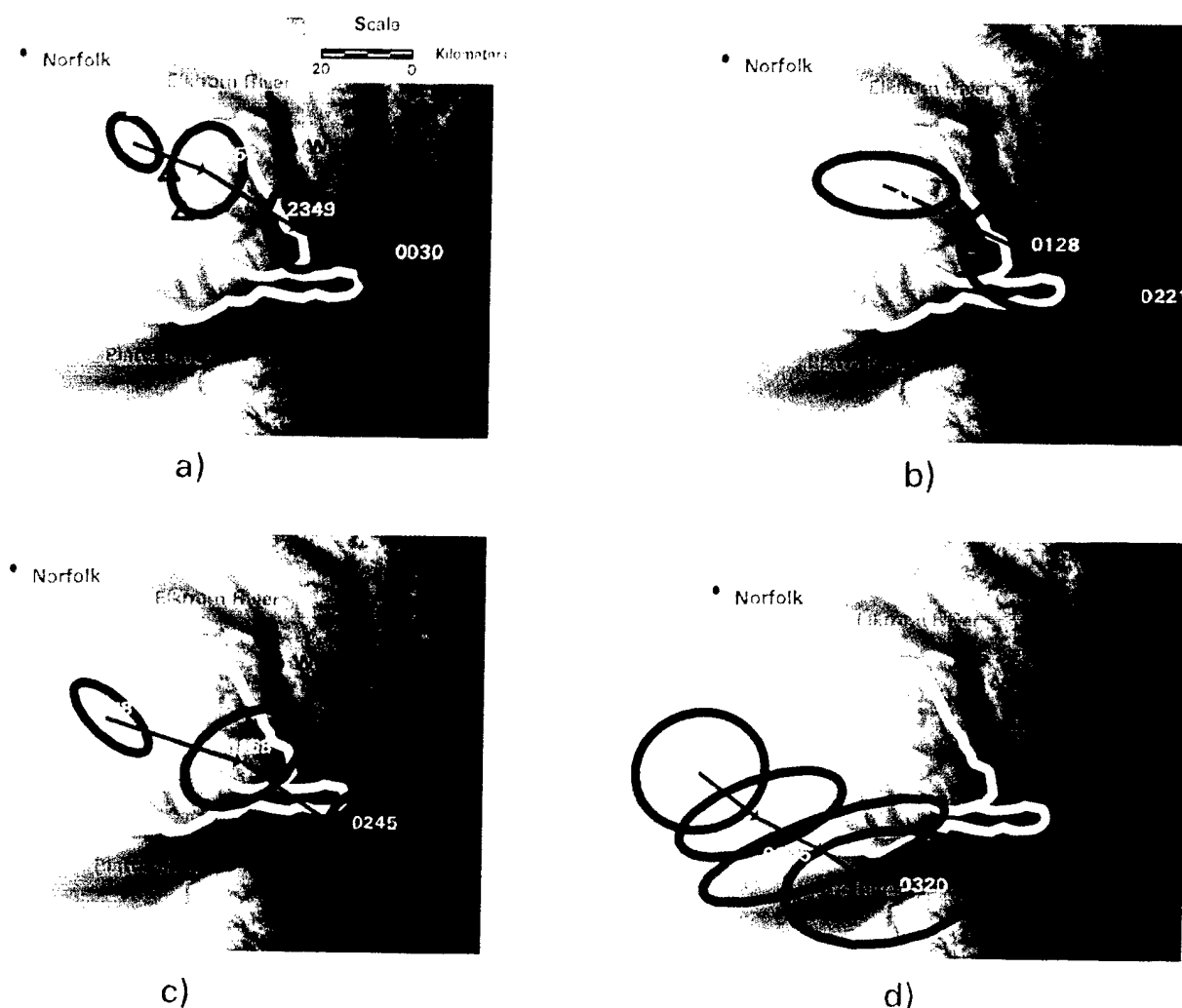


FIG. 14. Structure and motion of four supercell thunderstorms that passed over Maple and Pebble Creeks from 2300 UTC 20 Jun to 0300 UTC 21 Jun 1996. Ellipses contain the 45-dBZ boundary of the storm (in three dimensions). Volume-scan times are shown for each ellipse. Red triangles denote locations of tornado reports. The Pebble Creek basin boundary is outlined in white and is bordered on the southwest by the Maple Creek boundary (see Fig. 13a). The Platte and Elkhorn Rivers are labeled, along with the towns of Norfolk, West Point, and Fremont, NE.

tection of tornadoes with time. Even with these detection problems, it is clear that tornadic thunderstorms are a significant contributor to the flood behavior of the region. Six of the largest 14 flood peaks in the 40-yr Maple Creek record are linked to tornadic storm systems. Included are large floods during major tornado outbreaks on 14 June 1967, 17 June 1984, and 4 June 1992.

Extreme flooding in Pebble Creek on 21 June 1996 resulted from a series of four supercell storms that passed over the basin during a 4-h period from 2300 UTC June 20 to 0300 UTC June 21 (Fig. 14). For each of the storms and for the time periods shown in Fig. 14, storm motion was rapid and toward the southeast. Average storm speed during the periods shown in Fig. 14 was approximately  $60 \text{ km h}^{-1}$ . Each of the storms produced one or more tornadoes (Fig. 14) as they passed over Pebble Creek and Maple Creek. The storm systems that produced extreme rainfall in Dallas and Orlando

were dissipating supercells, in contrast to the Nebraska storms, which produced six tornadoes in and adjacent to Pebble Creek.

Structure and motion of the four storms illustrated in Fig. 14 played a prominent role in determining space-time variability of rainfall viewed from the Eulerian perspective imposed by the Pebble Creek drainage basin (Figs. 15–16). Rainfall analyses are based on WSR-88D volume-scan reflectivity observations and are computed using the standard WSR-88D  $Z-R$  relationship  $Z = 300R^{1.4}$  with a 55-dBZ hail threshold. The fractional coverage of heavy rainfall (Fig. 16) is the fractional basin area with rainfall rates that exceed  $25 \text{ mm h}^{-1}$ . The normalized distance (Fig. 16; see Smith et al. 2001, manuscript submitted to *J. Hydrometeor.*) is the rainfall-rate-weighted distance to the basin outlet (with distance measured along the drainage network) divided by the maximum distance to the outlet. Values close to 0 in-

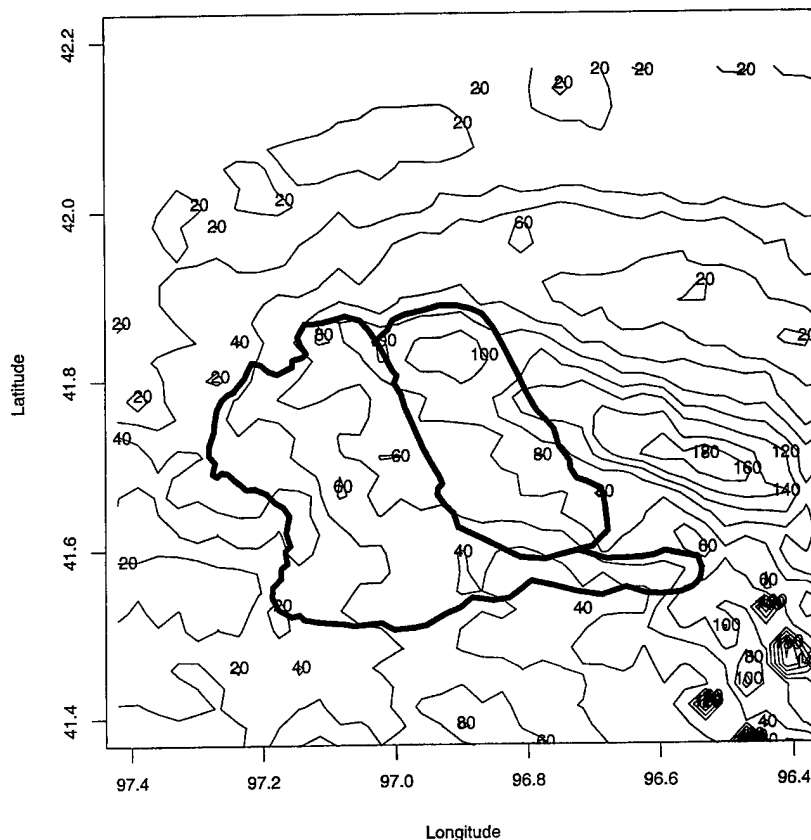


FIG. 15. Storm total rainfall (cm) field (2000 UTC 20 Jun–0600 UTC 21 Jun 1996) derived from volume-scan WSR-88D reflectivity observations using the WSR-88D Z–R relationship ( $Z = 300R^{1.4}$ ) and a 55-dBZ reflectivity threshold. Basin boundaries for Pebble Creek and Maple Creek are shown.

dicate a spatial rainfall distribution concentrated at the outlet of the basin; values close to 1 indicate that rainfall is concentrated at the periphery of the basin. Spatially uniform rainfall (solid line in Fig. 16) results in a value of 0.56 for the normalized distance.

The storm total rainfall distribution (Fig. 15) reflects southeast motion of the four storm elements and the southwestward shift of the tracks of the storms (Fig. 14). Basin-averaged rainfall for Pebble Creek was 85 mm. The rainfall accumulations estimated by radar are large, but not as exceptional as implied by the measured runoff. The basin-averaged runoff of 43 mm resulted in a runoff ratio (i.e., runoff divided by rainfall) greater than 50%. The average runoff ratio for the summer season in Pebble Creek is less than 10%. The 43 mm of runoff is 40% of the average annual runoff for Pebble Creek. Given the difficulties in measuring supercell rainfall by radar described in section 2, it is possible that the rainfall estimates are low.

A key element of the 20–21 June storms for flood production in Pebble Creek was the organization of heavy rainfall into a 4-h time period. The lag time of 10.3 h for the Pebble Creek flood peak was approxi-

mately 2.5 times the duration of extreme rainfall (4 h). Similar timing characterized the Turtle Creek flooding in Dallas at 20-km<sup>2</sup> scale with a lag time of 1.2 h and heavy rainfall duration of approximately 30 min. The temporal maximum in rainfall distribution occurred at approximately 2330 UTC on 20 June and was associated with storm 1 (Fig. 14). Fractional coverage of heavy rainfall reached a maximum of 50% (more than 250 km<sup>2</sup>) at 0120 UTC as storm 2 passed through the watershed (compare with spatial analyses of extreme rain area for the Dallas Supercell from dense rain gauges in section 2). The southeasterly motion of the storm elements resulted in downbasin storm motion, as reflected in decreasing values of the normalized distance (Fig. 16) during the two periods of heaviest rainfall: 2300–0000 UTC and 0030 UTC–0230 UTC. Storm size, motion at 528-km<sup>2</sup> and net duration all contributed to the peak discharge in Pebble Creek scale.

##### 5. Pennsylvania: 18–19 July 1996

The western margin of the central Appalachian region rivals the Edwards Plateau of Texas (as typified by the

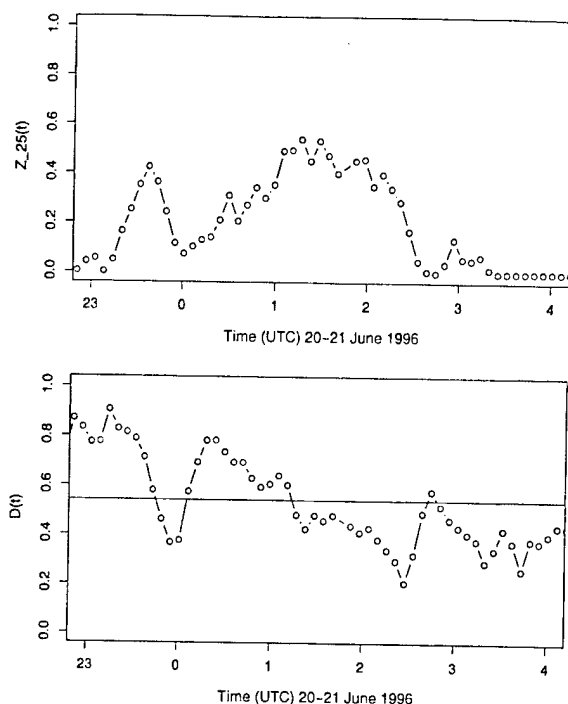


FIG. 16. Time series of (top) fractional coverage of heavy rainfall [ $Z_{25}(t)$ ; fraction of basin area with rain rate  $>25 \text{ mm h}^{-1}$ ] and (bottom) normalized distance function (see text). The solid line denotes the normalized distance for spatially uniform rainfall.

May 1935 D'Hannis storm noted in the introduction; see Costa 1987) for observations of extreme rainfall. The 483-mm rainfall accumulation in 2 h and 10 min on 18 July 1889 at Rockport, West Virginia (Finley 1889; Jennings 1950), was produced by a "terrific thunderstorm, accompanied by torrents of rainfall and vivid lightning" (Finley 1889). The world record rainfall accumulation of 782 mm in 4 h was produced by a thunderstorm complex in western Pennsylvania during the night and morning of 18–19 July 1942. Frequent lightning and hail accompanied the storms (Eisenlohr 1952). Extreme flooding occurred in the Redbank Creek watershed of western Pennsylvania on 18–19 July 1996 in connection with a major tornado outbreak in Pennsylvania (Pearce et al. 1998). The date of occurrence of the 1889, 1942, and 1996 flood events, 18–19 July is not purely fortuitous. There is a sharp seasonal maximum in heavy rainfall occurrence around 18 July (Fig. 17) that coincides with the peak in tornado occurrence for the region (not shown). Other major summer-season flood episodes in the western margin of the central Appalachians are described in Showalter (1941), Erskine (1951), NOAA (1991), and Bosart and Sanders (1981). The July 1996 Redbank Creek storm and flooding are examined in this section as a prototype for summer-season storms that produce catastrophic rainfall along the western margin of the central Appalachians and to

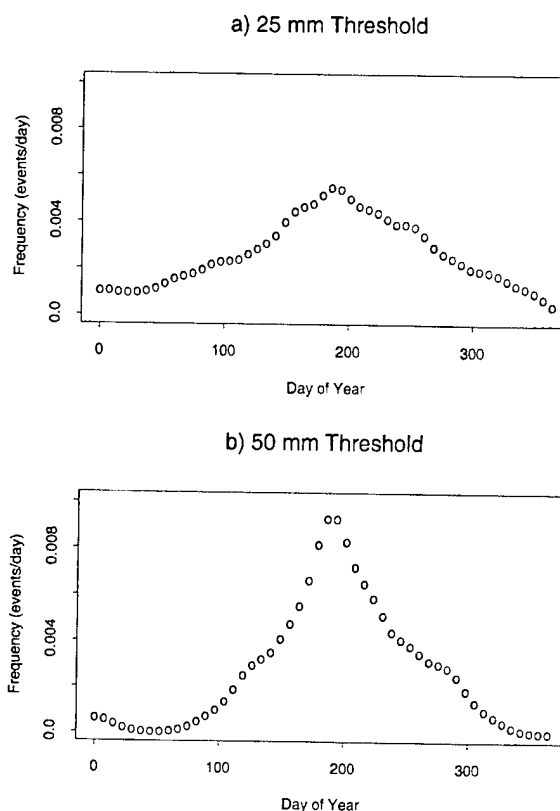


FIG. 17. Rate of occurrence of rainfall accumulations (24 h) exceeding (a) 25 and (b) 50 mm for the Franklin rain gauge in western PA.

illustrate the role of supercell storms in central Appalachian flood occurrence.

The 18–19 July 1996 storm produced the flood of record in Redbank Creek at a drainage area of  $1368 \text{ km}^2$  from a stream-gauging record of more than 70 yr. The July 1996 flood peak of  $1877 \text{ m}^3 \text{ s}^{-1}$  was 33% larger than the previous record peak. The second- and third-largest flood peaks resulted from the rain and snowmelt event of March 1936 and Hurricane Agnes in June of 1972 (note the striking connection to the three-floods paradigm of Miller 1990). The heaviest rainfall from the 1942 Smethport storm fell in upstream reaches of the Allegheny River (Redbank Creek is a tributary to the Allegheny River below the area of heaviest rainfall in 1942). The peak discharge of the Allegheny River at Eldred ( $1425 \text{ km}^2$ ) in July of 1942 was slightly smaller than the peak discharge from Redbank Creek in July of 1996. Peak discharge estimates for the July 1942 event (which are based on an extensive set of slope-area peak measurements conducted by the USGS) were most exceptional at the  $1\text{--}100\text{-km}^2$  scale (Eisenlohr 1952, Costa 1987). Unlike the July 1942 storm (Eisenlohr 1952), there is no record of peak discharges at small basin areas within Redbank Creek for the July 1996 storm.

Extreme flooding in Redbank Creek resulted from a

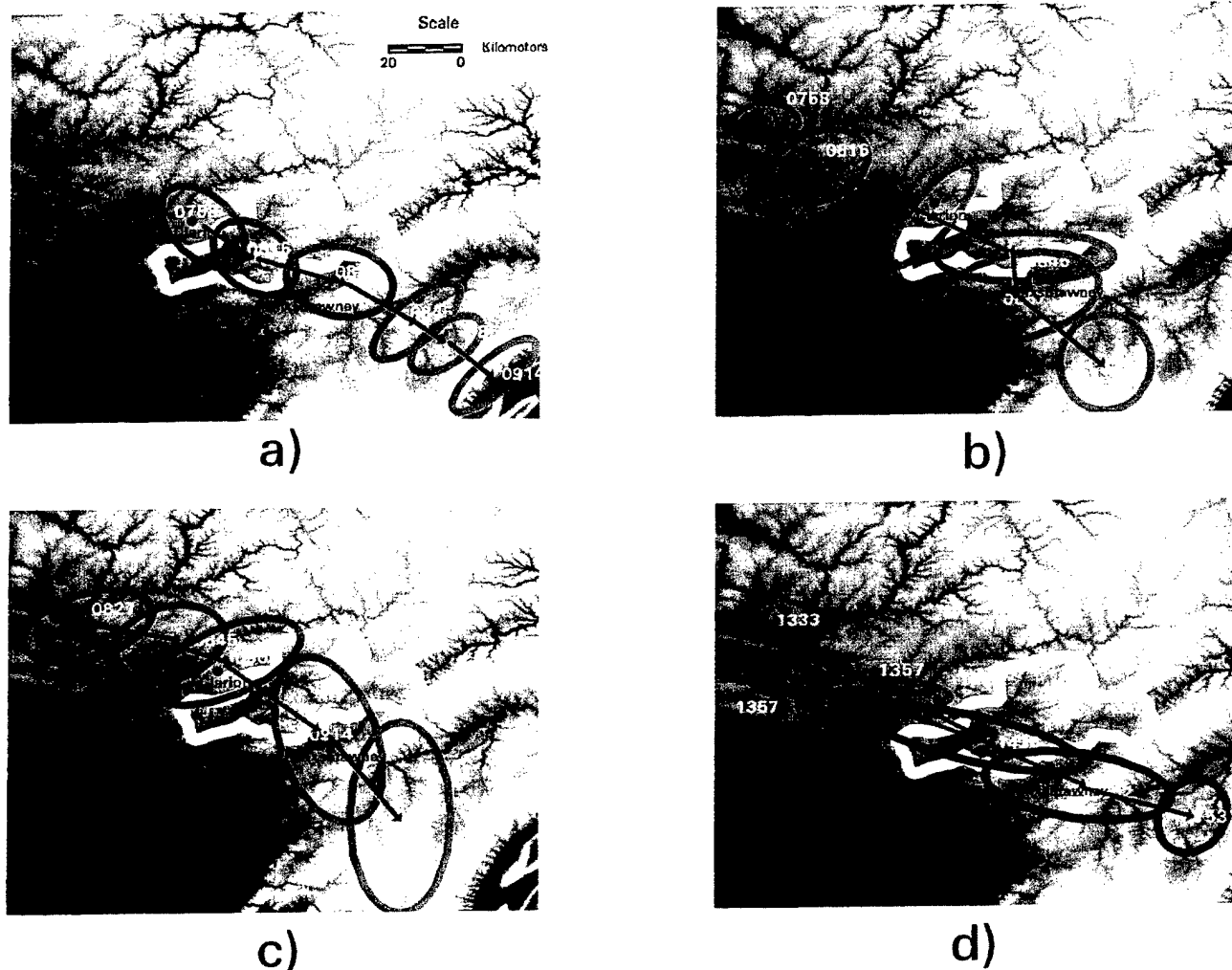


FIG. 18. Structure and motion of four storms that passed over Redbank Creek from 0600 to 1500 UTC 19 Jul 1996. Ellipses contain 45-dBZ boundary of the storm (in three dimensions). Volume-scan times are shown for each ellipse. The Redbank Creek basin boundary is outlined in white. The Allegheny River is labeled, along with the towns of Kittanning, Clarion, and Punxsutawney, PA. The storm ellipse for 1438 in (d) results from the merger of the two 1357 storm elements.

series of storms that passed over the basin from 0600 to 1500 UTC on 19 July 1996. Structure and motion of four storm elements are illustrated (Fig. 18) through a series of storm locations and storm area. Storms 1–3 (Figs. 18a–c) moved along similar paths from Lake Erie southwest over Redbank Creek at storm speeds approaching  $100 \text{ km h}^{-1}$ . Storm 4 (Fig. 18d) moved over the same path but at somewhat lower speed. Storms 1, 2, and 3 produced damaging winds and copious lightning but did not exhibit the mesocyclone signatures of supercell storms. The fourth storm element was a “borderline supercell” (Pearce et al. 1998) and produced a tornado in the Redbank Creek basin at 1330 UTC.

The Redbank Creek storms can be contrasted with the Orlando and Nebraska storms as a third setting in which supercell storms contribute to extreme flooding. The Orlando storm illustrates that an individual storm can produce extreme rainfall rates in small area and short time intervals. The Nebraska storms represent a

setting in which a series of supercell storms produces extreme flooding. The Redbank Creek storms represent a storm setting in which supercell storms combine with other storms to produce extreme floods.

An open question is how peak rainfall rates from supercell storms compare with rainfall rates from other forms of convective storms. For the Redbank Creek storm, a rain gauge at Brookville, Pennsylvania (see location in Fig. 19), was located in the path of all four storms. The storm total rainfall accumulation was 233 mm, of which 33 mm were recorded during a period of approximately 10 min (rainfall rate of  $200 \text{ mm h}^{-1}$ ) from the periphery of the supercell storm. Rainfall accumulations to the southwest of the Brookville gauge likely were significantly larger because of a combination of higher rainfall rates and longer rainfall duration.

The storm total rainfall distribution (Fig. 19) reflects southeast motion of the storm elements. Tracks of the four storm elements cover the same area, producing a

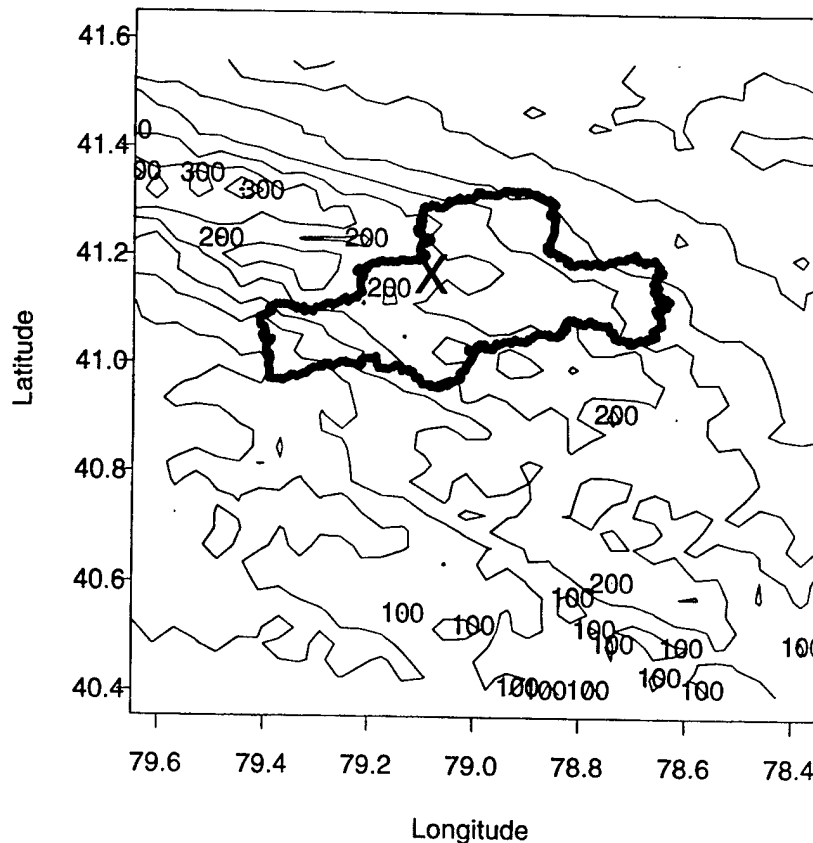


FIG. 19. Storm total rainfall (mm) field (0000–1600 UTC 19 Jul 1996) derived from volume-scan WSR-88D reflectivity observations using the WSR-88D  $Z-R$  relationship ( $Z = 300R^{1.4}$ ) and a 55-dBZ reflectivity threshold. Basin boundaries for Redbank Creek are shown. The location of the Brookville gauge is denoted by an "X."

narrow swath of heavy rainfall oriented from northwest to southeast. During the period of peak fractional coverage of heavy rainfall (Fig. 20) from 0800 to 0915 UTC, heavy rainfall covered an area of more than 500 km<sup>2</sup>. Fractional coverage of heavy rainfall from the supercell storm produced an area of more than 400 km<sup>2</sup> with heavy rainfall in the lower portion of the Redbank Creek watershed. The contribution of the supercell storm was to produce the rapid increase of the Redbank Creek hydrograph to its peak discharge. Extreme rainfall from the supercell storm occurred in the lower portion of the basin (Fig. 20) and fell on terrain that had been moistened by the previous storms of the sequence.

## 6. Summary and observations

There are 10 principal observations from our work.

- 1) The Dallas Supercell resulted in 16 flash-flood deaths in the Dallas metropolitan area and more than \$1 billion in property damages over the Dallas-Fort Worth metroplex. Peak storm total rainfall for Dallas of 120 mm was not exceptional for Texas.
- 2) Rainfall rates from the Dallas Supercell were most exceptional at 15–60-min time intervals. Peak rainfall rates at 5- (231 mm h<sup>-1</sup>), 15- (210 mm h<sup>-1</sup>), and 60-min (115 mm h<sup>-1</sup>) time intervals from the Dallas Supercell were 87%, 110%, and 115% of the 100-yr rainfall rates for the region. Peak rainfall rates for the Orlando Supercell were most extreme at 1–5-min timescales. The peak 1-min rainfall rate was 330 mm h<sup>-1</sup>. The peak 5-min rainfall rate of 222 mm h<sup>-1</sup> is 85% of the 100-yr rainfall rate for east Florida.
- 3) Catastrophic flash flooding in Dallas resulted from three elements of storm motion: (a) motion of the supercell precipitation cascade centered at the inflow notch, (b) motion of the rear-flank downdraft of the supercell, and (c) motion of the trailing squall line. Fundamental differences in rainfall distribution and resulting flood response between the Orlando and Dallas storms are linked to the contrasting storm motion. The uniformly rapid storm motion of the Orlando storm resulted in concentration of heavy rainfall on smaller timescales and space scales than for the Dallas storm.

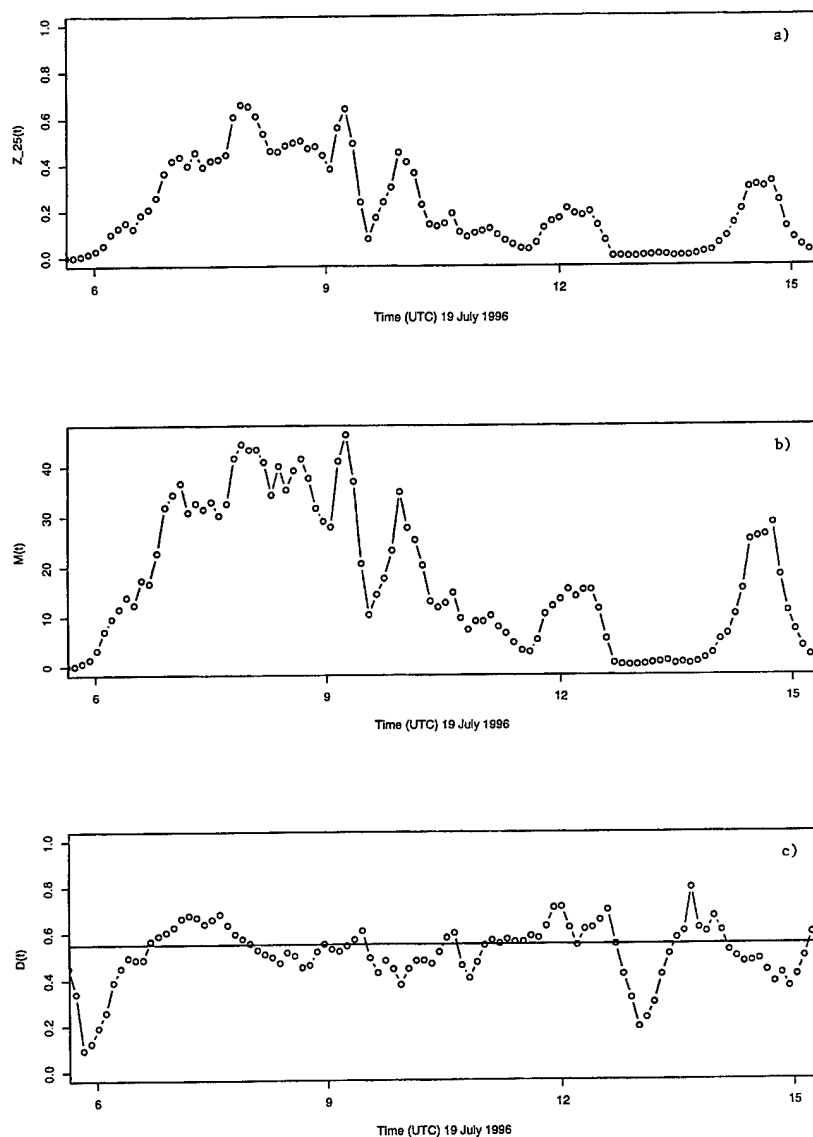


FIG. 20. Time series of (a) fractional coverage of heavy rainfall [ $Z_{25}(t)$ ]; fraction of basin area with rain rate  $>25 \text{ mm h}^{-1}$ ], (b) basin-averaged rainfall ( $\text{mm h}^{-1}$ ), and (c) normalized distance function (see text) for Redbank Creek.

- 4) Spatial variations of rainfall rate were associated with supercell structure for both the Dallas and the Orlando Supercells. For the Dallas Supercell, combined analyses of rain gauge and radar observations showed that distinct maxima in rainfall were organized around the precipitation cascade and rear-flank downdraft.
- 5) Systems of multiple supercell storms can produce extreme flooding at basin scales significantly larger than  $100 \text{ km}^2$ . The 20–21 June 1996 flood episode in eastern Nebraska was produced by a series of tornadic, supercell storms. Four storms tracked over the  $528\text{-km}^2$  Pebble Creek catchment during a period of less than 4 h.
- 6) The flood occurrence behavior of eastern Nebraska has a sharp seasonal maximum around 20 June, which coincides closely with the maximum in tornado occurrence for the region. For Maple Creek, 6 of the largest 14 flood peaks can be linked to tornadic storms.
- 7) The western margin of the Appalachian region has experienced some of the largest measured rainfall accumulations in the world at short time intervals (less than 6 h). All are associated with severe thun-



- derstorms, and the maximum in heavy rainfall for the region is tightly concentrated around 19 July. The 18–19 July 1996 flooding in western Pennsylvania was produced by a series of severe thunderstorms that tracked rapidly from northwest to southeast. The final storm element that passed through Redbank Creek was a tornadic supercell storm.
- 8) For the Orlando and Dallas Supercells, extreme rainfall rates were produced during the dissipating phase of the storm. For the Nebraska storm, extreme rainfall and flooding in Pebble Creek resulted from a succession of supercell storms that produced seven tornadoes in and adjacent to Pebble Creek. Similar, for the Redbank Creek flood episode, flood-producing rainfall and a tornado were produced at the same time.
  - 9) Fundamental rainfall measurement problems exist for supercell storms. Measurements from conventional radar are very useful but are limited in estimating extreme rainfall rates because of problems associated with hail contamination and anomalous raindrop size distributions (relative to those assumed in deriving standard  $Z-R$  relationships). Conventional rain gauge networks do not sample supercell rainfall at relevant space scales and timescales. Radar polarimetric measurements provide a promising avenue for overcoming the hail problem and problems associated with anomalous raindrop spectra (Zrnić and Ryzhkov 1999).
  - 10) Supercell thunderstorms play a significant role in determining the occurrence pattern of extreme rainfall rates at short timescales and small spatial scales for much of the United States east of the Rocky Mountains. These storms are of particular significance for urban hydrological behavior because of the fundamental role of extreme 1–30-min rain rates for design and water management problems in urban regions. As noted above, it is difficult to assess the climatological role of supercell storms from radar and conventional rain gauge networks. New observing systems and novel analysis procedures are needed to characterize the contributions of these storms to the occurrence of extreme rainfall precisely.
- Acknowledgments.** This research was funded in part by the U.S. Army Research Office (Grant DAAD19-99-1-0163), the National Science Foundation (Grant EAR-99-09696), NASA (Grant NAG5-7544), and NWS. This support is gratefully acknowledged. The comments and suggestions of an anonymous reviewer were most helpful in revising the manuscript.
- ### REFERENCES
- Baeck, M. L., and J. A. Smith, 1998: Estimation of heavy rainfall by the WSR-88D. *Wea. Forecasting*, **13**, 416–436.
- Band, L. F., E. Schroeder, and B. Hampton, 1982: Techniques for estimating magnitude and frequency of floods in the Dallas metropolitan area. Water Resources Investigation Rep. 82-18, U.S. Geological Survey, 55 pp.
- Bosart, L. F., and F. Sanders, 1981: The Johnstown flood of July 1977: A long-lived convective system. *J. Atmos. Sci.*, **38**, 1616–1642.
- Costa, J. E., 1987: Hydraulics and basin morphometry of the largest flash floods in the conterminous United States. *J. Hydrol.*, **93**, 313–338.
- Cotton, W. R., and R. A. Anthes, 1989: *Storm and Cloud Dynamics*. Academic Press, 883 pp.
- Dalrymple, T., 1937: Major Texas floods of 1935. U.S. Geological Survey Water-Supply Paper 796-G, 287 pp.
- Dixon, M., and G. Wiener, 1993: TITAN: Thunderstorm Identification, Tracking, Analysis, and Nowcasting—a radar-based methodology. *J. Atmos. Oceanic Technol.*, **10**, 785–797.
- Doswell, C. A., III, 1998: Seeing supercells as heavy rain producers. Preprints, *14th Conf. on Hydrology*, Dallas, TX, Amer. Meteor. Soc., 73–79.
- , and D. W. Burgess, 1993: Tornadoes and tornadic storms: A review of conceptual models. *The Tornado: Its Structure, Dynamics, Hazards and Prediction*, *Geophys. Monogr.*, No. 79, Amer. Geophys. Union, 161–172.
- , H. E. Brooks, and R. A. Maddox, 1996: Flash flood forecasting: An ingredients-based methodology. *Wea. Forecasting*, **11**, 560–581.
- Eisenlohr, W. S., Jr., 1952: Floods of July 18, 1942 in north-central Pennsylvania. U.S. Geological Survey Water-Supply Paper 1134-B, 100 pp.
- Erskine, H. M., 1951: Flood of August 4–5, 1943, in central West Virginia. U.S. Geological Survey Water-Supply Paper 1134-A, 47 pp.
- Finley, J. P., 1889: Local storms. *Mon. Wea. Rev.*, **17**, 184.
- Foufoula-Georgiou, E., and L. L. Wilson, 1990: In search of regularities in extreme rainstorms. *J. Geophys. Res.*, **95**, 2061–2072.
- Frederick, R. H., V. A. Myers, and E. P. Auciello, 1977: Five- to 60-minute precipitation frequency for the eastern and central United States. NOAA Tech. Memo. NWS Hydro-35, 35 pp.
- Groisman, P. Y., and D. R. Legates, 1994: The accuracy of United States precipitation data. *Bull. Amer. Meteor. Soc.*, **75**, 215–227.
- Gupta, V. K., O. Mesa, and D. R. Dawdy, 1994: Multiscaling theory of flood peaks: Regional quantile analysis. *Water Resour. Res.*, **30**, 3405–3421.
- Jennings, A. H., 1950: World's greatest observed point rainfalls. *Mon. Wea. Rev.*, **78**, 4–5.
- Lemon, L. R., and C. A. Doswell III, 1979: Severe thunderstorm evolution and mesocyclone structure as related to tornadogenesis. *Mon. Wea. Rev.*, **107**, 1184–1197.
- Miller, A. J., 1990: Flood hydrology and geomorphic effectiveness in the central Appalachians. *Earth Surf. Proc.*, **15**, 119–134.
- Moller, A. R., C. A. Doswell III, and R. Przyblinski, 1990: High-precipitation supercells: A conceptual model and documentation. Preprints, *16th Conf. Severe Local Storms*, Kananaskis Park, AB, Canada, Amer. Meteor. Soc., 52–57.
- , —, M. P. Foster, and G. R. Woodall, 1994: The operational recognition of supercell thunderstorm environments and storm structures. *Wea. Forecasting*, **9**, 327–347.
- NOAA, 1991: National disaster survey report: 20 June 1990 Shadyside, Ohio, flash flood. National Weather Service, Silver Spring, MD, 43 pp.
- , 1995: National disaster survey report: The Fort Worth–Dallas hailstorm and flash flood of May 5, 1995. National Weather Service, Silver Spring, MD, 39 pp.
- NRC, 1994: *Estimating Bounds on Extreme Precipitation Events*. National Academy Press, 30 pp.
- Pearce, M. L., G. S. Forbes, and E. Ostuno, 1998: Storm-scale aspects of non-classic, borderline supercell thunderstorms over Pennsylvania. Preprints, *16th Conf. on Weather Analysis and Forecasting*, Phoenix, AZ, Amer. Meteor. Soc., 109–111.
- Przyblinski, R. W., 1995: The bow echo: Observations, numerical simulations and severe weather detection methods. *Wea. Forecasting*, **10**, 203–218.
- Riedel, J. T., and L. C. Schreiner, 1980: Comparison of generalized estimates of probable maximum precipitation with greatest ob-

- served rainfalls. NOAA Tech. Rep. NWS 25, Office of Hydrology, Silver Spring, MD, 66 pp.
- Showalter, A. K., 1941: Meteorology of the storm. Flood of August 1935 in the Muskingum River basin, Ohio. C. V. Youngquist and W. B. Langbein, Eds., U.S. Geological Survey Water-Supply Paper 869, 29–31.
- Smith, J. A., 1992: The representation of basin scale in flood peak distributions. *Water Resour. Res.*, **28**, 2993–2999.
- , M. L. Baeck, J. E. Morrison, and P. Sturdevant-Rees, 2000: Catastrophic rainfall and flooding in Texas. *J. Hydrometeor.*, **1**, 5–25.
- Weisman, M. L., and J. B. Klemp, 1986: Characteristics of isolated convective storms. *Mesoscale Meteorology and Forecasting*, P. S. Ray, Ed., Amer. Meteor. Soc., 331–358.
- WMO, 1986: Manual for estimation of probable maximum precipitation. 2d ed. WMO No. 332, 250 pp.
- Woods, R., and M. Sivapalan, 1999: A synthesis of space–time variability in storm response: Rainfall, runoff generation and routing. *Water Resour. Res.*, **35**, 2469–2485.
- Zrnić, D. S., and A. V. Ryzhkov, 1999: Polarimetry for weather surveillance radar. *Bull. Amer. Meteor. Soc.*, **80**, 389–406.



# Scaling Properties of Flood Peaks

JULIA E. MORRISON

*Department of Operations Research and Financial Engineering, Princeton University, Princeton,  
New Jersey 08544*

*E-mail: egorova@princeton.edu*

JAMES A. SMITH

*Department of Civil and Environmental Engineering, Princeton University, Princeton, New Jersey 08544*

*E-mail: jsmith@princeton.edu*

[Received March 10, 2000; Revised January 31, 2001; Accepted February 28, 2001]

**Abstract.** The scaling behavior of flood peak distributions is examined using a statistical model of the spatio-temporal distribution of rainfall and a hydrological model that describes the transformation of rainfall to discharge within a drainage network. Of particular interest is the empirical observation made by a number of investigators that the coefficient of variation (CV) of annual flood peaks for a region increases with drainage area up to drainage areas of approximately  $100 \text{ km}^2$ , and decreases with drainage area for larger drainage basins. This observation is neither consistent with simple scaling models, in which the coefficient of variation does not vary with drainage area, nor multiscaling models, in which the coefficient of variation decreases monotonically with drainage area. Model analyses illustrate that knowledge of the spatial and temporal organization of the rainfall, together with the details of the network structure of the drainage basin, is sufficient information with which to explain the observed behavior of sample CV. The interaction between the temporal variability of rainfall, relative to basin size, and the network structure is shown to be of particular importance.

**Key words.** flood peaks, scaling, coefficient of variation, simulations

## 1. Introduction

The development of methods for estimating flood peak distributions for drainage basins has resulted in the identification of several classical problems in both hydrology and extreme value statistics [9,25]. One important line of research involving these methods is focused on the estimation of flood peak distributions for ungauged drainage basins (see [10]). A point of departure for many studies concerns the role of scale, which for a drainage basin is most often characterized by the drainage area. Two major theories for the areal dependence of the annual flood peak distribution have been developed: the simple-scaling (index-flood) theory, and the multiscaling theory [9,10,25].

To illustrate these two theories, let  $X_A$  be a random variable denoting the magnitude of the annual flood peak in a basin with drainage area  $A$ . The theory of simple scaling suggests that there is a positive function  $g$  such that for any two basins in a particular region with drainage areas  $A_1$  and  $A_2$ , the random variables  $X_{A_1}$  and  $g(A_1/A_2)X_{A_2}$  have the same distribution. Multiscaling theory allows the function  $g$  to be random and statistically

independent of  $X_A$ . Both theories lead to the conclusion that all moments  $\mathbb{E}[(X_A)^m]$  of  $X_A$  exhibit log-log linearity with the drainage basin area  $A$ . Under the assumptions of simple-scaling theory, the slopes of these linear relations change linearly with the order of the moment,  $m$ . In addition, the coefficient of variation (CV), defined as the ratio of the standard deviation of  $X_A$  to the expected value of  $X_A$ , should not change with basin area [9,10]. In the multiscaling framework, however, the CV decreases with increasing basin area [9,10].

Both theories were tested on annual flood peak data for 104 gauging stations in the central Appalachians region in Maryland and Virginia [25]. It was shown that the logarithms of the moments of  $X_A$  do vary linearly with  $\log A$ , although the CVs exhibit a very peculiar dependence on basin area ( $A$ ): CV increases with increasing  $A$  for basins with drainage areas smaller than some critical area  $A_c$ , and decreases with increasing  $A$  for basins larger than  $A_c$ . This effect is shown in Figure 1. For the central Appalachians region, the critical area  $A_c$  was determined to be approximately  $50 \text{ km}^2$ . Subsequently, similar results have been obtained by other investigators for a diverse collection of study sites in the United States and abroad [8,2]. The annual flood peak data from the set of stations in the central Appalachians region has been further studied [12] by fitting it with possible textbook annual flood peak distributions. The generalized extreme value distribution has also been fit to the data from each station, and the scaling behavior of the ensuing parameter estimates studied [14]. In this paper, we focus on the scaling behavior of moments and CVs estimated from the data, without any assumptions about the distribution of annual flood peaks.

It has been suggested that the spatial variability of rainfall is the predominant factor for the decrease of CV at large scales while the structure of the drainage network controls the behavior of CV on smaller scales [7,8,20]. In this paper, the dominant factors influencing the behavior of CV are explored by studying the interaction between the spatial and temporal properties of rainfall and the network structure of river basins. The principal tools used in this study are a statistical model of rainfall, which produces a rainfall field

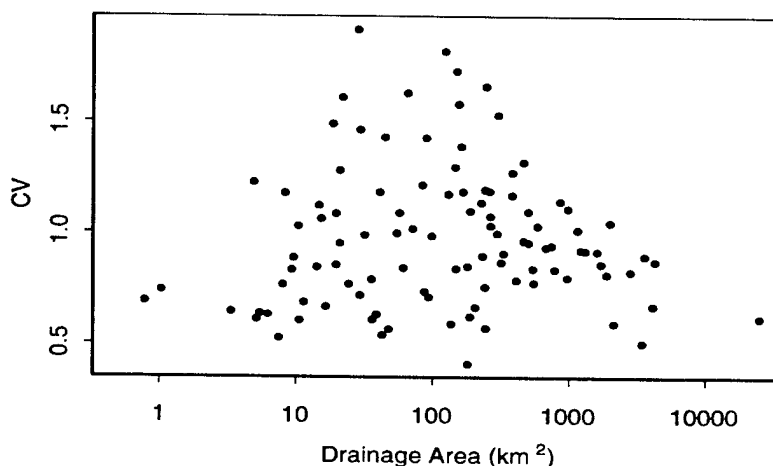


Figure 1. CV—Drainage area relationship for central Appalachian floods [25].

that varies both in space and time, and a simple, network-based drainage model for converting that rainfall field to a discharge at the drainage basin outlet. The study region is a  $\sim 5000 \text{ km}^2$  area in the Edwards Plateau, Texas (see Figure 2 for location). The Edwards Plateau is an interesting study site because it has experienced some of the largest floods in the continental US [4].

Our model assumes that flood peaks are due to storms with exceptionally heavy rainfall ("extreme rainfall events"), and we are interested in computing the peak discharge generated by these heavy storms. Randomly sampled river basins are drawn from the population of river basins in our area of study, and checked to ensure that they are not nested inside one another (that is, none of them is a sub-basin of any other). We can then assume that runoff generated at the outlet of one basin does not influence the runoff from any other basin. Additionally, comparison of the results from different random samples of basins will assure us that they are not an artifact of the basin choice.

Because the rainfall field is a complicated stochastic process, its interaction with the river network makes direct theoretical computation of the flood peak distribution difficult. Instead, numerical simulations are used to infer the properties of the distribution. To simulate the rainfall field, the models of [29] and [18] were combined, leading to the model described in Section 2 (see [11,17–19,23,29,30] for additional discussion of space-time rainfall models). To compute the discharge at basin outlets, a Network Model [26], which depends only on the structure of the network (i.e. two different basins with an

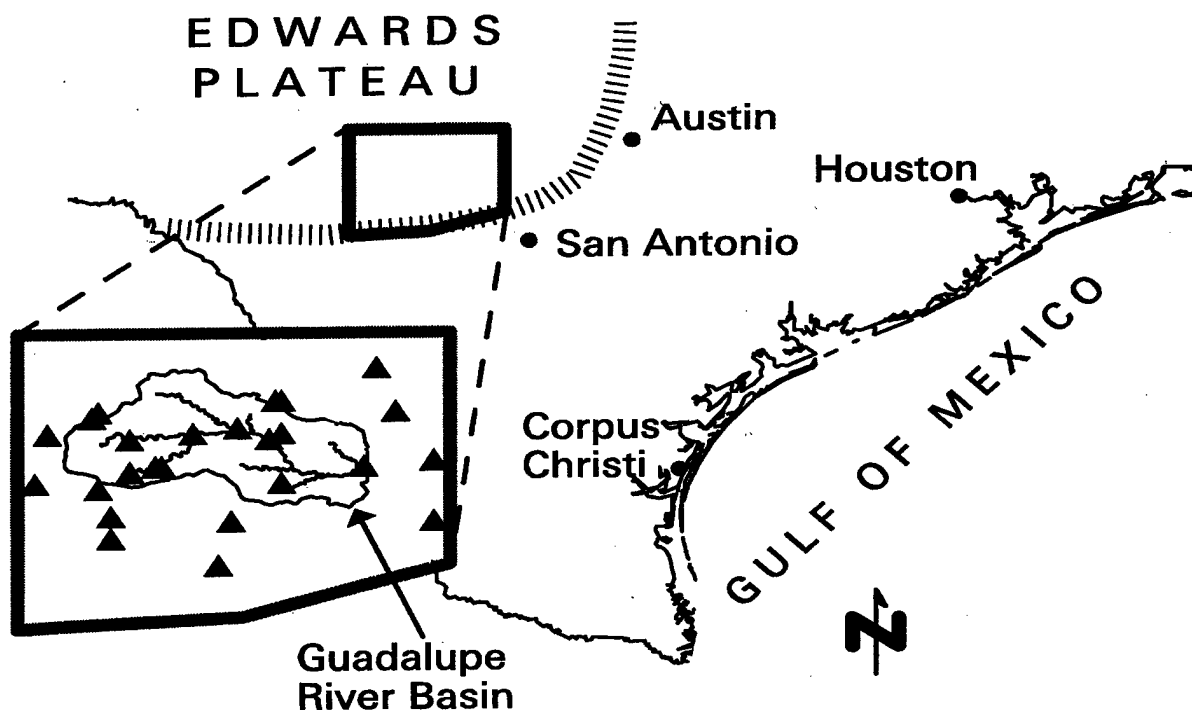


Figure 2. Partial map of Texas, showing the regions mentioned in the text. The inset corresponds to the area of interest. Triangles represent rain gauge locations.

identical network structure will respond the same to the same rainfall field) was used (see [24, Chapter 7] for a detailed discussion of network models). Using this model, the maximum discharge for each basin is determined for each simulated storm, allowing analysis of flood peak moments and CVs.

## 2. Storm model

Simulating an extreme rainfall event over an area of  $\sim 5000 \text{ km}^2$  is a complicated task. Accordingly, there are a number of spatio-temporal stochastic models for extreme rainfall that have been developed in the literature [5,15,23,30]. In order to determine which model will work the best for us, we note that the only extended record of data available in our area of interest (for the purpose of parameter estimation) is the daily rainfall accumulation measured by 23 rain gauges, which limits the number of models for which we would be able to estimate parameters. In addition, because our data is daily accumulation totals, there is no information available on the temporal structure of the rainfall for each event, so we modeled the spatial accumulations and the temporal structure independently. For modeling the spatial structure of the rainfall, we used a model [29] with a small number of parameters in comparison to other models to facilitate parameter estimation. The use of more complicated models [15,23] would be practical and desirable if additional rain gauge or radar data were available for parameter estimation. For modeling the temporal structure, we used a cascade model [18].

To simulate the extreme rainfall totals, the statistical model described in Smith and Karr [29] was used with the additional assumption of spatial homogeneity in the region. This model can be described as follows:

- The arrival times of extreme rainfall events form a Poisson process  $N$  on the time axis with seasonally-varying mean  $\lambda(t)$ . Because it is only the annual flood peaks that are of interest, only the annual frequency of extreme rainfall events  $\Lambda$  is utilized in the simulations.
- A rain field is constructed as a collection of distinct storm cells. The centers of these cells form a Poisson process  $M$  (independent of  $N$ ) on the plane with spatial rate  $a$ .
- For a particular storm, the total rainfall  $S_c$  in the center of each cell is independent of  $N$  and  $M$ , and has an exponential distribution with parameter  $b$ .
- The storm-total rainfall associated with each cell is assumed to be distributed symmetrically about the center of the cell with spread function

$$h(r) = e^{-2c^2 r^2},$$

and a magnitude equal to  $S_c$  at  $r = 0$ .

Suppose that, for the  $i$ th storm, there are  $M$  storms cells with coordinates  $Y_1, Y_2, \dots, Y_M$

and center accumulations  $S_{c,1}, S_{c,2}, \dots, S_{c,M}$ , respectively. Under the assumptions above, the storm-total rainfall  $S_i(x)$  from the storm at a point  $x$  on the plane is

$$S_i(x) = \sum_{j=1}^M S_{c,j} h(\|x - Y_j\|). \quad (1)$$

Moreover, note that the points  $\{(Y_1, S_{c,1}), (Y_2, S_{c,2}), \dots, (Y_M, S_{c,M})\}$  form a Poisson process on  $\mathbb{R}^2 \times \mathbb{R}_+$  with intensity measure  $abe^{-bs}$  dyds. This property is used to derive the moment parameter estimators for the model.

Smith and Karr computed the moments for this field [29], giving the mean  $\mu$  and the variance  $\sigma^2$  for the amount of storm-total rainfall at all locations  $x$  (the “storm totals”) as

$$\mu = \frac{\pi}{2} \cdot \frac{a}{c^2 b}$$

$$\sigma^2 = \frac{\pi}{2} \cdot \frac{a}{c^2 b^2},$$

and the correlation coefficient  $\rho$  for the storm totals between two locations with a distance  $r$  between them as

$$\rho(r) = e^{-c^2 r^2}.$$

The mean, variance, and correlation coefficient do not depend upon  $x$  because of the assumption of homogeneity in the region.

This model, then, has four parameters to be estimated: the rate of storm occurrence  $\lambda(t)$ , the mean number  $a$  of storm cells per unit area for a particular event, the mean total rainfall  $b^{-1}$  at the center of the cell, and the decay length  $c^{-1}$  of the spread function  $h(r)$ . To find characteristic parameters for the model from the Edwards Plateau study region, daily-total rainfall accumulations from 23 rain gauges were used. This data spans a period of 48 years (from 1948 to 1996), and, though there were gaps in the data sequence for most of the gauges, there were on average nine gauges reporting each day (see Figure 2 for the gauge locations).

An extreme rainfall event (storm) is defined as any period of three days with a total rain accumulation of more than 130 mm at one or more rain gauges [29]. This definition certainly describes the extreme rainfall events we are studying, since the accumulation measured for flood peaks above the median annual flood peak value for our basins all satisfy this criterion. We use the same definition of storms as Smith and Karr [29] to allow comparison of the model parameter estimates computed for the central Appalachians region and Edwards Plateau. The definition was tested by comparing the annual flood peak data from the four stream gauging stations and rain gauge data in the area of interest. The measured annual flood peak data for the majority of basins describes peaks that are orders of magnitude smaller than for the large floods we are interested in, as illustrated in Figure 3

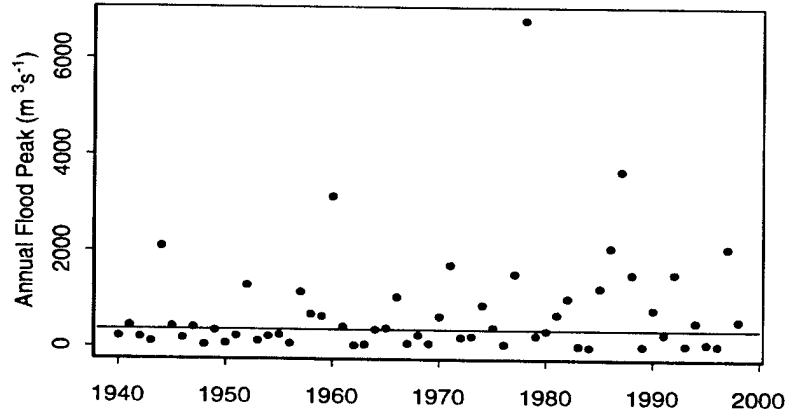


Figure 3. Measured annual flood peaks for the stream gauging station at Guadalupe river at Comfort. The line represents the median value.

for the stream gauging station at Guadalupe river at Comfort. In our framework, the small peaks correspond to the fact that there is a strictly positive probability of no extreme rainfall event occurring during a given year. We computed the total rainfall accumulation reported by the rain gauges for the three day period ending the day of the annual flood peak for each year. When we then exclude the peaks below the median flood peak values for each of the four basins, the minimum value of the recorded storm total accumulations is 125 mm.

We denote the total number of gauges in the region as  $\nu$ , and the total number of years of observation as  $n$ . The storm arrival times are denoted as  $T_i$ , and the total number of storms detected during the  $n$  years as  $N$ . For the  $i$ th storm, the total accumulation of rainfall  $S_{ij}$  for the  $j$ th gauge ( $j = 1, \dots, \nu$ ) is computed. The estimators derived in Smith and Karr [29] can then be used to find approximate values for the parameters in our model.

In our notation, the estimator for the annual frequency  $\Lambda$  is

$$\hat{\Lambda} = \frac{N}{n}.$$

The estimated value for  $\Lambda$  from our data set is 1.53 storms/year. To conveniently express the seasonally-varying rate  $\lambda(t)$ , one can think of a year as a time interval from 0 to 1, where 0 corresponds to January 1 and 1 to December 31. If the arrival times  $T_i$  are expressed in years, then the mantissa of the arrival time  $\{T_i\}$  indicates the time of year of the event. Then, for the seasonally-varying rate  $\lambda(t)$ , the window estimator

$$\hat{\lambda}(t) = \frac{1}{n} \frac{1}{\Delta t} \sum_{i=1}^N 1_{(t-\Delta t/2, t+\Delta t/2)}(\{T_i\}),$$

is used, where  $\Delta t$  is the width of the time window. The estimate for  $\lambda(t)$ , obtained using a



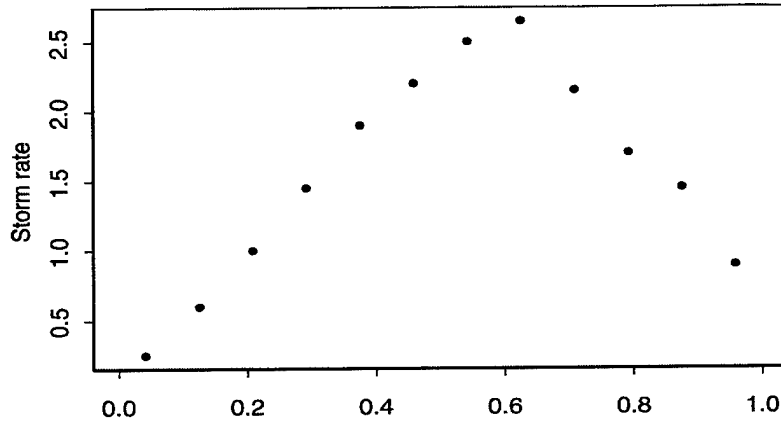


Figure 4. Estimate of the seasonally-varying rate of storm occurrence. Time index 0 corresponds to January 1, and time index 1 to December 31.

five month window [29], is shown in Figure 4. The seasonally-varying intensity varies from 0.6 in January to 2.65 storms per year in August.

In order to estimate the spread function parameter  $c$ , estimates of pairwise correlation coefficients  $\rho$  of the storm totals between gauges are plotted against the distance between the gauges. Each estimate  $\hat{\rho}$  was computed as a sample correlation coefficient for exactly 20 observations per pair of gauges. Pairs of rain gauges for which data exists for fewer than 20 storms were excluded from the analyses to eliminate uncertainties in the parameter estimates. A least squares estimator for  $c$  is used:  $\hat{c}$  is the number that minimizes

$$\sum \left( \hat{\rho}(r) - e^{-c^2 r^2} \right)^2,$$

giving an estimate of 30 km for  $c^{-1}$ .

The estimators for the parameters  $a$  and  $b$  of the model are obtained from the moment equations:

$$\hat{b} = \frac{\hat{\mu}}{\hat{\sigma}^2},$$

$$\hat{a} = \frac{2 \hat{\mu}^2}{\pi \hat{\sigma}^2} \hat{c}^2.$$

Estimates of  $\mu$  and  $\sigma$  are readily computed from the data, giving estimates of 50 mm for  $b^{-1}$  and 0.0015 storm cells  $\text{km}^2$  for  $a$ . The mean number of storm cells in the region of interest (area  $\sim 5000 \text{ km}^2$ ) during an extreme rainfall event is then 7.5.

It is interesting to compare our model parameter estimates for the Edwards Plateau with those for the Appalachians, as obtained by Smith and Karr [29]. Both sets of estimates are listed in Table 1. We note that this region of Texas has approximately three times as many heavy storms per year as the Appalachian region. Although each storm has, on average,

Table 1. Estimated values for the Storm Model parameters.

Parameter	Edwards Plateau (present study)	Central Appalachians Smith and Karr, 1990 [29]
$\Lambda$ (storms/year)	1.53	0.45
$a$ (cells per km <sup>2</sup> )	0.0015	0.0027
$b^{-1}$ (mm)	50	15–40
$c^{-1}$ (km)	30	34

fewer storm cells than do those in the Appalachians, each cell has, on average, higher rain accumulation. Each comparison in the table agrees with the qualitative understanding of the climatic differences between the Edwards Plateau and the central Appalachians [3,28].

Although analysis of daily rainfall accumulation is useful for the estimation of storm totals, it does not provide information about the temporal evolution of the storm. To represent the temporal structure of the rainfall, a cascade model [18] was used. The cascade model used is outlined as follows: For each storm cell with total rainfall  $S_c$  at its center, we assign a lifetime  $\tau$  such that the average rain rate  $\bar{Z}$  at the center of the cell during the period  $\tau$  is  $\bar{Z} = S_c/\tau$ . Next we divide the time interval  $(0, \tau)$  into two halves. We assign a rain rate  $W_{1,1}\bar{Z}$  to the interval  $(0, \tau/2]$ , and  $W_{1,2}\bar{Z}$  to the interval  $(\tau/2, \tau)$ , where  $W_{i,j}$  are independent random variables having the same distribution as a chosen positive random variable  $W$ . The expected amount of rain in every interval should be conserved, necessitating the condition  $\mathbb{E}[W] = 1$ . The next step is to divide each subinterval (each half) into two new intervals, giving four subintervals with length  $\tau/4$ . Again, we take independent positive random variables  $W_{2,1}$ ,  $W_{2,2}$ ,  $W_{2,3}$ , and  $W_{2,4}$  with the same distribution as  $W$ , and assign rain rates  $W_{2,1}W_{1,1}\bar{Z}$  to the first subinterval,  $W_{2,2}W_{1,1}\bar{Z}$  to the second,  $W_{2,3}W_{1,2}\bar{Z}$  to the third, and  $W_{2,4}W_{1,2}\bar{Z}$  to the fourth. Continuing in this fashion, we will have at the  $k$ th stage  $2^k$  intervals, each with a length  $\tau/2^k$  and rain rate  $Z_c(t) = \bar{Z} \prod_{i=1}^k W_{i,j}$ . A schematic of this construction is pictured in Figure 5.

The distribution of the storm total for a given storm cell in time is assumed to be independent of that for all other cells. Because storm cells represent different storm systems, it is natural to assume that they will evolve independently in time. In general, the temporal evolution of a storm cell might depend on changing meteorological conditions and interactions with other storm cells, but this is at a finer degree of detail than present in the spatial model of rainfall described above, and the runoff model described below.

For our analyses,  $\tau$  is taken to be characteristic of all the storms cells in the simulated storms and assumed to be a normally distributed random variable with mean 72 hours and standard deviation 3.0 hours (since we used three-day rain gauge accumulations to obtain estimates of storm-totals, the long storm length is required for the discharges to have reasonable values).  $k$ , the parameter corresponding to the number of cascades used, was varied from 4 to 10, giving a range of rainfall patterns averaged from over a period of a few hours to patterns averaged every minute. Random variable  $W$  is taken to have a lognormal distribution [18], i.e.  $W = e^{\gamma + \varsigma U}$ , where  $U$  is a standard Gaussian random variable, and  $\gamma$  and  $\varsigma$  are parameters of the distribution. The condition  $\mathbb{E}[W] = 1$  then corresponds to the condition  $\gamma = -\varsigma^2/2$ . The parameter  $\varsigma$  in our simulations was varied from 0.4 to 0.8.

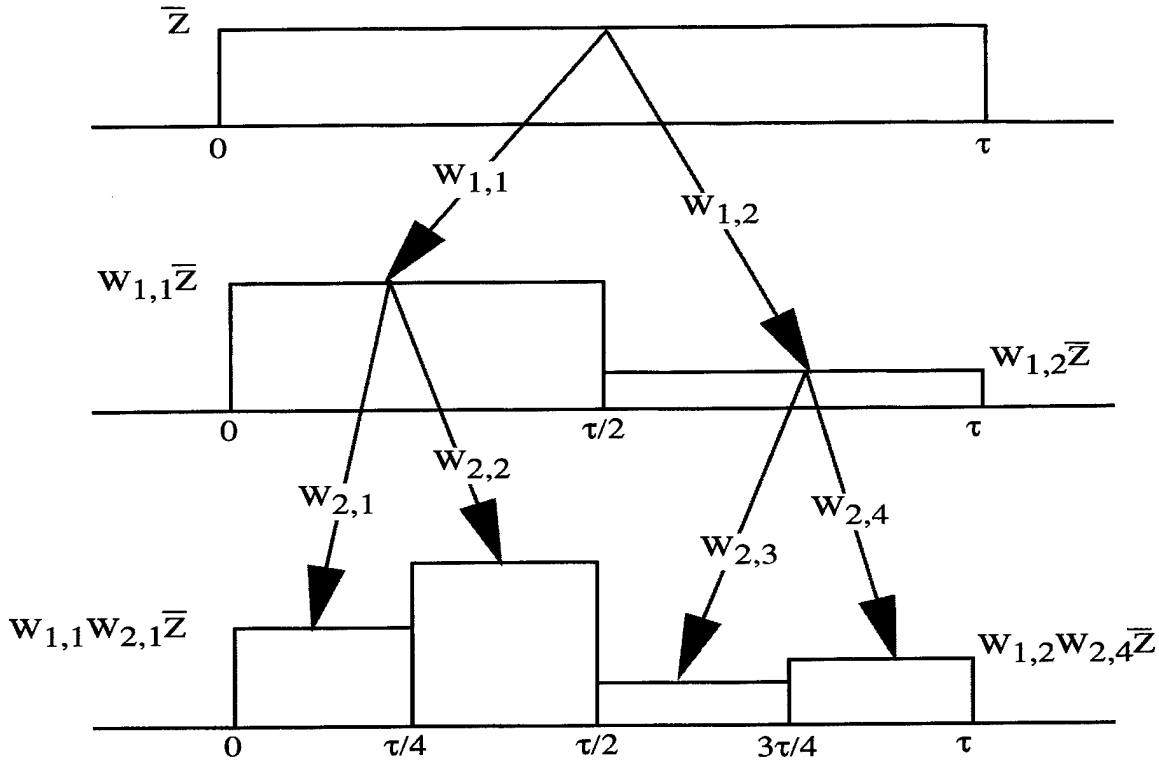


Figure 5. A schematic of the cascade model construction.

To summarize, we simulate the rainfield from a storm as follows:  $M$  storm cell centers  $Y_j$  are simulated as a realization of a Poisson process on the plane with spatial rate  $a$ , and the storm length  $\tau$  is taken from the Gaussian distribution. Each cell is assigned a total rain accumulation  $S_{c,j}$  in its center taken from an exponential distribution with parameter  $b$ . A cascade model is used for distributing  $S_{c,j}$  over the interval  $(0, \tau)$  to form the rain rate function  $Z_{c,j}(t)$ . A spread function  $h(r)$  is used to describe the proportion of the  $S_{c,j}$  that falls at a point at a distance  $r$  from the center of cell  $j$ . The rainfield  $Z(x, t)$  at a point  $x$  is then

$$Z(x, t) = \sum_{j=1}^M h(\|x - Y_j\|) Z_{c,j}(t).$$

### 3. Drainage network runoff model

In our Network Runoff Model, a discharge at the outlet of the basin is computed by the direct extension of the inverse GIUH function (geomorphological instantaneous unit hydrograph, defined as the basin's response to instantaneous rainfall with a unit magnitude

[24, page 477]). We represent the river network as a binary tree with  $n$  links. We will denote an individual link by  $e$ . Each link has a certain length  $l_e$ , an upper vertex  $\bar{e}$ , and a lower vertex  $\underline{e}$ . We know the position and geometry of every link, and the way that links are connected (i.e., we know the structure of a network similar to the one represented in Figure 6).

We make the assumption that, from every point in the basin, water flows to the nearest channel following the paths of steepest descent on the underlying elevation. After reaching the channel, the water follows the river network to the outlet. Under these assumptions, we can compute the travel distance  $f_e(x)$  to the outlet  $\underline{e}$  for each point  $x$  in the basin, and, assuming a constant flow velocity  $v$  both over the land and in the channels, the discharge  $Q_e$  at the outlet is given by:

$$Q_e(t) = \int_{\mathcal{B}} R\left(x, t - \frac{f_e(x)}{v}\right) dx, \quad (2)$$

where  $\mathcal{B}$  denotes that the integral is taken over the basin and  $R(x, t)$  denotes the runoff generated at location  $x$  at time  $t$ . Note that if  $R(x, t)$  is nonzero only for a certain time period  $(0, T)$ , then the discharge at the outlet will be nonzero at most during the period  $(0, T_0)$ , with  $T_0 = T + \max f_e(x)/v$ .

To approximate the effects of infiltration, the runoff field  $R(x, t)$  is computed from the rainfall field  $Z(x, t)$  by

$$R(x, t) = (Z(x, t) - K_s)^+,$$

where  $K_s$  is a parameter similar to the saturated hydraulic conductivity, and  $y^+ = \max(0, y)$ . We assume that  $K_s$  is the same throughout the basin. This representation of the infiltration process is reasonable for extreme rainfall events [16].

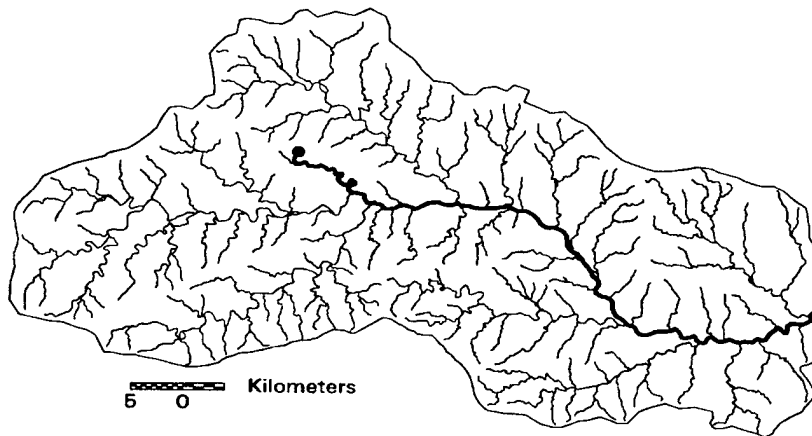


Figure 6. The network structure of the Guadalupe river. The bold line shows path of the water from the marked point in the basin to the outlet.

This model provides a useful tool for studying drainage basin response to extreme rainfall. It has only two parameters: the average surface flow velocity  $v$ , and the value of  $K_s$ . We can estimate the values of these parameters from reconstructed hydrographs for extreme events for which we have both good rainfall measurements and discharge measurements at one or more nodes. The assumption of constant velocity in the channels for extreme events has been discussed previously [10]. The analyses of measured velocity in different channels suggests that the velocity is effectively the same if the respective discharge levels in the channels have the same probability of occurrence [24, page 14].

We have implemented this model for several extreme events in Texas and other areas [26,27], and achieved acceptable reconstruction of discharge hydrographs. For the purposes of our simulations, we varied the flow velocity from 0.6 to 3.0 m s<sup>-1</sup>, and  $K_s$  from 0 to 20 mm h<sup>-1</sup>.

#### 4. Scaling analyses

We simulated flood peaks for 100 non-nested sub-basins of the Guadalupe river basin in the Edwards Plateau for a period of 50 years (see Figure 2 for the location of the Guadalupe river basin). For the river network structure, we used EPA RF3 river reach data (Figure 6), which corresponds to the blue lines on USGS topographical maps. Rainfall was simulated according to the Storm Model described in Section 2, and the ensuing runoff for each sub-basin was computed using the Network Runoff Model described in Section 3.

For each sub-basin, the annual flood peaks were identified as the maximum computed discharge from the simulated storms in that year. Since extreme rainfall events form a Poisson process on the time axis, there is a nonzero probability of obtaining zero events in a given year. For years with zero events, the annual flood peak was taken to be zero. As was noted earlier, this is justified by the fact that the measured annual flood peak data for most basins includes peaks that are orders of magnitude smaller than the large flood peaks of interest (Figure 3). The computations were repeated for different values of the Storm Model time cascade parameters,  $K_s$  value, and channel velocity, and different catchment sampling (choice of sub-basins). The dependence of the behavior of the flood peaks upon the values of the Network Runoff Model parameters was not statistically significant.

The first and second sample moments of the simulated flood peak data set for one set of sampled sub-basins are plotted against sub-basin area in Figure 7 (for  $v = 1$  m s<sup>-1</sup>,  $K_s = 0.5$  mm h<sup>-1</sup>,  $\zeta = 0.6$ , and  $k = 8$ ). The logarithms of the moments clearly exhibit a linear relationship with the logarithms of the sub-basin drainage areas. The slope of the linear regression for the sample means is 0.72, which is consistent with typical slopes for the real data [10,14,21]. Mean annual flood peaks computed from the measurements of several stream gauging stations in our area of interest are also shown in Figure 7 (squares). There are no small gauged basins in the area of interest with a long (> 30 years) record of maximum annual flood peaks.

The dependence of the coefficients of variation on the sub-basin drainage area is shown in Figure 8 (triangles). The overall shape of this dependence is similar to that obtained

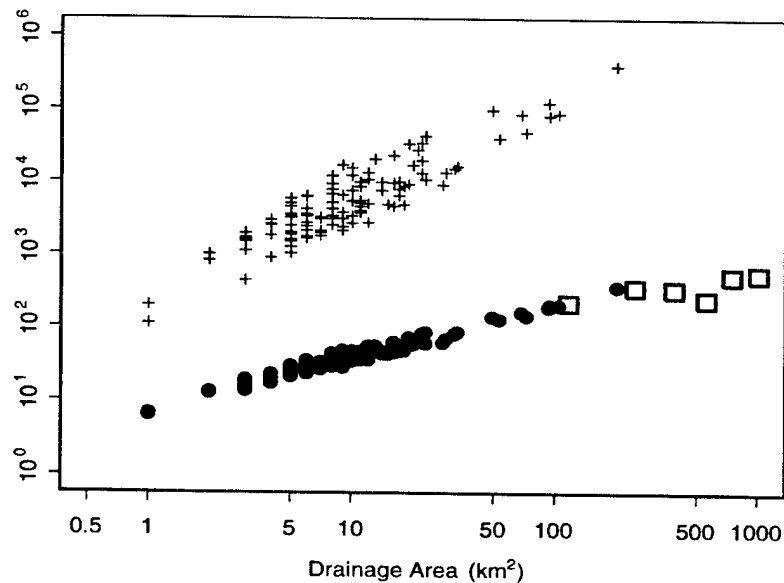


Figure 7. Log-log plot of first (solid circles) and second (crosses) sample moments of the simulated flood peaks versus drainage area. Empty squares represent estimated values of mean annual flood peak for actual basins in the area of interest. The units of the y axes are  $\text{m}^3 \text{s}^{-1}$  for the first moments and  $\text{m}^6 \text{s}^{-2}$  for the second. The parameters used to obtain this plot were:  $v = 1 \text{ m s}^{-1}$ ,  $K_s = 0.5 \text{ mm h}^{-1}$ ,  $\zeta = 0.6$ , and  $k = 8$ .

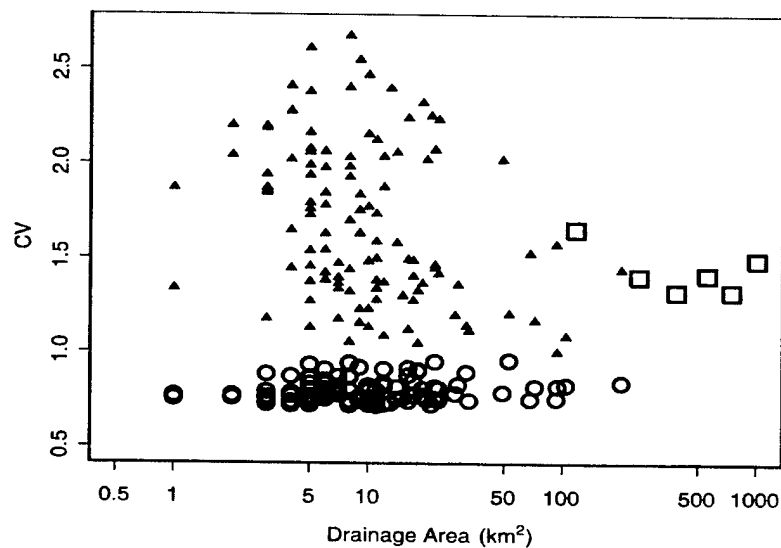


Figure 8. CV—Drainage area relationship for the simulated flood peaks. Triangles indicate values obtained with the rainfall simulated with the Storm Model, empty circles indicate values where the rainfall was simulated without the time cascade structure. Squares represent estimated values for CV for actual basins in the area of interest. The parameters of the models are as in Figure 7.

from an empirical study of actual flood peak data (Figure 1). There tends to be an increase of CV with increasing drainage basin area for catchments with areas smaller than  $A_c = 10 \text{ km}^2$ , and a decrease of CV with increasing drainage basin area for larger catchments. Similar results were obtained for all input parameters used in the simulation models. It is interesting to note that the CVs computed from annual peak data from several stream gauging stations in our area of interest is of the same order of magnitude (Figure 1, squares) as the simulated results. The inference that behavior of CVs for annual flood peaks can be largely explained in terms of spatial and temporal properties of the rainfall and the structure of the river networks is supported by the observation that only these three elements were included in our simulations.

In order to gain further understanding of the factors that influence the behavior of CVs, the simulation experiments were repeated with a stationary rainfall field, i.e., the time cascade construction was removed from the Storm Model. This simulation was performed in an attempt to isolate the effects of the spatial properties of the rainfall and the network on CV. CVs obtained without the cascade structure are also shown in Figure 8 (empty circles). They were computed with the same rainfall field spatial structure as the CVs obtained with the cascade structure (triangles) for each simulated event. The areal dependence of the prior analyses is no longer present. Because similar results were obtained for a wide range of simulation parameters, we infer that the temporal structure of the simulated rainfall is important for producing the small area behavior of CVs in our results.

There are multiple explanations for the change in low-area scaling in the context of our model. Because small basins have much shorter response times than larger basins, their instantaneous discharges depend on the rainfall during a shorter period of time than do larger basins' discharges. For the runoff calculated using the Network Runoff Model this effect is readily apparent, since, for each link  $\underline{e}$  at time  $t$ , the discharge  $Q_{\underline{e}}(t)$  is calculated from the rainfall during the time interval  $[t - \max(f_{\underline{e}}(x)/v), t]$ . Moreover, the form of equation (2) is similar to a resampling and averaging of the rainfall. A plot of  $\max(f_{\underline{e}}(x)/v)$  as a function of basin drainage area is shown in Figure 9 for the sub-basins of the Guadalupe river (assuming  $v = 1.0 \text{ m/s}$ ). We see that the largest transit time scales are roughly  $\sim 1$  hour for small basins and 30 hours for large basins. In the simulation experiments, the rainrates generated by the Storm Model generally changed every 10 minutes, so small catchments experienced little averaging of the temporal structure. This plays a role in determining the importance of rainfall temporal structure for small basin CVs, and especially for the discharges calculated using the Network Model.

The spatial structure of the simulated rainfall might also be suspected as the explanation for the low-area dependence. The two parameters that determine the spatial scale of the Storm Model are  $a$  and  $c$ . According to the estimates from Table 1, the average distance between storm cells is  $a^{-1/2} = 26 \text{ km}$  and the characteristic scale of a single storm cell is  $c^{-1} = 30 \text{ km}$ . These scales are somewhat larger than the resolution observable by the rain gauge network (the average distance between a particular rain gauge and its nearest neighbor was about 12 km), so the rain gauge network adequately captures the spatial structure considered. However, the error in the estimation of the parameters  $a$  and  $c$  is

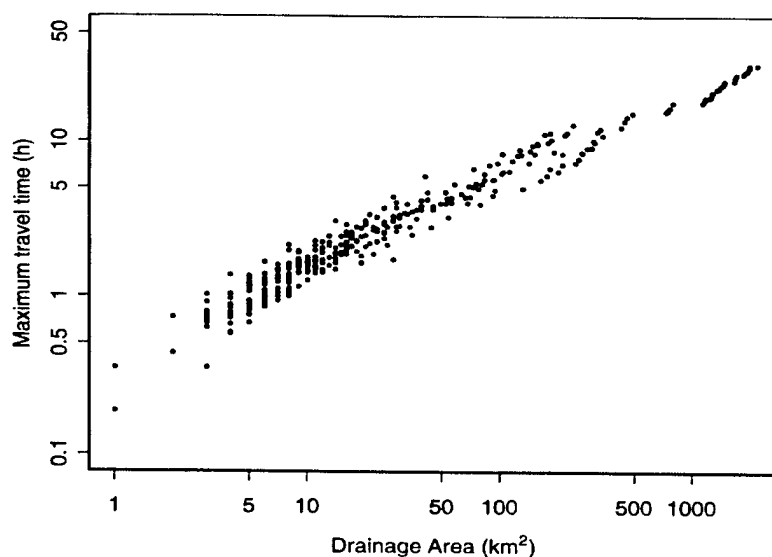


Figure 9. In the Network Runoff Model, the time scale of a basin response is  $\max(f_e(x)/v)$ . Here, values of  $\max(f_e(x)/v)$  are plotted as a function of drainage area for  $v = 1 \text{ m s}^{-1}$ .

large (see Bloschl [1]), and the CV results are dependent on the estimated characteristic spatial scale of the simulated rainfall.

To address the issue of the uncertainty in determining the spatial scale of the rainfall patterns, we simulated rainfall with several different values of  $a$  and  $c$ . The results are presented in Figure 10, which shows the envelope curves for four different simulation experiments with unique values of the parameters  $a$  and  $c$ . The shapes of these curves are

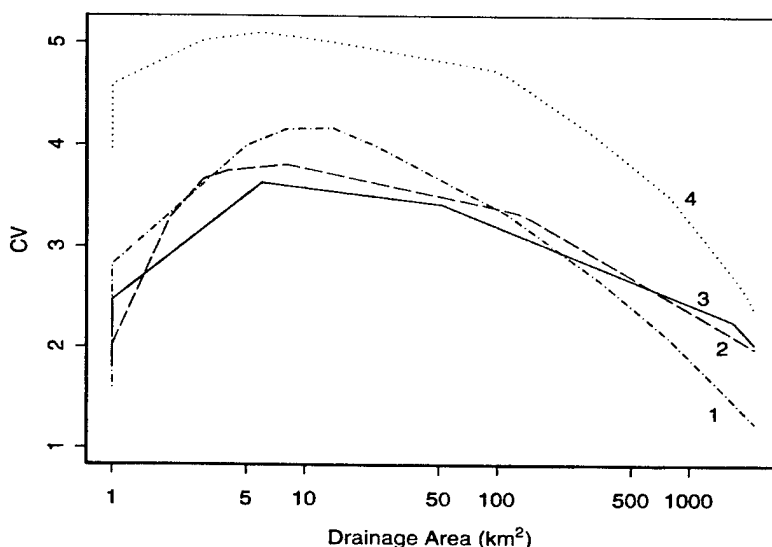


Figure 10. The envelope curves for the CV-area relationship resulted from simulated rainfall with different spatial scales. (1)  $a^{-1/2} = 60$ ,  $c^{-1} = 60$ ; (2)  $a^{-1/2} = 30$ ,  $c^{-1} = 15$ ; (3)  $a^{-1/2} = 15$ ,  $c^{-1} = 15$ ; (4)  $a^{-1/2} = 15$ ,  $c^{-1} = 30$  (km).



all similar to that of the real CVs (Figure 1). So while the particular estimates of the spatial structure might be imprecise, the scaling behavior of the simulated CVs does not change significantly.

Many authors [7,9,20] have stressed the importance of the network structure of the basin in determining the behavior of CVs for small catchments. In this study, we used a network taken from an actual basin, so realistic basin network properties were employed. In order to further understand the importance of employing actual river networks, though, we tested the same rainfall model with the Peano network.

The Peano network is an idealized model of a channel network [6,10,13]. An example of a Peano network, along with its basic properties, can be found in Rodriguez-Iturbe and Rinaldo [24, page 123], and a Peano network of order 5 is shown in Figure 11. Under the assumption of constant rainfall and constant water velocity in streams, the peak discharge in a Peano network exhibits simple scaling [10]. The scaling of flood peaks in a Peano basin with the spatial cascade model for rainfall has been studied both analytically and computationally [6], and it has been concluded that the peaks exhibit multiscaling in this case.

We studied the response of a Peano basin to rainfall generated by the Storm Model through simulations, and discharges at the end of each link were computed using the Network Model. The area of the entire Peano basin was taken to be approximately the same as the area of the Guadalupe river at Comfort basin ( $2190 \text{ km}^2$ ), and the order of the Peano basin was taken to be 5 (Figure 11) so that the drainage density is approximately the same as for the Guadalupe river basin. Figure 12 shows the flood peak CVs obtained with

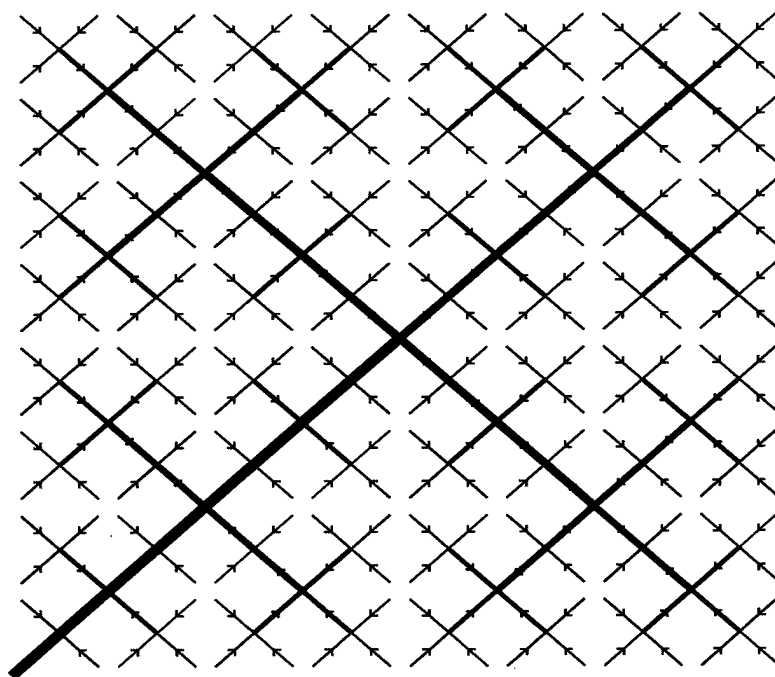


Figure 11. Peano network of order 5.

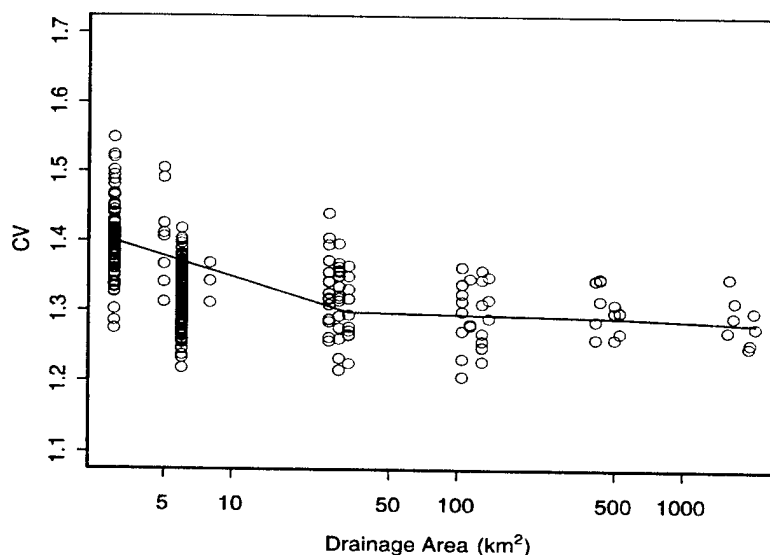


Figure 12. CVs of annual flood peak simulated in the sub-basins of Peano basin. Parameters of the models are as in Figure 7.

the same set of model parameters as used for Figures 7 and 8. It is clearly seen that CVs decrease with increasing drainage area for all scales. Although it is difficult to study the distribution of flood peaks with our rainfall model even in the Peano basin, this simulation experiment supports the hypothesis of multiscaling. This simulation experiment with a Peano basin shows that the network structure of the drainage basin is an important factor for determining the scaling behavior of flood peaks CVs, which agrees with the cited findings [7,9,20]).

Finally, we observe that our results provide a starting point from which to further test additional influences on the behavior of CVs. Much research has been performed to determine the features in the basins' morphology, dynamic response, and rainfall that produce the greatest effects on the behavior of flood peaks [2,7,21]. It has been suggested that the basin response to rainfall on a small scale is largely controlled by the spatial variability of basin's morphological properties [31], which are therefore critical for the scaling of annual flood peaks. It has also been hypothesized that the transfer of water from hill slopes to channels may be the key process defining the characteristic spatial scales of regional hydrology [22]. Another hypothesis, that nonlinearities in runoff generation contribute to the increase in CVs for small scales [2], is supported by the effect of the temporal structure of the model rainfall on the small scale behavior of CVs that was observed in this study. This study did not directly model any of the processes mentioned above. That our results reflect the observed behavior of CVs does not rule out any of these additional influences, but merely demonstrates that the overall response of the real system can be mimicked by the fundamental response of a much less complex system we can tractably analyse.

It is further encouraging to note that many of the additional processes not included in our results are coming within the reach of computational models with the recent increases

in computing power, while they would be prohibitively computationally intensive only two years ago.

## 5. Summary and conclusions

There are three primary results from our work:

- The simulation of rainfall over an area, coupled with the Network Runoff Model, provides a useful tool for studying flood peaks. Estimation of most of the parameters for such simulations can be done based on analysis of daily-accumulation rain gauge data.
- The areal scaling properties of flood peaks (log-log linearity of moments vs. basin drainage area and the peculiar behavior of the coefficients of variation) can be explained by the spatial and temporal structure of the rainfall and the spatial structure of the stream network.
- There is evidence that the interaction between the temporal structure of the rainfall and the network structure of the basin might be important to the scaling behavior of the flood peak coefficients of variation for basins with a sufficiently small area.

## Acknowledgments

This research was funded in part by the U.S. Army Research Office (Grant No. DAAH04-95-1-0113), the National Science Foundation (Grant No. EAR-9706259 and EAR-9528886), and NASA (Grant Nos. NAG8-1521 and NAG5-7544). This support is gratefully acknowledged. We thank the reviewers for their valuable comments and suggestions.

## References

- [1] Blöschl, G., "Scaling issues in snow hydrology," *Hydrol. Proc.* 13, 2149–2175, (1999).
- [2] Blöschl, G. and Sivapalan, M., "Process controls on regional flood frequency: Coefficient of variation and basin scale," *Water Resour. Res.* 33(12), 2967–2980, (1997).
- [3] Caracena, F. and Fritch, J.M., "Focusing mechanisms in the Texas Hill Country flash floods of 1978," *Mon. Wea. Rev.* 111, 2319–2332, (1983).
- [4] Costa, J.E., "Hydraulics and basin morphometry of the largest flash floods in the conterminous United States," *J. Hydrol.* 93, 313–338, (1987).
- [5] Cox, D.R. and Isham, V.S., "Stochastic spatial-temporal models for rain," In: *Stochastic Methods in Hydrology* (O.E. Barnoff-Nielsen, V.K. Gupta, V. Perez-Abreu, and E. Waymire, eds), World Scientific, New York, (1998).
- [6] Gupta, V.K., Castro, S., and Over, T.M., "On scaling exponents of spatial peak flows from rainfall and river network geometry," *J. Hydrol.* 187, 81–104, (1996).
- [7] Gupta, V.K. and Dawdy, D.R., "Physical interpretations of regional variations in the scaling exponents of flood quantiles," *Hydrological. Proc.* 9, 347–361, (1995).

- [8] Gupta, V.K., Messa, O.J., and Dawdy, D.R., "Multiscaling theory of flood peaks: Regional quantile analysis," *Water Resour. Res.* 30(12), 3405–3421, (1994).
- [9] Gupta, V.K. and Waymire, E., "Multiscaling properties of spatial rainfall and river flow distributions," *J. Geophys. Res.* 95(D3), 1999–2009, (1990).
- [10] Gupta, V.K. and Waymire, E., "Spatial variability and scale invariance in hydrologic regionalization," In: *Scale Dependence and Scale Invariance in Hydrology*, Cambridge University Press, 1998.
- [11] Harris, D., Menabde, M., Seed, A., and Austin, G., "Multifractal characterization of rain fields with a strong orographic influence," *J. Geophys. Res.* 101(D21), 26405–26414, (1996).
- [12] Hosking, J.R.M. and Wallis, J.R., "The theory of probability weighted moments," Research report RC20349, IBM Research, Yorktown Heights, NY, (1996).
- [13] Marani, A., Rigon, R., and Rinaldo, A., "A note on fractal channel structure," *Water Resour. Res.* 27, 3041–3049, (1991).
- [14] Morrison, J.E. and Smith, J.A., "Stochastic modeling of flood peaks using generalized extreme value distribution," submitted to *Water Resour. Res.*
- [15] Northrop, F., "A clustered spatial-temporal model of rainfall," *Proc. Roy. Soc. Series A* 454, 1875–1888, (1998).
- [16] Ogden, F.L. and Sagharian, B., "Green and Ampt infiltration with redistribution," *J. of Irrigat. and Drainage Eng. – ASCE* 123(5), 386–393, (1997).
- [17] Onof, C., Northrop, P., Wheeler, H.S., and Isham, V., "Spatiotemporal storm structure and scaling property analysis for modeling," *J. Geophys. Res.* 101(D21), 26415–26425, (1996).
- [18] Over, T.M. and Gupta, V.K., "A space-time theory of mesoscale rainfall using random cascades," *J. Geophys. Res.* 101(D21), 26319–26331, (1996).
- [19] Perica, S. and Foufoula-Georgiou, E., "Model for multiscale disaggregation of spatial rainfall based on coupling meteorological and scaling description," *J. Geophys. Res.* 101(D21), 26347–26361, (1996).
- [20] Robinson, J.S. and Sivapalan, M., "Catchment scale runoff generation model by aggregation and similarity analysis," In: *Scale Issues in Hydrologic Modeling* (J. Kalma and M. Sivapalan, eds), Wiley, New York, 311–330, (1995).
- [21] Robinson, J.S. and Sivapalan, M., "An investigation into the physical causes of scaling and heterogeneity of regional flood frequency," *Water Resour. Res.* 33(5), 1045–1059, (1997).
- [22] Robinson, J.S., Sivapalan, M., and Snell, J., "On the relative roles of hillslope processes, channel routing, and network geomorphology in the hydrologic response of natural catchments," *Water Resour. Res.* 31, 3089–3101, (1995).
- [23] Rodriguez-Iturbe, I., Cox, D.R., and Isham, V., "Some models for rainfall based on stochastic point processes," *Proc. R. Soc. London, Ser. A* 410, 269–288, (1987).
- [24] Rodriguez-Iturbe, I. and Rinaldo, A., *Fractal River Basins: Chance and Self-Organization*, Cambridge University Press, 1998.
- [25] Smith, J.A., "Representation of basin scale in flood peak distributions," *Water Resour. Res.* 28(11), 2993–2999, (1992).
- [26] Smith, J.A., Baeck, M.L., Morrison, J.E., and Sturdevant-Rees, P., "Catastrophic rainfall and flooding in Texas," *J. of Hydrometeor.* 1, 5–25, (2000).
- [27] Smith, J.A., Baeck, M.L., Morrison, J.E., Sturdevant-Rees, P., Turner-Gillespie, D., and Bates, P., "The regional hydrology of extreme floods in an urban environment," submitted to *J. of Hydrometeor.*
- [28] Smith, J.A., Baeck, M.L., Steiner, M., and Miller, A., "Catastrophic rainfall from an upslope thunderstorm in the central Appalachians: The Rapidan storm of June 27, 1995," *Water Resour. Res.* 32(10), 3099–3113, (1996).
- [29] Smith, J.A. and Karr, A.F., "A statistical model of extreme storm rainfall," *Journal of Geophysical Research* 95(D3), 2083–2092, (1990).
- [30] Waymire, E., Gupta, V.K., and Rodriguez-Iturbe, I., "A spectral theory of rainfall intensity at the meso- $\beta$  scale," *Water Resour. Res.* 20(10), 1453–1465, (1984).
- [31] Wood, E.F., Sivapalan, M., Beven, K., and Band, L., "Effects of spatial variability and scale with implications to hydrologic modeling," *J. Hydrol.* 102, 29–47, (1988).

## Tropical storms and the flood hydrology of the central Appalachians

Paula Sturdevant-Rees,<sup>1</sup> James A. Smith,<sup>2</sup> Julia Morrison,<sup>3</sup> and Mary Lynn Baeck<sup>2</sup>

**Abstract.** Flooding from Hurricane Fran is examined as a prototype for central Appalachian flood events that dominate the upper tail of flood peak distributions at basin scales between 100 and 10,000 km<sup>2</sup>. Hurricane Fran, which resulted in 34 deaths and more than \$3.2 billion in damages, made land fall on the North Carolina coast at 0000 UTC, September 6, 1996. By 1200 UTC on September 6, Fran had weakened to a tropical storm, and the center of circulation was located at the North Carolina–Virginia border. Rain bands surrounding the tropical depression produced extreme rainfall and flooding in Virginia and West Virginia, with the most intense rainfall concentrated near ridge tops in the Blue Ridge and Valley and Ridge physiographic provinces. The most severe flooding occurred in the Shenandoah River watershed of Virginia, where peak discharges exceeded the 100-year magnitude at 11 of 19 U.S. Geological Survey stream-gaging stations. The availability of high-resolution discharge and rainfall data sets provides the opportunity to study the hydrologic and hydrometeorological mechanisms associated with extreme floods produced by tropical storms. Analyses indicate that orographic enhancement of tropical storm precipitation plays a central role in the hydrology of extreme floods in the central Appalachian region. The relationships between drainage network structure and storm motion also play a major role in Appalachian flood hydrology. Runoff processes for Hurricane Fran reflected a mixture of saturation excess and infiltration excess mechanisms. Antecedent soil moisture played a significant role in the hydrology of extreme flooding from Hurricane Fran. Land use, in particular, the presence of forest cover, was of secondary importance to the terrain-based distribution of precipitation in determining extreme flood response.

### 1. Introduction

The central Appalachian region has been a workshop for hydrologists and geomorphologists to study extreme floods. Analyses of central Appalachian flood properties have played a central role in assessments of scaling theories of flood response [Gupta *et al.*, 1994; Miller, 1990; Robinson and Sivalapan, 1997; Smith, 1992]. The Shenandoah River basin was the study site for J. T. Hack's seminal studies of fluvial geomorphology, especially related to the role of catastrophic events [Hack, 1957, 1965; Hack and Goodlett, 1960; see also Jacobson *et al.*, 1989; Miller, 1990]. Extreme flooding occurred in the Shenandoah River basin on September 6, 1996, as the remnants of Hurricane Fran moved through the central Appalachians of Virginia (see Plate 1 for regional setting and summary rainfall analyses). The Shenandoah River basin lies in the Valley and Ridge physiographic province and is bounded on the east by the Blue Ridge.

Tropical storms play a major role in the hydrology of extreme floods in the central Appalachian region. Flood peaks that were produced by tropical storm rainfall dominate the

upper tail of flood frequency distributions for the central Appalachian region, particularly for drainage areas larger than 500 km<sup>2</sup> as illustrated in Figure 1 for the Shenandoah River at 7827 km<sup>2</sup> and the South River of the South Fork Shenandoah River at 549 km<sup>2</sup>. In the 80-year stream gaging record of the Shenandoah River, six of the eight largest flood peaks have resulted from tropical storms (Figure 1 and Table 1). Table 1 summarizes information on the eight largest flood peaks in the Shenandoah River basin and places them in the context of the larger Potomac River basin. The tracks of the six tropical storms (Plate 2) show south-to-north movement through the eastern United States. Orographic thunderstorms [Eisenlohr, 1952; Hack and Goodlett, 1960; Miller, 1990; Smith *et al.*, 1996] have produced many of the largest unit discharge flood peaks in the central Appalachian region. Extreme rainfall and flooding for these events is typically restricted to areas smaller than 500 km<sup>2</sup>. Flooding from Hurricane Fran is examined as a prototype for central Appalachian flood events that dominate the upper tail of flood peak distributions for basin scales between 500 and 10,000 km<sup>2</sup>.

A key feature of extreme tropical storm rainfall in the central Appalachian region is orographic enhancement of precipitation in mountainous regions [Bailey *et al.*, 1975; Clark *et al.*, 1987; Schwartz, 1970]. The largest measured rainfall totals from Hurricane Fran (400 mm in less than 12 hours) occurred along high-elevation regions of the Virginia Blue Ridge. These rainfall accumulations have recurrence intervals exceeding 100 years in the study area [Clark *et al.*, 1987; Hershfield, 1961] and are comparable to the maximum recorded precipitation associated with many of the events listed in Table 1 [Miller, 1990].

<sup>1</sup>Department of Civil and Environmental Engineering, University of Massachusetts, Amherst, Massachusetts.

<sup>2</sup>Department of Civil and Environmental Engineering, Princeton University, Princeton, New Jersey.

<sup>3</sup>Department of Operations Research and Financial Engineering, Princeton University, Princeton, New Jersey.

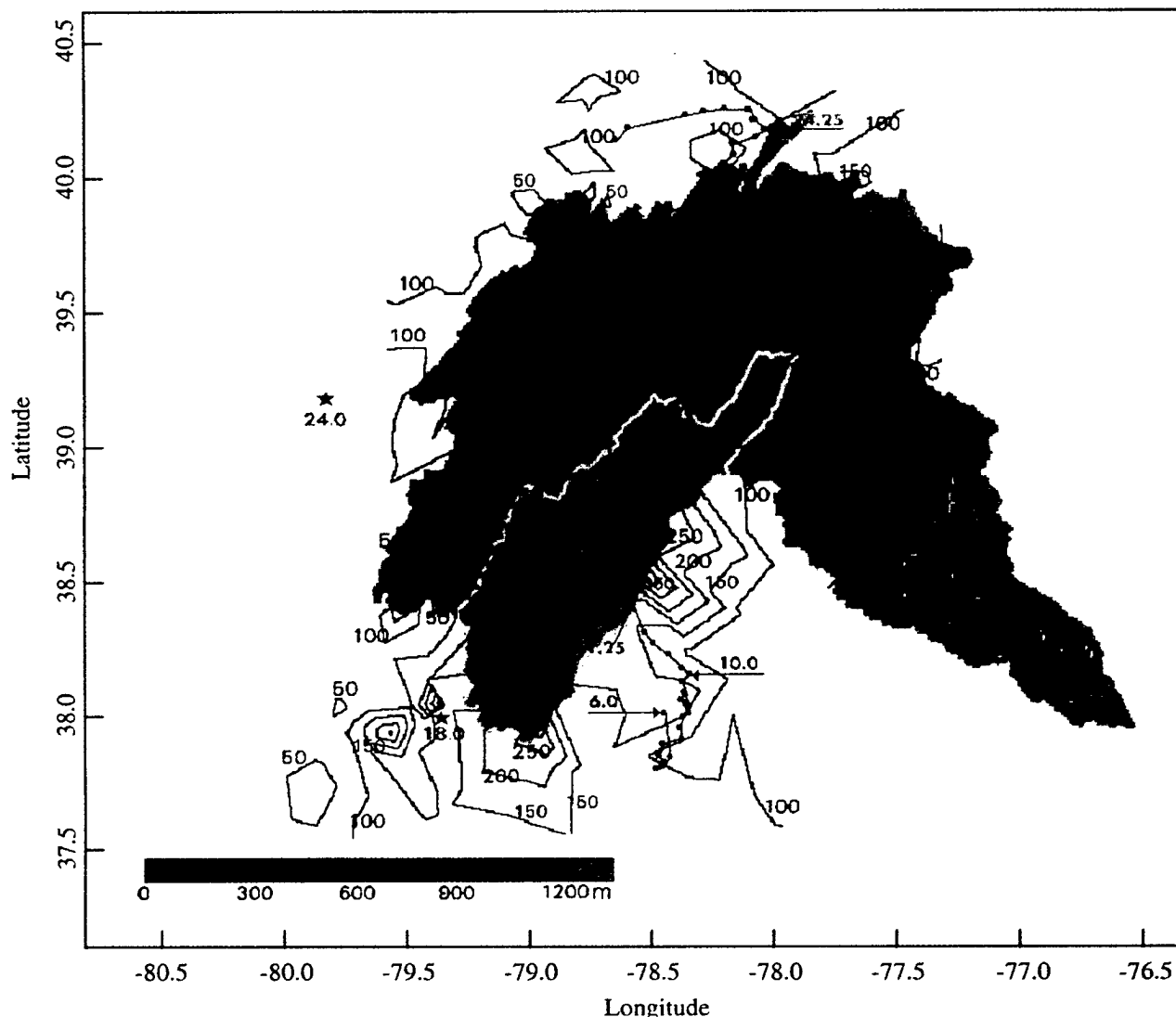


**Plate 1.** Regional setting and summary rainfall analyses for the September 6, 1996, flooding from Hurricane Fran in the Shenandoah River basin (yellow outline). The background map is a false color representation of topography derived from 30-m USGS digital elevation map (DEM) for the Potomac River basin. Contour plot of storm total rainfall (in mm; solid black lines) was derived from the IFLOWS network. Storm centroid locations (red line tracks), derived from WSR-88D volume scan reflectivity observations, are shown from 0600 to 2400 UTC on September 6. The blue stars show the center of circulation of the tropical storm at 1800 and 2400 UTC on September 6.

Hypotheses concerning flood hydrology that are addressed in this paper include the following:

1. Dependence of flood properties on a basin scale derives from space-time scaling properties of rainfall [Gupta *et al.*, 1994; Perica and Foufoula-Georgiou, 1996; Smith, 1992].
2. Antecedent soil moisture is of little importance in determining the magnitude of *extreme* floods [Wood *et al.*, 1990].
3. Runoff production for extreme floods is solely via the saturation excess mechanism in humid, vegetated environments [Dunne, 1991].
4. Extreme flood response of forested basins is markedly different from nonforested regions; forest cover promotes striking attenuation of flood response [Hewlett *et al.*, 1977].

The paper is organized as follows: Section 2 includes a description of the data sets used for both the precipitation analyses and analyses of flood response. The spatial and temporal

variability of rainfall along with the atmospheric environment of the storm are discussed in section 3. This information is combined with land surface information introduced in section 4 to assess the hypotheses presented above.

## 2. Data

A key element of precipitation analyses for the storm was availability of 15-min rain gage observations from the Integrated Flood Observing and Warning System (IFLOWS) network of high-elevation rain gages. Table 2 summarizes observations from the IFLOWS gages in and around the Shenandoah River basin. Locations of IFLOWS gages are shown in Plate 3. Of comparable importance for storm analyses are volume scan reflectivity observations at a 6-min time-scale from Weather Surveillance Radar-1988 Doppler (WSR-

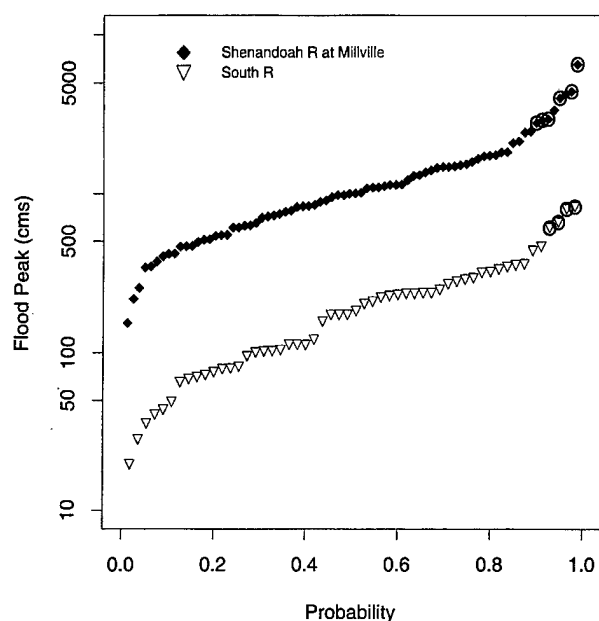


**Figure 1.** Exceedence probability of annual flood peaks for the Shenandoah River at Millville at 7827 km<sup>2</sup> (80-year record) and the South River of the South Fork Shenandoah River at 549 km<sup>2</sup> (55-year record). Circled symbols indicate large annual peaks associated with tropical storms. For Millville, six of the seven largest flood peaks are associated with tropical storms (note that for smaller flood peaks no distinction between tropical storms or other events are implied). For the South River the largest four flood peaks are associated with tropical storms (as above, numerous other smaller flood peaks associated with tropical storms are not marked).

88D) radars located in Sterling, Virginia, and Roanoke, Virginia. Both the Sterling and Roanoke radars suffer from problems of terrain blockage in the Shenandoah basin. Observations from the Geostationary Operational Environmental Satellite (GOES) satellite provided a synoptic-scale depiction of tropical storm motion and evolution.

U.S. Geological Survey (USGS) discharge observations were used to examine hydrologic response to rainfall produced by Hurricane Fran. Unit values discharge data were obtained from the USGS for all available stations in the Shenandoah River basin during the period of flooding resulting from Hurricane Fran (13 sites). The time resolution of unit values data for most stations was 15 min. At the largest drainage areas the

time resolution was hourly. USGS peak discharge measurements were available at seven additional sites throughout the Shenandoah basin. Mean daily discharge and annual flood peak observations for each station were also utilized in this study. The locations of USGS streamflow gaging stations within the Shenandoah are shown in Figure 2.

USGS digital elevation data (DEM) were used in conjunction with U.S. Environmental Protection Agency (EPA) River Reach 3 (RF3) data to define basin boundaries and to derive basin morphological characteristics. Soil distribution at a 1-km resolution was derived from the Pennsylvania State Conterminous United States (CONUS) soils database [Miller and White, 1998]. Land use-land cover distribution at a 30-m resolution was derived from the EPA region 3 land use-land cover data set (based on Landsat thematic mapper images from 1990, 1991, and 1992; [see Loveland and Shaw, 1996; also <http://www.epa.gov/mrlc>]).

### 3. Precipitation Analyses

Hurricane Fran made landfall as a category 3 hurricane near Wilmington, North Carolina, around 0000 UTC on September 6, 1996. The storm system continued to move north-northwesterly through North Carolina, Virginia, and West Virginia during the next 24 hours (Plate 1). The southeasterly steering flow was the product of an upper level low that developed over the Tennessee and lower Mississippi valley and a strong subtropical ridge located over the western Atlantic, which formed in the wake of Hurricane Edouard's northward passage off the East Coast from August 31 to September 2 [Mayfield, 1996]. During the 24-hour period after landfall, storm intensity decreased from category 3 hurricane to tropical depression, as illustrated in the GOES IR images from 0645 and 1245 UTC (Plates 4a and 4b).

Plate 1 provides a detailed view of storm motion through the central Appalachian region. The locations of the center of circulation of the tropical storm, as determined by the National Hurricane Center, are shown at 1800 and 2400 UTC on September 6. The average speed of the tropical storm from 0645 to 1845 UTC (the period of rainfall in the Shenandoah River basin) was 26 km h<sup>-1</sup> (7.3 m s<sup>-1</sup>). The rapid motion of Fran contrasts sharply with motion of the other five tropical storms shown in Plate 2. Heavy rainfall from these storms was associated with rain periods greater than 24 hours. As discussed below, a distinctive feature of Hurricane Fran was the combination of rapid tropical storm motion and anomalously high rainfall rates.

The track of rainfall centroids (i.e., the spatial centroid of rainfall mass flux) through the region (Plate 1), based on 6-min

**Table 1.** Largest Flood Peaks Occurring During the 100-year Record of the Shenandoah and Potomac Rivers

Event	Shenandoah River at Millville, cm	Potomac River at Hancock, cm	Potomac River at Point of Rocks, cm	Ranking at POR <sup>a</sup>
Oct. 1896 <sup>b</sup>	2970	NA	5,780	8
May 1924	3370	4530	7,840	6
March 1936	4280	9630	13,590	1
Oct. 1942 <sup>b</sup>	6510	4390	11,840	2
Aug. 1955 <sup>b</sup>	2800	3480	6,100	7
June 1972 <sup>b</sup>	2920	3170	9,830	3
Nov. 1985 <sup>b</sup>	4020	5860	8,750	4
Sept. 1996 <sup>b</sup>	4420	4200	8,740	5

<sup>a</sup>With regards to historical flood peaks in the Potomac River at Point of Rocks (POR) basin. NA, not available.

<sup>b</sup>Flood peaks were produced by tropical storm rainfall.

**Table 2.** IFLOWS Rain Gage Data<sup>a</sup>

Station	Code	Latitude	Longitude	Elevation, m	Rain, mm	Max Rate, mm h <sup>-1</sup>
Toms Branch	TB <sup>b</sup>	37.9639	78.9469	469	363	64.0
Sherando	SHE	37.9958	78.9917	442	203	39.6
Robinson Hollow	RBH	38.0042	78.9197	448	212	39.6
Spottswood	SPO	37.9617	79.2122	575	196	47.8
Middlebrook	MID	38.0483	79.2292	591	137	51.8
Stoney Creek	STC	37.9900	79.1228	488	205	35.6
Stokesville	STK	38.3550	79.1500	465	148	43.7
Craigsville	CRI	38.0614	79.3997	549	342	72.14
Upper Sherando	US	37.9167	79.0167	594	264	55.9
Elkhorn Lake	ELK	38.3233	79.2275	634	180	32.5
Mills Creek Dam	MLC	37.9536	79.0008	579	263	43.7
Hearthstone Lake	HRS	38.3950	79.1600	567	184	39.6
Mill Creek/County Line	MIC	38.1492	79.4644	658	164	32.5
Lovington	LOV	37.7719	78.8711	283	168	55.9
Montebello Fish	MON	37.8442	79.1303	808	240	39.6
Rockfish	ROC	37.8008	78.7536	149	132	32.5
Brent Gap	BRN	37.8447	78.9281	369	245	47.85
Devils Knob	DK	37.9083	78.9378	1049	296	72.1
Afton Mountain	AFT	38.0289	78.8597	622	134	39.6
Lewis Mountain Camp	LEW	38.4367	78.4792	1036	229	32.5
Ida	IDA	38.5872	78.4261	1006	256	76.2
Skyland	SKY	38.5914	78.3800	1149	249	39.6
Rocky Branch	RO	38.6917	78.3336	506	308	88.4
Big Meadows	BM <sup>b</sup>	38.5217	78.4361	1076	400	72.1
South Fork	LYW	38.3225	78.7550	309	192	47.8
Shenandoah River at						
Lynnwood						
Cootes Store	CO <sup>b</sup>	38.6369	78.8531	320	146	43.7
Bergton NW	BRG	38.7514	79.0686	942	177	32.5
Long Run Road	LR	38.5981	79.0592	975	256	39.6
Dundore Mountain	DUN	38.5264	79.1347	1201	198	24.4
Briery Branch	BRB	38.4439	79.0900	539	185	32.5
Swift Run	SFT	38.3661	78.5786	433	194	47.8
Camp Roosevelt	CAM	38.7256	78.5100	567	156	68.1
Detrick	DET	38.8431	78.4172	274	167	47.8
Smith Creek	SM	38.6214	78.6639	317	162	28.5
Bryce Mountain	BRC	38.8083	78.7703	512	177	43.7
Jerome Gap	JE <sup>b</sup>	38.8769	78.7508	415	223	68.8
Woodstock Reservoir	WOD	38.9058	78.6525	411	147	55.9
Fetzer Gap	FET	38.9708	78.5064	573	129	51.8
Mount Olive	MTL	38.9850	78.4594	299	122	68.1
Strasburg Reservoir	ST <sup>b</sup>	38.9442	78.3550	472	182	96.5
Hogback Mountain	HOG	38.7619	78.2750	1058	261	59.9
Limeton	LIM	38.8808	78.2467	195	96	35.6
Chester Gap	CHT	38.8500	78.1483	610	123	64.0
Manassas Gap	MAN	38.9094	78.0764	283	133	47.8
Nineveh	NIN	39.0069	78.1689	189	101	43.7
Browntown	BRW	38.8040	78.2342	299	203	59.9

<sup>a</sup>Station name, code name, latitude and longitude in decimal degrees, elevation, rainfall accumulation, and maximum recorded 15-min rainfall rate.

<sup>b</sup>Rain gage locations depicted in WSR-88D radar images (Plates 6a–6f).

WSR-88D volume scan reflectivity observations, provides a representation of storm motion that reflects the composite movement of the storm center and the major rain bands associated with the storm. Before reaching the Blue Ridge, the storm centroid moved at a speed of 24 km h<sup>-1</sup>; the speed decreased to 18 km h<sup>-1</sup> as the rain centroid moved along the Shenandoah valley. Shortly after 1500 UTC, the storm centroid passed into the South Branch Potomac watershed. Rainfall time centroids (i.e., the time prior to and after which 50% of rainfall occurs) were calculated for the IFLOWS rain gages in and surrounding the Shenandoah basin. These values were used to compute basin-averaged rainfall time centroids (Table 3). Analyses of the track of spatial rainfall centroids and the basin-averaged time centroids of rain gage observations reflect: (1) the southeast to northwest movement of the tropical storm

system, (2) curvature of rain band precipitation, which resulted in rain bands reaching the eastern Shenandoah basins earlier than western portions of the basin, and (3) intensification of rain band precipitation from east to west, which also resulted in east-to-west time differences in precipitation distribution.

The periods of greatest rainfall accumulation and intensity in the Shenandoah basin preceded the remnants of the hurricane eye. Passage of the center of circulation to the south and west of the Shenandoah basin resulted in strong, low-level easterly flow perpendicular to the Blue Ridge [see also Schwarz, 1970] and Shenandoah Mountain, which is the western ridge of the Shenandoah basin. These aspects of the storm environment played a major role in the orographically enhanced distribution of rainfall.

The storm total rainfall distribution (Plate 1) exhibited two



**Table 3.** Basin-Averaged Rainfall Time Centroids<sup>a</sup>

Basin	Rainfall Mass Centroid, hours	Time of Peak Discharge, hours	Lag Time, hours
SF Shenandoah			
South River			
Dooms	12.5	21.0	8.5
Harriston	12.5	20.5	8.0
Middle River	13.0	28.0	15.0
North River	14.7	23.8 <sup>b</sup>	9.1 <sup>b</sup>
Lynnwood	13.2	30.5	17.3
Front Royal	13.8	51.5	37.7
NF Shenandoah			
Cootes Store	15.5	22.5 <sup>b</sup>	7.0 <sup>b</sup>
Smith Creek	15.3	21.5	6.2
Mount Jackson	15.5	26.5	10.9
Strasburg	15.0	40.8	25.8
Passage Creek	13.8	22.0	8.2
Shenandoah			
Millville	14.5	60.0	45.5

<sup>a</sup>Time of rainfall mass centroid for Shenandoah basins is based on IFLOWS data; time of peak discharge for Shenandoah basins is based on unit discharge data; and lag time is calculated as the difference between occurrence time of the rainfall mass centroid and the peak discharge. All values are in fractional hours from 0000 UTC on September 6, 1996. SF, South Fork; NF, North Fork.

<sup>b</sup>Estimates based on the available data.

local peaks along the Blue Ridge with accumulations exceeding 350 mm (see also Table 2). The largest accumulation was at Big Meadows, which is <10 km north of the point where the rainfall centroids passed over the Blue Ridge and into the Shenandoah basin. The second peak was along the Blue Ridge in the southernmost portion of the Shenandoah basin. A dense network of IFLOWS rain gages in and near the South River basin provides a detailed picture of orographic enhancement of precipitation by the Blue Ridge (Plate 5). Along a southeast-to-northwest transect originating in the lower right-hand corner of Plate 5, rainfall accumulation increased from 132 mm in the valley of the neighboring watershed to 296 mm at the crest of the Blue Ridge. The largest South River storm total accumulation of 363 mm was located on the western slope of the Blue Ridge near the crest. At the northwest end of the transect, rainfall accumulation dropped below 200 mm in the Shenandoah Valley. Peak rainfall accumulations from Hurricane Fran occurred at or near ridge tops (compare with analyses of *Smith et al.* [1996] of the June 27, 1995, Rapidan storm, which produced rainfall accumulations exceeding 600 mm east of the Blue Ridge; see also *Hack and Goodlett* [1960]).

WSR-88D radar reflectivity observations show that rainfall was produced by a combination of weak, structured rain band convection, remnant eyewall convection, and broader-scale stratiform rainfall. The temporal and spatial structure of catastrophic flood-producing rainfall in the Shenandoah River basin and adjacent area is illustrated through time series of 15-min rainfall rate observations at 10 IFLOWS gages (Figures 3a–3e) and radar reflectivity fields from the Sterling WSR-88D at six times (1058, 1200, 1345, 1438, 1635, and 1734) (Plates 6a–6f). All times are in UTC on September 6.

Peak rainfall rates at most locations in the Shenandoah basin were associated with embedded convection in rain bands. The peak rainfall rate in the South River at Devil's Knob occurred around 1100 UTC (see Figure 3a) and was associated with the major band of rainfall (Plate 6a) that moved northward over the Shenandoah basin (at the same time, a secondary peak in 15-min rainfall rate occurred at the nearby Tom's Branch rain gage; Figure 3a). Rainfall from this rainband played a major

role in the Shenandoah River flooding (as illustrated in all time series plots of Figure 3 and reflectivity fields in Plate 6). Organization of embedded convection within the rain band structure imposed large spatial gradients in rainfall rates. At 1100 UTC the Devil's Knob and Tom's Branch gages were contained within the same region of embedded convection (Plate 6a) that produced 15-min rainfall rates ranging from 40 to 75 mm h<sup>-1</sup> at IFLOWS sites over which it passed.

The peak 15-min rainfall rate at Big Meadows of 72 mm h<sup>-1</sup> (Figure 3b) occurred at 1230 UTC and was associated with the primary rainband which passed the South River region 90 min earlier (see Plate 6b). Extreme rainfall accumulations at Big Meadows (the site of the largest storm total accumulation and one of the highest observed rainfall rates, as noted above) were not solely the result of intense rainband convection. Of the 400-mm storm total accumulation at Big Meadows, 175 mm fell from 1330 to 1800 UTC at rain rates between 30 and 50 mm h<sup>-1</sup>. Rainfall during this period was produced by a combination of stratiform precipitation and weak convection. At 1345 UTC (Plate 6c) an elongated, narrow band of elevated reflectivity extended from central Virginia to Big Meadows. Reflectivity values ranged from 30 dBZ (light green/light blue) in central Virginia, to 36 dBZ (dark blue/purple) in a 40-km swath extending southeast of Big Meadows to 42 dBZ (pink) immediately southwest of Big Meadows. Elevated reflectivity values (35–40 dBZ; blue/purple color codes in Plate 6c) occurred along and immediately to the east of the Blue Ridge from Big Meadows southward to the South River. Peaks in Big Meadows rainfall rates from 1330 to 1800 UTC were associated with periods when weak convection embedded in rain bands passed over the gage site (see also Plate 6d at 1438 UTC). The background stratiform rainfall rates did not drop below 20 mm h<sup>-1</sup> until after 1915 UTC.

The narrow rainbands that passed Big Meadows at and after 1438 UTC intensified as they moved northward, producing a narrow ribbon of high rainfall rates (Plates 6e and 6f). At 1635 UTC (Plate 6e), a thin line of convection extended from 80 km east of the Blue Ridge to Rocky Branch (RO) near the crest of the Blue Ridge, and across the Shenandoah Valley to Jerome

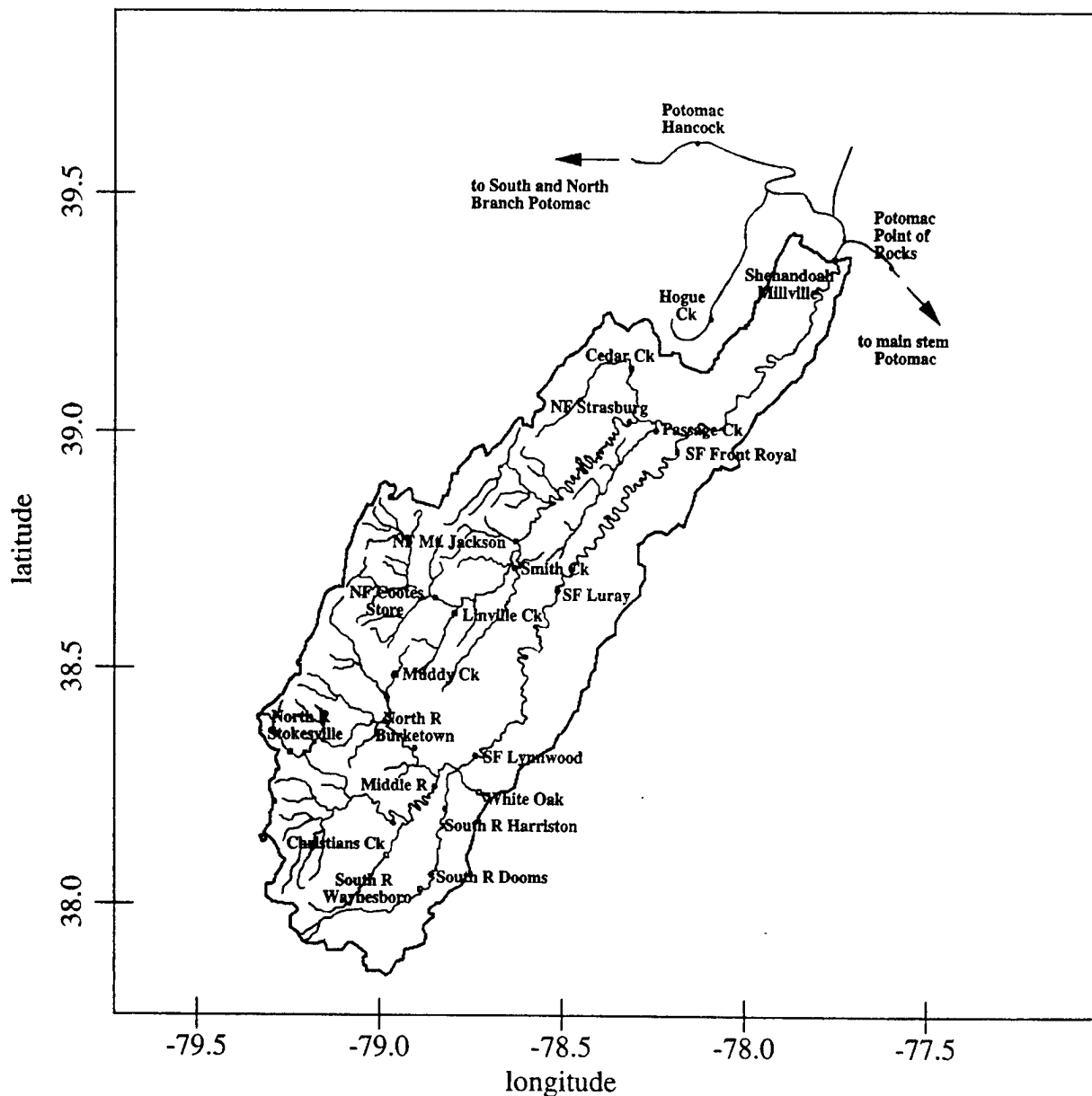


**Figure 2.** Drainage network structure for the Shenandoah River basin with the locations of USGS streamflow gaging stations noted. Solid squares indicate sites where unit values data were obtained for Hurricane Fran. Open squares indicate sites where only peak discharge and mean daily values data were available. The abbreviations SF and NF stand for South Fork Shenandoah River and North Fork Shenandoah River, respectively.

Gap (JE) in the Shenandoah Mountains. The Rocky Branch and Jerome Gap rainfall time series show spikes in rainfall rate to 90 and 70  $\text{mm h}^{-1}$ , respectively (Figures 3b and 3d).

Heavy rainfall in the South River from 1330 to 1530 UTC was associated with a storm element that originated in North Carolina as eyewall convection. In North Carolina this element of the storm resulted in catastrophic flooding in the Tar River basin [Baeck and Smith, 1998]. The area of convection can be tracked from near Raleigh, North Carolina, at 0600 UTC through southern Virginia into the Shenandoah basin. At 1058 UTC it was located at the extreme southwestern area of the Sterling WSR-88D coverage (Plate 6a). The region of convection moved separately from the remnant center of circulation

of Fran. At 1200 UTC it was located 78 km northeast of the storm center. From 1438 UTC (Plate 6d) to 1635 UTC (Plate 6e) the storm element moved down the South River into South Fork Shenandoah basin. Motion of this storm element played an important role in the magnitude and timing of flood peaks in the South River and South Fork Shenandoah, as discussed further in section 4. As previously noted, the peak rainfall rate at Tom's Branch in the South River basin did not occur with the major rainband, but during this extended period of 45–65  $\text{mm h}^{-1}$  rain rates from 1330 to 1530 UTC (Figure 3a). At other sites in the South River, this period produced high rainfall rates that were exceeded only by rain rates from the major rain band.

The composite effects of storm structure, storm evolution

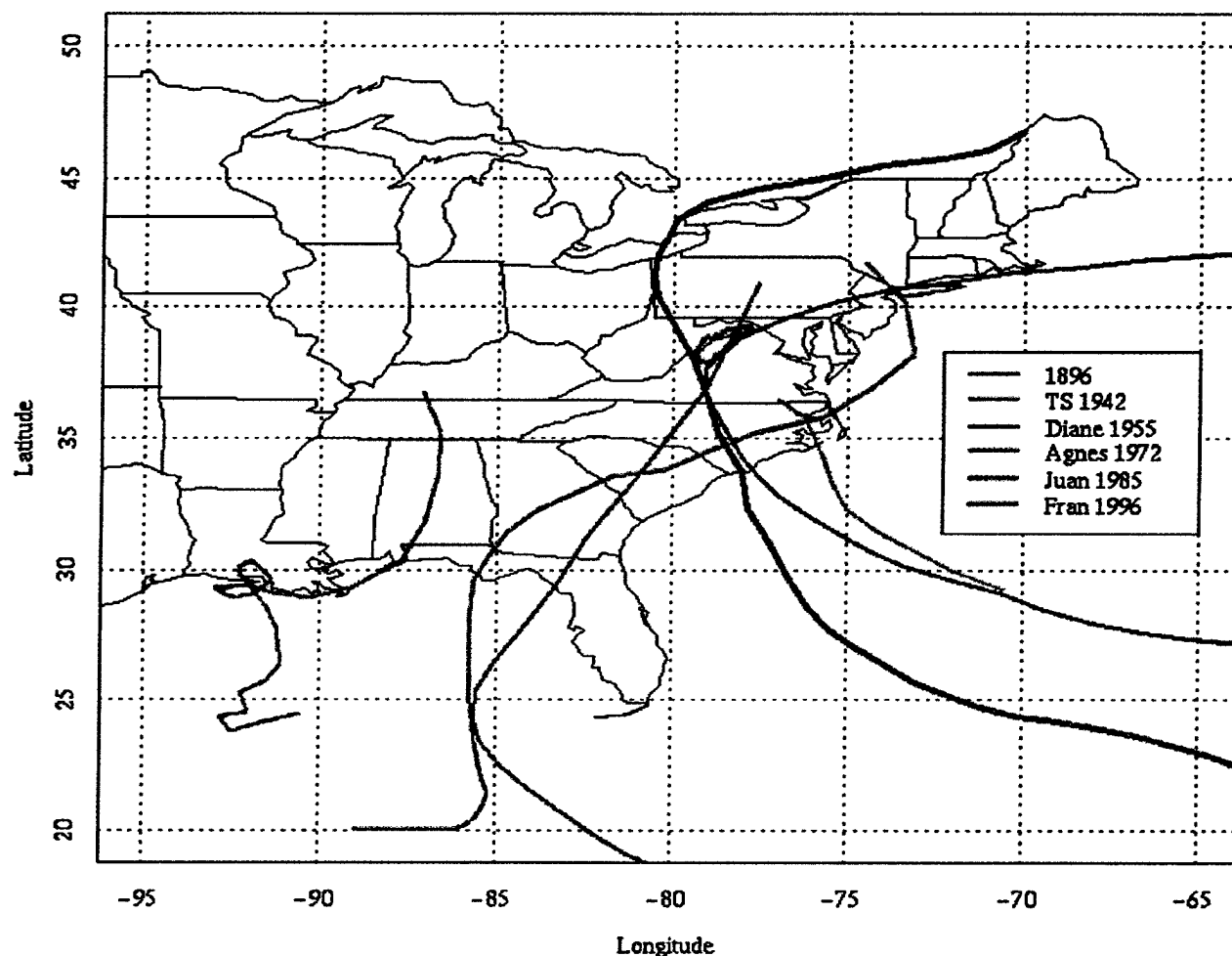


**Plate 2.** Tracks of six tropical storms which produced major flood peaks in the Potomac River basin during the past 110 years. The Shenandoah watershed boundary is outlined in orange.

and orographic enhancement of precipitation on the regional distribution of precipitation are illustrated in Figures 4 and 5 through the relationship between (1) storm total rainfall and maximum 15-min rainfall rate (Figure 4) and (2) storm total rainfall and the fraction of storm total rainfall produced by heavy rainfall rates (i.e., 15-min rainfall rates exceeding  $25 \text{ mm h}^{-1}$ ; Figure 5). The North River and southern North Fork Shenandoah region (open squares, color-coded orange in Plate 3) had relatively low rainfall rates. In contrast, the northern North Fork Shenandoah River watershed (solid squares, color-coded maroon in Plate 3) had anomalously large rainfall rates for a given rainfall accumulation due to intensification of rainband precipitation in the upper watershed (see discussion above). The Blue Ridge (open triangles, color-coded pink in Plate 3) and South River (solid triangles, color-coded blue in Plate 3) regions, with their mix of rainband convection, remnant eyewall convection and extended period of elevated stratiform precipitation, produced large rainfall rates and the largest storm total accumulations. As noted earlier, the lowest rainfall accumulations and rainfall rates occurred in portions of the Shenandoah Valley that were farthest removed from the elevated terrain of the Blue Ridge, Shenandoah, or Massanutten Mountains.

The fraction of storm total rainfall with 15-min intensity  $>25$

$\text{mm h}^{-1}$  increased sharply with storm total rainfall accumulation (Figure 5). Rainfall rates greater than  $25 \text{ mm h}^{-1}$  accounted for  $>70\%$  of the rainfall measured at the two sites where accumulations were greatest (Big Meadows and Toms Branch). Greater than  $25 \text{ mm h}^{-1}$  fractional intensity values were largest in the South River due to the combined effects of the main rainband and the remnant eyewall convection on rainfall rates. The  $25 \text{ mm h}^{-1}$  fractional intensity was also greater in the northern North Fork due to the intensification of rainbands after passing Big Meadows, discussed above.

Rainfall intensities  $>25 \text{ mm h}^{-1}$  exceed saturated hydraulic conductivity values in the Shenandoah basin and suggest the potential for significant infiltration excess runoff (see section 4 for additional discussion). Pronounced nonlinearity in runoff response to precipitation underlies the importance of short-term variability of rainfall rate.

The peak rainfall rates from Hurricane Fran at 15-min time-scale of nearly  $100 \text{ mm h}^{-1}$  are larger than those documented for any of the tropical storms of Table 1 [see Bosart and Carr, 1978; Clark et al., 1987; Costa, 1974; Engman et al., 1974; Miller, 1990]. Much larger rainfall rates have been reported for orographic thunderstorms in the central Appalachians (the June 27, 1995, Rapidan storm produced rainfall rates  $>300 \text{ mm h}^{-1}$  for time periods  $>15 \text{ min}$  [see Smith et al., 1996]) and for

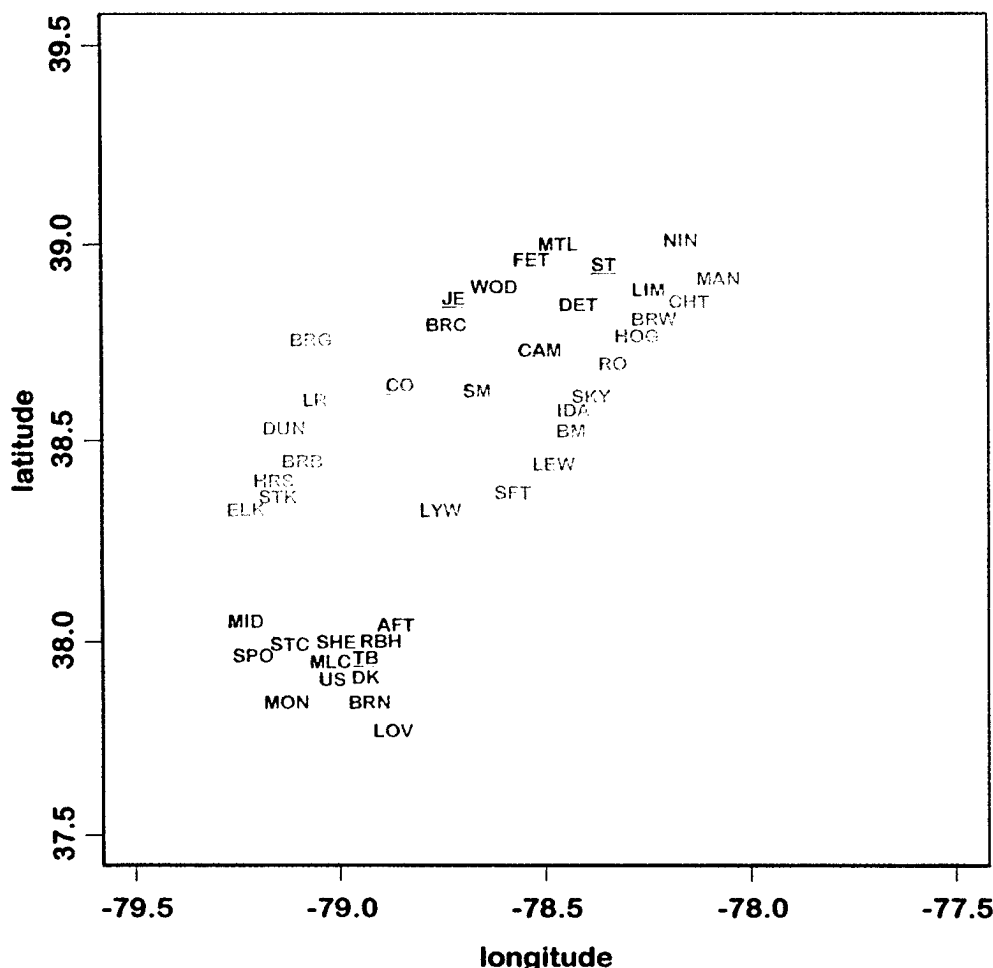


**Plate 3.** The locations of IFLOWS rain gages in and around the Shenandoah River basin. The gages are color coded based on five regional classifications: blue, South River; pink, Blue Ridge; green, valley; maroon, northern North Fork Shenandoah and Passage Creek; and orange, southern North Fork Shenandoah and North River South Fork Shenandoah. The underlined gages are included in the WSR-88D radar images (Plate 6).

tropical storms in more southerly locations. The remnants of Hurricane Camille likely produced rainfall rates comparable to the Rapidan storm over small areas along the east slope of the Blue Ridge near the Shenandoah River basin. As noted by Smith *et al.* [1996], however, this storm is more closely related to the Rapidan storm than to the tropical storms which produced extreme flooding over a wide range of basin scales in the central Appalachians (Table 1). From the perspective of the tropical storms of Table 1, distinctive features of Hurricane Fran were its rapid motion and anomalously large rainfall rates. The combined influence of rapid storm motion and large rainfall rates on runoff response during Hurricane Fran are examined in detail in section 4.

#### 4. Analyses of Flood Response

Rainfall produced by Hurricane Fran resulted in severe flooding throughout the Shenandoah River basin (Figure 6a). Flood peaks with recurrence intervals greater than 100 years occurred in 11 of 19 basins ranging in size from 5 to 8000 km<sup>2</sup>. Record peak discharges were set in 11 and equaled in 3 of the 20 basins for which data were available. The most severe flood-

ing occurred at basin scales <3000 km<sup>2</sup>. Flood peaks at drainage basin scales exceeding 3000 km<sup>2</sup> were characterized by recurrence intervals of ~50 years. Hydrologic response to Hurricane Fran is summarized in Table 4 through flood peak and water balance summaries and in Figures 7a–7f through nested flood hydrograph plots throughout the basin. The contrasting flood response properties of Shenandoah drainage basins are examined below in terms of (1) orographic enhancement of precipitation, (2) drainage network structure, (3) storm structure and motion, (4) land use–land cover properties, (5) soil moisture properties, and (6) runoff production mechanisms.

##### 4.1. Orographic Enhancement of Precipitation

The spatial distribution of storm total runoff (Figure 6b; compare with the rainfall accumulation map of Plate 1) illustrates the primary role of orographic enhancement of tropical storm precipitation for extreme flood response. Storm total runoff (in mm) was computed from USGS discharge observations by integrating volumetric water flux (in m<sup>3</sup> s<sup>-1</sup>) over the period of the flood (September 5–9) and dividing by the drainage area.

The largest runoff volumes were concentrated in the high-elevation regions of the western Shenandoah basin (194 mm

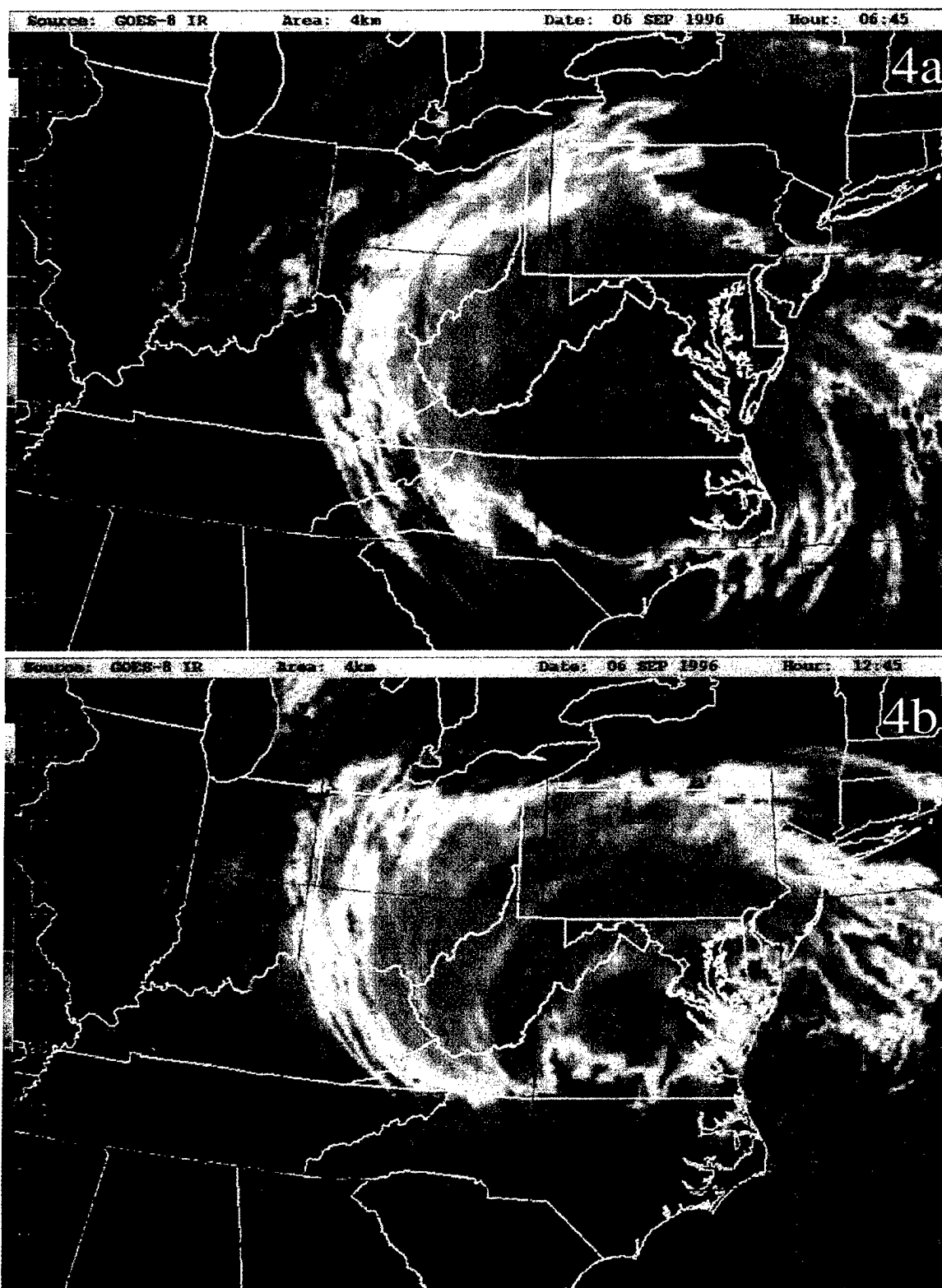


**Plate 4.** GOES IR images of Hurricane Fran on September 6, 1996 at (a) 0645 UTC, located over northern North Carolina and (b) 1245 UTC, located in central Virginia. The brightness temperature color scale is provided on the left side. The most intense convection is associated with the coldest temperatures. At coldest temperatures are approximately  $-80^{\circ}\text{C}$ . At 1245 UTC, coldest temperatures are approximately  $-60^{\circ}\text{C}$ .

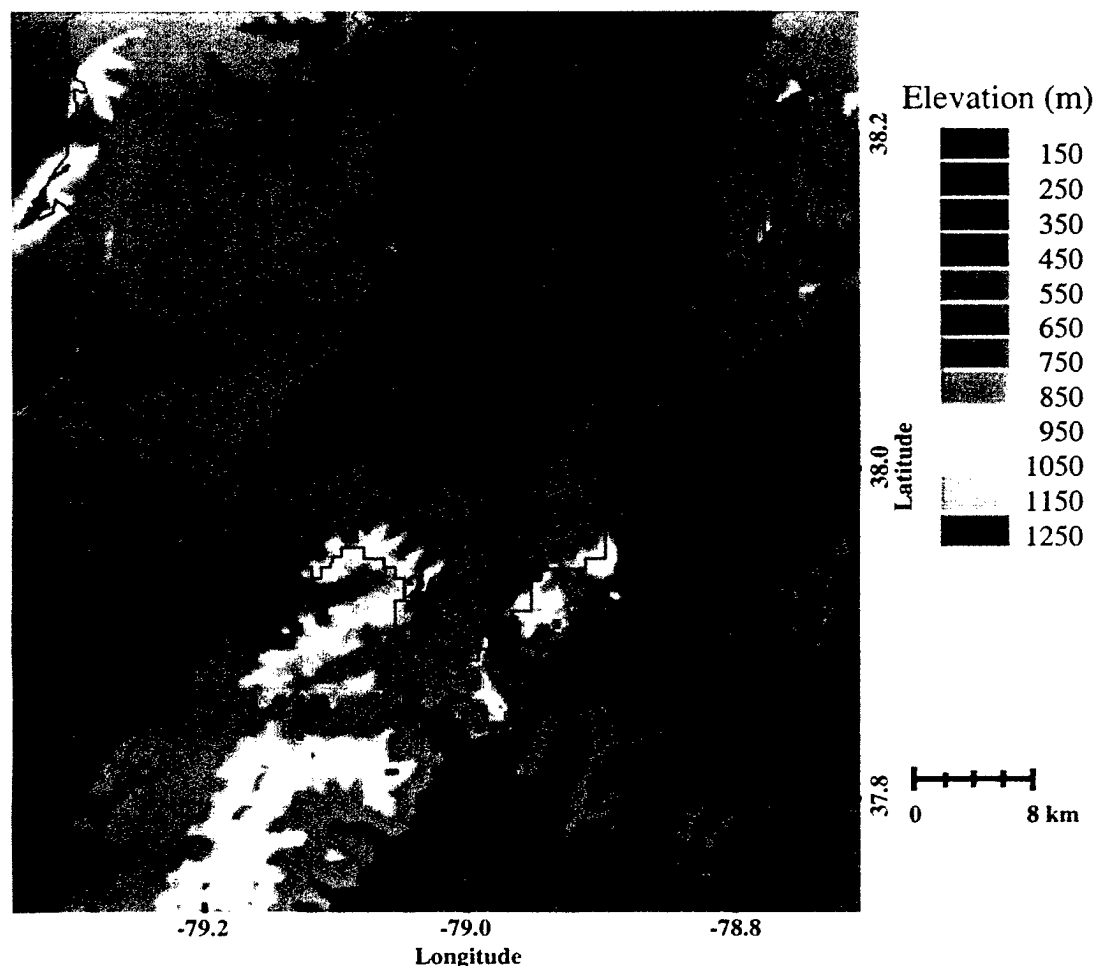


**Plate 5.** Detail of storm rainfall accumulations in the South River of the South Fork Shenandoah River and surrounding region. Red dots show the locations of IFLOWS gages, with accumulation given in millimeters. The background map is a false color representation of topography derived from 30-m USGS DEM for the region.

for the North River at Stokesville, 182 mm for the North Fork Shenandoah at Cootes Store, and 157 mm for Muddy Creek). High runoff volumes also occurred along the Blue Ridge, resulting in the increase in unit area runoff in the South Fork Shenandoah between Lynnwood (97 mm) and Front Royal (114 mm). Storm total runoff for the South Fork Shenandoah basin between Lynnwood and Front Royal was 147 mm. In the reach between Luray and Front Royal the runoff volume was 161 mm. This region of the Blue Ridge was the location of the largest rainfall accumulations observed throughout the Shenandoah basin (corresponding to the rain gages at Big Meadows and Rocky Branch, Figure 3b and Table 2). The smallest runoff volumes were concentrated in the low-elevation basins draining the Shenandoah Valley (for example, Smith Creek at 78 mm).

The contrasting spatial characteristics of flood response for Hurricane Fran, associated with orographic enhancement of precipitation, play a fundamental role in determining the regional variation of flood frequency. Orographic enhancement of precipitation results in the occurrence of larger unit discharge values in high-elevation basins not only for Hurricane Fran but throughout the flood frequency distribution. This point is illustrated in Figure 8 through sample flood frequency distributions for the high-elevation North Fork Shenandoah

River at Cootes Store (544 km<sup>2</sup>) and the low-elevation Smith Creek catchment (241 km<sup>2</sup>; see Figure 2 for basin locations).

#### 4.2. Drainage Network Structure

The role of drainage network structure in controlling basin-scale flood response can be illustrated through the geomorphological instantaneous unit hydrograph (GIUH)  $f(t)$ , which represents the basin response at time  $t$  to a unit mass input of rainfall at time 0 uniformly distributed over the catchment (see *Rodriguez-Iturbe and Rinaldo* [1997] for additional discussion). *Gupta et al.* [1986] show that the GIUH  $f(t)$  is proportional to  $W'(tV)$ , where the width function  $W(x)$  is the number of channel segments at length  $x$  from the outlet,  $V$  is a uniform flow velocity, and  $t$  is time. From nested hydrograph analyses a wave celerity of 1.9 m s<sup>-1</sup> was estimated for both the South Fork and North Fork Shenandoah (see Figures 7c and 7e). The width function for the Shenandoah River basin was extracted from EPA RF3 river reach data. GIUH representation of basin response, determined by using the estimated width function and wave celerity as the uniform flow velocity, is summarized in Figure 9 through a contour map of travel time to the basin outlet. A key observation from this analysis is that the surface runoff travel time of 45 hours at the southern end of the basin

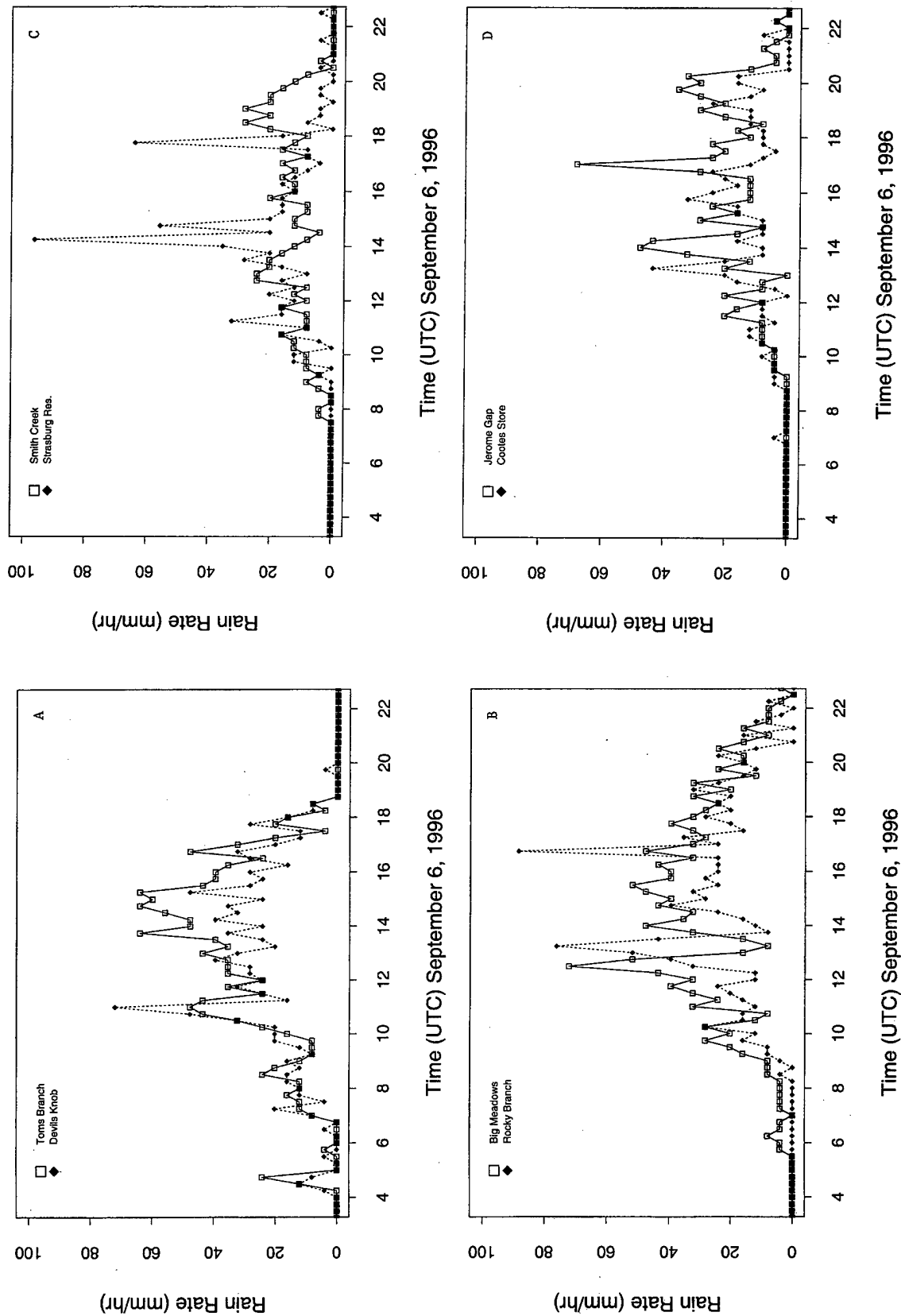


Figure 3. Time series of 15-min rainfall rate data at 10 IFLOWS gages: (a) Toms Branch and Devils Knob, (b) Big Meadows and Rocky Branch, (c) Smith Creek and Strasburg Reservoir, (d) Jerome Gap and Cootes Store, and (e) Long Run Road and Stokesville (see Plate 3 and Table 2 for gage locations).

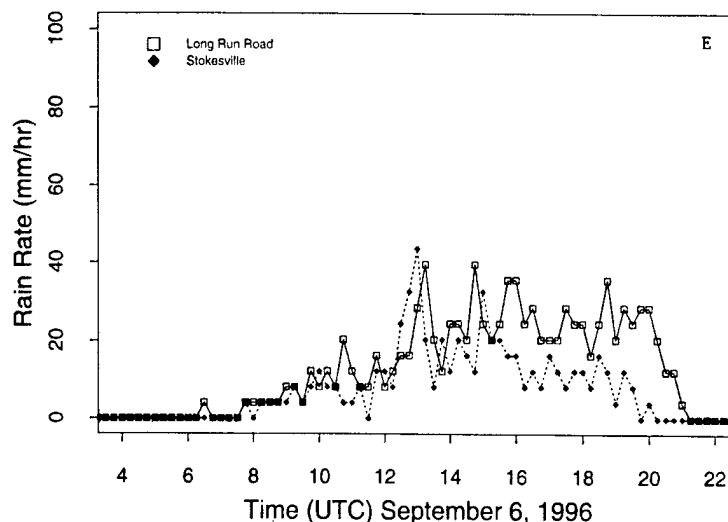


Figure 3. (continued)

is  $\sim 4$  times longer than the time required for the storm to traverse the basin from south to north (see section 4.3).

The drainage network structure, as represented by the GIUH, provides a reasonable simulation of flood magnitude and timing at the basin outlet (Figure 10). These results are based on uniform runoff over the catchment during the 10-hour rainfall period. The GIUH simulations result in distinct peaks from the North Fork and South Fork at the basin outlet, in contrast to the observed hydrograph (solid line), which indicates that the two basins contributed synchronously to the peak discharge (Figure 10, top right). Conversely, in the South

Fork Shenandoah the GIUH simulation has less distinct peaks than the observed hydrograph (Figure 10, middle right). The initial GIUH peak in the South Fork Shenandoah is too small and the second peak too large (Figure 10, middle right), reflecting the heterogeneity in runoff distribution that is not accounted for by the GIUH analysis. Timing of the GIUH response in the North Fork Shenandoah is much too fast (Figure 10, bottom right), reflecting the elements of storm motion and structure that controlled the time-varying runoff production throughout the basin.

The assumption of spatially and temporal uniform runoff is

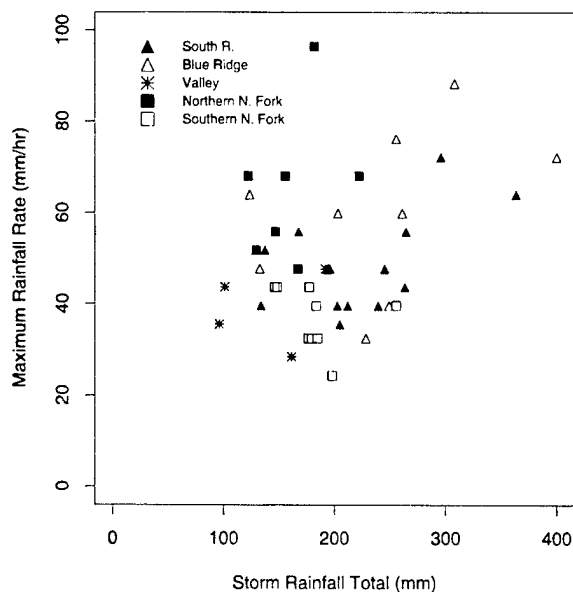


**Figure 4.** Maximum rainfall rate (in  $\text{mm h}^{-1}$ ) versus storm total rainfall (in mm) for IFLOWS rainfall data grouped by five regions (South River, Blue Ridge, Valley, northern North Fork, and southern North Fork, see Plate 3).

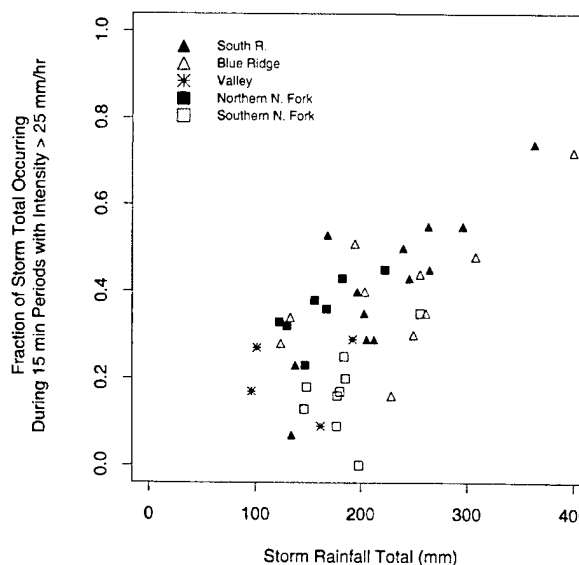


**Figure 5.** Fraction of the storm total which occurred during 15-min time periods with rainfall intensity  $> 25 \text{ mm h}^{-1}$ , versus storm rainfall total in millimeters for IFLOWS rainfall data grouped by five regions (South River, Blue Ridge, Valley, northern North Fork, and southern North Fork, see Plate 3).



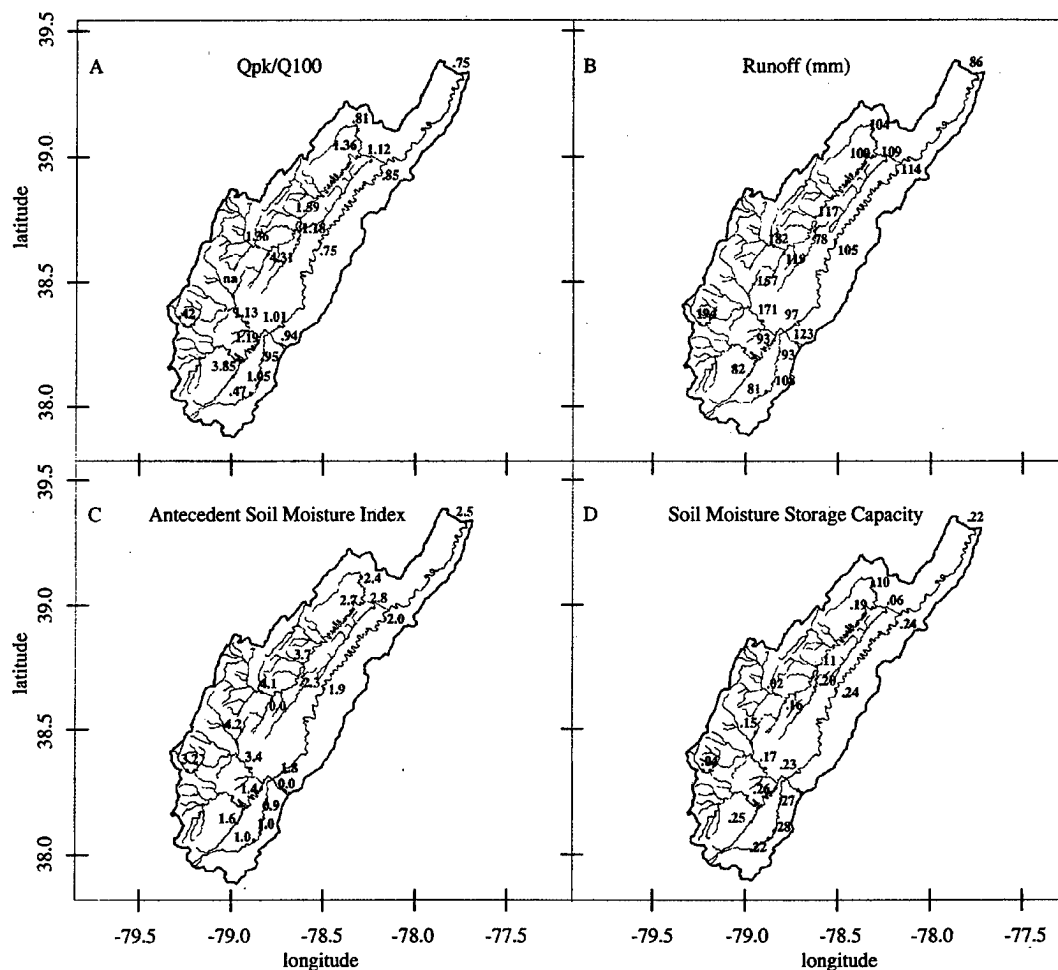


**Figure 6.** (a) Ratio of the peak discharge associated with Hurricane Fran to the generalized extreme value (GEV) distribution, using  $L$  moment estimators of Hosking [1990], estimate of the 100-year return interval discharge at USGS streamflow gaging sites throughout the Shenandoah. The record for Muddy Creek (refer to Figure 2) is too short to accurately determine the 100-year return interval discharge and is not included. Values  $>1$  indicate  $>100$ -year events. (b) Spatial distribution of storm total runoff (mm) throughout the Shenandoah River basin. (c) Antecedent soil moisture index values at USGS streamflow gaging sites throughout the Shenandoah basin. The antecedent index was computed based on the ratio of discharge preceding Fran to the median discharge value for September. (d) Soil moisture storage capacities throughout the Shenandoah River basin, represented as the ratio of the daily discharge exceeded 90% of the time to the mean daily flow.

at odds with the orographically controlled spatial distribution of rainfall (section 4.1) and with the temporal and spatial distribution of rainfall determined by storm structure and motion (as discussed in section 4.3). The assumption of uniform flow velocities is also not valid over the entire watershed. There are significant contrasts between response times (Table 3) of low-gradient, Shenandoah Valley basins (for example, Middle River (Figure 7b) and Smith Creek (Figure 7d)) and high-elevation basins (North River (Figure 7b), North Fork Shenandoah (Figure 7d), and South River (Figures 7a and 7b), for example). The low gradient environment of Shenandoah Valley basins combines with lowest values of drainage density (Table 5) to produce markedly slower flood response than in other portions of the Shenandoah basin.

#### 4.3. Storm Structure and Motion

Storm structure and motion (see section 3) were important elements of flood response in the Shenandoah watershed for basin scales ranging over 2 orders of magnitude (from  $<100$   $\text{km}^2$  to  $10,000$   $\text{km}^2$ ). Drainage network analyses of section 4.2 and nested flood hydrographs (Figure 7) for the Shenandoah River basin provide a background for interpreting the role of storm structure and motion for the scale-dependent flood response.

The large-scale motion of the storm system (Plate 1) from south to north served to amplify the peak discharge at the basin outlet (note, in particular, the anomalously low volume-to-peak ratios inferred in Table 6). Storm motion was, however, far from that which would optimize peak discharge for a given

**Table 4.** Summary of Flood Response in the Shenandoah River Basin to Extreme Rain Produced by Remnants of Hurricane Fran<sup>a</sup>

Basin	DA, km <sup>2</sup>	Peak, m <sup>3</sup> s <sup>-1</sup> km <sup>-2</sup>	Runoff, mm	Rainfall, mm	Runoff Ratio
SF Shenandoah					
South River					
Dooms	386	1.55	108	240	0.45
Harriston	549	1.49	93	225	0.41
Middle River	971	1.29	93	170	0.55
North River	982	2.03	171 <sup>b</sup>	210	0.81
Lynnwood	2808	1.08	97	190	0.51
Luray	3566	0.89	105	200	0.53
Front Royal	4253	0.81	114	215	0.53
NF Shenandoah					
Cootes	544	3.30	182 <sup>b</sup>	220	0.83
Smith Creek	241	1.46	78	150	0.52
Mount Jackson	1311	2.22	117	180	0.65
Strasburg	1989	1.62	100	175	0.57
Passage Creek	228	2.86	109	150	0.73
Shenandoah					
Millville	7827	0.56	86	185	0.46

<sup>a</sup>The value for the intervening area between the SF Shenandoah at Front Royal and Lynnwood is not included. Basin-averaged rainfall over this region was 240 mm, while runoff was 147 mm, resulting in a runoff-to-rainfall ratio of 0.61. Volume-to-peak ratios are not given explicitly due to space constraints but may be inferred from the provided data. DA, drainage area.

<sup>b</sup>Estimates based on water mass balance.

runoff volume (see *Smith et al.* [2000] for an example of storm motion and structure which optimizes peak discharge). As noted in section 4.2, the time for the storm to pass through the basin was approximately 1/4 of the time for runoff produced in the southernmost portion of the basin to move the drainage network to the basin outlet at Millville.

Structure, motion, and evolution of rain bands strongly influenced the timing of flood response in the South Fork and North Fork of the Shenandoah. Motion of the principal rain band (Plates 6a–6c) affected runoff production along the South Fork Shenandoah at Lynnwood, Luray, and Front Royal, which were characterized by near simultaneous hydrograph rise times (Figure 7c). This response was due to rapid motion of the primary rain band (timescale <2 hours; see discussion in section 3) and the long response times from the South Fork headwaters to Front Royal (~30 hours; see Figure 9). Storm motion and organization influenced the form of the flood hydrographs at Luray and Front Royal, which were characterized by an initial rise followed by a primary rise to the observed peak discharge. The initial rise is attributable to runoff occurring over the intervening drainage area; the primary peak is attributable to downstream advection from Lynnwood to Luray and from Luray to Front Royal.

Initial stream response to rainfall moved progressively from the eastern to western portion of the Shenandoah basin, as seen in the flood hydrographs for the Shenandoah at Millville, South Fork Shenandoah at Front Royal, and the North Fork Shenandoah at Strasburg (Figure 7f). Downstream advection of the flood peak along the North Fork Shenandoah between Mount Jackson and Strasburg (Figure 7e) suggests that the bulk of the North Fork flood originated in the high-elevation headwater region, supporting earlier analyses indicating the importance of orographic enhancement of rainfall. The flood wave passed through the North Fork Shenandoah valley bottom without significant attenuation or augmentation.

The importance of storm motion for flood response at scales <100 km<sup>2</sup> is clearly illustrated in the South River, where the downstream flood peak at Harriston occurred simultaneously

with the upstream peak at Dooms (Figure 7a). The peak at Harriston was augmented by movement of the remnant eye-wall convection (as discussed in section 3 and shown in Plates 6c–6e) down the South River basin (see also the peak rain period at the Toms Branch IFLOWS rain gage, Figure 3a).

#### 4.4. Land Use–Land Cover Properties

The interaction between land cover and streamflow has been studied for some time [see, e.g., *Hewlett et al.*, 1977; *Potter*, 1991; *Swank and Crossley*, 1986; *Zon*, 1927], but the influence of land use and cover on extreme floods is still not well understood. The idea that forest cover attenuates flood peaks by increasing infiltration has found particular resonance with those involved in watershed management and policy development (see, for example, discussion of Hurricane Fran impacts in the context of Chesapeake Bay water quality [*Potomac Basin Reporter*, 1996]).

Analyses of Shenandoah hydrologic response to Hurricane Fran rainfall and its relation to land cover (see especially Tables 3, 4, and 7 and Figure 7 and Plate 7) provide little direct evidence for attenuation of flood peaks or reduction of runoff production. The largest runoff volumes and flood peaks occurred in the forested, high-elevation portions of the basin. Multiple linear regression analyses with lag time (i.e., the time interval between the occurrence of the mass centroid of rainfall over a basin and the peak discharge at its outlet; see Table 3) as the response variable indicate that flood response time is most sensitive to drainage basin area (1% significance level) but is also influenced by drainage density (10% significance level) and aspect ratio A1 (5% significance level). Lag time is relatively insensitive to land use and cover (Table 8).

The extensive forest cover throughout the Shenandoah River basin (Plate 7, and Table 7) is new-growth forest dating from the late 1800s. Conversion of forest land to other uses during the twentieth century has been concentrated along valley bottoms, while upland areas, which experience the heaviest rainfall during extreme events, have remained forested. It is possible that flood response would have been faster and

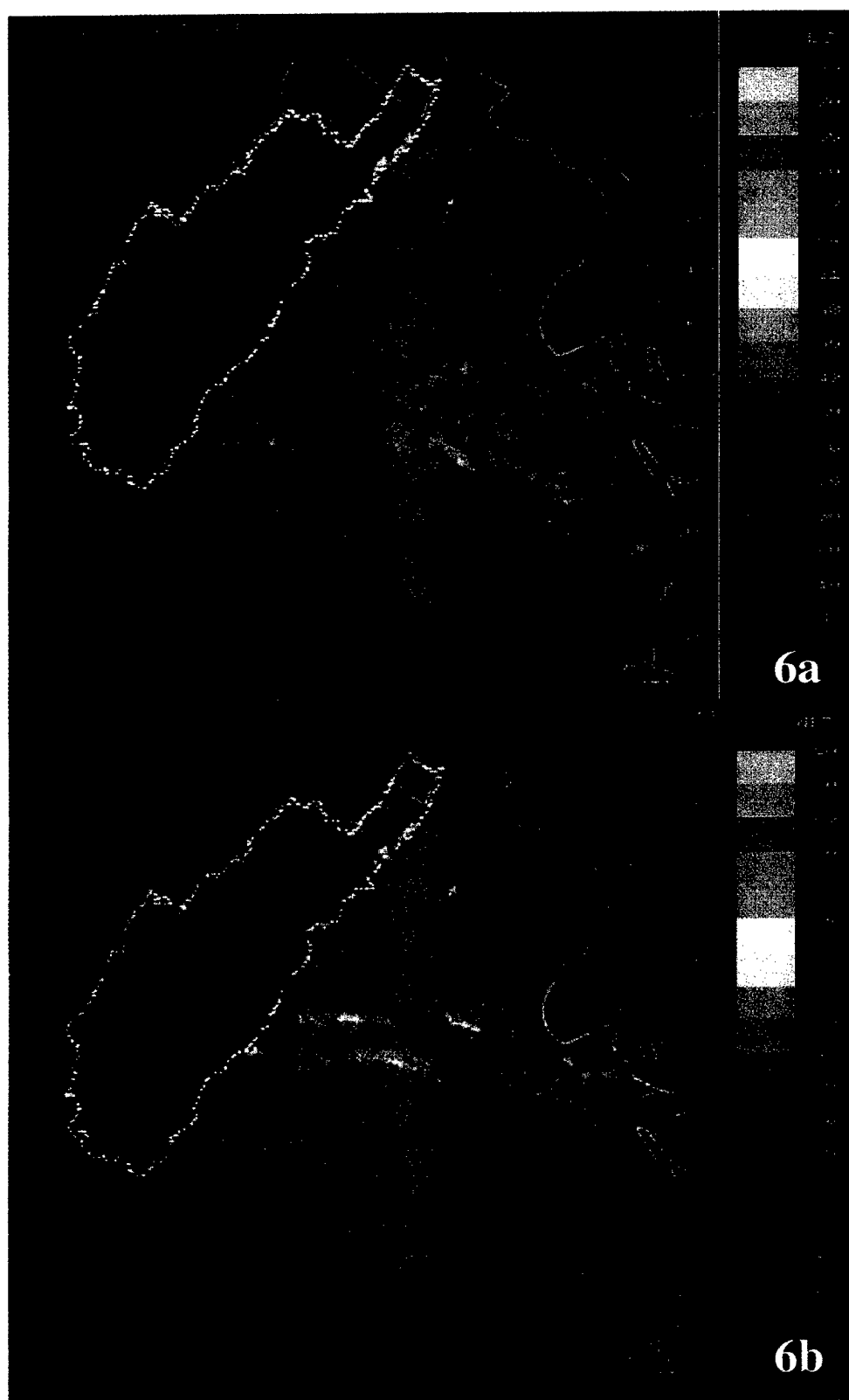


**Plate 6.** WSR-88D radar reflectivity fields from the Sterling WSR-88D at (a) 1058, (b) 1200, (c) 1345, (d) 1438, (e) 1635, and (f) 1734 UTC on September 6. The code names of IFLOWS gages identified in Plate 3 and Table 2 are included for reference. The basin boundary for the Shenandoah River basin is depicted as a white dotted line.

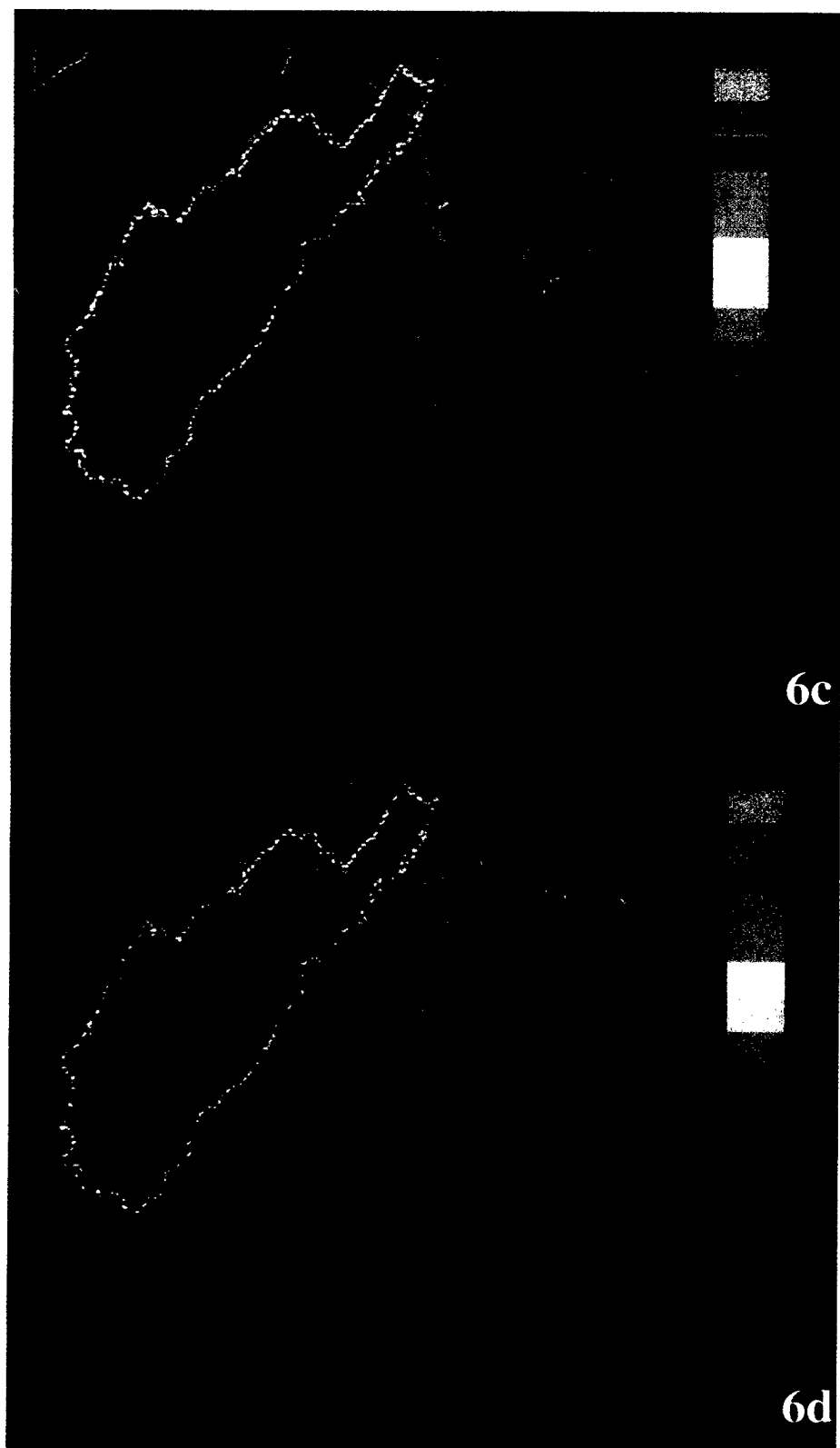


Plate 6. (continued)

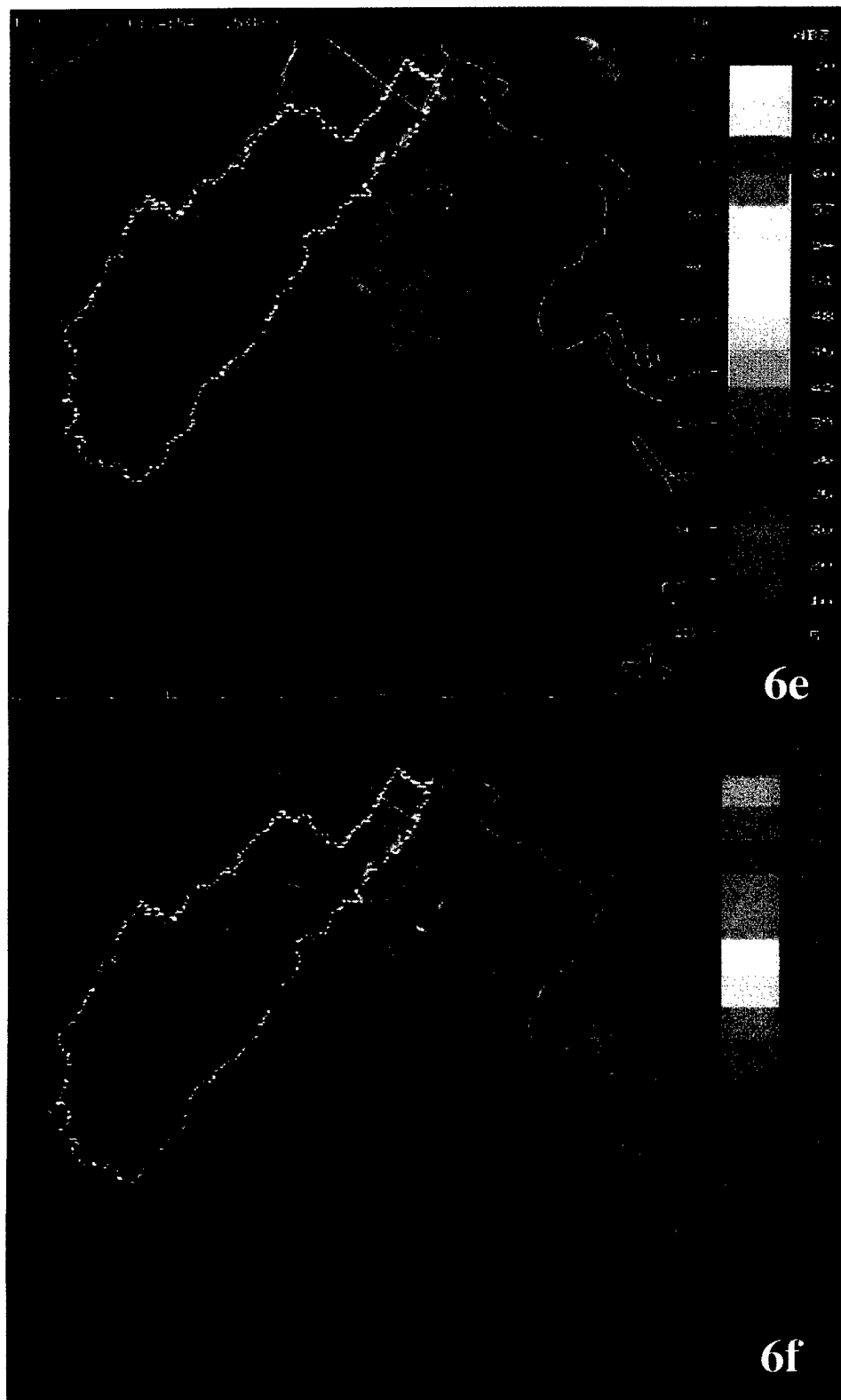
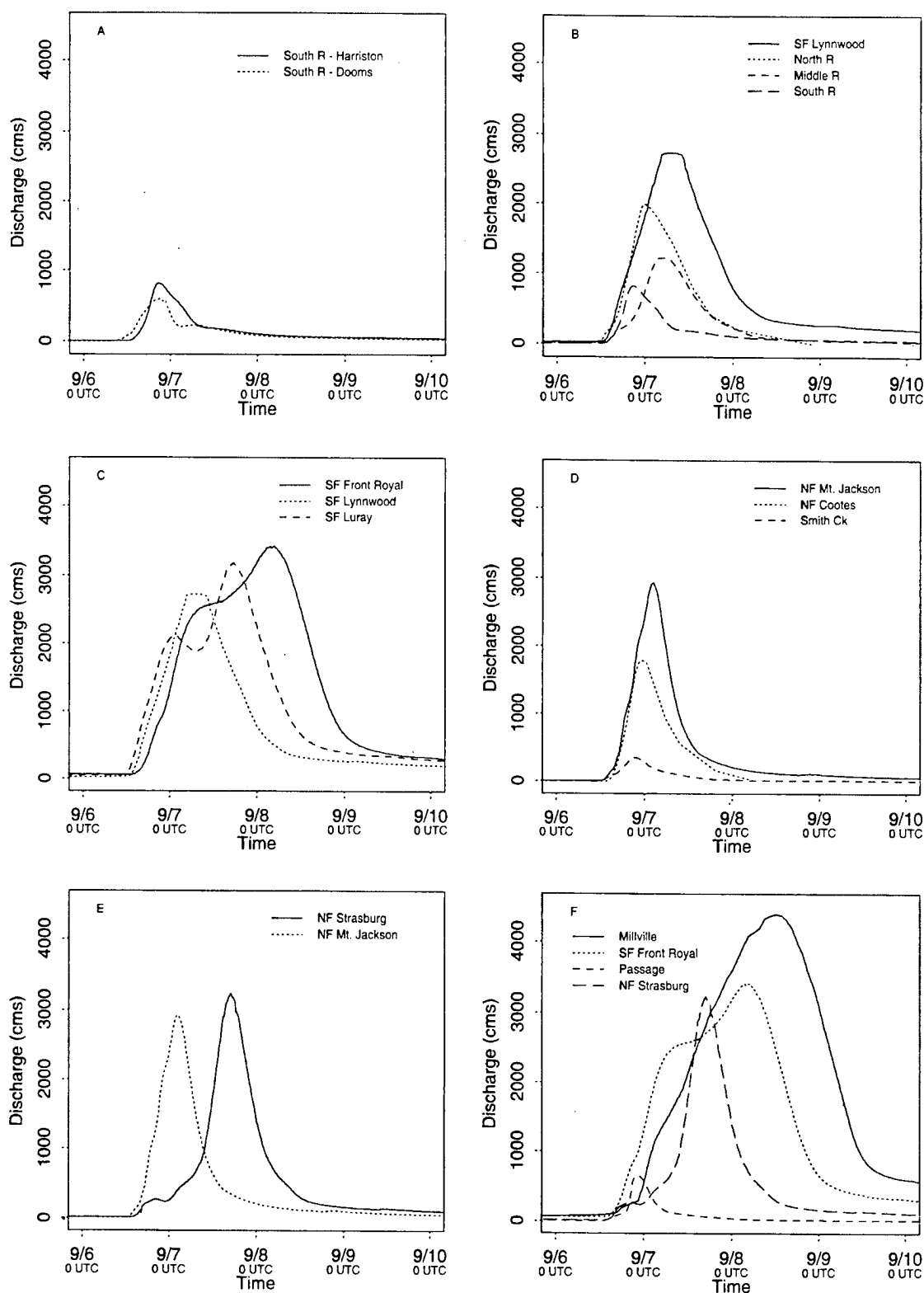
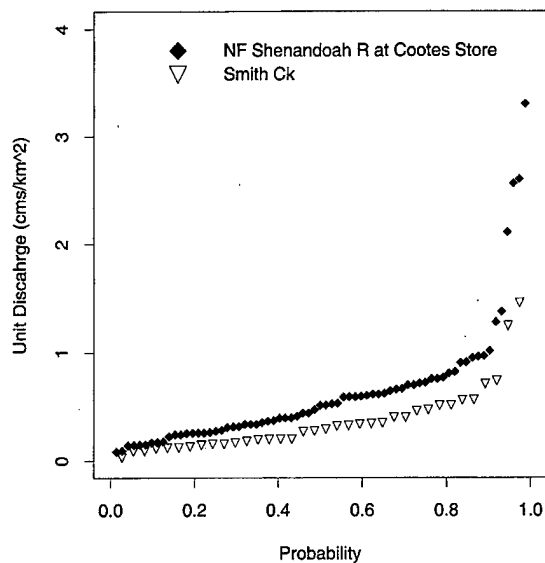


Plate 6. (continued)



**Figure 7.** Nested flood hydrograph plots for locations throughout the Shenandoah where unit values data are available. Details of the drainage network structure are shown in Figure 2, and information for the individual basins is available in Tables 4 and 5. (a) Discharge at South River gaging stations. (b) Discharge at gaging stations at and upstream of the South Fork Shenandoah River at Lynnwood. (c) Discharge along the main stem of the South Fork Shenandoah River. (d) Discharge at gaging stations at and upstream of the North Fork Shenandoah River at Mount Jackson. (e) Discharge along the main stem of the North Fork Shenandoah River. (f) Discharge at the most downstream gaging station of major Shenandoah River tributaries.



**Figure 8.** Sample flood frequency distributions for the North Fork Shenandoah River at Cootes Store, a high-elevation basin with a drainage area of 544 km<sup>2</sup>, and for Smith Creek, a low-elevation basin with a drainage area of 241 km<sup>2</sup>. The annual peak data have been scaled by drainage area.

greater if some of the high-elevation mountainous regions were unforested.

#### 4.5. Soil Moisture Properties

Wood *et al.* [1990] note that for large floods the role of antecedent soil moisture for flood response should decrease with increasing return interval. An open question is where "large" begins. In other words, how rare must floods be for antecedent soil moisture to have negligible importance for flood response? An antecedent moisture index for each sub-basin was derived by dividing the discharge preceding Fran by the median discharge value for September. Results are shown in Figure 6c. Values greater than one indicate wetter than average conditions for the month of September. Soil conditions in the western half of the Shenandoah watershed were significantly wetter in the prestorm environment than the remainder of the basin. Of particular note are values for the North River, North Fork Shenandoah at Cootes Store, and North Fork Shenandoah at Mount Jackson. Extraordinary peak discharge and storm total runoff values were observed at these stations (Figures 6a and 6b). In addition, runoff-to-rainfall ratios were generally higher in the North Fork Shenandoah than the South Fork Shenandoah (Table 4). These results suggest that in the central Appalachian region, antecedent moisture conditions can play a significant role in determining land-surface response to extreme rainfall for events with return intervals exceeding 100 years.

In the central Appalachian region, soil moisture storage capacity is closely linked to spatial variations in bedrock and surficial geology. Folded sedimentary rocks underlie most of the Shenandoah River basin. Thin, low-permeability soils cover shales and sandstones in the North River, North Fork Shenandoah River, and Passage Creek [Smith *et al.*, 1982]. These regions are characterized by low storage capacities and are poor sources of baseflow [Smith *et al.*, 1982]. Relatively thick surficial deposits, developed from colluvium and under-

lain by carbonate rocks, are characteristic of the South Fork Shenandoah River, Middle River, and South River [Ciolkosz *et al.*, 1979; Hack, 1965]. These are regions of high groundwater storage and high baseflow [Smith *et al.*, 1982; White, 1976, 1977]. The ratio of daily discharge exceeded 90% of the time to the mean daily flow,  $Q_{90}/Q_A$ , illustrates the variability in soil moisture storage capacity in the Shenandoah River basin (Figure 6d). Soil moisture storage capacities along the western Shenandoah basin are significantly lower than those in the eastern portion of the basin. The more extreme flood response in the western Shenandoah basin suggests that soil moisture storage capacity is an important factor determining land-surface response to extreme rainfall.

Higher antecedent soil moisture conditions (Figure 6c) and lower soil moisture storage capacity (Figure 6d) contributed to the more extreme flood response observed in the western Shenandoah basin despite the fact that measured rainfall rates and rainfall accumulations were greatest in the eastern portion of the basin along the Blue Ridge. The relative difference between rainfall rate and potential infiltration rate, as represented by saturated hydraulic conductivity (Plate 8 and Table 9), may also affect runoff generation.

#### 4.6. Runoff Production Mechanisms

The interactions between soil moisture deficit, soil hydraulic properties (especially, saturated hydraulic conductivity), and rainfall rate determine whether infiltration excess or saturation excess runoff production mechanisms control flood response. In this section, numerical simulation studies are used to examine the runoff production mechanisms at play in the Shenandoah River basin during Hurricane Fran.

Simulations are based on Richards equation for one-dimensional unsaturated flow in the soil column (see Appendix

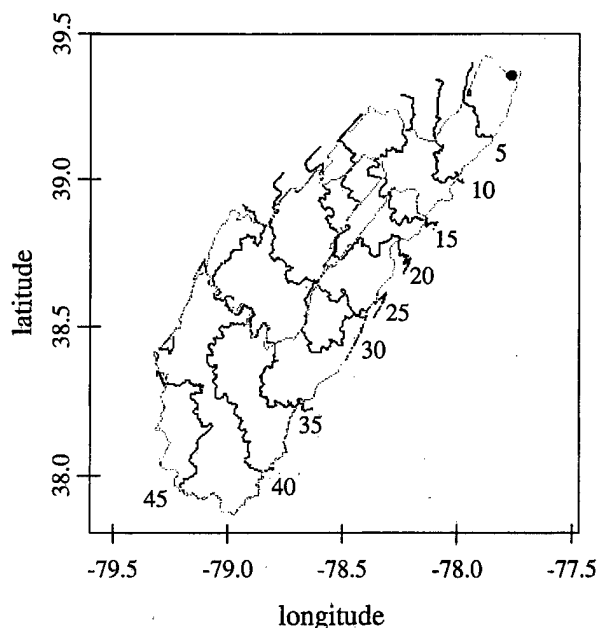


**Figure 9.** Contour map of travel time to the basin outlet based on GIUH analyses. The basin boundaries of the Shenandoah River at Millville, North Fork Shenandoah, and South Fork Shenandoah are shown in grey. The basin outlet at Millville is highlighted with a star.

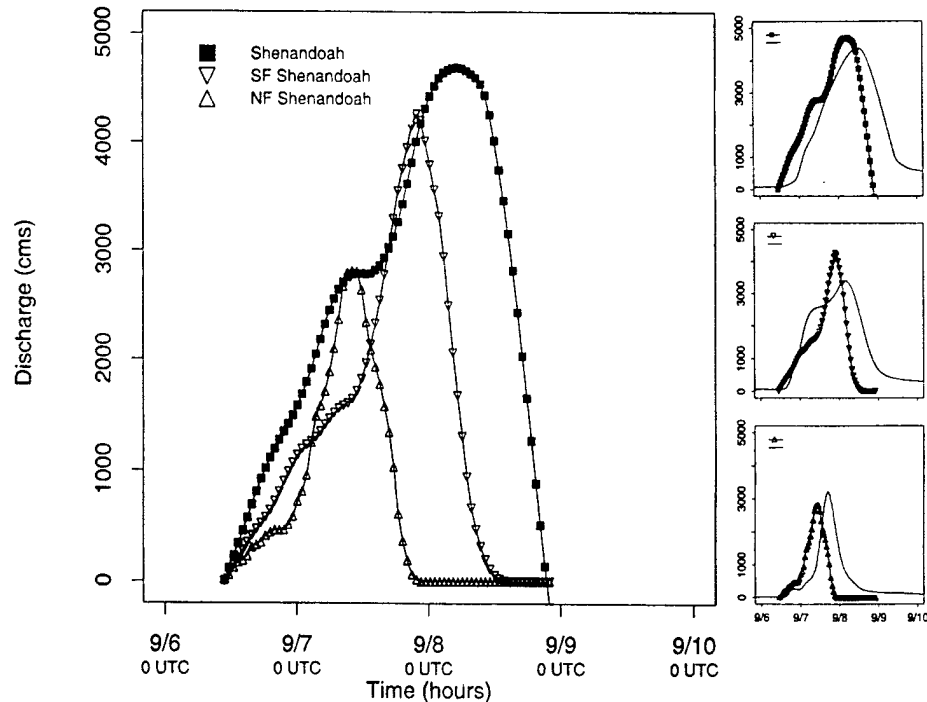


**Figure 10.** (left) GIUH representation of flood magnitude and timing of the Shenandoah River at Millville (solid square), South Fork Shenandoah River (inverted triangle), and the North Fork Shenandoah River (triangle), assuming uniform runoff over the catchment during a 10-hour period. (right) Differences between the actual streamflow response (depicted by solid lines) and the GIUH representation of response (depicted by symbols on lines) for (top) the Shenandoah River at Millville, (middle) SF Shenandoah River, and (bottom) NF Shenandoah River.

A for details). Rainfall forcing is based on the observed rainfall time series from the Toms Branch (Figure 3a) rain gage. Solution of Richards equation is obtained by a modified Picard procedure [Celia *et al.*, 1990] for time-varying rainfall. Van

Genuchten constitutive relationships are used with parameter values for a silt loam soil with a low ( $2.1 \text{ mm h}^{-1}$ ) and medium ( $6.8 \text{ mm h}^{-1}$ ) saturated hydraulic conductivity [Maidment, 1993; van Genuchten, 1980]. A silt loam soil was chosen due to

**Table 5.** Drainage Basin Area, Average Stream Slope, Aspect Ratio, Drainage Density, and Relief Ratio of Select Shenandoah Drainage Basins<sup>a</sup>

Basin	DA, km <sup>2</sup>	Stream Slope, m m <sup>-1</sup>	Aspect Ratio, m <sup>2</sup> m <sup>-2</sup>		Drainage Density, m km <sup>-2</sup>	Relief Ratio, m m <sup>-1</sup>
			A1	A2		
SF Shenandoah						
South River						
Dooms	386	0.030	0.44	0.86	810	0.0080
Harriston	549	0.031	0.42	0.69	752	0.0070
Middle River	971	0.009	0.54	0.85	395	0.0055
North River	982	0.040	0.57	0.94	488	0.0080
Lynnwood	2808	0.028	0.61	0.73	520	0.0078
Front Royal	4253	0.027	0.45	0.49	499	0.0042
North Fork Shenandoah						
Cootes	544	0.044	0.64	0.79	493	0.0164
Smith Creek	241	0.026	0.48	0.39	408	0.0065
Mount Jackson	1311	0.033	0.65	0.88	416	0.0092
Strasburg	1989	0.028	0.50	0.68	424	0.0064
Passage Creek	228	0.021	0.64	0.17	409	0.0084
Shenandoah						
Millville	7827	0.025	0.55	0.38	512	0.0029

<sup>a</sup>Stream slope is defined as the difference in elevation between the basin headwaters and stream outlet divided by channel length. Aspect ratio A1 is defined as  $A/(L1 \cdot L2)$  and A2 is defined as  $L1/L2$  where  $A$  is drainage basin area,  $L1$  is the length of the longest side of a rectangle enclosing the basin, and  $L2$  is the length of the shortest side of the rectangle [see Patton and Baker, 1976]. Drainage density is defined as total length of the channels divided by drainage basin area [Costa, 1987]. Relief ratio is defined as the difference between the average elevation of the drainage basin divide and the basin outlet divided by the basin length parallel to the main stream [Patton and Baker, 1976].



**Table 6.** Event Volume-to-Peak Ratio<sup>a</sup>

Basin	1936	1942	1972	1985	1996
South Fork Shenandoah					
South River Doods	NA	NA	NA	0.99	0.46
South River Harriston	1.06	0.63	0.87	0.90	0.42
Middle River	0.81	0.71	0.78	0.69	0.52
North River	0.51	0.49	0.97	0.43	0.59
Lynnwood	0.72	0.64	0.80	0.83	0.57
Front Royal	0.83	0.71	0.81	0.81	0.72
North Fork Shenandoah					
Cootes	0.60	0.68	1.12	0.87	0.55
Smith Creek	NA	NA	0.77	0.96	0.55
Mount Jackson	NA	NA	0.89	0.81	0.44
Strasburg	0.58	0.50	1.02	0.58	0.42
Passage Creek	0.43	0.57	0.98	1.00	0.34
Shenandoah					
Millville	0.74	0.68	0.85	0.80	0.75

<sup>a</sup>Standardized by the mean volume-to-peak ratio for a basin for key historical extreme flood events in the Shenandoah; NA, not available.

its relative abundance throughout the Shenandoah watershed. Water table depth and the assumption of a hydrostatic pressure distribution are used to specify a range of initial conditions. The water table depth is determined by solving the storage deficit function for a given moisture deficit.

Numerical simulation results summarizing the relative contributions of Hortonian overland flow (infiltration excess) and saturation overland flow (saturation excess) contributing to the total runoff over a range of antecedent moisture conditions (initial water table depth) are summarized in Figures 11a and 11b for the low- and medium-saturated hydraulic conductivity soils. In order to also depict the change in net infiltration with antecedent moisture conditions, the numerical results have been normalized by the total storm rainfall. The fraction of precipitation contributing to infiltration excess (shown by crosses), saturation excess (shown by circles) and infiltration (shown by pluses) thus sum to one. As the depth to water table increases, the fraction of total rainfall contributing to infiltration increases for both soils and total runoff decreases accordingly.

Numerical results derived for the low-saturated hydraulic conductivity soil (Figure 11a) show that due to elevated rainfall

rates early in the event, small amounts of infiltration excess runoff (around 1%) occur even when the initial water table depth is less than a meter from the surface. The amount of rainfall partitioned to infiltration excess runoff increases sharply between initial water table depths of 1.5 and 2.2 m while saturation excess runoff decreases sharply. For an initial depth of 1.8 m, runoff is equally distributed between infiltration excess and saturation excess runoff generating mechanisms. The sharp increase in the fraction of infiltration excess runoff with water table depth is a function of interaction between the rainfall time series and the available water storage capacity. When initial water table depths are greater than ~2.2 m, all runoff is partitioned to infiltration excess.

Numerical results derived for the medium saturated hydraulic conductivity soil (Figure 11b) are significantly different. Saturation excess generating mechanisms dominated runoff production for initial water table depths <2.0 m. Infiltration excess runoff occurred only when initial water table depths were >2.0 m; significant (>20%) partitioning of rainfall to infiltration excess did not occur until the initial water table depth was >2.4 m. At initial water table depths >2.6 m, however, more than 50% of the runoff was generated by infiltration

**Table 7.** Percent of Land Classified as Developed, Agricultural, and Forested in the Shenandoah Basins<sup>a</sup>

Basin	Land Use-Land Cover, %		
	Developed	Agriculture	Forested
South Fork Shenandoah			
South River			
Doods	5.9	30.2	62.2
Harriston	5.1	31.5	61.9
Middle River	3.5	55.5	40.2
North River	3.1	33.0	63.3
Lynnwood	3.5	43.1	52.4
Front Royal	3.2	37.8	57.9
North Fork Shenandoah			
Cootes	0.3	7.9	91.0
Smith Creek	4.8	51.2	43.1
Mount Jackson	1.9	37.2	60.1
Strasburg	2.5	37.1	59.5
Passage Creek	0.6	11.9	85.9
Shenandoah			
Shenandoah River at Millville	2.8	37.4	58.6

<sup>a</sup>Data are based on the EPA 30-m MRLC data.

**Table 8.** Regression Equations

Regression Equation	$R^2$
lag = $6.5 + 0.0055 \text{ area}$	0.89
lag = $11.6 + 0.0034 \text{ area} - 173.6 \text{ basin slope}$	0.90
lag = $11.7 + 0.0054 \text{ area} - 175.5 \text{ stream slope}$	0.90
lag = $9.1 + 0.0054 \text{ area} - 0.041\% \text{ forest}$	0.89
lag = $52.6 + 0.0053 \text{ area} - 68.6 \text{ A1} - 2.79\% \text{ developed}$	0.96
lag = $40.1 + 0.0053 \text{ area} - 0.021 \text{ drainage density} - 42.1 \text{ A1}$	0.94
lag = $40.1 + 0.0050 \text{ area} - 0.021 \text{ drainage density} - 42.1 \text{ A1} + 0.13\% \text{ forest}$	0.95
lag = $42.4 + 0.0054 \text{ area} - 0.042 \text{ drainage density} - 65.7 \text{ A1} + 0.184\% \text{ forest} + 0.15\% \text{ silt loam}$	0.97

excess mechanisms (equivalent to around 35% of the total rainfall). Results for larger values of saturated hydraulic conductivity result in progressively deeper initial water table depths before infiltration excess runoff becomes significant.

The numerical infiltration studies provide a context for interpreting the runoff processes that occurred throughout the Shenandoah River basin, given the distribution of soil hydraulic properties (Plate 8), rainfall (Figures 3a–3e and Table 4), and runoff (Figure 6b and Table 4). Rainfall rates were significantly larger than saturated hydraulic conductivity values throughout the basin (Figure 5 and Plate 8). The eastern margin of the Shenandoah basin is underlain by carbonate terrain and is characterized by thick soils with high storage capacity and some of the largest depths to bedrock (typically >1.3 m) observed throughout the Shenandoah. These characteristics, combined with relatively low initial soil moisture content, suggest that infiltration excess runoff may constitute a significant fraction of the runoff generated in these basins during Hurricane Fran. Infiltration excess runoff mechanisms likely contributed less to total runoff volumes in the western Shenandoah due to low storage capacity, high initial moisture contents, and shallow depth to bedrock. The potential importance of infiltration excess runoff generation during Hurricane Fran, particularly along the forested ridges of the South Fork Shenandoah, underscores the role rainfall intensity plays in controlling storm runoff volume and peak discharge (compare, for example, with *Hewlett et al.* [1977]).

## 5. Summary and Conclusions

There are eight principal observations from our work.

1. Hurricane Fran produced record flooding in the Shenandoah River watershed at basin scales ranging from 35 to 10,000 km<sup>2</sup>. The magnitude of flooding was comparable to that observed for other tropical storms producing extreme flooding at these scales in the central Appalachians, including Hurricane Juan (1985), Hurricane Agnes (1972), Hurricane Diane (1955), and the tropical storm of 1942.

2. Moist, upslope easterly flow sustained by the hurricane circulation resulted in orographically enhanced precipitation in the Shenandoah basin, with rainfall accumulation maxima (>350 mm) located near ridge tops. Rain gage accumulations were greater along the Blue Ridge (eastern boundary of the basin) than along Shenandoah Mountain (western boundary of the basin). Significantly lower accumulations (<200 mm) occurred in the Shenandoah Valley. Orographic enhancement of tropical storm precipitation plays a major role in determining the regional flood hydrology for the central Appalachian region.

3. Extreme rainfall from Hurricane Fran was produced by a combination of rain band convection, broader-scale stratiform precipitation and remnant eyewall convection. Peak rainfall rates in rain band convection approached 100 mm h<sup>-1</sup> at 15-min timescale. Hurricane Fran is distinguished from other flood-producing tropical storms in the central Appalachian region through the anomalously high magnitudes of rainfall rates.

**Table 9.** Percent of Soil Classified as Sandy Loam, Silt Loam, Loam, or Silty Clay Loam in the Shenandoah Basins<sup>a</sup>

Basin	Soil, %				Average $K_{sat}$ mm h <sup>-1</sup>
	Sandy Loam	Silt Loam	Loam	Silty Clay Loam	
South Fork Shenandoah					
South River					
Dooms	12.2	87.8	0.0	0.0	8.6
Harrison	14.6	85.4	0.0	0.0	9.0
Middle River	6.5	80.9	0.0	12.7	7.2
North River	40.9	51.3	0.0	7.9	12.6
Lynnwood	20.7	71.0	0.0	8.4	9.5
Front Royal	22.5	67.1	4.3	6.2	10.2
North Fork Shenandoah					
Coates	26.6	73.0	0.4	0.0	10.8
Smith Creek	27.4	44.6	0.0	28.0	9.6
Mount Jackson	18.7	65.1	0.2	16.0	8.9
Strasburg	21.6	64.5	0.11	13.78	9.4
Passage Creek	61.1	38.9	0.0	0.0	16.0
Shenandoah					
Shenandoah River at Millville	22.0	66.7	2.8	8.5	9.9

<sup>a</sup>Data are based on the CONUS 1-km data set.

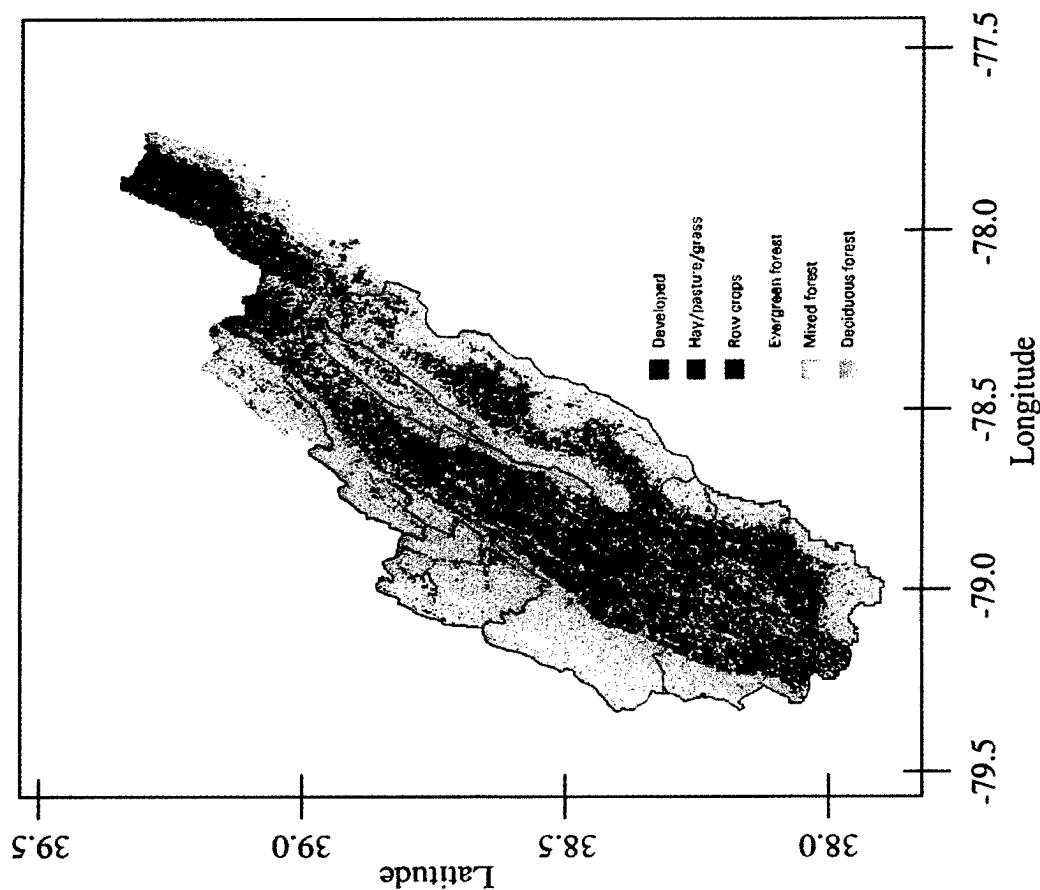


**Plate 7.** EPA multiresolution land characteristic (MRLC) 30-m land use-land cover map, derived from Landsat thematic mapper (TM) data, for the Shenandoah River basin. Basin boundaries are included as black lines, with basin outlet locations marked by black dots. The percentages of land use in three categories are given in Table 7 for the individual basins.

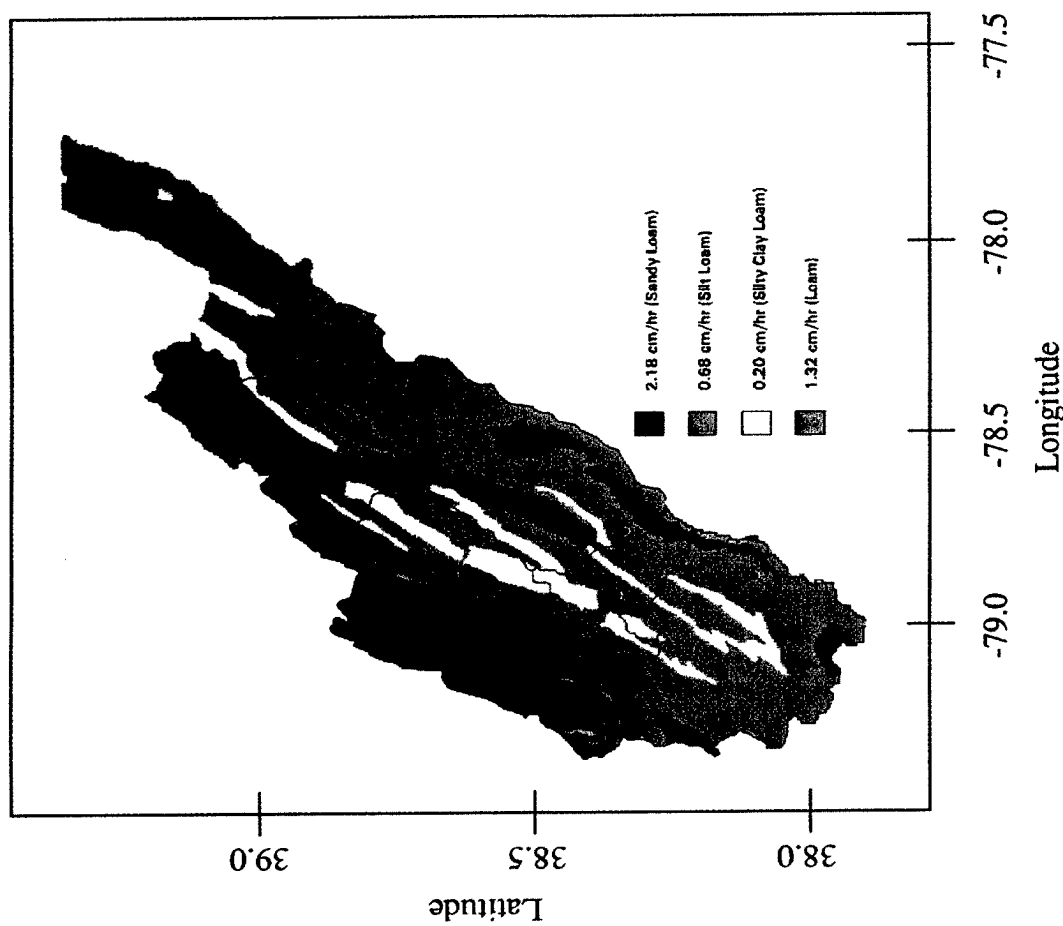


**Plate 8.** Soil distribution at a 1-km resolution, derived from the Pennsylvania State CONUS soils database, for the Shenandoah River basin. Basin boundaries are included as black lines, with basin outlet locations marked by red dots. Standard saturated hydraulic conductivity values have been assigned to the individual soil texture classifications (see text for details). Individual basin percentages are given in Table 9.

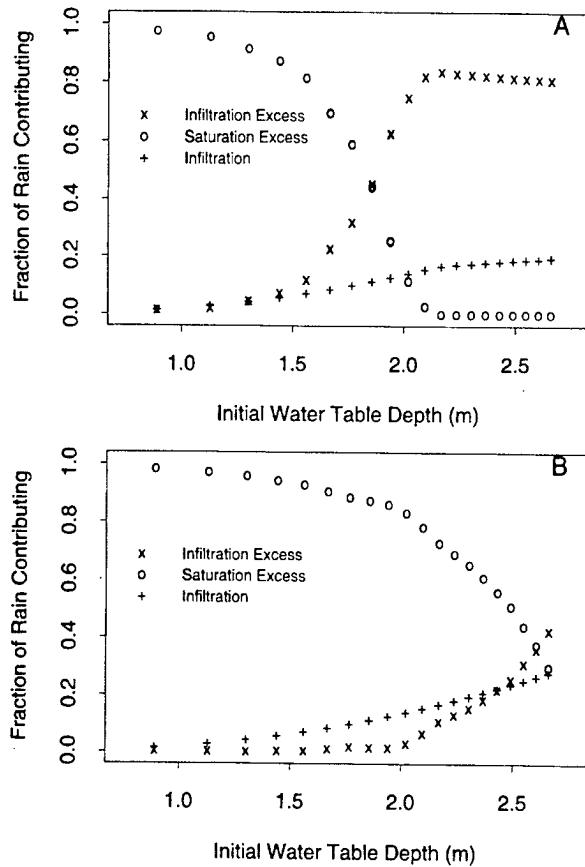


**Figure 11.** Numerical infiltration experiment results for (a) the low-saturated hydraulic conductivity soil and (b) the medium-saturated hydraulic conductivity soil. Experiments were based on the rainfall time series from the IFLOWS rain gage at Toms Branch and for initial water table depths ranging from <1 m to almost 3 m. The fraction of storm total rainfall contributing to storm total infiltration excess, saturation excess, and infiltration is shown (see text for details).

4. Hurricane Fran was also distinguished from other extreme flood-producing tropical storms through its rapid storm motion. Several elements of storm motion were important for flood response. The south-to-north motion of the tropical storm circulation amplified peak discharge at the outlet of the south-to-north flowing Shenandoah River. The rapid south-to-north motion of the principal rain band was especially important for runoff distribution in the South Fork Shenandoah River. The east-to-west motion and amplification of embedded rainband convection played a significant role in the spatial and temporal runoff distribution throughout the Shenandoah basin. Motion of remnant eyewall convection played a dominant role for flood response in the South River of the South Fork Shenandoah.

5. Antecedent soil moisture distribution appears to have played an important role in flood response. Larger unit discharges and runoff ratios in the western Shenandoah basin were likely related to the relatively higher initial moisture conditions. Spatial variability in soil moisture storage capacity was also an important aspect of the contrasting runoff production over the basin.

6. Numerical model experiments using Richards equation suggest that significant portions of the basin, including the for-

ested, high-elevation South Fork Shenandoah basin, experienced infiltration excess production. Infiltration excess runoff becomes more significant as the initial depth to the water table increases.

7. The principal forested regions of the Shenandoah River basin are concentrated in the high-elevation areas of the basin which received largest storm total accumulations. Any influences of forest cover on flood response, either through enhanced infiltration or increased roughness, were masked by the pronounced orographic amplification of rainfall accumulations.

## Appendix A

Infiltration analyses in section 4 are based on Richards equation of unsaturated zone flow in the form

$$\frac{\partial \theta}{\partial t} = \frac{\partial}{\partial z} [D(\theta)] \frac{\partial \theta}{\partial z} + \frac{\partial K}{\partial z}, \quad (\text{A1})$$

where

$$D(\theta) = K \frac{\partial h}{\partial \theta}. \quad (\text{A2})$$

A flux boundary condition is specified at the ground surface whenever the surface moisture content is less than saturation, i.e., for  $\theta(t, 0) < \theta_s$ . In this setting, the surface flux is equivalent to the rainfall rate  $R(t)$  (in  $\text{mm h}^{-1}$ )

$$q(t, 0) = R(t). \quad (\text{A3})$$

When the surface becomes saturated, expressed as  $\theta(t, 0) = \theta_s$ , then

$$h(t, 0) = 0. \quad (\text{A4})$$

The flux out of the soil column is assumed to be zero:

$$q(t, L) = 0. \quad (\text{A5})$$

The van Genuchten constitutive relationships are used to solve Richards equation. They are specified in terms of five parameters,  $\alpha$ ,  $n$ ,  $\theta_r$ ,  $\theta_s$ , and  $K_s$ . The constitutive relationships are expressed as

$$\Theta(t, z) = \frac{\theta(t, z) - \theta_r}{\theta_s - \theta_r}, \quad (\text{A6})$$

$$\Theta = \left[ \frac{1}{1 + (\alpha|h|)^n} \right]^{(n-1)/n}, \quad (\text{A7})$$

$$K(\theta) = K_s \Theta^{1/2} [1 - (1 - \Theta^{n/(n-1)})^{(n-1)/n}]^2, \quad (\text{A8})$$

$$D(\theta) = \frac{(1-m)K_s}{\alpha m(\theta_s - \theta_r)} \Theta^{1/2-1/m} [(1 - \Theta^{1/m})^m + (1 - \Theta^{1/m})^m - 2]. \quad (\text{A9})$$

Initial conditions are specified by a water table depth  $\omega_0$ , i.e.,  $W(0) = \omega_0$  and the assumption of a hydrostatic pressure distribution, i.e.,

$$h(z, 0) = z - \omega_0. \quad (\text{A10})$$

It follows from the constitutive relationship that

$$\theta(0, z) = \frac{\theta_s - \theta_r}{[1 + (\alpha[\omega_0 - z])^n]^{(n-1)/n}} + \theta_r, \quad (\text{A11})$$

for  $z \leq \omega_0$ .

The storage deficit function

$$S(t) = \int_0^{\infty} [\theta_s - \theta(t, z)] dz \quad (A12)$$

can be used to explicitly distinguish infiltration excess and saturation excess runoff. The infiltration rate  $I(t)$  is the time-varying Darcy flux at the surface:

$$I(t) = q(t, 0). \quad (A13)$$

The surface runoff rate is the difference between rainfall rate and infiltration rate:

$$\begin{aligned} Q(t) &= R(t) - I(t) & R(t) > I(t) \\ Q(t) &= 0 & R(t) \leq I(t). \end{aligned}$$

The saturation excess runoff rate  $Q_s(t)$  is the surface runoff that occurs when the storage deficit equals 0, i.e.,

$$\begin{aligned} Q_s(t) &= Q(t) & S(t) &= 0 \\ Q_s(t) &= 0 & S(t) &\geq 0. \end{aligned}$$

The infiltration excess runoff rate  $Q_i(t)$  is the surface runoff that occurs when the storage deficit is positive, i.e.,

$$\begin{aligned} Q_i(t) &= Q(t) & S(t) &> 0 \\ Q_i(t) &= 0 & S(t) &= 0. \end{aligned}$$

## Notation

- $t$  time (in hours),  $t \in [0, T]$ .
- $T$  total run time (in hours).
- $z$  depth from the surface (in mm, positive downward),  $z \in [0, L]$ .
- $L$  depth of zero-flow boundary (in mm).
- $\theta(t, z)$  moisture content at time  $t$  and depth  $z$ .
- $q(t, z)$  Darcy flux (in  $\text{mm h}^{-1}$ ) at time  $t$  and depth  $z$ .
- $h(t, z)$  pressure head (in mm) at time  $t$  and depth  $z$ .
- $W(t)$  water table depth at time  $t$  (in mm).
- $K(z, \theta)$  hydraulic conductivity at depth  $z$  for moisture content  $\theta$ .
- $D(z, \theta)$  soil water diffusivity at depth  $z$  for moisture content  $\theta$ .
- $K_s(z)$  saturated hydraulic conductivity at depth  $z$ .
- $\theta_r$  residual moisture content.
- $\theta_s$  saturated moisture content.
- $D(\theta)$  soil water diffusivity.
- $n$  exponent.
- $\alpha$  scale parameter.
- $S(t)$  storage deficit function (in mm).
- $I(t)$  infiltration rate (in  $\text{mm h}^{-1}$ ).
- $Q(t)$  excess rainfall (in  $\text{mm h}^{-1}$ ).
- $Q_s(t)$  saturation excess runoff (in  $\text{mm h}^{-1}$ ).
- $Q_i(t)$  infiltration excess runoff (in  $\text{mm h}^{-1}$ ).

**Acknowledgments.** This research was funded in part by the U.S. Army Research Office (grant DAAH04-95-1-0113), the National Science Foundation (grants EAR-9706259 and EAR-9528886), and NASA (grants NAG8-1521 and NAG5-7544). This support is gratefully acknowledged.

## References

Baeck, M. L., and J. A. Smith, Estimation of heavy rainfall by the WSR-88D, Weather and Forecasting, *Weather Forecasting*, 13, 416–436, 1998.

- Bailey, J. F., J. L. Patterson, and J. L. H. Paulhus, Hurricane Agnes rainfall and floods, June–July 1972, *U.S. Geol. Surv. Prof. Pap.*, 924, 403 pp., 1975.
- Beven, K., and P. Germann, Macropores and water flow in soils, *Water Resour. Res.*, 18(5), 1311–1325, 1982.
- Bosart, L. F., and F. H. Carr, A case study of excessive rainfall centered around Wellsville, New York, 20–21 June 1972, *Mon. Weather Rev.*, 106, 348–362, 1978.
- Celia, M. A., E. T. Bouloutas, and R. L. Zarba, A general mass-conservative numerical solution for the unsaturated flow equation, *Water Resour. Res.*, 26(7), 1483–1496, 1990.
- Ciolkosz, E. J., G. W. Petersen, R. L. Cunningham, and R. P. Matelski, Soils developed from colluvium in the ridge and valley area of Pennsylvania, *Soil Sci.*, 128(3), 153–162, 1979.
- Clark, G. M., R. B. Jacobson, J. S. Kite, and R. C. Linton, Storm-induced catastrophic flooding in Virginia and West Virginia, November, 1985 in *Catastrophic Flooding, Binghamton Symp. Geomorphol.*, vol. 18, edited by L. Mayer and D. Nash, pp. 355–377, Allen and Unwin, Concord, Mass., 1987.
- Costa, J. E., Response and recovery of a Piedmont watershed from tropical storm Agnes, June 1972, *Water Resour. Res.*, 10(1), 106–112, 1974.
- Costa, J. E., Hydraulics and basin morphometry of the largest flash floods in the continental United States, *J. Hydrol.*, 93, 313–338, 1987.
- Dunne, T., Effects of rainfall, vegetation and microtopography on infiltration and runoff, *Water Resour. Res.*, 27(9), 2271–2285, 1991.
- Eisenlohr, W. S., Jr., Floods of July 18, 1942 in north-central Pennsylvania, *U.S. Geol. Surv. Water Supply Pap.*, 1134-B, 100 pp., 1952.
- Engman, E. T., L. H. Parmele, and W. J. Gburek, Hydrologic impact of Tropical Storm Agnes, *J. Hydrol.*, 22, 179–193, 1974.
- Gupta, V. K., W. Waymire, and I. Rodriguez-Iturbe, On scales, gravity and network structures in basin runoff, in *Scale Problems in Hydrology*, edited by V. K. Gupta, I. Rodriguez-Iturbe, and E. F. Wood, pp. 159–184, D. Reidel, Norwell, Mass., 1986.
- Gupta, V. K., O. J. Mesa, and D. R. Dawdy, Multiscaling theory of flood peaks, *Water Resour. Res.*, 30(12), 3405–3422, 1994.
- Hack, J. T., Studies of longitudinal stream profiles in Virginia and Maryland, *U.S. Geol. Surv. Prof. Pap.*, 294-B, 97 pp., 1957.
- Hack, J. T., Geomorphology of the Shenandoah Valley, Virginia and West Virginia, *U.S. Geol. Surv. Prof. Pap.*, 347, 84 pp., 1965.
- Hack, J. T., and J. C. Goodlett, Geomorphology and forest ecology of a mountain region in the central Appalachians, *U.S. Geol. Surv. Prof. Pap.*, 347, 66 pp., 1960.
- Hershfield, D. M., Rainfall atlas of the United States, *Tech. Pap.*, 40, Weather Bur., Washington, D. C., 1961.
- Hewlett, J. D., J. C. Fortson, and G. B. Cunningham, The effect of rainfall intensity on storm flow and peak discharge from forest land, *Water Resour. Res.*, 13(2), 259–266, 1977.
- Hosking, J. R. M., L-moments: Analysis and estimation of distributions using linear combinations of order statistics, *J. R. Stat. Soc., Ser. B*, 52(2), 105–124, 1990.
- Jacobson, R., A. Miller, and J. Smith, The role of catastrophic geomorphic events in central Appalachian landscape evolution, *Geomorphology*, 2, 257–284, 1989.
- Loveland, T. R., and D. M. Shaw, Multi-Resolution land characterization: building collaborative partnerships, in *GAP Analysis: A Landscape Approach to Biodiversity Planning*, edited by J. M. Scott et al., pp. 83–90, Am. Soc. for Photogram. and Remote Sens., Bethesda, Md., 1996.
- Maidment, D. R. (Ed.), *Handbook of Hydrology*, McGraw-Hill, New York, 1993.
- Mayfield, M., Preliminary report: Hurricane Fran 23 August–8 September, *Natl. Hurricane Cent.*, Miami, Fla., 1996.
- Miller, A., Flood Hydrology and geomorphic effectiveness in the central Appalachians, *Earth Surf. Processes*, 15, 119–134, 1990.
- Miller, D. A., and R. A. White, Conterminous United States multi-layer soil characteristics data set for regional climate and hydrology modeling, *Earth Interact.*, 2, 1998. (Available on-line at <http://EarthInteractions.org>)
- Patton, P. C., and V. R. Baker, Morphometry and floods in small drainage basins subject to diverse hydrogeomorphic controls, *Water Resour. Res.*, 12(5), 941–952, 1976.
- Pearce, A. J., M. K. Stewart, and M. G. Sklash, Storm runoff generation in humid headwater catchments, 1, Where does the water come from?, *Water Resour. Res.*, 22(8), 1263–1272, 1986.
- Perica, S., and E. Foufoula-Georgiou, Linkage of scaling and thermo-

- dynamic parameters of rainfall: Results from midlatitude mesoscale convective systems, *J. Geophys. Res.*, 101(D3), 7431-7448, 1996.
- Potomac Basin Reporter*, Potomac summer a wash: September brings another deluge, 52(4), July/Aug. 1996.
- Potter, K. W., Hydrological impacts of changing land management practices in a moderate-sized agricultural catchment, *Water Resour. Res.*, 27(5), 845-855, 1991.
- Robinson, J. S., and M. Sivapalan, An investigation into the physical causes of scaling and heterogeneity of regional flood frequency, *Water Resour. Res.*, 33(5), 1045-1059, 1997.
- Rodriguez-Iturbe, I., and A. Rinaldo, *Fractal River Basins: Chance and Self-Organization*, Cambridge Univ. Press, New York, 1997.
- Schwarz, F. K., The unprecedented rains associated with the remnants of Hurricane Camille, *Mon. Weather Rev.*, 98(11), 851-859, 1970.
- Smith, J. A., Representation of basin scale in flood peak distributions, *Water Resour. Res.*, 28(11), 2993-2999, 1992.
- Smith, J. A., D. P. Sheer, and J. C. Schaake Jr., The use of hydrometeorological data in drought management: Potomac River basin case study, paper presented at International Symposium on Hydrometeorology, Am. Water Resour. Assoc., Denver, Colo., June 1982.
- Smith, J. A., M. L. Baeck, M. Steiner, and A. J. Miller, Catastrophic rainfall from an upslope thunderstorm in the Central Appalachians: The Rapidan Storm of June 27, 1995, *Water Resour. Res.*, 32(10), 3099-3113, 1996.
- Smith, J. A., M. L. Baeck, J. L. Morrison, and P. Sturdevant Rees, Catastrophic rainfall and flooding in Texas, *J. Hydrometeorol.*, 1(1), 5-25, 2000.
- Swank, W. T., and D. A. Crossley Jr., *Forest Hydrology and Ecology at Coweeta*, Springer-Verlag, New York, 1988.
- van Genuchten, M. T., A closed-form equation for predicting the hydraulic conductivity of unsaturated soils, *Soil Sci. Soc. Am. J.*, 44, 892-898, 1980.
- White, E. L., Role of carbonate rocks in modifying flood flow behavior, *Water Resour. Bull.*, 12(2), 351-370, 1976.
- White, E. L., Sustained flow in small Appalachian watersheds underlain by carbonate rocks, *J. Hydrol.*, 32, 71-86, 1977.
- Wood, E. F., M. Sivapalan, and K. Beven, Similarity and scale in catchment storm response, *Rev. Geophys.*, 28(1), 1-18, 1990.
- Zon, R., Forests and water in the light of scientific investigation, U.S. Dep. of Agric., For. Serv., Washington, D. C., 1927.
- M. L. Baeck and J. A. Smith, Department of Civil and Environmental Engineering, Princeton University, Princeton, NJ 08544.
- J. Morrison, Department of Operations Research and Financial Engineering, Princeton University, Princeton, NJ 08544.
- P. Sturdevant-Rees, Department of Civil and Environmental Engineering, University of Massachusetts, Amherst, MA 01003. (rees@ecs.umass.edu)

(Received January 3, 2000; revised September 15, 2000; accepted September 26, 2000.)